ASME
SETTING THE STANDARD

Transactions of the ASME, Journal of Applied Mechanics (ISSN 0021-8936) is published bimonthly (Jan., Mar., May, July, Sept., Nov.) by The American Society of Mechanical Engineers, Three Park Avenue, New York, NY 10016. Periodicals postage paid at New York, NY and additional mailing offices. POSTMASTER: Send address changes to Transactions of the ASME, Journal of Applied Mechanics, c/o THE AMERICAN SOCIETY OF MECHANICAL ENGINEERS, 22 Law Drive, Box 2300, Fairfield, NJ 07007-2300. **CHANGES OF ADDRESS** must be received at Society headquarters seven weeks before they are to be effective. Please send old label and new address. **STATEMENT from By-Laws.** The Society shall not be responsible for statements or opinions advanced in papers or printed in its publications (B7.1, Para. 3).

Journal of Applied Mechanics

Published Bimonthly by ASME

VOLUME 73 • NUMBER 6 • NOVEMBER 2006

Special Issue on Computational Mechanics

GUEST EDITORIAL

TECHNICAL PAPERS

(Contents continued on inside back cover)

This journal is printed on acid-free paper, which exceeds the ANSI Z39.48-1992 specification for permanence of paper and library materials. ♾™
♻ 85% recycled content, including 10% post-consumer fibers.

Journal of Applied Mechanics Volume 73, Number 6 NOVEMBER 2006

The ASME Journal of Applied Mechanics is abstracted and indexed in the following:

Alloys Index, Aluminum Industry Abstracts, Applied Science & Technology Index, Ceramic Abstracts, Chemical Abstracts, Civil Engineering Abstracts, Compendex (The electronic equivalent of Engineering Index), Computer & Information Systems Abstracts, Corrosion Abstracts, Current Contents, EEA (Earthquake Engineering Abstracts Database), Electronics & Communications Abstracts Journal, Engineered Materials Abstracts, Engineering Index, Environmental Engineering Abstracts, Environmental Science and Pollution Management, Fluidex, Fuel & Energy Abstracts, GeoRef, Geotechnical Abstracts, INSPEC, International Aerospace Abstracts, Journal of Ferrocement, Materials Science Citation Index, Mechanical Engineering Abstracts, METADEX (The electronic equivalent of Metals Abstracts and Alloys Index), Metals Abstracts, Nonferrous Metals Alert, Polymers Ceramics Composites Alert, Referativnyi Zhurnal, Science Citation Index, SciSearch (Electronic equivalent of Science Citation Index), Shock and Vibration Digest, Solid State and Superconductivity Abstracts, Steels Alert, Zentralblatt MATH

Journal of Applied Mechanics

Guest Editorial

This special issue of the *Journal of Applied Mechanics* contains 19 articles originally presented at ENIEF 2004, the XIV Congress on Numerical Methods and Their Applications, held in San Carlos de Bariloche, Argentina, on November 8–11, 2004. The first Congress in this series was held in 1983. Participation has grown consistently since then, with the 14th Congress attracting over 300 contributing participants—mainly from North and South America and Europe.

Some selected contributions to ENIEF 2004 were expanded and improved by their authors for consideration for this special issue. These submissions were then reviewed by the Guest Editors, and some were then sent out for external reviews. The usual ASME rules governing the selection of journal articles were applied throughout. The outcome of the review process is the 19 articles appearing in this issue.

The topics covered in this issue fairly represent the areas covered by the Association of Computational Mechanics of Argentina. We feel that they will also be of interest to the applied mechanics community at large.

There are nine articles from the field of solid mechanics. They deal with fiber-reinforced composites, fracture, finite deformation, localization, solid mechanics, and plate tectonics.

There are seven articles from the field of fluid mechanics. They deal with velocity-vorticity numerical formulations, prediction of stability boundaries, density currents, internal combustion, and free-surface flows.

The three remaining articles address the simulation of solidification and heat treatment of metals, and fluid-structure interactions.

It is our hope that the readers of the *Journal of Applied Mechanics* will find the width and depth of the coverage in this special issue of interest. We are indebted to the numerous anonymous reviewers who participated in the editorial process: Their critical but helpful reviews greatly aided the authors and the Guest Editors in maintaining the high standards expected in ASME journal publications. We are also grateful to the Editor of the *Journal of Applied Mechanics* for entertaining the proposal of this special issue.

Gustavo Buscaglia
Bassam A. Younis

Ricardo Daniel Ambrosini[1]
Professor
National University of Cuyo,
CONICET,
Los Franceses 1537,
5600 San Rafael, Mendoza,
Argentina
e-mail: dambrosini@uncu.edu.ar

Bibiana María Luccioni
Associate Professor
Structures Institute,
National University of Tucumán,
CONICET,
J.B. Terán 375,
Yerba Buena, Tucumán,
Argentina
e-mail: bluccioni@herrera.unt.edu.ar

Craters Produced by Explosions on the Soil Surface

Explosives are commonly used in terrorist attacks and the craters formed by blast waves can be used as a diagnostic tool. For example, the focus of the explosion and the mass of the explosive used in the attack can be deduced by examining the location, geometry, and dimensions of the crater. However, studies about craters produced by explosions on or above ground level, which would be the case when the explosive charge is situated in a vehicle, are rarely found in the open technical literature. In this paper, a numerical study on craters formed by explosive loads located on the soil surface is presented. The soil parameters used in the numerical model, as well as the analysis procedure, were validated against experimental observations of the crater diameters. Results of numerical tests performed with different amounts of explosive on the soil surface are presented. Moreover, the effect of elevation of the center of energy release of explosive loads located on the soil surface is analyzed and discussed. Simple predictive equations for the crater diameter are presented. [DOI: 10.1115/1.2173283]

1 Introduction

Blasting loads have come to be forefront of attention in recent years due to a number of accidental and intentional events that affected important structures all over the world, clearly indicating that this issue is important for purposes of structural design and reliability analysis. In consequence, extensive research activities in the field of blast loads have taken place in the last few decades.

Dynamic loads due to explosions result in strain rates of the order of 10^{-1} to 10^{3} s^{-1} which imply short time dynamic behavior of the materials involved, characterized mainly by a great overstrength and increased stiffness, in comparison with normal, static properties. In the case of soils, the response and the mechanism of crater formation are particularly complex due to the usual anisotropy and nonlinear nature of the material, and to the variability of mechanical properties and coexistence of the three phases: solid, liquid, and gaseous. Generally, simplifying assumptions must be made in order to solve specific problems. Until now, most practical problems have been solved through empirical approaches. Years of industrial and military experience have been condensed in charts or equations [1,2]. These are useful tools, for example, to establish the explosive weight to yield a perforation of certain dimensions or to estimate the type and amount of explosive used in a terrorist attack, from the damage registered. Most research is related to underground explosions and only a few papers are concerned with explosions at ground level. Studies about craters produced by explosions above ground level, which would be the case when the explosive charge is situated in a vehicle, are rarely found in the open technical literature. Some reports are classified and access is limited to government agencies.

Most of the information about explosively formed craters found in the literature is based on experimental data. Numerical studies were scarce until recently.

However, with the rapid development of computer hardware over the last years, it has become possible to make detailed numerical simulations of explosive events in personal computers, significantly increasing the availability of these methods. New developments in integrated computer hydrocodes complete the tools necessary to carry out the numerical analysis successfully. Nevertheless, it is important to be aware that both these models and analysis procedures still need experimental validation.

The main objective of this paper is to propose a simple relationship between the mass and location of the explosive used and the diameter of the generated crater, which is sometimes an easy-to-measure parameter. A numerical study related to craters produced by explosive charges located on the soil surface is presented in this paper. The analysis is performed with a hydrocode and material models and analysis procedures are validated with experimental results. Additionally, the crater diameters for explosive charges of up to 500 kg of TNT situated on the ground at the ground level are obtained. The effect of elevation of the center of energy release of explosive loads located on the soil surface is analyzed and discussed. All the results are compared with empirical equations used nowadays for the prediction of crater dimensions and new simple equations are proposed.

2 Theory and Previous Results

2.1 Crater Formation. A crater produced by an explosive charge situated on or above the ground level is schematized in Fig. 1. The crater dimensions defined by Kinney and Graham [3] are used in this paper (Fig. 1): D is the apparent crater diameter, D_r is the actual crater diameter, and H_2 is the apparent depth of the crater. The depth of the crater created by an explosion ordinarily is about one-quarter of the diameter of the crater, but this ratio depends on the type of soil involved. The diameter of the crater produced by an explosion also depends on the relative location of the explosive charge from the ground level. Thus, explosions above surface level may not create any crater at all [3].

Tests of crater formation are appropriate tools to study the blast phenomena, the behavior and destructive power of different explosives, and the response of soils and rocks under this type of load [4]. The mechanism of crater formation is complex and it is related to the dynamic physical properties of air, soil, and soil-air interface. Even very carefully performed cratering tests give deviations in the dimensions measured of the order of 10%, while differences of as much as 30% to 40% are common [5].

A cavity is always formed when a confined explosion is produced in a mass of soil. If the explosion is close to the surface, a crater is formed and a complex interaction between gravity effects, soil strength, and transient load conditions takes place. The most important variables in defining the crater shape and size are the mass W of the explosive and the depth of the detonation be-

[1]To whom correspondence should be addressed.

Contributed by the Applied Mechanics Division of ASME for publication in the JOURNAL OF APPLIED MECHANICS. Manuscript received May 23, 2005; final manuscript received December 20, 2005. Review conducted by G. C. Buscaglia. Discussion on the paper should be addressed to the Editor, Prof. Robert M. McMeeking, Journal of Applied Mechanics, Department of Mechanical and Environmental Engineering, University of California – Santa Barbara, Santa Barbara, CA 93106-5070, and will be accepted until four months after final publication of the paper itself in the ASME JOURNAL OF APPLIED MECHANICS.

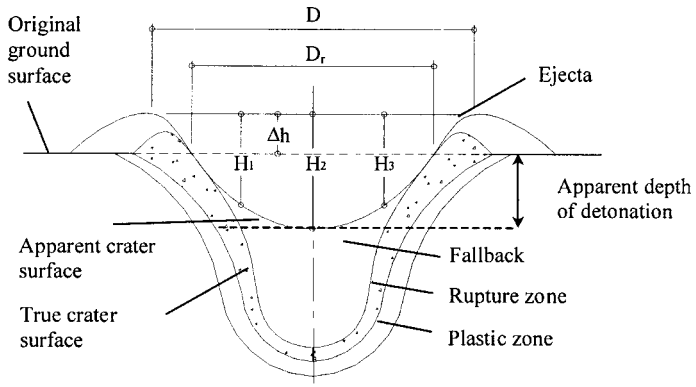

D: Apparent crater diameter
D_r: Crater diameter

Fig. 1 Definitions of the crater dimensions

neath the air/soil interface d. When $d<0$, the explosive is detonated over the air/soil interface, $d=0$ when the detonation occurs in the air/soil interface, and $d>0$ when the explosive is detonated beneath the soil surface. For $d>0$, the crater mechanism is altered by gravitational effects. When the depth of the detonation increases, larger amounts of subsoil must be expelled by the explosion. Thus, the crater radius and the depth of the crater increase when d increases, until a certain limit value, from which they rapidly decrease [5].

Studies concerned with the characteristics of craters caused by explosions usually resort to dimensional analysis and statistics. The scaling law establishes that any linear dimension "L" of the crater can be expressed as a constant multiplied by W^{α} divided by the distance of the charge from the ground, where W represents the equivalent TNT mass of explosive and α is a coefficient that is dependent on whether the gravitational effects can be neglected or not. When the gravitational effects can be neglected the cubic root law is applicable ($\alpha=0.33$) and in the other cases the functional dependence can be quite complex.

Baker et al. [6] present a dimensional study to model the crater formation phenomenon in the case of underground explosions. Six parameters are chosen to define the problem: the explosive mass W, the depth of the explosive charge d, the apparent crater radius R, the soil density ρ, and two strength parameters to define the soil properties: one with the dimensions of stress σ, related to soil strength, and the other with the dimensions of a force divided by a cubic length $(\mathrm{Nm}^{-3})K$, which takes into account gravitational effects.

After a dimensional analysis and many empirical observations, the following functional relation may be obtained [6].

$$\frac{R}{d}=f\left(\frac{W^{7/24}}{\sigma^{1/6}K^{1/8}d}\right) \tag{1}$$

If R/d (scaled radius of the crater) is plotted as a function of $W^{7/24}/d$ [6], it can be seen that this relation is close to experimental results and can be approximately simplified by two straight lines, one with a moderate slope for $W^{7/24}/d>0.3$ and one steeper for $W^{7/24}/d<0.3$. For $W^{7/24}/d<0.3$, the scaled radius of the crater is sensitive to small changes in the independent parameter and, due to this fact, the independent parameter or the scaled radius may exhibit great variability. Experimental conditions are better controlled for $W^{7/24}/d>0.3$.

It can be deduced [6] that the specific weight ρg is the best measure for K and that ρc^2 is the best measure for σ, where c is the seismic velocity in the soil. If experimental results for different types of soils are plotted in a R/d vs. $W^{7/24}/\rho^{7/24}c^{1/3}g^{1/8}d$ graph, it may be clearly seen that there is very little variability in the results.

The preceding paragraphs refer to underground explosions. There is less information about explosions at ground level. Statistical studies of about 200 accidental above-ground explosions of relatively large magnitude are presented by Kinney and Graham [3]. The results exhibit a variation coefficient in the crater diameter of about 30%. From these results, the following empirical equation for the crater diameter was proposed.

$$D(m)=0.8W\ (\mathrm{Kg})^{1/3} \tag{2}$$

Additional experimental evidence was obtained during the surface explosions performed by EMRTC (Energetic Materials Research Center of the Mineralogical and Technologic Institute of New Mexico). EMRTC conducted experimental determinations to explore alternative ways of controlling the blasting power. In this program, the explosion of 250 kg of TNT situated at ground level formed a 3.8 m diameter crater.

In connection with the morphological and structural types of the craters, Melosh [7] determine four different basic types: (a) bowl-shaped, (b) flat-floored with central uplift, (c) flat floored with a peak ring, and (d) flat floored with >2 asymmetric rings (multiring basins). One of the factors that determine the shape is the height of burst. On the other hand, numerical and independent research results presented by Iturrioz et al. [8] confirm preliminarily the formation of the same shapes of craters. Additionally, there are important contributions in the literature related to cratering studies, but many of them are about predicting *rock* damage, for example, works by Yang et al. [9], Liu and Katsabanis [10], and Wu et al. [11], and others are related with *buried* explosions, for example, works by Wang and Lu [12] and Zhou et al. [13].

2.2 Experimental Tests. In a previous paper, Ambrosini et al. [14] presented the results of a series of tests performed with different amounts of explosive at short distances above and below ground level, as well as on the soil surface. These results were used in the present paper to calibrate the soil parameters of the numerical model as well as to validate the analysis procedure. The description of the test will be summarized in this point.

The tests were performed in a large flat region, without rock formations, normally used for agriculture. Two exploratory drillings and two test pits were used to determine the mechanical properties of the soil. The exploratory holes were drilled to depths of 2 and 5 m, respectively, with standard penetration tests (SPTs) performed at 1 m intervals. The test pits were dug to a depth of

Table 1 Soil properties of experimental tests—drilling S-1. WD: wet density; DD: dry density; *w*: moisture content; T200: percentage that passes through sieve 200; LL: liquid limit; PI: plastic index; Clas. /UCS: classification according to UCS; (1) 0 to 0.70 m: Brown clayey silt with organic matter; (2) 0.70 to 5.0 m: Reddish brown clayey silt of low plasticity, classification CL, very dry

Depth (m)	Free water level	Type of soil	SPT tests Depth (m)	SPT tests *N*	WD (t/m^3)	DD (t/m^3)	*w*	T200	LL (%)	PI (%)	Clas. /UCS
0.7		(1)	0.5–1.0	6	1.25	1.14	9.6	87	28.1	12.3	CL
1.0	without free water surface		1.5–2.0	12	1.43	1.27	12.7	91	27.9	8.6	CL
2.0											
3.0		(2)					19.3	95	31.0	10.4	CL
4.0											
5.0					End of the drilling						

2 m in order to collect undisturbed soil samples for triaxial testing and for a more precise determination of the in situ density. Partial results of the soil tests are presented in Table 1. The soil profile was quite uniform in the entire 40×50 m^2, testing area, being characterized by:

1) 0 to 0.70 m Brown clayey silt with organic matter.
2) 0.70 to 5.0 m Reddish brown clayey silt of low plasticity, classification CL, very dry.

The crater tests were performed in a selected 40×50 m^2 area. A grid with 10 m spacing was used to locate the explosive charges at its nodes, as shown in Fig. 2. Each row of the grid corresponded to loads of the same magnitude. Charges equivalent to 1, 2, 4, 7, and 10 kg of TNT were located on the five rows. All the charges were spherical. In the first two columns indicated as "A" in Fig. 2,

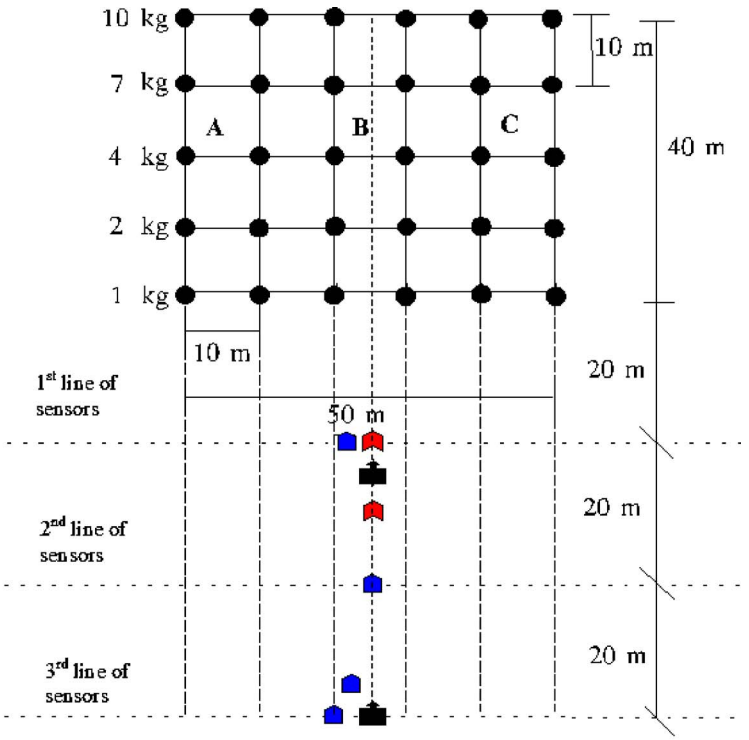

Fig. 2 Loads and measurement equipment locations

Fig. 3 Superficial explosion crater obtained in a test

the explosives were situated tangential to the surface. In the following columns designated as "B" in Fig. 2, the explosives were located 0.5 m above ground level. Finally, in the last two columns indicated as C1 and C2 in Fig. 2, the loads were situated 1 m above ground level and 1 m underground, respectively. The charges above ground level were located hanging on wood tripods. The explosive used in the tests was Gelamón 80, a NG based gelatinous explosive theoretically equivalent in mass to 80% TNT.

The following comments apply to the craters size measurement procedure:

a. The apparent crater diameter D (Fig. 1) was measured in all cases according to the definition given by Kinney and Graham [3].
b. Three measurements of the crater diameter and three of the crater depth were performed (Fig. 1).
c. In general, the craters produced by explosives situated at ground level presented a small mound in the center formed by the loose soil that fell down on the site after the explosion.
d. The shape of most of the craters was flat-floored with central uplift.

As illustration, the crater due to a surface explosion is shown in Fig. 3. The results about the dimensions of the craters are presented in Ambrosini et al. [14].

3 Numerical Model

3.1 Introduction and Numerical Tool. Computer codes normally referred as "hydrocodes" encompass several different numerical techniques in order to solve a wide variety of nonlinear problems in solid, fluid, and gas dynamics. The phenomena to be studied with such a program can be characterized as highly time dependent with both geometric nonlinearities (e.g., large strains and deformations) and material nonlinearities (e.g., plasticity, failure, strain hardening and softening, and multiphase equations of state). Different numerical tools are used in some papers in order to solve similar problems of crater determination, for example, ABAQUS [9], AUTODYN [11,12], SALE2D [15,16], and CTH [17].

In this paper, the program AUTODYN-2D [18], which is a "hydrocode" that uses finite difference, finite volume, and finite element techniques to solve a wide variety of nonlinear problems in solid, fluid, and gas dynamics, is used. The various numerical processors available in AUTODYN generally use a coupled finite difference/finite volume approach similar to that described by Cowler and Hancock [19]. The first-order Euler approach scheme is based upon the method developed by Hancock [20].

While finite element codes are usually based on the equilibrium condition, the hydrocode utilizes the differential equations governing unsteady material dynamic motion: the local conservation of mass, momentum, and energy. In order to obtain a complete solution, in addition to appropriate initial and boundary conditions, it is necessary to define a further relation between the flow variables. This can be found from a material model, which relates stress to deformation and internal energy (or temperature). In most cases, the stress tensor may be separated into a uniform hydrostatic pressure (all three normal stresses equal) and a stress deviatoric tensor associated with the resistance of the material to shear distortion.

The relation between the hydrostatic pressure, the local density (or specific volume), and local specific energy (or temperature) is known as an equation of state. Since solids are able to withstand a certain amount of tensile stress, it is necessary to consider extending the equations of state into limited regions of negative values of the pressure (tension). However, since the analytic forms derived for ranges of positive pressure may not be valid for extrapolation into the negative regions special attention should be paid in using some forms of equation of state. The *hydrodynamic tensile limit*, sometimes referred to as $p_{\min}$, is the minimum pressure at which the material can sustain continuous expansion. If the material pressure drops below this limit in a cell, it is assumed that the material will fracture or in some way lose its uniform and continuous ability to sustain a tensile pressure. This would then form the lower limit of the analytic equation of state. Regardless of the definition of a value of $p_{\min}$, it may be necessary to provide a different analytic form for negative pressure values from that used for positive values (but taking care to ensure continuity of function and derivatives at $p=0$).

While there are many problems that can be calculated using a hydrodynamic equation of state, there are many applications where material strength effects (i.e., its resistance to shearing forces) cannot be ignored and indeed may even dominate. If the material is solid and has finite shear strength, then, in addition to the calculation of the hydrostatic pressure, it is necessary to define relations between shear stress and strain. The methodology followed in this paper is that first one formulated by Wilkins [21] to extend conventional numerical hydrodynamic codes to include the effects of material strength and resistance to shear distortion.

A relation to define the transition between elastic and plastic strain, both in compression and release, and a relation to define the onset of fracture are also required. The yield criterion governing the transition from elastic to plastic behavior may involve only constant yield strength, or this strength may itself be a function of the degree of strain (work hardening), the rate of strain, and/or the temperature of the material (energy dependency).

Real materials are not able to withstand tensile stresses that exceed the material local tensile strength. The computation of the dynamic motion of materials assuming that they always remain continuous, even if the predicted local stresses reach very large negative values, will lead to unphysical solutions. For this reason the model has to be constructed to recognize when tensile limits are reached, to modify the computation to deal with this, and to describe the properties of the material after this formulation has been applied.

3.2 Numerical Mesh. A Euler formulation is used to model both air and soil in this paper. The Euler solver uses a fixed numerical mesh where the physical material flows through the mesh. Free surfaces and material interfaces can move through the fixed Euler mesh. Because the mesh is fixed, large material deformations are easily handled. Limiting numerical diffusion requires complex computations to accurately maintain material interfaces. AUTODYN is able to model the strength and failure of materials with the Euler solver.

In Euler processors, a control volume method is used to solve the equations that govern conservation of mass, momentum, and energy. The finite volume method is a method for representing and evaluating partial differential equations as algebraic equations. Similar to the finite difference method, values are calculated at discrete places on a meshed geometry. "Finite volume" refers to the small volume surrounding each node point on a mesh. In the finite volume method, volume integrals in a partial differential

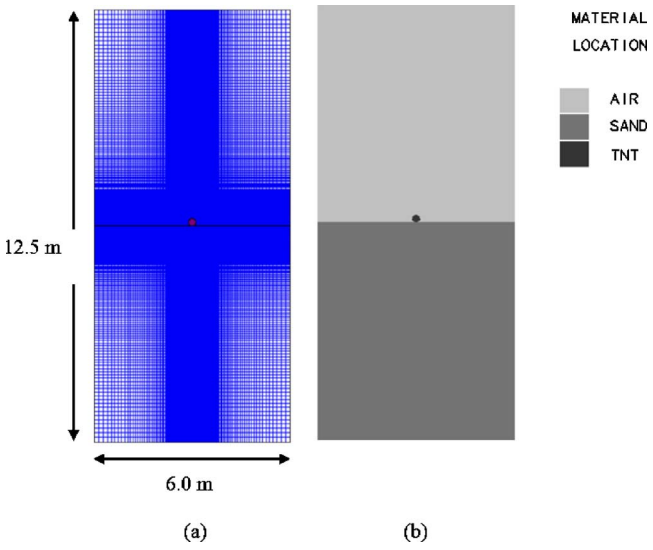

Fig. 4 Numerical model for explosives charges situated on the ground level: (*a*) mesh and (*b*) material location

equation that contain a divergence term are converted to surface integrals, using the divergence theorem. These terms are then evaluated as fluxes at the surfaces of each finite volume. Because the flux entering a given volume is identical to that leaving the adjacent volume, these methods are conservative. Another advantage of the finite volume method is that it is easily formulated to allow for unstructured meshes. The method is used in many computational fluid dynamics packages.

In AUTODYN the integral and discrete forms of the problem equations are expressed in conservation form to obtain accurate, stable solutions. Terms producing changes in conserved variables are divided into two groups: Lagrangian or transport (convective). A two-step numerical procedure is used to solve the finite-difference equations. In the first step, the Lagrange step, the Lagrangian forms of the equations are updated or advanced one time interval (time step). In the second step, the Euler step, the updated variables are mapped onto the Euler mesh. Multiple materials are handled through either a volume fraction technique or an interface technique originally developed by Youngs [22]. All variables are cell centered. This allows arbitrarily shaped control volumes to be formed more readily at the interface between Euler and Lagrange grids, facilitating the computation of fluid-structure or gas-structure interaction problems.

The use of symmetry conditions allows using a two-dimensional (2D) mesh considering axial symmetry. The number of cells required to produce accurate solutions is greatly reduced when compared with a full 3D model. The mesh used for explosive charges situated on the ground level is shown in Fig. 4(*a*). The mesh was filled with different materials: air, TNT, and soil, indicated in Fig. 4(*b*).

In the case of charges of 1 to 10 kg of TNT a 6×12.5 m^2 mesh was used, while a 10×12.5 m^2 mesh was used for charges of 50 kg of TNT or greater.

3.3 Materials Models. All the terms in the equations presented in this section could be in any congruent system units, but the SI units are recommended.

3.3.1 Air. The ideal gas equation of state was used for the air. This is one of the simplest forms of the equation of state for gases. In an ideal gas, the internal energy is a function of the temperature alone and, if the gas is polytropic the internal energy is simply proportional to temperature. It follows that the equation of state for a gas, which has uniform initial conditions, may be written as,

Table 2 Material properties for air

EOS: Ideal gas
$\gamma=1.4$
Reference density: $\rho_a=1.225\times10^{-3}$ g/cm^3
Reference temperature: $T_o=288.2$ K
Specific heat: $c_v=717.3$ J/kgK

$$p=(\gamma-1)\rho e \tag{3}$$

in which p is the hydrostatic pressure, ρ is the density, and e is the specific internal energy.

γ is the adiabatic exponent, it is a constant equal to $1+R/c_v$, where constant R may be taken to be the universal gas constant R_0 divided by the effective molecular weight of the particular gas and c_v is the specific heat at constant volume. The values of the constants used for air are presented in Table 2.

3.3.2 TNT. High explosives are chemical substances which, when subject to suitable stimuli, react chemically, very rapidly (in order of microseconds) releasing energy. In the hydrodynamic theory of detonation, this very rapid time interval is shrunk to zero and a detonation wave is assumed to be a discontinuity which propagates through the unreacted material, instantaneously liberating energy and transforming the explosive into detonating products. The normal Rankine-Hugoniot relations, expressing the conservation of mass, momentum, and energy across the discontinuity, may be used to relate the hydrodynamic variables across the reaction zone. The only difference between the Rankine-Hugoniot equations for a shock wave in a chemically inert material and those for a detonation wave is the inclusion of a chemical energy term in the energy conservation equation.

Since the 1939–1945 war, when there was naturally extensive study of the behavior of high explosives, there has been a continuous attempt to understand the detonation process and the performance of the detonation products, leading to considerable improvements in the equation of state of the products. The most comprehensive form of the equation of state developed over this period, the "Jones-Wilkins-Lee" (JWL) equation of state, is used in this paper.

$$p=C_1\left(1-\frac{\omega}{r_1v}\right)e^{-r_1v}+C_2\left(1-\frac{\omega}{r_2v}\right)e^{-r_2v}+\frac{\omega e}{v} \tag{4}$$

where $v=1/\rho$ is the specific volume, C_1, r_1, C_2, r_2, and ω (adiabatic constant) are constants, and their values have been determined from dynamic experiments and are available in the literature for many common explosives. The values used for TNT are presented in Table 3.

It can be shown (AUTODYN [18]) that at large expansion ratios the first and second terms on the right-hand side of Eq. (4) become negligible and hence the behavior of the explosive tends towards that of an ideal gas. Therefore, at large expansion ratios, where the explosive has expanded by a factor of approximately 10

Table 3 Material properties for TNT

EOS: JWL
Reference density $\rho=1.63$ g/cm^3
$C_1=3.7377\times10^8$ kPa
$C_2=3.73471\times10^6$ kPa
$r_1=4.15$
$r_2=0.9$
$\omega=0.35$
C-J detonation velocity: 6.93×10^3 m/s
C-J energy/unit volumen: 6×10^6 KJ/m^3
C-J pressure: 2.1×10^7 kPa

from its original volume, it is valid to switch the equation of state for a high explosive from JWL to ideal gas. In such a case the adiabatic exponent for the ideal gas, γ, is related to the adiabatic constant of the explosive, ω, by the relation $\gamma=\omega+1$. The reference density for the explosive can then be modified and the material compression will be reset. Potential numerical difficulties are therefore avoided.

An explosion may be initiated by various methods. However, whether an explosive is dropped, thermally irradiated, or shocked, either mechanically or from a shock from an initiator (of more sensitive explosive), initiation of an explosive always goes through a stage in which a shock wave is an important feature. The Lee-Tarver equation of state [23] was used to model both the detonation and expansion of TNT in conjunction with the JWL EOS to model the unreacted explosive.

3.3.3 Soil. A shock equation of state combined with an elastoplastic strength model based on Mohr Coulomb criterion and a hydro tensile limit were used for the soil.

A Mie-Gruneisen form of equation of state based on the shock Hugoniot was used (AUTODYN [18]). The Rankine-Hugoniot equations for the shock jump conditions can be regarded as defining a relation between any pair of the variables ρ, p, e, u_p (material velocity behind the shock), and U (shock velocity). In many dynamic experiments (AUTODYN [18]) it has been found that for most solids and many liquids over a wide range of pressure there is an empirical linear relationship between u_p and U.

$$U = c_o + s u_p \tag{5}$$

in which c_0 is the initial sound speed and s is a dimensionless parameter.

This is the case even up to shock velocities around twice the initial sound speed c_0 and shock pressures of order 100 Gpa (AUTODYN [18]). In this case the equation of state is:

$$p = p_H + \Gamma\rho(e - e_H) \text{ with } p_H = \frac{\rho_o c_o^{\,2}\mu(1+\mu)}{[1-(s-1)\mu]^2}; \tag{6}$$

$$e_H = \frac{1}{2}\frac{p_H}{\rho_o}\frac{\mu}{1+\mu}; \quad \mu = \frac{\rho}{\rho_o} - 1$$

where p is the hydrostatic pressure, ρ_0 is the initial density, e is the specific internal energy, and Γ is the Gruneisen gamma parameter and it is assumed that, $\Gamma_\rho=\Gamma_o\rho_o=$const.

An elastoplastic model with Mohr Coulomb yield criterion was used for the strength effects. This model is an attempt to reproduce the behavior of dry soil where the cohesion and compaction result in an increasing resistance to shear up to a limiting value of yield strength as the loading increases. This is modeled by a piecewise linear variation of yield stress with pressure. In tension (negative values of p) soils have little tensile strength and this is modeled by dropping the curve for $Y(p)$ rapidly to zero as p goes negative to give a realistic value for the limiting tensile strength.

A nonassociated flow rule (Prandtl-Reuss type) that avoids the problem of shear-induced dilatancy in soils was used. A constant hydrodynamic tensile limit was specified as failure criterion. All the material properties initially used for the soil model are presented in Table 4. However, a study about the variability of soil properties is presented in Sec. 4.4.

3.4 Boundary Transmit. In order to fulfil the radiation condition, a transmitting boundary was defined for air as well as soil subgrids external limits. The transmit boundary condition allows a stress wave to continue "through" the physical boundary of the subgrid without reflection. The size of the numerical mesh can be reduced by use of this boundary condition. The transmit boundary is only active for flow out of a grid. The transmit boundary is calculated as follows.

Table 4 Material properties for soil

EOS: Shock	Strength: Mohr Coulomb
Reference density $\rho=1.92$ g/cm^3	
Gruneisen gamma $\Gamma=0.11$	
$c_o=1.614\times10^3$ m/s	
$S=1.5$	
Shear modulus $G=2.0\times10^5$ kPa	
Pressure 1=0 kPa,	Yield stress 1=6.2×10^3 kPa
Pressure 2=1.1×10^4 kPa,	Yield stress 2=6.2×10^3 kPa
Pressure 3=1.0×10^8 kPa,	Yield stress 3=6.2×10^3 kPa
Hydro tensile limit $p_{\min}=-100$ kPa	

Let the normal velocity at the boundary be U_n, where U_n is positive for outflow. Then the boundary pressure (P) is computed as follows:

for $U_n > 0$

$$P = P_{\text{ref}} + (U_n - U_{\text{ref}})I \tag{7a}$$

for $U_n < 0$

$$P = P_{\text{ref}} \tag{7b}$$

in which P_{ref} and U_{ref} are the pressure and velocity of reference, respectively (material model properties) and I is the material impedance (density*soundspeed). If the impedance at the boundary is undefined, it is taken from values in adjacent cells.

4 Results and Discussion

The process of crater formation and crater dimension for explosive charges up to 500 kg of TNT situated on the ground level were analyzed with the procedure described.

4.1 Crater Formation and Wave Propagation. The process of crater formation for a spherical explosive load of 10 kg of TNT lying on the ground is illustrated in Fig. 5 where the soil, the explosive (TNT), and the air are shown. It must be pointed out that, at large expansion ratios, where the explosive has expanded by a factor of approximately 10 from its original volume, the equation of state for JWL was switched to ideal gas. For this reason, the air as well as the TNT are in an ideal gas state in Fig. 5.

It can be seen that the explosive expands its volume in the air quickly and starts to make the crater in the solid semispace (soil). It takes about 10 ms for the hole crater to be formed.

In Fig. 6, the final state of the crater is shown as well as a detail of the numerical grid used for calculations. The values of the craters diameters were measured on figures showing the final state of the crater like Fig. 6. Comparing the crater obtained from the numerical analysis (Fig. 6) with the theoretical crater (Fig. 1) and the real crater (Fig. 3) from a morphological point of view, it can be observed that the numerical crater has a semi spherical shape in contrast with the flat-floored with central uplift shape or flat-floored with a peak ring shape observed [7]. This fact may be attributed to the use of a Euler processor together with a continuum model, which is not able to simulate disintegration, to represent the soil. It is well known that soils are granular materials with low cohesion that are pulverized when exposed to close explosions. As a result, many soil particles are thrown into the air and then fall down, forming a crater with the shape shown in Figs. 1 and 3.

The morphological differences found should not be interpreted as a limitation of the numerical simulation. For this reason, only the diameter value is used in the numerical-experimental comparison and in the numerical predictions (Eqs. (9) and (10)).

Moreover, the wave propagation in the air and in the soil is

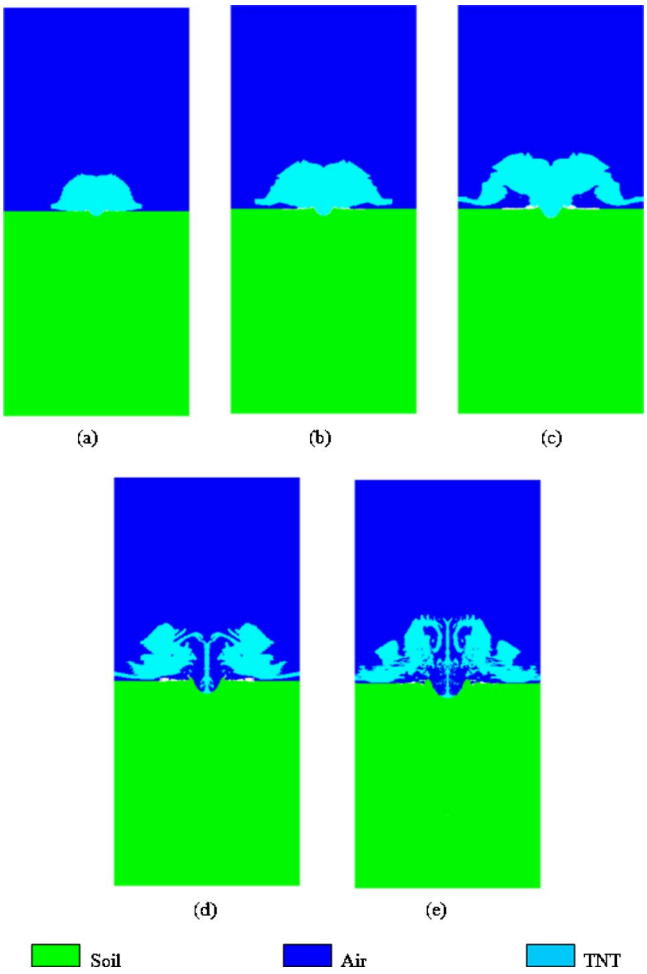

Fig. 5 Crater formation (10 kg TNT on the ground). (*a*) *t* =0.5 ms. (*b*) *t*=1.1 ms. (*c*) *t*=2.0 ms. (*d*) *t*=5.2 ms. (*e*) *t* =10.0 ms (AUTODYN-2D [18]). Model of 12.5×6.0 m^2.

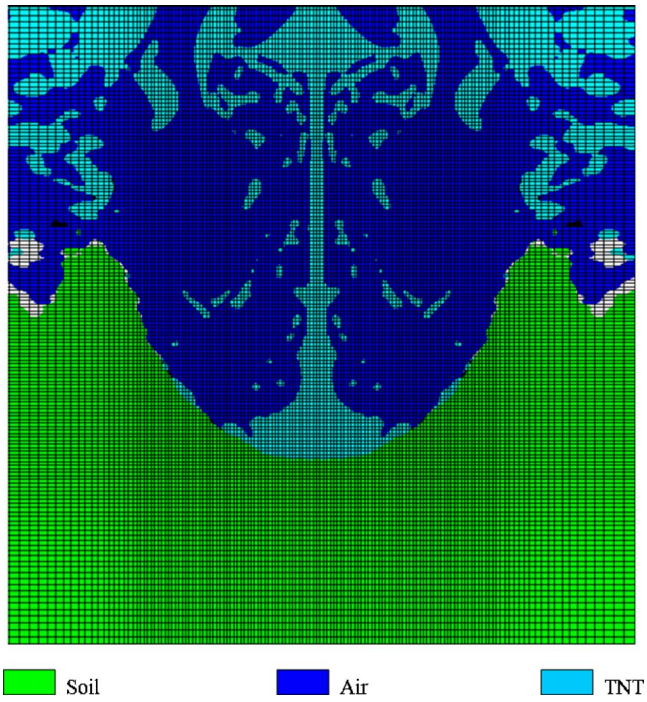

Fig. 6 Crater formation. Final state of the crater obtained numerically.

illustrated in Figs. 7(*a*) and 7(*b*). Finally, in Fig. 7(*c*), the Von Mises stresses developed in the soil are shown at 1.17 ms for the case of 50 kg of TNT with the energy release center at the ground level. Figure 7(*a*) shows that the shock wave propagates freely in the air with a hemispherical wavefront as expected. In Figs. 7(*b*) and 7(*c*) it may be observed that the wavefront is propagating into the soil and the transmitting boundary applied (see Sec. 3.4) is working properly because reflections of the waves in the boundary are not observed, except for a small reflection that appears in the bottom of the soil grid. This reflection has null effect on the crater formation because most of the TNT liberated energy has been consumed at this time.

The detonation produces a shock wave and very high initial gas pressures. (As an example, a value of the order of 35,000 atm is obtained for a 50 kg TNT half buried load.) This causes crushing, compaction, and plastic deformation of the subgrade immediately below and surrounding the detonation together with the formation of a near semispherical cavity. The high-pressure gases generate a shock wave across the semispherical surface and there is a sharp discontinuity in the physical state of the subgrade. On the shock wave front the subgrade is compressed due to the collapse of the pores. The subgrade then breaks into particles and behind the shock wave front the subgrade expands. As the shock wave moves outwards from the point of detonation the peak pressure falls. For pressures above the dynamic crushing strength of the subgrade, work on the subgrade appears in the form of crushing, heating, and physical displacement. In regions outside the limit of crushing, the shock wave produces permanent deformation by plastic flow until the peak pressure in the shock wave front has decreased to a value equal to the plastic limit for the subgrade.

4.2 Comparison With Experimental Results. In order to validate not only the material models and material properties but also the analysis procedures, a comparison with experimental results was first performed. The results of a series of tests performed with different amounts of explosive from 1 to 10 kg of TNT on the soil surface [14] were used to calibrate the materials parameters.

In this section, the properties of the soil incorporated in the numerical model are obtained from real properties of the soil at the test site (see [14] and Table 1). Then, the initial density adopted is 1250 kg/m^3. The value of the shear modulus G can be obtained from the SPT test by using the empirical relationship

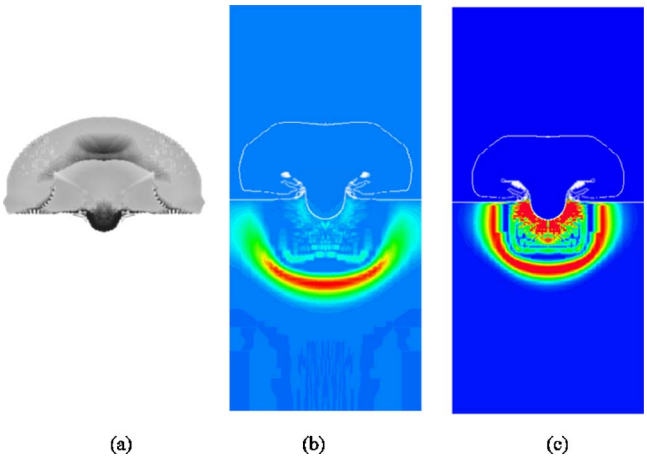

Fig. 7 Wave propagation. (*a*) Velocity field in the air. (*b*) Pressure contours in the soil. (*c*) Von Mises stresses. 50 kg of TNT with the energy release center at the ground level. 1.17 ms.

Table 5 Apparent crater diameter. Comparison with experimental results.

Experimental program	W (kg of TNT)	Experimental results[14] D[m]	Numerical results D[m]	Numerical/ Experimental
Ref. [14]	1	0.58	0.60	1.03
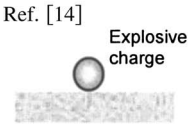	2	0.74	0.72	0.97
	4	0.84	1.03	1.23
	7	1.48	1.12	0.76
	10	1.56	1.54	0.99
EMRTC 	250	3.80	3.94	1.04

(8*a*) given by Ohsaki and Iwasaki [24] for sands or, alternatively, the expression (8*b*) given by Hara et al. [25] for cohesive soils.

$$G_o = 12N^{0.8} \text{ MPa} \tag{8a}$$

$$G_o = 15.8N^{0.67} \text{ MPa} \tag{8b}$$

For the soils found at the test site, the bounds are given by the expression (8*a*): $G=50$ to 88 MPa. A value of 70 MPa was adopted. Some authors disagree with using SPT results in order to obtain elastic properties of the soil. However, in Sec. 4.4 it will be shown that the variation of the shear modulus does not affect the dimensions of the crater significantly.

An additional comparison with EMRTC experimental determinations was made. Numerical results for the crater diameter and the comparison with experimental ones are presented in Table 5. Moreover, the diameters obtained in the numerical study are represented in Fig. 8 as a function of the diameters measured in the experimental program for the same explosive weight and location. The 45 deg trend line represents the perfect correlation. Figure 8 indicates that the research program can be considered successful.

Table 5 and Fig. 8 show that a mean difference of about 10% is obtained with respect to experimental results for charges ranging from 1 to 10 kg of TNT and a difference of about 4% for greater charges. Obviously, the last value, corresponding to a 250 kg4 TNT load, should not be considered in a quantitative sense because it is only the comparison of one result. However, the qualitative tendency of the numerical model seems to be good for both small and big charges.

4.3 Numerical Results. The crater dimensions for explosive charges from 50 to 500 Kg of TNT situated on the ground (case (a)) and with the energy release center at ground level (case (b)) are calculated in this section. These charge values were used because they are in the medium range of terrorist attacks to buildings. The range of explosive masses used in terrorist attacks is discussed in some papers [26,27] and it is strongly dependent on the way the explosive is supposed to have been transported. In order to carry out a comparative analysis, the mass of the explosive is defined by TNT masses. The corresponding masses for other explosives can be obtained through the concept of TNT equivalence [28].

The results obtained are presented in Table 6. These results are obtained with the soil properties indicated in Table 4. However, a study about the variability of soil properties is presented in Sec. 4.4.

It may be observed that the crater is always smaller when the

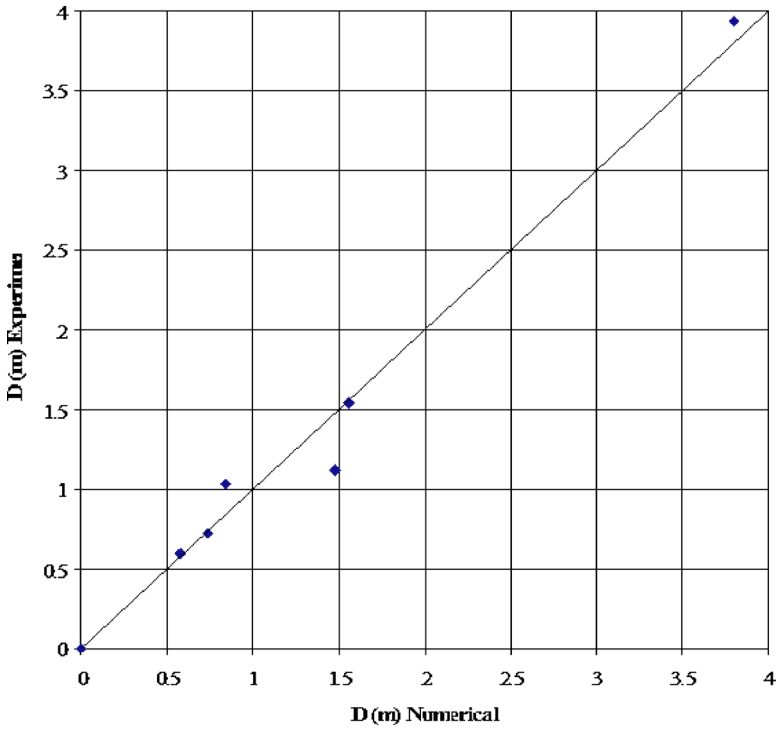

Fig. 8 Comparison of numerical and experimental crater diameters

Table 6 Apparent crater diameter. Numerical results.

W	(a)	(b)	Comparison
(kg of TNT)	D (m)	D (m)	$D_{(a)}/D_{(b)}$
50	2.10	2.76	0.76
100	2.52	3.06	0.82
150	2.62	3.40	0.77
200	3.06	3.76	0.81
250	3.10	4.14	0.75
300	3.20	4.36	0.73
400	3.40	4.60	0.74
500	4.22	5.30	0.80

explosive is lying on the ground level than when the energy release center is at ground level. The difference is attributed to the fact that the energy release center is elevated from the ground level in case (a). Nevertheless, the ratio between apparent crater diameters of both cases is almost constant, about 0.77 (coefficient of variation 4.4%), for all the charges studied.

The results of this numerical analysis are also plotted in Fig. 9 to be compared with experimental ones and empirical equation (4).

In a graphic representing crater diameter as a function of the cubic root of the explosive mass, numerical results are presented in Fig. 9 for the cases when the explosive is lying on the ground level (case (a) in Fig. 9) and when the energy release center is at the ground level (case (b) in Fig. 9). These results can be approximately represented with two straight lines through the origin. These straight lines are similar to that described in Eq. (4) that was also included in Fig. 9 together with its upper and lower limits. Numerical results (b) for explosions with the energy release center at the ground level and EMRTC experimental result are very close to the lower limit of Eq. (4). Another linear approximation must be used for explosives lying on the ground like those simulated in numerical series (a).

4.4 Influence of Soil Properties. In order to analyze the influence of soil properties on the size of the craters, additional studies were carried out varying the elastic, failure, and yield strength properties.

4.4.1 Shear Modulus. The value of the shear modulus was varied in a wide range: 30 MPa (soft soil) to 1000 MPa (sound rock). The results are presented in Table 7.

Table 7 Apparent crater diameter. Influence of shear modulus. $D_{ref.}$ = diameter corresponding, G=200 MPa.

W	G	Numerical results	
(kg of TNT)	(MPa)	D[m]	D_{ref}/D
10	30	1.564	0.96
	200	1.500	—
	1000	1.388	1.08
250	30	4.350	0.95
	200	4.140	—
	1000	3.950	1.05

4.4.2 Mass Density. In this case, a wide range was also considered for the density 1250 kg/m^3 to the reference (maximum) density 1950 kg/m^3. The results are presented in Table 8.

Tables 7 and 8 show that the elastic properties of the soil do not affect significantly the diameter of the crater. However, a variation of ±5% could be obtained in particular cases.

4.4.3 Failure Criteria. The hydro tensile limit was varied from −100 to −200 kPa. The results are presented in Table 9.

4.4.4 Yield Strength. The three yield functions considered are presented in Table 10. The first one corresponds to a Tresca criterion and the last two to a Mohr Coulomb criterion with different yield strength. The results for the diameter of the crater obtained for each one of these yielding criteria are shown in Table 11.

Tables 9 and 11 show that, when the failure limit and the yield function are changed between reasonable limits, the diameter of the crater remains unchanged.

4.5 Summary of Results. From the results obtained in Secs. 4.1–4.4, Eqs. (9) and (10) can be proposed for the prediction of crater dimensions in cases (a) and (b), respectively. These equations represent the linear approximation of the numerical result by minimum least-fit squares. The variation of ±5% accounts for the differences between soil properties that could be found in different sites.

$$\text{Case (a)} \quad D\,(\text{m}) = 0.51 W\,(\text{Kg})^{1/3} \pm 5\% \tag{9}$$

$$\text{Case (b)} \quad D\,(\text{m}) = 0.65 W\,(\text{Kg})^{1/3} \pm 5\% \tag{10}$$

It must be noted that there are very important differences between the previous results found in the literature ([3], Eq. (2)) and

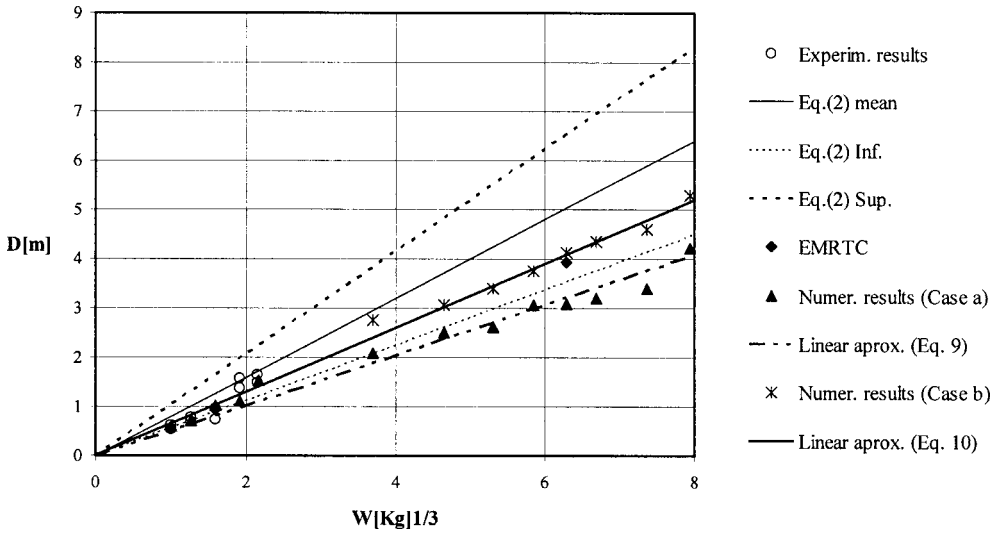

Fig. 9 Apparent crater diameter for explosions on and above the ground level

Table 8 Apparent crater diameter. Influence of density.

W  (kg of TNT)	Numerical results, D (m) (a) Mass density 1250 kg/m^3	(b) Mass density 1920 kg/m^3	$D_{(a)}/D_{(b)}$
50	2.76	2.76	1.00
100	3.06	2.92	1.05
150	3.40	3.40	1.00
200	3.76	3.58	1.05
250	4.14	3.78	1.10
300	4.36	3.94	1.11
400	4.60	4.50	1.02
500	5.30	4.60	1.15

those presented in this paper in Eqs. (9) and (10). Moreover, the dispersion obtained is significantly smaller in this case.

5 Conclusions

A numerical study of craters produced by explosive loads was presented in this paper. Taking into account the results obtained, the following conclusions and observations may be drawn:

- Material models and analysis procedures were validated with experimental results. A good agreement was found with existing results for apparent diameters of this type of crater.
- It was observed, as it was expected, that the crater is always smaller when the explosive is lying at ground level than when the energy release center is at ground level. The difference is attributed to the fact that the energy release center is elevated from the ground level in case (a). Nevertheless, the ratio between apparent crater diameters of both cases is almost constant: about 0.77 (coefficient of variation 4.4%) for all the charges studied.
- It was demonstrated that the elastic properties of the soil do not significantly affect the diameter of the crater obtained. However, a variation of ±5% could be obtained in particular cases.
- It was demonstrated that when the failure limit and the yield function are changed between reasonable limits, the diameter of the crater remains unchanged.
- The crater diameters for explosive loads from 50 to 500 kg of TNT on the soil surface and with the energy release center at the ground level were obtained. The results obtained confirm that the simple empirical linear laws proposed in the paper can be used to predict the apparent crater diameter, which is a function of the cubic root of the explosive mass. Moreover, the effect of the elevation of the energy release center when the explosive is on the ground is clearly shown in the numerical results and in the proposed empirical relationship.
- The results obtained in this paper show that the proposed empirical laws can be used for different types of soil having mechanical properties in the range studied, without introducing large errors.

Table 9 Apparent crater diameter. Influence of hydro tensile limit.

W  (kg of TNT)	Numerical results, D (m) (a) HTL −100 kPa	(b) HTL −200 kPa	$D_{(a)}/D_{(b)}$
50	2.10	2.10	1.00
500	4.22	4.22	1.00

Table 10 Yield functions adopted

Pressure (kPa)	Yield stress (kPa) (a)	(b)	(c)
0	6.20×10^3	1.00×10^2	2.00×10^2
3.6×10^4	6.20×10^3	3.80×10^2	7.60×10^2
1.4×10^5	6.20×10^3	1.14×10^3	2.28×10^3
2.7×10^5	6.20×10^3	1.14×10^3	2.28×10^3

Table 11 Apparent crater diameter. Influence of yield function.

W  (kg of TNT)	Numerical results, D (m) Yield function (a)	Yield function (b)	Yield function (c)
50	2.10	2.10	2.10
500	4.22	4.22	4.22

Acknowledgment

The authors wish to thank the help received from Amelia Campos for the English revision. The financial support of the CONICET (Argentina) and the National University of Tucumán is gratefully acknowledged.

References

[1] Baker, W. E., Cox, P. A., Westine, P. S., Kulesz, J. J., and Strehlow, R. A., 1983, *Explosion Hazards and Evaluation*, Elsevier, Amsterdam.

[2] Smith, P. D., and Hetherington, J. G., 1994, *Blast and Ballistic Loading of Structures*, Butterworth-Heinemann Ltd., UK.

[3] Kinney, G. F., and Graham, K. J., 1985, *Explosive Shocks in Air*, 2nd ed., Springer Verlag, New York.

[4] Persson, P. A., Holmberg, R., and Lee, J., 1994, *Rock Blasting and Explosives Engineering*, CRC Press, Boca Raton, FL.

[5] Bull, J. W., and Woodford, C. H., 1998, "Camouflets and Their Effects on Runway Supports," Comput. Struct., **69**(6), pp. 695–706.

[6] Baker, W. E., Westine, P. S., and Dodge, F. T., 1991, *Similarity Methods in Engineering Dynamics*, Elsevier, Amsterdam.

[7] Melosh, H. J., 1989, *Impact Cratering—A Geologic Process*, The Clarendon Press, Oxford University Press, New York.

[8] Iturrioz, I., and Riera, J. D., 2001, "Numerical Study of the Effect of Explosives on a Plane Surface," XII Congress on Num. Methods and Their Applications, ENIEF 2001, Argentina.

[9] Yang, R., Bawden, W. F., and Katsabanis, P. D., 1996, "A New Constitutive Model for Blast Damage," Int. J. Rock Mech. Min. Sci. Geomech. Abstr., **33**(3), pp. 245–254.

[10] Liu, L., and Katsabanis, P. D., 1997, "Development of a Continuum Damage Model for Blasting Analysis," Int. J. Rock Mech. Min. Sci., **34**(2), pp. 217–231.

[11] Wu, C., Lu, Y., and Hao, H., 2004, "Numerical Prediction of Blast-Induced Stress Wave From Large-Scale Underground Explosion," Int. J. Numer. Analyt. Meth. Geomech., **28**, pp. 93–109.

[12] Wang, Z., and Lu, Y., 2003, "Numerical Analysis on Dynamic Deformation Mechanism of Soils Under Blast Loading," Soil Dyn. Earthquake Eng., **23**, pp. 705–714.

[13] Zhou, X. L., Wang, J. H., and Lu, J. F., 2003, "Transient Dynamic Response of Poroelastic Medium Subjected to Impulsive Loading," Comput. Geotech., **30**, pp. 109–120.

[14] Ambrosini, R. D., Luccioni, B. M., Danesi, R. F., Riera, J. D., and Rocha, M. M., 2002, "Size of Craters Produced by Explosive Charges on or Above the Ground Surface," Shock Waves, **12**(1), pp. 69–78.

[15] Baratoux, D., and Melosh, H. J., 2003, "The Formation of Shatter Cones by Shock Wave Interference During Impacting," Earth Planet. Sci. Lett., **216**, pp. 43–54.

[16] Nolan, M. C., Asphaug, E., Greenberg, R., and Melosh, H. J., 2001, "Impacts on Asteroids: Fragmentation, Regolith Transport, and Disruption," Icarus, **153**, pp. 1–15.

[17] Pierazzo, E., and Melosh, H. J., 1999, "Hydrocode Modeling of Chicxulub as an Oblique Impact Event," Earth Planet. Sci. Lett., **165**, pp. 163–176.

[18] AUTODYN, 2002, *Interactive Non-Linear Dynamic Analysis Software*, Version 4.3, User's Manual, Century Dynamics Inc.

[19] Cowler, M. S., and Hancock, S. L., 1979, "Dynamic Fluid-Structure Analysis of Shells Using the PISCES 2DELK Computer Code," 5th Int. Conf. on Structural

Mechanics in Reactor Technology, Paper No. B1/6, Berlin, West Germany, August.
[20] Hancock, S., 1976, "Finite Difference Equations for PISCES-2DELK," TCAM-76-2, Physics International Company Technical Memo TCAM 76-2.
[21] Wilkins, M. L., 1964, "Calculation of Elastic-Plastic Flow," Methods Comput. Phys., **3**, pp. 211–263.
[22] Youngs, D. L., 1982, "Time-Dependent Multimaterial Flow With Large Fluid Distortion," Numer. Methods Fluid Dyn., K. W. Morton and M. J. Baines, eds., pp. 273–285.
[23] Lee, E. L., and Tarver, C. M., 1980, "Phenomenological Model of Shock Initiation in Heterogeneous Explosives," Phys. Fluids, **23**(12), pp. 2362–2372.
[24] Ohsaki, Y., and Iwasaki, R., 1973, "On Dynamic Shear Moduli and Poisson′s Ratios of Soil Deposits," Soils Found., **13**, pp. 61–73.
[25] Hara, A., Ohta, T., Niwa, M., Tanaka, S., and Banno, T., 1974, "Shear Modulus and Shear Strength of Cohesive Soils," Soils Found., **14**, pp. 1–12.
[26] Elliot, C. L., Mays, G. C., and Smith, P. D., 1992, "The Protection of Buildings Against Terrorism and Disorder," Proc. Inst. Civ. Eng., Struct. Build., **94**, pp. 287–297.
[27] Millington, G., 1994, "Discussion of ′The Protection of Buildings Against Terrorism and Disorder," Proc. Inst. Civ. Eng., Struct. Build., **104**, pp. 343–350.
[28] Formby, S. A., and Wharton, R. K., 1996, "Blast Characteristics and TNT Equivalence Values for Some Commercial Explosives Detonated at Ground Level," J. Hazard. Mater., **50**, pp. 183–198.

Constitutive Model for Fiber-Reinforced Composite Laminates

Bibiana M. Luccioni
CONICET,
Structures Institute,
National University of Tucumán,
Av. Roca 1800,
4000 San Miguel de Tucumán,
Tucumán, Argentina

Nowadays, conventional materials have been progressively replaced by composite materials in a wide variety of applications. Particularly, fiber reinforced composite laminates are widely used. The appropriate design of elements made of this type of material requires the use of constitutive models capable of estimating their stiffness and strength. A general constitutive model for fiber reinforced laminated composites is presented in this paper. The model is obtained as a generalization of classical mixture theory taking into account the relations among the strains and stresses in the components and the composite in principal symmetry directions of the material. The constitutive equations for the laminated composite result from the combination of lamina constitutive equations that also result from the combination of fibers and matrix. It is assumed that each one of the components are orthotropic and elastoplastic. Basic assumptions of the proposed model and the resulting equations are first presented in the paper. The numerical algorithm developed for the implementation in a three-dimensional (3D) finite element nonlinear program is also described. The paper is completed with application examples and comparison with experimental results. The comparison shows the capacity of the proposed model for the simulation of stiffness and strength of different composite laminates.
[DOI: 10.1115/1.2200654]

1 Introduction

In recent years, considerable attention has been focused on the modeling of composite materials as conventional materials are continuously being replaced by a variety of composite materials. Several approaches have been developed but there is still a strong need of predicting models that can be used for stiffness and strength assessment of this type of materials in actual situations without the need of many empirical constants.

Constitutive models for fiber reinforced composite laminates can be classified according to the scale in which they are defined [1]. In macro-models the composite material is represented as a unique material with average properties. This type of approach generally results insufficient to describe the overall inelastic behavior and failure of the laminate. In meso-models the composite is assumed to be formed by unidirectional laminas for which macroscopic equations are derived. The constitutive properties of individual laminas are obtained from experimental tests. In contrast, micro-models use the constitutive equations of the elemental constituents: Matrix, fibers, interfaces, etc. This approach has the advantage of allowing the identification of the failure mode but requires accurate experimental data for the individual components, which is not generally available. An alternate approach is the use of multi-scale models [2].

Many micromechanical models have been developed for fiber reinforced composites but most of them have considerable limitations. Theories are generally too complicated or, when they are simple, they are only able to reproduce a few aspects of the behavior in fiber directions or they are only valid for composites in which stiffness and strength of the fibers are significantly greater than those of the matrix [3].

Contributed by the Applied Mechanics Division of ASME for publication in the JOURNAL OF APPLIED MECHANICS. Manuscript received May 21, 2005; final manuscript received March 27, 2006. Review conducted by G. C. Buscaglia. Discussion on the paper should be addressed to the Editor, Prof. Robert M. McMeeking, Journal of Applied Mechanics, Department of Mechanical and Environmental Engineering, University of California–Santa Barbara, Santa Barbara, CA 93106-5070, and will be accepted until four months after final publication of the paper itself in the ASME JOURNAL OF APPLIED MECHANICS.

Hinton and Soden recently organized a "failure exercise" to compare the predictive capabilities of a number of the most important strength theories for laminated composites in current usage [4–8]. The results of that exercise [9–12] were used for the assessment of the accuracy of current theoretical methods of failure prediction in composite laminates. According to Soden et al. [12], the most reliable theories for the designer are the theories of Zinoviev et al. [13,14], Bogetti [15], Tsai [16,17], Puck [18,19], and Cuntze [20].

None of these five theories is based on a micromechanics analysis. Huang [3] developed a micromechanical model to estimate the strength of unidirectional fibre reinforced composites. Fibers and matrix are considered to be elastoplastic with very simple linear hardening laws defined for each direction. The stress in each component is expressed in terms of the global stress using a bridging matrix. Nevertheless, the accuracy of the strength predictions for this theory is moderate [12].

A numerical model for general composite materials, appropriate for the mechanical analysis of fiber reinforced composite laminates, is presented in this paper. The model is based on an analysis at component materials level that allows obtaining, at a first stage, the behavior of the lamina from the mechanical properties of matrix and fibers, their volume ratio and their orientation. Then, the behavior of the laminate can be obtained composing laminas with different fiber orientations. The model is completely general and can be used for other types of composites.

The model is based on very simple kinematical and equilibrium assumptions that, properly handled, lead to composite constitutive equation and the strain and stress tensors in all the components. In this way, elastic properties of the laminate can be obtained. Nonlinear behavior and the progressive failure can be analyzed and failure envelopes can be defined.

The novelty of the model presented is the development of a formalism that allows dealing with equal stress or equal strain in correspondence with each stress (or strain) component in a systematic way and that is applicable to various kinds of composite topologies. The model can be interpreted as a generalization of Reuss' and Voight's theories that can also deal with general orthotropic elastoplastic models for each one of the constituents mate-

rials. Moreover, resulting equations are very simple and resemble those of mixing theory [21] allowing a similar numerical treatment.

2 Proposed Model

2.1 Introduction. This model assumes that the composite can be subsequently decomposed in sub-composites to arrive to composites with simple structure for which simple kinematical and equilibrium hypothesis relating stress and strain of the components can be stated. Basically, for this composite with simple structure it should be clear which strain components are common to all components (parallel behavior) and which stress components are common to all components (series behavior).

Successive decompositions are generally required in order to state these assumptions. Particularly, in the case of reinforced fiber laminated composites, the laminate should be separated in laminas and each lamina should be analyzed first. It will be noted later in application examples that even the precise analysis of one individual unidirectional lamina should require more than one decomposition.

2.2 Constitutive Model for the Components. It is well known that fibers present a strong anisotropic behavior, generally assumed as transversely isotropic, characterized not only by the elastic orthotropy like in the case of carbon fibers but also by the marked difference of strength in principal directions. Another important property of fibers is their slightly lower strength in compression than in tension.

In general, epoxy resins have lower tension than compression strength like brittle materials. In the case of polymeric matrix the material itself can be supposed to be isotropic. Nevertheless, as the fiber/matrix interface is not explicitly modeled, the constitutive model of the matrix is modified including the interface constitutive model [22,23]. Orthotropic elastoplastic or damage interface models can be used to simulate fiber debonding or delamination. As a result, the constitutive model of the matrix including interface exhibits a tension strength much lower in perpendicular direction to fiber than in longitudinal direction.

Taking into account the above considerations, each one of the basic components is supposed to have a general orthotropic elastoplastic behavior covering the case of fibers, matrix, and interface included in matrix.

The orthotropic model used is based on the assumption that there are two spaces [24–26]: (a) A real anisotropic space and (b) a fictitious isotropic space. The problem is solved in the fictitious isotropic space allowing the use of elastoplastic models originally developed for isotropic materials. The isotropic elastoplastic model used in this paper includes energy-based criteria to make it suitable for brittle materials [27].

Stress tensors in both spaces are related by a tensor transformation that can be written as,

$$\boldsymbol{\tau} = \boldsymbol{A}(\boldsymbol{\sigma}, \kappa^p) : \boldsymbol{\sigma} \tag{1}$$

where $\boldsymbol{\tau}$ and $\boldsymbol{\sigma}$ are the stress tensors in spaces (a) and (b), respectively, and $\boldsymbol{A}$ is a fourth-order transformation tensor that contains the information about strength anisotropy depending on material symmetry. In the most general case, this tensor varies with the stress state and the evolution of the inelastic process represented by the isotropic plastic hardening variable κ^p [26]. In this paper, all the components materials are assumed initially orthotropic with 3 axes of material symmetry. There are different alternatives to define tensor $\boldsymbol{A}$ for this case [25,26,28–30]. The simplest way is a diagonal fourth-order tensor [27],

$$A_{ijkl} = \delta_{im}\delta_{jn}\delta_{km}\delta_{\ln}\bar{\tau}/\bar{\sigma}_{mn} \tag{2}$$

where $\bar{\tau}$ is the strength in the fictitious isotropic space and $\bar{\sigma}_{mn}$ is the actual strength in the direction m in the plane with normal n. A better approach has been proposed by Oller et al. [30].

The model is thermodynamically consistent and it is based on the assumption of uncoupled elasticity. The free energy density can be supposed to be formed by two independent parts: An elastic part Ψ^e and a plastic part Ψ^p,

$$\Psi = \Psi^e + \Psi^p \quad \Psi^e = \tfrac{1}{2}\boldsymbol{\varepsilon}^e : \boldsymbol{C} : \boldsymbol{\varepsilon}^e \tag{3}$$

where $\boldsymbol{C}$ is the stiffness tensor and $\boldsymbol{\varepsilon}^e$ is the elastic strain tensor.

The secant constitutive equation can be deduced from the free energy density as follows,

$$\boldsymbol{\sigma} = \partial\Psi^e/\partial\boldsymbol{\varepsilon}^e = \boldsymbol{C} : \boldsymbol{\varepsilon}^e = \boldsymbol{C} : (\boldsymbol{\varepsilon} - \boldsymbol{\varepsilon}^p) \tag{4}$$

where $\boldsymbol{\varepsilon}$ is the strain tensor and $\boldsymbol{\varepsilon}^p$ is the plastic strain tensor.

The plastic threshold is defined through a yielding function,

$$F(\boldsymbol{\sigma}; \alpha) = \bar{F}(\boldsymbol{\tau}; \bar{\alpha}) = 0 \tag{5}$$

where F and $\bar{F}$ represent the yielding function in the real anisotropic space and in the fictitious isotropic space, respectively; α and $\bar{\alpha}$ are internal variables in correspondence with both spaces.

The transformation defined by Eq. (1) allows the use of yielding functions $\bar{F}$ defined for isotropic materials in the fictitious isotropic space. It should be noted that this space is isotropic with respect to yielding thresholds and strength but not necessarily with respect to other properties like elastic stiffness.

Evolution of plastic strain in real space is defined with the well-known flow rule,

$$\dot{\boldsymbol{\varepsilon}}^p = \dot{\lambda}(\partial G/\partial\boldsymbol{\sigma}) \tag{6}$$

where G is the plastic potential function defined in the real stress space. Instead of working with this function that should be anisotropic, function $\bar{G}$ defined in the fictitious isotropic space could be used.

$$G(\boldsymbol{\sigma}, \alpha) = \bar{G}(\boldsymbol{\tau}, \bar{\alpha}) \tag{7}$$

Equation (5) can be then rewritten as,

$$\dot{\boldsymbol{\varepsilon}}^p = \dot{\lambda}(\partial\bar{G}/\partial\boldsymbol{\sigma}) = \dot{\lambda}(\partial\bar{G}/\partial\boldsymbol{\tau}) : (\partial\boldsymbol{\tau}/\partial\boldsymbol{\sigma}) = \dot{\lambda}(\partial\bar{G}/\partial\boldsymbol{\tau}) : \boldsymbol{H} = \dot{\lambda}\bar{\boldsymbol{h}}$$

$$\text{with} \quad \boldsymbol{H} = \partial\tau/\partial\boldsymbol{\sigma} \quad \text{and} \quad \bar{\boldsymbol{h}} = (\partial\bar{G}/\partial\boldsymbol{\tau}) : \boldsymbol{H} \tag{8}$$

where $\boldsymbol{H}$ is a fourth-rank tensor and $\bar{\boldsymbol{h}}$ is a second-rank tensor and represents the plastic flux in the real orthotropic space.

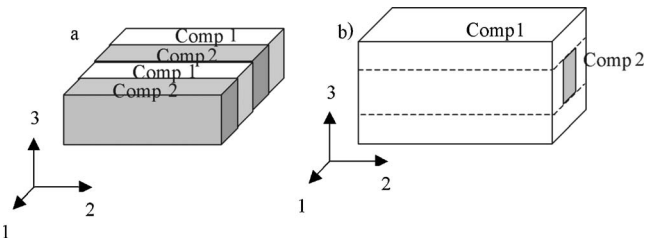

Fig. 1 Schematic representation of composite structure. (*a*) Simple structure, (*b*) more complex structure.

2.3 Kinematical and Equilibrium Assumptions. In a composite with a simple structure there are three orthogonal directions referred to which some strain components are common to all constituents (parallel behavior) and the rest of the components are associated to equal stress in all constituents (series behavior). A parallel behavior in correspondence with one component means that all the composite constituents have the same value for this strain component. A series behavior in correspondence with one component means that all the composite constituents have the same value for this stress component. As an example, consider a composite with the representative structure shown in Fig. 1(*a*). It is clear that σ_{11} is common for both components (series behavior) while ε_{22} and ε_{33} are common for both components (series behavior). For a more complex structure like that represented in Fig.

1(*b*), this type of conclusions can not be stated a priori, but the composite can be considered to be formed by the sub-composites with simple structure indicated with dashed lines.

Based on this analysis, stress and strain components could be rearranged. All the stress and strain components that are common to all components are grouped in tensor $\boldsymbol{\varepsilon}^*$, while all the stress and strain components that will be obtained as a superposition of the contribution of all constituents are grouped in tensor $\boldsymbol{\sigma}^*$.

In order to express this rearrangement the following fourth order tensors are defined,

$$\alpha^{\sigma}_{ijkl} = \delta_{ir}\delta_{js}\delta_{kr}\delta_{ls}H(p_{rs})$$
$$\alpha^{\varepsilon}_{ijkl} = \delta_{ik}\delta_{jl} - \alpha^{\sigma}_{ijkl}$$
$$with\ p_{rs} = \begin{cases} 1 \text{ if the } rs \text{ component works in parallel} \\ 0 \text{ if the } rs \text{ component works in series} \end{cases} \tag{9}$$

H: Threshold function.

According to Eq. (9), the product $\boldsymbol{\alpha}^{\sigma}:\boldsymbol{\sigma}$ preserves the stress components that are assumed to have a parallel behavior and make the other components zero.

Stress and strain components are rearranged as follows,

$$\begin{matrix} \boldsymbol{\sigma}^* = \boldsymbol{\alpha}^{\sigma}:\boldsymbol{\sigma} + \boldsymbol{\alpha}^{\varepsilon}:\varepsilon \\ \boldsymbol{\varepsilon}^* = \boldsymbol{\alpha}^{\varepsilon}:\boldsymbol{\sigma} + \boldsymbol{\alpha}^{\sigma}:\boldsymbol{\varepsilon} \end{matrix} \quad \text{and} \quad \begin{matrix} \boldsymbol{\sigma} = \boldsymbol{\alpha}^{\sigma}:\boldsymbol{\sigma}^* + \boldsymbol{\alpha}^{\varepsilon}:\boldsymbol{\varepsilon}^* \\ \boldsymbol{\varepsilon} = \boldsymbol{\alpha}^{\varepsilon}:\boldsymbol{\sigma}^* + \boldsymbol{\alpha}^{\sigma}:\boldsymbol{\varepsilon}^* \end{matrix} \tag{10}$$

where $\boldsymbol{\sigma}^*$ contains stress components in correspondence with directions of parallel behavior and strain components in correspondence with directions of series behavior. Tensor $\boldsymbol{\varepsilon}^*$ contains strain components in correspondence with directions of parallel behavior and stress components in correspondence with directions of series behavior

2.4 Alternative Way of Writing Constitutive Equations of the Components. An alternative way of writing constitutive equations of the components that makes the development of the constitutive equation of the composite easier is proposed in this section.

Combining Eqs. (3) and (10), the following secant constitutive relation can be obtained,

$$\boldsymbol{\sigma}^* = \boldsymbol{C}^*:\boldsymbol{\varepsilon}^* - \boldsymbol{\sigma}^{p^*} \tag{11}$$

where,

$$\boldsymbol{C}^* = (\boldsymbol{\alpha}^{\sigma}:\boldsymbol{C} + \boldsymbol{\alpha}^{\varepsilon}):(\boldsymbol{\alpha}^{\varepsilon}:\boldsymbol{C} + \boldsymbol{\alpha}^{\sigma})^{-1} \tag{12}$$

$$\boldsymbol{\sigma}^{p^*} = (\boldsymbol{C}^*:\boldsymbol{\alpha}^{\sigma} - \boldsymbol{\alpha}^{\varepsilon}):\boldsymbol{\varepsilon}^p \tag{13}$$

2.5 Composite Constitutive Equation. First, the case of a composite with simple structure where principal directions and tensors $\boldsymbol{\alpha}^{\sigma}$ and $\boldsymbol{\alpha}^{\varepsilon}$ are coincident for all the constituents is analyzed. In such composite, the following condition is verified,

$$\boldsymbol{\varepsilon}^*_c = \boldsymbol{\varepsilon}^* \tag{14}$$

where *c* indicates an arbitrary component material.

Assuming that the plastic strain of the composite in the directions in which the material works in series can be obtained as the sum of the plastics strains of the components multiplied by their respective volume fractions, the following secant equation is obtained,

$$\boldsymbol{\sigma}^* = \boldsymbol{C}^*:\boldsymbol{\varepsilon}^* - \boldsymbol{\sigma}^{p^*} \tag{15}$$

where,

$$\boldsymbol{C}^* = \sum k_c \boldsymbol{C}^*_c \quad \boldsymbol{\sigma}^{p^*} = \sum k_c (\boldsymbol{C}^*_c:\boldsymbol{\alpha}^{\sigma} - \boldsymbol{\alpha}^{\varepsilon}):\boldsymbol{\varepsilon}^p_c \tag{16}$$

And k_c represents the volume fraction of a generic constituent material.

Equation (15) can be rearranged with the aid of Eqs. (10) to give,

$$\boldsymbol{\sigma} = \boldsymbol{C}:\boldsymbol{\varepsilon} - \boldsymbol{\sigma}^p \tag{17}$$

where,

$$\boldsymbol{C} = (\boldsymbol{\alpha}^{\sigma}:\boldsymbol{C}^* + \boldsymbol{\alpha}^{\varepsilon}):(\boldsymbol{\alpha}^{\varepsilon}:\boldsymbol{C}^* + \boldsymbol{\alpha}^{\sigma})^{-1}$$

$$\boldsymbol{\sigma}^p = -\boldsymbol{C}:\boldsymbol{\alpha}^{\varepsilon}:\boldsymbol{\sigma}^{p^*} + \boldsymbol{\alpha}^{\sigma}:\boldsymbol{\sigma}^{p^*} = (\boldsymbol{\alpha}^{\sigma} - \boldsymbol{C}:\boldsymbol{\alpha}^{\varepsilon}):\boldsymbol{\sigma}^{p^*} \tag{18}$$

Numerical implementation in a finite element program requires the evaluation of the strain tensor for each one of the components from the composite strains. In this way, once the strains are known, constitutive equations can be independently integrated for each constituent and information at the constituents material level (fiber and matrix) level can be recorded through the corresponding internal variables.

Starting from condition (14) and Eqs. (10) and (17), the following relation can be written,

$$\boldsymbol{\varepsilon}_c = \boldsymbol{\phi}_c:\boldsymbol{\varepsilon} + \tilde{\boldsymbol{\varepsilon}}^p_c \tag{19}$$

where,

$$\boldsymbol{\phi}_c = (\boldsymbol{\alpha}^{\varepsilon}:\boldsymbol{C}^*_c + \boldsymbol{\alpha}^{\sigma}):(\boldsymbol{\alpha}^{\varepsilon}:\boldsymbol{C}^* + \boldsymbol{\alpha}^{\sigma})^{-1}$$

$$\tilde{\boldsymbol{\varepsilon}}^p_c = \boldsymbol{\phi}_c:\boldsymbol{\alpha}^{\varepsilon}:\boldsymbol{\sigma}^{*P} - \boldsymbol{\alpha}^{\varepsilon}:\boldsymbol{\sigma}^{*P}_c \tag{20}$$

The elastoplastic tangent tensor can be obtained from the derivation of Eq. (16)

$$\dot{\boldsymbol{\sigma}} = \boldsymbol{C}:\dot{\boldsymbol{\varepsilon}} - \dot{\boldsymbol{\sigma}}^p = \boldsymbol{C}^T:\dot{\boldsymbol{\varepsilon}} \tag{21}$$

and results,

$$\boldsymbol{C}^T = \boldsymbol{C} - (\boldsymbol{\alpha}^{\sigma} - \boldsymbol{C}:\boldsymbol{\alpha}^{\varepsilon}):\sum k_c(\boldsymbol{C}^*_c:\boldsymbol{\alpha}^{\sigma} - \boldsymbol{\alpha}^{\varepsilon}):(\boldsymbol{I} - \boldsymbol{C}^{-1}_c:\boldsymbol{C}^T_c):\boldsymbol{\phi}_c \tag{22}$$

where $\boldsymbol{C}^T_c$ is the elastoplastic tangent tensor of component *c*.

All the preceding equations are only valid in the composite local system of reference coincident with its principal symmetry directions. For an arbitrary reference system, all tensors must be rotated.

2.6 More Complex Composites. The constitutive equations for a laminated composite or for a composite material with a more complex structure, where the tensors $\boldsymbol{\alpha}^{\sigma}$ and $\boldsymbol{\alpha}^{\varepsilon}$ are not the same for all components, can be obtained in different steps. The composite must be decomposed in more simple sub-composites for which the correspondent constitutive equations can be obtained as described above. Then, the constitutive equation of the composite, can be written with a similar approach, composing the constitutive equations already found for the sub-components. For example, the constitutive equation of a laminate composed by *n* fiber reinforced laminas with different properties, in principal directions of the laminate would look like Eqs. (17) and (18) where the tensors $\boldsymbol{\alpha}^{\sigma}$ and $\boldsymbol{\alpha}^{\varepsilon}$ are related to the laminate structure and the tensors $\boldsymbol{C}^*$ and $\boldsymbol{\sigma}^{p*}$ are calculated as follows,

$$\boldsymbol{C}^* = \sum_{c=1}^{n} k_c \boldsymbol{C}^*_c \tag{23}$$

$$\boldsymbol{C}^*_c = (\boldsymbol{\alpha}^{\sigma}:\boldsymbol{R}_c \,.\, \boldsymbol{R}_c \,.\, \boldsymbol{C}_c \,.\, \boldsymbol{R}^t_c \,.\, \boldsymbol{R}^t_c + \boldsymbol{\alpha}^{\varepsilon}):(\boldsymbol{\alpha}^{\varepsilon}:\boldsymbol{R}_c \,.\, \boldsymbol{R}_c \,.\, \boldsymbol{C}_c \,.\, \boldsymbol{R}^t_c \,.\, \boldsymbol{R}^t_c + \boldsymbol{\alpha}^{\sigma})^{-1} \tag{24}$$

$$\boldsymbol{C}_c = \left(\boldsymbol{\alpha}^{\sigma}_c:\sum_{i=1}^{2} k_{ci}\boldsymbol{C}^*_{ci} + \boldsymbol{\alpha}^{\varepsilon}_c\right):\left(\boldsymbol{\alpha}^{\varepsilon}_c:\sum_{i=1}^{2} k_{ci}\boldsymbol{C}^*_{ci} + \boldsymbol{\alpha}^{\sigma}_c\right)^{-1} \tag{25}$$

$$\boldsymbol{C}^*_{ci} = (\boldsymbol{\alpha}^{\sigma}_c:\boldsymbol{C}_{ci} + \boldsymbol{\alpha}^{\varepsilon}_c):(\boldsymbol{\alpha}^{\varepsilon}_c:\boldsymbol{C}_{ci} + \boldsymbol{\alpha}^{\sigma}_c)^{-1} \tag{26}$$

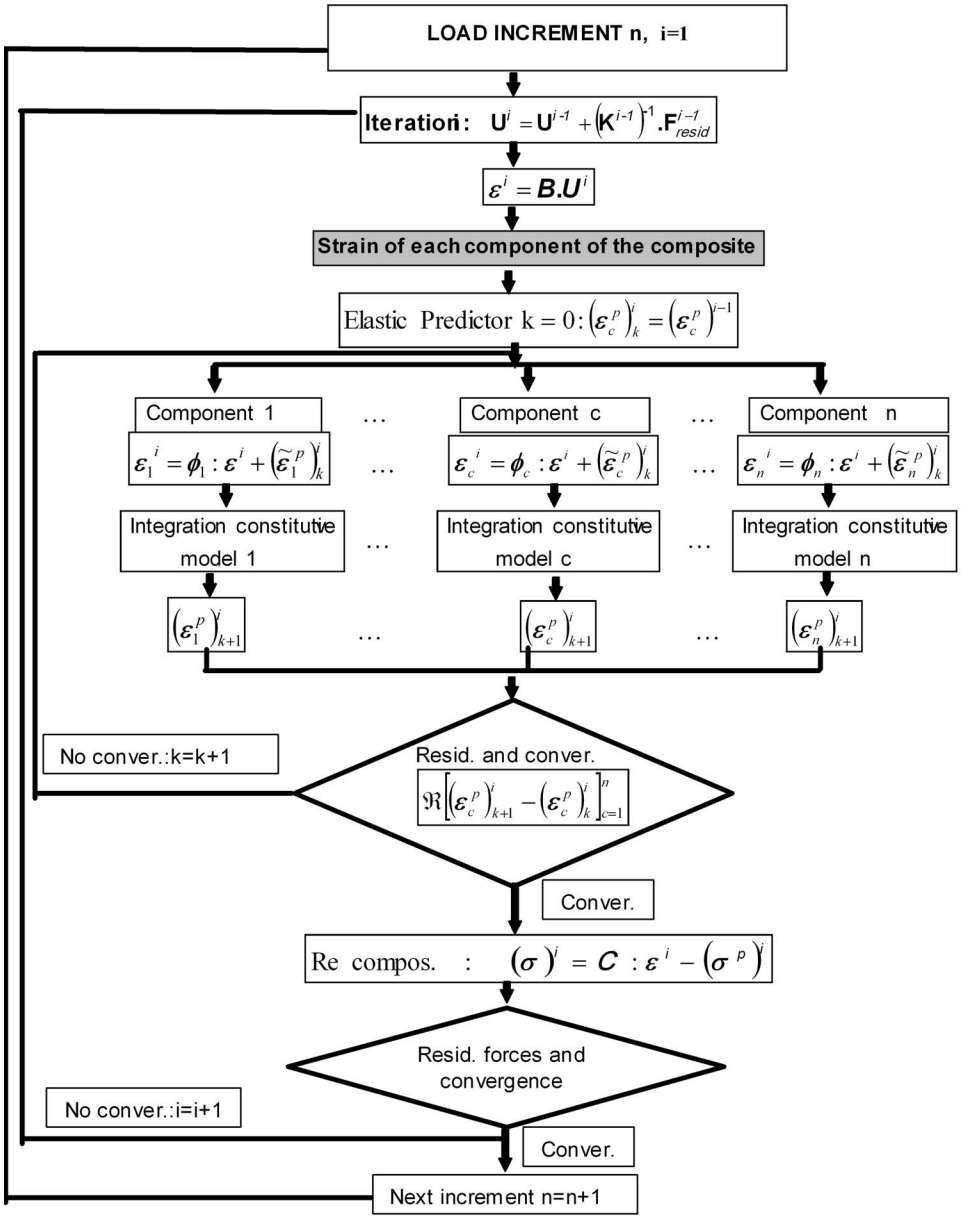

Fig. 2 Numerical scheme for the solution of a nonlinear problem

$$\boldsymbol{\sigma}^{p^*} = \sum_{c=1}^{n} k_c(\boldsymbol{C}_c^*:\boldsymbol{\alpha}^\sigma - \boldsymbol{\alpha}^\varepsilon):\boldsymbol{R}^{t-1}\,.\,\boldsymbol{\varepsilon}_c^p\,.\,\boldsymbol{R}^{-1} \tag{27}$$

$$\boldsymbol{\varepsilon}_c^p = \boldsymbol{C}_c^{-1}:\boldsymbol{\sigma}_c^p = \boldsymbol{C}_c^{-1}:(\boldsymbol{\alpha}_c^\sigma - \boldsymbol{C}_c:\boldsymbol{\alpha}_c^\varepsilon):\boldsymbol{\sigma}_c^{p^*} \tag{28}$$

$$\boldsymbol{\sigma}_c^{p^*} = \sum_{i=1}^{2} k_{ci}(\boldsymbol{C}_{ci}^*:\boldsymbol{\alpha}_c^\sigma - \boldsymbol{\alpha}_c^\varepsilon):\boldsymbol{\varepsilon}_{ci}^p \tag{29}$$

where $\boldsymbol{R}_c$ is the rotation matrix from lamina c principal coordinates to laminate principal coordinates, the tensors $\boldsymbol{\alpha}_c^\sigma$ and $\boldsymbol{\alpha}_c^\varepsilon$ are related to the lamina c, k_c is the volume fraction of lamina c, k_{ci} is the volume fraction of the component i in lamina c, $\boldsymbol{C}_{\mathrm{ci}}$ is the secant stiffness tensor of the same component in lamina local coordinates, and $\boldsymbol{\varepsilon}_{ci}^p$ is the permanent strains tensor of component i in lamina c in local lamina coordinates.

Delamination can be included in the model presented using an approach similar to that used for fiber debonding [22,23]. A term due to differential strains among laminas, depending on interlaminar stress, should be added in Eq. (27).

3 Numerical Implementation

The model presented can be implemented in a nonlinear finite element program using the iterative scheme presented in Fig. 2. A composite with simple structure strains in each component can be evaluated with Eq. (19) if plastic strains are known. In case of a more complex composite, this scheme must be used to decompose the composite in sub-composites and again inside each sub-composite to arrive to each one of the constituents.

In any case, plastic strains of all components are required for the evaluation of the strains in each component. As a result, the problem cannot be explicitly solved and, for example, an iterative scheme must be used. The algorithm schematized in Fig. 2 is based on a predictor-corrector iterative procedure using the norm of plastic strains as convergence measure.

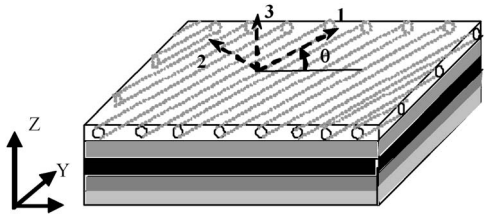

Fig. 3 Fiber reinforced laminated composite

Once the strains of each one of the constituents have been obtained, the correspondent constitutive equations can be integrated using well-known procedures like Euler backward or return mapping algorithms.

Failure envelopes can be obtained with a finite element program loading an element with different stress combinations up to failure. Each stress ratio gives a point of the failure envelope. Alternatively, failure envelopes for composites with simple structure can be analytically obtained writing the yielding criteria of each component, Eq. (5), in terms of the composite stress tensor. In this type of composites it is simple to analyze which is the failure mechanism without any nonlinear calculation.

4 Application Examples

4.1 Introduction. A scheme of a laminated is shown in Fig. 3 where the principal directions used as references are also indicated. In the case of unidirectional laminas, the components can be supposed to work in parallel in fiber directions 1 and 3 (the same strain for all components) and in series in direction 2 (the same stress for all components). The way in which shear is resisted is not so clear and depends, among other factors, on the shape of the fibers transverse section. In general, a more complex combination is required to accurately reproduce shear transfer inside the composite.

In the case of the laminate, principal directions X and Y are contained in the laminate plane and direction Z is orthogonal to that plane. Each lamina can exhibit a different fiber orientation that is defined through the angle θ that forms lamina principal direction 1 with principal direction X of the laminate (see Fig. 4). It can be assumed that laminas work in parallel in the laminate plane and in series in the orthogonal direction.

In general, structures are not designed with all the fibers aligned in a unique direction if the structure is expected to be exposed to stresses in the orthogonal direction. However, unidirectional laminas constitute the basic elements of the laminate and, inside it, they can be exposed to stresses normal to the fiber direction and shear stresses. It is important then to know first if the models are able to reproduce the behavior of individual laminas.

4.2 Elastic Properties of an Unidirectional Lamina. Elastic properties of an epoxy lamina with carbon fibers are studied in this section. Elastic properties of each one of the constituents are the following,

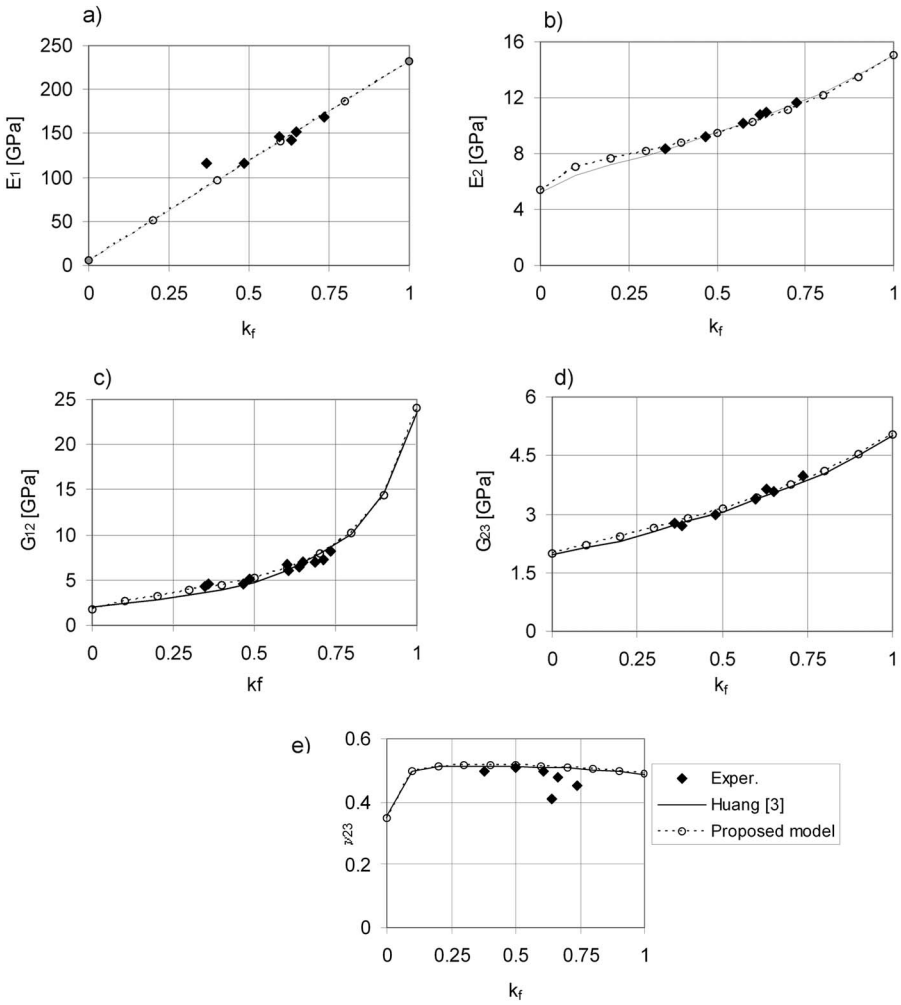

Fig. 4 Elastic properties of the lamina as a function of fiber fraction. (*a*) E_1, (*b*) E_2, (*c*) G_{12}, (*d*) G_{23}, (*e*) ν_{23}.

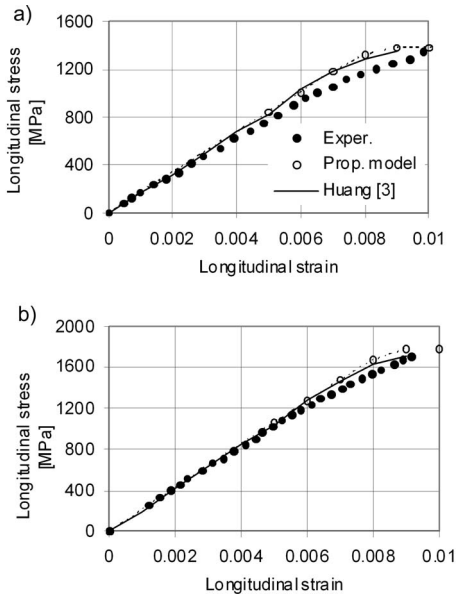

Fig. 5 Stress-strain behavior in the fiber direction. (*a*) $k_f = 0.20$, (*b*) $k_f = 0.35$.

$$E_{1f} = 232 \text{ GPa}; \quad E_{2f} = 15 \text{ GPa}; \quad \nu_{12f} = 0.279;$$

$$\nu_{23f} = 0.49; \quad G_{12f} = 30.2 \text{ GPa};$$

$$E_m = 5.35 \text{ GPa}; \quad \nu_m = 0.22$$

The variations of longitudinal and transverse Young modulus E_1 and E_2, longitudinal and transverse shear modulus G_{12} and G_{23} and Poisson ratio ν_{23} as a function of fiber volume fraction k_f are shown in Fig. 4. The experimental results obtained by Kriz and Stinchcomb [31] and analytical results by Huang [3] are also plotted on Fig. 4. In all cases, a good agreement between the proposed model and experimental results is obtained. It should be noted that in this case where fibers are supposed to be orthotropic, elastic modulus E_2 can be accurately estimated with the assumption of series behavior in direction 2. In contrast, for transverse elastic modulus G_{12} and G_{23} a series/parallel combination gives better results.

4.3 Strength and Nonlinear Behavior of an Unidirectional Lamina. The nonlinear behavior of a lamina composed of unidirectional SiC brittle fibers and a Titanium matrix is analyzed in this section. The mechanical properties of the constituent materials are the following,

$$E_f = 400 \text{ GPa}; \quad \nu_f = 0.25; \quad Y_f^u = 1000 \text{ MPa};$$

$$E_m = 106 \text{ GPa}; \quad E_m^T = 7.6 \text{ GPa}; \quad Y_m^y = 850 \text{ MPa};$$

$$Y_m^u = 1000 \text{ MPa}; \quad \nu_m = 0.33$$

where Y_m^y and Y_m^u are the matrix yield stress and ultimate strength, respectively, and Y_f^u is the fibers ultimate strength.

The stress-strain behavior in the direction of the fibers for two different fiber volume fractions is presented in Fig. 5. Numerical results are compared with experimental ones obtained by Gundel [32] and analytical ones given by Huang [3]. A good agreement with analytical and experimental results is obtained.

4.4 Composite Laminates. Material data and the different types of analysis presented in this section correspond to the failure exercise previously mentioned [5,7]. All the laminates studied are formed by laminas composed of a soft matrix with continuous unidirectional fibers. The mechanical properties of four types of epoxy resins and four types of glass and carbon fibers are presented in Tables 1 and 2, respectively. The determination of the mechanical properties is not always straightforward. As a consequence, variability and inaccuracy are expected to be found.

Table 1 Matrix mechanical properties [5]

Type of Matrix	3501-6 epoxy	BSL914C epoxy	LY556/HT907/DY063 epoxy	MY750/HY917/DY063 epoxy
Young modulus, E_m (GPa)	4.2	4.0	3.35	3.35
Shear modulus, G_m (GPa)	1.567	1.481	1.24	1.24
Poisson ratio, ν_m	0.34	0.35	0.35	0.35
Tension strength, Y_{mt} (MPa)	69	75	80	80
Compres. strength, Y_{mc} (MPa)	250	150	120	120
Shear strength, S_m (MPa)	50	70	⋯	⋯
Ultimate tension strain., ε_{mt} (%)	1.7	4	5	5

Almost all experimental results used were derived from tests on tube specimens. Numerical results were all obtained for a 100 mm × 100 mm model with the lamina or laminate thickness and a three-dimensional analysis was performed. The use of these models is justified by the fact that in tube specimens a global plane stress state for the lamina or the laminate is obtained.

4.4.1 Unidirectional Laminas. Before analyzing the behavior of the laminate it is interesting to analyze the behavior of unidirectional laminas under biaxial tension tests to obtain the corresponding failure envelopes. In all cases, a Mohr Coulomb failure criterion was used for the matrix while a Drucker Prager criterion was used for the fibers failure.

Figure 6 shows the comparison of the failure envelope obtained using the proposed model with experimental results [7] and with other numerical models [12] for an unidirectional glass fiber reinforced lamina (E-Glass/LY556/HT907/DY063), with a fiber volume fraction $k_f = 0.62$, under shear stresses and normal stresses orthogonal to fiber direction. Experimental results correspond to tubes of 60 mm internal diameter and 2 mm thick. It can be observed that the model closely reproduces the experimental failure envelope. For this particular example, the failure is always produced by the matrix failure.

Figure 7 shows the comparison of failures stresses obtained using the model proposed and other numerical models [11] with experimental ones [7] for an unidirectional carbon fiber reinforced lamina (T300/BSL914C epoxy), with a fiber volume fraction $k_f = 0.60$, under shear stresses and normal stresses in the direction of

Table 2 Fibers mechanical properties [5]

Type of fiber	AS4	T300	E-Glass 21 × 43 Gevetex	Silenka E-Glass 1200 tex
Long. Young modulus, E_{f1} (GPa)	225	230	80	74
Transv. Young modulus, E_{f2} (GPa)	15	15	80	74
Long. shear. modulus, G_{f12} (GPa)	15	15	33.33	30.8
Poisson ratio ν_{f12}	0.2	0.2	0.2	0.2
Transv. shear modulus., G_{f23} (GPa)	7	7	33.33	30.8
Long. tensile strength, X_{ft} (MPa)	3350	2500	2150	2150
Long. compres. strength, X_{fc} (MPa)	2500	2000	1450	1450
Ultimate tensile strain, ε_{f1T} (%)	1.488	1.086	2.687	2.905
Ultimate compres. strain, ε_{f1c} (%)	1.111	0.869	1.813	1.959

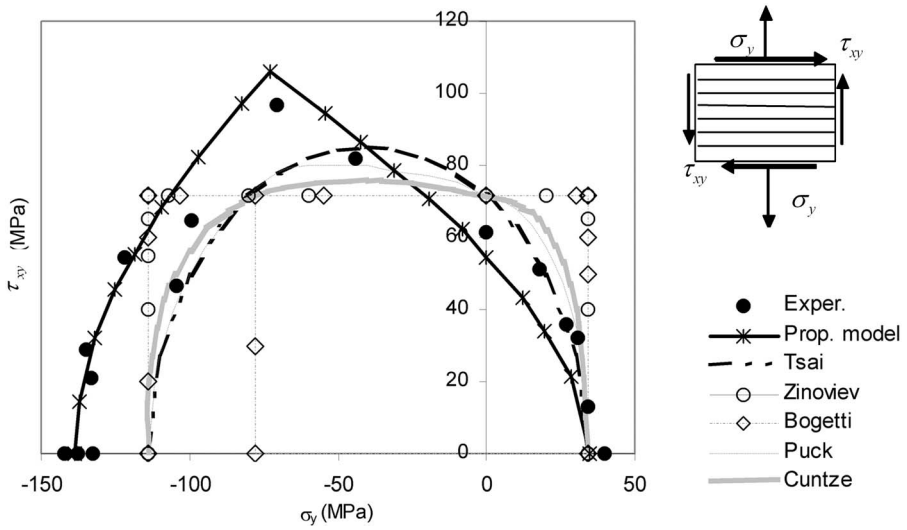

Fig. 6 Failure envelope for a unidirectional lamina (E-Glass/LY556/HT907/DY063)

the fibers. Experimental results were obtained from tubes tested under combined axial tension or compression and torsion. The tubes were 32 mm diameter and 1.9–2.3 mm thick. In this example, failure is generated by the failure of the fibers for moderated shear stresses or by the matrix failure for greater shear stresses. It could be seen that the model approximately reproduces the lamina failure envelope but does not result conservative in the zone corresponding to compression in fiber direction because it is not able to capture buckling and associated failure.

Figure 8 shows the comparison of the failure envelope obtained using the model and other numerical models [12] with experimental results [7] for an unidirectional glass fiber reinforced lamina (Silenka E-Glass 1200 tex MY750/HY917/DY063 epoxy),l with a fiber volume fraction $k_f=0.60$ under normal stresses in the direction of the fibers and in the orthogonal one. Most of the experimental results were obtained from testing nearly circumferentially wound tubes under combined internal pressure and axial load. The specimens were 100 mm inner diameter, 300 mm long and approximately 0.95 mm or 1.2 mm thick. In this case, the failure is produced by the fibers failure when the stress in fiber direction is prevalent or by the matrix failure in the directional perpendicular to the fibers.

4.4.2 Laminates

4.4.2.1 $(90\ \text{deg}/\pm 30\ \text{deg})_s$ *laminate (E-Glass/LY556/HT907/DY063).* The structure of this laminate is indicated in Fig. 9. Soden et al. [5] use a different nomenclature but refer to a $(90/\pm 30\ \text{deg})_s$ laminate. The angle indicated corresponds to the angle of the fibers to axe X that is coincident with the axe of the tubes experimentally tested. The total thickness of the laminate is 2 mm, while $h_1=0.172$ mm and $h_2=0.414$ mm. As a consequence, laminas at ±30 deg represent 82.8% of the total thickness and laminas at 90 deg represent the remaining 17.2%. The laminate is not isotropic and, therefore, different types of failure under biaxial stresses can take place, not only those due to fibers failure. The fiber volume fraction of each lamina is $k_f=0.62$. Experimental results were obtained from 60 mm inside diameter and 2 mm thick tubes tested under combined pressure and axial load and combined torsion and axial load.

Figures 9(*a*) and 9(*b*) show the failure envelopes obtained with the model for this laminate under biaxial stresses and their comparison with experimental results [7] and other theories [11]. Figure 9(*a*) corresponds to different combinations of normal stresses

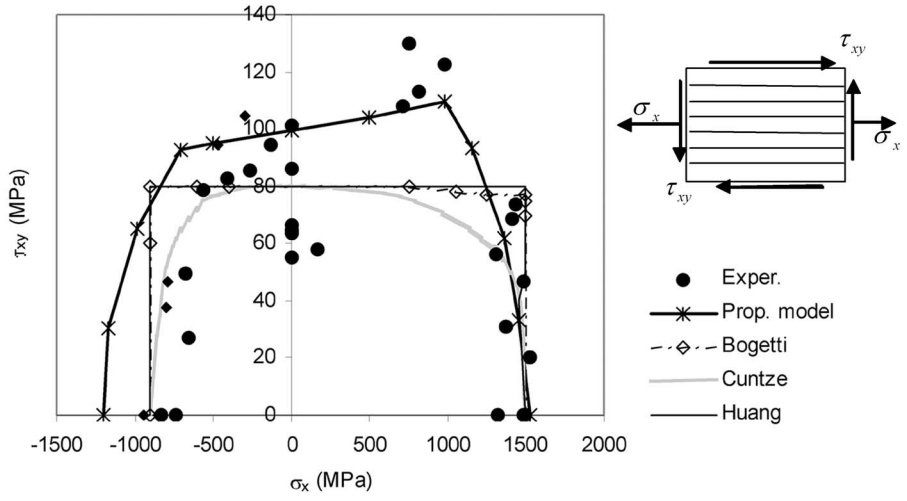

Fig. 7 Failure envelope for a unidirectional lamina (T300/BSL914C epoxy)

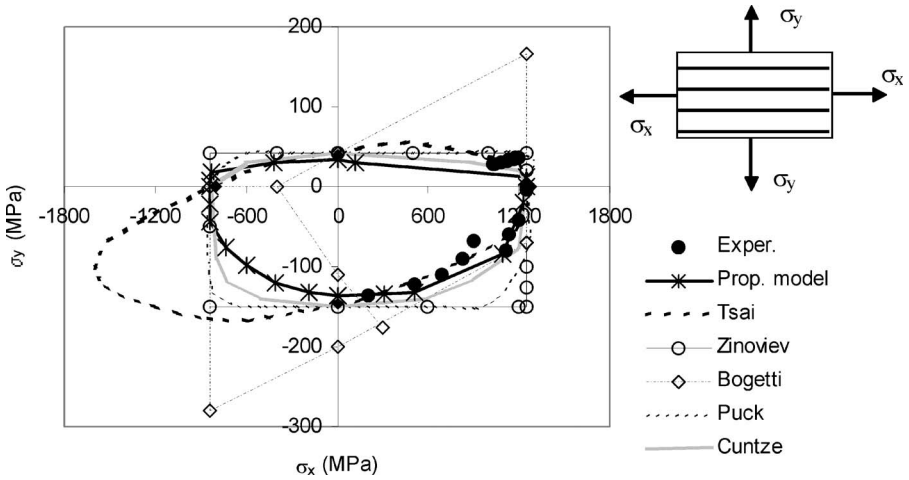

Fig. 8 Failure envelope for a unidirectional lamina (Silenka E-Glass 1200 tex MY750/HY917/DY063 epoxy)

in the plane. Failure is due to matrix failure in the compression-compression zone and it is caused by fiber failure for most of the other stress combinations. Figure 9(*b*) represents a combination of normal and shear stresses. Composite failure is due to matrix failure in compression zone and it is mostly due to fiber failure in pure shear and tension zones. In general, the model reproduces experimental results but leads to nonconservative results under biaxial compression stress states.

4.4.2.2 $(90\ \text{deg}/\pm 45\ \text{deg}/0\ \text{deg})_s$ *laminate AS4/3501-6.* The

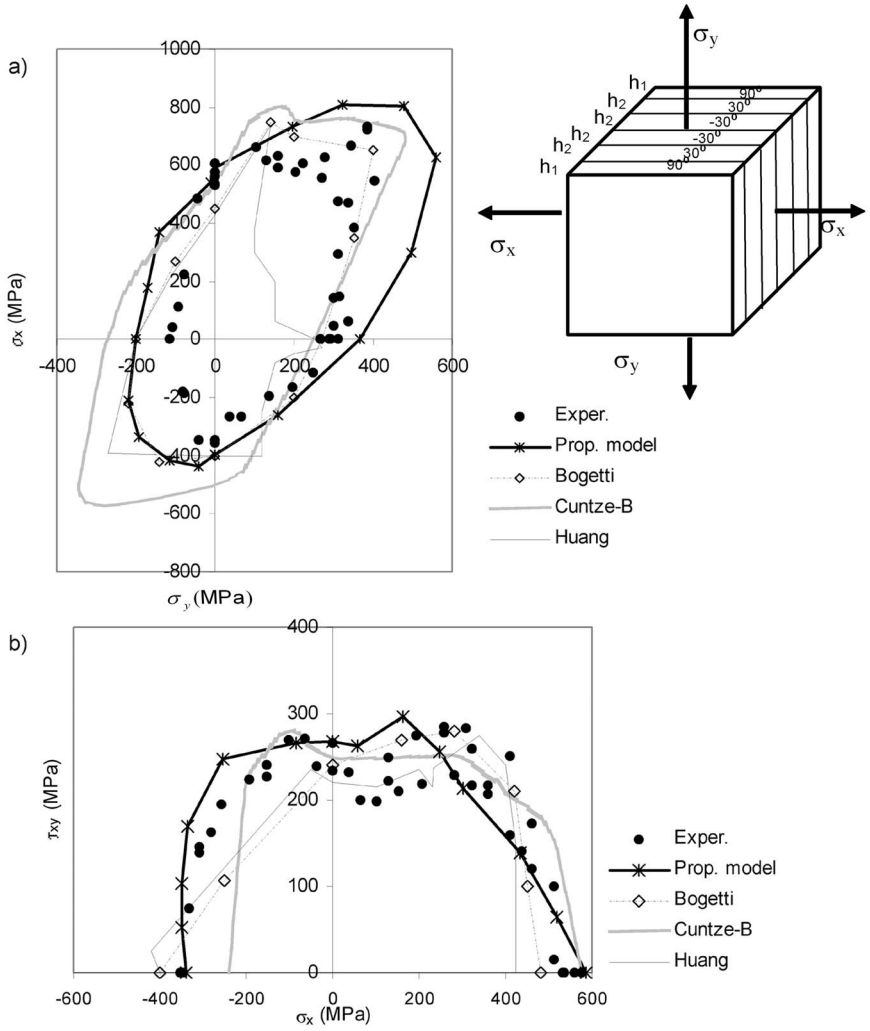

Fig. 9 Failure envelope for a $(90\ \text{deg}/\pm 30\ \text{deg})_s$ laminate (E-Glass/LY556/HT907/DY063). (*a*) σ_x versus σ_y; (*b*) τ_{xy} versus σ_x.

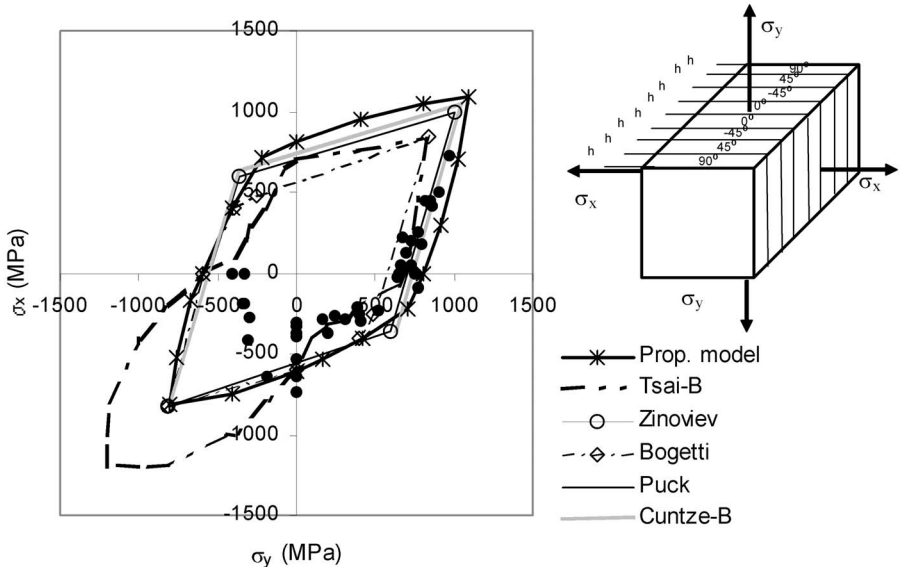

Fig. 10 Failure envelope for $(90\ \text{deg}/\pm 45\ \text{deg}/0\ \text{deg})_s$ laminate (AS4/3501-6)

structure of this quasi isotropic laminate is shown in Fig. 10. The total thickness of the laminate is 1.1 mm and all the laminas have the same thickness. The fiber volume fraction of each lamina is k_f=0.60. The tests were carried out by subjecting 96 mm inside diameter tubular specimens to pressure and axial loads.

Figure 10 shows the failure envelope obtained with the model and its comparison with experimental results [7] and other theories [12] for biaxial stress states. In general, the tests have shown failure by fibers fracture being the failure controlled by fibers strength. Experimental results in the compression-compression quadrant represent structural failure produced by buckling of the laminate and not by crushing of the material. Numerical results confirm that composite failure is due to fiber failure and dependent on fibers compressive and tensile strength. In general, the model results are close to experimental ones except those in the compression-compression zone where the model is not able to reproduce buckling failure.

4.4.2.3 $(\pm 55\ \text{deg})_s$ *laminate (Silenka E-Glass 1200 tex MY750/HY917/DY063 epoxy).* The structure of this laminate is shown in Fig. 11. The total thickness of the laminate is 1 mm and all the laminas have the same thickness. The fiber volume fraction of each lamina is k_f=0.60. Experimental results were obtained from tubes with 100 mm inner diameter and 1 mm thick.

Figure 11 also shows the failure envelope obtained with the model and its comparison with experimental results [7] and other theories [12]. Numerical results show that failure is mostly due to fiber failure, except for the zone where the failure envelope narrows that corresponds to matrix tensile failure. A good agreement between numerical and experimental results is achieved.

5 Conclusions

A general model for composite materials that starts from a simple idealization of the behavior at individual constituents level has been presented in this paper. The model gives the behavior of a composite material from the constitutive models of the components, their location in the composite and volume fraction. Due to its assumptions the model is especially appropriate for the treatment of fiber reinforced composite laminates. It allows the anisotropy and nonlinear behavior of the materials to be considered.

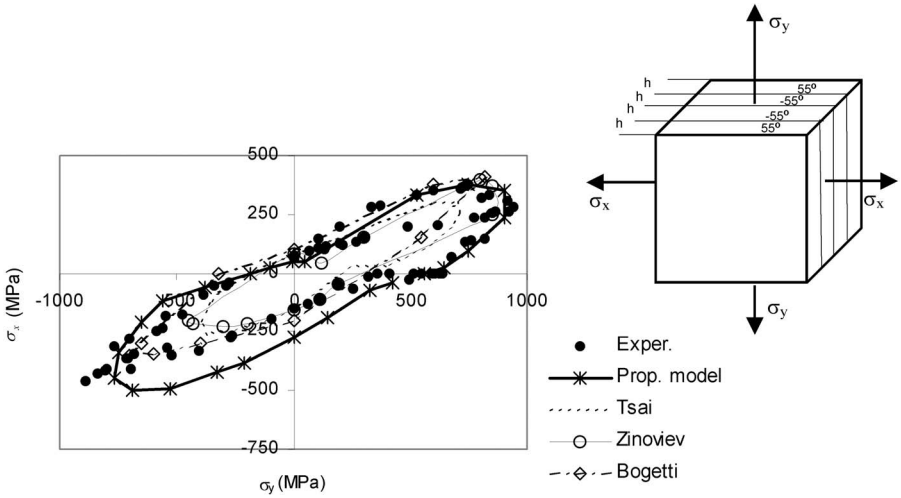

Fig. 11 Failure envelope for $(\pm 55\ \text{deg})_s$ laminate (Silenka E-Glass 1200 tex MY750/HY917/DY063 epoxy)

The resulting model describes the behavior and the failure of the composite taking into account what is happening in each component and it is able to identify the failure mode of the composite produced by the failure of one or more components. It is capable of reproducing complex failure modes that change from the matrix to the fibers depending on the type of stress state.

In contrast to most existing models for laminated composites, the model presented is of relatively simple numerical implementation in a nonlinear finite element program and it is able to reproduce nonlinear behavior of laminates. The model approximately reproduces the stiffness of the laminas and the failure of unidirectional laminas and composite laminates. The differences with experimental results are not greater than those obtained with the best-ranked models at the failure exercise [9–12].

Acknowledgment

The author wishes to thank the economical support of CONICET and CIUNT and Mrs. Amelia Campos for the English revision.

References

[1] Chaboche, J. L., Lesne, O., and Pottier, T., 1998, "Continuum Damage Mechanics of Composites: Towards a Unified Approach," *Damage Mechanics in Engineering Materials, Studies in Applied Mechanics 46*, Elsevier Voyiadjis, Ju and Chaboche, Elsevier, Vol. 46, pp. 3–26.

[2] Oller, S., Miquel, J., and Zalamea, F., 2005, "Composite Material Behavior Using a Homogenization Double Scale Method," J. Engrg. Mech. Div., **131**, pp. 65–79.

[3] Huang, Z., 2001, "Micromechanical Prediction of Ultimate Strength of Transversely Isotropic Fibrous Composites," Int. J. Solids Struct., **38**, pp. 4147–4172.

[4] Hinton, M. J., and Soden, P. D., 1998, "Predicting Failure in Composite Laminates: The Background to the Exercise," Compos. Sci. Technol., **58**, pp. 1001–1010.

[5] Soden, P. D., Hinton, M. J., and Kaddour, A. S., 1998, "Lamina Properties, Lay-Up Configurations and Loading Conditions for a Range of Fibre-Reinforced Composite Laminates," Compos. Sci. Technol., **58**, pp. 1011–1022.

[6] Hinton, M. J., Kaddour, A. S., and Soden, P. D., 2002, "Evaluation of Failure Prediction in Composite Laminates: Background to 'Part B' of the Exercise," Compos. Sci. Technol., **62**, pp. 1481–1488.

[7] Soden, P. D., Hinton, M. J., and Kaddour, A. S., 2002, "Biaxial Test Results for Strength and Deformation of a Range of E-Glass and Carbon Fiber Reinforced Composite Laminates: Failure Exercise Benchmark Data," Compos. Sci. Technol., **62**, pp. 1489–1514.

[8] Hinton, M. J., Kaddour, A. S., and Soden, P. D., 2004, "Evaluation of Failure Prediction in Composite Laminates: Background to 'Part C' of the Exercise," Compos. Sci. Technol., **64**, pp. 321–327.

[9] Soden, P. D., Hinton, M. J., and Kaddour, A. S., 1998, "A Comparison of the Predictive Capabilities of Current Failure Theories for Composite Laminates," Compos. Sci. Technol., **58**, pp. 1225–1254.

[10] Kaddour, A. S., Hinton, M. J., and Soden, P. D., 2004, "A Comparison of the Predictive Capabilities of Current Failure Theories for Composite Laminates: Additional Contributions," Compos. Sci. Technol., **64**, pp. 449–476.

[11] Hinton, M. J., Kaddour, A. S., and Soden, P. D., 2004, "A Further Assessment of the Predictive Capabilities of Current Failure Theories for Composite Laminates: Comparison with Experimental Evidence," Compos. Sci. Technol., **64**, pp. 549–588.

[12] Soden, P. D., Kaddour, A. S., and Hinton, M. J., 2004, "Recommendations for Designers and Researchers Resulting From the World-Wide Failure Exercise," Compos. Sci. Technol., **64**, pp. 589–604.

[13] Zinoviev, P., Grigoriev, S. V., Labedeva, O. V., and Tairova, L. R., 1998, "Strength of Multilayered Composites Under Plane Stress State," Compos. Sci. Technol., **58**, pp. 1209–1224.

[14] Zinoviev, P., Labedeva, O. V., and Tairova, L. R., 2002, "Coupled Analysis of Experimental and Theoretical Results on the Deformation and Failure of Laminated Composites Under a Plane State of Stress," Compos. Sci. Technol., **62**, pp. 11711–11724.

[15] Bogetti, T. A., Hoppel, C. P. R., Harik, V. M., Newill, J. F., and Burns, B. P., 2004, "Predicting the Nonlinear Response and Progressive Failure of Composite Laminates," Compos. Sci. Technol., **64**, pp. 477–485.

[16] Liu, K. S., and Tsai, S. W., 1998, "A Progressive Quadratic Failure Criterion of Alaminate," Compos. Sci. Technol., **58**, pp. 1023–3102.

[17] Kuraishi, A., Tsai, S. W., and Liu, K. A., 2002, "A Progressive Quadratic Failure Criterion Part B," Compos. Sci. Technol., **62**, pp. 1682–1696.

[18] Puck, A., and Schurmann, H., 1998, "Failure Analysis of FRP Laminates by Means of Physically Based Phenomenological Models," Compos. Sci. Technol., **58**, pp. 1045–1068.

[19] Puck, A., and Schurmann, H., 2002, "A Failure Analysis of FRP Laminates by Means of Physically Based Phenomenological Models—Part B," Compos. Sci. Technol., **62**, pp. 11633–11672.

[20] Cuntze, R. G., and Freund, A. A., 2004, "The Predictive Capability of Failure Mode Concept-Based Strength Criteria for Multidirectional Laminates," Compos. Sci. Technol., **64**, pp. 343–377.

[21] Oller, S., Oñate, E., Miquel, J., and Botello, S., 1996, "A Plastic Damage Constitutive Model for Composite Materials," Int. J. Solids Struct., **33**(17), pp. 2501–2518.

[22] Luccioni, B., and López, D., 2002, "Modelo Para Materiales Compuestos Con Deslizamiento de Fibras," Análisis y *Cálculo de Estructuras de Materiales Compuestos*, CIME, Barcelona, España, Chap. 13 pp. 411–431.

[23] Luccioni, B., López, D., and Danesi, R., 2005, "Bond Slip in Reinforced Concrete Elements," J. Struct. Eng., **131**(11), pp. 1690–1698.

[24] Betten, J., 1988, "Application of Tensor Functions to the Formulation of Yield Criteria for Anisotropic Materials," Int. J. Plast., **4**, pp. 29–46.

[25] Oller, S., Botello, S., Miquel, J., and Oñate, E., 1995, "An Anisotropic Elasto-Plastic Model Based on an Isotropic Formulation," Eng. Comput., **12**, pp. 245–262.

[26] Luccioni, B., Oller, S., and Danesi, R., 1995, "Plastic Damaged Model for Anisotropic Materials," Appl. Mech. Eng., **1**, pp. 124–129.

[27] Luccioni, B., Oller, S., and Danesi, R., 1996, "Coupled Plastic-Damaged Model," Comput. Methods Appl. Mech. Eng., **129**, 81–89.

[28] Car, E., Oller, S., and Oñate, E., 1999, "A Large Strain Plasticity Model for Anisotropic Material—Composite Material Application," Int. J. Plast., **17**(11), pp. 1437–1463.

[29] Oller, S., Car, E., and Lubliner, J., 2003, "Definition of a General Implicit Orthotropic Yield Criterion," Comput. Methods Appl. Mech. Eng., **192**, pp. 895–912.

[30] Luccioni, B., and Martín, P. E., 1997, "Modelo Elastoplástico Para Materiales Ortótropos," Mét. Num. Cálc. Dis. Ing. RIMNI, **13**(4), pp. 603–614.

[31] Kriz, R. D., and Stinchomb, W. W., 1979, Exp. Mech., **19**, 41.

[32] Gundel, D. B., and Wawner, F. E., 1997, "Experimental and Theoretical Assessment of the Longitudinal Tensile Strength of Unidirectional SiC-Fiber/Titanium-Matrix Composites," Compos. Sci. Technol., **57**, pp. 471–481.

Numerical Aspects on the Prediction of Stability Boundaries of Two-Phase Natural Circulation Circuits, Considering Flashing Evaluation

P. Zanocco
e-mail: zanoccop@cab.cnea.gov.ar

D. Delmastro

M. Giménez

Centro Atómico Bariloche, CNEA,
Av.a Bustillo Km. 9,500,
San Carlos de Bariloche,
R8402AGP Río Negro,
Argentina

In this work, the stability of a two-phase, natural circulation circuit is analyzed, using a specially developed model. This thermohydraulic model results in a set of coupled, nonlinear, first-order partial differential equations, which are solved by means of the up-wind finite difference method, using combinations of explicit and implicit methods for the numerical integration of the different balance equations. An adaptive nodalization scheme is implemented, minimizing the error of the propagation of small perturbations through the discretized volumes and especially the ones having two-phase flow regime. A linearization method is implemented by means of numerical perturbations. Frequency domain calculations are carried out, allowing a rapid visualization of the stability of the linearized system. Two cases are analyzed: a test case, where the code is compared in a wide range of qualities with an analytical model, and an application case, where the model is used to analyze the stability of an integral reactor cooled by natural circulation. The CAREM prototype is taken as a reference. In both cases, the numerical diffusion and integration errors are analyzed in the stability limit prediction by means of a convergence analysis using different nodalization and numerical integration criteria.
[DOI: 10.1115/1.2178835]

1 Introduction

It is well known that boiling systems may oscillate because of two-phase dynamics and may be unstable under particular conditions. This problem has been widely studied under classical boiling water reactors (BWR) conditions [1,2].

In many cases, analytical solutions have been used by means of Laplace transforming the simplified and linearized equations [3]. This allows stability analysis in the frequency domain and determining the margin to instability. Most of the stability maps for the most common BWR reactors were constructed with these tools. Nevertheless, they were not able to predict unstable behaviors and, due to the complexity of the mathematical formulations, they were often limited to very simplified cases.

Detailed-system codes were developed to study mainly accidents or operational transients involving well-defined transitions. Numerical methods were validated under these conditions. In most cases, high artificial diffusion is introduced in the numerical solution [4], usually looking for robustness. However, stability events are initiated by very small perturbations, which are usually damped as a result of numerical diffusion.

Numeric considerations of time-domain codes were enhanced in order to reduce the impact of numerical diffusion and to enable the study of the nonlinear behavior [5]. In some cases, simplified phenomenological models were developed, in order to understand the basic phenomena involved in the nonlinearities [6,7]. Some detailed-system codes were also improved in order to cope with stability considerations [8], which in some cases showed good agreement with experiments [9].

In the last decade, interest was focused on boiling natural circulation systems. A number of studies were carried out, motivated by the intention of developing an advanced BWR without recirculation pumps [10,11]. A different kind of instability was studied more deeply, promoted by the combination of natural circulation and a low void-fraction regime. This kind of instability was pointed out in experimental observations [12] and was reported for the Dodewaard natural circulation BWR [13]. Some theoretical analyses were carried out regarding these instabilities [14], and a set of planned experimental studies has recently been announced [15] and is meant to serve as a future validation database.

In an integral self-pressurized reactor, the control of pressure is achieved by thermal imbalance within the primary loop. Therefore, in order to control pressure, the water of the primary circuit must be coupled thermodynamically with the steam located in the dome. This implies a heat sink within the steam zone to promote a continuous condensation [16]. This configuration achieves an excellent self-regulation. Nevertheless, since the system is very close to saturation pressure, it works with a continuous steam flow from the riser, in order to compensate for the condensation in the dome. This condition, together with the natural circulation, could make the reactor subject to instabilities. Moroever, the long riser provokes an important pressure change due to the hydraulic height. This allows the possibility of the occurrence of boiling in this region due to the decrease of saturation enthalpy, an effect known as flashing. This was pointed out as an important factor within these conditions [17,18].

In this work, the HUARPE numerical code is used, a purpose-designed code that was originally developed to model the reactor dynamics during thermal imbalance transients. It was compared against other codes (RETRAN and RELAP) and experimental data from the full height, full pressure natural circulation circuit

Contributed by the Applied Mechanics Division of ASME for publication in the JOURNAL OF APPLIED MECHANICS. Manuscript received May 24, 2005; final manuscript received December 29, 2005. Review conducted by G. C. Buscaglia. Discussion on the paper should be addressed to the Editor, Prof. Robert M. McMeeking, Journal of Applied Mechanics, Department of Mechanical and Environmental Engineering, University of California-Santa Barbara, Santa Barbara, CA 93106-5070, and will be accepted until four months after final publication of the paper itself in the ASME JOURNAL OF APPLIED MECHANICS.

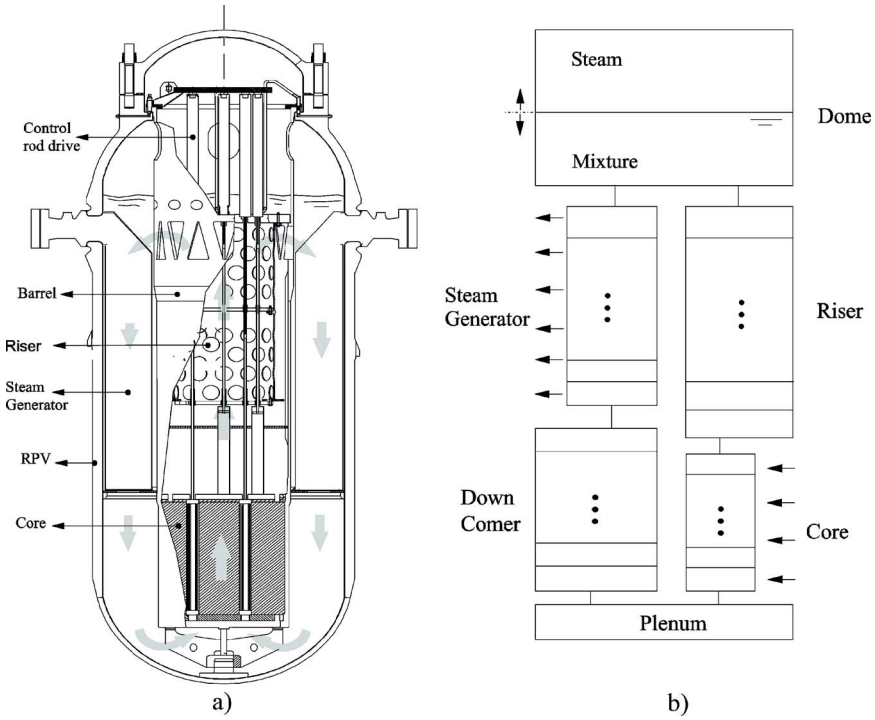

Fig. 1 Carem-25 primary system: (*a*) diagram and (*b*) used nodalization scheme

(CAPCN) which simulates the CAREM primary system [19–21], showing good agreement in all cases. The code is computationally efficient and has been used for parametric analyses for design purposes [22]. Moreover, the use of our own code allows us to introduce modifications in order to analyze the different physical and numerical models. This encouraged us to improve it to perform stability analyses, with a special emphasis on minimizing the numerical diffusion and integration errors, and the implementation of a linearization method. Linear and nonlinear aspects were recently studied for the CAREM prototype reactor [23,24]. In these works, interest was focused on studying the impact of different physical models in the stability prediction, involving varying degrees of detail: the basic ones, which are typical in simplified models used to obtain analytical solutions and to understand the nature of oscillations, and also the study of the impact of specific phenomenology, such as self-pressurization and the flashing effect.

The purpose of this work is to focus on the numerical model and its ability for stability prediction. Two main aspects are concerned: the use of different options for numerical integration (i.e., explicit or implicit methods, or their combination) and the nodalizations employed in the predictions. The second one has been recognized as an important factor in conventional codes. We have also studied the use of an adaptive nodalization scheme, proposed in HUARPE code, designed to optimize the nodalization in order to minimize the damping of small perturbations.

2 CAREM Reactor Description

The CAREM reactor prototype (CAREM-25, 100 MWth) [25–28] is taken as a reference. A diagram of the primary system of this reactor is shown in Fig. 1(*a*). The main design features consist of an integral primary cooling system, primary cooling by natural circulation, self-pressurization, and safety systems relying on passive features.

The steam dome is located inside the upper zone of the pressure vessel. The coolant (water), confined all along the RPV by a barrel, leaves the reactor core and enters the riser. It then proceeds towards the outer annular volume through the barrel windows, finally entering the steam generators (SGs). The circuit is completed by the down-comer and the lower plenum.

The control-rod-drive (CRD) mechanisms are hydraulically operated and are located within the RPV. This design therefore avoids the use of mechanical shafts passing through the RPV wall, which in turns eliminates the possibility of a control-rod ejection and a large LOCA.

Due to self-pressurization, the system keeps the pressure very close to saturation value. The continuous condensation promoted by the flow controlling the CRD and, to a lesser extent, by the RPV structures, ensures the thermodynamical coupling of the steam zone with the primary circuit. The negative reactivity feedback coefficients and the large water inventory of the primary circuit, combined with the self-pressurization features, support an excellent response under operational transients. Nevertheless, stability phenomena should be studied to guarantee this behavior.

3 Theoretical Model

The model developed includes the coolant circuit and steam dome, according to the balance equations (mass, energy, and momentum) and the core behavior, taking into account the neutronic feedback. A complete description of the theoretical model can be found in [23]. The main hypotheses of the model are as follows:

- One-dimensional flux.
- Two-phase drift-flux equilibrium model for the circuit (a homogeneous equilibrium model is also available).
- Two-phase, nonequilibrium, stratified model for the dome.
- Time-dependent pressure with a hydraulic-height correction for the calculation of fluid saturation properties.
- No carry-under of bubbles to the SG.
- Point-kinetic ordinary equations for the core neutronics.
- One-dimensional model for the core structure, axially nodalized.

4 Basic Equations

This section introduces the equations especially relevant for the stability analysis. The four-equation drift-flux model is used in the

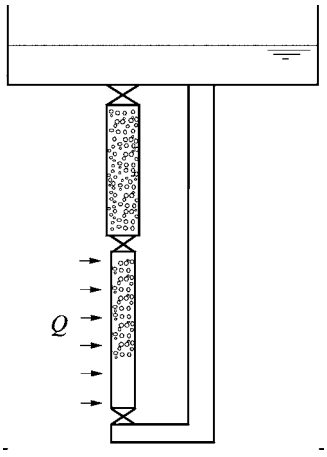

Fig. 2 Natural circulation loop used in the test case

program [29], where a relative velocity between phases is predicted in terms of two flow-regime-dependent parameters, the drift velocity and the distribution parameter.

In order to obtain the mass flow due to the buoyancy force (natural circulation), the momentum and mass equations have been solved, the spatial distribution of flow being obtained with the mass equation:

$$\frac{\partial \rho}{\partial t} + \frac{1}{A}\frac{\partial GA}{\partial z} = 0 \tag{1}$$

where ρ is the density, G is the mass flow, A is the flow area, and z is the spatial coordinate.

The momentum equation is solved by integrating analytically over the whole loop; thus:

$$\frac{d\hat{G}}{dt} = -\oint \rho g \cos\theta dz - \oint \frac{f\Phi_{f0}^2 |G|G}{2D_h\rho_l} dz - \sum \left(K\frac{|G|G}{2\rho} \right) - \sum \frac{G^2}{2\rho}\left(1 - \frac{A_i}{A_o}\right) \tag{2}$$

where g is the gravity, D_h is the hydraulic diameter, θ is the vertical angle, f is the Moody friction factor, K is the local friction, subscripts i and o are input and output, respectively, and Φ_{f0}^2 is the two-phase friction loss multiplier. $\hat{G}$ is the total momentum of the system, expressed as:

$$\hat{G} \equiv \oint G dz \tag{3}$$

To obtain the enthalpies of the circuit, the energy equation is solved:

$$\rho\frac{\partial h}{\partial t} + \frac{1}{A}\frac{\partial (G\hat{h}A)}{\partial z} - \frac{h}{A}\frac{\partial (GA)}{\partial z} = \frac{q'}{A} + \frac{\partial P}{\partial t} \tag{4}$$

where P is the pressure, q' is the linear heat flux, and h and $\hat{h}$ are enthalpies averaged with mass and flow, respectively.

4.1 Fuel Dynamics. Fuel structure is modeled as one-dimensional, nodalized in the axial direction. The time derivative for the fuel temperature is proportional to the difference between the power generated and that transferred to the fluid. An axial temperature distribution is assumed, neglecting axial conduction. Thus:

$$\frac{M_c Cp_c}{L_c}\frac{dT_c(z)}{dt} = W(z)\frac{Q_c}{L_c} - h'\mathrm{Per}[T_c(z) - T(z)] \tag{5}$$

T is temperature, M is the mass, Cp is the specific heat, Per is the heated perimeter, Q is generation power, L is the length, and the subscript c stands for "core." W is the power-axial-profile weighting factor.

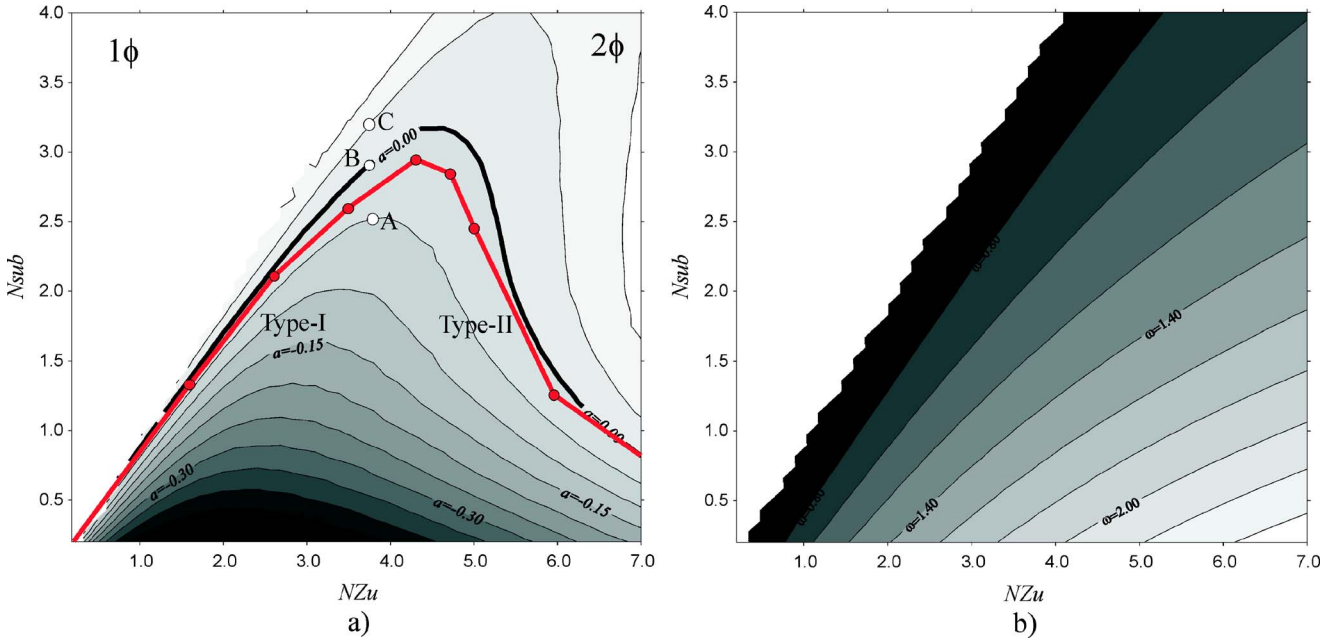

Fig. 3 (*a*) Level diagram obtained with the numerical model, and the stability limit obtained with the analytical model. (*b*) Frequencies of oscillations, according to the numerical model.

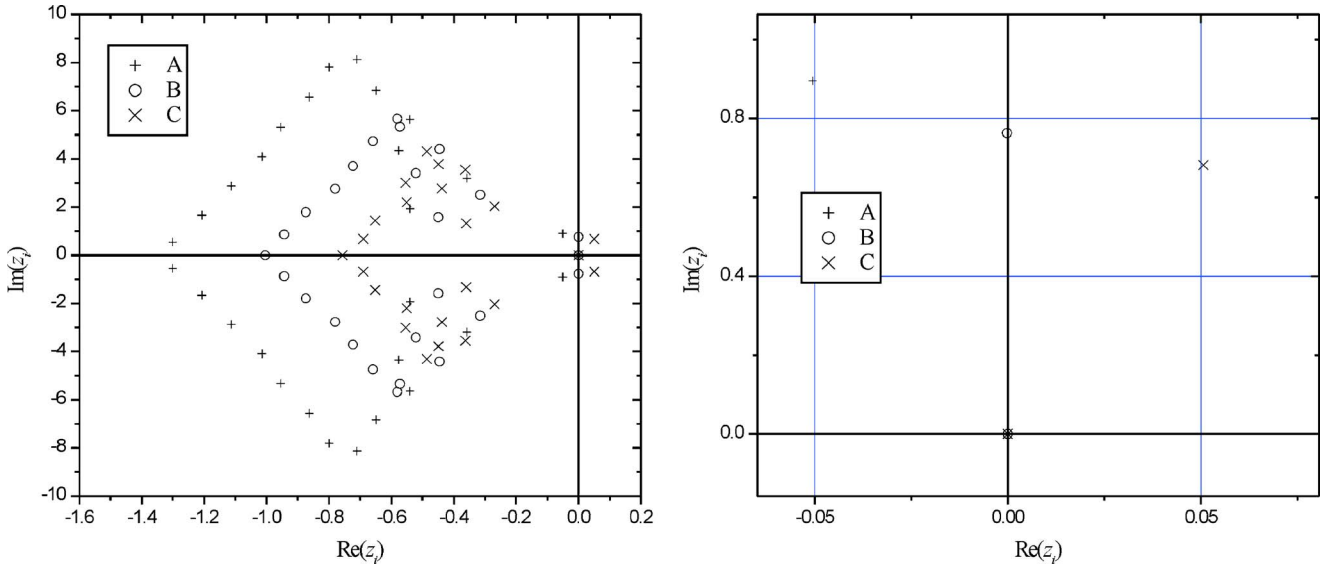

Fig. 4 Eigenvalues of the discretized and linealized system, in the three points analyzed

5 Numerical Solution

A diagram of the reactor nodalization is shown in Fig. 1(*b*). The dome is divided into two variable volumes to represent the steam and the mixture zones. The equations are discretized according to the explicit, up-wind scheme. A special effort was made to minimize the numerical diffusion in the mixture drift-flux energy equation.

5.1 Numerical Integration Scheme. The stated equations form a set of nonlinear, first-order partial differential equations, which are strongly coupled because the flow profile in a certain time depends on the time derivative of the density in the same time. This depends on the time derivatives of enthalpies, which in turns depends on the flow profile. The variables need to be made to converge by an internal iteration, in order to achieve a well-converged solution. This procedure minimizes the instabilities caused by numerical factors involving convergence problems, which could mask the stability analysis.

5.2 Adaptive Nodalization. The concept of adaptive node boundaries is frequently used, for example, to improve the representation of λ movements [30] or to achieve an appropriate representation of enthalpy fronts [31]. In our case, an adaptive nodalization scheme is adopted in order to achieve a nondiffusive propagation through the system when small perturbations are concerned, keeping the nodalization fixed in time.

An interesting aspect of the combination of up-wind discretization and explicit integration is that the numerical error or numerical diffusion is minimized when the time step equals exactly the fluid residence time in a volume. This condition coincides the Courant numerical stability limit [32]; in this condition, a small perturbation would be appropriately propagated through the volume.

In order to achieve a nondiffusive propagation through the system, the adaptive nodalization scheme allows us to reach the Courant limit in all nodes, with special attention to the core and riser zones; these components are allowed to have a two-phase regime and are therefore potentially a cause of instability.

In the program, a first nodalization is used in the initialization subroutine in order to set all variables at a steady-state condition. In particular, the fluid velocity profile is calculated and the node length at any position can be set up in order to establish the same fluid residence time in all the discretized volumes.

This scheme is applied to the riser, where the time step is defined as the time of residence/number of nodes ratio. The same algorithm is applied to the core, save the first volume in the inlet; this operates as a "regulating node" in order to allow all the above nodes to match the same Courant limit, without violating the geometry condition due to different fluid-residence time for core and riser. In the rest of the circuit, the nodalization is automatically made with the maximum number of nodes for a component which assures a maximum Courant ratio, without violating the numerical stability limit.

When nodalization refining in a component is needed, it is possible to introduce intermediate time steps in the energy equation (NIT) for solving the enthalpies of that single component, while keeping constant the remaining variables over the time step. This is used in the core, where a large number of nodes are needed to reproduce a nonuniform axial power. This avoids penalization in nodalization in the rest of the circuit.

The adaptive nodalization strategy is made just after the initialization stage in the calculations and will reduce the damping of small perturbation movements, especially in the whole two-phase region.

5.3 Linearization Method. To perform a stability analysis in the frequency domain, the system is linearized around a steady-state condition. This is carried out by means of the small-perturbations method, of which some details are explained in [23,33]. This representation allows a rapid visualization of the stability of the linearized system in a very simple manner, avoiding an exhaustive analysis of all possible transients in a time-domain approach. The discretized equations governing a given stability problem and their boundary conditions can be written in a compact form as:

$$\frac{d\delta y}{dt} \approx F(y_0, p, \Delta t)\delta y^n \tag{6}$$

where y represents the vectors of independent variables or state variables, p is a vector of physical and numerical parameters, and δ denotes a deviation from the steady-state condition. F embeds the continuous-time system predicted by the discrete-time numerical method, and its eigenvalues are relevant for the stability analysis: the imaginary component is the frequency of an oscillation mode, and the real part is the amplification or damping of that oscillation mode. It is therefore possible to evaluate the amplification and frequency of the longer surviving mode of oscillation, a and ω, which correspond to the real and imaginary parts, respectively, of the matrix F eigenvalue having the largest real part. The

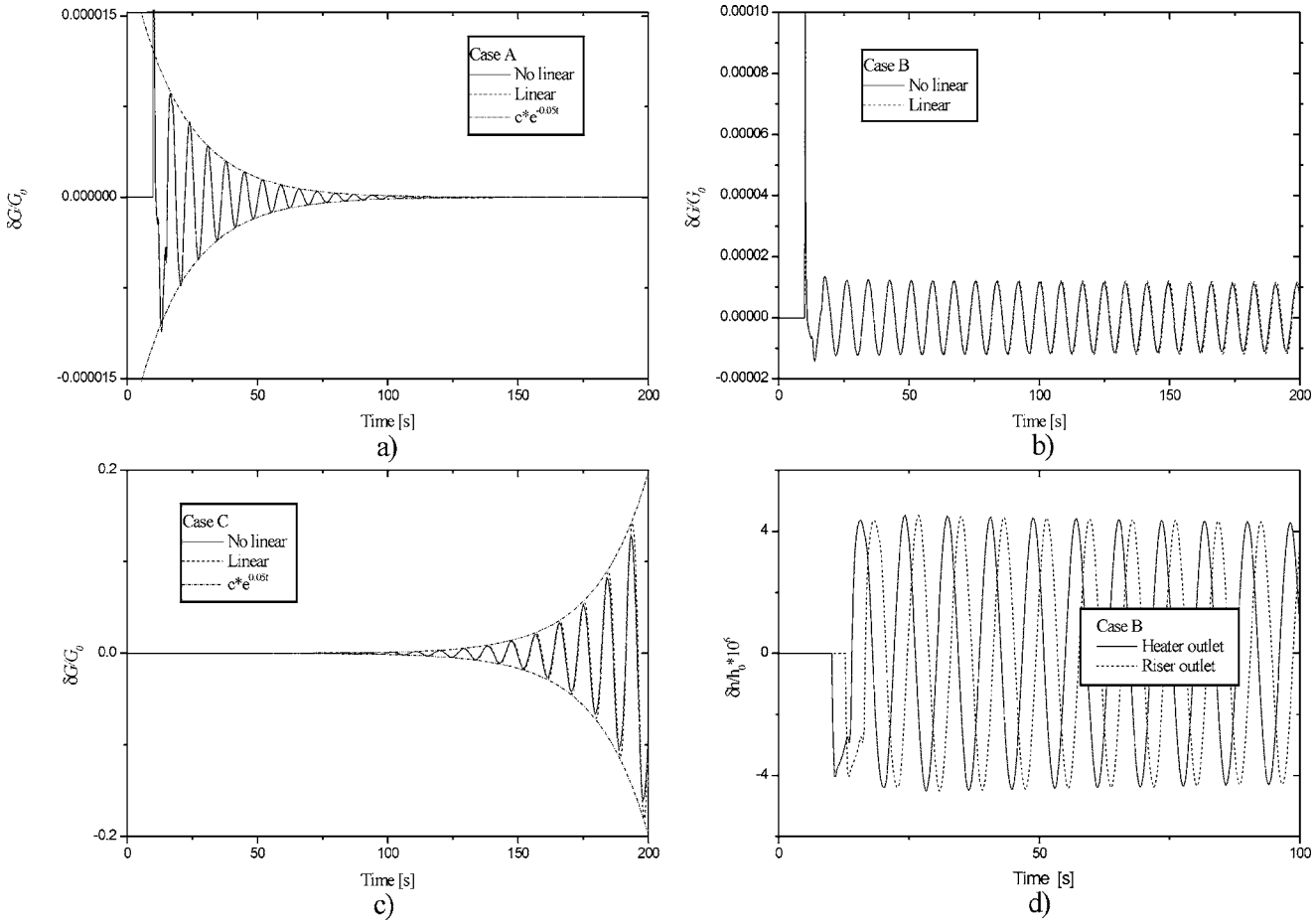

Fig. 5 Time evolutions for the averaged nondimensionalized flow, according to the linear and nonlinear system, at points (*a*) stable, (*b*) neutral, and (*c*) unstable (points A, B and C). (*c*) Heater outlet and riser outlet enthalpy, showing propagation.

amplification factor a is used in this work to define stability: positive or negative values imply unstable or stable conditions, respectively. In particular, the asymptotic oscillation period and the decay ratio are given by

$$T_{osc} = \frac{2\pi}{\omega} \quad DR = e^{2\pi a/\omega} \tag{7}$$

6 Results

Results obtained with the model developed are analyzed below, with reference to two cases:

- A "test case," where the results are compared with an analytical model. The purpose of the comparison is to verify that numerical diffusion is low enough to prevent masking of the physical instability phenomena. In this case a wide range of vapor qualities at the heater exit are analyzed.
- An "application case," where the model developed is used to analyze CAREM reactor-prototype stability, without pressure feedbacks. In this case the low-quality range is analyzed in more detail, because it is characteristic of self-pressurized reactors.

6.1 Test Case. In this section, the stability boundary prediction of this model is checked against a frequency-domain model [34]. This model, which we will hereafter call the "analytical model," was specifically developed to analyze the system shown in Fig. 2, which is a simplification of a vertical U-tube recirculation-type steam generator. This method is strictly nondiffusive.

In the analytical model, the following simplifying assumptions were adopted:

- homogeneous two-phase flow
- constant system pressure
- no subcooling boiling
- constant inlet subcooling
- uniform heat flux in the heater zone
- saturation density for subcooling conditions
- localized friction in core inlet and outlet, and in riser outlet

In order to be able to compare the results, the same hypotheses are applied to the numerical model. For the analysis, characteristic values were introduced to enable obtaining typical stability limits of a BWR reactor type in natural convection or of a U-type steam generator.

Figure 3(*a*) shows a level graph of the amplification factor obtained with the numerical model and the stability limit obtained with the analytical model. Figure 3(*b*) shows the level graph of frequencies. The number of nodes in the riser N_r was fixed to eight for the entire range, accommodating the number of nodes in the heated region by the adaptive nodalization. In the figure, subcooling number N_{sub} and Zuber number N_{Zu} are introduced for this comparison:

$$N_{\text{Zu}} \equiv \frac{Q_c}{G_c A_c h_{fg}} \frac{\rho_f - \rho_g}{\rho_g} \quad N_{\text{sub}} \equiv \frac{h_f - h_{c,i}}{h_{fg}} \frac{\rho_f - \rho_g}{\rho_g} \tag{8}$$

When the Zuber number is larger than the subcooling number, a two-phase mixture leaves the heated section, a good agreement

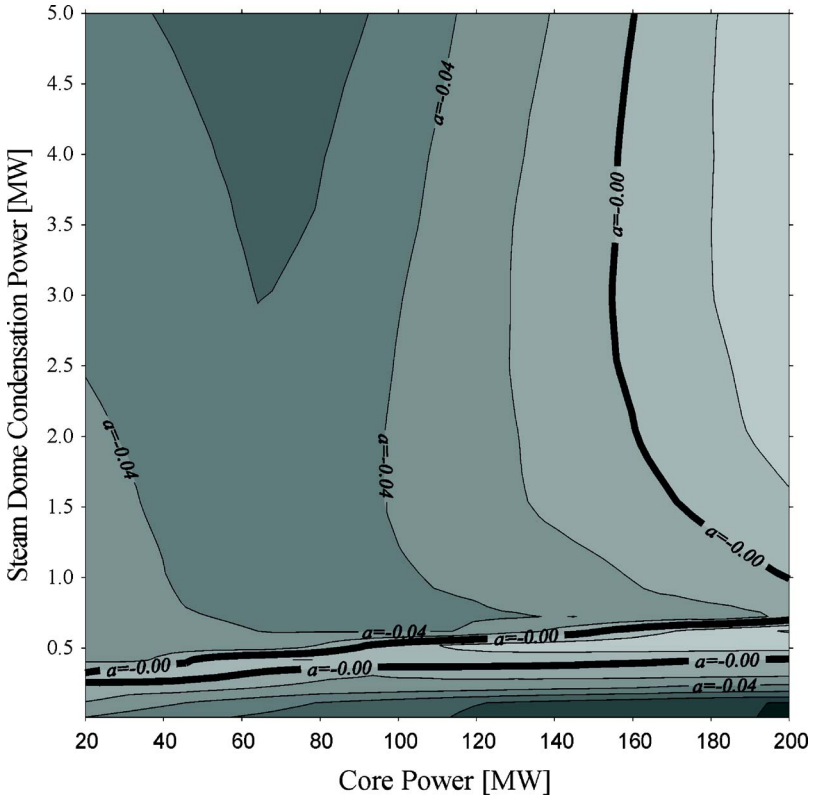

Fig. 6 Stability map for the application case, without pressure feedback

between the models being verified. This shows that the numerical model is suitable to analyze cases near the stability boundary. Two main zones of instability may be observed, as shown in previous analytical and experimental observations [12,14]. They are the so-called type-I and type-II oscillations. Type-I oscillations are important under low power conditions and are caused by the gravitational pressure drop along the riser. They are important in the case of self-pressurized reactors. Type-II oscillations are dominant at high-power BWR conditions and are caused by the interaction between one- and two-phase frictional pressure drops. Nevertheless, the transition between the two zones is gradual, and there is no clear-cut boundary line.

It can be noted that there is a more abrupt slope near the type-I instabilities than near the type II. This causes the type-II instability limit to depend more on models. The frequency variations are continuous, meaning that there is only one dominant eigenvalue in the entire range. The type-I oscillations have a lower frequency than those in type II.

Figure 4 shows the eigenvalues (z_i) at the points indicated in Fig. 3(a): A is in the stable zone ($a=-0.05\ s^{-1}$), B is at the stability limit ($a=0\ s^{-1}$), and C is in the unstable zone ($a=0.05\ s^{-1}$). All the characteristic frequencies of the system (imaginary axis) and their decay constants (real axis) can be seen. The dominant eigenvalues are the ones with the larger real part, which produces the longer surviving oscillations. It can be noted that there is a substancial difference between the dominant eigenvalues and the remaining ones.

Figures 5(a)–5(c) show the temporal evolution of a perturbation on $\hat{G}$ (nondimensional), for the previous three points on the nonlinear (original) model, compared with the linearized one. The system is initialized in a steady-state condition, and at 10 s a small perturbation on $\hat{G}$ is introduced. In the first place, a total concordance may be seen between the linearized and the original system in the three cases, the respective evolutions being almost superimposed. Diminishing oscillations are observed for point A, self-supported oscillations for point B, and increasing oscillations for point C, showing agreement between the decay (growth) constants and the calculated amplification factor, according with the previous analysis. We can also observe a concordance between the period of the oscillation and the frequency of the calculated oscillation. Figure 5(d) shows the spread of the enthalpy disturbance along the chimney, in which it can be noticed that both the amplitude and period of the wave at the entry remain unaffected while it is transported up to the exit. This shows the low diffusion obtained with the adaptive nodalization scheme.

6.2 Application Case. In this section CAREM prototype stability at nominal conditions is analyzed. The geometries, friction distributions, and power profile are taken from the CAREM-25 reactor. Figure 6 shows the stability map for a constant dome pressure, which would be equivalent to an infinite vapor volume. This case will be used in Sec. 7.2 as a base case for the convergence analysis.

Q_c is used as the abscise variable, and the condensation of steam in the dome, Q_V, is used instead of the core inlet subcooling as the ordinate variable, thus allowing a better visualization of the region of interest, covering a wide range of Q_c values in correspondence with small Q_V ones. In this region, oscillations take place due to the counteraction between buoyancy force and flow. The case of $Q_V=0$ coincides with the case of $N_{Zu}=N_{sub}$, and increasing Q_V is equivalent to decreasing the core inlet subcooling.

When Q_V is relatively high (above approximately 0.75 MW), the boiling occurs within the core. The sensitivity of the buoyancy force due to enthalpy perturbations is magnified when increasing Q_c; hence, the system is less stable in this direction.

At low Q_V (below 0.75 MW), the boiling boundary position (λ) is located in the riser due to the decrease of pressure with hydraulic height (flashing). The location of λ is more sensitive, increasing the buoyancy force sensitivity, and the system is less stable.

For very low Q_V values, λ is near located the riser outlet; the two-phase region decreases, stabilizing the system.

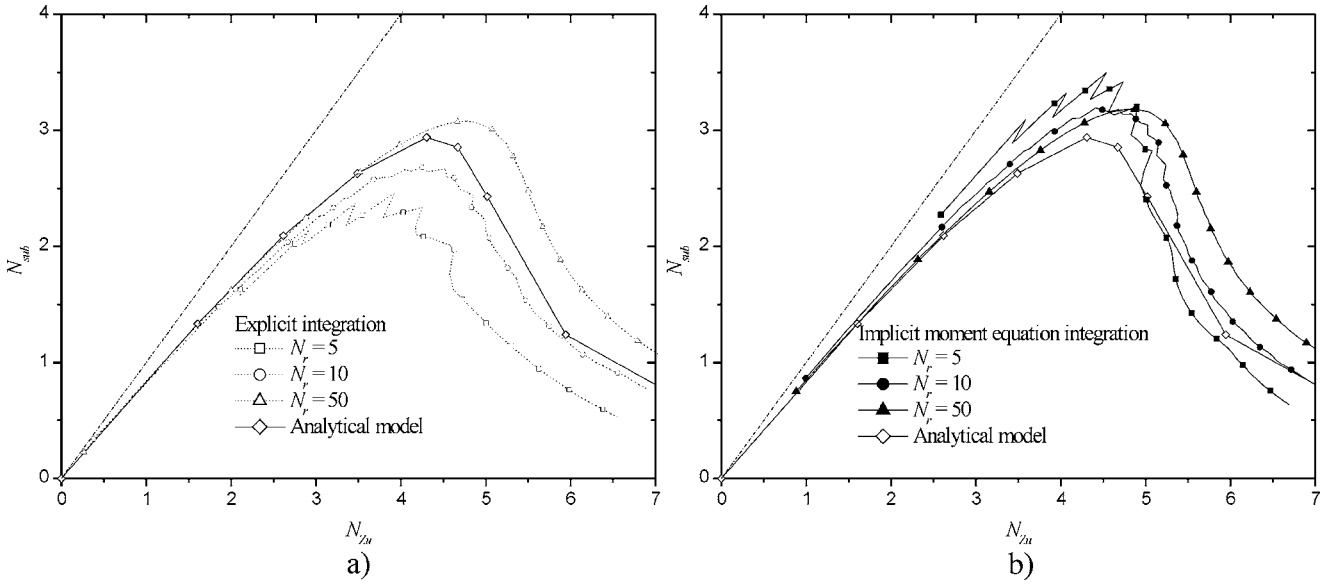

Fig. 7 Convergence analysis of the numerical model by using the adaptive nodalization: (*a*) Fully explicit and (*b*) implicit momentum equation

This case is conservative from the stability point of view. The effect of pressure feedback is analyzed in [23,24], where a strong stabilizing effect is observed; this is because an increment in the void fraction expands all the coolant, immediately pressurizing the system, and this tends to decrease the void fraction. Therefore, the natural consequence is to balance density changes along the system. In this work, pressure is kept constant to simplify the convergence analysis.

7 Linear Convergence Analysis

For stability analysis, the code combines the methods of linearization and frequency domain calculations by means of eigenvalue calculation. This representation allows a straightforward visualization of the stability of the linearized system, therefore avoiding an exhaustive analysis of all possible transients in a time-domain approach.

In this section, linear convergence is analyzed for the numerical scheme, for the two cases shown in Sec. 6. The "test case" is of interest because a wide range of qualities is studied, including both type-I and type-II oscillations. Moreover, this case relies on an analytical solution of the problem. The "application case" is of particular interest because it includes most of the models postulated for the primary system of the reactor analyzed in this work.

7.1 Test Case. In order to analyze the convergence of the model, the stability limit is calculated using different nodalizations. The aim is to analyze the influence of numerical errors, associated with nodalization and time integration, in the stability prediction, focusing on the momentum and energy equations.

In the first place, the convergence of the method is analyzed, applying explicit integration to the whole scheme. The cases $N_r = 5$, 10, and 50 are analyzed, arranging the nodes in the heated

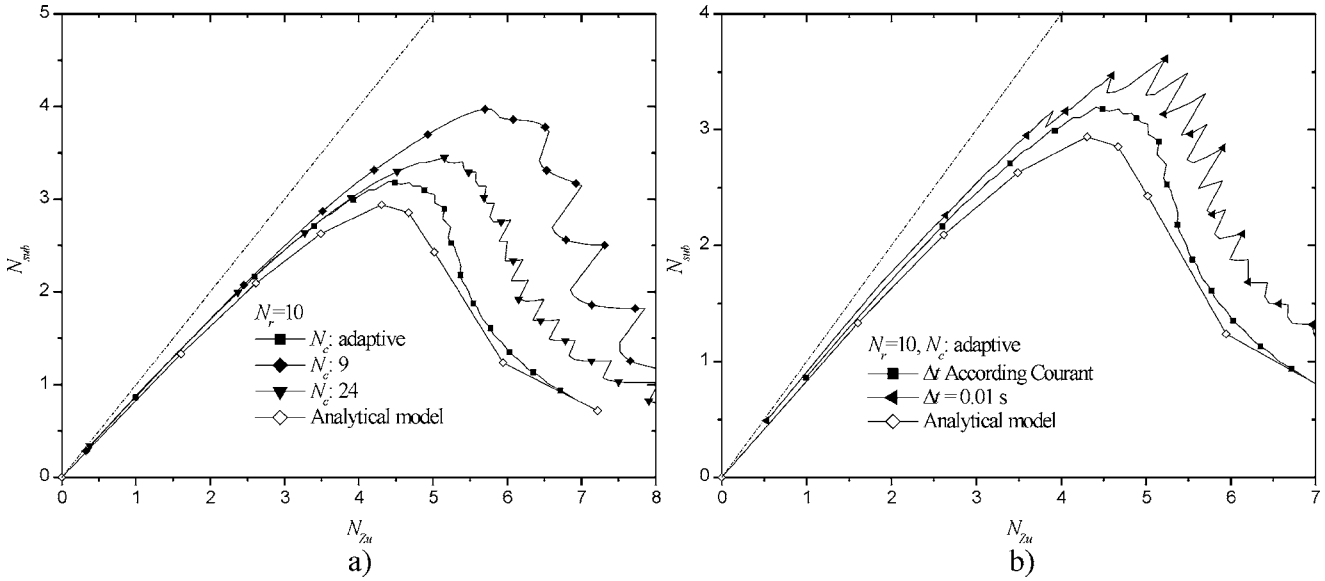

Fig. 8 Comparison of stability limit prediction using (*a*) adaptive nodalization and fixed nodalization and (*b*) Courant limit and lower time step

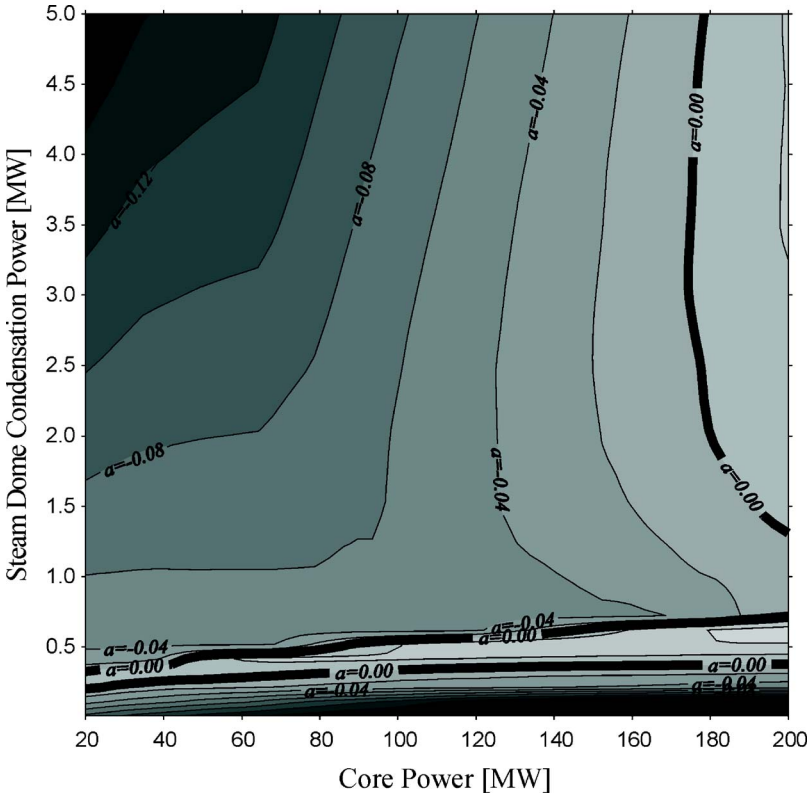

Fig. 9 Stability map showing the core influence, in the case of constant core inlet coolant temperature

zone according to the adaptive nodalization, without the use of intermediate steps. The case of 50 nodes was found to be a converged solution. The results are shown in Fig. 7(*a*).

In the case of a coarse nodalization, as is the case of $N_r=5$, discontinuities may first be observed that match the changes in the number of nodes in the heater. This results from discontinuities in the Courant relation in the first node, which acts as an adjustment node, as explained in Sec. 5.2. These discontinuities becomes almost imperceptible beyond $N_r=10$, where the weight of the first node is sufficiently low. On the other hand, in the case of low quality the required time step due to the Courant relation overcomes the limit of numerical stability in the momentum equation; the stability study is therefore not possible in this zone. An overprediction of the instability, weakening when the nodalization is refined, can also be observed, which causes the limit to converge from the stable zone. This behavior is contrary to the one that might be expected from the point of view of the diffusion of enthalpy fronts, in which the diffusion should be larger for larger nodes, stabilizing the system. In this case, provided that the adaptive nodalization scheme minimizes the problem of enthalpy front diffusion, this source of error is reduced regarding others and the resulting effect is the inverse one. In this case, the integration error of the momentum equation is of a higher order in relation to the energy equation. The explicit integration error can be understood as a "negative diffusion" effect, in the sense that it is opposite to the spatial discretization one, which provokes an error cancellation in the energy equation when the Courant limit is fulfilled. Due to the fact that the momentum equation has only a temporary dimension, the error cancellation effect does not take place, introducing a destabilizing factor that is increased with the time step. This would provoke the instability overestimation which has already been observed in other applications [35].

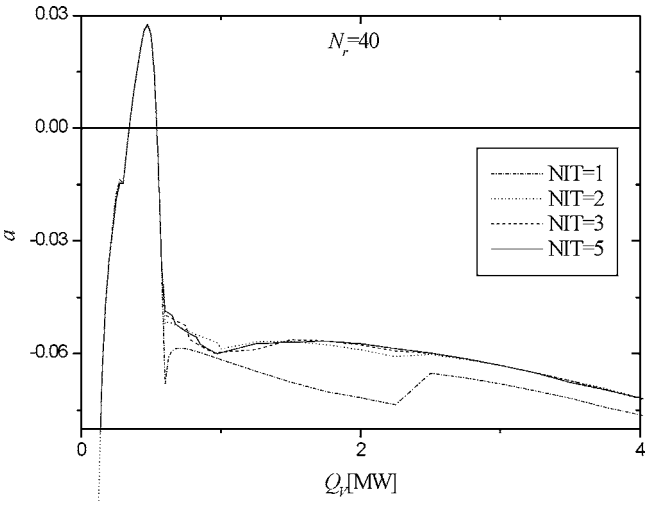

Fig. 10 Amplification factor as a function of QV, using different numbers of intermediate steps (NIT) in the core

One alternative is to apply a pseudo-implicit scheme to the momentum equations by using an estimated density $\rho_j^{(n+1)+}$ from the following expression:

$$\rho_j^{(n+1)+} = \left.\frac{d\rho}{dt}\right|_j^+ \Delta t + \rho_j^n \tag{9}$$

This is used for the buoyancy force calculation in Eq. (2).

Figure 7(*b*) shows the result, in which a significant improvement can be observed in the convergence in relation to the fully explicit case. The trend towards overestimation is reversed in the case of type-I oscillations. Both cases (explicit or pseudo-implicit momentum equation integration) converge to the same value when increasing the nodalization.

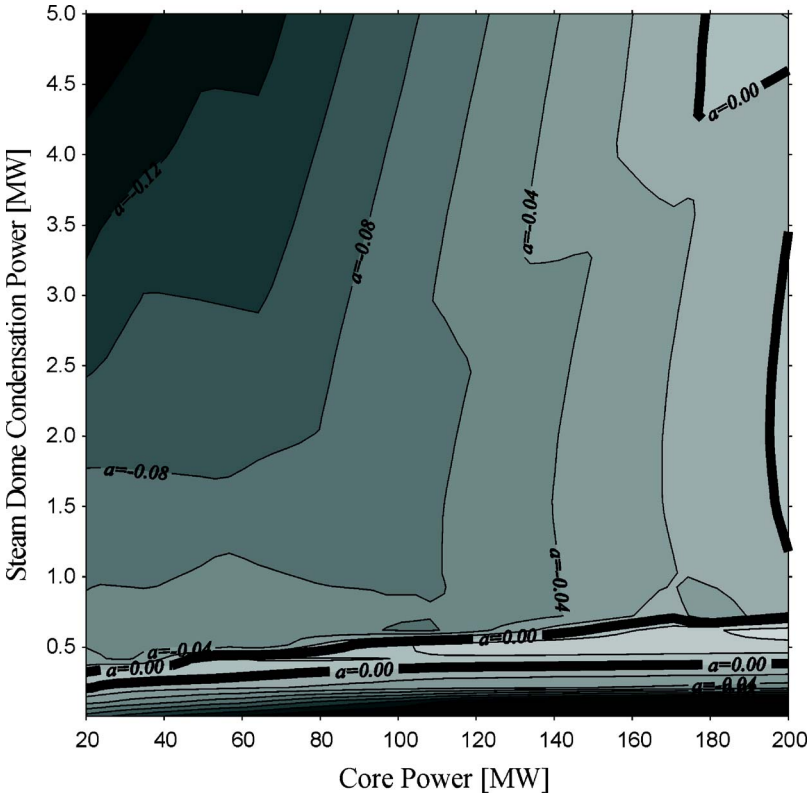

Fig. 11 Stability map obtained without intermediate steps in the core

Another interesting point is the comparison of the results obtained with adaptive and fixed nodalizations. For this purpose, the case for $N_r=10$ is analyzed, the time step calculated according to the Courant criterion, using both fixed and adaptive nodalizations. In the case of an adaptive nodalization, N_c varies between 9 and 24 along the stability limit. For the purposes of comparison, these extreme values are used for two fixed nodalizations. The results are shown in Fig. 8(*a*).

In the fixed nodalizations, an amplification of the stable zone may be observed, which is a consequence of the numerical diffusion existent in these cases; this is more noticeable in the zone of type-II instabilities. This effect diminishes when increasing the number of nodes in the heater. Nevertheless, it is not possible to approach the stability limit predicted by the adaptive nodalization without also increasing the nodalization in the riser.

Discontinuities in the stability limit may additionally be seen in the case of fixed nodalizations, which match the movement of the boiling boundary (λ) from node to node. When this happens, the fluid residence time in these nodes changes sharply, causing a discontinuity in the numerical diffusion of the model in the volumes containing two phases. This effect does not take place in the adaptive nodalization, whereas in the case of fixed nodalizations it is reduced as the nodalization is increased.

The time-step effect will now be analyzed. In the case of adaptive nodalizations, Δt is adjusted in agreement with the Courant criterion, varying from 0.05 to 0.8 s along the stability limit. Figure 8(*b*) shows the comparison when imposing $\Delta t=0.01$ s on the whole range, using the same adaptive nodalization scheme.

As explained in Sec. 5.2, the discretization and time integration errors tend to cancel each other out when Δt fulfills Courant's criterion in all nodes. When Δt is reduced the time integration error diminishes, leaving only that due to spatial discretization, which tends to spread the enthalpy fronts, stabilizing the system. As in the case of fixed nodalizations, some discontinuities can also be noted matching the movement of the boiling boundary (λ) from node to node, and which are associated with the up-wind scheme.

7.2 Application Case. In this section, the case shown in Sec. 6.2 is taken as a base case for the convergence analysis, that is to say, the reactor primary system without the pressure feedback modeling.

The nodalization effect can be observed in the diffusion of small perturbations along the circuit. In this case, flow variations cause two types of perturbations:

1. Those at the core exit, propagating along the riser. These perturbations are produced in the two-phase zone and are the cause of the system instabilities.
2. Those at the SG exit (on the primary side), which will propagate along the downcomer. These perturbations are produced in the single-phase zone and are dominant only in the more stable regions.

Figure 9 shows the stability map when the propagation of perturbations in the SG and the downcomer are not modeled, the same nodalization for the hot branch being used. This results in a condition of constant temperature at the core inlet. As can be seen, the stability map obtained is similar to the one in Fig. 6, showing some differences in the more stable region (high Q_c, low Q_V) due to the fact that the dominant oscillation modes in this region are the ones related to the propagation of disturbances along the cold branch. Nevertheless, in the more unstable regions the amplification factor is similar, provided that the two-phase dynamic is dominant in these conditions. Therefore, the prediction of the stability limit is more or less independent of the nodalization in the cold leg, due to the strong dependence on the hot leg nodalization.

Therefore, the constant core inlet temperature condition is adopted for the convergence analysis of the adaptive nodalization. The time step and core and riser nodalizations are specially analyzed.

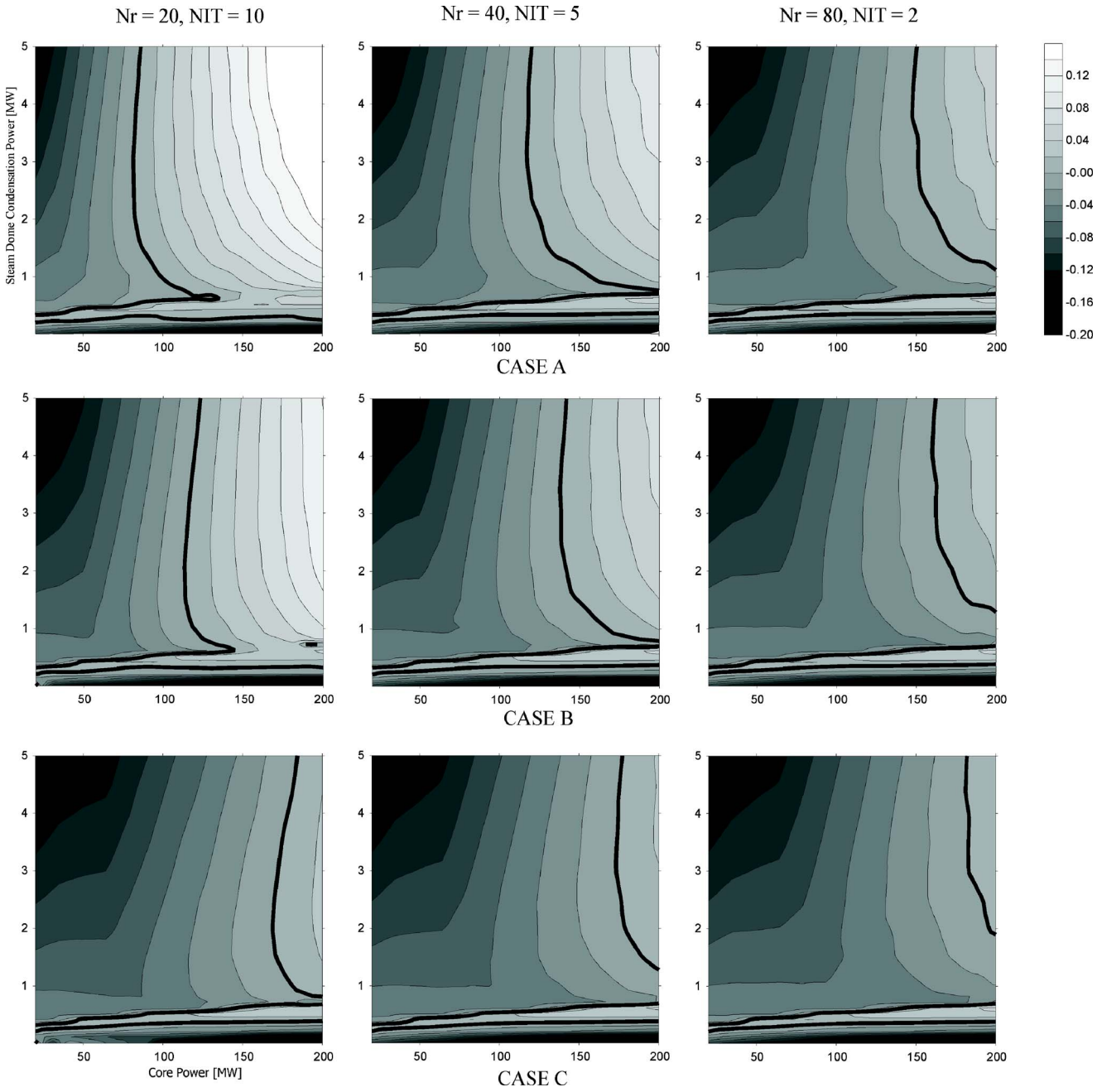

Fig. 12 Convergence analysis for points A, B, and C, using N_r=20, 40, and 80 and NIT=10, 5, and 2, respectively, in order to keep $N_c \approx$const

Figure 10 shows the amplification factor when Q_V increases, keeping Q_c constant at 100 MW. The different curves illustrate different NIT steps in the core region, keeping constant the time step and the nodalization in the riser; this is equivalent to different nodalizations in the core. There is no difference while λ is located in the riser. Conversely, when λ moves into the core, there are some discontinuities when moving from node to node. This is, to a certain extent, due to the fact that in this range the oscillation periods are comparable to the typical fluid residence time in the core. Thus, the changes in power affect the system to different extents according to the size, location, and transferred power to the volume containing the boiling boundary. Figure 11 shows the stability map obtained with the adaptive nodalization without introducing intermediate steps. In this case the problem becomes evident, where a "step" caused by this phenomenon can be observed. These discontinuities diminish when increasing the core nodalization, in this case by increasing the intermediate step number, becoming almost imperceptible for NIT=5, the value finally adopted.

The time-step effect is now analyzed. This is performed by varying N_r, in order to fulfill the Courant criterion, imposed by the adaptive nodalization. N_c is kept approximately constant by introducing intermediate steps. In the analysis, three cases are compared:

Case A: A fully explicit scheme is used.

In Fig. 12 the stability maps for different time steps may be seen. There are no appreciable variations within the flashing zone. Conversely, the region where the boiling occurs within the core is relatively more sensitive to numerical errors. In the same way as that observed in Sec. 7.1, it can be noted that the convergence

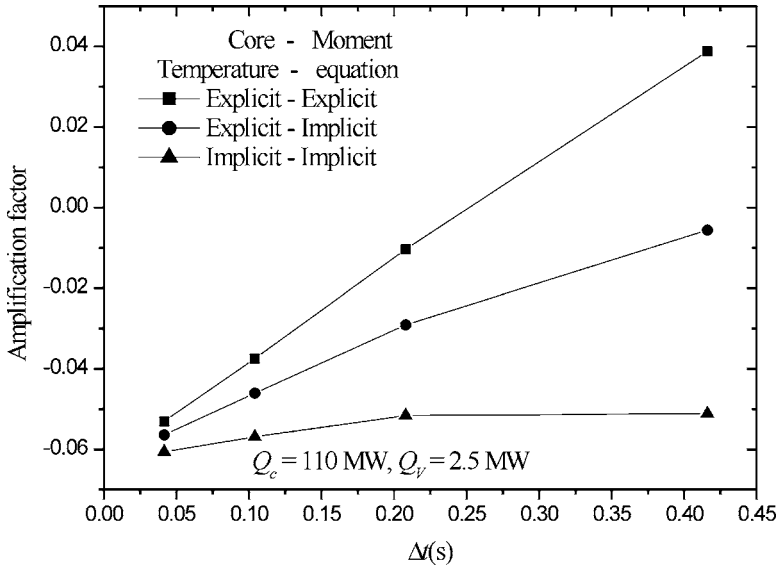

Fig. 13 Convergence analysis for cases A, B, and C

takes place from the stable zone (becoming more stable as the time step is reduced), that is to say an inverse behavior from the expected one from the spatial diffusion point of view. As already observed, one possible reason is the explicit integration of the equations which depend solely on time.

Case B: Implicit (or "pseudo-implicit") integration of the momentum equation.

The same scheme detailed in Sec. 7.1 is used. The stability map presented in Fig. 12 shows the convergence for this case. Some improvement is observed in relation to the fully explicit case, while still preserving the convergence trend from the stable zone.

Case C: Implicit (or "pseudo-implicit") integration of the momentum and fuel temperature equations.

The fuel-temperature equation is integrated by using an estimated temperature for the calculation of the power transferred to the coolant. The equation is included in the convergence loop of the program. Equation (5) is thus:

$$\left.\frac{dT_c}{dt}\right|_j^n = \frac{L_c}{M_c Cp_c}\left(W_j \frac{Q_c^N}{L_c} - h^t \mathrm{Per}(T_{cj}^{(n+1)+} - T_j^n)\right) \tag{10}$$

where

$$T_{cj}^{(n+1)+} = \left.\frac{dT_c}{dt}\right|_j^n \Delta t + T_{cj}^n \tag{11}$$

The convergence in this case is shown in Fig. 12. A remarkable improvement is observed in relation with the fully explicit cases (case A) and implicit momentum equations (case B).

The comparison of these three cases is presented in Fig. 13, showing the amplification factor for $Q_c = 110$ MW, $Q_V = 2.85$ MW, taken as a "test" point in the region with boiling within the core (out of the flashing zone), as a function of the time step used in each case.

In the first place, it can be observed that the three cases converge to the same value when the time step is reduced. Case B converges faster than the fully explicit case, as already observed in Sec. 7.1. Nevertheless, case C presents the best convergence, being virtually converged even for the largest time-step. Case C is the scheme finally adopted for calculations, with the exception of the ones explicitly stated.

8 Conclusions

From the results obtained, it can be said that the numerical scheme is suitable for the stability analysis, and its flexibility allows the parametric study of different hypotheses and numerical schemes.

The linearization method assures a total conformity of the linearized system, with identical behavior with respect to the nonlinear system when small deviations from the steady state are concerned, regarding both the amplification factor and the frequency of the oscillations.

The adaptive nodalization scheme shows a very low diffusion in the transport of small disturbances. This remarkably improves convergence regarding fixed nodalizations. Moreover, the stability limit obtained with the fixed nodalizations evidences discontinuities that correspond with movements of the boiling boundary from one node to another. These discontinuities are minimized in the case of the adaptive nodalization.

In the case analyzed, the fully explicit integration produces an overestimation of the instability, with convergence from the stable zone. The implicit integration of the momentum and fuel temperature equations inverts this trend in some cases and notably improves the convergence both in type-I and type-II oscillations. The results obtained with a converged numerical model predict a more stable behavior with respect to the one obtained with the analytical model.

In the case of the reactor studied, the disturbances of the steam generators in the single-phase primary zone are dominant only in the more stable regions; therefore, the prediction of the stability limit is roughly independent of the cold-leg nodalization.

The gradient of the amplification factor near the stability limit is larger in oscillations of type I than in those of type II. Therefore, the stability limit in the latter is more sensitive to changes in the model or nodalization.

Nomenclature

A = flow area
a = amplification factor
Cp = specific heat
D_h = hydraulic diameter
DR = decay ratio
f = Moody friction factor
G = mass flow
$\hat{G}$ = total momentum

g = gravity
h = mass averaged enthalpy
$\hat{h}$ = flow averaged enthalpy
h^t = heat transfer coefficient
K = local friction
L = length
M = mass
N = number of nodes
NIT = intermediate time steps in the energy equation
N_{sub} = Zuber number
N_{Zu} = subcooling number
P = pressure
Per = heated perimeter
Q_c = core power
Q_V = condensation power in the steam zone within the upper dome
q' = linear heat flux
T = temperature
T_{osc} = oscillation period of asymptotic oscillation
t = time coordinate
W = power-axial-profile weighting factor
y = state variables vector
z = spatial coordinate/eigenvalue

Greek Letters

δ = deviation from the steady-state condition
Φ_{f0}^2 = two-phase friction loss multiplier
λ = boiling boundary position
θ = vertical angle
ρ = density
ω = frequency of asymptotic oscillation

Subscripts and Superscripts

c = core
f = saturated liquid
g = saturated steam
i = input
n = time level
l = liquid
o = output
r = riser

References

[1] March-Leuba, J., and Rey, J. M., 1993, "Coupled Thermohydraulic-Neutronic Instabilities in Boiling Water Nuclear Reactors: A Review of the State of the Art," Nucl. Eng. Des., **145**, pp. 97–111.

[2] D'Auria, F., Ambrosini, W., Anegawa, T., Blomstrand, J., In De Betou, J., Langenbuch, S., Lefvert, T., and Valtonen, K., 1997, "State of the Art Report on Boiling Water Reactor Stability," OCDE/GD(97)13.

[3] Wallis, G. B., and Heasley, J. H., 1961, "Oscillations in Two-Phase Flow Systems," ASME J. Heat Transfer, **83**, pp. 363–369.

[4] Mahaffy, J. H., 1993, "Numerics of Codes: Stability, Diffusion and Convergence," Nucl. Eng. Des., **145**, pp. 131–145.

[5] Takigawa, Y., Takeuchi, Y., Tsunoyama, S., Ebata, S., Chan, K. C., and Tricoli, C., 1987, "Caorso Limit Cycle Oscillation Analysis With Three-Dimensional Transient Code TOSDYN-2," Nucl. Technol., **79**(2), pp. 210–227.

[6] Karve, A., Rizwan-uddin, and Dorning, J. J., 1997, "Stability Analysis of BWR Nuclear-Coupled Thermal-Hydraulics Using a Simple Model," Nucl. Eng. Des., **177**, pp. 155–177.

[7] Van Bragt, D., Riswan-uddin, and Vand Der Hagen, T., 1999, "Nonlinear Analysis of a Natural Circulation Boiling Water Reactor," Nucl. Sci. Eng., **131**, pp. 23–44.

[8] Paulsen, M. P., Shatford, J. G., and Westacott, J. L., 1992, "A Nondifussive Solution Method for RETRAN-03 Boiling Water Reactor Stability Analysis," Nucl. Technol., **100**, pp. 162–173.

[9] Cheung, Y. K., and Klebanov, L. A., 2001, "TRACG Analyses of Two-Phase Flow Instability Data From SIRIUS Loop at Relatively High System Pressure," Proceedings of International Conference on Nuclear Engineering, Nice, France.

[10] Shiralkar, B. S., Alamgir, M., and Andersen, J. G. M., 1993, "Thermal Hydraulic Aspects of the SBWR Design," Nucl. Eng. Des., **144**, pp. 213–222.

[11] Arnold, H., Yadigaroglu, G., Stop, P. M., Gonzales, A., Sawyer, C. D., and Rao, A., 1997, "ESWR—The Latest Passive BWR," Nucl. Eng. Int., **42**(511), pp. 20–22.

[12] Kyung, I., and Lee, S., 1994, "Experimental Observations on Flow Characteristics in an Open Two-Phase Natural Circulation Loop," Nucl. Eng. Des., **159**, pp. 163–176.

[13] Van Der Hagen, T., Van Bragt, D., Van Der Kaa, F. J., Karuza, J., Killian, D., Nissen, W. H. M., Stekelenburg, A. J. C., and Wouters, J. A. A., 1997, "Exploring the Dodewaard Type-I and Type-II Stability; From Start-up to Shutdown, From Stable to Unstable," Ann. Nucl. Energy, **24**(8), pp. 659–669.

[14] Van Bragt, D., and Vand Der Hagen, T., 1998, "Stability of Natural Circulation Boiling Water Reactors: Part II—Parametric Study of Coupled Neutronic—Thermohydraulic Stability," Nucl. Technol., **121**, pp. 52–62.

[15] Kruijf, W. J. M., Ketelaar, K. C. J., Avakian, G., Gubernatis, P., Caruge, D., Manera, A., Van der Hagen, T. H. J. J., Yadigaroglu, G., Dominicus, G., Rohde, U., Prasser, H. M., Castrillo, F., Huggenberg, M., Henning, D., Munoz-Cobo, J. L., and Aguirre, C., 2003, "Planned Experimental Studies on Natural-Circulation and Stability Performance of Boiling Water Reactors in Four Experimental Facilities and First Results (NACUSP)," Nucl. Eng. Des., **221**, pp. 141–250.

[16] Zanocco, P., Giménez, M., and Delmastro, D., 2003, "Self-Pressurization Behavior in Integrated Reactors," Int. J. Heat Technol., **21**, pp. 149–155.

[17] Van Bragt, D., Kruijf, W. J. M., Manera, A., Van Der Hagen, T. H. J. J., and Van Dam, H., 2002, "Analytical Modeling of Flashing-Induced Instabilities in a Natural Circulation Cooled Boiling Water Reactor," Nucl. Eng. Des., **215**, pp. 87–98.

[18] Inada, F., Furuya, M., and Yasuo, A., 2000, "Termo-Hydraulic Instability of Boiling Natural Circulation Loop Induced by Flashing (Analytical Consideration)," Nucl. Eng. Des., **200**, pp. 187–199.

[19] Zanocco, P., 1998, "Integral Reactor Design Criterion Based on Transients," Nuclear Engineering Degree Dissertation, Balseiro Institute (in Spanish).

[20] Zanocco, P., Gimenez, M., and Delmastro, D., 1998, "HUARPE: A Thermohydraulic Code for Transient Simulations in Integrated Reactors," XXV reunión anual de la Asociación Argentina de Tecnología Nuclear (AATN), Buenos Aires.

[21] Zanocco, P., Gimenez, M., and Delmastro, D., 2002, "Modelling of Self-Pressurized Natural Circulation Circuits," XXIX reunión anual de la Asociación Argentina de Tecnología Nuclear (AATN), Buenos Aires.

[22] Zanocco, P., Giménez, M., and Delmastro, D., 2003, "Safety Design Maps: An Early Evaluation of Safety to Support Reactor Design," Nucl. Eng. Des., **225**, pp. 271–283.

[23] Zanocco, P., Giménez, M., and Delmastro, D., 2004, "Modeling Aspects in Linear Stability Analysis of a Self-Pressurized Natural Circulation Integral Reactor," Nucl. Eng. Des., **231**, pp. 283–301.

[24] Zanocco, P., Delmastro, D., and Giménez, M., 2004, "Linear and Nonlinear Stability Analysis of a Self-Pressurized, Natural Circulation, Integral Reactor," ICONE12, International Conference on Nuclear Engineering, Washington, DC.

[25] IAEA-TECDOC-1391, 2004, "Status of Advanced Light Water Reactor Designs," IAEA, Vienna.

[26] Delmastro, D., Santecchia, A., Mazzi, R., Ishida, M. V., Gómez, S. E., Gómez, S., and Ramilo, L., 2001, "CAREM: An Advanced Integrated PWR," Proceedings of International Seminar on Status and Prospects for Small and Medium Sized Reactors, Cairo, Egypt, 27–31 May.

[27] Giménez, M., Schlamp, M., Zanocco, P., González, J., and Vertullo, A., 2001, "CAREM-25 Accident Analysis," Proceedings of International Seminar on Status and Prospects for Small and Medium Sized Reactors, Cairo, Egypt, 27–31 May.

[28] Giménez, M., Grinblat, P., Schlamp, M., Zanocco, P., González, J., and Vertullo, A., 2003, "A Cost-Effective Methodology to Internalize Nuclear Safety in Nuclear Reactor Conceptual Design," Nucl. Eng. Des., **226**, pp. 293–309.

[29] Wallis Graham, B., 1969, *One-Dimensional Two-Phase Flow*, McGraw-Hill, New York.

[30] Van Bragt, D., and Vand Der Hagen, T., 1998, "Stability of Natural Circulation Boiling Water Reactors: Part I—Description Stability Model and Theoretical Analysis in Terms of Dimensionless Groups," Nucl. Technol., **121**, pp. 40–51.

[31] Clausse, A., Delmastro, D., and Lahey, R. T., 1990, "The Analysis of Chaotic Instabilities in Natural Circulation Boiling Systems," Eurotherm Seminar No. 16, pp. 161–167.

[32] Press, W. H., Flannery, B. P., Teukolsky, S. A., and Vetterin, W. T., 1989, *Numerical Recipes, the Art of Scientific Computing*, Cambridge University Press, Cambridge.

[33] Ambrosini, W., 2001, "On Some Physical and Numerical Aspects in Computational Modeling of One-Dimensional Flow Dynamics," Proceedings of VII International Seminar on Recent Advances in Fluid Mechanics, Physics of Fluids an Associated Complex Systems, Buenos Aires, October.

[34] Delmastro, D., Clausse, A., and Converti, J., 1991, "The Influence of Gravity on the Stability of Boiling Flows," Nucl. Eng. Des., **127**, pp. 129–139.

[35] Ambrosini, W., and Ferreri, J. C., 1998, "The Effect of Truncation Error on the Numerical Prediction of Linear Stability Boundaries in a Natural Circulation Single-Phase Loop," Nucl. Eng. Des., **183**, pp. 53–76.

Direct Numerical Simulations of Planar and Cylindrical Density Currents

Mariano I. Cantero[1]
Department of Civil and Environmental Engineering,
University of Illinois at Urbana-Champaign,
Urbana, IL 61801
e-mail: mcantero@uiuc.edu

S. Balachandar
Department of Theoretical and Applied Mechanics,
University of Illinois at Urbana-Champaign,
Urbana, IL 61801
e-mail: s-bala@uiuc.edu

Marcelo H. García
Department of Civil and Environmental Engineering,
University of Illinois at Urbana-Champaign,
Urbana, IL 61801
e-mail: mhgarcia@uiuc.edu

James P. Ferry
Center for the Simulation of Advanced Rockets,
University of Illinois at Urbana-Champaign,
Urbana, IL 61801
e-mail: jferry@uiuc.edu

The collapse of a heavy fluid column in a lighter environment is studied by direct numerical simulation of the Navier-Stokes equations using the Boussinesq approximation for small density difference. Such phenomenon occurs in many engineering and environmental problems resulting in a density current spreading over a no-slip boundary. In this work, density currents corresponding to two Grashof (Gr) numbers are investigated (10^5 and 1.5×10^6) for two very different geometrical configurations, namely, planar and cylindrical, with the goal of identifying differences and similarities in the flow structure and dynamics. The numerical model is capable of reproducing most of the two- and three-dimensional flow structures previously observed in the laboratory and in the field. Soon after the release of the heavier fluid into the quiescent environment, a density current forms exhibiting a well-defined head with a hanging nose followed by a shallower body and tail. In the case of large Gr, the flow evolves in a three-dimensional fashion featuring a pattern of lobes and clefts in the intruding front and substantial three-dimensionality in the trailing body. For the case of the lower Gr, the flow is completely two dimensional. The dynamics of the current is visualized and explained in terms of the mean flow for different phases of spreading. The initial phase, known as slumping phase, is characterized by a nearly constant spreading velocity and strong vortex shedding from the front of the current. Our numerical results show that this spreading velocity is influenced by Gr as well as the geometrical configuration. The slumping phase is followed by a decelerating phase in which the vortices move into the body of the current, pair, stretch and decay as viscous effects become important. The simulated dynamics of the flow during this phase is in very good agreement with previously reported experiments. [DOI: 10.1115/1.2173671]

Introduction

Two fluids having different densities that are initially separated by a physical boundary and are suddenly allowed to mix, interact freely forming a density current. Depending on the situation, the density current can be in the form of a denser intrusion penetrating horizontally into the lighter fluid along the bottom boundary, in the form of a lighter intrusion spreading into the heavier fluid along the top boundary, or as a combination of both conditions. Examples are snow avalanches, thunderstorm fronts, volcano eruptions, oil spills in the ocean, the release of contaminants in the environment and flows generated by the collapse of a building. Many more examples can be found in the books by Simpson [1] and Allen [2]. In most environmental and industrial flows of this type, the density difference is only a few percent and it is caused either by scalar fields, such as temperature, salinity and a chemical species, or by particles in suspension leading to the development of turbidity currents [3,4].

Consider the case of a denser fluid released into a lighter environment. Soon after the release a density current develops, which presents a front, a body, and a tail. The front is a discontinuity in density that penetrates into the lighter fluid. The denser fluid rides over a thin layer of light fluid that remains attached to the bottom boundary as a consequence of the no-slip condition. This results in a front whose nose is somewhat lifted above the bottom boundary. The front of the current is a complex, dynamic region where most of the mixing occurs. This mixing, driven by Kelvin–Helmholtz instabilities and vortex shedding, plays an important role regulating the flow since it modifies the driving force by entraining ambient fluid into the current, and thus, diminishing density differences. Behind the front, the body and the tail of the current follow, and their length depends on the amount of dense fluid initially released. In this region, the vortices shed from the front pair, stretch, and eventually break down.

The earliest theoretical attempts to describe the spreading rate of these types of flows were made by von Kármán [5] and Benjamin [6]. Benjamin [6] proposed that in a lock-exchange configuration the front should move at a speed of $\sqrt{1/2g(\rho_1-\rho_0)/\rho_0 h_0}$, where ρ_0 and ρ_1 are the densities of the lighter and heavier fluids, respectively, h_0 is the channel half height and g is the acceleration of gravity. Later works used shallow water theory, along with an empirical Froude condition to close the model, in order to describe the propagation of the front [7–11]. Most of these analyses do not account for the mixing with the ambient fluid.

Several experiments have also been performed to study the front dynamics. Huppert and Simpson [12] have studied experimentally the release of a fixed volume of denser fluid in a lighter ambient. They found that initially a given current spreads at an approximately constant speed and then continuously decelerates until it is dissipated by viscous effects, calling them the slumping, inertial, and viscous phases, respectively. If the Reynolds number of the flow is large enough the deceleration starts with the beginning of the inertial phase. However, for low Reynolds numbers the inertial phase is not present and the deceleration of the flow occurs dominated by viscous effect during the final viscous phase. They also proposed an empirical Froude condition that has been

[1]To whom correspondence should be addressed.

Contributed by the Applied Mechanics Division of ASME for publication in the JOURNAL OF APPLIED MECHANICS. Manuscript received May 24, 2005; final manuscript received December 19, 2005. Review conducted by G. C. Buscaglia. Discussion on the paper should be addressed to the Editor, Prof. Robert M. McMeeking, Journal of Applied Mechanics, Department of Mechanical and Environmental Engineering, University of California–Santa Barbara, Santa Barbara, CA 93106-5070, and will be accepted until four months after final publication of the paper itself in the ASME JOURNAL OF APPLIED MECHANICS.

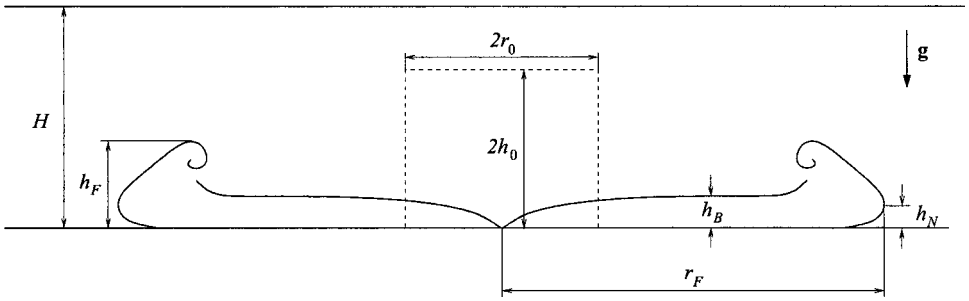

Fig. 1 Sketch of a density current in cylindrical configuration showing the main features of the flow. The dashed line shows the initial condition; this is a cylindrical region of denser fluid located at the center of the domain. After the release a density current develops.

used in box models and to close integral shallow water models of density currents. The propagating front undergoes three-dimensional instability in the form of lobes and clefts. Allen [13] and Simpson [14] devoted a great deal of effort to studying the lobe and cleft patterns. Simpson [14] proposed that the lobe and cleft instability forms only in no-slip surfaces and it is caused by denser fluid overrunning on top of less dense fluid. However, the exact origin of this instability is still not well known and recent work [15] has brought Simpson's theory back into discussion. García and Parsons [16] and Parsons and García [17] studied the similarity of density currents fronts finding that the Reynolds number of the current front plays an important role in the mixing with the ambient fluid. Very recent observations of density current activity in the Chicago River, Illinois, by García et al. [18] supports the observation that the front dynamics is affected by scale (i.e., Reynolds number effects).

Recently, high-resolution numerical computations have been performed in both two and three dimensions to explore the dynamics of density currents [19–23]. These works have provided a detailed description of the flow topology at the foremost portion of the current. The simulations have concentrated on planar and axisymmetric configurations and, to date, no such effort has been attempted for the corresponding cylindrical three-dimensional configuration. In this work, the release of a fixed volume of a homogeneous fluid into a slightly less dense environment in a cylindrical configuration is considered, and the results are compared with the planar case.

The planar lock-exchange configuration studied by Härtel, Meiburg, and Necker [22] is considered first. We present results from a three-dimensional simulation with the same conditions as reported by them and compare the results qualitatively as well as quantitatively. Then we consider the release of a cylindrical region of denser fluid into a less dense ambient and compare our results qualitatively with previously reported experiments [24].

Numerical Formulation

We consider the case of an initial cylindrical volume of heavier fluid surrounded by an infinite extent of lighter fluid. The released volume is a cylinder of radius r_0 and height $2h_0$ (see Fig. 1) and the lighter fluid extends between top and bottom boundaries separated vertically by a distance H. Here we consider both the top and bottom boundaries to be rigid and no slip. Attention will be restricted to the case where the density difference is due to a scalar field (e.g., salinity or temperature).

The density difference is assumed to be small enough so that the Boussinesq approximation can be adopted. With this approximation density variations are important only in the buoyancy term. The dimensionless equations of motion read [22]

$$\frac{\partial \tilde{u}_i}{\partial \tilde{t}} + \tilde{u}_k \frac{\partial \tilde{u}_i}{\partial \tilde{x}_k} = \tilde{\rho} e_i - \frac{\partial \tilde{p}}{\partial \tilde{x}_i} + \frac{1}{\sqrt{\mathrm{Gr}}} \frac{\partial^2 \tilde{u}_i}{\partial \tilde{x}_k \partial \tilde{x}_k}, \tag{1}$$

$$\frac{\partial \tilde{u}_k}{\partial \tilde{x}_k} = 0, \tag{2}$$

$$\frac{\partial \tilde{\rho}}{\partial \tilde{t}} + \frac{\partial}{\partial \tilde{x}_k}(\tilde{\rho} \tilde{u}_k) = \frac{1}{\mathrm{Sc}\sqrt{\mathrm{Gr}}} \frac{\partial^2 \tilde{\rho}}{\partial \tilde{x}_k \partial \tilde{x}_k}. \tag{3}$$

Here $\tilde{u}_i$ is the velocity vector, $\tilde{p}$ is the dynamic pressure, $\tilde{\rho}$ is the density, Gr is the Grashof number, Sc is the Schmidt number and e_i is a unit vector pointing in the gravity direction. We have adopted the initial condition half height, h_0, as the length scale. Since there is no externally imposed velocity scale for the flow, the following velocity scale is defined

$$U_0 = \sqrt{g \frac{\rho_1 - \rho_0}{\rho_0} h_0}. \tag{4}$$

Consequently, the time scale is h_0/U_0. Here ρ_1 is the density of the denser fluid and ρ_0 is the density of the ambient fluid. The dimensionless density and dynamic pressure are given by

$$\tilde{\rho} = \frac{\rho - \rho_0}{\rho_1 - \rho_0}, \quad \tilde{p} = \frac{p}{\rho_0 U_0^2}. \tag{5}$$

The two dimensionless numbers in Eqs. (1)–(3) are given by

$$\mathrm{Gr} = \left(\frac{U_0 h_0}{\nu} \right)^2 \text{ and} \tag{6}$$

$$\mathrm{Sc} = \frac{\nu}{\kappa}, \tag{7}$$

where ν is the kinematic viscosity and κ is the diffusivity of temperature or salinity responsible for the density difference. The definitions are similar to those employed by Härtel, Meiburg, and Necker [22] in their study of planar case. Note that the Grashof number is essentially the square of the Reynolds number. The ratios r_0/h_0 and h_0/H are additional geometric parameters introduced by the initial condition. In this work we will concentrate on the condition $H=2h_0$, where the denser fluid initially extends vertically over the entire height of the layer.

The governing equations are solved using a de-aliased pseudospectral code [25]. Fourier expansions are employed for the flow variables along the horizontal directions (x and y). In the nonhomogeneous vertical direction (z) a Chebyshev expansion is used with Gauss–Lobatto quadrature points. The flow field is time advanced using a Crank–Nicolson scheme for the viscous and scalar diffusion terms. The advection term in the momentum equation is handled with the Arakawa scheme, where the nonlinear term is alternately considered in its convective form (as written in Eq. (1)) followed by the conservative form. A third-order Runge–Kutta scheme is used to advance the nonlinear terms. The buoyancy term is also advanced with a third-order Runge–Kutta

scheme. More details on the implementation of this numerical scheme can be found in the work by Cortese and Balachandar [26].

For the planar lock-exchange configuration the computational domain is a box of size $\tilde{L}_x=30\times\tilde{L}_y=3\times\tilde{L}_z=2$, where the spanwise width of the domain ($\tilde{L}_y=3$) has been shown to be more than adequate to capture the lobe and cleft instability [22]. For the cylindrical configuration the computational domain is also a box of size $\tilde{L}_x=30\times\tilde{L}_y=30\times\tilde{L}_z=2$. Periodic boundary conditions are enforced in the horizontal directions for all variables. At the top and bottom walls no-slip and zero-gradient conditions are enforced for velocity and density, respectively. The use of a rectangular grid to solve a cylindrical problem may seem odd. However, a Cartesian grid with equi-spaced grid points provides uniform resolution along the horizontal directions over the entire domain. This allows adequate resolution as the cylindrical front propagates radially out and we are able to better resolve the fine structures of the flow at the front (lobes and clefts). With a cylindrical grid, the circumferential resolution will be far more than what is needed as the center is approached. Furthermore, a cylindrical computational domain requires to carefully address the singularity presented by the pole at the origin as well as the outflow boundary condition at the outer extent of the computational domain. Herein, by adopting a rectangular domain and periodic boundary conditions these difficulties are clearly avoided.

For the case of the cylindrical current, periodic boundary conditions along the horizontal directions strictly imply an infinite layer of lighter fluid with a doubly periodic array of cylindrical regions of heavier fluid released into it. Here we consider the initial nondimensional radius of the cylindrical region to be $\tilde{r}_0=2$ and thus the released volume is of unit aspect ratio. Owing to the periodic boundary conditions, the lateral spacing between the cylindrical releases is 30 along both the x and y directions. Only when the head of the gravity current approaches the lateral boundaries of the computational domain, it begins to interact with the front of the adjacent currents. Based on simulation results we observe that this interaction effect can be neglected till the front reaches about 2 nondimensional units from the lateral boundaries. This behavior is similar to that observed by Härtel, Meiburg, and Necker [22] for the planar case along the x direction. As the cylindrical gravity current expands from the initial radius of 2 to about 13, its evolution is not influenced by the periodic boundary condition and can, thus, be taken as an isolated cylindrical density current spreading into an infinite lighter medium.

In this work, two different Grashof numbers will be considered: $\mathrm{Gr}=10^5$ and $\mathrm{Gr}=1.5\times10^6$. As will be discussed below, with increasing Gr the complexity of the flow increases and thus the simulation at the higher Grashof number requires increased resolution. In the cylindrical configuration the flow was solved using approximately 12 millions grid points for $\mathrm{Gr}=10^5$ ($N_x=420\times N_y=420\times N_z=72$) and 28 millions for $\mathrm{Gr}=1.5\times10^6$ ($N_x=512\times N_y=512\times N_z=110$). For the lock-exchange configuration approximately 2 million grid points were used for $\mathrm{Gr}=1.5\times10^6$ ($N_x=560\times N_y=48\times N_z=64$). The numerical resolution for each simulation was selected to have between 6 and 8 decade decay in the energy spectrum for all the variables, i.e., the three velocity components and density. The time step was selected to produce a Courant number smaller than 0.5 for all time steps.

The flow was started from rest and a small random disturbance superposed on the density field to accelerate the three-dimensional development. The following initial condition was used in all the cylindrical simulations to be reported:

$$\tilde{u}_i=0 \quad \forall\,(\tilde{x},\tilde{y},\tilde{z}), \tag{8}$$

$$\tilde{\rho}=\frac{1+\gamma_1}{2}\,\mathrm{erf}\{\sqrt[4]{\mathrm{GrSc}^2}[\tilde{r}-(\tilde{r}_0+\gamma_2)]\}. \tag{9}$$

Here $\tilde{r}=\sqrt{\tilde{x}^2+\tilde{y}^2}$, $\gamma_1\in(-0.05,0)$ and $\gamma_2\in(-\Delta x/2,\Delta x/2)$. These last two parameters are random numbers chosen from a uniform distribution. For the planar case we use the same initial condition as that of Härtel, Michaud, and Stein [27], where they justify the use of an error function to prescribe the initial density profile based on the solution to the pure diffusion equation for early times when the flow has not yet developed. The values of γ_1 and γ_2 were selected to produce a decorrelated interface with a white noise energy spectrum. In this way we assure that there is no artificially selected wavelength that could evolve in an artificial lobe and cleft pattern. The solution was advanced in time until the front reached the radial location of $\tilde{r}=13$ to avoid the influence of the lateral boundaries [27]. The above initial condition ensures that the rectangular planform of the domain and the grid do not introduce any bias in the evolution of a cylindrical front.

Results

Planar Lock-Exchange Configuration. In order to validate the code, we have performed a planar lock-exchange simulation under the same conditions reported by Härtel, Meiburg, and Necker [22], i.e., $\mathrm{Gr}=1.5\times10^6$ and $\mathrm{Sc}=0.71$. This configuration can also be seen as the limiting case of a cylindrical configuration with the condition of $\tilde{r}_0\to\infty$.

Figure 2 shows three-dimensional views of the flow time evolution visualized by a surface of constant density ($\tilde{\rho}=0.5$). The flow starts as two dimensional ($\tilde{t}=5$), forming the head of the current and the nose. Kelvin–Helmholtz instabilities are also observed in the interface between light and heavy fluid. The flow turns into a three-dimensional state ($\tilde{t}=10$ and 15) starting with instabilities at the bottom foremost part of the current that grow very rapidly, forming a pattern of lobes and clefts. Then, the whole flow becomes three dimensional ($\tilde{t}=20$) presenting vortex pairing at the rear end of the head. These results are in complete agreement with the findings of Härtel, Meiburg, and Necker [22] and with laboratory observations [3].

Figure 3 shows the mean flow visualized by density contours. Mean variables are computed as spanwise averages of the three-dimensional results, i.e.

$$\bar{f}(\tilde{x},\tilde{z})=\frac{1}{\tilde{L}_y}\int_0^{L_y} f(\tilde{x},\tilde{y},\tilde{z})\,d\tilde{y}. \tag{10}$$

In this figure the dynamics of the Kelvin–Helmholtz instabilities can be more clearly appreciated. Observe that the flow is initially symmetric, but as it becomes three dimensional the symmetry is lost. The last snapshot ($\tilde{t}=15$) also shows the beginning of vortex pairing on the lower-advancing front.

The front velocity has also been computed from two-dimensional simulations of the lock-exchange configuration with $\mathrm{Gr}=10^5$ and $\mathrm{Gr}=10^7$. The results are presented in Fig. 4. For comparison, the result of Härtel, Meiburg, and Necker [22] is also shown. Observe that the agreement is not only qualitative as mentioned above, but also quantitative. The trend of the front velocity with the Gr number is also correct.

We will not expand any further on the planar lock-exchange problem, since Härtel et al. [22,28] have presented a very fine and detailed analysis of the flow for this configuration. Now we turn into the cylindrical configuration.

Cylindrical Configuration

Flow Structure. To study the structure of the flow, simulations for $\mathrm{Gr}=10^5$ and $\mathrm{Gr}=1.5\times10^6$ were performed. The Sc number was set to 1. As addressed by Härtel, Meiburg, and Necker [22] its

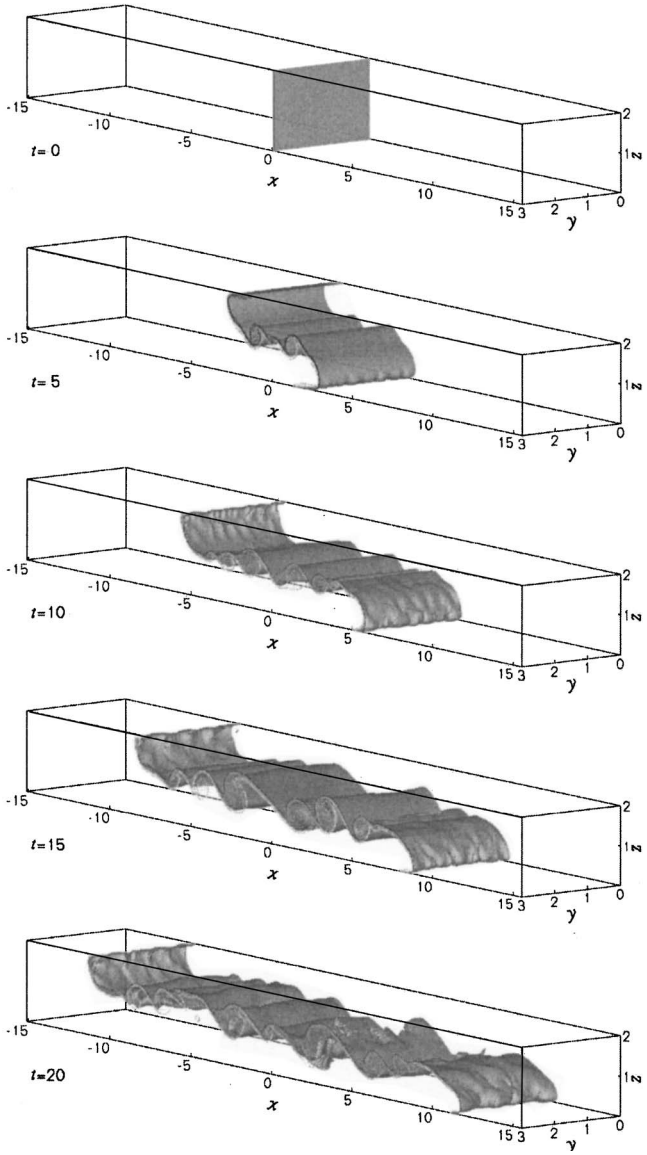

Fig. 2 Three-dimensional planar current in lock-exchange configuration for Gr=1.5×10^6 and Sc=0.71. Flow visualized by an isosurface of density $\tilde{\rho}$=0.5. At $\tilde{t}$=0 the left half of the domain has $\tilde{\rho}$=1 and the right half $\tilde{\rho}$=0. The flow starts as two-dimensional forming the head of the current ($\tilde{t}$=5), then the flow turns three dimensional ($\tilde{t}$=10, 15, and 20) developing the lobes and clefts observed in experiments.

influence on the flow is weak as long as it is kept order 1.

Figure 5 shows the time development of the flow structure for the higher Gr=1.5×10^6. In this figure the flow is visualized by a surface of constant density $\tilde{\rho}$=0.25. After the release of the denser fluid, an intrusive front forms. Initially, the flow evolves in an axisymmetric fashion in which Kelvin–Helmholtz rolls develop and form the front and the nose. Below the nose, which is raised from the bottom, an unstable stratified region forms as a consequence of the no-slip condition. In this region, three-dimensional instabilities develop and evolve into a lobe and cleft pattern in the foremost part of the current. This feature has been observed in experiments for both planar [14] and cylindrical currents [29]. Behind the front, the flow develops into a very intense three-dimensional structure where the Kelvin–Helmholtz billows shed from the front deform, bend, and break up. This behavior is similar to the planar case [22,30].

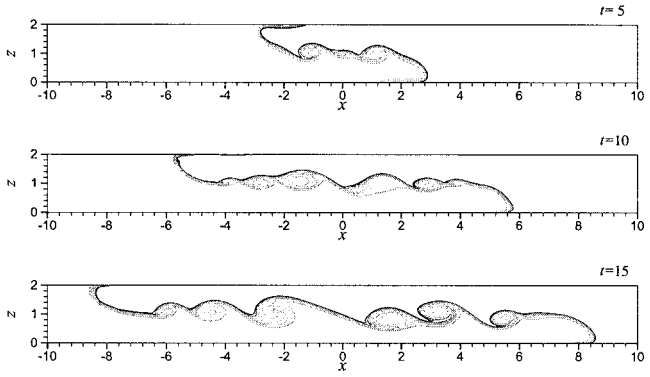

Fig. 3 Mean flow of planar current in lock-exchange configuration for Gr=1.5×10^6 and Sc=0.71. Flow visualized by density contours. The flow starts symmetrically, but this symmetry is lost as the flow becomes three dimensional. Observe also the beginning of vortex pairing at $\tilde{t}$=15 in the front advancing to the right.

One of the main differences between the cylindrical (finite volume release) and the planar lock-exchange configurations is the maximum density value inside the current. Figure 6 shows the time evolution of the maximum density, $\tilde{\rho}_{max}$, with time for planar lock-exchange and cylindrical currents with Gr=1.5×10^6. In a truly planar lock-exchange configuration, which corresponds to infinite volume release, at all finite times the maximum and minimum concentration levels remain at 1.0 and 0.0, and, respectively, correspond to unmixed heavy and light fluids. In the present periodic finite volume planar lock exchange, over the time interval computed and shown in Fig. 2, the maximum and minimum concentrations remain 1.0 and 0.0, respectively. In the cylindrical configuration the small finite volume release of heavy fluid quickly mixes with the surrounding light fluid as it flows out. Thus the maximum concentration remains equal to 1.0 only for a short duration after which the concentration decreases. In the present periodic case the final well mixed concentration will be 2.8% and it depends on the ratio of volume released to the volume of the periodic box. From Fig. 6 it is clear that the released heavy fluid is everywhere diluted by entrainment of lighter fluid, but the mixing process is far from complete. While $\tilde{\rho}_{max}$ remains equal to the initial value ($\tilde{\rho}_{max}$=1) the cylindrical current moves at approximately constant velocity. This phase of spreading is called

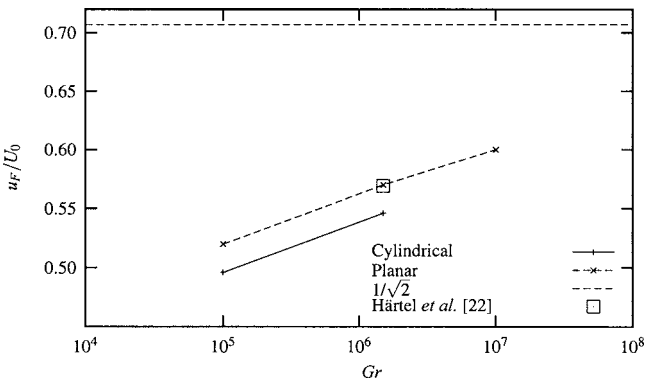

Fig. 4 Front velocity in the slumping phase as a function of Gr number. Planar refers to the planar lock-exchange configuration and Cylindrical to the finite volume release in cylindrical configuration. The open square is the outcome of the simulation by Härtel, Meiburg, and Necker [22] in good agreement with our results.

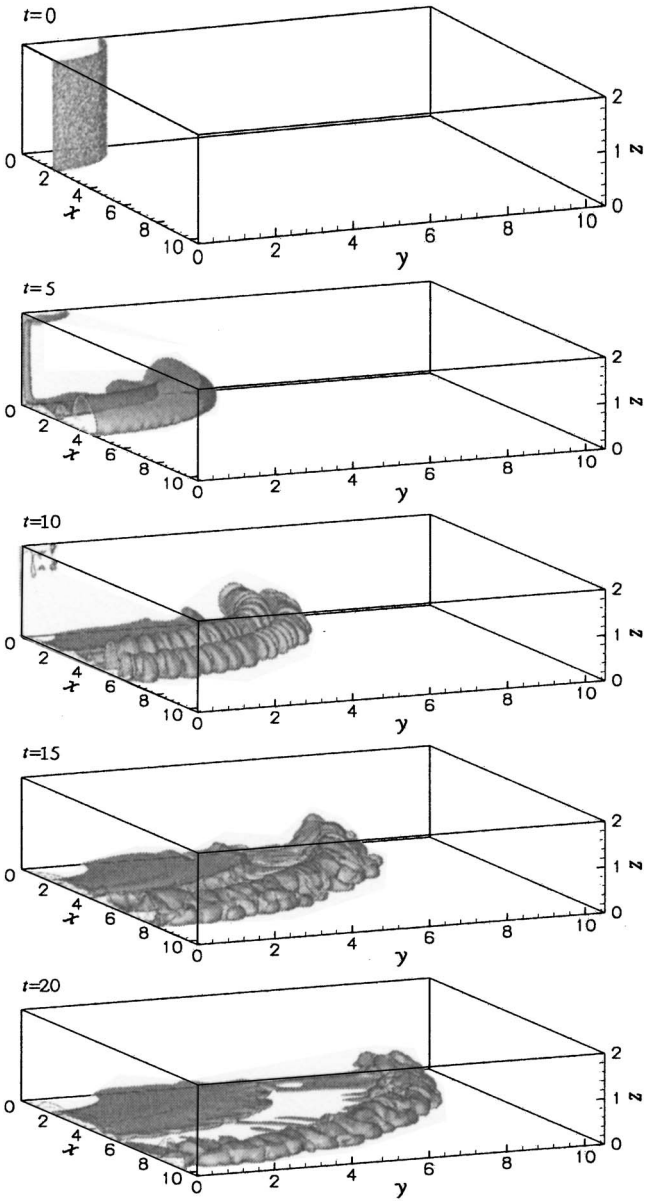

Fig. 5 Three-dimensional cylindrical current for Gr=1.5×10^6 and Sc=1. Flow visualized by an isosurface of density $\tilde{\rho}$=0.25. The figure shows only one quarter of the simulation domain. At $\tilde{t}$=0 the cylindrical region has $\tilde{\rho}$=1 and everywhere outside it $\tilde{\rho}$=0. The flow starts as two dimensional, but soon after it develops three-dimensional instabilities at the front. The flow becomes completely three dimensional eventually.

slumping phase [12]. In the case of the planar lock exchange, $\tilde{\rho}_{\max}=1$ for all the computation time and the front spreads at constant speed.

The lobe and cleft structure of the front is shown in detail in Fig. 7. Figure 7(*a*) is a visualization of the front in a laboratory experiment for Gr$\sim 10^8$ and Sc=700 using the same geometrical configuration of the numerical simulations. Figure 7(*b*) is a close view of the numerical results for Gr$=1.5\times 10^6$ and Sc=1. We can observe in this figure the similitude between the experimental and numerical results despite the difference in the Sc (Sc in the experiment is two order of magnitude larger than in the numerical simulation). This is in agreement with the findings of Härtel, Meiburg, and Necker [22] who state that the Sc does not influence the flow as long as it is kept order 1 or larger. In contrast to the planar case [22], the number of lobes in the front stays almost

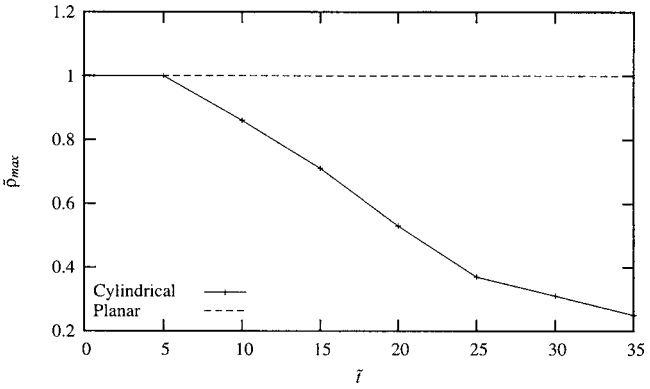

Fig. 6 Maximum value of $\tilde{\rho}$ ($\tilde{\rho}_{\max}$) over time. Planar refers to the planar lock-exchange configuration and Cylindrical to the finite volume release in cylindrical configuration, both for Gr =1.5×10^6. The value of $\tilde{\rho}_{\max}$ in the current is related to the front velocity. While $\tilde{\rho}_{\max}$=1 the current moves at approximately constant velocity.

constant as the front evolves. However, since the current is spreading radially, the size of the lobes grows as the current spreads out until it is dissipated by mixing of light fluid. The origin and dynamics of this instability are still not well understood. Simpson [14] states that the lobe and cleft instability forms only in no-slip surfaces and it is caused by denser fluid overrunning less dense fluid. However, recent work by McElwaine and Patterson [15] suggests that this is not necessarily the case and that lobes and clefts may still form in free-slip surfaces provided the Gr number of the flow is large enough. Our simulations show that the formation of lobes and clefts is highly Gr dependent even in the case of no-slip surfaces. For example, the solution for Gr $=10^5$ does not present this feature. The solution is completely axisymmetric for all time (see Fig. 8).

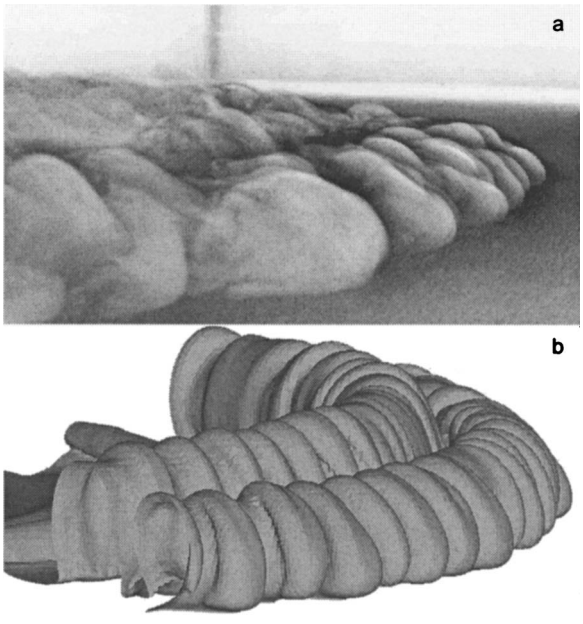

Fig. 7 Lobe and cleft instability in a cylindrical current. (*a*): Visualization of the front in a laboratory experiment for Gr ~10^8 and Sc=700 using the same geometrical configuration of the numerical simulations. (*b*): Numerical result for Gr=1.5 ×10^6 and Sc=1.

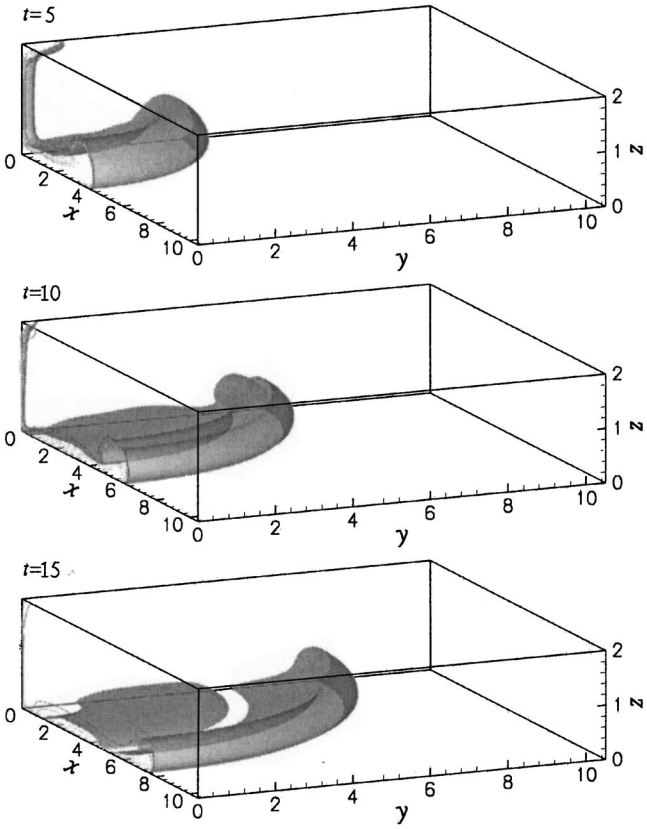

Fig. 8 Three-dimensional cylindrical current for Gr=10^5 and Sc=1. Flow visualized by surface of density $\tilde{\rho}=0.25$. The figure shows only one quarter of the simulation domain. For this case, the pattern of lobes and clefts is not observed.

The structure of the mean flow is also dependent on the Gr number. In the cylindrical configuration the mean flow is computed as

$$\bar{f}(\tilde{r},\tilde{z}) = \frac{1}{2\pi}\int_0^{2\pi} f(\tilde{r},\tilde{\theta},\tilde{z})d\tilde{\theta}. \tag{11}$$

Figures 9 and 10 show the mean flow visualized by contours of constant density for Gr=1.5×10^6 and Gr=10^5, respectively. The main structures of the flow, namely head, nose, and body are

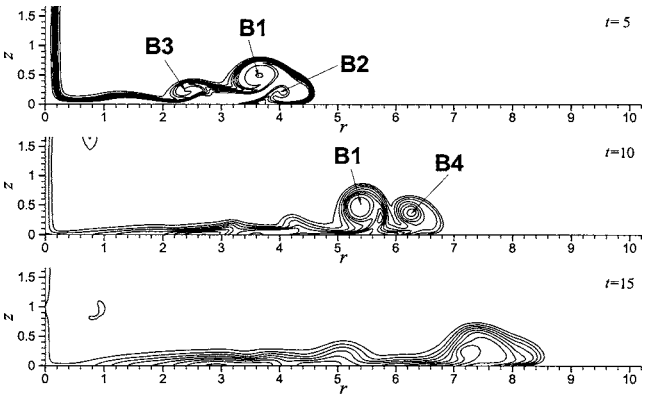

Fig. 9 Mean flow of cylindrical current for Gr=1.5×10^6 and Sc=1. Flow visualized by density contours. The main vortex structures are indicated in the figure. The dynamic of the vortical structures is in complete agreement with the experimental results of Alahyari and Longmire [24] for Gr$\sim10^7$.

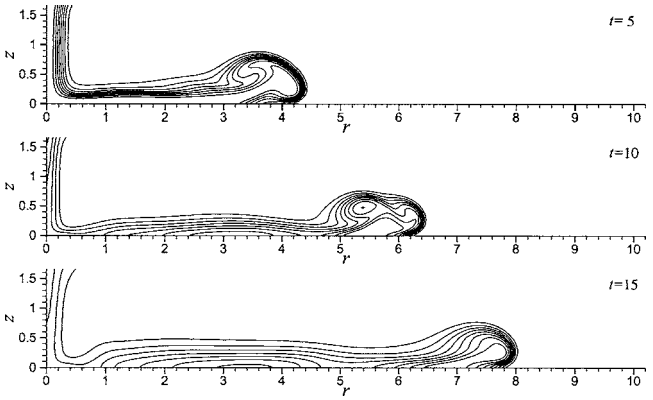

Fig. 10 Mean flow of cylindrical current for Gr=10^5 and Sc=1. Flow visualized by density contours. For this case the flow presents weak vortex structures.

present for both Gr investigated, however, there are substantial differences. The head of the current for Gr=10^5 features a single vortex that evolves in time to become a rounded structure. On the other hand, the current for Gr=1.5×10^6 features two vortices in the head that eventually pair and form a triangular structure. It is also clearly seen from these figures that the nose location (h_N in Fig. 1) of the current for Gr=10^5 is always higher compared to the current for Gr=1.5×10^6. This feature is in agreement with experimental observations [31]. In contrast to the behavior of the nose location, the height of the head (h_F in Fig. 1) is approximately the same for both Gr. However, h_F diminishes over time transforming the potential energy of the head into kinetic energy of the flow, which is subsequently expended in mixing light fluid into the current and dissipated by viscous effects. Another clear difference between the two Gr solutions is the structure and height of the body (h_B in Fig. 1) of the current. The lower Gr current presents a higher body with a regular structure while the higher Gr current presents a lower body with vortical structures in it.

Mean Flow Dynamics. When viscous effects are not important (high Gr) the current that develops from the release of a fixed volume of heavy fluid passes through three different phases [12], provided that the volume of released fluid is large enough. Soon after the release, the current enters the slumping phase, which is characterized by a nearly constant front velocity. Huppert and Simpson [12] proposed that this phase lasts until $h_B=0.075H$. Then, the current enters a self-similarity phase called the inertial phase. During this phase the front decelerates and the front velocity evolves as $t^{-1/2}$ (cylindrical configuration). This self-similar phase lasts until viscous effects take over, and the current enters the viscous phase. Depending on the initial configuration of the flow, the inertial phase may or may not be present. In the following we will describe the dynamics of the mean flow during the slumping and inertial/viscous phases.

An idea of how the flow evolves can be gained from Figs. 9 and 10 that show the time evolution of the mean flow for Gr=1.5×10^6 and Gr=10^5, respectively. The development of the mean flow starts with a short acceleration phase. In this phase, the nose is formed and the front reaches the slumping phase velocity. After the initial acceleration phase, the flow enters the slumping phase and moves at approximately constant speed, which depends on Gr. In this phase the flow presents a very interesting behavior. First, a large billow is formed in the front (B1 in Fig. 9), which gives the current the characteristic structure of front (or head) and body. Then, two more billows are formed. One counter-rotating billow is formed in the lower region of the front (B2), which has been interpreted as boundary layer separation by Alahyari and Longmire [24] caused by the adverse pressure gradient produced by the first billow (B1). The other billow (B3) is formed in the body of

the current and rotates in the same direction as the first billow (B1). Finally, the first billow formed in the front (B1) retards the upper part of the front, which gives place to the formation of another billow at the front (B4). At the same time, billows B2 and B3 loose their identity.

After the slumping phase, the flow enters into the inertial/viscous phases. During these phases the third billow formed at the front (B4) becomes more prominent and undergoes the same dynamics as the first billow (B1) in the slumping phase. Billow B4 retards the front and pair with billow B1 to form a triangular wedge that eventually dissipates.

The dynamics of the flow described here is in good agreement with the findings of Alahyari and Longmire [24] based on their laboratory experiments. It is worth noticing that the Gr of their experiment is larger ($\mathrm{Gr} \simeq 10^7$) than our simulation, however, the dynamics and structure of the flow are quite similar.

Front Velocity. The planar lock-exchange configuration (infinite volume release) from the previous section can be seen as the limiting case of the cylindrical configuration with infinite radius. Thus, the planar lock-exchange density current will stay in the slumping phase and will never reach the inertial phase, while the corresponding cylindrical current started from a finite volume release will transition from the initial slumping phase to an inertial phase and finally to a viscous phase. The time at which these transitions take place depend on the amount of fluid being released and on the Reynolds number of the flow. The slumping phase is characterized by a constant front velocity, which based on theory [5,6] takes a value of $1/\sqrt{2}$ for the case of $2h_0=H$. Based on a best fit to experimental data, Huppert and Simpson (12) proposed the same nondimensional front velocity for both planar and cylindrical currents. In this section we present front velocity results in the slumping phase obtained from our simulations of planar lock-exchange and cylindrical currents for two values of Gr.

The front velocity is computed by tracking the front location over time. If $\tilde{r}_F$ denotes the front location, the front velocity is computed as

$$\tilde{u}_F = \frac{d\tilde{r}_F}{d\tilde{t}}. \tag{12}$$

The front location is defined as the largest radial location where the mean flow density equals a preset density value (for example, $\tilde{\rho}=0.01$).

Figure 4 shows the front velocity for the planar lock-exchange configuration and for the slumping phase of the cylindrical configuration. The figure also shows the value reported by Härtel, Meiburg, and Necker [22] (open square) in good agreement with our results. There is a clear dependency of the front velocity on Gr number, which was originally observed by Simpson and Britter [31]. This Gr dependency is less strong for larger Gr (see Härtel, Meiburg, and Necker [22]) and it is likely to be negligible for large enough values of Gr, reaching an asymptotic state close to the theoretical value.

There is also a well defined dependency on the geometrical configuration of the current. The cylindrical current is slower than the planar current. This is in contradiction with the findings of Huppert and Simpson (12), who reported the front velocity to be independent of the geometrical configuration. It can be argued that the numerical simulations are at lower Gr and over a narrow range compared to the experimental results, and that for larger Gr the cylindrical currents could reach the same asymptotic state as the planar lock-exchange configuration. The answer to this question will be addressed in a forthcoming work.

Concluding Remarks

In the present work, we have presented and discussed the results of three-dimensional direct numerical simulations of density currents in planar lock-exchange and cylindrical configurations. There were two main objectives in this paper. The first one was to validate the present computational methodology by comparing our results with previously published experimental and numerical works [22,24] and with experimental visualizations produced for this work. The second one was to present a detailed analysis and visualization of three-dimensional density currents in cylindrical configuration. The simulations were performed employing a dealiased pseudospectral code, which allows accurate representation of all length scales.

We have presented three-dimensional results for $\mathrm{Gr}=1.5\times10^6$ and $\mathrm{Sc}=0.71$ and two-dimensional results for $\mathrm{Gr}=10^5$ and $\mathrm{Gr}=10^7$ with $\mathrm{Sc}=1$ in the planar lock-exchange configuration. The flow starts as two dimensional and preserves the initial symmetry for early times. For later times the flow becomes three dimensional, presents a pattern of lobes and clefts at the front, and the symmetry of the flow is lost. These results are in complete agreement with the results reported by Härtel, Meiburg, and Necker [22], qualitatively as well as quantitatively. We have also presented three-dimensional simulations in cylindrical configuration for $\mathrm{Gr}=10^5$ and $\mathrm{Gr}=1.5\times10^6$, and $\mathrm{Sc}=1$. These highly resolved simulations allowed for a detailed analysis and visualization of the flow structures (two- and three-dimensional structures) and dynamics. The simulation for $\mathrm{Gr}=1.5\times10^6$ exhibits the main features observed in laboratory experiments [14,29] (see also Fig. 7), and the dynamics of the flow computed in this simulation is in agreement with experimental observations [24] at higher Gr ($\sim10^7$).

The results for front velocity indicate dependencies on both the Gr and on geometrical configuration. However, it is possible that with increasing Gr the front velocity will reach an asymptotic state that is independent of Gr and geometrical configuration. Simulations for larger Gr are under way and the answer to this question will be presented in a forthcoming paper.

Acknowledgment

We gratefully acknowledge the support of the Coastal Geosciences Program of the Office of Naval Research (Award No. N00014-03-1-0143), the Chicago District of the U.S. Army Corps of Engineers, and the Metropolitan Water Reclamation District of Greater Chicago. Support from the National Center for Supercomputer Applications at the University of Illinois at Urbana-Champaign is also acknowledged. Mariano Cantero was supported by a Graduate Student Fellowship from the Computational Science and Engineering Program at UIUC. Computer time was provided by Dr. Fady Najjar and Dr. Nahil Sobh.

References

[1] Simpson, J., 1997, *Gravity Currents*, 2nd ed., Cambridge University Press.
[2] Allen, J., 1985, *Principles of Physical Sedimentology*, George Allen and Unwin Ltd..
[3] García, M., and Parker, G., 1989, "Experiments on Hydraulic Jumps in Turbidity Currents Near a Canyon-Fan Transition," Science, **245**, pp. 393–396.
[4] García, M., 1994, "Depositional Turbidity Currents Laden With Poorly Sorted Sediment," J. Hydraul. Eng., **120**(11), pp. 1240–1263.
[5] von Kármán, T., 1940, "The Engineer Grapples With Nonlinear Problems," Bull. Am. Math. Soc., **46**, pp. 615–683.
[6] Benjamin, T., 1968, "Gravity Currents and Related Phenomena," J. Fluid Mech., **31**, pp. 209–248.
[7] Rottman, J., and Simpson, J., 1983, "Gravity Currents Produced by Instantaneous Releases of a Heavy Fluid in a Rectangular Channel," J. Fluid Mech., **135**, pp. 95–110.
[8] Bonnecaze, R., Huppert, H., and Lister, J., 1993, "Particle-Driven Gravity Currents," J. Fluid Mech., **250**, pp. 339–369.
[9] Choi, S.-U., and García, M., 1995, "Modeling of One-Dimensional Turbidity Currents With a Dissipative-Galerkin Finite Element Method," J. Hydraul. Res., **33**(5), pp. 623–648.
[10] Hallworth, M., Huppert, H., Phillips, J., and Sparks, R., 1996, "Entrainment Into Two-Dimensional and Axisymmetric Turbulent Gravity Currents," J. Fluid Mech., **308**, pp. 289–311.
[11] Hallworth, M., Huppert, H., and Ungarish, M., 2001, "Axisymmetric Gravity Currents in a Rotating System: Experimental and Numerical Investigations," J. Fluid Mech., **447**, pp. 1–29.
[12] Huppert, H., and Simpson, J., 1980, "The Slumping of Gravity Currents," J. Fluid Mech., **99**, pp. 785–799.

[13] Allen, J., 1971, "Mixing at Turbidity Current Heads, and its Geological Implications," J. Sediment. Petrol., **41**(1), pp. 97–113.
[14] Simpson, J., 1972, "Effects of the Lower Boundary on the Head of a Gravity Current," J. Fluid Mech., **53**(4), pp. 759–768.
[15] McElwaine, J., and Patterson, M., 2004, "Lobe and Cleft Formation at the Head of a Gravity Current," *Proceedings of the XXI International Congress of Theoretical and Applied Mechanics*, Warsaw, August 15–21.
[16] García, M., and Parsons, J., 1996, "Mixing at the Front of Gravity Currents," Dyn. Atmos. Oceans, **24**, pp. 197–205.
[17] Parsons, J., and García, M., 1998, "Similarity of Gravity Current Fronts," Phys. Fluids, **10**(12), pp. 3209–3213.
[18] García, C., Manríquez, C., Oberg, K., and García, M., 2005, "Density Currents in the Chicago River, Illinois," *Proceedings of the 4th IAHR Symposium on River, Coastal and Estuarine Morphodynamics*, G. Parker and M. García, eds., Urbana, IL, October 4–7, Vol. 1, pp. 191–201.
[19] Droegemeier, K., and Wilhelmson, R., 1987, "Numerical Simulation of Thunderstorm Outflows Dynamics. Part I: Outflow Sensitivity Experiments and Turbulence Dynamics," J. Atmos. Sci., **44**(8), pp. 1180–1210.
[20] Terez, D., and Knio, O., 1998, "Numerical Study of the Collapse of an Axisymmetric Mixed Region in a Pycnoclyne," Phys. Fluids, **10**(6), pp. 1438–1448.
[21] Terez, D., and Knio, O., 1998, "Numerical Simulation of Large-Amplitude Internal Solitary Waves," J. Fluid Mech., **362**, pp. 53–82.
[22] Härtel, C., Meiburg, E., and Necker, F., 2000, "Analysis and Direct Numerical Simulation of the Flow at a Gravity-Current Head. Part 1. Flow Topology and Front Speed for Slip and No-Slip Boundaries," J. Fluid Mech., **418**, pp. 189–212.
[23] Necker, F., Härtel, C., Kleiser, L., and Meiburg, E., 2002, "High-Resolution Simulations of Particle-Driven Gravity Currents," Int. J. Multiphase Flow, **28**, pp. 279–300.
[24] Alahyari, A., and Longmire, E., 1996, "Development and Structure of a Gravity Current Head," Exp. Fluids, **20**, pp. 410–416.
[25] Canuto, C., Hussaini, M., Quarteroni, A., and Zang, T., 1988, *Spectral Methods in Fluid Dynamics*, Springer-Verlag.
[26] Cortese, T., and Balachandar, S., 1995, "High Performance Spectral Simulation of Turbulent Flows in Massively Parallel Machines With Distributed Memory," Int. J. Supercomput. Appl., **9**(3), pp. 187–204.
[27] Härtel, C., Michaud, L. K. M., and Stein, C., 1997, "A Direct Numerical Simulation Approach to the Study of Intrusion Fronts," J. Eng. Math., **32**, pp. 103–120.
[28] Härtel, C., Carlsson, F., and Thunblom, M., 2000, "Analysis and Direct Numerical Simulation of the Flow at a Gravity-Current Head. Part 2. The Lobe-and-Cleft Instability," J. Fluid Mech., **418**, pp. 213–229.
[29] Spicer, T., and Havens, J., 1987, "Gravity Flow and Entrainment by Dense Gases Released Instantaneously Into Calm Air," *Proceedings of the Third International Symposium on Stratified Flows*, E. List and G. Jirka, eds., Pasadena, CA, February 3–5, pp. 642–651.
[30] Cantero, M., García, M., Buscaglia, G., Bombardelli, F., and Dari, E., 2003, "Multidimensional CFD Simulation of a Discontinuous Density Current," *Proceedings of the XXX IAHR International Congress*, Thessaloniki, Greece, August 24–29.
[31] Simpson, J., and Britter, R., 1979, "The Dynamics of the Head of a Gravity Current Advancing Over a Horizontal Surface," J. Fluid Mech., **94**, pp. 477–495.

Modeling Mixture Formation in a Gasoline Direct Injection Engine

Rossella Rotondi
Dipartimento di Ingegneria Meccanica,
Università di Roma "Tor Vergata",
Viale del Politecnico 1,
00133 Roma, Italy
e-mail: rossella.rotondi@uniroma2.it

Mixture formation and combustion in a gasoline direct injection (GDI) engine were studied. A swirl-type nozzle, with an inwardly opening pintle, was used to inject the fuel directly in a four stroke, four cylinder, four valves per cylinder engine. The atomization of the hollow cone fuel spray was modeled by using a hybrid approach. The most important obstacle in the development of GDI engines is that the control of the stratified-charge combustion over the entire operating range is very difficult. Since the location of the ignition source is fixed in SI engines the mixture cloud must be controlled both temporally and spatially for a wide range of operating conditions. Results show that the volume of the spark must be considered when discretizing the computational domain because it highly influences the flow field in the combustion chamber. This is because the volume occupied by the plug cannot be neglected since it is much bigger than the ones used in port fuel injection engines. The development of a successful combustion system depends on the design of the fuel injection system and the matching with the in-cylinder flow field: the stratification at part load appears to be the most crucial and critical step, and if the air motion is not well coupled with the fuel spray it would lead to an increase of unburned hydrocarbon emission and fuel consumption [DOI: 10.1115/1.2173284]

1 Introduction

To satisfy CO_2 emissions restrictions that will be introduced in the industrialized countries, brake-specific fuel consumption (BSFC) has to be reduced. Gasoline port-fuel injection engines that are in production today have a higher BSFC compared to the direct-injection (DI) Diesel engines. This is due to the higher compression ratio and the unthrottled operation typical of diesel engines, that, however, have higher NO_x and soot emissions, slightly higher noise level, and lower startability. The ideal would be to put together the best features of both, combining diesel efficiency with gasoline-specific power. Studies in this direction have shown that this may be achieved with gasoline direct injection (GDI) unthrottled engine [1,2]. Fuel is injected directly into the combustion chamber in order to have a mixture with an ignitable composition near the spark plug at the time of ignition for all loads. Power is controlled by varying the amount of fuel injected in a diesel-like manner, and with the unthrottled operation pumping losses are significantly reduced. The charge cooling during injection, higher compression ratio, lower octane requirement, and increased volumetric efficiency lead to an improved BSFC up to 30%. The critical step in the development of such engines is the stratification at partial loads, at which an erroneous mechanism of mixture formation leads to an increase of engine-specific fuel consumption and unburned hydrocarbon emissions.

2 Fuel Injection System in GDI Engines

GDI injectors can either be single-fluid or air-assisted (two phase) and may be classified by atomization mechanism (sheet, turbulence, pressure, cavitation), by actuation type, by nozzle configuration (that can be either swirl, slit, multihole or cavity type), or by spray configuration (hollow cone, solid cone, fan, multi plume). A detailed classification of GDI injectors may be found in [1]. Currently the most widely used injector for GDI applications, the one analyzed in this paper, is the single-fluid, swirl-type unit that uses an inwardly opening pintle, a single exit orifice, and a fuel pressure, in the range of 70–100 bar.

The liquid emerges from the single discharge orifice as an annular sheet that spreads radially outwards to form an initially hollow-cone spray. Pressure energy is transformed into rotational momentum that enhances atomization. The initial spray angle ranges between 25–150 deg and the Sauter mean diameter (SMD) varies from 14 to 23 μm. Surface roughness may, however, produce streams of fuel in the fuel sheet, resulting in formation of pockets of locally rich mixture. The spray has a leading edge (the main spray tip) that penetrates away from the nozzle tip for about 50 mm in less than 20 ms. A toroidal vortex is also attached to the periphery. The leading edge of the spray contains a separate sac.

The fuel injection system needs to provide different operating modes for the different loads. Fuel injection pressure varies in a range from 40 to 130 bar. In the full-load case a stratified homogenous charge is needed and this is done with an early injection, during the induction. A well-dispersed spray is desirable, with bigger cone angle and a conical shape. At part load, a late injection is needed in order to allow stratified charge combustion, with a well-atomized compact spray to control the stratification. The fuel is injected during the compression stroke when the cylinder pressure is about 10 bar, which requires a relatively higher injection pressure compared to the full-load case. The higher injection pressure is necessary to reduce the Sauter mean radius (SMD) of the liquid spray, because the fuel must vaporize before the spark event occurs in order to limit unburned hydrocarbons (UBHC) emissions and to have a repeatable ignition process. The smaller the droplet size, the faster the vaporization occurs. GDI systems require fuel droplets of under 20 μm SMD (diesel engines require SMD lower than 8 μm).

3 The Experimental Engine

The numerical code has been tested comparing numerical results with experiments [3] on a GDI, four cylinder, four valves per cylinder engine, whose characteristics are reported in Table 1.

This engine is fueled by the injector previously described. Compared to a multi-point injection (MPI) engine it is characterized by a higher compression ratio typical of this class of engines. As load increases the combustion varies from stratified to homogeneous. The engine, as it can be seen in the CAD design of Fig. 1, has in one of each of the cylinder's intake duct a swirl valve able to modify the air motion in the cylinder as a function of the

Contributed by the Applied Mechanics Division of ASME for publication in the JOURNAL OF APPLIED MECHANICS. Manuscript received May 26, 2005; final manuscript received December 19, 2005. Review conducted by G. C. Buscaglia. Discussion on the paper should be addressed to the Editor, Prof. Robert M. McMeeking, Journal of Applied Mechanics, Department of Mechanical and Environmental Engineering, University of California-Santa Barbara, Santa Barbara, CA 93106-5070, and will be accepted until four months after final publication of the paper itself in the ASME JOURNAL OF APPLIED MECHANICS.

Table 1 Basic engine geometric characteristics

Bore	7.2 (cm)
Stroke	10.2 (cm)
Displacement	459.5 (cm^3)
No. of cylinders	4
Compression ratio	12.5

engine operating conditions. For the full-load case, requiring a homogeneous charge (stoichiometric air/fuel ratio), the above-mentioned valve is completely open, determining a well-organized swirl motion in the cylinder, while at part load, when a stratified charge is needed, the valve is throttled in order to have a tumble motion in the chamber. In Fig. 1 a CAD design of the engine and the related computational grid are shown.

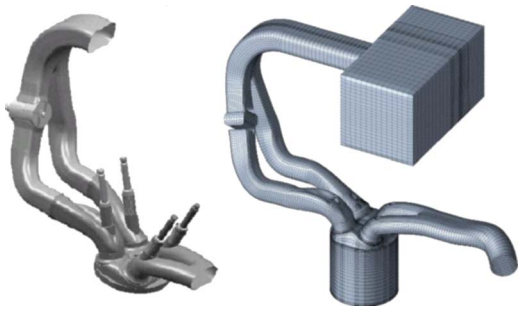

Fig. 1 CAD design of the engine and related computational grid

4 Numerical Code

The developed numerical computation tool "NCF 3D" is based on the well-known KIVA III code originally developed by the Los Alamos Laboratory [4,5]. It employs a finite volume approximation of the governing 3D Navier-Stokes (N-S) equations in a Cartesian or cylindrical reference system in which a multi-block grid structure is generated. A modified $\kappa-\varepsilon$ turbulence model, accounting for compressibility effects, is used during the arbitrary Lagrangian Eulerian (ALE) integration of the averaged N-S equations. The original version has been enhanced by a certain number of specific submodels necessary for GDI engine modeling as listed in the following:

4.1 Boundary Conditions—1D Simulations. The whole engine was first simulated following a fully 1D approach [6], at different full- and part-load conditions. Figure 2 shows the intake system, the plenum collector, the four cylinders, and the exhaust system. Ambient conditions are set at the intake and exhaust boundaries, while the experimental in-cylinder pressure was imposed for the combustion.

Then 3D simulations, at the same load conditions, were performed, and the boundaries conditions at the inlet of the 3D domain (plenum) and the exhaust were imposed by the corresponding values in the 1D simulations.

Comparisons were made between experimental pressure, the 1D and the 3D numerical ones, in the intake duct, at the location shown in Fig. 1. The related diagrams are reported in Fig. 3 for a part-load case (left) and a full-load case (right).

It can be seen that the experimental and numerical pressure profile versus crank angle present the same frequency while some discrepancies in the magnitude are present. This is due to the heat transfer and friction effects evaluations, but in order to provide boundary conditions to the 3D code the 1D results are acceptable, having a volumetric efficiency error lower than 8%.

Comparisons were also made between the experimental and 1D numerical pressure in the plenum and experimental and 3D numerical pressure in the cylinder at different loads. Results show an agreement with a discrepancy of 7% in the worst case.

For the 3D simulations following cycles were also simulated in order to evaluate the influence of initial conditions. At high engine speed (up to 5000 rpm), up to three following cycles were simulated in order to minimize the differences. Differences were slightly bigger for the part-load cases.

4.2 Injection and Atomization Models. A Lagrangian treatment of stochastic particle injection is used for the liquid drops that simulate the spray. The fuel spray enters the computational domain as an annular sheet, but in the KIVA spray model this continuous liquid is artificially divided into discrete Lagrangian parcels injected into the gas. Each computational parcel represents a group of physically similar droplets that exchange mass momentum and energy with the surrounding air through source terms in the gas phase equations. The liquid jet is simulated by injecting blobs with characteristic size equal to the sheet thickness.

Following Nagaoka's approach [7] the liquid jet exiting the injector is treated as a liquid sheet until it reaches its breakup length. The sheet is analyzed discretizing its volume in small quantities to which the momentum conservation equation is applied.

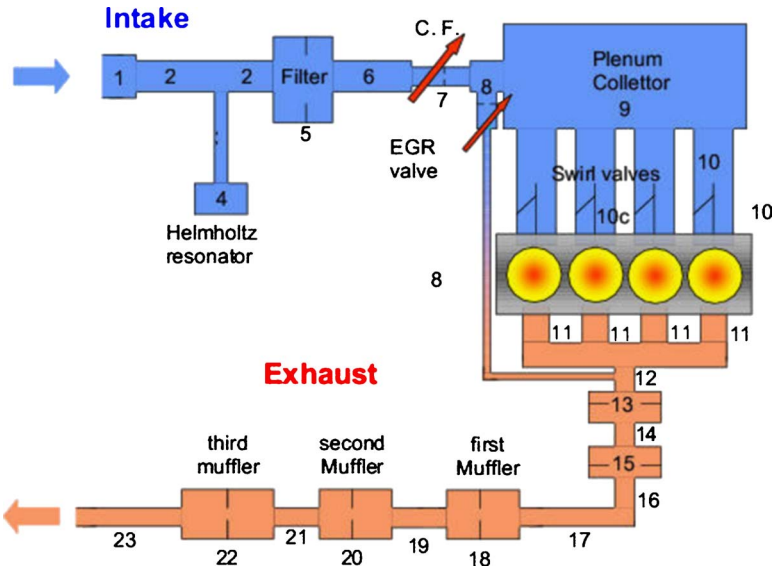

Fig. 2 Schematic of the whole engine in the 1D approach

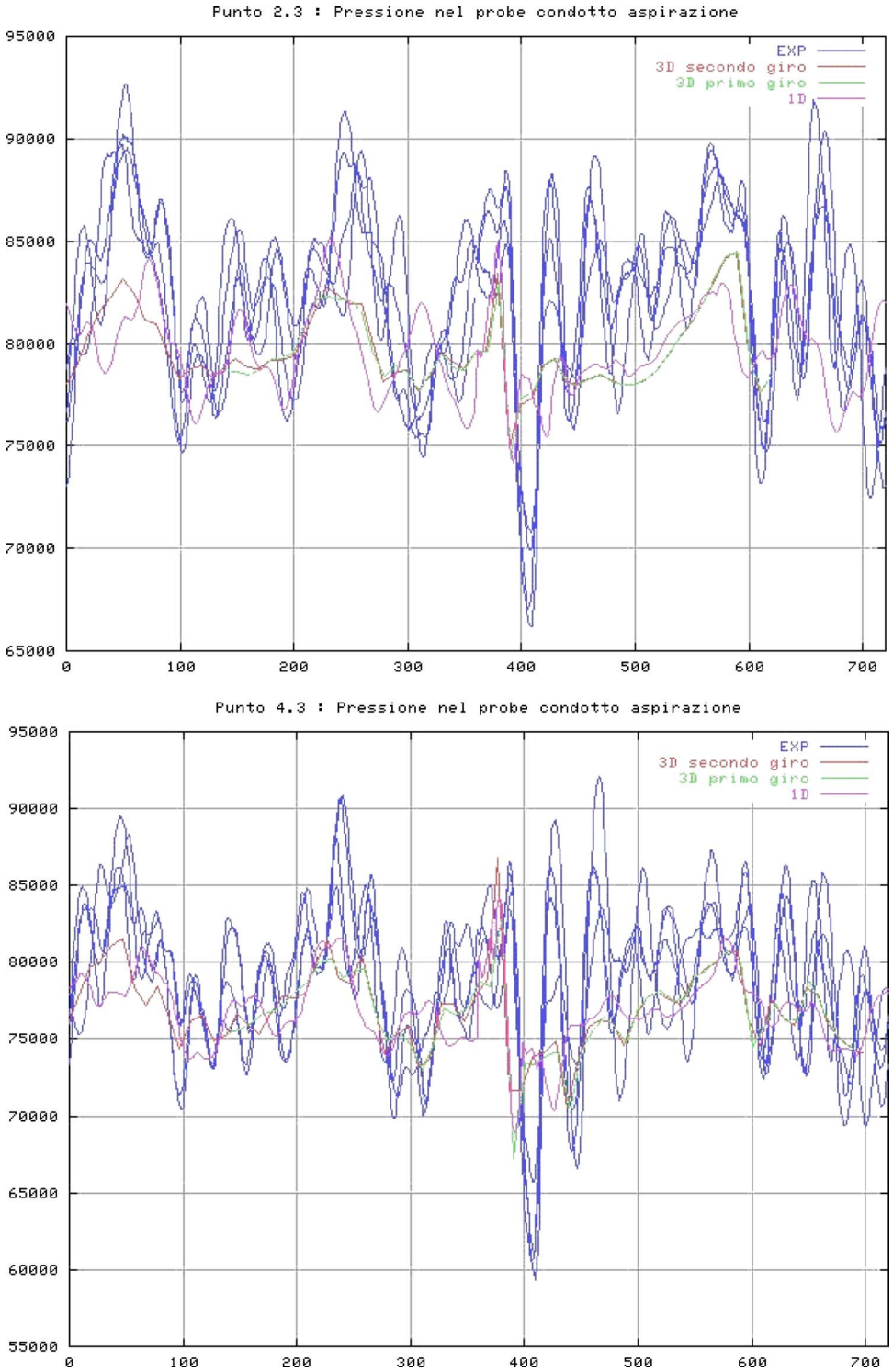

Fig. 3 Comparison between numerical (1D and 3D) and experimental pressure (Pascal) in the intake duct. Part load case (top) and full load case (bottom).

$$\frac{d\bar{u}_f}{dt} = C_s \frac{\rho_g |(\bar{u}_g - \bar{u}_f)_n|}{\rho_f} (\bar{u}_g - \bar{u}_f)_n + \frac{1}{\rho_f} \frac{\partial p}{\partial n}$$

in which $\bar{u}_g$ is the velocity vector related to the gas comprehensive of the turbulence term (for which the k-ε model implemented in KIVA was used), and $\bar{u}_f$ is the velocity vector related to the liquid "sheet." Subscript n refers to the sheet normal direction, g and f to gas and fluid, respectively. The variation of the sheet thickness during the injection period is evaluated imposing mass conservation:

$$h_f = \frac{K_0}{L + K_0/h_0} \qquad K_0 = h_0(w_0 - h_0)\cos\theta/(2\sin\theta)$$

where K_0 represents the sheet thickness variation, L is the distance from the injector, and θ is the angle with respect to the injector axis [8]. In the previous expression h_0 represents the sheet thick-

Table 2 Summary of combustion model constants

B_m	30.5
B_ϕ	−54.9
Φ_m	1.21
C_μ	0.09
C_1	8.0
C_2	0.142

Table 3 Spark model constants

Parameter	Arc discharge	Glow discharge
η_{0B}	36	8
η_∞	50	30
A (m/s)	500	700

ness at the exit of the injector, while w_0 represents the characteristic length so it was put equal to the nozzle diameter, d_0. The breakup length is evaluated by means of the formula [9]

$$L_b = \frac{18\sqrt{2}}{F}\sqrt{\frac{\rho_f}{\rho_g}}\frac{h_f}{\sqrt{\mathrm{We}_h}}$$

where F is the ratio between the amplitude of the pressure waves that arise in viscous flow over those in a inviscid flow. F is evaluated as follows:

$$F = \sqrt{N(2-N)}\left[\left(1+\frac{N^3V^2}{4(2-N))}\right)^{3/2} - \frac{3}{2}\sqrt{\frac{N^3V^2}{4(2-N))}}\right]$$

$$N \approx (1+2.29V)^{-0.677}$$

$$V = \frac{\sqrt{2}}{4}Z$$

$$Z = \mathrm{Oh}\cdot\mathrm{We}$$

$$\mathrm{Oh} = \frac{\mu_f}{\sqrt{\rho_f\sigma_f h_f}}$$

$$\mathrm{We} = \frac{\rho_g u_{\mathrm{rel}}^2 h_f}{\sigma_f}$$

where u_{rel} is the relative velocity between gas and liquid, σ_f is the surface tension force of the liquid, and μ_f is the liquid viscosity. Before the droplet detaches from the liquid sheet, because of the interaction between the two phases, ligaments of characteristic size d_L are formed on the surface of the conical sheet:

$$d_L = \left(\frac{8}{9}\right)^{1/3}\left[\frac{K_0^2\sigma_f^2}{\rho_g\rho_f u_{\mathrm{rel}}^4}\right]^{1/6}\left[1+2.6\mu_f\left(\frac{K_0\rho_g^4 u_{\mathrm{rel}}^7}{72\rho_f^2\sigma_f^5}\right)^{1/3}\right]^{1/5}$$

These ligaments detach as droplets of diameter d_D related to the ligament size by the following correlation:

$$d_D = 1.88\cdot d_L\cdot(1+3\cdot\mathrm{Oh}_L)^{1/6} \quad \mathrm{Oh}_L = \frac{\mu_f}{\sqrt{\rho_f\sigma d_L}}$$

in which Oh_L is the Ohnesorge number of the ligament [10].

d_D is proportional to the characteristic size to be put in the Rosin-Rammler distribution function [11]

$$1 - V = e^{-(D^q/\bar{D})}$$

$$\bar{D} = C_1 d_D$$

(that is widely used in spray applications) to determine the post breakup sizes of the primary parcels. Usually for internal combustion engines applications $1.5 < q < 4$, and it was put equal to 3.5 [12]. C_1 is an empirical factor [13] put equal to 1. In the present simulation this model was used for primary atomization as was done in previous work [14].

Once the droplets are formed they may undergo secondary breakup. This was modeled using different approaches in the different regimes as the droplet Weber number changes as done in previous works [15].

The droplets formed after the atomization of the annular liquid sheet may undergo secondary breakup. Because of the forces acting on a droplet, as it moves in the surrounding gas, a nonuniform pressure distribution is developed around it. This process leads to droplet deformation and subsequent breakup. The relevant forces in this physical phenomenon are those related with surface tension, viscosity, inertia, and surface instabilities responsible for wave growth. Different regimes can be observed as the relative magnitude of these forces varies. One possible classification [16] can be made over different ranges of droplet Weber number ($\mathrm{We}=\rho_l u_r^2 d_D/\sigma_l$).

In the *vibrational mode* (We=12) fragmentation is caused by the amplification of droplet deformation originated by vibrational resonance of the liquid surface. In the *bag regime* ($12<\mathrm{We}<45$) the drop breakup is due to the deformation of the droplet in a baglike structure that disintegrates after a critical value of deformation is reached. The *chaotic regime* ($45<\mathrm{We}<100$) is a transitional regime in which droplet breakup is due to both ballooning and breaking of filaments resulting from the liquid surface layer ripping. In the *stripping regime* ($100<\mathrm{We}<1000$) the flow over the drop causes the ripping of the surface inducing a thin laminar boundary on it. After a certain stage of deformation, the boundary layer is stripped from the periphery because of K-H instability effects, in the form of film and fragments (boundary layer stripping). Drop diameter gradually reduces and, when a critical value is reached, the drop disintegrates in smaller ones with bimodal distribution. The *catastrophic regime* occurs at $\mathrm{We}>100$ where both R-T and K-H instabilities are involved. The first, due to droplet deceleration and related to higher values of wavelength and amplitude, leads to the formation of bigger drops then those related with K-H instabilities associated with lower values of wavelength and amplitude.

For a GDI pressure system the injection velocities can reach maximum values of about 100 m/s, so the catastrophic regime is unlikely to happen. During their lifetime drops may decelerate, breakup, and evaporate and different ranges of droplet Weber number can be reached, so different secondary breakup mechanisms can then be simultaneously present.

The TAB [17] and DDB [18] models are based on the dynamic of a single droplet and can therefore be considered as a secondary breakup model. In the first model the breakup is due to the amplification of droplet deformation resulting from vibrational resonance of the surface and therefore was chosen to model droplet breakup in the vibrational regime. The second is a deformation-induced secondary breakup model and is used in the bag regime. The WAVE [19] model considers K-H instability effects and can be used to simulate the breakup of secondary droplets in the stripping regime. In the chaotic regime, in which bag breakup and stripping coexist, a competition between the DDB model and the WAVE model was implemented.

All the models are used with the original value of the constants except for the WAVE model. For the latter a customized value of

Table 4 Operating condition for the homogeneous case

	rpm	mep	EGR	Lambda	Spark advance
Case 0	3000	6 bar	10%	0.954	21.4 deg

the size constant (B_0=0.59) was chosen, while the time constant B_1 was set equal to 80 according to previous work [20,21] in which the values of the constants were determined for the low injection pressure range, comparing numerical droplet sizes and velocities to the experimental ones evaluated by means of a phase Doppler particle analyzer (PDPA) technique.

4.3 Combustion Model. The approach used is based on a suggestion made by Abraham et al. [22] and subsequently modified by Reitz [23] and is particularly suitable for GDI combustion computation in highly stratified charge conditions due to the strong influence that the value of the local air/fuel ratio exerts on the formulation of the burning rate. In this combustion model the time rate of change of the partial density of species i, due to the conversion from one chemical species to another, is given by:

$$\frac{dY_i}{dt} = -\frac{Y_i - Y_i^*}{\tau_c}$$

where Y_i is the mass fraction of species i and Y_i^* is the local and instantaneous thermodynamic equilibrium value of the mass fraction. τ_c is defined as the characteristic time scale to achieve the equilibrium. The characteristic time scale is assumed to be the same for all the considered species. The characteristic conversion time scale τ_c is assumed to be expressed as:

$$\tau_c = \tau_l + \tau_t$$

where τ_l is the laminar conversion time scale and τ_t the turbulent mixing time scale.

The characteristic laminar conversion time scale for gasoline has been evaluated as a function of pressure p, temperature T, and equivalence ratio ϕ, using the procedure described in [22]. A power law was used to determine the laminar burning velocity for the gasoline combustion in each computational cell [24]:

$$S_l = S_{lo}\left(\frac{T_u}{T_0}\right)^{\alpha}\left(\frac{p}{p_0}\right)^{\beta}$$

where for gasoline α, β are given by:

$$\alpha = 2.4 - 0.271\phi^{3.51} \quad \beta = -0.357 + 0.14\phi^{2.77}$$

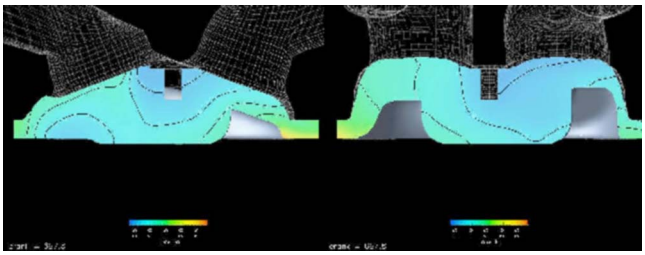

Fig. 4 Lambda distribution in the combustion chamber. Homogeneous case.

$$S_{lo} = B_m + B_\phi(\phi - \phi_m)$$

Once the laminar burning velocity in the flame is determined, it is possible to evaluate the flame thickness and the laminar conversion time by means of the following expressions:

$$\delta_l = \frac{\bar{D}_l}{S_l} \quad \tau_l = \frac{\delta_l}{S_l}$$

$\bar{D}$ being an average value of the laminar diffusion coefficient in the flame front.

The turbulent mixing time scale can be estimated according to Magnussen and Hjertager [25] and introduces a delay coefficient as suggested in [22,26]. The use of this coefficient takes into consideration the delay of the turbulent mixing, allowing, during the delay period, the laminar flame to move a distance equal to two or three times the length scale of the turbulent eddies. The delay coefficient f can be expressed as:

$$f = -\exp\left(-\frac{t - t_s}{\tau_d}\right)$$

where:

$$\tau_d = C_t\frac{l_t}{S_l} \quad l_t = C_\mu^{3/4}\frac{k^{3/2}}{\varepsilon \cdot \kappa}$$

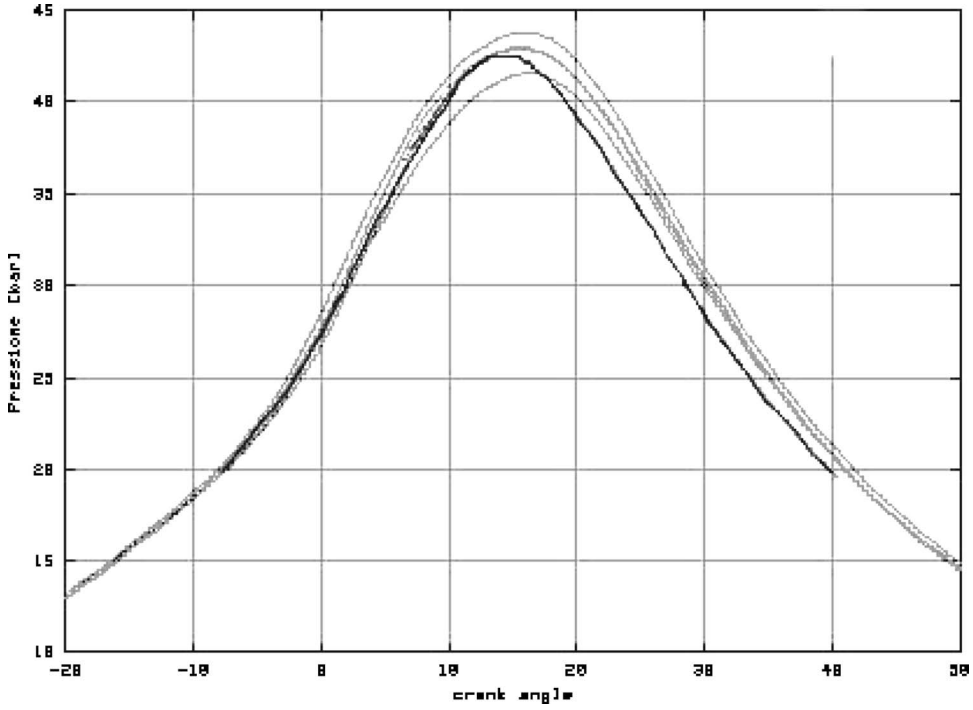

Fig. 5 Experimental and numerical indicated cycle for nominal crank timing: 21.4 deg

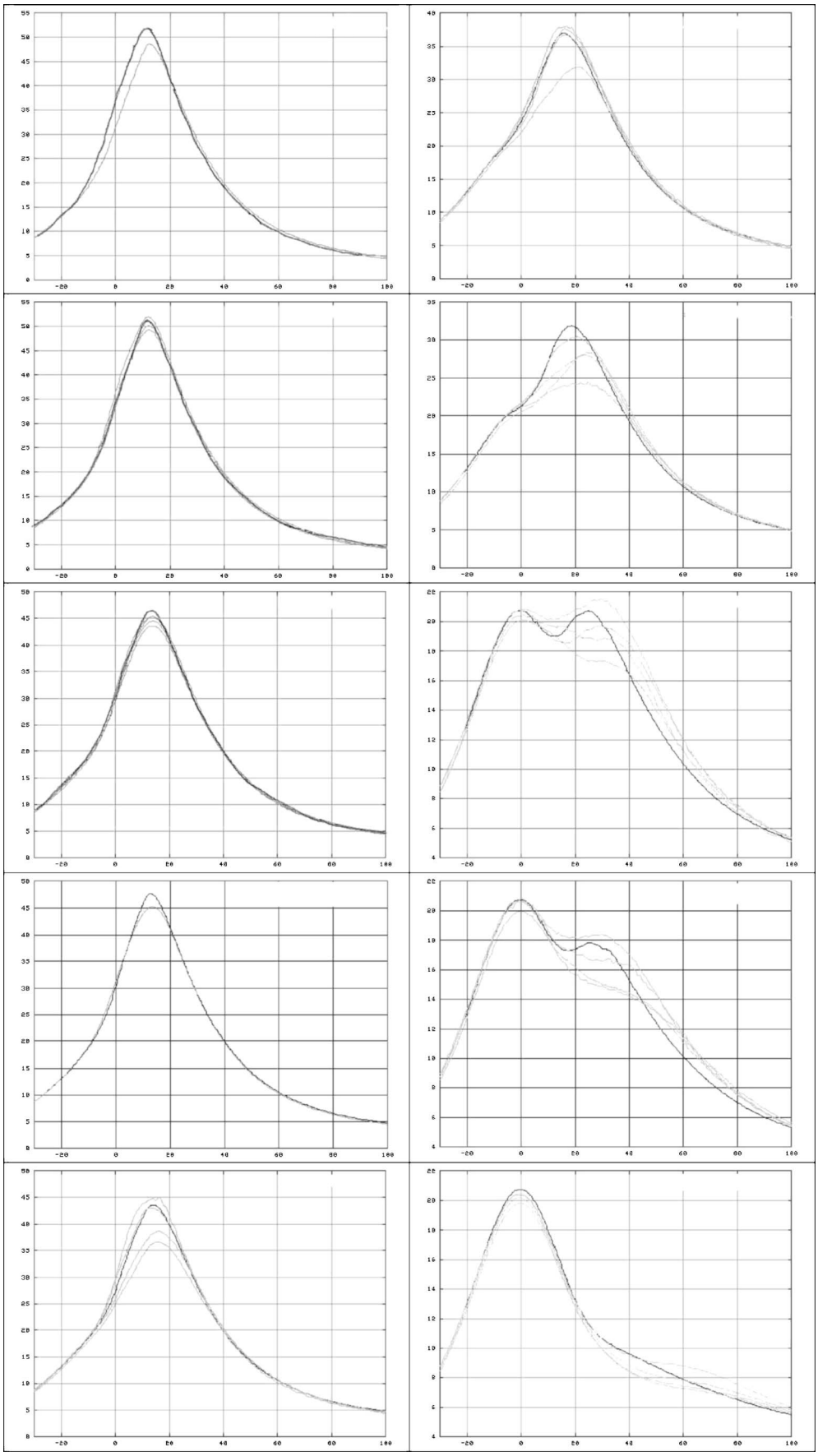

Fig. 6 Numerical (dark line) and experimental (lighter lines) indicated cycle for different crank timing: 29, 27, 25, 24, 22, 17, 12, 7, 4, 1, and –2 deg

Table 5 Operating conditions of three different cases

	rpm	mep (bar)	EGR	Lambda	Spark advance	Injected mass (mg)	Start of injection (deg)
Case 1	1000	4	15%	1.477	18.9	12.94	637.2
Case 2	2000	4	10%	1.58	22.1	12.73	626.6
Case 3	2000	2	20%	2.072	24.1	8.150	638

with $k=0.41$ (the von Karman constant).

The turbulent mixing time scale can then be expressed as:

$$\tau_t = C_2 \frac{k}{\varepsilon} \chi \cdot f$$

where

$$\chi = 1 \quad \text{for } h < 1$$

$$\chi = 1/h \quad \text{for } h \geqslant 1$$

with

$$h = \frac{0.6(Y_p - Y_{ps})}{(Y_f - Y_f^* + Y_{0_2} - Y_{0_2}^*)}$$

where subscripts p and ps refer to products of combustion at actual and stoichiometric conditions, respectively, and f refers to fuel. The constants are given in Table 2.

4.4 Spark Plug Model. A model that simulates the initial flame kernel formation and development in SI engines was used according to [27,28]. The ignition phase includes electrical discharge, plasma breakdown, and shock wave propagation. The mixture in the combustion chamber is ignited by the electrical discharge between the spark plug electrodes. The spark discharges the electrical energy through the arc and glow phases. Plasma is created and the flame kernel is produced by the plasma. All these phenomena occur in a very short period of time (less than 10^{-6} s) and in a relatively small domain, which has a size ranging from the spark gap distance to the order of the turbulence integral length scale [24].

The initial temperature and diameter of the plasma are given by:

$$T_i = \left[\frac{1}{\gamma} \left(\frac{T_b}{T_0} - 1 \right) + 1 \right] T_0$$

$$d_i = 2 \left[\frac{\gamma - 1}{\gamma} \frac{E_b}{\rho_0 d (1 - T_0/T_i) \pi} \right]^{1/2}$$

where γ is the specific heat ratio, E_b and T_b are the breakdown energy and temperature respectively, d is the gap distance between the electrodes, and T_0 and p_0 temperature and pressure in the combustion chamber.

Heat is dissipated in all directions following the equation:

$$\frac{\partial T}{\partial r} = \alpha \left(\frac{\partial^2 T}{\partial^2 r} + \frac{2}{r} \frac{\partial T}{\partial r} \right) + \frac{\eta_{B,G} U(t) I(t) + E_{che}}{\rho_{\text{pl}} c_p V_k}$$

with the following initial conditions:

$$T(0,r) = T_i \quad \text{if } 0 < r < d_i/2$$

$$T(0,r) = T_0 \quad \text{if } r > d_i/2$$

in which α is the thermal diffusivity, ρ_{pl} is the gas density of plasma, c_p is the specific heat at constant pressure, $I(t)$ and $U(t)$ are current and voltage as measured across the spark gap, and $\eta_{B,G}$ is the energy transfer efficiency for arc and glow discharge, respectively, given by the following expression [28]:

$$\eta_{B,G} = \eta_{0B,G} + \frac{(\eta_{\infty B,G} - \eta_{0B,G}) U^3}{A_{B,G} + U^3}$$

in which $\eta_{0B,G}$ and $\eta_{\infty B,G}$ are the energy transfer efficiency for a quiescent mixture and for very high velocities ($v \geqslant 15$ m/s), respectively. $A_{B,G}$ are given constants (see Table 3) and U is the voltage as measured across the spark gap.

Kernel radius r_k is then determined as the location at which the temperature equals the adiabatic flame temperature. The kernel velocity v_k is then calculated as the time derivative of r_k. Two distinct transition criteria can be used to switch from the ignition model to the combustion model. The one proposed by Herweg and Maly [28], used in present simulations, states that the ignition process should be finished when the kernel velocity reaches the laminar burning velocity. Another criteria proposed by Reitz et al. [29] imposes the kernel size to reach the order of the integral length scale:

$$d_k \geqslant C_k l_T$$

where $C_k=3.5$ and l_T is the turbulence length scale related to the turbulent kinetic energy, k, and its dissipation rate, ε, by:

$$l_T = 0.16 \frac{k^{1.5}}{\varepsilon}$$

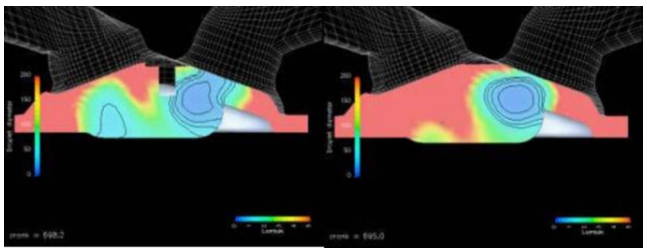

Fig. 7 Lambda distribution at ignition crank angle. Case 3. Grid considering the volume of the plug (left) and grid neglecting it (right).

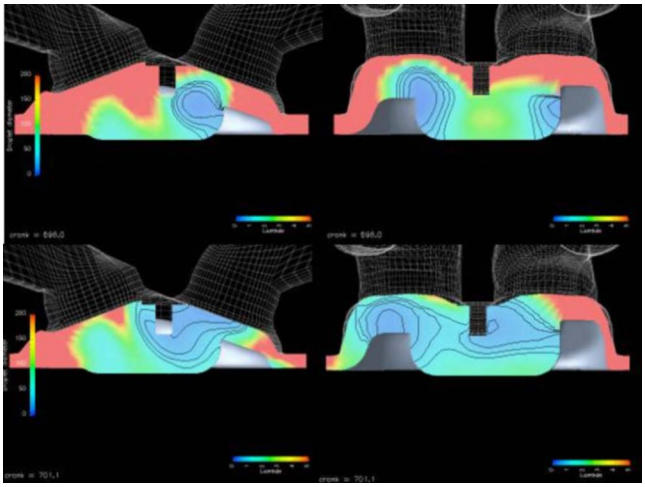

Fig. 8 Lambda distribution at ignition crank angle. Case 1 (up) and case 2 (down) in two different planes.

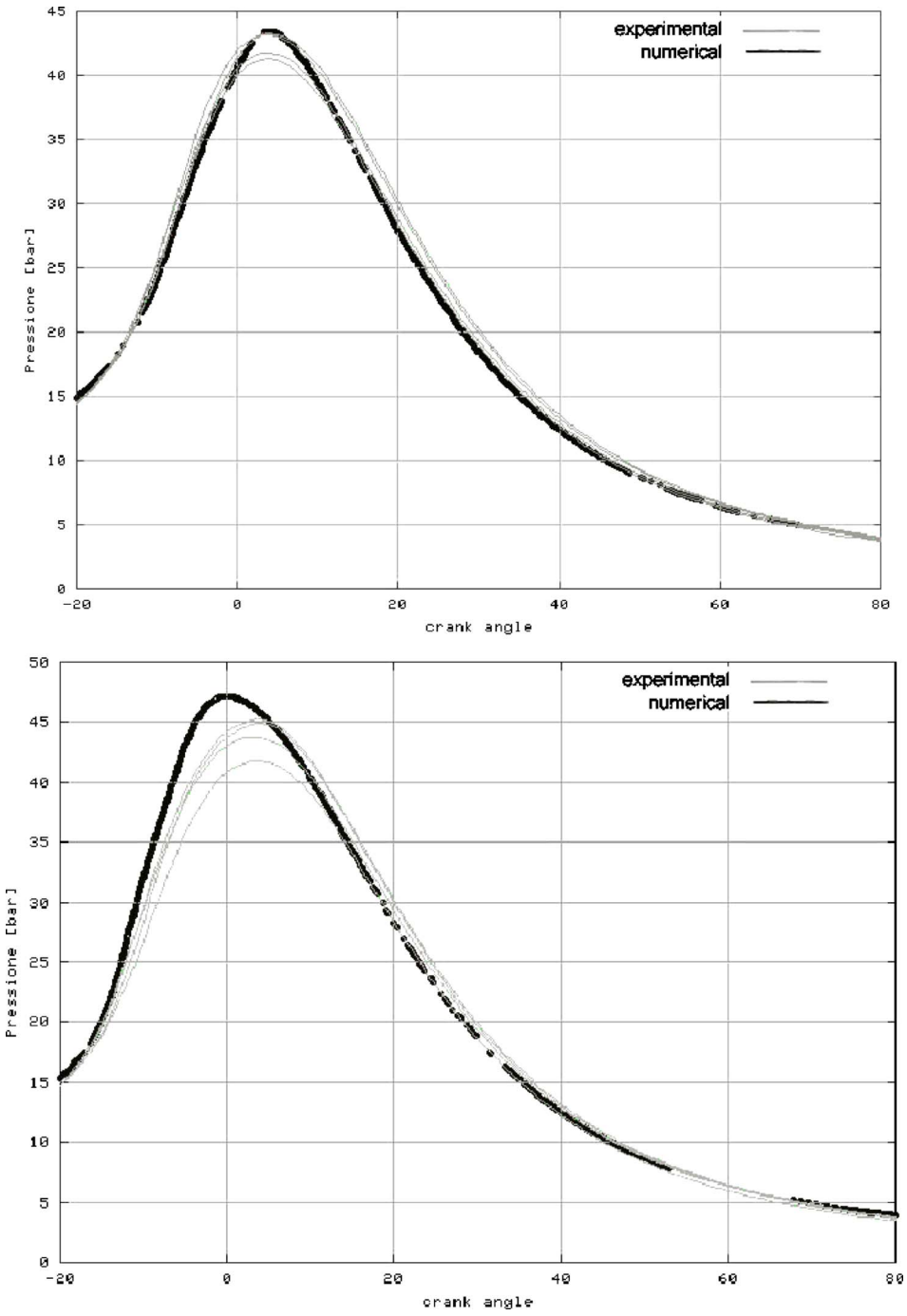

Fig. 9 Indicated cycle for cases 1 and 3

5 Engine Simulations

To correctly predict the combustion phase a precise mixture formation modeling is absolutely necessary, so present simulation must involve also the intake and exhaust stroke to have a right prediction of the air motion inside the cylinder which highly influences the mixture formation.

The grid generation is generated within the main frame of the original design in CAD-CATIA, while the final multi-block mesh for the KIVA III solver is made by the IBM created interface, the ENGAGE code. The resulting computational domain was shown in Fig. 1. The grid has about 160,000 computational cells and discretizes the cylinder and part of the intake and exhaust systems.

Different simulations were performed at different loads (from 0 to 6 bar mean effective pressure, mep), engine speed (from 750 to 5000 rpm), and EGR, for homogeneous and stratified charge cases. Homogeneous mixture in this kind of engine is a globally stoichiometic mixture with a local nonhomogeneity that can go up to about 5%. This produces significant variations in ignition delay and in unburned hydrocarbon emission. Locally rich zones can give, for these engines, soot emissions.

For the homogeneous case results concerning the configuration shown in Table 4 will be presented. In Fig. 4 two plots of the lambda distribution are reported in different planes. It can be seen how the mixture is nearly homogeneous around the stoichiometric value (lambda=1).

To test the predictive capability of the spark model several simulations were performed for this case varying the spark advance timing and comparing numerical results with experiments. In Fig. 5 the numerical and experimental indicated cycles are

reported for the nominal spark timing 21.4 deg. The agreement is very good. Then different simulations were performed changing the spark timing (29, 27, 25, 24, 22, 17, 12, 7, 4, and −2 deg), comparing the experimental indicated cycle to the numerical one as shown in Fig. 6. The model constants were set once for the nominal spark advance timing and never changed in all the different simulations. The experimental curves are an average of 64 consecutive cycles. As it can be seen in most cases four experimental diagrams are shown and this is because, in some operating conditions, there were big differences between the four cylinders. This is probably due to the plenum's particular shape. The numerical cycle was acceptable if laying between the four experimental ones. The results show very good agreement, if not considering the second plot (29 deg spark advance). This case being very stable (the four cylinders have the same history), this could be due to an erroneous modeling of the ignition process since, because of the shorter time from the start of injection, the air/fuel mixture presents strong gradients near the plug.

As mentioned before, for GDI engines, the most challenging problem is the charge stratification and combustion at part load, so results concerning some cases in the stratified mode will be presented in the following, as listed in Table 5. As it can be evinced from the table the part load cases with higher EGR are reported. These are certainly the most difficult cases since there is little fuel that needs a very high stratification of the charge, made harder by the high levels of EGR.

As it can be evidenced in the following figures the volume of the spark was considered when discretizing the computational domain. This is fundamental in GDI engine modeling since the volume occupied by the spark plug is not neglectable, being it is much bigger than the ones used in port fuel injection engines. Figure 7 shows on the left-hand side, for case 3, the lambda distribution when the spark volume is considered and it is much different from the one we have on the right-hand side in which the same case, but in a grid in which this volume is neglected, is reported.

The reason for this completely different air-fuel distribution is that the tumble motion, which determines the mixing, is different in the two cases. If not considering the plug, the tumble in a vertical plane through the cylinder axis has a characteristic length equal to half the combustion chamber, but, if the plug is considered, this characteristic length is half of the previous one. Instead of having one big vortex, in a vertical plane, we have two distinct tumble motions on each side of the chamber and this can be seen in a second cloud of fuel on the left side of the chamber completely absent in the second picture. In Fig. 8 the lambda distribution at the ignition crank angle is reported for cases 1 and 2.

In Fig. 9 pressure is plotted against crank angle, comparing the experimental (in each of the four cylinders) and numerical ones for cases 1 and 3.

6 Conclusions

Mixture formation and combustion in a four-stroke, four-cylinder, four valves per cylinder gasoline direct injection engine fueled by a swirl injector with a inwardly opening pintle were studied [1,2].

At first a 1D simulation of the whole engine was performed in order to provide more realistic boundary conditions to the NCF-3D code. Both stratified charge (atpart load) and nearly homogeneous charge (at higher loads) were modeled for different engine speeds and different percentage of EGR. Stratified charge is obtained at part load by throttling a swirl valve in one of the two intake ducts of each cylinder. This determines a tumble motion in the chamber that helps in the formation of a stratified mixture near the spark plug. A modified ignition model was used and tested varying the spark advance timing in the homogeneous case. Results show good agreement. Results also show that the spark plug, which is an internal obstacle, may affect the in-cylinder flow field and the subsequent mixture formation, especially at part load. Therefore the plug volume was considered when generating the computational grid.

The numerical results globally show that the stratification at part load is the most crucial and critical step, and if the air flow motion is not well coupled with the fuel spray, the combustion could be incomplete with higher exhaust emissions.

References

[1] Zhao, F. F., Harrington, D. L., and Lai, M. C., 2002, *Automotive Gasoline Direct-Injection Engines*, SAE.

[2] Zhao, F. Q., Lai, M. C., and Harrington, D. L., 1997, "A Review of Mixture Preparation and Combustion Strategies for Spark-Ignited Direct Injection Gasoline Engine," SAE, Paper No. 970627.

[3] Nu, M. I. D. I. A., 2003, private communications.

[4] Amsden, A. A., Ramshaw, J. D., O'Rourke, P. J., and Dukowicz, J. K., 1993, "A Computer Program for Two and Three Dimensional Fluid Flows With Chemical Reaction and Fuel Spray," Los Alamos Labs., LS 12503 MS.

[5] Amsden, A., 1993, "KIVA-3: A KIVA Program With Block-Structured Mesh for Complex Geometries," Los Alamos National Laboratory.

[6] Alessandri, M., 2000, "Simulazione Della Fase di Ricambio Della Carica in un Motore Benzina ad Iniezione Diretta," Tesi di Laurea Università di "Tor Vergata."

[7] Nagaoka, M., and Kawamura, K., 2001, "A Deforming Droplet Model for Fuel Spray in Direct-Injection Gasoline Engines," SAE Paper No. 2001-01-1225.

[8] Dombrowski, N., Hasson, D., and Ward, D., 1960, "Some Aspects of Liquid Flow Through Fan Spray Nozzles," Chem. Eng. Sci., **12**, pp. 35–50.

[9] Dombrowski, N., and Johns, D., 1963, "The Aerodynamic Instability and Disintegration of Viscous Liquid Sheets," Chem. Eng. Sci., **18**, pp. 203–214.

[10] Ohnesorge, W., 1936, "Formation of Drops by Nozzles and the Breakup of Liquid Jets," Z. Angew. Math. Mech., **16**, pp. 355—358.

[11] Sauter, J., 1926, "Determining Size of Drops in Fuel Mixture of Internal Combustion Engines," NACA TM 390.

[12] Han, Z., Parrish, S., Farrel, P. V., and Reitz, R. D., 1997, "Modeling Atomization Processes of Pressure Swirl Hollow-Cone Fuel Sprays," Atomization Sprays, **7**, pp. 663–684.

[13] Hayakawa, M., Takada, S., Yonesige, K., Nagaoka, M., and Takeda, K., 2002, "Fuel Spray Simulation of a Slit Nozzle Injector for Direct-Injection Gasoline Engine," SAE Paper No. 2002-01-1135.

[14] Beccaria, M., Bella, G., and Lanzafame, R., 2003, "Simulazione Fluidodinamica di uno Spray di Combustibile per Motori ad Accensione Comandata GDI," ATI.

[15] Rotondi, R., Bella, G., Grimaldi, C., and Postrioti, L., 2001, "Atomization of High-Pressure Diesel Spray: Experimental Validation of a New Breakup Model," SAE Paper No. 2001-01-1070.

[16] Giffen, E., and Muraszew, A., *The Atomisation of Liquid Fuels*, Chapman & Hall, London.

[17] O'Rourke, P. J., and Amsden, A. A., 1987, "The Tab Method for Numerical Calculation of Spray Droplet Breakup," SAE Paper No. 872089.

[18] Ibrahim, E. A., Yang, H. Q., and Przekwas, A. J., 1993, "Modeling of Spray Droplets Deformation and Breakup," J. Propul. Power, **9**, pp. 651–654.

[19] Reitz, R. D., 1996, "Computer Modeling of Sprays," Spray Technology Short Course, Pittsburgh, PA, May.

[20] Bella, G., Rotondi, R., Corcione, F. E., and Valentino, G., 1999, "Experimental and Computational Analysis of a Diesel Spray," 4th International Conference ICE99, Internal Combustion Engines: Experiments and Modeling, Capri.

[21] Devita, A., Alaggio, M., and Rotondi, R., 2000, "Experimental and Numerical Studies of Diesel Fuel and Biodiesel Spray," ASME Technical Paper No. 2000-ICE-333.

[22] Abraham, J., Bracco, F. V., and Reitz, R. D., 1985, "Comparison of Computed and Measured Premixed Charge Engine Combustion," Combust. Flame, **60**, pp. 309–322.

[23] Reitz, R. D., and Kuo, T. W., 1989, "Modelling of HC Emissions Due to Crevice Flows in Premixed Charge Engines," SAE Paper No. 892085.

[24] Heywood, J. B., 1995, *Internal Combustion Engine Fundamentals*, McGraw Hill Book Co., New York.

[25] Magnussen, B. F., and Hjertager, B. H., 1971, 16th Symposium (International) on Combustion, The Combustion Institute, Pittsburgh, PA, pp. 649–657.

[26] Reitz, R. D., 1991, "Assessment of Wall Heat Transfer Models for Premixed-Charge Engine Combustion Computations," SAE Paper No. 910267.

[27] Song, J., and Sunwoo, M., 2000, "A Modeling and Experimental Study of Initial Flame Kernel Developement and Propagation in SI Engines," SAE Paper No. 2000-01-0960R.

[28] Herweg, R., and Maly, R. R., 1992, "A Fundamental Model for a Flame Kernel Formation in S.I. Engines," SAE Paper No. 922243.

[29] Fan, L., Li, G., Fan, Z., and Reitz, R. D., 1999, "Modeling Fuel Preparation and Stratified Combustion in a Gasoline Direct Injection Engine," SAE Paper No. 1999-01-0175.

Cassio M. Oishi
e-mail: oishi@icmc.usp.br

José A. Cuminato
e-mail: jacumina@icmc.usp.br

Valdemir G. Ferreira
e-mail: pvgf@icmc.usp.br

Murilo F. Tomé
e-mail: murilo@icmc.usp.br

Antonio Castelo
e-mail: castelo@icmc.usp.br

Departamento de Ciências de Computação e Estatística, ICMC,
Universidade de São Paulo, USP,
Av. Trabalhador São Carlense, 400,
C.P. 668, 13251-900, São Carlos, SP,
Brazil

Norberto Mangiavacchi
Departamento de Engenharia Mecânica,
Universidade do Estado do Rio de Janeiro, UERJ,
Rua Sao Francisco Xavier, 524,
20550-900 Rio de Janeito, RJ,
Brazil
e-mail: norberto@uerj.br

Sean McKee
Department of Mathematics,
University of Strathclyde,
Livingstone Tower,
Glasgow, UK
e-mail: smck@maths.strath.ac.uk

A Stable Semi-Implicit Method for Free Surface Flows

The present work is concerned with a semi-implicit modification of the GENSMAC method for solving the two-dimensional time-dependent incompressible Navier-Stokes equations in primitive variables formulation with a free surface. A projection method is employed to uncouple the velocity components and pressure, thus allowing the solution of each variable separately (a segregated approach). The viscous terms are treated by the implicit backward method in time and a centered second order method in space, and the nonlinear convection terms are explicitly approximated by the high order upwind variable-order nonoscillatory scheme method in space. The boundary conditions at the free surface couple the otherwise segregated velocity and pressure fields. The present work proposes a method that allows the segregated solution of free surface flow problems to be computed by semi-implicit schemes that preserve the stability conditions of the related coupled semi-implicit scheme. The numerical method is applied to both the simulation of free surface and to confined flows. The numerical results demonstrate that the present technique eliminates the parabolic stability restriction required by the original explicit GENSMAC method, and also found in segregated semi-implicit methods with time-lagged boundary conditions. For low Reynolds number flows, the method is robust and very efficient when compared to the original GENSMAC method.
[DOI: 10.1115/1.2173672]

1 Introduction

In dimensionless conservative form, the Navier-Stokes equations for incompressible viscous Newtonian flows can be written as

$$\frac{\partial \mathbf{u}}{\partial t} + \nabla \cdot (\mathbf{uu}) = -\nabla p + \frac{1}{\mathrm{Re}}\nabla^2 \mathbf{u} + \frac{1}{\mathrm{Fr}^2}\mathbf{g} \tag{1}$$

$$\nabla \cdot \mathbf{u} = 0 \tag{2}$$

where t is time, $\mathbf{u}$ is the velocity vector field, p is pressure and $\mathbf{g}$ is the gravity field. The nondimensional parameters $\mathrm{Re}=LU/\nu$ and $\mathrm{Fr}=U/\sqrt{gL}$ are the Reynolds and Froude numbers, respectively, where L and U are appropriate length and the velocity scales, and ν is the kinematic viscosity of the fluid.

Contributed by the Applied Mechanics Division of ASME for publication in the JOURNAL OF APPLIED MECHANICS. Manuscript received June 1, 2005; final manuscript received December 30, 2005. Review conducted by G. C. Buscaglia. Discussion on the paper should be addressed to the Editor, Prof. Robert M. McMeeking, Journal of Applied Mechanics, Department of Mechanical and Environmental Engineering, University of California—Santa Barbara, Santa Barbara, CA 93106-5070, and will be accepted until four months after final publication of the paper itself in the ASME JOURNAL OF APPLIED MECHANICS.

To solve Eqs. (1) and (2) appropriate boundary conditions need to be invoked. On solid boundary (rigid walls), no-slip conditions are applied, i.e, the normal and tangential components of the velocity are taken to be zero.

Boundary conditions on the inflow and outflow need to be prescribed. On the inflow they are given by

$$u_n = u_{\mathrm{inflow}} \quad \text{and} \quad u_\tau = 0 \tag{3}$$

where u_n is the normal velocity to the boundary and u_τ is the tangential velocity to the boundary. On the outflow they are given by

$$p = 0 \quad \text{and} \quad \frac{\partial u_\tau}{\partial n} = \frac{\partial u_n}{\partial n} = 0 \tag{4}$$

On the free surface, it is necessary to impose conditions on the velocity and pressure. For two-dimensional flows, these conditions, in the absence of surface tension, are

$$(\mathbf{T}\cdot\mathbf{n})\cdot\mathbf{n} = 0, \quad \text{and} \quad (\mathbf{T}\cdot\mathbf{n})\cdot\mathbf{m} = 0 \tag{5}$$

where $\mathbf{n}=(n_x,n_y)$ is the unit normal vector, external to the free surface, and $\mathbf{m}=(m_x,m_y)$ is the tangent vector to the free surface. Substituting the total tensor $\mathbf{T}=-p\mathbf{I}+\boldsymbol{\tau}$, with $\boldsymbol{\tau}$ the viscous stress tensor and $\mathbf{I}$ the identity tensor, into Eq. (5) we obtain

$$-p+\frac{2}{\mathrm{Re}}\left[\frac{\partial u}{\partial x}n_x^2+\frac{\partial v}{\partial y}n_y^2+\left(\frac{\partial u}{\partial y}+\frac{\partial v}{\partial x}\right)n_x n_y\right]=0 \tag{6}$$

$$2\frac{\partial u}{\partial x}n_x m_x+2\frac{\partial v}{\partial y}n_y m_y+\left[\frac{\partial u}{\partial y}+\frac{\partial v}{\partial x}\right](n_y m_x+n_x m_y)=0 \tag{7}$$

In this paper the central issue will be the development of a semi-implicit method for the Navier-Stokes equations for free surface flows with weaker stability constraints than the explicit method and such that the resulting linear systems for the velocity and pressure fields can be solved independently.

Free surface fluid flows have the added difficulty that not only must the Navier-Stokes equations be solved, but at the same time the position of a free surface or surfaces, where the conditions (6) and (7) are applied, need to be determined. Based on the well known marker-and-cell (MAC) method [1], many numerical schemes have been developed with the objective of solving these types of flows. One example of such methods is the generalized simplified marker-and-cell (GENSMAC) method [2]. The GENSMAC method is an explicit time-dependent algorithm, and consequently the size of the time step is subject to the usual parabolic stability restriction in common with explicit methods for the heat equation. This means that the maximum allowable time-step size is computed according to the Reynolds number and to the square of the spatial step size. In many fluid flow problems the viscous forces are dominant, and the Reynolds number is often much smaller than 1. Thus explicit numerical techniques, such as GENSMAC, often require very small time steps and consequently very large CPU times. Implicit and semi-implicit schemes offer the opportunity to overcome these difficulties. Authors such as [3–8] and others have presented an overview of implicit methods for the Navier-Stokes equations. The majority of these methods solve the Navier-Stokes equations in primitive variables using coupled or decoupled formulations. Henceforth those methods that solve Eqs. (1) and (2) simultaneously at each time step shall be known as *coupled*, and those that solve them separately shall be referred to as *segregated*.

Coupled methods are highly influenced by the nonlinearities of the convective terms, are more difficult to implement and tend to have high computational cost. Pracht [3] presents an implicit version of the MAC method, the marker-and-cell-Reynolds-low (MACRL) method, which solves the Navier-Stokes equations simultaneously, coupling the components of velocity and pressure. However, at each time step a complete set of linear equations for the primitive variables has to be solved and that can be very costly. Thus we see that decoupling the equations is a strategy for lowering computational costs which has been in practice for a long time. Another example of a numerical scheme that uses this strategy was proposed by Armenio [4], and called semi-implicit-marker-and-cell (SIMAC). The SIMAC method is a modification of the MAC method for the solution of free surface flows with high Reynolds number using a semi-implicit numerical discretization. However, as the SIMAC method aims at the simulation of high Reynolds number flows it uses a simplification of Eq. (6) and assumes that $p=0$ on the free surface. In this work we are concerned with low Reynolds number flows, so that the same simplification of Eq. (6) cannot be employed.

This paper is concerned with a semi-implicit finite difference numerical method for solving incompressible viscous free surface fluid flow problems. The method differs from the MACRL method since it solves decoupled linear systems for velocity and pressure, and is distinct from the SIMAC method since it does not make any simplification to Eq. (6). By using a semi-implicit formulation, the method we shall describe overcomes the parabolic stability restrictions of the explicit formulation. We are proposing a modification to the GENSMAC methodology that uses implicit discretization of the governing equations and boundary conditions for the pressure field at the free surface. It will be shown that the boundary conditions on the free surface need to be treated implicitly; the efficiency of the resulting semi-implicit method will be demonstrated by verifying that a considerable saving in CPU time can be achieved.

2 Numerical Method

The proposed numerical method for solving Eqs. (1) and (2) is basically a modification of the GENSMAC method, which is an improved version of the MAC method. The essence of the MAC method is the use of virtual marker particles on cells defined on an Eulerian grid. Marker particles are moved from their positions at time t to their new positions at time $t+\delta t$ according to the newly calculated velocities. In GENSMAC, marker particles are placed on the free surface only as opposed to other techniques where particles are placed on the whole domain. The free surface is approximated by a piecewise linear surface and represented by a specific data structure (see [9]), supporting the representation of complex flow geometries. Breakup and recombination may be dealt with and it has indeed been implemented in the axisymmetric case in [10] and in the tri-dimensional case when surface tension effects are not dominant [11]. The main thrust of this paper is the study of implicit techniques for incompressible viscous free surface flows, purporting to assess their stability properties for this class of problems. Hence, we shall mainly be dealing with simple geometry problems.

As the GENSMAC method was designed originally to solve problems with free surfaces, a classification strategy of the cells of the mesh is used to represent the movement of the fluid. Figure 1 illustrates the classification of the cells in the mesh for a two-dimensional flow at a fixed instant of time. Note the empty cells have been left blank. In the present work the same classification of cells is used, namely:

- Empty Cell (E): Cells that do not contain fluid;
- Full Cell (F): Cells that do not have any face in contact with empty cells;
- Surface Cell (S): Cells that contain fluid and have one or more faces in contact with empty cells;
- Boundary Cell (B): Cells that belong to the rigid domain;
- Inflow Cell (I): Cells that are on the fluid entrance into the domain;
- Outflow Cell (O): Cells that are on the fluid exit out of the domain.

A first order time discretization of Eqs. (1) and (2) can be written as

$$\mathbf{u}^{n+1}-\frac{\delta t}{\mathrm{Re}}\nabla^2\mathbf{u}^{n+\delta_1}=\mathbf{u}^n+\delta t\left\{-\nabla\cdot(\mathbf{uu})^{n+\delta_2}-\nabla p^{n+1}+\frac{1}{\mathrm{Fr}^2}\mathbf{g}^n\right\} \tag{8}$$

$$\nabla\cdot\mathbf{u}^{n+1}=0 \tag{9}$$

where δ_1 and δ_2 are integers that assume the values 0 or 1 only. If $\delta_1=\delta_2=0$ we have an explicit scheme as in the case of GENSMAC. Taking $\delta_1=1$ and $\delta_2=0$ the semi-implicit (backward implicit) method is obtained. Note that Eqs. (8) and (9) couple the primitive variables even for the case of the explicit scheme. The projection method is one technique that can be applied to decouple the velocity components from the pressure.

In this work, the time-marching procedure is based on the projection method [4,12,13]. Several different formulations of semi-implicit and fractional step methods have been developed in the past. Gresho [14] provided a theoretical foundation that made it possible to solve the Navier-Stokes equations via a semi-implicit projection method. The main idea of the projection method is the use of an approximation of Eq. (8) to determine a tentative velocity field $\tilde{\mathbf{u}}$, as in

(a)

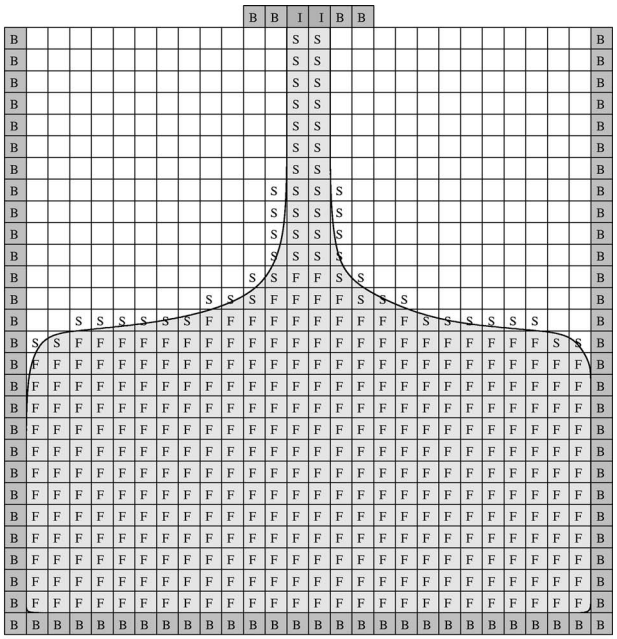

(b)

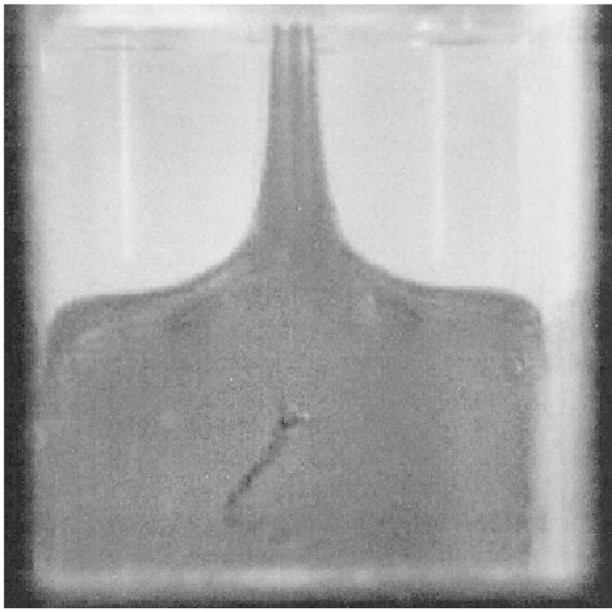

Fig. 1 (*a*) Cell classification. (*b*) Flow visualization of glucose syrup. For details see [13].

$$\tilde{\mathbf{u}} - \frac{\delta t}{\mathrm{Re}}\nabla^2\tilde{\mathbf{u}} = \mathbf{u}^n + \delta t\left\{-\nabla\cdot(\mathbf{uu})^n - \nabla\tilde{p} + \frac{1}{\mathrm{Fr}^2}\mathbf{g}^n\right\} \tag{10}$$

where $\tilde{p}$ is a tentative pressure. Generally, this provisional velocity field is not a solenoidal field. For $t=t_0$, $\mathbf{u}(\mathbf{x},t_0)$ and $\tilde{\mathbf{u}}(\mathbf{x},t_0)$ are required to satisfy the same boundary conditions, so that on the boundary $\mathbf{u}(\mathbf{x},t_0)=\tilde{\mathbf{u}}(\mathbf{x},t_0)$.

The role of the pressure in incompressible flows is to make sure that the velocity field satisfies the continuity Eq. (9). Using the Helmholtz–Hodge decomposition theorem [15,16] (also known as Ladyzhenskaja theorem), which plays a fundamental role in the derivation of the projection methods commonly used for the numerical solution of the incompressible Navier-Stokes equations, a general velocity field $\tilde{\mathbf{u}}$ can be decomposed into a solenoidal field $\mathbf{u}^{n+1}$ and the gradient of a potential $\nabla\psi$ of the following form

$$\tilde{\mathbf{u}} = \mathbf{u}^{n+1} + \nabla\psi \tag{11}$$

Taking the divergence of Eq. (11), and taking into account Eq. (9), a Poisson equation for the potential ψ is derived, as

$$\nabla^2\psi^{n+1} = \nabla\cdot\tilde{\mathbf{u}} \tag{12}$$

The boundary conditions necessary for solving Eq. (12) on a domain like the one in Fig. 1 are

- Homogeneous boundary conditions of Neumann type on the rigid boundaries (*B* cells), that is

$$\frac{\partial\psi}{\partial n} = 0$$

  This boundary condition will also be used on the inflows (*I* cells) when they exist.
- Boundary conditions for the free surface (*S* cells) will be given in Sec. 3.
- Homogeneous boundary conditions of Dirichlet type on the outflows (*O* cells), that is

$$\psi = 0.$$

The pressure field is updated by the equation

$$p^{n+1} = \tilde{p} + \frac{\psi^{n+1}}{\delta t} \tag{13}$$

Equations (10)–(13) are approximated on a staggered mesh. On this mesh, the pressure is stored at cell centers and the components of the velocity u and v are stored in the middle of the lateral faces. As in [2], the diffusion terms and the pressure gradient in Eq. (10) are approximated by central differences. The convective terms are discretized by the variable-order nonoscillatory scheme (see [17]), which is a high order bounded upwind technique. In this paper, an implementation of the above algorithm known as FREEFLOW2D (see [18]) was employed.

2.1 Stability of the Explicit and the Semi-Implicit Methods. The use of an explicit time integration in the GENSMAC methodology can impose severe restrictions on the allowable values of the time step (δt) in problems where the viscous terms of Eq. (1) are predominant. In particular, this occurs when the flow has a low Reynolds number, as in the case of *creeping flow*. The stability restriction due to the explicit treatment of the viscous terms demands that

$$\delta t_{\mathrm{visc}} \leqslant \frac{\mathrm{Re}}{2}\left(\frac{1}{(\delta x)^2} + \frac{1}{(\delta y)^2}\right)^{-1} \tag{14}$$

where δt_{visc} is the non-dimensional time step resulting from the stability condition on the viscous terms.

The GENSMAC method is also subject to another stability restriction that relates the time step both to the mesh spacing and to a reference velocity. That is, a fluid particle cannot travel, in each time step, a distance larger than the width of a cell. This condition is known in the literature as the Courant–Friedrichs–Lewy (CFL) condition and can be written in the form

$$\delta t_{\mathrm{CFL}x} \leqslant \left(\frac{\delta x}{|u|_{\max}}\right) \text{ and } \delta t_{\mathrm{CFL}y} \leqslant \left(\frac{\delta y}{|v|_{\max}}\right) \tag{15}$$

where $|u|_{\max}$ and $|v|_{\max}$ are the maximum modulus of the velocities in the directions x and y, respectively.

The point of using a semi-implicit discretization of Eq. (10) is to overcome restriction (14). The only restriction then to be imposed on the time step would be Eq. (15), thus allowing a larger time step than that required by GENSMAC.

3 Free Surface Boundary Conditions Schemes

As explained in Sec. 2, the projection method is used to decouple Eqs. (8) and (9). The boundary conditions at the free surface (Eqs. (6) and (7)), when discretized implicitly, again couple the otherwise segregated velocity and pressure fields. The ap-

Table 1 Comparison of maximum time step for the *F*1 formulation (δt), for the explicit method (δt_{exp}) and the time step calculated by restriction (14) for *Hagen-Poiseuille* (confined) and *fountain* (free surface) flows with $\delta x = \delta y = 0.05$

Problem	δt	δt_{exp}	δt_{visc}	Re
Confined	1.25×10^{-2}	2.5×10^{-5}	6.25×10^{-5}	0.1
Free surface	8.75×10^{-5}	2.5×10^{-5}	6.25×10^{-5}	0.1
Confined	1.25×10^{-2}	2.5×10^{-6}	6.25×10^{-6}	0.01
Free surface	8.5×10^{-6}	2.5×10^{-6}	6.25×10^{-6}	0.01
Confined	1.25×10^{-2}	2.5×10^{-7}	6.25×10^{-7}	0.001
Free surface	8.25×10^{-7}	2.5×10^{-7}	6.25×10^{-7}	0.001
Confined	1.25×10^{-2}	2.25×10^{-8}	6.25×10^{-8}	0.0001
Free surface	8.25×10^{-8}	2.25×10^{-8}	6.25×10^{-8}	0.0001

proach employed in the discretization of these boundary conditions may substantially affect the overall stability of the methods. In this paper, two different approaches to the discretization of the free surface boundary conditions are studied. Both result in a segregated method.

3.1 *F*1 Formulation and Results. The first formulation, which we refer to as *F*1, uses the implicit Eq. (10) with an explicit discretization of the boundary conditions (6) and (7). The pressure p^{n+1} at the free surface boundary is computed by an explicit (time-lagged) approximation of Eq. (6)

$$p^{n+1} = \frac{2}{\mathrm{Re}}\left[\frac{\partial u}{\partial x}n_x^2 + \frac{\partial v}{\partial y}n_y^2 + \left(\frac{\partial u}{\partial y} + \frac{\partial v}{\partial x}\right)n_x n_y\right]^n \tag{16}$$

Equation (7) is used to obtain explicit boundary conditions for the tangential velocity component while the continuity Eq. (2) is employed, again explicitly, to compute the normal velocity component. The solution procedure begins by computing velocity and pressure at the boundaries, employing Eqs. (7) and (16) in the case of free surface boundary conditions. After solving Eq. (10) and solving the Poisson Eq. (12), the velocity and pressure fields are updated from Eqs. (11) and (13), respectively. In this formulation, the boundary conditions on the free surface for solving the Poisson equation are homogeneous Dirichlet type ($\psi=0$). The linear systems resulting from Eqs. (10) and (12) are sparse, symmetric, and positive definite. Consequently, we employed the conjugate gradient method for solving them, obtaining a robust and efficient solver. The last step in the computing cycle is the movement of the marker particles to their new positions. This is accomplished by solving the ordinary differential equations

$$\frac{dx}{dt} = u \text{ and } \frac{dy}{dt} = v \tag{17}$$

by Euler's method. The fluid surface is defined by a list of particles and the visualization of the free surface boundary is obtained by connecting them by straight lines.

The *F*1 formulation was applied to simulate the flow of a fluid between two parallel plates, separated by a distance $L=1m$, forming a channel. Two different flows were simulated:

- *Hagen-Poiseuille* flow, in which the channel is initially full and there is no free surface, i.e., confined flow;
- *Fountain* flow, in which the channel is initially empty and fluid is injected at the channel's entrance with a parabolic velocity profile. In this problem there is a free surface moving along the channel.

Table 1 displays the maximum time step for different values of Re that rendered a stable calculation. It can be observed in Table 1 that for the confined problem the maximum time step used is larger than that of the explicit method, as one would expect. On the other hand, for the free surface flow problem the maximum time step used was very close to the one used by the explicit method. That is, for the free surface problem the stability restriction is no longer imposed by the CFL condition alone. As can also be observed from Table 1 the time step for this formulation is only about four times larger than that of the explicit method. The conclusion seems to be that the presence of the free surface greatly influences the stability of the numerical method, and points towards the need for discretizing the free surface condition implicitly. Therefore, to construct a more stable semi-implicit method a special treatment of Eq. (6) is required. This leads us to the next section.

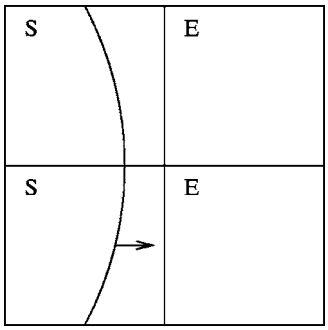

Fig. 2 Cell of the free surface in contact, in its right lateral face, with an empty cell

3.2 *F*2 Formulation and Results. In the second formulation, referred to as *F*2, Eq. (6) is discretized implicitly and written in the form

$$-p^{n+1} + \frac{2}{\mathrm{Re}}\left[\frac{\partial u^{n+1}}{\partial x}n_x^2 + \frac{\partial v^{n+1}}{\partial y}n_y^2 + \left(\frac{\partial u^{n+1}}{\partial y} + \frac{\partial v^{n+1}}{\partial x}\right)n_x n_y\right] = 0 \tag{18}$$

Notice that Eq. (18) couples the velocity and pressure fields leading to the coupling of the linear systems arising from Eqs. (10) and (12). This coupling is undesirable as it makes the solution of the linear system much harder to solve.

In this section we present a technique for decoupling Eq. (18) in such a way that Eqs. (10) and (12) may be solved separately. This technique makes use of Eq. (11) for updating the velocity and of Eq. (13) for updating the pressure fields to construct new equations for the potential ψ. To deduce the new equations, consider first the case where an *S* cell on the free surface is in contact with an *E* cell as depicted in Fig. 2. In this case, the normal vector is $\mathbf{n}=(1,0)$ and Eq. (18) reduces to

$$p^{n+1} = \frac{2}{\mathrm{Re}}\left(\frac{\partial u^{n+1}}{\partial x}\right) \tag{19}$$

From the continuity Eq. (2) discretizated at the time level t_{n+1} we get

$$\frac{\partial u^{n+1}}{\partial x} = -\frac{\partial v^{n+1}}{\partial y} \tag{20}$$

which when substituted into Eq. (19) produces

$$p^{n+1} = -\frac{2}{\mathrm{Re}}\left(\frac{\partial v^{n+1}}{\partial y}\right) \tag{21}$$

From Eq. (11) the final velocity in the *y* direction discretizated at time level t_{n+1} is

$$v^{n+1} = \tilde{v} - \frac{\partial \psi^{n+1}}{\partial y} \tag{22}$$

Substituting Eq. (22) into Eq. (21) gives

$$p^{n+1} = -\frac{2}{\mathrm{Re}}\left(\frac{\partial \tilde{v}}{\partial y} - \frac{\partial^2 \psi^{n+1}}{\partial y^2}\right) \tag{23}$$

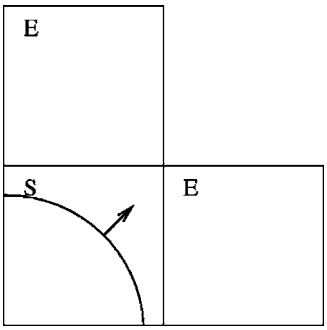

Fig. 3 Cell on the free surface with two adjacent empty cells

Finally, substituting Eq. (23) into Eq. (13) we have

$$\psi^{n+1} - \frac{2\delta t}{\mathrm{Re}}\left(\frac{\partial^2 \psi^{n+1}}{\partial y^2}\right) = -\frac{2\delta t}{\mathrm{Re}}\left(\frac{\partial \tilde{v}}{\partial y}\right) - \delta t \tilde{p} \tag{24}$$

This equation is used as a boundary condition to define ψ on the free surface for the case depicted in Fig. 2.

The second case is given by the configuration of Fig. 3 where $\mathbf{n}=\left(\frac{\sqrt{2}}{2}, \frac{\sqrt{2}}{2}\right)$, and then Eq. (18) becomes

$$p^{n+1} = \frac{1}{\mathrm{Re}}\left(\frac{\partial u^{n+1}}{\partial y} + \frac{\partial v^{n+1}}{\partial x}\right) \tag{25}$$

From Eq. (11) the velocity in the x direction discretized at time level t_{n+1} is

$$u^{n+1} = \tilde{u} - \frac{\partial \psi^{n+1}}{\partial x} \tag{26}$$

Substituting Eqs. (26) and (22) into (25) gives

$$p^{n+1} = \frac{1}{\mathrm{Re}}\left(\frac{\partial \tilde{u}}{\partial y} - \frac{\partial^2 \psi^{n+1}}{\partial x \partial y} + \frac{\partial \tilde{v}}{\partial x} - \frac{\partial^2 \psi^{n+1}}{\partial x \partial y}\right) \tag{27}$$

which, after taking Eq. (13) into account, yields

$$\psi^{n+1} + \frac{2\delta t}{\mathrm{Re}}\left(\frac{\partial^2 \psi^{n+1}}{\partial x \partial y}\right) = \frac{\delta t}{\mathrm{Re}}\left(\frac{\partial \tilde{u}}{\partial y} + \frac{\partial \tilde{v}}{\partial x}\right) - \delta t \tilde{p} \tag{28}$$

This equation is used as a boundary condition to define ψ on the free surface for the case depicted in Fig. 3. The construction of the equations for ψ in the other cases where a surface cell (S) is in contact with empty cells (E) is very similar, and will not be derived here.

The solution procedure for the $F2$ formulation is analogous to that for the $F1$ formulation, except for the calculation of the potential ψ. In the $F1$ formulation, the Poisson equation for the potential ψ is calculated in the whole domain that contains fluid. In the $F2$ formulation, in addition to the Poisson equation, the new equations for the potential ψ at the free surface are solved. Now, the linear system for ψ is sparse, but nonsymmetric, and therefore the method used was the bi-conjugated gradients with preconditioning (BCGP). There are, of course, other alternatives to the BCGP: generalized minimum residual and preconditioned conjugate gradient squared are two such examples.

The same problem proposed in the previous subsection is now used to illustrate the $F2$ formulation. The results are presented in Table 2.

As can be seen from Table 2, for creeping flow problems, the $F2$ formulation has superior stability characteristics both to the original explicit method and the $F1$ formulation. As the Reynolds number decreases, the stability restriction on the implicit $F2$ formulation becomes less severe (in comparison with the explicit method) and it appears that the restriction on the time-step δt is wholly dominated by the CFL condition. In fact, it would appear that the time step cannot get as large as the CFL bound would suggest. This is clearly due to the fact that these are linearized stability restrictions. Furthermore, not only is the underlying problem nonlinear, the (virtual) particle motion is determined by the solution of Euler's method which itself requires a step length restriction to ensure stability. From Table 2, it can be seen that the $F2$ formulation allowed δt to be about 5×10^2 to 5×10^5 times larger than the explicit method (see Table 1), as Re is decreased. Therefore, the use of the implicit free surface boundary Eq. (18) was enough to make the semi-implicit method considerably more stable for problems with free surfaces. Perhaps we should stress that in the $F2$ formulation, Eq. (7) continued being calculated explicitly, avoiding the need for the solution of an equation that couples the velocities u and v. This proved to be very important for savings in CPU time. In conclusion, the $F2$ formulation seems to produce an efficient semi-implicit method with a simple formulation.

Table 2 Maximum δt for the $F2$ formulation for *Hagen-Poiseuille* (confined) and *fountain* (free surface) flows with $\delta x = \delta y = 0.05$

Problem	δt	Re
Confined/free surface	1.25×10^{-2}	0.1
Confined/free surface	1.25×10^{-2}	0.01
Confined/free surface	1.25×10^{-2}	0.001
Confined/free surface	1.25×10^{-2}	0.0001

4 Validation and Benchmarking

In this section numerical results using both the implicit formulations are presented, and compared to the explicit method. The efficiency (in terms of CPU time) of the $F2$ formulation is compared to that of the $F1$ formulation and that of the explicit scheme for problems with $\mathrm{Re}<1$. The results are encouraging, both in terms of accuracy and computer time. The following test cases are considered.

Implementation of the numerical software for the $F1$ and $F2$ formulations was tested for *fountain* flows. For this simple test case, comparisons between the numerical and analytical solutions (see [19]) are possible. The model used in the comparisons is the same that was presented in the previous section, i.e., the channel filling problem with the free surface. The $F1$ and $F2$ formulations were employed with three spatial meshes: coarse (**M**1, where $\delta x = \delta y = 0.1$); medium (**M**2, where $\delta x = \delta y = 0.05$), and fine (**M**3, where $\delta x = \delta y = 0.025$).

It was observed that the numerical results are very close to the analytical solution, as are the numerical results produced by the explicit method. In order to demonstrate the convergence of the methods, the relative error, in the l_2 norm, between the numerical and the analytical solutions was calculated. These are presented in Table 3.

Up to this point we have developed a semi-implicit segregated finite difference method for the simulation of free surface flows. This method would appear to enjoy unrestricted stability properties rather akin to implicit schemes for parabolic problems. However, we should stress that the semi-implicit method computing cycle is considerably more expensive than the same cycle for the explicit method. This is due to the fact that in the semi-implicit method two extra linear systems had to be solved at each time step for the velocities $\tilde{u}$ and $\tilde{v}$. So, for the semi-implicit method to be competitive with the explicit method the time step used by the semi-implicit must be large enough to compensate for the extra work. To show that this appears to be the case we present the comparison of the CPU times between the semi-implicit method and the explicit method for the channel flow test problem.

Tables 4–6 show the CPU times for these methods when solving *fountain* flow test problem. These tables also display the relative error (E_r) and the maximum step size used, so that the accu-

Table 3 Time step (δt) and relative error (Er) for *fountain* flow with Re=0.1 and the meshes M1, M2 and M3. The relative error is computed from the analytical solution given in [19].

	M1		M2		M3	
Method	δt	Er	δt	Er	δt	Er
Explicit	1.0×10^{-4}	3.4E−05	2.5×10^{-5}	2.3E−06	6.25×10^{-6}	2.6E−07
$F1$ Formulation	4.0×10^{-3}	2.2E−04	8.75×10^{-5}	2.1E−05	2.0×10^{-5}	1.1E−06
$F2$ Formulation	5.0×10^{-2}	3.4E−05	1.25×10^{-2}	2.3E−06	6.25×10^{-3}	2.6E−07

racy of the results can be assessed. The time step for the $F2$ formulation is larger than that of both the $F1$ and explicit schemes. On the other hand, the CPU times are considerably larger for both methods. All the calculations discussed in this section were performed on a Dual Athlon XP MP 2200 MHz with 1.0 Gb memory.

5 Numerical Simulation of the Transient Planar Jet Extrudate-Swell

In this section we present a simulation of the planar Newtonian extrudate-swell problem: the extrusion of a viscous fluid through a die into an inert medium. This is a well-known free surface problem: at low Reynolds numbers, the fluid swells as it comes out of the die. Implicit formulations are capable of accurately predicting the swelling ratio of a Newtonian jet, and should therefore provide a firm numerical foundation for extension to viscoelastic jets where the swelling ratio is of considerable industrial importance.

Extrusion is one of the major processing methods in the polymer industry. Polymeric materials when extruded are commonly found to have larger dimensions than the die. This phenomenon is known as die swell or extrudate swell. Due to its importance in industrial applications, this phenomenon has been investigated by many researchers through experiments and numerical simulations.

Many results have been presented for Newtonian fluids, for instance, the experimental work of [20,21] among others, and the numerical results of [22–25], etc. Most of these numerical schemes were used to solve the axisymmetric extrudate-swell problem, due largely to the existence of experimental results for this problem. In the case of plane flows, experimental results are more difficult to obtain and, consequently, only numerical results would appear to have been presented in the literature (see [22,26–35]). An important aspect of the extrudate-swell problem is the influence of the Reynolds number and the surface tension since both can affect the swelling (see [22,25,27,34]). We have chosen to neglect the surface tension (as in [22,33,35]). We have done so because the main thrust of this paper is to assess the efficiency (in terms of the time-step size employed and CPU time) of the implicit formulation for low-Reynolds number free surface flows.

The extrudate-swell ratio S_r (or swelling ratio) is defined as

$$S_r = \frac{Le}{L} \tag{29}$$

where Le is the width of the extruding liquid and L is the diameter (or width) of the capillary (see Fig. 4(b)). For planar problems various values of S_r can be found in the literature. The following authors, for example, have obtained the results: 1.155 (Chang, Patten, and Finlayson [26]), 1.161 (Dutta and Ryan [29]), 1.170 (Chang, Patten, and Finlayson [26]), 1.186 (Georgiou and Boudouvis [35]), 1.190 (Tanner [22] and Omodei [27]), 1.196 (Ahn and Ryan [32]), 1.200 and 1.227 (Crochet and Keunings [30]). Tanner [22] makes the point that the substantial disparity between these results is due to the different numerical methods employed and to the choice of meshes in addition to using a range of Reynolds number and surface tension coefficients.

Table 4 Results for *fountain* flow with Re=0.1 for the M2 mesh and non-dimensional time t =20

Method	Er	δt	**CPU time**-(m:s)
Explicit	2.2915×10^{-6}	2.5×10^{-5}	104:40
$F1$ Formulation	2.0654×10^{-5}	8.75×10^{-5}	60:08
$F2$ Formulation	2.2977×10^{-6}	1.25×10^{-2}	5:20

Table 5 Results for *fountain* flow with Re=0.01 for the M2 mesh and non-dimensional time t =20

Method	Er	δt	**CPU time**-(m:s)
Explicit	2.1915×10^{-6}	2.5×10^{-6}	875:16
$F1$ Formulation	1.2528×10^{-5}	8.5×10^{-6}	544:55
$F2$ Formulation	2.2958×10^{-6}	1.25×10^{-2}	5:37

Table 6 Results for *fountain* flow with Re=0.001 for the M2 mesh and non-dimensional time t=20

Method	Er	δt	**CPU time**-(m:s)
Explicit	2.0511×10^{-6}	2.5×10^{-7}	7054:50
$F1$ Formulation	1.4544×10^{-5}	8.25×10^{-7}	5812:40
$F2$ Formulation	2.305×10^{-6}	1.25×10^{-2}	5:33

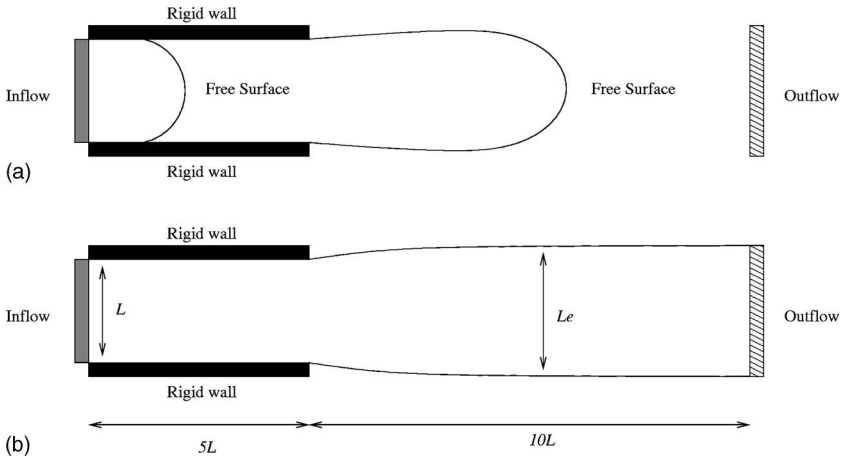

Fig. 4 Geometry and boundaries for the extrudate-swell problem: (*a*) unsteady state and (*b*) steady state

We consider the time-dependent flow of a two-dimensional jet flowing through a slit with a uniform input velocity, extruded into the air. The no-slip condition is imposed on the walls of the slit, resulting in a parabolic profile at the slit exit where the jet might be expected to exhibit the phenomenon of swelling. The flow geometry for the incompressible extrudate-swell problem is depicted in Fig. 4.

The input velocity is set to $u_{\text{inflow}}=1.0\ \text{m s}^{-1}$ and the kinematic viscosity coefficient is chosen to be $\nu=100.0\ \text{m}^2\ \text{s}^{-1}$. The scaling parameters were taken to be $L=1.0$ m and $U=1.0\ \text{m s}^{-1}$ resulting in Re=0.01.

The plane extrudate-swell problem was solved by the $F1$ and $F2$ methods and by the explicit method. However, due to the severe restrictions of the time step for the explicit method and for the $F1$ formulation, a convergence analysis is presented for the $F2$ formulation only. The meshes used were: **M**1, **M**2, and **M**3 defined previously, and **M**4 ($\delta x=\delta y=0.0125$). Figure 5 shows the configuration of the free surface at different times for the $F2$ formulation using the mesh **M**2.

For the $F2$ formulation, Table 7 shows the effect of mesh refinement on the swelling ratio, on the time step, and on the time step that would be required by the parabolic restriction (14) and by CFL restriction (15). For the $F2$ formulation the swelling ratio increases from 1.081 to 1.182 as the mesh is refined. The results for the swelling ratio are considered to be in reasonable agreement with previous numerical predictions. For example, for **M**3 the swelling ratio is in agreement with the calculations of [26], and for **M**4 with [26,35].

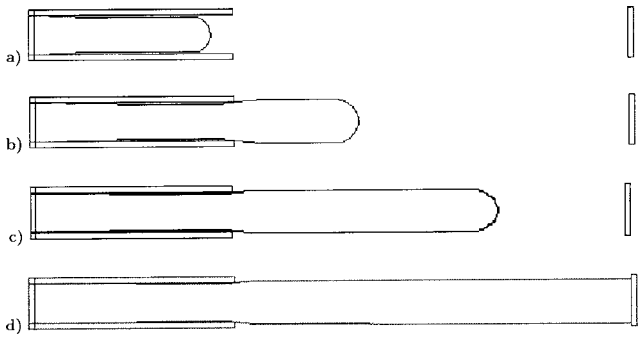

Fig. 5 Free surface profile for extrudate swell of a Newtonian jet using *F*2 formulation at different non-dimensional times: (*a*) *t*=6.0, (*b*) *t*=12.0, (*c*) *t*=18.0 and (*d*) *t*=24.6

The CPU time required for the simulation of the extrudate-swell problem using the $F2$ formulation was small compared to those for the explicit method and the $F1$ formulation. However, as the problem is unsteady, the free surface particles are continually moving, so it was necessary to reduce the CFL number in order to ensure good numerical resolution in the area where the fluid is in contact with the atmosphere (see Figs. 5(*b*) and 5(*c*)). That fact becomes more important when the mesh is refined. Therefore, the value of the time step for the $F2$ formulation was calculated using a slightly more restricted CFL condition than Eq. (15) (see Table 7). Table 8 presents a comparison between the CPU time for the numerical schemes for the mesh **M**2.

6 Conclusion

A new implicit version of the GENSMAC method has been developed and tested for the solution of free surface low-Reynolds numbers flows. The new method, like the GENSMAC method, employs the SMAC strategy based on the projection method but is designed to provide a segregated solution of the velocity components and pressure.

The new method employs a backward-implicit discretization of the viscous terms, thus producing a scheme that does not have a parabolic stability restriction for confined flows. The complete viscous free surface boundary conditions were considered. Implicit implementation of these boundary conditions requires a coupling of the velocity and pressure fields at the boundaries. Two

Table 7 Results of the extrudate-swell ratio for Re=0.01 using *F*2 formulation

Mesh	S_r	δt	δt_{visc}	δt_{CFL}
M1	1.081	7.5×10^{-3}	2.5×10^{-5}	1.0×10^{-1}
M2	1.115	5.0×10^{-3}	6.25×10^{-6}	5.0×10^{-2}
M3	1.150	1.0×10^{-3}	1.5625×10^{-6}	2.5×10^{-2}
M4	1.182	5.0×10^{-4}	3.90625×10^{-7}	1.25×10^{-2}

Table 8 Results of the extrudate-swell problem for the M2 mesh for Re=0.01 and non-dimensional time *t*=30

Method	S_r	δt	CPU time-(m:s)
Explicit	1.114	2.5×10^{-6}	8093:30
$F1$ Formulation	1.096	8.5×10^{-6}	6126:18
$F2$ Formulation	1.115	5.0×10^{-3}	65:22

different implementation strategies were addressed: an implicit formulation employing explicit (time-lagged) free surface boundary conditions ($F1$ formulation), and an implicit formulation employing semi-implicit (semi-time-lagged) free surface boundary conditions ($F2$ formulation).

The $F1$ formulation allows larger time steps than the original (explicit) GENSMAC formulation, for confined flows. However, for free surface flows, it is still subject to a parabolic-like stability criteria. The $F2$ formulation was developed to overcome this stability problem without requiring the simultaneous solution of the velocity components and pressure. An implicit boundary condition for the Poisson equation was developed involving only the tentative components of velocity and pressure. The resulting boundary conditions are implicit, they involve only the pressure correction ψ, and they do not involve the velocities at time t_{n+1}. The introduction of the Poisson equation with this special boundary condition requires the solution of an augmented linear system which includes the boundary values, but it is not symmetric and so requires a suitable iterative solution method.

Numerical results for the simulation of low-Reynolds fountain flows, obtained with the $F2$ formulation, show that the method does not have a parabolic stability restriction and from the limited numerical evidence it appears to have a large stability range.

Benchmarking of the method shows that it is very efficient for the solution of low-Reynolds number flows, requiring total CPU times several orders of magnitude smaller than the CPU times required by GENSMAC for the same problem.

The extension of the present approach to second order time accurate schemes, employing Crank–Nicholson time discretization and second order projection methods, is currently being studied and it will be reported in future work.

Another extension is related to the implementation of semi-implicit methods for the three-dimensional incompressible Navier-Stokes equations with free surfaces. To our understanding, this extension should not be very complex because the formulation used in this work can easily be extended to the three-dimensional case. The main modification will be in the technique for decoupling the velocity and pressure fields in the free surface equations. For three-dimensional free surface flows, the normal component of the stress tensor Eq. (5) will have to be implemented using an implicit formulation, as was done in this work for the case of the $F2$ formulation. Therefore, to deduce the equations for ψ on the free surface, one additional base case will have to be considered (see [36]).

Acknowledgment

The authors thank the financial support of the Brazilian Agency FAPESP (Fundação de Amparo a Pesquisa do Estado de São Paulo). This research has been part of Projects 03/12612-9 and 00/03385-0.

References

[1] Harlow, F. H., and Welch, J. E., 1965, "Numerical Calculation of Time-Dependent Viscous Incompressible Flow of Fluid With Free Surface," Phys. Fluids, **8**, pp. 2182–2189.
[2] Tomé, M. F., and McKee, S., 1994, "GENSMAC: A Computational Marker-and-Cell Method For Free Surface Flows in General Domains," J. Comput. Phys., **110**, pp. 171–186.
[3] Pracht, W. E., 1971, "A Numerical Method for Calculating Transient Creep Flows," J. Comput. Phys., **7**, pp. 46–60.
[4] Armenio, V., 1997, "An Improved MAC Method (SIMAC) for Unsteady High-Reynolds Free Surface Flows," Int. J. Numer. Methods Fluids, **24**, pp. 185–214.
[5] Manna, M., and Vacca, A., 1999, "An Efficient Method for the Solution of the Incompressible Navier-Stokes Equations in Cylindrical Geometries," J. Comput. Phys., **151**, pp. 563–584.
[6] Briley, W. R., and McDonald, H., 2001, "An Overview and Generalization of Implicit Navier-stokes Algorithms and Approximate Factorization," Comput. Fluids, **30**, pp. 807–828.
[7] Kim, K., Baek, S., and Sung, H. J., 2002, "An Implicit Velocity Decoupling Procedure for the Incompressible Navier-stokes Equations," Int. J. Numer. Methods Fluids, **38**, pp. 125–138.
[8] Armfield, S., and Street, R., 2003, "The Pressure Accuracy of Fractional-Step Methods for the Navier-stokes Equations on Staggered Grids," Aust N. Z. Ind. Appl. Math. J., **44**, pp. 20–39.
[9] Mantyla, M., 1988, *An Introduction to Solid Modeling*, Computer Science, Rockville, MD.
[10] Mangiavacchi, N., Castelo, A., Tomé, M. F., Cuminato, J. A., de Oliveira, M. L. B., and McKee, S., 2005, "An Effective Implementation of Surface Tension Using the Marker and Cell Method for Axisymmetric and Planar Flow," SIAM J. Sci. Comput. (USA), **26**, pp. 1340–1368.
[11] de Sousa, F. S., Mangiavacchi, N., Nonato, L. G., Castelo, A., Tomé, M. F., Ferreira, V. G., Cuminato, J. A., and McKee, S., 2004, "A Front-Tracking/Front-Capturing Method for the Simulation of 3D Multi-Fluid Flows With Free Surfaces," J. Comput. Phys., **198**, pp. 469–499.
[12] Amsden, A. A., and Harlow, F. H., 1970, "A Simplified MAC Technique for Incompressible Fluid Flow Calculations," J. Comput. Phys., **6**, pp. 332–335.
[13] Tomé, M. F., McKee, S., Barratt, L., Jarvis, D. A., and Patrick, A. J., 1999, "An Experimental and Numerical Investigation of Container Filling With Viscous Liquids," Int. J. Numer. Methods Fluids, **31**, pp. 1333–1353.
[14] Gresho, P. M., 1990, "On the Theory of Semi-Implicit Projection Methods for Viscous Incompressible Flow and its Implemention via a Finite Element Method That Also Introduces a Nearly Consistent Mass Matrix," Int. J. Numer. Methods Fluids, **11**, pp. 587–620.
[15] Hodge, W. V. D., 1952, *The Theory and Applications of Harmonic Integrals*, Cambridge University Press, Cambridge.
[16] Denaro, F. M., 2003, "On the Applications of the Helmoltz-Hodge Decomposition in Projection Methods for Incompressible Flows With General Boundary Conditions," Int. J. Numer. Methods Fluids, **43**, pp. 43–69.
[17] Ferreira, V. G., Tomé, M. F., Mangiavacchi, N., Castelo, A., Cuminato, J. A., and McKee, S., 2002, "High Order Upwinding and the Hydraulic Jump," Int. J. Numer. Methods Fluids, **39**, pp. 549–583.
[18] Castelo, A. F., Tomé, M. F., Cesar, M. L., Cuminato, J. A., and Mckee, S., 2000, "Freeflow: An Intregated Simulation System for Three-Dimensional Free Surface Flows," Comput. Visualization Sci., **2**, pp. 199–210.
[19] Batchelor, G. K., 1970, *An Introduction to Fluid Dynamics*, Cambridge University Press, Cambridge, pp. 182–184.
[20] Tanner, R. I., 1970, "A Theory of Die-Swell," J. Polym. Sci. A, **8**, pp. 2067–2078.
[21] Hill, G. A., and Chenier, C. L., 1984, "Die Swell Experiments for Newtonian Fluids," Can. J. Chem. Eng., **62**, pp. 40–45.
[22] Tanner, R. I., 1988, *Engineering Rheology*, Clarendon, Oxford, pp. 305–343.
[23] Liu, T. J., Yu, A., and Cheng, S. H., 1991, "Finite Difference Solution of a Newtonian Jet Swell Problem," Int. J. Numer. Methods Fluids, **12**, pp. 125–142.
[24] Ngamaramvaranggul, V., and Webster, M. F., 1999, "Viscoelastic Simulation of Stick-Slip and Die-Swell Flows," Int. J. Numer. Methods Fluids, **29**, pp. 363–371.
[25] Housiadas, K., Georgiou, G., and Tsamopoulos, J., 2000, "The Steady Annular Extrusion of a Newtonian Liquid Under Gravity and Surface Tension," Int. J. Numer. Methods Fluids, **33**, pp. 1099–1119.
[26] Chang, P. W., Patten, T. W., and Finlayson, B. A., 1979, "Collocation and Galerkin Finite Element Methods for Viscoelastic Fluid Flow-II: Die Swell Problems With a Free Surface," Comput. Fluids, **7**, pp. 285–293.
[27] Omodei, B. J., 1979, "Computer Solutions of a Plane Newtonian Jet With Surface Tension," Comput. Fluids, **7**, pp. 79–96.
[28] Crochet, M. J., and Keunings, R., 1980, "Die Swell of a Maxwell Fluid: Numerical Prediction," J. Non-Newtonian Fluid Mech., **7**, pp. 199–212.
[29] Dutta, A., and Ryan, M. E., 1982, "Dynamics of a Creeping Newtonian Jet With Gravity and Surface Tension: A Finite Difference Technique for Solving Steady Free-Surface Flows Using Orthogonal Curvilinear Coordinates," Am. Inst. Chem. Eng. J., **28**, pp. 220–232.
[30] Crochet, M. J., and Keunings, R., 1982, "On Numerical Die Swell Calculation," J. Non-Newtonian Fluid Mech., **10**, pp. 85–94.
[31] Crochet, M. J., and Keunings, R., 1982, "Finite Element Analysis of Die Swell of a Highly Elastic Fluid," J. Non-Newtonian Fluid Mech., **10**, pp. 339–356.
[32] Ahn, Y. C., and Ryan, M. E., 1991, "A Finite Difference Analysis of the Extrudate Swell Problem," Int. J. Numer. Methods Fluids, **13**, pp. 1289–1310.
[33] Tomé, M. F., Duffy, B., and McKee, S., 1996, "A Numerical Technique for Solving Unsteady Non-Newtonian Free Surface Flows," J. Non-Newtonian Fluid Mech., **62**, pp. 9–34.
[34] Gifford, W. A., 1998, "The Effect of Surface Tension on Extrudate Swell From Square and Retangular Channels," Polym. Eng. Sci., **38**(7), pp. 1167–1174.
[35] Georgiou, G. C., and Boudouvis, A. G., 1999, "Converged Solutions of the Newtonian Extrudate-Swell Problem," Int. J. Numer. Methods Fluids, **29**, pp. 363–371.
[36] Tomé, M. F., Castelo, A., Cuminato, J. A., Mangiavacchi, N., and McKee, S., 2001, "GENSMAC3D: A Numerical Method for Solving Unsteady Three-Dimensional Free Surface Flows," Int. J. Numer. Methods Fluids, **37**, pp. 747–796.

Modeling of Crack Propagation in Thin-Walled Structures Using a Cohesive Model for Shell Elements

Pablo D. Zavattieri
GM Research and Development Center,
30500 Mound Road,
Warren, MI 48090-9055
e-mail: Pablo.zavattieri@gm.com

A cohesive interface element is presented for the finite element analysis of crack growth in thin specimens. In this work, the traditional cohesive interface model is extended to handle cracks in the context of three-dimensional shell elements. In addition to the traction-displacement law, a bending moment-rotation relation is included to transmit the moment and describe the initiation and propagation of cracks growing through the thickness of the shell elements. Since crack initiation and evolution are a natural outcome of the cohesive zone model without the need of any ad hoc fracture criterion, this model results in automatic prediction of fracture. In particular, this paper will focus on cases involving mode I/III fracture and bending, typical of complex cases existing in industrial applications in which thin-walled structures are subjected to extreme loading conditions (e.g., crashworthiness analysis). Finally, we will discuss how the three-dimensional effects near the crack front may affect the determination of the cohesive parameters to be used with this model. [DOI: 10.1115/1.2173286]

1 Introduction

The cohesive zone model (CZM) has gained significant importance in the modeling of crack propagation in solids in recent years. Although this model was first proposed by Barenblatt in 1962 [1] to describe material degradation and separation in a process zone in front of the crack tip in brittle materials and then applied to ductile fracture by Dugdale in 1959 [2], most of the advances in the implementation of this model into numerical methods have taken place during the last decade [3–7].

The most commonly used technique to incorporate the cohesive zone model into a finite element analysis is the discrete representation of the crack which is accomplished by introducing cohesive surfaces (or so-called zero-thickness interface elements) along interelement boundaries. In most cases, these special elements are governed by a cohesive constitutive law that relates the traction with the opening and shear displacement across the interface [3–7]. Although other techniques that make use of smeared or exact representation of the crack regardless of the initial mesh have been developed in the last few years [8–10], the utilization of interface elements remains attractive essentially due to the simplicity and effectiveness in some applications. In fact, the main advantage is that the complexity of crack initiation and evolution (including branching, coalescence, and arrest) can be modeled as a natural outcome of the model, without the need of any additional fracture criterion.

The first efforts to extend these cohesive models to fully three-dimensional problems were made by Ortiz and co-workers [11,12]. Thereafter, similar works have found this tool to be highly predictable of different kinds of three-dimensional problems [13,14]. However, there is a set of problems involving thin-walled structures (such as the analysis of thin plates, fuselage, sheet-metal forming, and crashworthiness) where the use of 3D solid elements would be prohibitive from the computational viewpoint. Generally, these engineering problems are solved with shell or other structural elements [15]. Li and Siegmund [16] made the first attempt to extend the cohesive zone model for shell elements. In their work, crack propagation under mode I/III conditions was studied in aluminum panels. However, the out-of-plane bending deformation was not contemplated in their cohesive model. It should be mentioned that, although the extension of the three dimension cases is relatively simple, shell elements present the challenge of having additional degrees of freedom (i.e., nodal rotations), which may help to identify other failure modes, such as surface crack propagating through the thickness of shells under bending conditions. Most recently, during the review of this paper, a new cohesive approach was proposed by Cirak et al. [17] in which the fracture of thin shells, including the out-of-plane bending mode, was accounted for in the framework of Kirchhoff-Love theory using subdivision elements, where only the nodal displacements were needed for the shell formulation.

In this work, the cohesive interface model is extended to handle cracks in the context of three-dimensional shell elements. In addition to the traction-displacement law, a bending moment-rotation relation is included to transmit the moment and describe the initiation and propagation of cracks growing through the thickness of the shell elements. Unlike the work presented in [17], the cohesive model proposed in this paper is intended for shell elements based on the Mindlin theory (commonly used in several applications) in which the nodal rotations are used for the out-of-plane bending modes. The paper is organized as follows: The description of the interface cohesive element and the constitutive law is given in Sec. 2. Simulations of simple mode I/III crack propagation problems and bending configuration in a thin elastic plate are discussed in Sec. 3. Comparisons with 3D simulations using solid elements showed that the new cohesive model for shell elements can predict the same material response using the same cohesive parameters. A study of ductile crack propagation of elastic-plastic materials and how this affects the determination of the cohesive parameters is included in Sec. 4. It is shown that when the same cohesive parameters are used in the solid and shell models, the results are appreciably different. This is because shell

Contributed by the Applied Mechanics Division of ASME for publication in the JOURNAL OF APPLIED MECHANICS. Manuscript received June 2, 2005; final manuscript received December 23, 2005. Review conducted by G. C. Buscaglia. Discussion on the paper should be addressed to the Editor, Prof. Robert M. McMeeking, Journal of Applied Mechanics, Department of Mechanical and Environmental Engineering, University of California—Santa Barbara, Santa Barbara, CA 93106-5070, and will be accepted until four months after final publication of the paper itself in the ASME JOURNAL OF APPLIED MECHANICS.

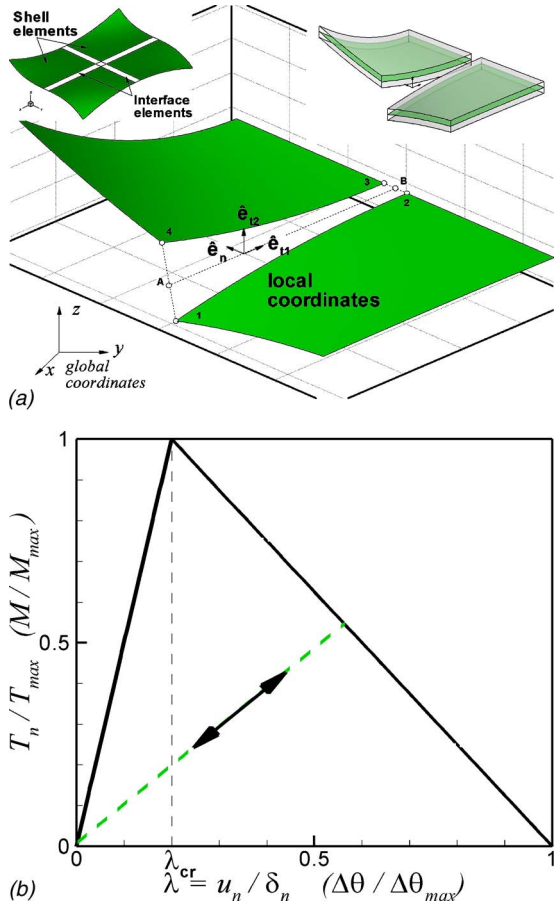

Fig. 1 (*a*) Schematics of the separation between two shell elements. The local coordinates are defined in the middle line of the interface elements. The upper-left box shows the cohesive interface elements embedded along quadrilateral shell elements (for illustration purposes, the shell elements have been separated). (*b*) Traction separation law for pure normal separation. The arrows indicate unloading and loading for $\lambda > \lambda_{cr}$. The same triangular law describes the bending moment-rotation relationship under pure rotation (denoted between parentheses).

elements cannot properly predict the three-dimensional deformational state ahead of the crack front that affects the overall behavior of the material. However, it is demonstrated that the cohesive zone model can still be used to represent this localized behavior by including a constitutive cohesive law that considers geometrical and material factors. A numerical technique to modify these cohesive laws to account for these effects is discussed in Sec. 4.1. Finally, a detailed analysis of the 3D cohesive zone reveals that the projection of the cohesive tractions and opening displacements lead to a well-defined "effective" cohesive law similar to those obtained by the numerical technique.

2 Model Description

2.1 Interface Elements for Shell Elements. The description for the formulation of the interface cohesive element for shell elements is based on the zero thickness four-node linear interface element described in previous works [6,7] extended to 3-D "*line*" interface elements connecting two quadrilateral shell elements. These interface elements are embedded along shell element boundaries as indicated in Fig. 1(*a*).

The model assumes that a perfect interface between two surfaces carries forces that oppose separation and shear between them until decohesion. From that point, the two surfaces will behave as distinct entities. The propagation of a crack can thus be simulated as the consecutive failure of interface elements. The cohesive relationship is expressed in terms of the opening displacement $\Delta=\{u_n,u_{t1},u_{t2}\}^T$ and the traction $\mathbf{T}=\{T_n,T_{t1},T_{t2}\}^T$, where the subscripts n, $t1$, and $t2$ denote the component of the traction and displacement in the direction of the local axes of coordinates. The magnitude of the opposing forces before debonding is a function of the relative normal and shear displacement jumps between the two surfaces, and this relationship is given by the constitutive cohesive law, $\mathbf{T}=f(\Delta)$. The interface between two shell elements is "intact" until the interface traction reaches a maximum value $T_{\max}$, and reduces to zero until the displacement jump reaches the maximum value. The reduction of cohesive traction can be interpreted as the progressive degradation of an otherwise intact stress state ahead of the crack tip. Details of the constitutive cohesive laws will be given in the following section.

This shell interface element should be compatible with the formulation of the shell element. In this work, the Belytschko-Lin-Tsay shell element [18] is considered. This shell element, which is the default shell element implemented in explicit finite element software DYNA3D [19], is widely used in several applications including crashworthiness and structural analysis. The formulation of this shell element uses the Mindlin theory of plates [20], which allows for transverse shear strains through the thickness of the plate, as well as thickness reduction. Since the displacements in a quadrilateral shell element can be approximated with classical C^0 interpolations, each node has six degrees of freedom, three translational, (x,y,z) and three rotational, $(\theta_x,\theta_y,\theta_z)$.

2.2 Constitutive Cohesive Law. In this work, the so-called triangular law introduced by Espinosa and Zavattieri [6,7] is extended to 3-D interface elements connecting quadrilateral shell elements. In formulating the cohesive law, a nondimensional effective displacement jump is defined by $\lambda=\sqrt{(u_n/\delta_n)^2+\beta_1^2(u_{t1}/\delta_{t1})^2+\beta_2^2(u_{t2}/\delta_{t2})^2}$, where u_n, u_{t1}, and u_{t2} are the actual normal and tangential displacement jumps at the interface estimated by the finite element analysis, and δ_n, δ_{t1} and δ_{t2} are the critical values at which the interface failure takes place.

Assuming a potential of the form $\Phi(u_n,u_{t1},u_{t1})=\delta_n T_{\max}(\lambda-\lambda^2/2)/(1-\lambda_{cr})$, then the components of the traction acting on the interface in the fracture process zone in the local configuration are given by

$$T_n=\frac{\partial\Phi}{\partial u_n}=\frac{\partial\Phi}{\partial\lambda}\frac{\partial\lambda}{\partial u_n}=\frac{1-\lambda}{\lambda}\left(\frac{u_n}{\delta_n}\right)\frac{T_{\max}}{(1-\lambda_{cr})}$$

$$T_{t1}=\frac{\partial\Phi}{\partial u_{t1}}=\frac{\partial\Phi}{\partial\lambda}\frac{\partial\lambda}{\partial u_{t1}}=\frac{1-\lambda}{\lambda}\left(\frac{u_{t1}}{\delta_{t1}}\right)\frac{\alpha_1 T_{\max}}{(1-\lambda_{cr})}$$

$$T_{t2}=\frac{\partial\Phi}{\partial u_{t2}}=\frac{\partial\Phi}{\partial\lambda}\frac{\partial\lambda}{\partial u_{t2}}=\frac{1-\lambda}{\lambda}\left(\frac{u_{t2}}{\delta_{t2}}\right)\frac{\alpha_2 T_{\max}}{(1-\lambda_{cr})} \quad (1)$$

where $\alpha_1=\beta_1^2(\delta_n/\delta_{t1})$ and $\alpha_2=\beta_2^2(\delta_n/\delta_{t2})$. λ is monotonically increasing and has the form $\lambda=\max(\lambda_{\max},\lambda)$ with $\lambda_{\max}=\lambda_{cr}$ at the beginning. Once the maximum traction is reached, the interface starts failing, the traction reduces to zero, and any unloading in the range $\lambda_{cr}<\lambda\leqslant 1$ takes place irreversibly. Once the effective displacement jump λ reaches or exceeds a value of 1, the interface element is broken and the crack is said to have initiated. Subsequent failure of neighboring interface elements leads to crack evolution. The most attractive feature of this new law is that this irreversible behavior is already incorporated in the law. Figure 1(*b*) shows the variation of the tensile cohesive traction $T_n/T_{\max}$ with respect to the nondimensional normal displacement. The area under the curve for normal traction in the absence of tangential traction gives the cohesive energy (work of separation) G_{Ic} for mode I, namely $G_{Ic}=\delta_n T_{\max}/2$. Similarly, the energies for modes II and III can be obtained as $G_{IIc}=\beta_1^2 G_{Ic}$ and $G_{IIIc}=\beta_2^2 G_{Ic}$, respectively. Once $\lambda\geqslant\lambda_{cr}$, the cohesive interface begins to irreversibly

dissipate energy defined as $G_{dis}=G_{Ic}(\lambda_{max}-\lambda_{cr})/(1-\lambda_{cr})$.

2.3 Fracture by Bending. In this section, a novel cohesive formulation that accounts for the effect of cracks growing through the thickness by bending is proposed. In addition to the traction-displacement law (Eq. (1)), a bending moment-rotation relation is included to transmit the moment and describe the initiation and evolution of cracks. In formulating this cohesive law, a nondimensional effective displacement jump is redefined by adding an extra term, $\lambda=\sqrt{(u_n/\delta_n)^2+\beta_1^2(u_{t1}/\delta_{t1})^2+\beta_2^2(u_{t2}/\delta_{t2})^2+\hat{\beta}^2(\Delta\theta/\Delta\theta_{max})^2}$. Since cracks are allowed to grow along interface elements, and assuming that the crack will grow in the direction of the maximum stress produced by bending, only the rotation θ_{t1} in the direction $\hat{\mathbf{e}}_{t1}$ (parallel to the middle line) will be considered.

Assuming the same potential of Sec. 2.2, the expressions of the normal and tangential tractions remain the same as in Eq. (1), except that λ has a contribution from the rotation and the bending moment is given by

$$M_{t1}=\frac{\partial\Phi}{\partial\Delta\theta}=\frac{\partial\Phi}{\partial\lambda}\frac{\partial\lambda}{\partial\Delta\theta}=\frac{1-\lambda}{\lambda}\left(\frac{\Delta\theta}{\Delta\theta_{max}}\right)\frac{\hat{\alpha}T_{max}}{(1-\lambda_{cr})} \tag{2}$$

where $\hat{\alpha}=\hat{\beta}^2(\delta_n/\Delta\theta_{max})$. Since $\hat{\beta}$ is nondimensional, $\hat{\alpha}$ has dimensions of length/radians and a maximum moment can be defined as $M_{max}=\hat{\alpha}T_{max}$. If there is only pure rotation along the axis $\hat{\mathbf{e}}_{t1}$, this bending moment-rotation relationship represents a nonlinear rotational spring carrying a moment that opposes the bending. Under theses circumstances, the cohesive law has the same triangular shape as the one shown in Fig. 1(*b*). The rising portion of the curve describes the elastic behavior of an intact shell and any loading/unloading takes place linearly with an initial bending stiffness given by $\kappa=M_{max}/(\lambda_{cr}\Delta\theta_{max})$. When the bending moment reaches a maximum value M_{max} a surface crack initiates and propagates through the thickness. Any unloading in the range $\lambda=[\lambda_{cr},1]$ will take place irreversibly with a bending stiffness lower than the initial value. That bending stiffness will decrease as the crack grows until the interface element *breaks* at $\lambda=1$.

In early works, the concept of including a rotational spring along shell element boundaries was introduced by Rice and Levy [21] and later extended to stationary elastic-plastic crack analysis by Parks and White [22]. In their work, the spring represents the additional compliance contributed by the presence of stationary part-through surface cracks. In this new model the same idea is applied in the context of the cohesive zone model, allowing the crack to propagate due to the bending moment and in-plane stresses.

3 Crack Propagation in Elastic Thin Panels

In this section, we will present a simple case of crack propagation in a precracked elastic thin panel under three different loading conditions: tension, torsion, and bending. The main purpose of this study is to compare the new cohesive model for shells with a fully three-dimensional model based on hexahedral continuum elements and their respective cohesive interface elements. Considering that the cohesive zone model has been successfully tested for solid elements in two and three dimensions [3–14], this comparison will allow us to determine how well the proposed model for shell elements is capable of predicting the same fracture behavior using less computational time.

The geometry of the precracked panel is presented in Fig. 2(*a*). The length of this panel is $L=30$ cm, the width $W=12.7$ cm, and thickness $t=6$ mm. The tensile axis is aligned with the y-direction and a crack of initial length $a_0=26$ mm lies along the line $y=0$. For all the cases, the specimen is simulated using both hexahedral and shell meshes (see Figs. 2(*b*) and 2(*c*)). The hexahedral mesh has been constructed using the same shell elements as base with four hexahedral elements through the thickness. The shell element selected is the Belytschko-Tsay shell with five integration points through the thickness. In this analysis, cohesive interface elements

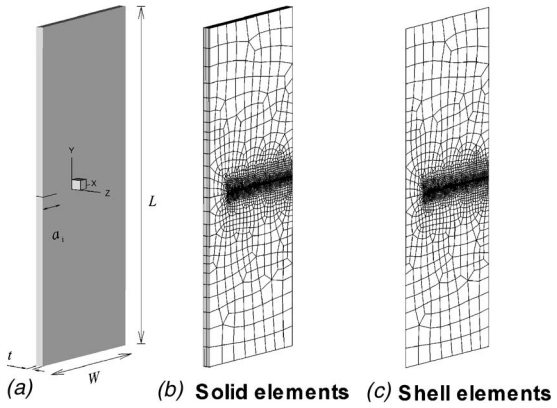

Fig. 2 (*a*) Geometry used for the crack propagation analysis of a precracked elastic thin panel under three different loading conditions: tension, torsion, and bending; (*b*) Hexahedral mesh. (*c*) Shell mesh.

are only embedded along the line $y=0$, so that the crack is constrained to grow along the initial crack line. Since the material used for these simulations (Steel C300) behaves in a brittle fashion, it is assumed that the crack will only grow under pure mode I and crack branching is not allowed. It should be mentioned that this kind of assumption is commonly used by several investigators [4,11,12,14,16,23]. The constitutive material parameters for steel C300 are $E=200$ GPa, $\nu=0.3$, $\rho=7830$ kg/m^3. The cohesive parameters are $T_{max}=700$ MPa, $\delta_n=\delta_{t1}=\delta_{t2}=70$ μm, $\beta_1=\beta_2=1.0$, and $\lambda_{cr}=0.3$. In addition to the condition that the element size has to be much smaller than the dimension of the block to provide an accurate representation of the stress near the crack tip, the cohesive element size should be also able to resolve the length over which the cohesive model plays a role in the elastic solution. For a simple cohesive law, under pure mode I conditions, Rice [24] proposed a simple expression of the cohesive zone length given by the elastic properties, and the cohesive parameters, $l_{cz}\approx(9\pi E/32)(G_{Ic}/T_{max}^2)$. Considering the material parameters for the case to be analyzed in this section, the cohesive zone length is $l_{cz}\approx 9$ mm. It is common practice to evaluate this characteristic length before the finite element meshes are built to ensure convergence in the results [5–7]. In addition to this, a convergence analysis with cohesive element size $L_e<l_{cz}$ was also performed. Finally, to satisfy all the length scales a cohesive element size of approximately $L_e=1$ mm was chosen. A similar convergence analysis was performed to determine the number of layers of elements needed through the thickness of the plate. It was then determined that for the elastic simulations presented in Secs. 3.1–3.3, five layers of elements through the thickness of the plate were sufficient. In this preliminary study, the material is treated as elastic, using the continuum elastic model for large deformations available in DYNA3D [19]. Discussion on elastic-plastic material is given in Sec. 4.

Cohesive interface elements connecting hexahedral elements: Similar to the case of shell elements, the formulation of the cohesive interface elements connecting the faces of two hexahedral elements is based on a zero-thickness eight-node bilinear interface element similar to that previously presented in [14]. Like in any traditional cohesive interface element for 2- and 3-D, only the displacement-traction relationship constitutes the cohesive law [3–7,11–14]. The components of the opening displacement are $\Delta=\{u_n,u_{t1},u_{t2}\}^T$, and the nondimensional effective displacement jump becomes $\lambda=[(u_n/\delta_n)^2+\beta_2^2(u_t/\delta_t)^2]^{1/2}$ where $(u_t/\delta_t)^2=(u_{t1}/\delta_{t1})^2+(u_{t2}/\delta_{t2})^2$. As a result, the cohesive law employed for these interface elements is the same as the one given by Eq. (1) considering $\delta_{t1}=\delta_{t2}=\delta_t$. The main difference between this cohesive law and the one proposed for the shell interface element in

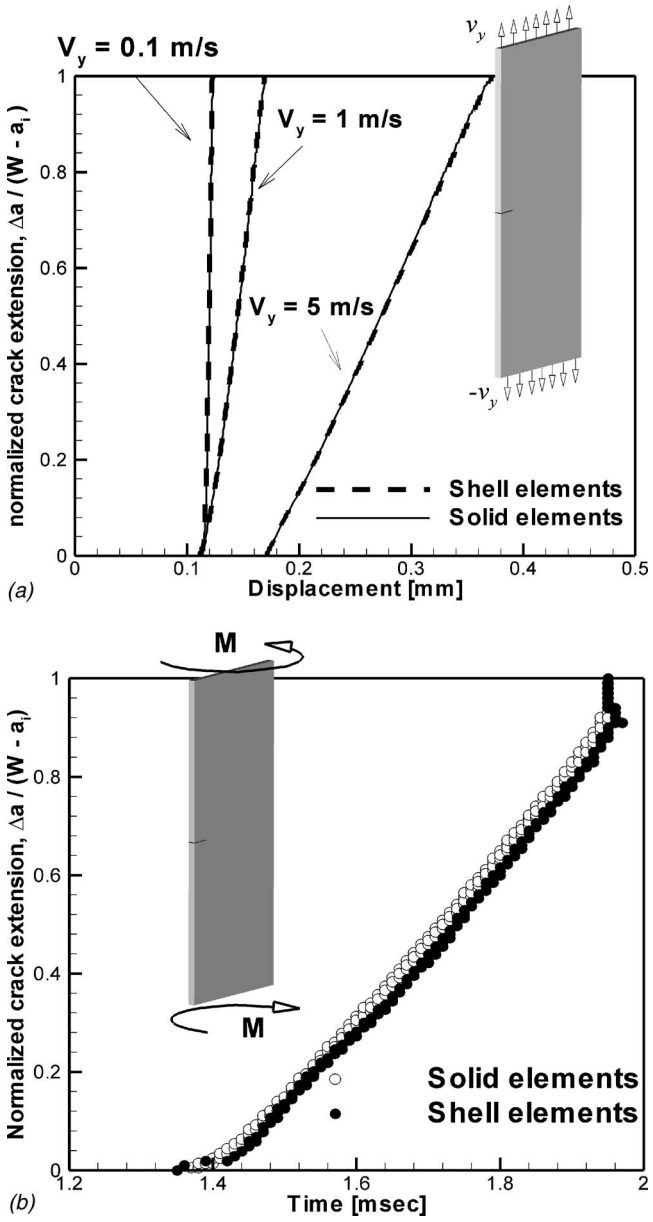

Fig. 3 (*a*) Tension test: crack tip position versus displacement for three different loading rates. (*b*) Torsion test: crack tip position as a function of time for the case where the elastic thin plate is loaded under mode III conditions.

Sec. 2.1 is that it is not necessary to make any difference between the tangential components.

3.1 Mode I Crack Propagation: Tension Test. In this case, the rectangular thin-walled specimen is subjected to dynamic tensile loading on both upper and bottom boundaries given by a uniformly applied velocity at the top and bottom boundaries, $v_y = \pm 0.1$, 1, and 5 m/s as shown in Fig. 3(*a*). The simulations were carried out until the crack reached the other end of the plate. An evaluation of the stress distribution, crack evolution, and force-displacement curves showed a good agreement between the fully three-dimensional model and the shell model.

Figure 3(*a*) shows the crack tip position as a function of the applied displacement for the three different loading rates. The crack tip position is determined by the global position of the integration point in which the condition $\lambda = 1$ is satisfied. In these figures the solid line represents the simulations with solids and the dashed line the simulations with shells. It is clear from these results that both models can predict exactly the same material response.

3.2 Mode III Crack Propagation: Torsion Test. To further test the model, the same specimen is simulated with solid and shell elements under torsion load. As in the previous case, the boundary conditions are only applied on the top and bottom boundaries, except that in this case a constant rotational velocity field of $\dot{\theta} = 0.08$ rad/s is applied. These geometry and loading conditions create a mode III stress field near the crack trip/front. The loading conditions and cohesive parameters are similar for both models. Given the asymmetric conditions at the crack plane, the moment-rotation relationship does not play an important role yet. However, this problem complements in some way the one considering only pure mode I. The results of these simulations are depicted in Fig. 3(*b*). The crack tip position as a function of time is similar for both cases. A closer examination of the middle plane in the solid case revealed that the stress field was similar to the one with shell elements.

3.3 Bending Test. In this case, the same precracked plate is loaded in a three-point bending setup. Unlike traditional setups to study crack propagation, in this specific problem the applied load is perpendicular to the plane of the plate such that out-of-plane bending is induced. The main idea behind this test is to provoke through-the-thickness crack propagation. The layout of this experiment is shown in Fig. 4(*a*). Two cylindrical rods are positioned under the plate, each one at 10 cm from crack plane. A third rod aligned with the crack plane is positioned just above the plate and it moves towards the plane with a constant velocity $v_z = 1$ m/s. The diameter of the rods is 1 cm. It was observed that one of the advantages of this setup is that the crack front propagates in two directions: (1) perpendicular to the plane of the plate, along the z-axis from the bottom to the top (through-the-thickness crack propagation) and (2) in the direction of the original crack along the x-axis, from the initial crack front to the other side of the plate (where the local axes are defined in Fig. 2). This leads to a more controlled crack growth, as opposed to the case without initial crack where the crack can grow through the thickness in an unrestrained mode. Although the shell model is not able to explicitly predict through-the-thickness crack growth, this configuration will test the capability of the model to predict the overall response of the structure.

As in previous cases, the cohesive parameters used for the shell model are the same as those used in the fully three-dimensional case. However, in this case the moment-rotation relationship of Eq. (2) becomes an important part of the overall constitutive cohesive law and, therefore, the cohesive parameters $\Delta\theta_{\max}$ and $\hat{\beta}$ need to be determined. Several simulations were performed with different parameters until a good match was achieved. Figure 4(*a*) shows the crack tip position as a function of time for best case with $\Delta\theta_{\max} = 0.05$ rad and $\hat{\beta} = 1.0$. In this figure, the crack evolution is represented by the x-coordinate of the centroid of the interface elements at the time where $\lambda = 1$ is satisfied. In the simulation with solid elements, several interface elements have the same x-coordinate. However, the time where the crack front passes through those points may be different. Figure 4(*a*) shows that the crack front evidently evolves differently along the various layers of elements. This confirms that the crack grows in two directions along the projected crack plane. Furthermore, it was observed that the crack initiates originally at the intersection of the initial crack front and the bottom surface and propagates to the upper surface as it grows in the x-direction.

A second configuration is tested to validate the model parameters. The thickness of the plate is reduced to 2 mm, and the impact velocity is increased to $v_z = 10$ m/s. The crack tip position as a function of time is shown in Fig. 4(*b*). Although the fully three-dimensional simulation case shows a strong through-the-

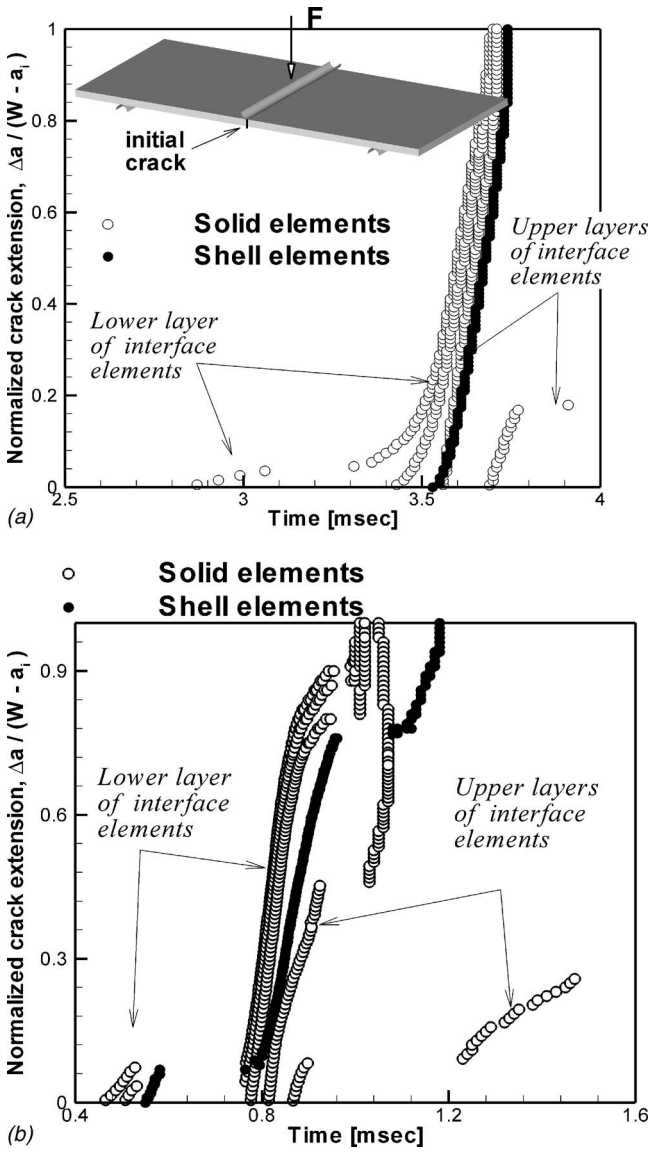

Fig. 4 Schematics of the three-point bending setup. (*a*) Crack tip position as a function of time for case with thickness t =6 mm and v_z=1 m/s. (*b*) Crack tip position as a function of time for the case with thickness t=2 mm and v_z=10 m/s. (Comment: The dots represent the x-coordinate of the centroid of the interface elements at the time where they fail. Clearly the simulation with solids shows the crack evolution in the different layers of elements.)

thickness crack propagation, the shell model is able to predict the crack propagation in the x-direction. Some of the discontinuities shown in these plots correspond to temporary arrests of the local crack front. The ability of the model with shell elements to capture such effects is remarkable. Moreover, it is observed that the overall force needed in the upper rod to break the plate is similar using both models.

The bottom views of the cracked plate and the stress field are shown in Fig. 5 for both models at three different times where the crack growth takes place. The position of the crack front/tip can be estimated from the stress field. It should be noted that the stress shown in the simulation with solid elements is that of the bottom surface of the plate, whereas the one shown in the case with shells represents the middle plane stress field. Therefore, the crack tip position of the model with shells as described in Fig. 4 can be considered as the position of the crack front at the middle plane.

4 Three-Dimensional Effects of Ductile Crack Propagation in Thin-Walled Specimens

The potential of the cohesive zone model to simulate crack propagation in elastic thin plates using shell elements has been examined in the last section. The material under consideration was only elastic, and in most cases the crack front was straight. Consequently, the plane stress formulation used by the shell elements may be suitable to model these kinds of problems. However, this desired behavior might not be observed in real ductile materials. The study of ductile fracture in elasto-plastic materials raises some concerns regarding the mechanical constraint imposed by the plastic deformation in the region near the crack front. Moreover, during ductile crack propagation of thin metals, a characteristic phenomenon called crack tunneling is observed. Crack tunneling occurs when the initially straight crack front grows more rapidly in the middle of the thin-walled specimen leading to the formation of rounded crack front profile. The plastic deformation around the tunneled crack front departures from the ideal deformational state observed in the elastic cases. As a consequence, additional out-of-plane components of shear stress become significant as the highly plastic deformation takes place near the crack region. In addition to crack tunneling, slant crack growth could also occur under certain conditions and materials. This is when the crack front turns into a 45 deg direction leading to a mixed mode I/III crack growth problem [25]. The study of slant fracture and its transition from flat crack is out of the scope of this analysis. Thus, we will restrict the current study to problems where crack fronts advance in flat mode.

All these complex mechanisms certainly affect the driving force of the crack and, consequently, the response of the material. It is then essential to make use of powerful tools that can accurately predict these localized phenomena. The cohesive zone model, in combination with the finite element method and continuum models, has proven to be a good choice for these kinds of analysis. Chen et al. [26–28] have extensively carried out fully three-dimensional analysis of crack growth in thick specimens using the cohesive model. Since ductile fracture in elasto-plastic materials is driven by void nucleation, growth, and coalescence, which are affected by the local constraint, they found a strong dependence of the cohesive parameters with the constraint conditions (stress triaxility), and as a result through-the-thickness variation of these parameters was considered. Moreover, they found that different cohesive parameters may be needed for different specimen geometries (i.e., double edge notched and compact test specimens). On the other hand, Roychowdhury et al. [14] have shown that for thin specimens, a three-dimensional model with constant cohesive parameters can fit the experimental results with good agreement, and yet were able to predict crack tunneling. Moreover, their work demonstrated the ability of the fully-three dimensional model to predict crack growth with different crack lengths and other geometries (including compact tests) with only one set of cohesive parameters.

The use of shell elements in conjunction with the cohesive model may require a special treatment to capture the fundamental nature of ductile crack propagation in thin specimens. Since shell theory is based on a bidimensional state of plane stress [15,20], all these three-dimensional effects mentioned in the previous paragraph are essentially ignored by the shell formulation, and any variation of thickness does not play any role in the simulated results [29]. It is then expected that the three-dimensional model and the shell model will lead to different results.

To illustrate the importance of the three-dimensional effect of tunneling in the crack region, an elasto-plastic specimen loaded in mode I is simulated with solid and shell elements. Details of this setup and material model are given later in Sec. 4.1. The same configuration is simulated with a pure elastic model for comparison purposes; however, the cohesive parameters are the same for all these simulations. Figure 6(*a*) compares the crack tip position as a function of the applied displacement for all these cases. Even

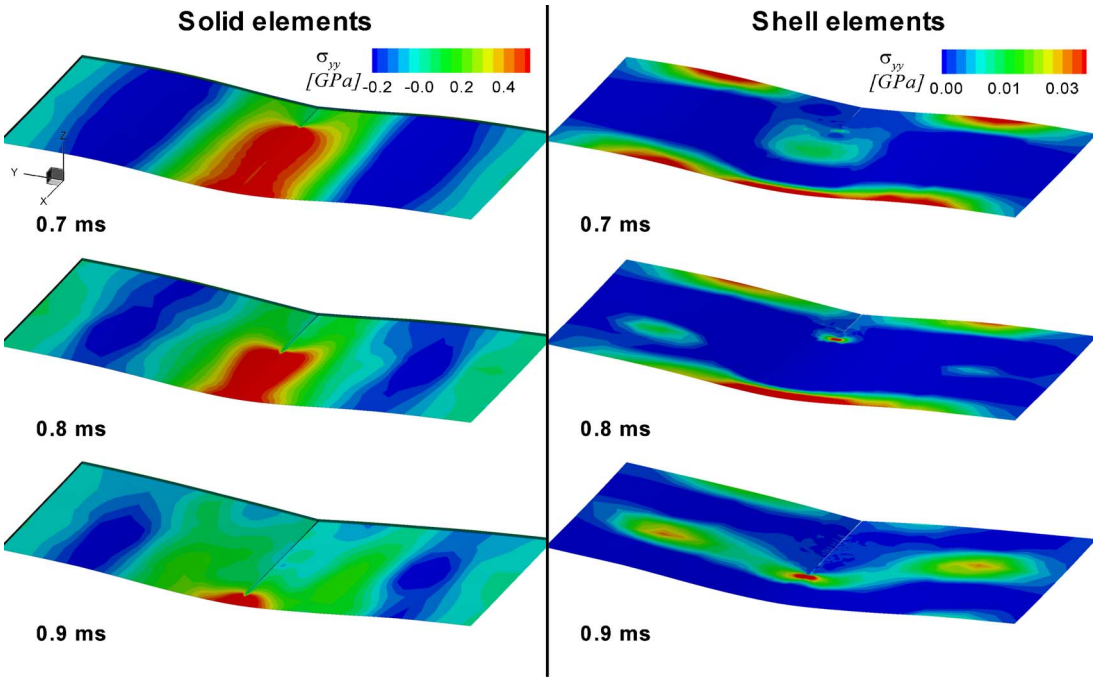

Fig. 5 Tensile stress σ_{yy} at different times during the propagation of the crack using a shell and solid mesh for the three-point bending configuration for t=2 mm and v_z=10 m/s.

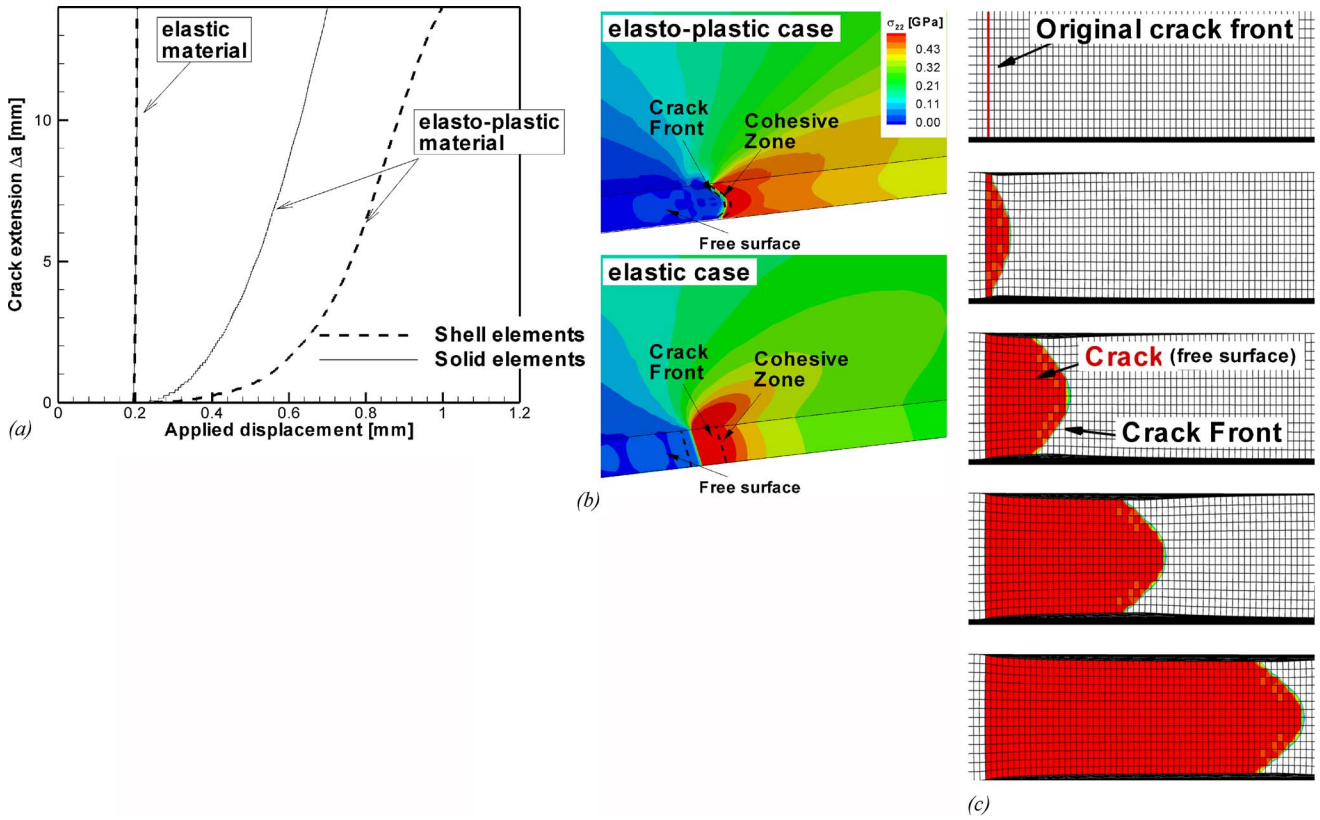

Fig. 6 (*a*) Crack tip position as a function of the applied displacement for a mode I ductile crack problem simulated with solid and shell elements. The solution for the solid mesh is given at the midsection of the panel. (*b*) Tensile stress field for the elasto-plastic and elastic material. (*c*) Details of the crack tunneling for the case modeled with 3D solid elements. The dark region indicates where G_{dis}/G_{Ic}=1.0.

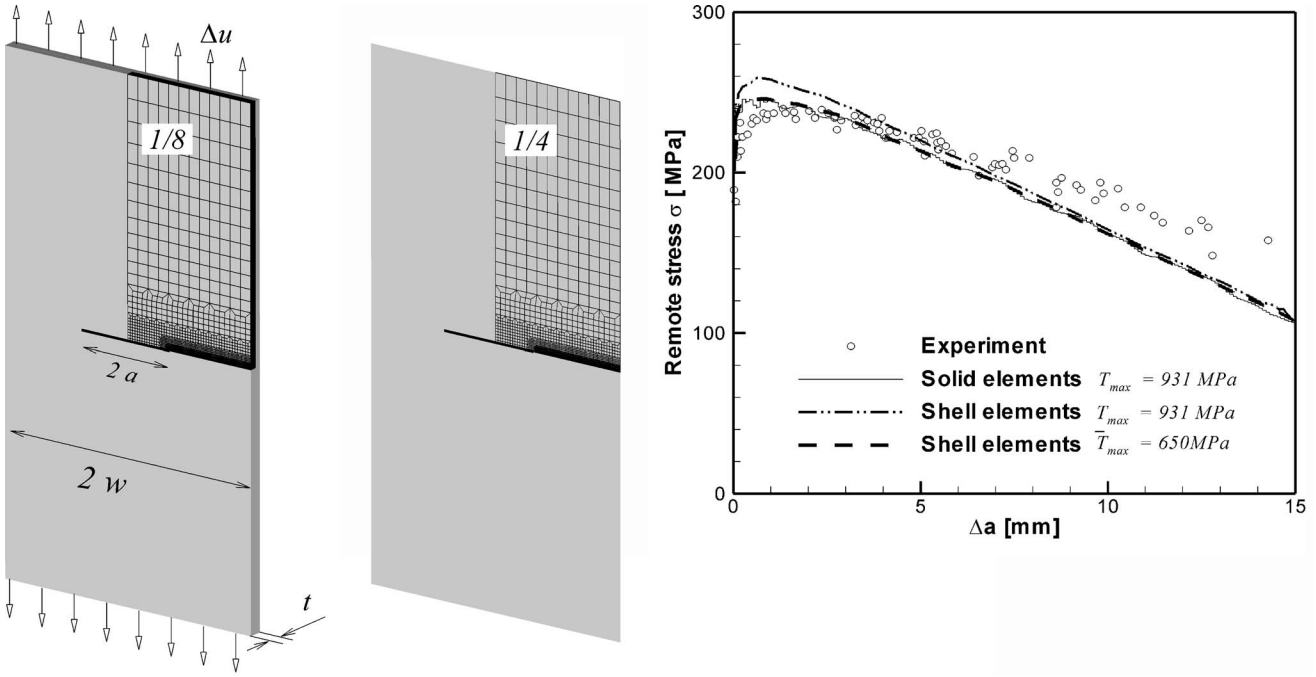

Fig. 7 (*a*) Details of the center-cracked aluminum panel. For simplicity purposes, the solid model considers only one-eighth of the geometry and (*b*) the shell model one-fourth. Symmetry boundary conditions are applied accordingly. (*c*) Predicted and measured load-crack growth response using both models (for comparison purposes the shell model uses two cohesive strengths).

though there is an excellent agreement when the material is elastic (as observed in Sec. 3.1), a noticeable disagreement in crack growth between the solid and shell model is obtained for the elasto-plastic case. Based on the hypothesis that the three-dimensional simulation contains the most reliable information about the true deformation process, there is clearly something missing in the model for shells. The three-dimensional tensile stress fields (σ_{yy}) for the elasto-plastic and pure elastic cases are shown in Fig. 6(*b*). For illustration purposes, only one half of the specimen from the crack plane is shown. The presence of a more complex three-dimensional stress state ahead of the crack front is evident in the elasto-plastic case. The same figure indicates the location of the crack front and the cohesive zone defined as the region where irreversible energy dissipation takes place $0 \leqslant (G_{\text{dis}}/G_{\text{Ic}}) < 1$ (see Sec. 2.2). Although not shown in this paper, the formation of "*shear lips*" caused by the plastic deformation on the free borders was also observed. Figure 6(*c*) shows the predicted crack front formation at different stages. The initial straight crack front evolves into a round-shaped crack front. The dark region indicates where the material has been totally separated (where $G_{\text{dis}}/G_{\text{Ic}}=1.0$). A thick black line on the free surfaces depicts evidence of thickness reduction.

Unfortunately, the localized three-dimensional deformational state near the crack front affects the overall response of the structure, and the bi-dimensional nature of the plane stress formulation is evidently not adequate to capture this phenomenon [29]. Nevertheless, it may still be possible to "*lump*" this localized behavior into the cohesive zone model. In this section, we will study this alternative by explicitly modifying the existing constitutive cohesive law to incorporate some geometrical and material factors that would eventually take into account the complexity of the tunneling effect. As an example, a mode I crack propagation experiment performed by Dodds and co-workers [23] on constrained center-cracked aluminum panel specimens will be used. It should be mentioned that, even though this experiment has been modeled with the cohesive zone model using both solid elements (Roychowdhury et al. [14]) and shell elements (Li and Siegmund [16]), both papers have reported different values of cohesive strength. This discrepancy will be discussed later in the section.

4.1 Analysis of a Center-Cracked Aluminum Panel. Following the work by Dodds and co-workers [14,23], simulations of an aluminum Al2024-T3 centered-crack panel are performed with the fully three-dimensional model. Following the description of Fig. 7(*a*), the width of the panel is $2w=75$ mm. The initial crack length is $a/w=0.333$ and the thickness of the plates is $t=2.3$ mm. Due to the symmetry of this configuration only one-eighth of the geometry is simulated. Thus, symmetry boundary conditions are employed accordingly. Cohesive elements are inserted in the projected crack plane/line. The element size in the fracture region is $L_e=0.1$ mm in the crack direction and $L_t=0.16$ mm in the thickness direction. This provides seven layers of elements across half-thickness. Mesh convergence studies performed by Dodds [14] demonstrated that $L_e=25$ mm and five layers of elements across the half-thickness were sufficient refinement to capture proper crack growth and tunneling formation. Due to the localized high plastic deformation ahead of the crack front, a convergence analysis was performed to evaluate the different element formulations to check for hourglass modes and undesired locking. Finally, it was found that, either, the fully integrated eight-node hexahedral elements using the mean dilatation method or the reduced integration hexahedral with stiffness form of the Flanagan-Belytschko hourglass method [19] could be safely used for this kind of analyses. Both formulations gave essentially the same results and were compared with the results reported by previous works and experiments [14,23].

In order to simulate the quasi-static test with displacement control loading using an explicit code such as DYNA3D, uniform low velocities are applied at the nodes on the top boundary. Previous calculations demonstrated that applied nodal velocities of about 500–750 mm/s were slow enough to prevent inertia effects in the calculation and satisfactorily fast to improve CPU efficiency. For the continuum material, the traditional isotropic elastic-plastic constitutive model that uses the Mises yield criterion is utilized. The elastic parameters for the Al2024-T3 are $E=71.3$ GPa and

$\nu=0.3$. The initial yield stress is $\sigma_y=345$ MPa and the plastic regimen is governed by $\sigma=\mathbf{K}\varepsilon^n$, where $\mathbf{K}=\sigma_y(E/\sigma_y)^n$, $n=0.1$ is the hardening exponent, σ is the true effective stress, and ε is the logarithmic strain. A systematic and parametric study performed by Roychowdhury et al. [14] led to the following calibrated cohesive parameters: $T_{\max}=2.7\cdot\sigma_y=931.5$ MPa and $G_{\mathrm{Ic}}=19$ kJ/m^2 (equivalent to a material toughness of $K_{\mathrm{Ic}}=38.5$ MPa$\sqrt{m}$). Figure 7(*c*) shows a good agreement between the numerical predictions and the experimental load-crack extension data. The simulation with shells will be discussed later.

Simulation with shell elements: Following the same scheme, the specimen is simulated with quadrilateral shell elements. In this case only one-quarter of the geometry is modeled with shells. As shown in Fig. 7(*b*), the shell mesh utilized is identical to one of the faces of the fully three-dimensional case. Keeping the same element size, the number of elements is therefore reduced from 21,700 solid elements and 1750 *plane* cohesive elements to only 3500 shell elements and 250 *line* cohesive elements. However, results using the same cohesive parameters as those used in the three-dimensional case are markedly different. Crack propagation is slower than in the real case and the applied peak force is significantly overpredicted. Figures 7(*c*) and 8(*a*) show the crack extension and normal applied force for the three-dimensional case and the shell simulation. The same effect has been observed in later simulations with specimens of different thicknesses. As expected, the fully three-dimensional simulations show a strong dependency of the overall material behavior with the specimen thickness, whereas the shell model predicts the same behavior; that is, the remote applied stress and crack extension are independent of the specimen thickness. It is clear that the cohesive law needs to be modified in order to take into account the three-dimensional effect that the shell elements cannot provide.

Calibration of the shell model: As mentioned before, Li and Siegmund [16] demonstrated that the cohesive zone model could certainly be used with shell elements to model these kinds of problems. Nevertheless, they reported a much lower value for the cohesive strength ($\bar{T}_{\max}=2\sigma_y$). Prior works on dynamic crack growth in thin sheets also led to similar findings [30]. This indicates that possible modifications of the cohesive zone model can involve a reduction of the cohesive strength. However, to the best of the author's knowledge, there is no work done on defining some sort of scaling law to relate the cohesive strength, $T_{\max}$, used in the three-dimensional calculations with the "modified" cohesive strength, $\bar{T}_{\max}$, for a 2D formulation. As previously discussed, the cohesive strength used in 3D simulations was shown to predict well different specimens and loading conditions [14]. On the other hand, the modified cohesive strength for shell elements should eventually contain information of the geometry and is expected to vary for different specimen thicknesses.

Looking at this trend, a series of numerical simulations with shell elements was performed for various values of the cohesive strength, $\bar{T}_{\max}$, and keeping the same cohesive energy G_{Ic} (the critical displacement is then computed as $\delta_n=2G_{\mathrm{Ic}}/\bar{T}_{\max}$). Figures 8(*a*) and 8(*b*) show the crack extension and force as a function of the remote applied displacement for different values of $\bar{T}_{\max}$ using the shell model. It is observed that crack growth is delayed for higher values of $\bar{T}_{\max}$. Conversely, the peak force increases with $\bar{T}_{\max}$. In conclusion, it was found that, with $\bar{T}_{\max}=1.88\ \sigma_y=650$ MPa, the shell model gives similar results to the three-dimensional model. The force-crack extension curve was also included in Fig. 7(*c*) using $\bar{T}_{\max}=931.5$ and 650 MPa for comparison purposes. This value is closer to Li and Siegmund's findings [16].

Certainly, this change in the value of $\bar{T}_{\max}$ is an "adhoc" modification of the cohesive law to take into account the three-dimensional effects for this specific thickness and material; hence,

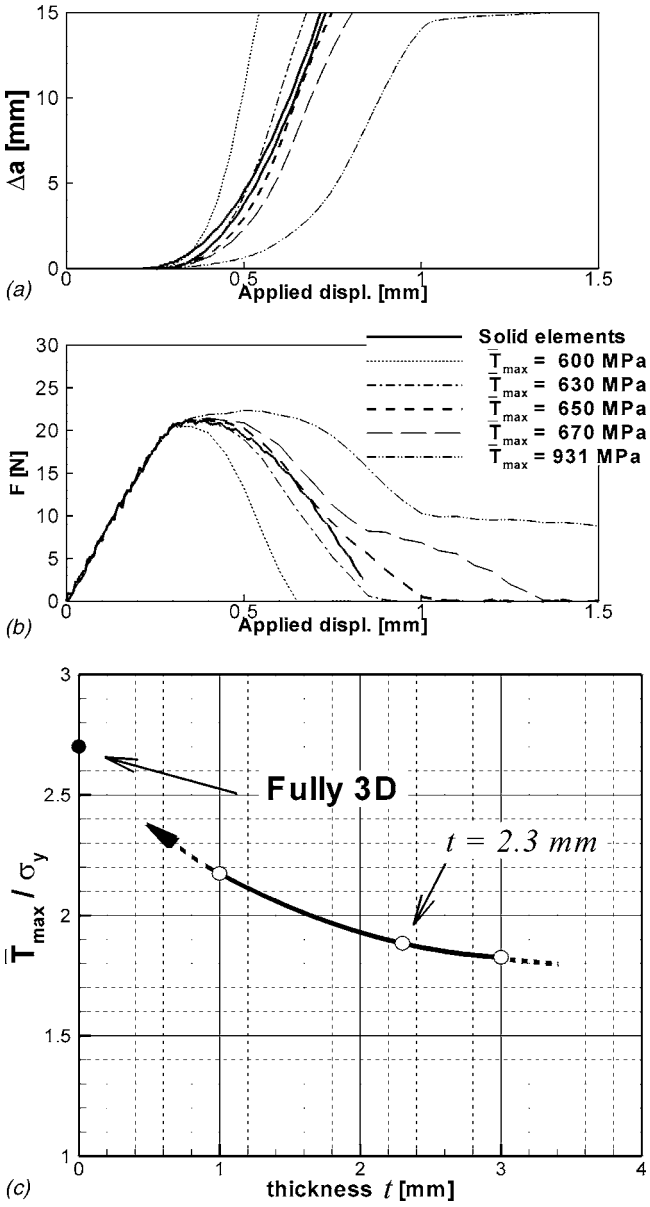

Fig. 8 (*a*) Crack extension and force as a function of the uniformly applied displacement obtained with the fully-three-dimensional model and with the shell model using different cohesive strength values. The two solid lines indicate the crack front position at the middle and outer surface of the specimen for the solid mesh with thickness $t=2.3$ mm. (*b*) Correction of the cohesive strength for shell elements as a function of the specimen thickness.

it should be expected that this correction would be different for other thicknesses or material (different values of E,ν,σ_y,n). Therefore, two more three-dimensional simulations were added for two more thicknesses, $t=1$ and 3 mm using the constant cohesive parameters $T_{\max}=931.5$ GPa and $G_{\mathrm{Ic}}=19$ kJ/m^2 used in [14]. Then, the same process was repeated for these two new specimens. Again, simulations with the shell model were performed for different values of $\bar{T}_{\max}$ for the two cases until good agreement was achieved. Finally, the best match was attained with $\bar{T}_{\max}=2.17\cdot\sigma_y$ for $t=1$ mm, and $\bar{T}_{\max}=1.82\cdot\sigma_y$ for $t=3$ mm. Figure 8(*c*) shows the best match $\bar{T}_{\max}$ versus the specimen thickness. This clearly demonstrates that the cohesive model for shell elements is affected by the geometry, at least for the modeling of

cracks under normal opening.

It should be mentioned that, although it is common practice to report only the force versus crack extension curves for these kinds of experiments (Fig. 7(*c*)), the individual evolutions of these two variables with respect to the applied remote displacement (Fig. 8(*a*)) are more sensitive to the cohesive parameters than just the combination of the two. Therefore, the two curves should be used simultaneously for calibration and validation purposes.

It should be repeated that this model is based on the assumption that the three-dimensional simulations give the best match to the experimental results, and the cohesive law proposed in this section is primarily an "adhoc" modification to modify crack growth under plane stress conditions to obtain an accurate response of the material. Certainly this modification can only take place whenever the three-dimensional model can accurately represent the experimental data in thin plates (where the crack extension and dimensions of the plate are much larger than the thickness of the plate). Extensions of this model can also be done for thicker plates if the right set of cohesive parameters is known for the three-dimensional model, even if these parameters vary with the local position with respect to the middle plane of the specimen, as found in [26–28]. However, in those cases where the cohesive parameters need to be changed for different specimens and boundary conditions in the 3D model, as in [27], the cohesive parameters will need to be changed for the shell model as well.

"Effective" cohesive law: Another way to look at this problem is by analyzing in detail the three-dimensional deformational state and extract from the calculations useful information that can eventually provide some guidelines to define a cohesive law for shell elements. Thus, it can then be possible to look at the bi-dimensional solution as a projection of the three-dimensional case. For instance, the three-dimensional cohesive zone ahead of the mode-I crack front, defined by the normal cohesive traction, is shown in Fig. 9(*a*) (upper corner). The maximum traction (when $T_n=T_{\max}$) follows a curved shape similar to the tunneled crack front. The same figure shows the profile of the normal traction along the x-axis in the direction of the crack growth. Data points represent the normal traction at each integration point of the three-dimensional calculation. The average *through-the-thickness* cohesive traction can be easily obtained by $\bar{T}_n=2/t'\int_0^{t'/2}T_n dz$ (shown as solid line), where $t'=t'(x)$ is the current thickness. The averaged maximum traction is then defined as $\bar{T}_{\max}$, which is notably lower than the cohesive strength used in the three-dimensional simulations. It was observed that this profile, as well as $\bar{T}_{\max}$, remains constant as the tunneling is fully developed and cracks propagate steadily. Three-dimensional simulations of different thicknesses reveal that this averaged maximum traction decreases for thicker panels.

Conversely, the opposite effect was found with the averaged normal opening (defined as $\bar{u}_n=2/t'\int_0^{t'/2}u_n dz$), in which the averaged maximum critical displacement is greater than the one used in the three-dimensional simulations and increases with the thickness of the panel. More remarkable is the combination of these two variables. Figure 9(*b*) shows the relationship between $\bar{T}_n$ and $\bar{u}_n$. Each dot represents the values at integration points of the plane cohesive elements at various stages of the crack propagation simulation. This well-defined "effective" cohesive law is shown for three thicknesses $t=1$, 2.3, and 3 mm. The original cohesive law ($T_{\max}=931.5$ MPa and $G_{\mathrm{Ic}}=19$ kJ/m^2) is also shown in dashed lines. Even though the shape of the cohesive laws departs from the original triangular shape, the overall cohesive energy does not deviate significantly from its original value, which confirms the assumption used in the previous section of keeping the same energy and only modifying the cohesive strength. In all the cases, the initial stiffness also remains unchanged. Consequently, these cohesive laws were implemented for shell elements, and simulations for each thickness were performed. Although, a similar trend to that described in the previous section was observed, the crack extension and applied force were not as accurate as the results obtained with the "calibrated" cohesive parameters. One possible explanation is that the averaged cohesive parameters are slightly greater than those obtained in the calibration process and, hence, do not take into consideration the real three-dimensional character of crack growth by only projecting in a 2D plane. However, this "effective" cohesive law provides some qualitative insight into the real mechanisms that need to be applied in order to define cohesive laws that can be compatible with a plane stress formulation.

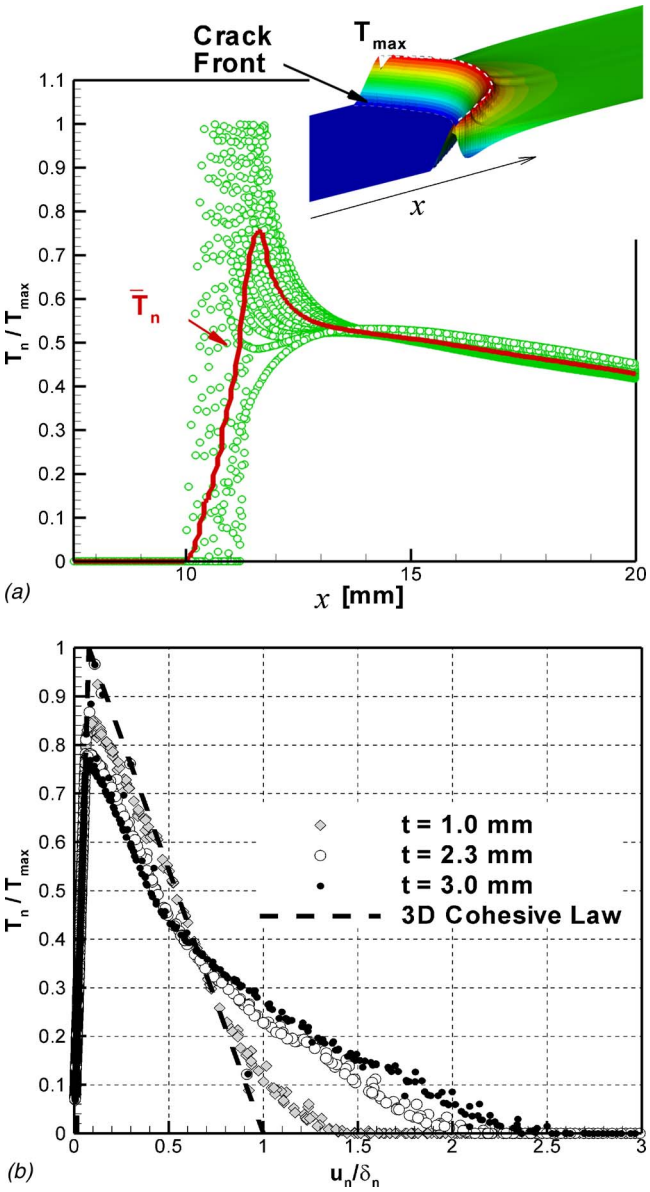

Fig. 9 (*a*) **Normal cohesive traction profile developed near the crack front. Each dot represents the value at each integration point and its *x*-coordinate (initial straight crack front is located at *x*=0). The solid line represents its average through the thickness $\bar{T}_n$. (*b*) Effective cohesive law ($\bar{T}_n$ vs. $\bar{u}_n$) for three different specimen thicknesses.**

5 Conclusions

In this paper, a three-dimensional finite-deformation cohesive element for shell elements for the finite element analysis of crack propagation in thin-walled structures was presented. A numerical

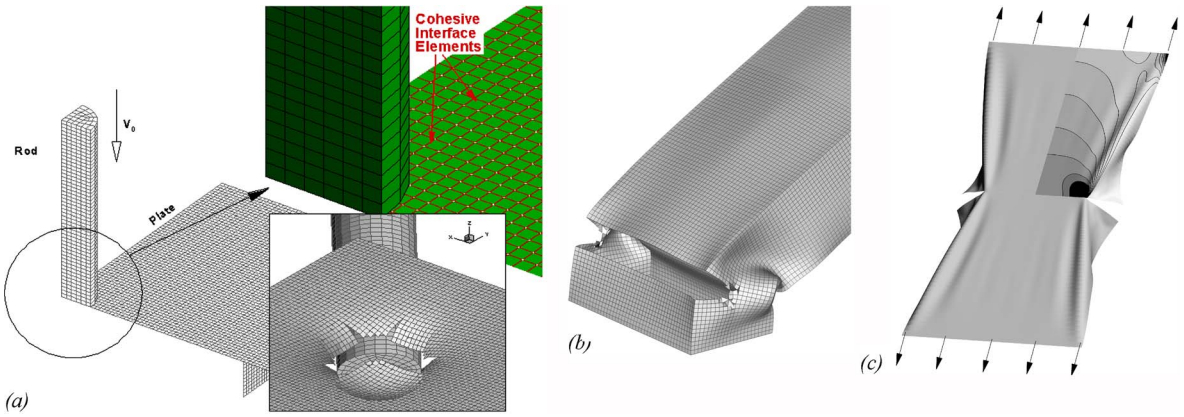

Fig. 10 (*a*) **Rod impacting a brittle plate.** (*b*) **Bending of an aluminum tube.** (*c*) **Fracture of polymer membranes.**

analysis for elastic thin plates was included to assess the capability of the model to predict crack growth under mode I/III and bending loading conditions. Unlike previous models [16], the proposed model incorporates a bending moment-rotation relation to transmit the moment and describe the initiation and propagation of cracks growing through the thickness of the shell elements. In addition, three-dimensional simulations of ductile crack propagation in elasto-plastic materials were used to emphasize the importance of plastic constrain in the region near the crack front. This numerical analysis suggested that the two-dimensional nature of plane stress shell elements together with the cohesive model may not be appropriate to accurately predict the three-dimensional deformational state ahead of the crack front that evidently affects the overall behavior of the material. Therefore, the cohesive law for shells needs to be modified to take into account these geometry and material factors. For that reason, a scaling law for the cohesive strength is proposed in this work (see Fig. 9). Future directions will be focused into a dimensional analysis where different geometry, as well as material parameters, will be included. Along these lines, it will be possible to come up with a dimensionless function for the "modified" cohesive strength as $\bar{T}_{\max}/\sigma_y = \Pi(t/l, E/\sigma_y, n, T_{\max}/\sigma_y)$, where the thickness t may be normalized by the ligament size (l) or the plastic zone length (Γ_p).

The versatility and ability of the model to predict crack growth under various loading conditions have been demonstrated in this work. This opens a new set of possible solutions for problems involving fracture in thin-walled structures that otherwise could not be solved with other models, such as dynamic impact and penetration of plates, deformation, and failure of tubes and tearing of membranes. Figure 10 shows some preliminary simulations performed with this model for various materials.

Finally, the limitations of this model were discussed in Sec. 4. The model is shown to work under the particular circumstances described in Sec. 4 and, clearly, a comprehensive and systematic dimensional analysis to determine clear limits of this model in terms of the geometric and material parameters (including the thickness and plastic zone size) is required, and further studies will be needed in future research works.

Acknowledgment

The author would like to thank Marcos Actis, Alejandro Patanella, and the Departmento de Aeronautica of Universidad Nacional de La Plata, Argentina, for their support during his stay, where the model was developed and implemented. He also would like to thank Nancy Johnson for helpful discussions and Carina Verzi for corrections of this paper. Finally, the support from the organizing committee for the XIV Congress on Numerical Methods and their Applications, ENIEF 2004 and its Chairman, Gustavo Buscaglia is greatly appreciated.

References

[1] Barenblatt, G. I., 1962, "The Mathematical Theory of Equilibrium Cracks in Brittle Fracture," Adv. Appl. Mech., **7**, pp. 55–129.
[2] Dugdale, D. S., 1959, "Yielding of Steel Sheets Containing Slits," J. Mech. Phys. Solids, **8**, pp. 100–104.
[3] Tvergaard, V., and Hutchinson, J. W., 1992, "The Relation Between Crack Growth Resistance and Fracture Process Parameters in Elastic-Plastic Solids," J. Mech. Phys. Solids, **40**, pp. 1377–1397.
[4] Xu, X.-P., and Needleman, A., 1994, "Numerical Simulations of Fast Crack Growth in Brittle Solids," J. Mech. Phys. Solids, **42**(9), pp. 1397–1434.
[5] Camacho, G., and Ortiz, M., 1966, "Computational Modeling of Impact Damage in Brittle Materials," Int. J. Solids Struct., **33**, pp. 2899–2938.
[6] Espinosa, H. D., Zavattieri, P. D., and Dwivedi, S., 1998, "A Finite Deformation Continuum/Discrete Model for the Description of Fragmentation and Damage in Brittle Materials," J. Mech. Phys. Solids, **46**(10), pp. 1909–1942.
[7] Zavattieri, P. D., and Espinosa, H. D., 2001, "Grain Level Analysis of Ceramic Microstructures Subjected to Normal Impact Loading," Acta Mater., **49**(20), pp. 4291–4311.
[8] Klein, P. A., Foulk, J. W., Chen, E. P., Wimmer, S. A., and Gao, H., 2001, "Physics-Based Modeling of Brittle Fracture: Cohesive Formulations and the Application of Meshfree Methods," Theor. Appl. Fract. Mech., **37**(1–3), pp. 99–166.
[9] Moes, N., and Belytschko, T., 2002, "Extended Finite Element Method for Cohesive Crack Growth," Eng. Fract. Mech., **69**, pp. 813–833.
[10] De Borst, R., 2003, "Numerical Aspects of Cohesive-Zone Models," Eng. Fract. Mech., **70**(14), pp. 1743–1757.
[11] Ortiz, M., and Pandolfi, A., 1999, "Finite-Deformation Irreversible Cohesive Elements for Three-Dimensional Crack-Propagation Analysis," Int. J. Numer. Methods Eng., **44**, pp. 1267–1282.
[12] Pandolfi, A., Guduru, P. R., Ortiz, M., and Rosakis, A. J., 2000, "Three Dimensional Cohesive-Element Analysis and Experiments of Dynamic Fracture in C300 Steel," Int. J. Solids Struct., **37**, pp. 3733–3760.
[13] Zhou, F., and Molinari, J. F., 2004, "Dynamic Crack Propagation With Cohesive Elements: a Methodology to Address Mesh Dependency," Int. J. Numer. Methods Eng., **59**, pp. 1–24.
[14] Roychowdhury, S., Arun Roy, Y. D., and Dodds, R. H., Jr., 2002, "Ductile Tearing in Thin Aluminum Panels: Experiments and Analices Using Large-Displacement, 3-D Surface Cohesive Elements," Eng. Fract. Mech., **69**, pp. 983–1002.
[15] Belytschko, T., Liu, W. K., and Moran, B. G., 2000, *Nonlinear Finite Elements for Continua and Structures*, John Wiley & Sons, Ltd., New York.
[16] Li, W., and Siegmund, T., 2002, "An Analysis of Crack Growth in Thin-Sheet Metal via a Cohesive Zone Model," Eng. Fract. Mech., **69**(18), pp. 2073–2093.
[17] Cirak, F., Ortiz, M., and Pandolfi, A., 2005, "A Cohesive Approach to Thin-Shell Fracture and Fragmentation," Comput. Methods Appl. Mech. Eng., **194**(21–24), pp. 2604–2618.
[18] Belytschko, T., 1984, "Explicit Algorithms for Nonlinear Dynamics of Shells," Comput. Methods Appl. Mech. Eng., **43**, pp. 251–276.
[19] Lin, J., 1998, "DYNA3D: A Nonlinear, Explicit, Three-Dimensional Finite Element Code for Solid and Structural Mechanics. User Manual," MDGME, LLNL.
[20] Mindlin, R. D., 1951, "Influence of Rotary Inertia and Shear on Flexural Motions of Isotropic, Elastic Plates," ASME J. Appl. Mech., **18**, pp. 31–38.
[21] Rice, J. R., and Levy, N., 1972, "The Part-Through Surface Crack in an Elastic Plate," ASME J. Appl. Mech., **39**, pp. 185–194.
[22] Parks, D. M., and White, C. S., 1982, "Elastic-Plastic Line-Spring Finite-Elements for Surface-Cracked Plates and Shells," ASME J. Pressure Vessel Technol., **104**, pp. 287–292.
[23] Gullerud, A. S., Dodds, R. H. Jr., Hampton, R. W., and Dawicke, D. S., 1999, "Three-Dimensional Modeling of Dutile Crack Growth in Thin Sheet Metals: Computational Aspects and Validation," Eng. Fract. Mech., **63**, pp. 347–374.

[24] Rice, R. J., 1980, "The Mechanics of Earthquake Rupture," in *Physics of the Earth's Interior*, A. M. Dziewonski and E. Boschi, eds., Italian Physical Society/North-Holland Publ. Co, Amsterdam, pp. 555–649.
[25] Mahgoub, E., Deng, X., and Sutton, M. A., 2003, "Three-Dimensional Stress and Deformation Fields Around Flat and Slant Cracks Under Remote Mode I Loading Conditions" Eng. Fract. Mech., **70**(18), pp. 2527–2542.
[26] Chen, C. R., Kolednik, O., Scheider, I., Siegmund, T., Tatschl, A., and Fischer, F. D., 2003, "On the Determination of the Cohesive Zone Parameters for the Modeling of Micro-Ductile Crack Growth in Thick Specimens," Int. J. Fract., **120**, pp. 517–536.
[27] Chen, C. R., and Kolednik, O., 2005, "Comparison of Cohesive Zone Parameters and Crack Tip Stress States Between Two Different Specimen Types," Int. J. Fract., **132**, pp. 135–152.
[28] Chen, C. R., Kolednik, O., Heerens, J., and Fischer, F. D., 2005, "Three-Dimensional Modeling of Ductile Crack Growth: Cohesive Zone Parameters and Crack Tip Triaxility," Eng. Fract. Mech., **72**(13), pp. 2072–2094.
[29] Kwon, S. W., and Sun, C. T., 2000, "Characteristics of Three-Dimensional Stress Fields in Plates With a Though-the-Thickness Crack," Int. J. Fract., **104**, pp. 291–315.
[30] Mathur, K. K., Needleman, A., and Tvergaard, V., 1996, "Three Dimensional Analysis of Dynamic Ductile Crack Growth in a Thin Plate," J. Mech. Phys. Solids, **44**(3), pp. 439–464.

R. Balderrama
Mechanical Engineering School,
Universidad Central de Venezuela,
Caracas, Venezuela

A. P. Cisilino[1]
Department of Mechanical Engineering,
Welding and Fracture Division – INTEMA – CONICET,
Universidad Nacional de Mar del Plata,
Av. Juan B. Justo 4302,
7600 Mar del Plata,
Argentina
e-mail: cisilino@fi.mdp.edu.ar

M. Martinez
Mechanical Engineering School,
Universidad Central de Venezuela,
Caracas, Venezuela

Boundary Element Method Analysis of Three-Dimensional Thermoelastic Fracture Problems Using the Energy Domain Integral

A boundary element method (BEM) implementation of the energy domain integral (EDI) methodology for the numerical analysis of three-dimensional fracture problems considering thermal effects is presented in this paper. The EDI is evaluated from a domain representation naturally compatible with the BEM, since stresses, strains, temperatures, and derivatives of displacements and temperatures at internal points can be evaluated using the appropriate boundary integral equations. Special emphasis is put on the selection of the auxiliary function that represents the virtual crack advance in the domain integral. This is found to be a key feature to obtain reliable results at the intersection of the crack front with free surfaces. Several examples are analyzed to demonstrate the efficiency and accuracy of the implementation. [DOI: 10.1115/1.2173287]

1 Introduction

Assessing the engineering integrity and life expectancy of thermally stressed components, either under service conditions or during the design stage, requires the determination of fracture parameters. Over the years much work has been done to evaluate stress intensity factors for these problems, resulting in collections of results published in handbook form [1,2]. However, most of these solutions are restricted to regular cracks in infinite or semi-finite solids and two-dimensional simple crack geometries. The solution of complicated three-dimensional crack problems usually requires such numerical techniques as the finite element method (FEM) and the boundary element method (BEM).

The attraction of the BEM can be largely attributed to the reduction in the dimensionality of the problem; for three-dimensional problems only the surface of the domain needs to be discretized [3]. At the same time, and due to the inherent characteristics of its formulation, the BEM provides very accurate results for problems containing strong geometrical discontinuities. This makes the BEM a powerful numerical tool for modeling crack problems [4]. In particular, thermoelastic BEM formulations have been presented, among others, by Raveendra and Banerjee [5], Mukherjee et al. [6], Prassad et al. [7], and dell'Erba and Aliabadi [8].

Evaluation of stress intensity factors using boundary elements has been done by a variety of methods, such as the extrapolation of displacements or stress, special crack tip elements, the subtraction of singularity technique, the strain energy release rate, and J-integral methods [9]. Techniques based on the extrapolation of displacements and stresses are easy to implement, but they require a very high level of mesh refinement in order to obtain accurate results. Alternating and virtual crack extension methods are also computationally expensive, as they require multiple computer runs to solve the problem. On the other hand, path-independent integrals, being an energy approach, eliminate the need to solve local crack tip fields accurately, since if integration domains are defined over a relatively large portion of the mesh, an accurate modeling of the crack tip is unnecessary because the contribution to J of the crack tip fields is not significant. At the same time, the BEM is ideally suited for the evaluation of path-independent integrals, since the required stresses, strains, temperatures, and derivatives of displacements and temperatures can be directly obtained from their boundary integral representations. Using the BEM, Prasad et al. [7] implemented the J-integral due to Kishimoto et al. [10] for the analysis of two-dimensional thermoleastic problems. Its extension to three dimensions was presented by dell'Erba and Aliabadi [8] together with a decomposition method for the computation of the mixed mode stress intensity factors. Among the available methods for calculating fracture parameters, the energy domain integral (EDI) [11] has shown to be well-suited for three-dimensional BEM analysis. Applications of the EDI to solve three-dimensional crack problems using the BEM have been reported by Cisilino et al. for elasticity [12], elastoplasticity [13], and fiber-matrix interfaces in composite materials [14]. To develop the domain integral the EDI incorporates an auxiliary function φ, which can be interpreted as a virtual crack front advance. This makes the EDI similar to the virtual crack extension technique, but with the advantage that only one computer run is necessary to evaluate the pointwise energy release rate along the complete crack front. In a recent paper, Cisilino and Ortiz[15] combined the EDI with the M_1-integral methodology, for the analysis of mixed-mode cracks. In that work special emphasis was put on the selection of the auxiliary function φ. The function φ was found to be a key feature to obtain reliable results at the intersection of the crack front with free surfaces.

This work presents a BEM formulation of the EDI for the analysis of three-dimensional cracks in thermally stressed bodies. To the authors' knowledge this is the first time the EDI is used for the analysis of three-dimensional thermoelastic problems using the BEM. Following dell'Erba and Aliabadi [8] the thermoelastic problem is solved first by using the dual formulation of the BEM (the dual boundary element method or DBEM). The formulation of the EDI is presented in a straightforward approach, and the auxiliary function φ assimilated to a virtual crack-front extension. The computation of the EDI is implemented as a postprocessing technique, and so it can be applied to the results from a particular model at a later stage. The implementation takes advantage of the

[1]To whom correspondence should be addressed.

Contributed by the Applied Mechanics Division of ASME for publication in the JOURNAL OF APPLIED MECHANICS. Manuscript received June 7, 2005; final manuscript received December 21, 2005. Review conducted by R. M. McMeeking. Discussion on the paper should be addressed to the Editor, Prof. Robert M. McMeeking, Journal of Applied Mechanics, Department of Mechanical and Environmental Engineering, University of California–Santa Barbara, Santa Barbara, CA 93106-5070, and will be accepted until four months after final publication of the paper itself in the ASME JOURNAL OF APPLIED MECHANICS.

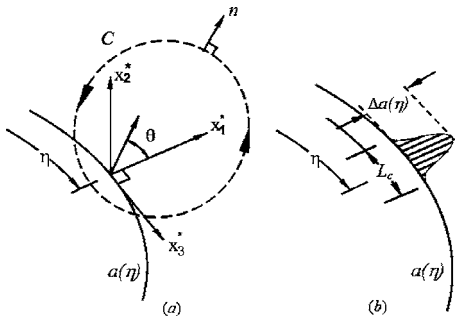

Fig. 1 (*a*) Definition of the local orthogonal Cartesian coordinates at point η on the crack front. (*b*) Virtual crack front advance.

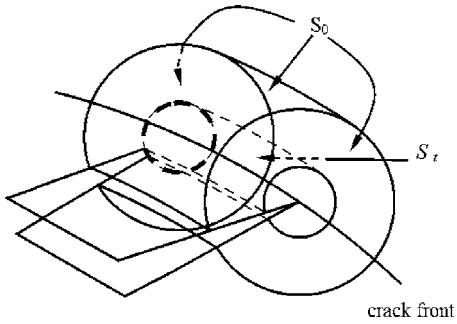

Fig. 2 Tubular domain surrounding a segment of the crack front

efficiency of the boundary integral equations to directly obtain the required stresses, strains, temperatures, and displacement and temperature derivatives. Two approaches are studied for the selection of the auxiliary function φ, and their results compared and discussed. Several examples are analyzed to demonstrate the efficiency and accuracy of the implementation.

2 The Energy Domain Integral

Consider a three-dimensional crack front with a continuously turning tangent as depicted in Fig. 1(*a*). Define a local coordinate system x^* at position η, where the crack energy release rate is evaluated, given by x_1^* normal to the crack front, x_2^* normal to the crack plane, and x_3^* tangent to the crack front.

Following Natha and Moran [16], the energy release rate $G(\eta)$ due to crack extension in its own plane along a three-dimensional crack front takes the form (see Fig. 1(*a*))

$$G(\eta) = \lim_{C\to 0} \xi_k(\eta) \int_{C(\eta)} (w \cdot \delta_{ki} - \sigma_{ij}^* u_{j,k}^*) n_i dC \tag{1}$$

where w is the strain energy density, σ_{ij}^* and $u_{j,k}^*$ are Cartesian components of stress and displacement derivatives expressed in the local system x^*, $\xi_k(\eta)$ is the unit outward normal to the crack front in the local crack plane $x_1^* - x_3^*$, n_i is the unit vector normal to the contour $C(\eta)$ (which lies in the $x_1^* - x_2^*$ plane), and dC is the differential of the arc length C. It is worth noting that, although Eq. (1) comes from a two-dimensional analysis, it applies for the three-dimensional case, as in the limit as $C \to 0$, plane strain conditions prevail so that three-dimensional fields approach to the plane problem.

Within the framework of uncoupled thermoelasticity, the strain is written as the sum of an elastic part ε_{ij}^e and a thermal part:

$$\varepsilon_{ij} = \varepsilon_{ij}^e + \alpha\theta\delta_{ij} \tag{2}$$

where α is the coefficient of linear thermal expansion and θ is temperature. If we make the additional restriction that thermal strains are bounded, a definition of w which can be used in Eq. (1) is:

$$w(\varepsilon_{ij}, \theta) = \int_0^{\varepsilon_{ij}^m} \sigma_{ij} \cdot d\varepsilon_{ij}^m \tag{3}$$

where $\varepsilon_{ij}^m = \varepsilon_{ij} - \alpha\theta\delta_{ij}$ are the mechanical strains.

In order to derive the equivalent domain representation of Eq. (1), we consider a small segment L_c of the crack front that lies in the local $x_1^* - x_3^*$ plane as shown in Fig. 1(*b*). Next we assume that the segment undergoes a virtual crack advance in the plane of the crack, and we define the magnitude of the advance at each point η as $\Delta a(\eta)$. Note that $\Delta a(\eta)$ varies continuously along L_c and it vanishes at each end of the segment. Now let

$$\bar{G}(\eta) = \int_{L_C} G(\eta)\Delta a(\eta) d\eta \tag{4}$$

where $G(\eta)$ is the integral defined in Eq. (1). Note that while $G(\eta)$ belongs to the point-wise energy release rate, $\bar{G}$ gives the total energy released when the finite segment L_c undergoes the virtual crack advance.

The appropriate domain form of the point-wise crack-tip contour integral can be obtained from Eq. (1) by considering a tubular domain V surrounding the crack segment (see Fig. 2). As shown in the figure, the surface S_t is formed by translating the contour C along the segment L_c, and S_o stands for the outer surface of V including the ends. Next an auxiliary function φ is introduced, which is sufficiently smooth in V and it is defined on the surfaces of V as follows:

$$\varphi_k = \begin{cases} \Delta a(\eta) \cdot \xi_k(\eta) & \text{on } S_t \\ 0 & \text{on } S_o \end{cases} \tag{5}$$

Finally, in the limit as the tubular surface S_t is shrunk onto the crack segment L_c, and after applying the divergence theorem, the domain integral is obtained:

$$\bar{G} = \int_V \{[(\sigma_{ij}^* u_{j,k}^* - w \cdot \delta_{ki})\varphi_{k,i} + \alpha\sigma_{ii}^* \theta_{,k}\varphi_k]\} dV \tag{6}$$

In the evaluation of the energy release rate, the integral given by Eq. (6) reduces to the domain representation of the familiar J-integral. A simple relationship between $J(\eta)$ and $\bar{G}$ can be obtained if it is assumed that $\bar{G}$ is constant along the segment L_c. It follows directly from Eq. (4) that

$$J(\eta) = \frac{\bar{G}}{\int_{L_c} \Delta a(\eta) d\eta} \tag{7}$$

Finally, it is worth mentioning that the above derivation of the EDI assumes the absence of crack face tractions. If present, an extra term needs to be included in Eq. (6). For a more comprehensive derivation of the EDI the reader is referred to [11].

3 The Dual Boundary Element Method for Thermoelasticity

Consider a linear-elastic, isotropic and homogeneous body occupying a domain $\Omega(X)$ enclosed by a boundary $\Gamma(x)$ as illustrated in Fig. 3(*a*). The two governing equations for steady-state thermoelasticity are the Laplace and the Navier equations which can be written as follows:

$$\theta_{,kk} = 0 \tag{8}$$

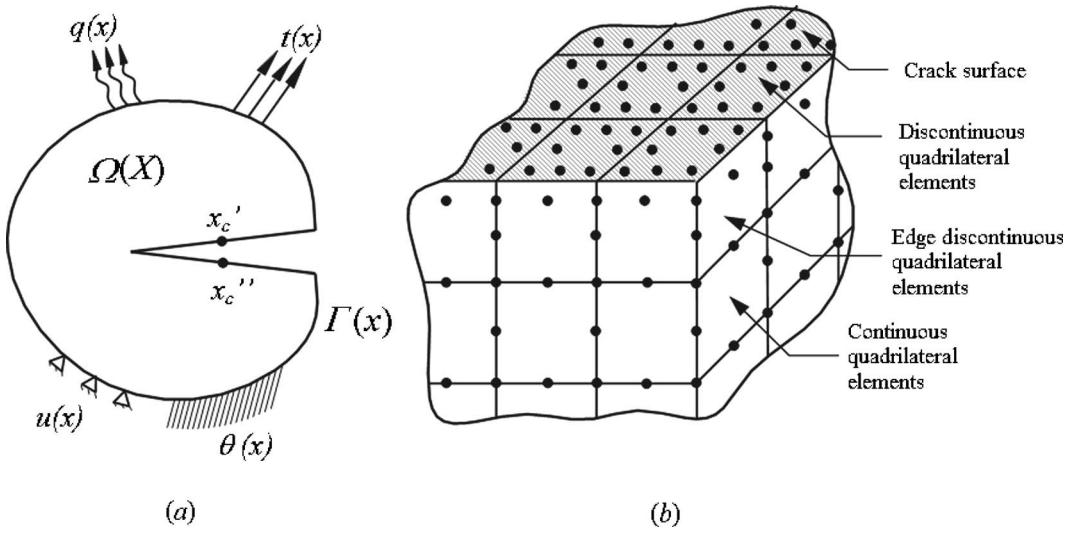

Fig. 3 (*a*) General cracked body with mechanical and thermal boundary conditions. (*b*) Crack discretization strategy.

$$\mu u_{i,jj} + \frac{\mu}{(1-2\nu)} u_{j,ij} - \frac{2\mu(1+\nu)}{(1-2\nu)} \alpha \theta_{,i} = 0 \tag{9}$$

where θ is the temperature and u_i are the displacement components, μ is the shear modulus, ν is the Poisson's ratio, and α is the coefficient of linear thermal expansion. Equations (8) and (9) are solved subject to boundary conditions in temperatures θ, fluxes q, displacements u, and tractions t (see Fig. 3(*a*)).

The dual boundary integral equations on which the thermoelastic formulation of the DBEM is based are the temperature and the flux boundary integral equations for the solution of the Laplace equation, and the displacement and the traction integral equations for the solution of the Navier equation. The boundary integral temperature equation relating the boundary temperature $\theta(x)$ with the boundary fluxes $q(x)$ can be written as

$$c(x')\theta(x') - \int_\Gamma q^*(x',x)\theta(x)d\Gamma = -\int_\Gamma \theta^*(x',x)q(x)d\Gamma \tag{10}$$

where $c(x')$ depends on the local geometry of the boundary surface at the position of point x'; $\theta^*(x',x)$ and $q^*(x',x)$ are the temperature and flux fundamental solutions at a boundary point x due to a unit source placed at location x'. Expressions for the fundamental solutions $\theta^*(x',x)$ and $q^*(x',x)$ are given in the Appendix.

Assuming continuity of both temperatures and fluxes at x' on a smooth boundary, the boundary flux integral equation is obtained by differentiating Eq. (10):

$$c(x')q(x') - n_i(x') \oint_\Gamma \theta_i^{**}(x',x)q(x)d\Gamma = -n_i(x') \neq_\Gamma q_i^{**}(x',x)\theta(x)d\Gamma \tag{11}$$

where $n_i(x')$ denotes the component of the outward unit normal to the boundary at x'. The symbols $\oint$ and $\neq$ represent integrals evaluated in the Cauchy and Hadamard principal value sense, respectively. Expressions for the kernels $\theta_i^{**}(x',x)$ and $q_i^{**}(x',x)$ are given in the Appendix.

If Eqs. (10) and (11) are used for collocation on coincident points on the crack surfaces (points x_c' and x_c'' in Fig. 3(*b*)) the temperature and flux boundary integral equations can be written as

$$\frac{1}{2}\theta(x_c') + \frac{1}{2}\theta(x_c'') - \int_\Gamma q^*(x_c',x)\theta(x)d\Gamma = -\int_\Gamma \theta^*(x_c',x)q(x)d\Gamma \tag{12}$$

and

$$\frac{1}{2}q(x_c'') - \frac{1}{2}q(x_c') - n_i(x_c'') \oint_\Gamma \theta_i^{**}(x_c'',x)q(x)d\Gamma = -n_i(x_c'') \neq_\Gamma q_i^{**}(x_c'',x)\theta(x)d\Gamma \tag{13}$$

where the normal vectors $n_i(x') = -n_i(x'')$ are assumed on the crack surface. At the same time it is also assumed that the crack surfaces at the position x_c' and x_c'' are always smooth. The later assumption makes $c(x') = 1/2$ in Eqs. (10) and (11).

Similarly to the boundary integral temperature equation, the displacement boundary integral equation relates the displacements $u_j(x)$ with the boundary tractions $t_j(x)$, temperatures $\theta(x)$, and fluxes $q(x)$:

$$c_{ij}(x')u_i(x') + \oint_\Gamma T_{ij}(x',x)u_j(x)d\Gamma - \int_\Gamma \bar{P}_i(x',x)\theta(x)d\Gamma = \int_\Gamma U_{ij}(x',x)t_j(x)d\Gamma - \int_\Gamma \overline{Q}_i(x',x)q(x)d\Gamma \tag{14}$$

where $U_{ij}(x',x)$ and $T_{ij}(x',x)$ are the Kelvin traction and displacement fundamental solutions for elasticity, and $\overline{P}_i(x',x)$ and $\overline{Q}_i(x',x)$ are the fundamental fields that account for the thermal expansion (see the Appendix).

Assuming continuity of both strains and tractions at x' on a smooth boundary, the boundary traction integral equation is obtained by differentiating Eq. (14) and by applying the material constitutive relationships

$$\frac{1}{2}t_i(x') + n_j(x')\int_\Gamma T_{kij}(x',x)u_k(x)d\Gamma - n_j(x')\int_\Gamma \bar{P}_{ij}(x',x)\theta(x)d\Gamma + \frac{\mu(1+\nu)}{(1-2\nu)}\alpha n_i(x')\theta(x') = n_j(x')\int_\Gamma U_{kij}(x',x)t_k(x)d\Gamma - n_j(x')\int_\Gamma \bar{Q}_{ij}(x',x)q(x)d\Gamma \quad (15)$$

where the kernels $T_{kij}(x_c',x)$, $U_{kij}(x_c',x)$, $\overline{P_{ij}}(x_c',x)$, and $\overline{Q_{ij}}(x_c',x)$ contain derivatives of the fundamental fields in Eq. (14) together with elastic constants.

If, as it has been done with their thermal counterparts, Eqs. (14) and (15) are used for collocation on coincident points on the crack surfaces, then the displacement and traction boundary integral equations can be written as

$$\frac{1}{2}u_i(x_c') + \frac{1}{2}u_i(x_c'') + \int_\Gamma T_{ij}(x',x)u_j(x)d\Gamma - \int_\Gamma \overline{P_i}(x',x)\theta(x)d\Gamma = \int_\Gamma U_{ij}(x',x)t_j(x)d\Gamma - \int_\Gamma \overline{Q_i}(x',x)q(x)d\Gamma \quad (16)$$

and

$$\frac{1}{2}t_j(x_c'') - \frac{1}{2}t_j(x_c') + n_j(x_c'')\int_\Gamma T_{kij}(x_c'',x)u_k(x)d\Gamma - n_j(x_c'')\int_\Gamma \overline{P_{ij}}(x_c'',x)\theta(x)d\Gamma + \frac{\mu(1+\nu)}{(1-2\nu)}\alpha n_i(x_c'')\theta(x_c'') = n_j(x_c'')\int_\Gamma U_{kij}(x_c'',x)t_k(x)d\Gamma - n_j(x_c'')\int_\Gamma \overline{Q_{ij}}(x_c'',x)q(x)d\Gamma \quad (17)$$

Following dell'Erba and Aliabadi [8], the general discretization strategy can be summarized as follows (see Fig. 3(*b*)):

- Crack surfaces are discretized using eight-node discontinuous quadratilateral elements in order to ensure the continuity requirements of the field variables for the existence of the flux and traction equations.
- Continuous elements are used over the remaining model boundary, except at the intersection of the crack with the boundary surface. Edge discontinuous elements are employed in this region in order to avoid common nodes at the intersection.
- The temperature integral equation (12) and the displacement integral equation (16) are applied for collocation on one of the crack surfaces.
- The flux integral equation (13) and the traction integral equation (17) are applied for collocation on the opposite crack surface.
- The temperature integral equation (10) and the displacement integral equation (14) are applied for collocation on all other surfaces.

4 Stresses, Strains, and Displacement and Temperature Derivatives

4.1 Internal Points. As it has been stated in Sec. 2, the computation of the EDI requires the stress, strain, and temperature fields, σ_{ij}, ε_{ij}, and θ, and the displacement and temperature derivatives, $u_{i,j}$ and $\theta_{,k}$, to be known within the integration volume V. Although these quantities must be expressed in the local crack-front coordinate system, in this work, and for the sake of simplicity, they are first computed in the global system and then transformed to the local crack-front coordinate system. Bearing this in mind, and in order to integrate the computation of the EDI into the DBEM formulation, derivatives of the displacements at internal points X' are obtained from their boundary integral representations. Thus, the integral equations for the displacement and temperature derivatives result from the analytical differentiation of the internal counterparts of Eqs. (10) and (14):

$$\theta_{,k}(X') = \int_\Gamma q_{,k}^{**}(X',x)\theta(x)d\Gamma - \int_\Gamma \theta_{,k}^{**}(X',x)q(x)d\Gamma \quad (18)$$

and

$$u_{i,k}(X') = -\int_\Gamma T_{ij,k}(X',x)u_j(x)d\Gamma + \int_\Gamma \overline{P_{i,k}}(X',x)\theta(x)d\Gamma + \int_\Gamma U_{ij,k}(X',x)t_j(x)d\Gamma - \int_\Gamma \overline{Q_{i,k}}(X'x)q(x)d\Gamma \quad (19)$$

where the kernels $q_{,k}^{**}(X',x)$, $\theta_{,k}^{**}(X',x)$, $T_{ij,k}(X',x)$, $U_{ij,k}(X',x)$, $\overline{P_{i,k}}(X',x)$, and $\overline{Q_{i,k}}(X',x)$ are the derivatives of the fundamental solutions.

Once the displacement derivatives $u_{j,k}$ are known, stresses σ_{ij} and strains ε_{ij} are computed using basic continuum mechanics relationships:

$$\varepsilon_{ij} = \tfrac{1}{2}(u_{i,j} + u_{j,i}) + \alpha\theta\delta_{ij} \quad (20)$$

$$\sigma_{ij} = \frac{E}{1+\nu}\left(\varepsilon_{ij} + \frac{\nu}{1-2\nu}\varepsilon_{kk}\delta_{ij}\right) - \frac{E}{1-2\nu}\alpha\theta\delta_{ij} \quad (21)$$

4.2 Boundary Points. Temperature and displacement derivatives $\theta_{,k}$ and $u_{i,j}$ at boundary nodes could be obtained from Eqs. (18) and (19) in a similar way to their internal counterparts, by taking the limit of Eqs. (18) and (19) as point X' moves to the boundary, i.e., $X' \to x'$. However, this procedure is computationally expensive because of the occurrence of hypersingular integrands. To avoid this difficulty, stresses and strains, as well as the displacements and temperatures on the model surface, are evaluated in this work from the boundary displacements, tractions, temperatures, and fluxes following a procedure similar to that used in FEM computations. Consider with this purpose a local Cartesian system, (x_1^0, x_2^0, x_3^0), such that x_3^0 is the unit vector in the normal direction to the boundary element and x_1^0 and x_2^0 are unit vectors which define the local tangential plane. If σ_{ij}^0 and t_i^0 are stresses and tractions in the local system, stress components in the normal direction can be written as

$$\sigma_{i3}^0 = t_i^0 \quad (22)$$

The remaining stress tensor components, σ_{11}^0, σ_{12}^0, and σ_{22}^0 can be expressed in terms of t_3^0 and the tangential strain tensor components ε_{11}^0, ε_{12}^0, and ε_{22}^0, by eliminating ε_{33}^0 from the general expression of Hooke's law. Thus,

$$\sigma_{11}^0 = \frac{1}{1-\nu}[\nu t_3^0 + 2\mu(\varepsilon_{11}^0 + \nu\varepsilon_{22}^0) - (1+\nu)\alpha\theta]$$

$$\sigma_{22}^0 = \frac{1}{1-\nu}[\nu t_3^0 + 2\mu(\varepsilon_{22}^0 + \nu\varepsilon_{11}^0) - (1+\nu)\alpha\theta]$$

$$\sigma_{12}^0 = 2\mu\varepsilon_{12}^0 \quad (23)$$

Strain components ε_{ij}^0 can be obtained using Eq. (20), now applied in the local coordinate system. It is worth nothing that displace-

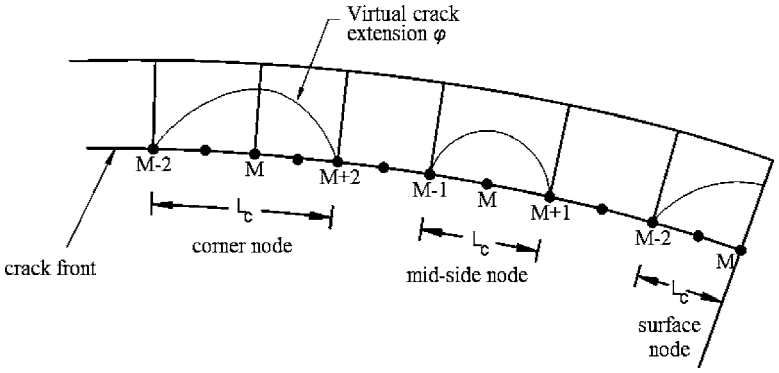

Fig. 4 Schematic of the volume cells in the crack front region illustrating the virtual crack extensions for a corner node, a mid-node, and a surface node

ment derivatives in Eq. (20) are initially evaluated in the intrinsic element directions (ξ_1, ξ_2) and then converted to the local coordinate system x^0 since, as usual in the BEM, boundary displacements are approximated in terms of the piecewise parametric representation (shape functions) of intrinsic coordinates:

$$u_i(\xi_1, \xi_2) = \sum_{n=1}^{8} \Phi^n(\xi_1, \xi_2) u_i^n \tag{24}$$

where Φ^n are the shape functions and u_i^n are the nodal values of the displacements.

From (24) it follows

$$\frac{\partial u_i}{\partial \xi_j} = \sum_{n=1}^{8} \frac{\partial \Phi^n}{\partial \xi_j} u_i^n \tag{25}$$

Finally, the derivatives of the displacements in the global system are computed. Using chain differentiation, derivatives of the displacements in the global system, $u_{i,m}$, can be related to the derivatives of the displacements in the intrinsic boundary element directions, $\partial u_i / \partial \xi_j$, as follows:

$$\frac{\partial u_i}{\partial \xi_j} = \frac{\partial u_i}{\partial x_m} \frac{\partial x_m}{\partial \xi_j} \tag{26}$$

where $\partial x_m / \partial \xi_j$ is the Jacobian matrix of the transformation. The nine components of the displacement derivatives $u_{i,m}$ can be retrieved by solving for each case a system of equations constructed using expressions (26). For further details the reader is referred to the works by Cisilino et al. [12,13,15].

A similar procedure can be employed for the computation of the temperature derivatives on the model boundary.

5 Boundary Element Implementation

5.1 Energy Domain Integral Evaluation. As it has been stated in Sec. 2, Eq. (6) allows computation of the *J*-integral at any position η on the crack front. This requires the evaluation of a volume integral within domains that enclose a segment of the crack front L_c. A natural choice here is to make η coincident with the element nodes on the crack front, while L_c is taken as the element or element sides at which points η lies (see Fig. 4).

The portion of the model domain in which the volume integrals are evaluated is discretized using 20-node isoparametric (brick) cells, over which stresses, strains, and displacements and temperature derivatives are approximated by products of the cell interpolation functions, ψ^n, and the nodal values of σ_{ij}, ε_{ij}, u_{ij}, and $\theta_{,k}$. Nodal values of these variables are computed following the procedures introduced in Secs. 4.1 and 4.2 depending on whether the node is internal or it lies on the model boundary. Volume discretization is designed to have a web-style geometry around the crack front, while the integration volumes are taken coincident with different rings of cells. This is illustrated for an example in Fig. 5, where one of the model faces has been removed to show the crack and the integration domains.

As depicted in Fig. 4, three different cases need to be considered, depending on whether the node of interest *M* is in the middle of an element side (mid-node), it is shared by two elements (cor-

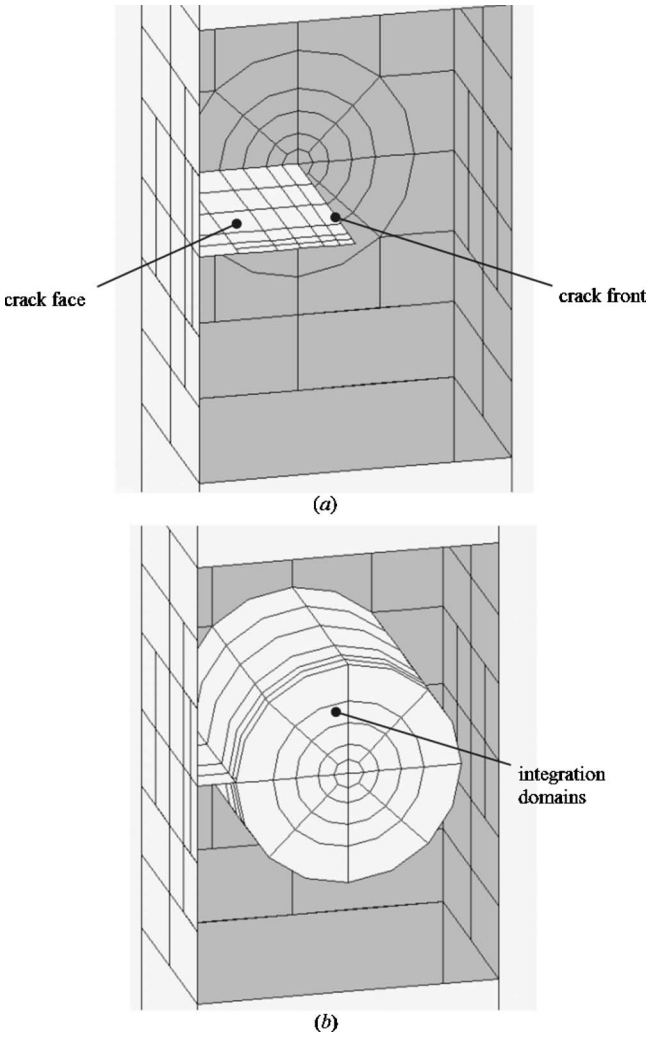

Fig. 5 Boundary element discretization and integration cells

ner node), or it is located coincident with the external surface (surface node). If the node M is a mid-node or surface node, L_c (the segment of the crack front over which the J-integral is computed) spans over one element, connecting nodes $M-1$, M, and $M+1$ and nodes $M-2$, $M-1$, and M, respectively. On the other hand, if M is a corner node, L_c spans over two elements, connecting nodes from $M-2$ to $M+2$.

The function φ is used to specify the virtual crack extension. For the sake of simplicity the direction of the crack extension is taken constant along L_c and coincident with the three orthogonal local directions defined at η (see Fig. 1(*a*)). Consistent with the isoparametric formulation, φ is given by

$$\varphi_k = \sum_{i=1}^{20} \Psi^i \varphi_k^i \tag{27}$$

where Ψ^i are the cell interpolation functions and φ_k^i are the nodal values for the ith node. From the definition of φ (see Eq. (5)), $\varphi_k^i=0$ if the ith node is on S_0 (the outer surface of the integration domain) and $\varphi_k^i \neq 0$ for the nodes on L_c. In particular $\varphi_k^i=1$ for the node at η (nodes labeled M in Fig. 4). Different criteria for specifying φ_k^i for the other nodes L_c and for the nodes inside the integration domain V are discussed in next section.

Following standard manipulations

$$\varphi_{k,j} = \sum_{i=1}^{20} \sum_{i=1}^{3} \frac{\partial \Psi'}{\zeta_n} \frac{\partial \zeta_n}{\partial x_j} \varphi_k^i \tag{28}$$

where ξ_n are the coordinates in the cell isoparametric space.

If Gaussian integration is used, the discretized form of Eq. (6) is given by

$$G = \sum_{\text{cells in } V} \sum_{p=1}^{m} \left[[(\sigma_{ij}^* u_{j,k}^* - w \cdot \delta_{ki}) \varphi_{k,i} + \alpha \sigma_{ii}^* \theta_{,k} \varphi_k] \det\left(\frac{\partial x_j}{\partial \zeta_k} \right) \right]_p w_p \tag{29}$$

where m is the number of Gaussian points per cell and w_p are the weighting factors.

5.2 The φ-Function. Since the virtual crack advance can adopt any arbitrary shape, the only requirement for the function φ is to be sufficiently smooth within the integration volume V as the evaluation of the EDI requires of its differentiation. Although Shih et al. [11] have shown that the EDI is insensitive to the assumed shape of the φ function, it has been found in a recent work by one of the authors of this paper [15] that the shape of the function φ could be relevant for the performance of the EDI computations. In this sense two different approaches for the shape of the function f are investigated.

5.2.1 Bi-quadratic φ. The bi-quadratic definition of φ has been employed with excellent results in the computation of EDI in previous works by Cisilino et al. [12–14]. Within this approach φ is defined to vary quadratically in the directions tangential and normal to the crack front. Considering that η is at the middle of the crack front segment L_c, and that r_0 is the radius of the integration domain, the function φ is written as:

$$\varphi(x) = \left\| 1 - \left(\frac{x_3}{L_c/2} \right)^2 \right\| \cdot \left[1 - \left(\frac{r}{r_0} \right)^2 \right] \tag{30}$$

where r is the distance from the crack front in the $x_1^*-x_2^*$ plane as depicted in Fig. 1.

5.2.2 Optimized φ. Saliva et al. [17] proposed an optimum shape for the function φ, which under certain considerations ensures the convergence of the EDI computations. The proposed function is

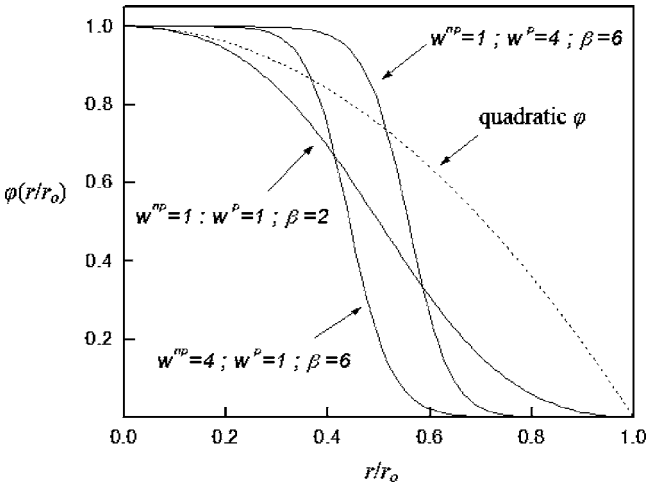

Fig. 6 Influence of parameters w^p, w^{np}, and β on the shape of function φ (one-dimensional case)

$$\varphi(x) = \frac{w^p \|x\|^{-\beta}}{w^p \|x\|^{-\beta} + \sum_{i=1}^{N} w_j^{np} \|x - z_i\|^{-\beta}} \tag{31}$$

where w^p, w^{np}, and β are parameters to be chosen, and z_i are the positions of the N points with null prescribed values of φ. These are given in this work by the N cell-nodes located on S_0, the outer surface of the integration volume V.

Using parameters w^p, w^{np}, and β, it is possible to control the shape of φ and consequently the parts of the domain with the most significant contribution to the integral in Eq. (6). In particular β is associated with the smoothness of φ. Greater values induce approximately null gradients around the crack front, where non-null values of φ are prescribed. In contrast, the field undergoes abrupt changes outside these regions. With w^p and w^{np}, the region with non-null gradients can be translated near the crack front or near the boundary of the integration volume where null values of φ are prescribed. Figure 6 illustrates the influence of the parameters as a function of the normalized distance r/r_0.

It is important to mention here that the previous works which made use of the optimized φ, Refs. [15,17], were devoted to the solution of linear elastic crack problems without the presence of body loads. Under these circumstances, the second term of the integral in Eq. (6), the term which accounts for body loads (thermal loads in our case), vanishes. The key feature for the excellent performance of the optimized φ for problems without body loads can be attributed to the behavior of φ in the crack tip vicinity. Note that for the optimized definition of φ, the gradient $\varphi_{,i}$ is zero in the vicinity of the crack front (see Fig. 6), resulting in that the contribution to G of the crack front fields is not significant. As a consequence, the zone of the integration domain with the lowest accuracy in the results has a marginal contribution to the value of G.

The formulation of the EDI for thermoelastic problems includes a term to account for the thermal loads (see Eq. (6)). Note that since this term is multiplied by φ, the justification given in the previous paragraph for the excellent performance of the optimized φ is not longer valid. However, and as it will be shown in the following sections, the shape of φ still contributes to the accuracy of the EDI computations.

6 Examples

6.1 Edge Crack in a Thin Panel Subjected to a Linear Thermal Field. An example with two-dimensional characteristics is proposed for the first example. It consists of an edge-cracked

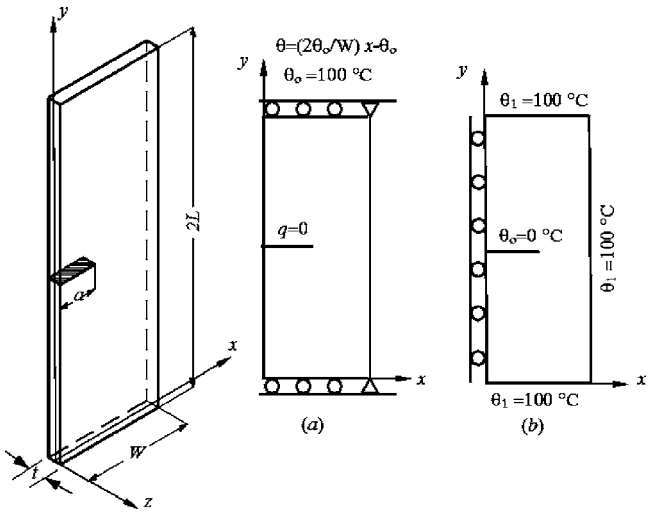

Fig. 7 Geometry, dimensions, and boundary conditions for the edge and center cracked specimens

thin panel illustrated in Fig. 7(*a*). The crack length is $a=10$ mm, and the specimen dimensions $W=2a$, $L=W$, and $t=a/10$. Material properties are Young modulus $E=1000$ N/mm^2, Poisson ratio $\nu=0.3$, coefficient of thermal expansion $\alpha=10^{-5}/°C$, and thermal conductivity $\lambda=1$ W/°C·mm. The specimen is subjected to a linear temperature variation throughout the width W, with zero temperature at mid-width, and temperatures $\theta_0=\pm 100°C$ at the right and left edges, respectively (see Fig. 7(*a*)). Crack surfaces are isolated. Displacement boundary conditions at the panel ends are illustrated in Fig. 7(*a*). Lateral faces of the specimen ($z=\pm t/2$) are isolated and their normal displacements are restricted in order to simulate the plane strain condition.

Model discretization follows the same pattern of that illustrated in Fig. 5, but with only one element in the direction of the specimen thickness. Two meshes are considered: a "coarse" mesh consisting of 242 elements and 899 nodes, and a "fine" mesh consisting of 374 elements and 1319 nodes. Seven rings of internal cells with radii ranging from 5% to 75% of the crack length are constructed around the crack tip for the J computations. For the so-called coarse mesh, 60 cells and 526 nodes are used. On the other hand, 116 cells and 958 nodes are used for the fine mesh. The bi-quadratic definition of the function φ is used for the solution of this problem.

Obtained results for the two discretizations are reported in Tables 1 and 2 in terms of normalized mode-I stress intensity factor K_I^*. Stress intensity factors were computed from J results via the well-known expression $K_I=\sqrt{J\cdot E/(1-\nu^2)}$ and later normalized using $K_I^*=K_I/\sigma_\theta\sqrt{\pi a}$. The symbol $\sigma_\theta=\alpha E\theta_0/(1-\nu)$ stands for the exact solution for the thermal stress in the y-direction at the right edge of an uncraked specimen. Results are reported for crack front points located on the specimen surface and on its mid-plane, and they are compared to the solution reported by Wilson and Yu [18] who solved the problem using finite elements. Differences between computed results and the reference solution are denoted as $\Delta\%$.

Tables 1 and 2 show the improvement of the results with the refinement of the model discretization. While for the coarse mesh the differences between the computed results and the reference value are close to 5%, they drop to less than 1% for the fine mesh. The only exception is the results obtained for the smallest integration domain ($r/a=0.05$) which is defined using only one ring of cells. It is also worth noting the excellent agreement between the interior and surface values and the independence of the results with the integration path. The overall performance of the implemented algorithm is found to be very good, with an accuracy level similar to other applications of the EDI [12–14]. As usual when dealing with J-integral computations, the most accurate results are obtained for integration paths defined over a relatively large portion of the mesh.

6.2 Thin Panel With a Central Crack Subjected to a Thermal Field. The second example consists in a center-cracked thin panel in plane strain condition. The model geometry is the same of the first example, but with the addition of the symmetry conditions (both thermal and displacement) at $x=0$ (see Fig. 7(*b*)). The thermal field is given as follows: temperature for crack surfaces are $\theta_0=0°C$ while the temperatures for all the surfaces perpendicular to the x-y plane ($x=W$, $y=0$ and $y=2L$) are $\theta_1=100°C$. As in the previous example, the lateral faces of the model are isolated and their normal displacements restricted in order to simulate the plane strain condition.

Normalized stress intensity factor results $K_I^*=K_I/\alpha E(\theta_1-\theta_0)\sqrt{W}$ are reported in Table 3 and compared to those reported by Murikami et al. [1]. All results were computed using the fine discretization and the bi-quadratic φ. As in the previous example K results are reported for crack front points located on the specimen surface and on the mid-plane. Excellent agreement is obtained between the computed and the reference results, with a difference less than 2% for all the integration domains.

6.3 Penny-Shaped Crack in a Cylindrical Bar Subjected to a Thermal Field. A bar of circular cross section containing an embedded penny-shaped crack is analyzed in this example (see

Table 1 Normalized K results $K_I^*=K_I/\sigma_\theta\sqrt{a\pi}$ for the edge crack in a thin panel (coarse discretization)

	r/a							Average	Ref. [18]
	0.05	0.09	0.15	0.225	0.338	0.50	0.75		
Surface	0.534	0.527	0.525	0.525	0.526	0.528	0.529	0.528	0.504
$\Delta\%$	5.95	4.56	4.17	4.17	4.37	4.76	4.96	4.71	...
Interior	0.538	0.529	0.527	0.526	0.528	0.53	0.532	0.530	0.504
$\Delta\%$	6.75	4.96	4.56	4.37	4.76	5.16	5.56	5.16	...

Table 2 Normalized K results $K_I^*=K_I/\sigma_\theta\sqrt{a\pi}$ for the edge crack in a thin panel (fine discretization)

	r/a							Average	Ref. [18]
	0.05	0.09	0.15	0.225	0.338	0.50	0.75		
Surface	0.482	0.497	0.501	0.501	0.502	0.502	0.502	0.498	0.504
$\Delta\%$	−4.37	−1.39	−0.60	−0.60	−0.40	−0.40	−0.40	−1.16	...
Interior	0.489	0.5	0.502	0.502	0.503	0.503	0.503	0.500	0.504
$\Delta\%$	−2.98	−0.79	−0.40	−0.40	−0.20	−0.20	−0.20	−0.74	...

Table 3 Normalized K results $K_I^* = K_I/\alpha E(\theta_1 - \theta_0)\sqrt{W}$ for the edge crack in a thin panel (coarse discretization)

	r/a							Average	Ref. [1]
	0.05	0.09	0.15	0.225	0.338	0.50	0.75		
Surface	0.497	0.489	0.487	0.486	0.486	0.486	0.496	0.490	0.495
Δ%	0.40	−1.21	−1.62	−1.82	−1.82	−1.82	0.20	−1.10	···
Interior	0.497	0.489	0.487	0.486	0.486	0.486	0.496	0.490	0.495
Δ%	0.40	−1.21	−1.62	−1.82	−1.82	−1.82	0.20	−1.10	···

Fig. 8(a)). The crack of radius $a=1$ mm is located in the center of the bar, in a plane perpendicular to the axis of the bar. In order to assimilate the problem to that of a penny-shaped crack embedded in an infinite body, the dimensions $R/a=10$ and $H/R=6$ are chosen. The temperature of the crack surfaces is set $\theta_0=0\,^\circ$C while for all the surfaces of the cylinder $\theta_1=100\,^\circ$C. The boundary element mesh consists of 1434 nodes and 224 elements. The crack is discretized using 152 elements. Three rings of cells with radii $r/a=0.2$, 0.35, and 0.50 are used for the J computations. With this purpose 832 cells are employed. Material properties are adopted the same as the previous examples. The bar is allowed to expand freely.

Normalized K results $K_I^*=K_I/(\alpha E\theta_0\sqrt{a\pi}/(1-\nu))$ calculated along the crack front using the bi-quadratic φ are reported in Table 4. Also included in Table 4 is the analytical solution due to Das [19] for comparison. Since the K result is constant along the crack front, results in Table 4 are reported only for a few positions. Table 4 shows that the EDI results deviate less than 3% from the reference solution, which is considered acceptable for the mesh used. No attempt was made to refine the mesh.

6.4 Circular Bar With an Annular Crack Subjected to a Thermal Field. The problem of an annular crack in a circular bar is considered in this example (see Fig. 8(b)). The crack is situated at the bar mid-length, on a plane perpendicular to its axis. Model dimensions are crack depth $a=20$ mm, cylinder radius $R/a=2.5$, and cylinder height $H/R=12$. The thermal field is given by temperatures $\theta_0=-50\,^\circ$C on the crack surfaces and $\theta_1=0\,^\circ$C on the top and the bottom ends of the cylinder. The lateral surface of the cylinder is isolated. The boundary element discretization consists of 1970 nodes and 328 elements, 192 of which are used for the crack faces. Three rings of cells with radii $r/a=0.2$, 0.35, and 0.50 are used for the J computations. Axial displacements are restricted for the top and bottom ends of the cylinder.

The picture in Fig. 8(c) illustrates boundary element mesh in the deformed configuration. Some of the elements in the lateral surface of the cylinder have been removed in order to see the crack discretization. Obtained results using the bi-quadratic φ are presented in Table 5 in terms of the normalized stress intensity factors $K_I^*=K_I/(\alpha E\theta_0\sqrt{a\pi})$ for a number of positions along the crack front. Although there is not reference solution available for comparison, the independence of the results with the integration path can be verified. Thus, the last column in Table 5 reports the maximum deviation of the results with respect to the average value. Maximum deviation is always less than 1%.

6.5 Edge Crack in a Thick Panel Subjected to a Linear Thermal Field. This example consists of a problem with three-dimensional characteristics for which the variation of J along the crack front is studied. The problem loading and geometry are the same as that of the example studied in Sec. 6.1, but considering now a panel of length $2L=6W$ and thickness $t=3a$. Since the problem is symmetric with respect to the plane $z=-t/2$ (see Fig. 7(a)), only one half of its geometry is modeled. The devised boundary element discretization consists of 292 elements and 1351 nodes. Six elements are placed along the crack front and a total of 35 elements are used in the crack discretization. Crack front elements are graded towards the free surface, the smallest one being equal to $t/32$ (see Fig. 5). Four rings of cells with radii $r/a=0.2$, 0.35, 0.5, and 0.75 are accommodated around the crack front for J computations. With this purpose 480 cells and 2302 nodes are employed.

J-integral values are computed using the two approaches introduced in Sec. 5 for the specification of φ. Afterwards, K-values are calculated from J results using $K_I=\sqrt{J\cdot E/(1-\nu^2)}$, and later normalized by doing $K_I^*=K_I/\alpha E\theta_0\sqrt{W}$. Results for the bi-quadratic definition of φ are plotted in Fig. 9(a), while results obtained using optimized φ are plotted in Fig. 9(b). Following Ortiz and Cisilino [14] the values of the parameters for the opti-

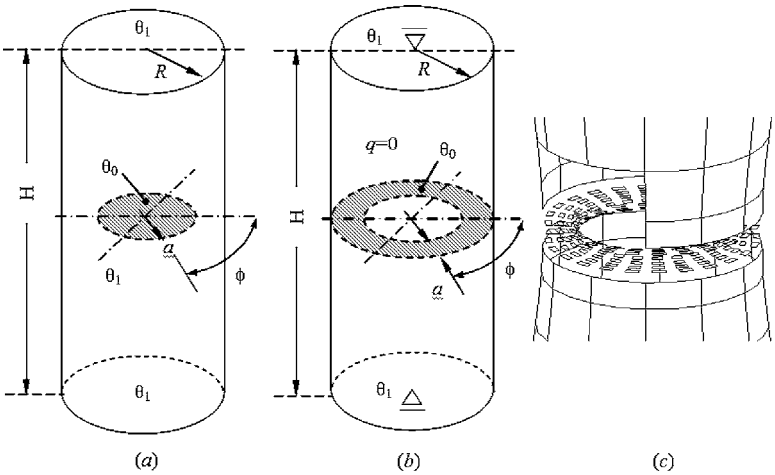

Fig. 8 Geometry, dimensions, crack discretization, and boundary conditions for the penny-shaped and annular cracks

Table 4 Normalized K results $K_I^* = K_I/(\alpha E\theta_0\sqrt{a/\pi}(1-\nu))$ for the penny-shaped crack in a cylindrical bar

$\phi/2\pi$	r/a			Average	Ref. [19]	$\Delta\%$
	0.20	0.35	0.50			
0.000	0.9580	0.9730	0.9779	0.9696	0.9418	2.95
0.125	0.9573	0.9720	0.9762	0.9685	0.9418	2.83
0.250	0.9575	0.9721	0.9764	0.9687	0.9418	2.85
0.375	0.9575	0.9720	0.9763	0.9686	0.9418	2.84
0.500	0.9576	0.9722	0.9764	0.9687	0.9418	2.86
0.625	0.9577	0.9722	0.9764	0.9688	0.9418	2.86
0.750	0.9576	0.9721	0.9764	0.9687	0.9418	2.85
0.875	0.9576	0.9721	0.9764	0.9687	0.9418	2.85

mized φ are chosen as $w^p=6$, $w^{np}=1$, and $\beta=6$. Error bars in the plots indicate the maximum deviation for the results obtained using the different integration domains. Reference values in the plots are those reported by dell'Erba et al. [8] using COD computations from BEM results. In the region near the symmetry plane, $z/t=0$, a plane strain condition is expected, and thus the result by Wilson and Yu [18] for two-dimensional analysis is also included for comparison.

Both approaches for φ provide results within a 4% error with respect to the plane strain solution at the position of the symmetry plane, $z/t=0$. For positions along the crack front located in the interior of the specimen, results computed using the bi-quadratic φ show a more stable and robust behavior than those obtained using the optimized φ. On the other hand, the optimized φ results are more reliable for the computations in the region of the crack front near to the free surface. Note that in such a case K values computed using the optimized φ are almost independent of the integration domains, while those computed using the optimized φ exhibit a relatively large dispersion. Finally, it is worth mentioning that results obtained using both approaches for φ are always higher than those reported by dell'Erba et al. [8] and closer to the plane strain solution. Both sets of results, those computed in this work and those reported by dell'Erba et al. [8], tend to the same value at the free surface.

6.6 Thick Panel With a Central Crack Subjected to Thermal Field. The last example consists of a thick panel with a central crack. Model geometry and boundary conditions are the same as that illustrated in Fig. 8(*b*) and used in the example in Sec. 6.2, but with the specimen the thickness increased to $t=3a$. Following the previous example, the J-integral and their corresponding K-values are computed along the crack front. Model discretization is the same as used in the previous example. Appropriate displacement boundary conditions are set in order to account for the symmetry conditions.

Normalized K-results $K_I^* = K_I/\alpha E(\theta_1-\theta_0)\sqrt{W}$ are reported in Figs. 10(*a*) and 10(*b*) for the bi-quadratic and optimized φ, respectively. Parameters for the optimized φ are chosen as $w^p=6$, $w^{np}=1$, and $\beta=6$. As for the previous example, error bars indicate the maximum deviation in the results with respect to the integration domains.

Table 5 Normalized K results $K_I^* = K_I/(\alpha E\theta_0\sqrt{a/\pi})$ for the penny-shaped crack in a cylinderical bar

$\phi/2\pi$	r/a	Average	Maximum deviation %		
	0.20	0.35	0.50		
0,000	0,164	0,166	0,166	0,166	0,618
0,104	0,166	0,168	0,168	0,167	0,605
0,208	0,165	0,167	0,167	0,166	0,872
0,313	0,166	0,168	0,168	0,167	0,604
0,417	0,165	0,167	0,167	0,166	0,872
0,521	0,166	0,168	0,168	0,167	0,605
0,625	0,165	0,167	0,167	0,166	0,872
0,729	0,166	0,168	0,168	0,167	0,605
0,833	0,165	0,167	0,167	0,166	0,872
0,938	0,166	0,168	0,168	0,167	0,604

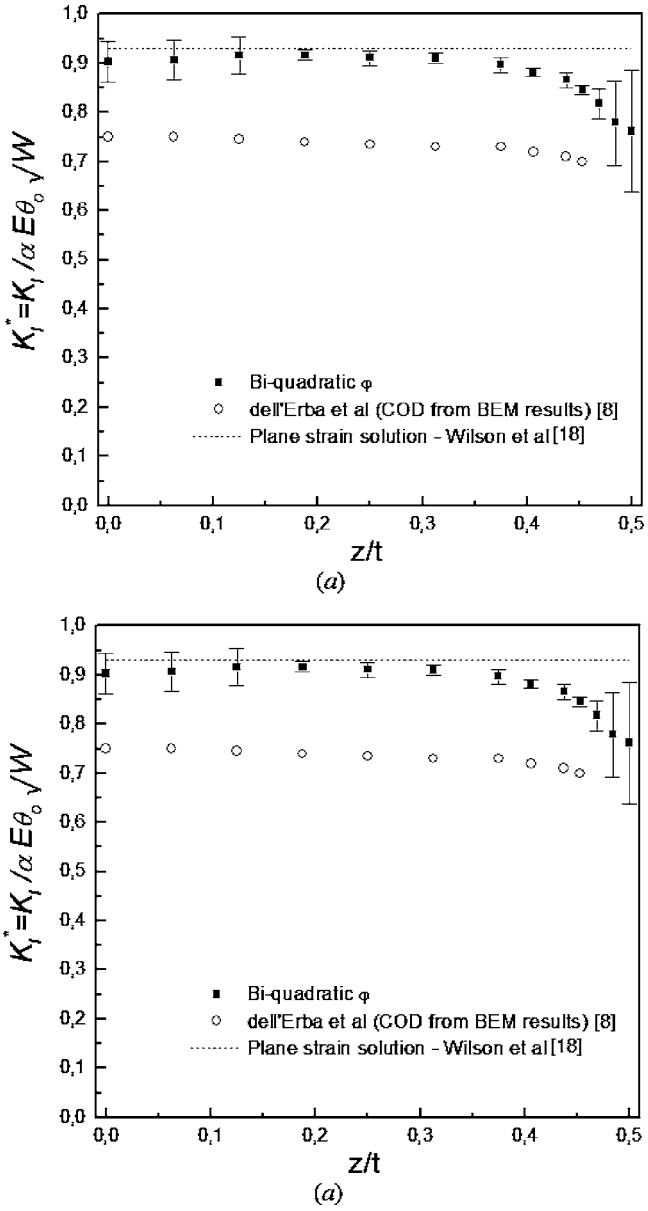

Fig. 9 Normalized mode I stress intensity factor along the crack front for the edge crack in a thick panel: (*a*) results using bi-quadratic φ and (*b*) results using optimized φ

Computed results show the same general behavior of the previous example: both approaches for φ provide results very close to the plane strain solution for the symmetry plane (position $z/t=0$), the bi-quadratic φ behaves more stable and robust than the optimized φ in the interior of the specimen, and the optimized φ results are more appropriate for the computations on the free surface. At this point it is worth noting that although both approaches result in the same K-value at the free surface (see Fig. 10), those computed using the bi-quadratic φ possess nearly 20% dispersion, while for the optimized φ the dispersion is only 3%.

7 Conclusions

A three-dimensional dual boundary element method formulation of the energy domain integral for the numerical analysis of thermoelastic fracture problems has been presented in this paper.

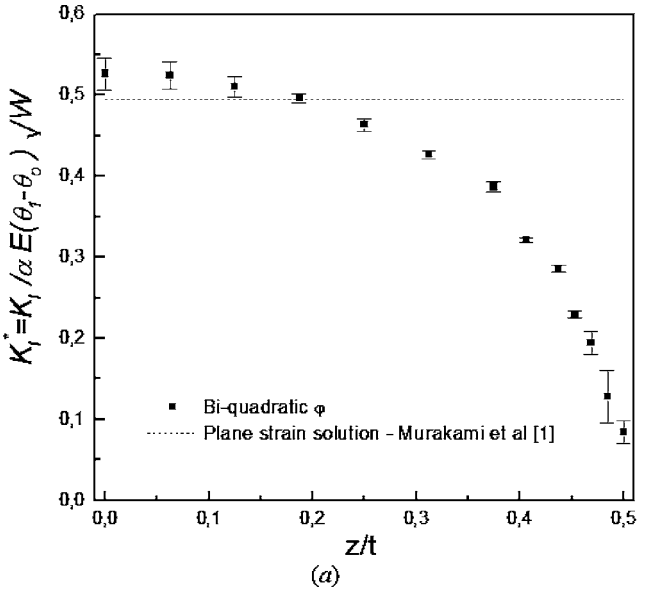

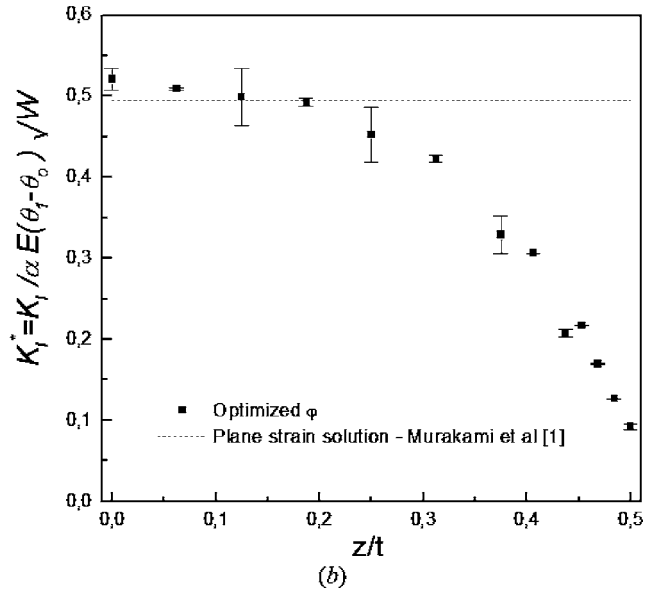

Fig. 10 Normalized mode I stress intensity factor along the crack front for the central crack in a thick panel: (*a*) results using bi-quadratic φ and (*b*) results using optimized φ

The proposed formulation has been implemented as a post-processing technique, and so it can be applied to the results from a particular model at a later stage. The implementation takes advantage of the efficiency of the boundary integral equations to directly obtain the required stress, strains, temperatures, and displacement and temperature derivatives. A number of examples have been solved to demonstrate the efficiency and accuracy of the proposed formulation. Obtained results are accurate and in good agreement with other results reported in the literature.

Special emphasis has been put on the appropriate selection of the auxiliary function φ present in the domain integral formulation. In this sense two approaches have been considered: a bi-quadratic variation and an optimized approach proposed in the paper by Saliva et al. [17].

It has been found that the function φ constitutes a key feature for the performance of the proposed methodology. Obtained results show that the optimized φ performs markedly better for the point located at the intersection of the crack front with the free surface, allowing obtaining reliable J results where the bi-quadratic φ fails. On the other hand, for crack front positions located in the interior of the specimen both approaches allow computing accurate J results, however the bi-quadratic φ presents a more robust behavior. These behaviors for the two definitions of φ are the same as those reported in a recent paper by one of the authors of this work [15] when dealing with the application of the EDI to linear elastic crack problems without the presence of body loads.

Acknowledgment

This work was financed by the Fondo Nacional de Ciencia y Tecnología de Venezuela (FONACIT) and by Grant No. PICT 12-12528 of the Agencia Nacional de Promoción Científica y Tecnológica de la República Argentina (ANPYCT).

Appendix

In this appendix the fundamental solutions for the implementation of the thermoelastic formulation of the dual boundary element method are provided. In what follows the symbol r stands for the distance from the field point $x$to the source point x':

$$r(x',x) = |x - x'| \tag{A1}$$

The notation $r_{,k}$ indicates the derivative at the source point, i.e.,

$$\frac{\partial r}{\partial x_k} = -r_{,k} \tag{A2}$$

The fundamental solutions in the temperature Eq. (10) are

$$\theta^*(x',x) = \frac{-1}{4\pi r} \tag{A3}$$

$$q^*(x',x) = \lambda \frac{r_{,k} n_k}{4\pi r^2} \tag{A4}$$

The fundamental solutions for the flux Eq. (11) can be found after the differentiation of the solutions (A3) and (A4) to yield

$$\theta_i^{**}(x',x) = \frac{\lambda}{4\pi r^2} r_{,i} \tag{A5}$$

$$q_i^{**}(x',x) = \frac{\lambda}{4\pi r^3}(3 r_{,i} r_{,k} n_k - n_i) \tag{A6}$$

The fundamental solutions in the displacement Eq. (14) are given by

$$T_{ij}(x',x) = \frac{-1}{8\pi(1-\nu)r^2}\left\{\frac{\partial r}{\partial n}[(1-2\nu)\delta_{ij} + 3 r_{,i} r_{,j}] - (1-2\nu)(n_j r_{,i} - n_i r_{,j})\right\} \tag{A7}$$

$$U_{ij}(x',x) = \frac{-1}{16\pi(1-\nu)\mu r}\{(3-4\nu)\delta_{ij} + r_{,i} r_{,j}\} \tag{A8}$$

$$\bar{P}_i(x',x) = \frac{\alpha(1+\nu)}{8\pi(1-\nu)r}\left(n_i - \frac{\partial r}{\partial n} r_{,i}\right) \tag{A9}$$

$$\bar{Q}_i(x',x) = \frac{\alpha(1+\nu)}{8\pi(1-\nu)} r_{,i} \tag{A10}$$

The fundamental solutions in the traction equation (15) are obtained by material constitutive relationships. This procedure results in

$$T_{kij}(x',x) = \frac{\mu}{4\pi(1-\nu)r^3}\left\{3\frac{\partial r}{\partial n}[(1-2\nu)\delta_{ij}r_{,k} + \nu(\delta_{ij}r_{,k} + \delta_{jk}r_{,i} - 5r_{,i}r_{,j}r_{,k})] + 3\nu(n_i r_{,j}r_{,k} + n_j r_{,i}r_{,k}) + (1-2\nu)(3n_k r_{,i}r_{,j} + n_k\delta_{ij} + n_i\delta_{jk}) - (1-4\nu)n_k\delta_{ij}\right\} \tag{A11}$$

$$U_{kij}(x',x) = \frac{1}{8\pi(1-\nu)r^2}[(1-2\nu)(\delta_{ik}r_{,j} + \delta_{jk}r_{,i} - \delta_{ij}r_{,k}) + 3r_{,i}r_{,j}r_{,k}] \tag{A12}$$

$$\bar{P}_{ij}(x',x) = 4\frac{\alpha\mu(1+\nu)}{8\pi(1-\nu)r^2}\left\{n_k r_{,k}\left[\frac{\delta_{ij}}{1-2\nu} - 3r_{,i}r_{,j}\right] + n_i r_{,j} + n_j r_{,i}\right\} \tag{A13}$$

$$\bar{Q}_i(x',x) = 4\frac{\alpha\mu(1+\nu)}{8\pi(1-\nu)r}\left(r_{,i}r_{,j} - \frac{\delta_{ij}}{1-2\nu}\right) \tag{A14}$$

References

[1] *Stress Intensity Factor Handbook*, 1987, Y. Murakami, ed., Pergamon Press, Oxford, UK.

[2] Tada, H., Paris, P. C., and Irwin, G. R., 2000, *The Stress Analysis of Cracks Handbook*, 3rd ed., ASME Press, New York.

[3] Brebbia, C. A., Telles, J. C. F., and Wrobel, L. C., 1984, *Boundary Element Techniques*, Springer-Verlag, Berlin.

[4] Aliabadi, M. H., 1997, "Boundary Element Formulations in Fracture Mechanics." Appl. Mech. Rev., **50**, pp. 83–96.

[5] Raveendra, S. T., and Banerjee, P. K., 1992, "Boundary Element Analysis of Cracks in Thermally Stressed Planar Structures," Int. J. Solids Struct., **29**, pp. 2301–2317.

[6] Mukherjee, Y. X., Shah, K., and Mukherjee, S., 1999, "Thermoelastic Fracture Mechanics with Regularized Hypersingular Boundary Integral Equations," Eng. Anal. Boundary Elem., **23**, pp. 89–96.

[7] Prasad, N. N. V., Aliabadi, M. H., and Rooke, D. P., 1994, "The Dual Boundary Element Method for Thermoelastic Crack Problems," Int. J. Fract., **66**, pp. 255–272.

[8] dell'Erba, D. N., and Aliabadi, M. H., 2001, "BEM Analysis of Fracture Problems in Three-Dimensional Thermoelasticity Using J-Integral," Int. J. Solids Struct., **38**, pp. 4609–4630.

[9] Aliabadi, M. H., and Rooke, D. P., 1992, *Numerical Fracture Mechanics*, Computational Mechanics Publications, Southampton, UK.

[10] Kishimoto, K., Auki, S., and Sakata, M., 1980, "On the Path Independent Integral-J," Eng. Fract. Mech., **13**, pp. 841–850.

[11] Shih, C. F., Moran, B., and Nakamura, T., 1986, "Energy Release Rate Along a Three-Dimensional Crack Front in a Thermally Stressed Body," Int. J. Fract., **30**, pp. 79–102.

[12] Cisilino, A. P., Aliabadi, M. H., and Otegui, J. L., 1998, "Energy Domain Integral Applied to Solve Center and Double-Edge Crack Problems in Three-Dimensions," Theor. Appl. Fract. Mech., **29**, pp. 181–194.

[13] Cisilino, A. P., and Aliabadi, M. H., 1999, "BEM Implementation of the Energy Domain Integral for the Elastoplastic Analysis of 3D Fracture Problems," Int. J. Electron., **96**, pp. 229–245.

[14] Cisilino, A. P., and Ortiz, J. E., 2005, "Three-Dimensional Boundary Element Assessment of Fibre/Matrix Interface Cracks Under Transverse Loading," Comput. Struct., **83**, pp. 856–869.

[15] Cisilino, A. P., and Ortiz, J. E., 2005, "Boundary Element Analysis of Three-Dimensional Mixed-Mode Cracks via the Interaction Integral," Comput. Methods Appl. Mech. Eng., **194**(11), pp. 935–956.

[16] Natha, R., and Moran, B., 1993, "Domain Integrals for Axisymmetric Interface Crack Problems," Int. J. Solids Struct., **30**(15), pp. 2027–2040.

[17] Saliva, R., Vènere, M. J., Padra, C., Taroco, E., and Feijoo, R. A., 2000, "Shape Sensitivity Analysis and Energy Release Rate of Planar Cracks Embedded in Three-Dimensional Bodies," Comput. Methods Appl. Mech. Eng., **188**, pp. 649–664.

[18] Wilson, W. K., and Yu, I. W., 1979, "The Use of J-Integral in Thermal Stress Crack Problems," Int. J. Fract., **15**, pp. 377–387.

[19] Das, B. R., 1977, "Thermal Stress in a Long Cylinder Containing a Penny-Shaped Crack," Int. J. Eng. Sci., **6**, pp. 497–516.

A Two-Dimensional Linear Assumed Strain Triangular Element for Finite Deformation Analysis

Fernando G. Flores
Department of Structures,
National University of Cordoba,
Casilla de correos 916,
5000 Cordoba, Argentina
e-mail: fflores@efn.uncor.edu

An assumed strain approach for a linear triangular element able to handle finite deformation problems is presented in this paper. The element is based on a total Lagrangian formulation and its geometry is defined by three nodes with only translational degrees of freedom. The strains are computed from the metric tensor, which is interpolated linearly from the values obtained at the mid-side points of the element. The evaluation of the gradient at each side of the triangle is made resorting to the geometry of the adjacent elements, leading to a four element patch. The approach is then nonconforming, nevertheless the element passes the patch test. To deal with plasticity at finite deformations a logarithmic stress-strain pair is used where an additive decomposition of elastic and plastic strains is adopted. A hyper-elastic model for the elastic linear stress-strain relation and an isotropic quadratic yield function (Mises) for the plastic part are considered. The element has been implemented in two finite element codes: an implicit static/dynamic program for moderately non-linear problems and an explicit dynamic code for problems with strong nonlinearities. Several examples are shown to assess the behavior of the present element in linear plane stress states and non-linear plane strain states as well as in axi-symmetric problems. [DOI: 10.1115/1.2173674]

1 Introduction

For practical industrial applications in the finite strain range, low order elements are almost exclusively used, specially in problems including contact. Also elements including only physical degrees of freedom are normally preferred. For two-dimensional problems these two aspects restrict the choice to linear triangles and bilinear quadrilaterals.

If only elements with translational degrees of freedom are considered, the linear triangle (constant strain triangle with six degrees of freedom) is not a good choice because it requires very fine meshes to obtain results of engineering precision, and also because it locks for quasi-incompressible problems, e.g., material models including J_2 plasticity or rubber-like materials in plane strain.

From the point of view of the present techniques for finite element development, the bilinear quadrilateral shows much more possibilities. Important efforts have been made in the past 30 years to obtain efficient and robust quadrilaterals which do not lock in the incompressible limit, or have a good performance in bending-dominated problems even with coarse meshes. Different practical approaches and their theoretical basis have been proposed in this direction, from the addition of incompatible modes to improving bending behavior or selective integration of the volumetric response to avoid locking, to the present more refined techniques of assumed strain and enhanced strain finite elements (see, for example, Refs. [1,2] and references listed therein).

From the point of view of industrial applications, the use of triangular elements is more convenient. This is mainly associated with the fact that mesh generators using triangles are more efficient and robust than those using quadrilaterals. This facility is especially important in processes in which large distortions of the original mesh are expected leading unavoidably to remeshing and/or to adaptive refinement.

These reasons have led to the developments of triangles with degrees of freedom that are not strictly displacements, including mixed or hybrid elements on one side and elements with drilling rotations or displacement derivatives on the other side. The extra degrees of freedom in mixed/hybrid (assumed stress) approaches have no associated mass, requiring special time integration techniques [3] when explicit integrators are used. This aspect is important in problems including strong nonlinearities, in which explicit integrators are more robust and preferred. Besides, the standard algorithmic framework for non-linear solid mechanics is typically *strain driven* and, from a practical perspective, algorithms for assumed stress elements are more involved. Elements with drilling freedoms are less common, and have been restricted to plane stress problems [4]. More recently an F-bar method (volumetric strain averaging) [5] that alleviates volumetric locking and an application of sub-grid scales in mixed elements [6] that avoids pressure oscillations were proposed, but none of them improve the poor in-plane behavior of the constant strain triangle.

In this paper a triangular element defined by only three nodes and with only translational degrees of freedom is presented. For the computation of the strains a four element patch including the three adjacent elements is used. This approach has a geometric definition similar to that used in Ref. [7] for the evaluation of the curvatures in a shell element and shares some aspects with the subdivision approach recently proposed for surfaces [8]. The proposed approach linearly interpolates the metric tensor evaluated at the midpoint of each side. The present development is intended to deal with elastic-plastic models at finite strains.

The outline of the paper is as follows. In Sec. 2, the essential governing equations for non-linear solid mechanics relevant to this work are presented. The next two sections are devoted to the finite element approximation: in Sec. 3 the original approach to

Contributed by the Applied Mechanics Division of ASME for publication in the JOURNAL OF APPLIED MECHANICS. Manuscript received June 8, 2005; final manuscript received December 19, 2005. Review conducted by G. C. Buscaglia. Discussion on the paper should be addressed to the Editor, Prof. Robert M. McMeeking, Journal of Applied Mechanics, Department of Mechanical and Environmental Engineering, University of California—Santa Barbara, Santa Barbara, CA 93106-5070, and will be accepted until four months after final publication of the paper itself in the ASME JOURNAL OF APPLIED MECHANICS.

the evaluation of the deformation gradient and the metric tensor is presented, while in Sec. 4 the stiffness matrix necessary for implicit algorithms is derived. Section 5 describes the element performance in linear plane stress problems, and Sec. 6 shows preliminary results for plane strain and axisymmetric problems in the non-linear range. Finally, some conclusions are drawn in Sec. 7.

2 Solid Kinematics

The most relevant aspects associated with the kinematic response of solids are initially presented. More detailed developments can be found in the literature devoted to the field [9].

Consider a solid with reference configuration Ω^0 in R^3 at the initial time $t=0$. Let us then denote with $\mathbf{X} \in \Omega^0$ the position vector of a material point that transforms to a point $\mathbf{x}$ at a time t, both referred to a fixed set of axis.

At each point $\mathbf{X}$ the deformation gradient is defined as

$$\mathbf{F}(\mathbf{X}) = \left[\frac{\partial \mathbf{x}}{\partial X_1}, \frac{\partial \mathbf{x}}{\partial X_2}, \frac{\partial \mathbf{x}}{\partial X_3} \right] = [\mathbf{a}_1 \ \mathbf{a}_2 \ \mathbf{a}_3] \tag{1}$$

The definition of the Lagrangian tensor $\mathbf{C}=\mathbf{F}^T\mathbf{F}=\mathbf{U}^2$ (with $\mathbf{U}$ the right stretch tensor, and $\mathbf{C}$ the right Cauchy–Green tensor, respectively) allows the introduction of the covariant metric tensor at each point

$$C_{\alpha\beta} = (U^2)_{\alpha\beta} = \mathbf{a}_\alpha \cdot \mathbf{a}_\beta = a_{\alpha\beta} \tag{2}$$

One advantage of the Lagrangian strains is that they are referred to material fibers leading to a simple handling of anisotropic materials. With $\mathbf{U}^2$ it is possible to define different Lagrangian strain measures. With this objective the spectral decomposition is performed as

$$\mathbf{U} = \sum_{\alpha=1}^{3} \lambda_\alpha \mathbf{r}_\alpha \otimes \mathbf{r}_\alpha \tag{3}$$

where λ_α and $\mathbf{r}_\alpha$ are the eigenvalues and eigenvectors, respectively, of the right stretch tensor $\mathbf{U}$.

To deal with plasticity at finite deformations an adequate stress-strain pair must be used. Here a logarithmic (Hencky) strain measure is adopted that, restricted to two-dimensional problems, can be explicitly expressed as

$$\mathbf{E}_{\ln} = \begin{bmatrix} \varepsilon_{11} & \varepsilon_{21} & 0 \\ \varepsilon_{12} & \varepsilon_{22} & 0 \\ 0 & 0 & \varepsilon_{33} \end{bmatrix} = \sum_{\alpha=1}^{3} \ln(\lambda_\alpha) \mathbf{r}_\alpha \otimes \mathbf{r}_\alpha \tag{4}$$

The conjugated stress measure $\mathbf{T}$ is used consistently. Besides this, in the framework of a total Lagrangian formulation, it may be convenient to work with the second Piola–Kirchhoff stress tensor ($\mathbf{S}$) for the residual force evaluation. The relation between the stress $\mathbf{T}$ and the stress $\mathbf{S}$ results from the definition of the rotated tensors

$$\mathbf{T}_L = \mathbf{R}_L^T \mathbf{T} \mathbf{R}_L \tag{5}$$

$$\mathbf{S}_L = \mathbf{R}_L^T \mathbf{S} \mathbf{R}_L \tag{6}$$

where $\mathbf{R}_L$ is the material rotation tensor associated with the principal stretches (eigenvectors of $\mathbf{U}$)

$$\mathbf{R}_L = [\mathbf{r}_1 \ \mathbf{r}_2 \ \mathbf{r}_3] \tag{7}$$

The relations between these rotated stress measures are

$$[S_L]_{\alpha\alpha} = \frac{1}{\lambda_\alpha^2} [T_L]_{\alpha\alpha} \tag{8}$$

$$[S_L]_{\alpha\beta} = \frac{\ln(\lambda_\alpha/\lambda_\beta)}{\frac{1}{2}(\lambda_\alpha^2 - \lambda_\beta^2)} [T_L]_{\alpha\beta} \tag{9}$$

They allow to compute

$$\mathbf{S} = \mathbf{R}_L \mathbf{S}_L \mathbf{R}_L^T \tag{10}$$

With the previous definitions, the weak form of the equilibrium equations in the reference configuration can be written as

$$\delta\Pi = \int_{\Omega^0} [\delta \mathbf{E}_{\mathrm{GL}} : \mathbf{S}] d\Omega^0 + \delta\Pi_{\mathrm{ext}} = 0 \tag{11}$$

where $\mathbf{E}_{\mathrm{GL}}$ are the Green–Lagrange strains conjugated to $\mathbf{S}$

$$\mathbf{E}_{\mathrm{GL}} = \sum_{\alpha=1}^{3} \frac{1}{2}(\lambda_\alpha^2 - 1) \mathbf{r}_\alpha \otimes \mathbf{r}_\alpha = \frac{1}{2}(\mathbf{U}^2 - \mathbf{1}) \tag{12}$$

Note that the stress-strain pair $\mathbf{S}-\mathbf{E}_{\mathrm{GL}}$ is used only to write the equilibrium equations in the reference configuration. Alternatively, an equivalent formulation to Eq. (11) using the spatial Kirchhoff stress tensor $\boldsymbol{\tau}$ on the actual configuration can be developed.

The constitutive model used in the numerical experiments below corresponds to an elastic-plastic material associated with a ductile metal. For this kind of material, where elastic strains are small and a logarithmic strain measure is used, it seems reasonable to adopt an additive decomposition of elastic and plastic strains $\mathbf{E}_{\ln}^e = \mathbf{E}_{\ln} - \mathbf{E}_{\ln}^p$, where plastic strains may be associated with a plastic deformation gradient $\mathbf{F}^p$ through

$$\mathbf{E}_{\ln}^p = \ln(\mathbf{F}^{pT} \mathbf{F}^p)^{1/2} \tag{13}$$

usually associated with a stress free intermediate configuration. For moderately large shear plastic strains, the results obtained with the additive formulation are similar to those obtained with the multiplicative decomposition of $\mathbf{F}$. See Ref. [10] for a comparison of results for both approaches. An associative Mises yield function (J_2) with non-linear isotropic hardening is considered. Also an anisotropic Hill-type function can be easily defined since the elastic strains are computed on the material axis. The elastic-plastic constitutive equations are integrated using a standard return mapping algorithm.

For the elastic part, a linear relation (constant) between stresses and elastic strains is also adopted. The constitutive relation is split into its deviatoric and volumetric components and in the numerical implementation the volumetric part is averaged at the element center to avoid volumetric locking.

3 Mapping Functions and Gradient Evaluation

In this approach we start from a three-node triangular finite element mesh of the domain. But in contrast with standard finite elements, for the evaluation of the deformations at an element, we resort also to the geometry of the adjacent elements to the triangle being considered (see Fig. 1(*a*)). A quadratic geometry is thus defined by the position of the six nodes

$$\mathbf{X} = \sum_{I=1}^{6} N^I \mathbf{X}^I \quad \mathbf{x} = \sum_{I=1}^{6} N^I \mathbf{x}^I \tag{14}$$

In the parametric space (master element) we keep the vertex positions, nodes 1–3, of the central or main triangle (standard linear triangle) which occupy the positions (see Fig. 1(*b*)).

$$(\xi^1, \eta^1) = (0,0), \quad (\xi^2, \eta^2) = (1,0), \quad (\xi^3, \eta^3) = (0,1)$$

while the three extra nodes forming the patch, denoted as 4–6, occupy the positions

$$(\xi^4, \eta^4) = (1,1), \quad (\xi^5, \eta^5) = (-1,1), \quad (\xi^6, \eta^6) = (1,-1).$$

The following set of shape functions can be defined over this quadratic non-standard six node triangle (with $\zeta = 1-\xi-\eta$)

$$N^1 = \zeta + \xi\eta \quad N^2 = \xi + \eta\zeta \quad N^3 = \eta + \zeta\xi$$

$$N^4 = \frac{\zeta}{2}(\zeta - 1) \quad N^5 = \frac{\xi}{2}(\xi - 1) \quad N^6 = \frac{\eta}{2}(\eta - 1) \tag{15}$$

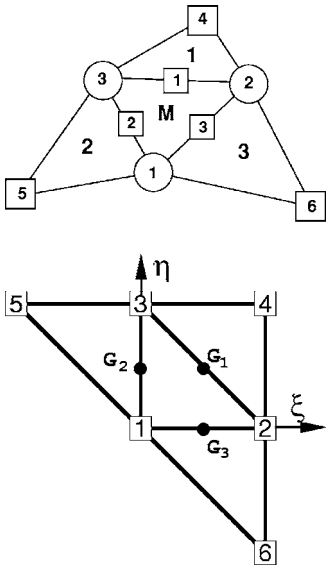

Fig. 1 Patch of elements (*a*) in spatial coordinates, (*b*) in natural coordinates

The aim of this mapping is the computation of the metric tensor at selected points in the central element to generate an assumed strain approach. For a linear interpolation in local natural coordinates three values are needed. The points used for evaluation are located at the middle of each side of the reference triangle (**M** in Fig. 1(*a*)). They are indicated as G_1, G_2 and G_3 in Fig. 1(*b*). This choice has the following properties:

- The gradient computed at each mid-side point depends exclusively on the positions of the nodes associated with the two elements adjacent to the side. This can be immediately checked by differentiating the shape functions and evaluating at the middle of each side.
- When the deformation gradients are computed at the common side of two neighbor triangles, the same four nodes will be used. Thus, at each side of the mesh, a unique deformation gradient exists.

The deformation gradient is then determined by the coordinates of a patch of four elements, which includes the element under consideration (**M** in Fig. 1(*a*)) as the central one. Note that the present approach is nonconforming because the quadratic geometry computed from two adjacent triangles is different along the common side.

Once the deformation gradient has been defined the derivation is standard, and some details are given in the sequel. We will denote by $\mathbf{t}_1$ and $\mathbf{t}_2$ the two orthogonal unit vectors in a local Cartesian system conveniently selected (e.g., the orthotropic principal directions of the constitutive material). The natural derivatives of the reference coordinates allow to compute the Jacobian matrix of the isoparametric mapping **J** and the Cartesian derivatives of the shape functions $N_1^I N_2^I$. With them the deformation gradient at the deformed configuration (respect to the original Cartesian system) can be computed as

$$[\mathbf{x}_{,1}, \mathbf{x}_{,2}] = [\mathbf{x}_{,\xi}, \mathbf{x}_{,\eta}]\mathbf{J}^{-1} \tag{16}$$

and the (in-plane) covariant metric tensor

$$\mathbf{C} = \begin{bmatrix} a_{11} & a_{12} \\ a_{21} & a_{22} \end{bmatrix} = \begin{bmatrix} \mathbf{x}_{,1}\cdot\mathbf{x}_{,1} & \mathbf{x}_{,1}\cdot\mathbf{x}_{,2} \\ \mathbf{x}_{,2}\cdot\mathbf{x}_{,1} & \mathbf{x}_{,2}\cdot\mathbf{x}_{,2} \end{bmatrix} \tag{17}$$

and finally any in-plane desired Lagrangian strain measure. For example, the Green–Lagrange strain tensor

$$\mathbf{E}_{\mathrm{GL}} = \frac{1}{2}\begin{bmatrix} \mathbf{x}_{,1}\cdot\mathbf{x}_{,1}-1 & \mathbf{x}_{,1}\cdot\mathbf{x}_{,2} \\ \mathbf{x}_{,2}\cdot\mathbf{x}_{,1} & \mathbf{x}_{,2}\cdot\mathbf{x}_{,2}-1 \end{bmatrix} = \frac{1}{2}\begin{bmatrix} a_{11}-1 & a_{12} \\ a_{21} & a_{22}-1 \end{bmatrix} \tag{18}$$

An element that has a side along the boundary does not have an adjacent element on this side. In this case the deformation gradient at this side is computed as the gradient of the central element using the standard linear interpolation. Once the metric tensor ($\mathbf{C}_i$) is computed at each mid-side point *i*, the element can be classified as an **assumed strain** element if the metric tensor is interpolated as a function of the computed values at the sides. This allows to associate a theoretical basis to the present approach.

$$\mathbf{C}(\xi,\eta) = (1-2\zeta)\mathbf{C}_1 + (1-2\xi)\mathbf{C}_2 + (1-2\eta)\mathbf{C}_3 \tag{19}$$

4 Stiffness Matrix

The derivative of the weak form (Eq. (11)) is needed for most of the implicit predictor-corrector algorithms. As usual, for nonlinear problems, the **material** and **geometric** parts are considered separately. The material part is almost standard and does not offer difficulties, it is the result of the integral

$$\delta\mathbf{u}^T\mathbf{K}_M\Delta\mathbf{u} = \delta\mathbf{u}^T\int_A \mathbf{B}^T\mathbf{D}\mathbf{B}\,dA\,\Delta\mathbf{u} \tag{20}$$

where matrix **B** results from the evaluation of the variation of the Green–Lagrange strain tensor (Eq. (18)). In the numerical implementation, adequate changes must be introduced for elements on the boundary. Matrix **D** is the tangent elasticity matrix or, in elastic-plastic problems, the tangent/algorithmic constitutive matrix $\mathbf{D}_{\mathrm{ep}}$.

The geometric part turns out from

$$\delta\mathbf{u}^T\mathbf{K}_G\Delta\mathbf{u} = \int_A \frac{\partial}{\partial\mathbf{u}}(\delta\mathbf{E}_{\mathrm{GL}}^T\mathbf{S})\Delta\mathbf{u}\,dA \tag{21}$$

which can be obtained by adding the contributions from the three mid-side points (written in matrix form):

$$\delta\mathbf{u}^T\mathbf{K}_G\Delta\mathbf{u} = \frac{1}{3}\sum_{K=1}^{3}\sum_{I=1}^{4}\sum_{J=1}^{4}\left\{\delta\mathbf{u}^I\int_A [N^I_{,1}\ N^I_{,2}]\begin{bmatrix} S_{11} & S_{12} \\ S_{21} & S_{22}\end{bmatrix}\times\begin{bmatrix} N^J_{,1} \\ N^J_{,2}\end{bmatrix}dA\,\Delta\mathbf{u}^J\right\}^{(K)} \tag{22}$$

where index $K=1,3$ is the side and $N^{I(K)}$ are the shape functions restricted to the four contributing nodes at each point ($I,J=1,4$).

In the numerical comparisons we denote by TR3 the present element when three points are used to integrate the deviatoric forces and corresponding stiffness matrix. And by TR1 when only one integration point is used, equivalent to averaging the metric tensors computed at each side. The latter is the usual case because it needs less storage for internal variables; it is more competitive for explicit codes and does not have spurious modes.

For the TR1 version the computational cost is slightly above the standard constant strain triangle (CST). Two aspects must be considered: (a) the evaluation of the internal forces, (b) the computations associated to the stiffness matrix. For codes with explicit integration of the momentum equations only the former is concerned, while for implicit integrators the latter is the most relevant. For the evaluation of the internal forces the differences with the CST amount to the computation of the average metric tensor (or the deformation gradient) than can be made quite efficiently. The same also applies to the stiffness matrix evaluation. It must be noted that also a slightly wider bandwidth will be obtained leading to higher CPU times to solve the equations systems.

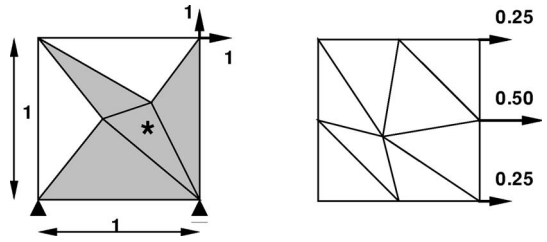

Fig. 2 Membrane patch test

5 Linear Numerical Examples

In this section and the next, a summary of the numerical experiments performed to assess the behavior of this element is presented. In this section linear problems in plane stress state are considered. An implicit static/dynamic program for moderately non-linear simulations developed by the author is used. For comparisons, the results obtained with other elements are included, namely: the constant strain triangle (CST), the linear strain triangle (LST) and three three-node triangles (ALL-3I, BER-85 and CF-OPT) with three degrees of freedom per node (both displacements and the drilling rotation) obtained with different formulations as reported in Ref. [4]. With ALL-3I we denote the element developed by Allman [11] integrated with three inner points; with BER-85 we denote the element developed by Bergan [12] using the free formulation and with CF-OPT we denote the element developed by Felippa and Militello based on the ANDES scheme [13] optimized to reproduce exactly constant bending states.

5.1 Membrane Patch Test. As the present approach is non-conforming, one of main aspects to be considered is the satisfaction of the patch test. To assess this a square domain of unit side subjected to nodal forces associated with a uniform unit stress state (both Cartesian directions and shear) have been used. Two possible patches of elements are shown in Fig. 2. In the first patch, the loads necessary to obtain a uniform stress state $S_{xx}=S_{xy}=S_{yy}=1$ are shown. In the second patch, only the loads corresponding to a uniform traction in the direction x are depicted. For both meshes unitary stresses are obtained at all elements, using one or three integration points.

Two very important things may be noted in this simple example. First, in the second case, note that the nodal forces are the loads associated with the linear triangle and not to the quadratic one. This has important implications in problems including contact, where the use of the standard LST implies non-uniform equivalent nodal forces for a uniform pressure leading to the well-known problems of quadratic elements in contact simulations. Second, note that the element patches used for gradient computations at each element are quite distorted. In the first mesh the element patch used to compute strains at element $*$ is shaded as an example. A LST element defined with the same six points will show a very strong sensitivity to such distortion leading to unpredictable results.

5.2 Short Cantilever Under Uniform Shear. This example (see Fig. 3), taken from Ref. [4], is used to assess the behavior and convergence properties of elements under bending and shear when the element aspect ratio is increased. Shear load is parabolically distributed according to beam theory. All displacements are constrained at the root, not allowing Poisson's contraction. A numerically converged solution of the deflection at point **C** of $\delta_C=0.35601$ is used for normalization. Mesh units are formed by four half-thickness overlaid triangles to avoid orientation influence. Along direction y (beam height) 2, 4, 8, 16, and 32 mesh units are considered while along direction x mesh is defined by element aspect ratio values $\gamma=1$, 2, and 4.

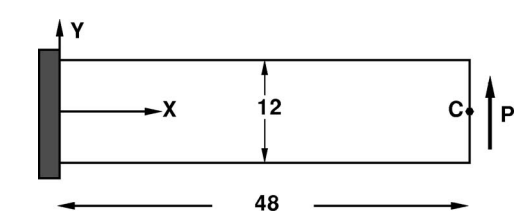

Fig. 3 Shear loaded short cantilever: no contraction allowed at the root. $E=30{,}000$, $\nu=0.25$, $h=1$.

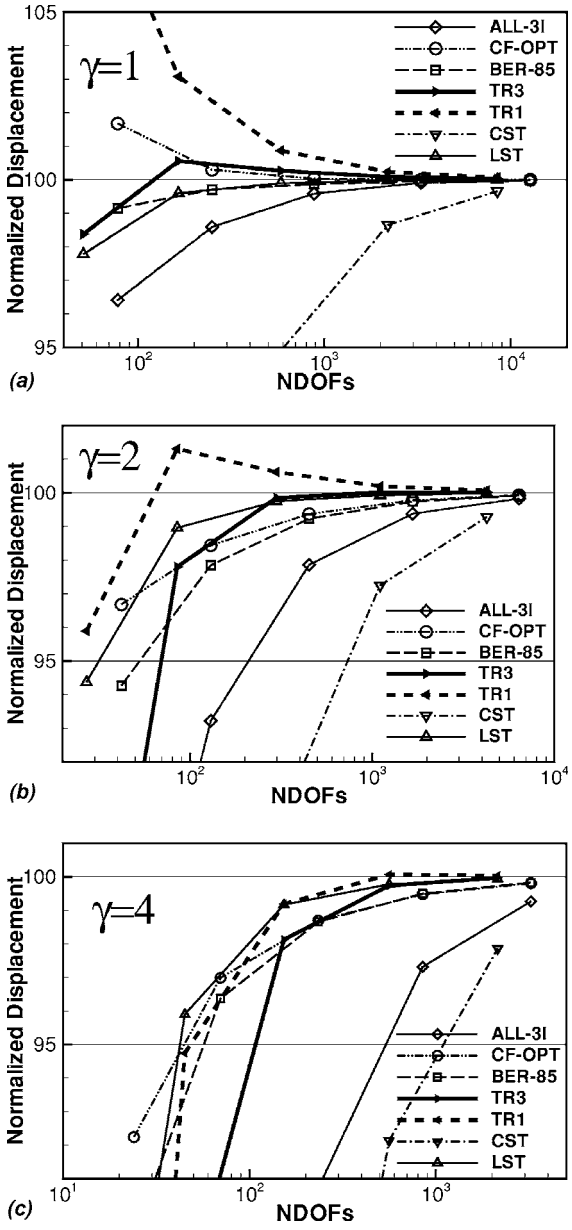

Fig. 4 Tip deflections for short cantilever under end load. (*a*) $\gamma=1$, (*b*) $\gamma=2$, (*c*) $\gamma=4$.

The results for the vertical displacements of point **C** are plotted in Figs. 4(*a*)–4(*c*) for the three element aspect ratios and for all the elements described above. In all the cases the best results are obtained with the linear strain triangle while the constant strain triangle is notoriously overstiff. The performance of elements with drilling freedom deteriorates as the aspect ratio increases, specially Allman's triangle. Present element fully integrated (TR3) converges rapidly and is less sensitive to aspect ratio than ele-

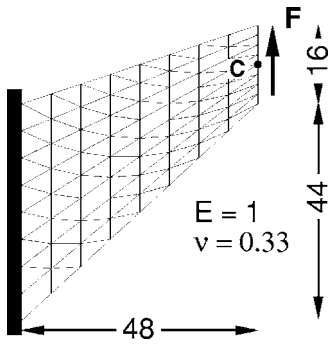

Fig. 5 Cook's membrane problem. Geometry and load.

ments with drilling freedoms. Present element with only one integration point (TR1) is slightly more flexible but converges to the correct solution.

5.3 Cook's Membrane Problem. One of the main targets of this proposal is to obtain a membrane approach with a behavior similar to the linear strain triangle in arbitrary domains. Such capacity is studied in this example [14], corresponding to a problem with an important amount of shear energy involved, intended also to assess the ability of the element to distort. Figure 5 shows the geometry of a tapered panel clamped on one side and with a uniformly distributed shear load on the opposite side. In Fig. 6 the vertical displacement of point **C** (midpoint of the loaded side) for the uniformly refined meshes considered are plotted as a function of the total number of degrees of freedom.

For the present element with three integration points, it can be seen that for the coarsest mesh (two linear elements), the measured displacement is slightly superior than the constant strain triangle; but when the mesh is refined, the values computed rapidly catch up with those obtained with the linear strain triangle. For the elements with drilling freedoms, the trends of the previous example are reverted. The more general Allman's element has a better performance than the other two (optimized for uniform bending) which give similar values and converge slower. The present element with only one integration point (TR1) shows excellent predictions for coarse meshes and fast convergence properties.

6 Nonlinear Numerical Examples

In this second part of the numerical experiments, examples in the geometric and material non-linear range are discussed. Due to the characteristics of the problems modeled, including strong non-linearities and contact with friction, a program with explicit integration of the governing equations was used [15]. This program allows to obtain pseudo-static solutions using dynamic relaxation. The problems analyzed in this second part are in plane strain or axisymmetric states. Special emphasis is placed in detecting if the element is capable of handling elastic-plastic problems with isochoric plastic flow or quasi-incompressible elastic problems.

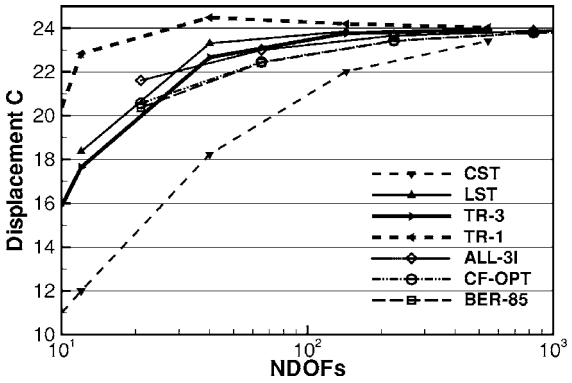

Fig. 6 Cook's membrane problem. Vertical deflections of point C (plane stress).

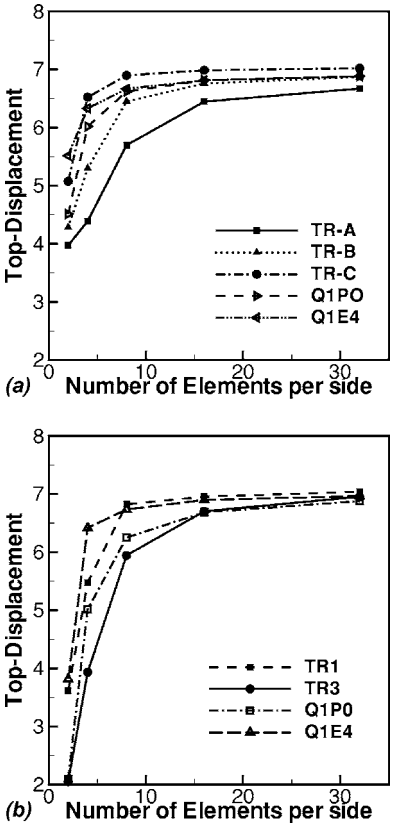

Fig. 7 Cook's problem in plane strain. Convergence of finite element solutions. (*a*) quasi-incompressible finite elasticity. (*b*) Finite Strain J_2 flow theory.

6.1 Cook's Problem in Plane Strain. The same geometry considered in Sec. 5.3 is used, but here in a state of plane strain. Two different materials are considered. First, a quasi-incompressible linear elastic material defined by a shear modulus $\mu=80.1938$ GPa and three possible values of the bulk modulus $K_A=401.0\times10^3$ GPa, $K_B=40.1\times10^3$ GPa and $K_C=4.01\times10^3$ GPa in correspondence with three values of the Poisson ratio $\nu=0.4999$, 0.4990, and 0.4900, respectively. Second, an elastic-plastic material defined by the elastic constants $\mu=80.1938$ GPa and $K=164.21$ GPa and J_2 plasticity with non-linear hardening defined by the yield stress $\sigma_y(e^p)=0.450+0.12924e^p+(0.715-0.450)(1-e^{-16.93e^p})$ [GPa]. The applied load is 100 kN for the elastic case, and 5 kN in the elastic-plastic case.

Figure 7 plots the vertical displacement of the upper corner versus the number of elements per side of the mesh. Figure 7(*a*) corresponds to the quasi-incompressible elastic case using one integration point for present element. Results are shown for the three bulk modulus considered, denoted as TR-A, TR-B, and TR-C. Curve TR-A (Poisson's ratio $\nu=0.4999$) shows clearly a slow convergence. For a Poisson's ratio of $\nu=0.4990$ convergence is reasonably good, while for the lowest considered value of $\nu=0.4900$ convergence is very good, similar to that obtained in the plane stress case. For comparative purposes, results for the highest Poisson's ratio obtained with two four node quadrilaterals are included. Q1P0 [16] is a mixed element equivalent to integrating the volumetric part with one point and the deviatoric part with four

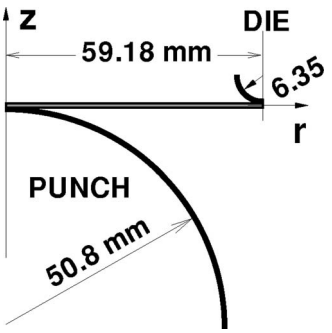

Fig. 8 Stretching of circular sheet with a hemispherical punch

points; Q1EA is an enhanced strain element [17]. Both quadrilaterals show a better performance than the proposed triangle (TR1) for this type of quasi-incompressible elastic problem.

Figure 7(*b*) corresponds to the elastic-plastic material. Results for the two versions (one and three integration points) of the present element and the two quadrilaterals mentioned in the previous paragraph are included. In this case, TR3 shows a stiffer behavior than quadrilaterals, but there is no locking. While the element version TR1 converges faster than both quadrilaterals used for comparison.

6.2 Stretching of a Circular Sheet With a Hemispherical Punch. The last example considered is an axisymmetric problem with moderately large strains. This *benchmark* was proposed in Ref. [18] and has been widely used to test two-dimensional solid elements. The simple geometry of this test is shown in Fig. 8. The sheet thickness is 1 mm and the material is defined by the elastic constants $E=69.004$ GPa and $\nu=0.3$, and J_2 plasticity with an isotropic hardening law $\sigma_y=0.589(10^{-4}+e^p)^{0.216}$ GPa. Contact between the tools and the sheet is modeled using penalization and the friction coefficient adopted is $\mu=0.3$. A uniform mesh of 28 elements in direction r and four elements in the thickness was used ($28\times4\times2$ TR1 elements).

Figure 9(*a*) plots the force on the punch versus the punch travel along the process. These values are in agreement with most of the simulations where solid elements (as opposite to shell elements) have been used, as they can deal with local effects associated with shear distortion due to the small radius of the die and to the frictional contact with the tools [16]. Figure 9(*b*) shows the thickness along the radius for different punch travels, and Fig. 9(*c*) the effective plastic strain on the middle surface of the sheet for different punch travels. These results agree quite well with most of the data published for this benchmark including solid [16] and shell elements [7].

7 Conclusions

A triangular finite element for the simulation of two-dimensional solids has been presented. The geometry is defined by three nodes and only translational degrees of freedom are used, which makes the element convenient for implementation in codes with explicit integration of the governing equations for problems including contact and adaptive remeshing. The element is nonconforming but satisfies the *patch test* and the numerical test computed did not show problems.

In uniform bending plane stress states, the element displays a reasonable behavior. For more general problems including a massive discretization, the element shows a performance similar to the linear strain element. Thus the element turns out to be an excellent candidate for the membrane part of a shell element [19], specially if it is oriented to sheet metal forming, where the membrane behavior is of utmost importance and requires a detailed discretization of the domain.

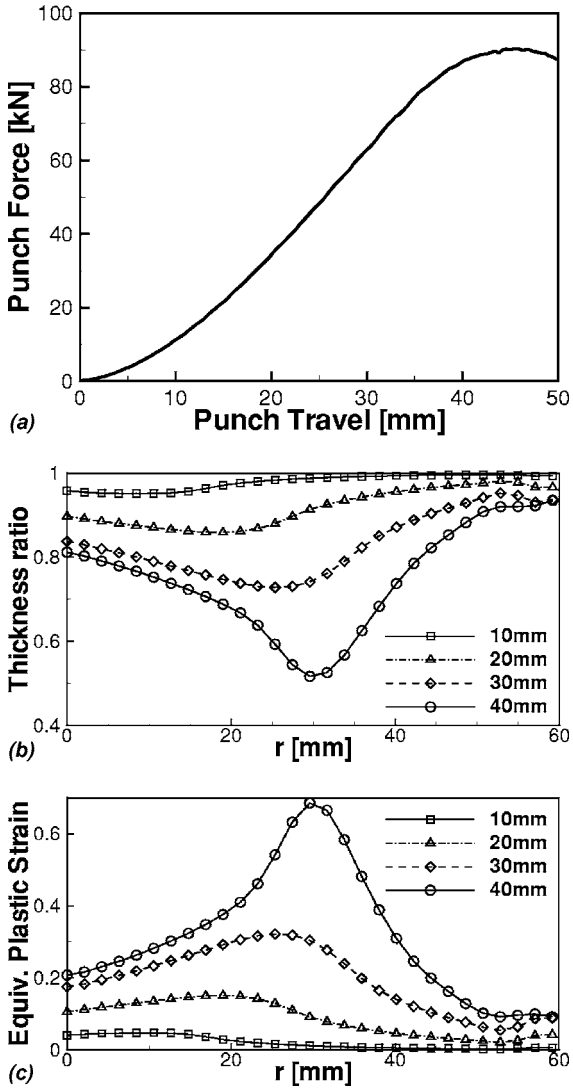

Fig. 9 Stretching of circular sheet with a hemispherical punch. (*a*) Punch force vs punch travel. (*b*) Thickness ratio along the radius for different punch travels. (*c*) Equivalent plastic strain along the radius for different punch travels.

For plane strain and axisymmetric states with finite strains in the plastic range, the element performance is very good, similar to the enhanced strain quadrilaterals. For quasi-incompressible elastic problems the element is rather stiff for Poisson's ratio greater than 0.4999 but is quite good for Poisson's ratio below 0.4990

A more detailed assessment of the element must be performed. In particular the behavior in problems including very large strains (exceeding 1) and the convergence properties in complex domains and meshes where large gradients of the element size exist.

Acknowledgment

The author is a member of the scientific staff of the Science Research Council of Argentina (CONICET). The support provided by grants of CONICET is gratefully acknowledged.

References

[1] Simo, J. C., and Rifai, M. S., 1990, "A Class of Mixed Assumed Strain Methods and the Method of Incompatible Modes," Int. J. Numer. Methods Eng., **29**, pp. 1595–1638.
[2] Armero, F., 2000, "On the Locking and Stability of Finite Elements in Finite Deformations Plane Strain Problems," Comput. Struct., **75**, pp. 261–290.
[3] Zienkiewicz, O. C., Rojek, J., Taylor, R. L., and Pastor, M., 1998, "Triangles and Tetrahedra in Explicit Dynamic Codes for Solids," Int. J. Numer. Methods

Eng., **43**, pp. 565–583.
[4] Felippa, C. A., 2003, "A Study of Optimal Membrane Triangles With Drilling Freedoms," Comput. Methods Appl. Mech. Eng., **192**, pp. 2125–2168.
[5] de Souza Neto, E. A., Andrade Pires, F. M., and Owen, D. R. J., 2005, "F-Bar-Based Linear Triangles and Tetrahedra for Finite Strain Analysis of Nearly Incompressible Solids. Part I: Formulation and Benchmarking," Int. J. Numer. Methods Eng., **62**, pp. 353–383.
[6] Cervera, M., Chiumenti, M., Valverde, Q., and Agelet de Saracibar, C., 2003, "Mixed Linear/Linear Simplicial Elements for Incompressible Elasticity and Plasticity," Comput. Methods Appl. Mech. Eng., **192**, pp. 5249–5263.
[7] Flores, F. G., and Oñate, E., 2001, "A Basic Thin Shell Triangle With Only Translational DOFs for Large Strain Plasticity," Int. J. Numer. Methods Eng., **51**, pp. 57–83.
[8] Cirak, F., and Ortiz, M., 2000, "Subdivision Surfaces: A New Paradigm for Thin-Shell Finite Element Analysis," Int. J. Numer. Methods Eng., **47**, pp. 2039–2072.
[9] Marsden, J. E., and Hughes, T. J. R., 1994, *Mathematical Foundations of Elasticity*, Dover, New York.
[10] Miehe, C., and Apel, N., 2004, "Anisotropic Elastic-Plastic Analysis of Shells at Large Strains. A Comparison of Multiplicative and Additive Approaches to Enhanced Finite Element Design and Constitutive Modelling," Int. J. Numer. Methods Eng., **61**, pp. 2067–2113.
[11] Allman, D. J., 1984, "A Compatible Triangular Element Including Vertex Rotations for Plane Elasticity Analysis," Comput. Struct., **19**, pp. 1–8.
[12] Bergan, P. G., and Felippa, C. A., 1985, "A Triangular Membrane Element With Rotational Degrees of Freedom," Comput. Methods Appl. Mech. Eng., **50**, pp. 25–69.
[13] Felippa, C. A., and Militello, C., 1992, "Membrane Triangles With Corner Drilling Freedoms: II. The ANDES Element," Finite Elem. Anal. Design, **12**, pp. 189–201.
[14] Cook, R. D., 1974, "Improved Two-Dimensional Finite Element," J. Struct. Div. ASCE, **100**, ST6, pp. 1851–1863.
[15] STAMPACK, 2005, *A General Finite Element System for Sheet Stamping and Forming Problems*, Quantech ATZ, Barcelona, Spain, ver. 6.00.
[16] Garino, C. García, 1993, "A Numerical Model for the Analysis of Elastic-Plastic Solids Subjected to Large Strains," Ph.D. thesis (in Spanish) Universidad Politécnica de Cataluña, Barcelona.
[17] Glaser, S., and Armero, F., 1997, "On the Formulation of Enhanced Strain Finite Elements in Finite Deformations," Eng. Comput., **14**, pp. 757–791.
[18] Lee, J. K., Wagoner, R. H., and Nakamachi, E., 1990, "A Benchmark Test for Sheet Metal Forming," Technical Report, Ohio State University.
[19] Flores, F. G., and Oñate, E., 2005, "Improvements in the Membrane Behaviour of the Three Node Rotation-Free BST Shell Triangle Using an Assumed Strain Approach," Comput. Methods Appl. Mech. Eng., **194**, pp. 907–932.

Patricia M. Dardati
Department of Industrial Engineering,
Regional Faculty at Córdoba,
National Technological University,
M. López and Cruz Roja Argentina,
Córdoba, Argentina
e-mail: pdardati@industrial.frc.utn.edu.ar

Luis A. Godoy
Department of Structures,
Faculty of Exact, Physical and Natural Sciences,
National University of Córdoba and CONICET,
Av. Vélez Sarsfield 1601,
Córdoba, Argentina
e-mail: lgodoy@com.uncor.edu

Diego J. Celentano
Department of Mechanical Engineering,
University of Santiago de Chile,
3363 O'Higgins Ave.,
Santiago, Chile
e-mail: dcelenta@lauca.usach.cl

Microstructural Simulation of Solidification Process of Spheroidal-Graphite Cast Iron

This paper presents a new micro-macro approach for the thermo-microstructural behavior of the solidification process of an eutectic ductile cast iron. The thermal balance is written at a macroscopic level and can take into account both the structural component being cast and its mold. Models of nucleation and growth represent the evolution of the microstructure, following a multinodular solidification theory with independent nucleation of graphite and austenite and a dendritic growth of austenite. The resulting formulation is solved using a finite element discretization of the macro domain, in which the evolution of the microstructure is taken into account at the Gauss integration points. The quantitative agreement between experimental and computational values in terms of cooling curves is acceptable. [DOI: 10.1115/1.2189876]

1 Introduction

This paper presents a simulation of the solidification process of eutectic spheroidal-graphite (SG) cast iron, by means of a coupled macro-microstructural formulation. This is a thermal-microstructural formulation, in which two different but interdependent problems are coupled: the macroscopic problem is governed by the heat flow equation, while the microscopic problem is governed by the microstructure formation during solidification. Both models are coupled and lead to a nonlinear problem.

SG cast iron, also known as ductile cast iron, nodular iron, or ductile iron, plays a key role in metallurgical industries and in some engineering processes. Because of its advantageous mechanical properties, SG cast iron has substituted cast steel and forged steel in a number of applications. The new feature is that the spherical structure of graphite can be obtained as a result of the solidification process instead of the long and expensive thermal treatments that are needed following the solidification of white cast iron. However, the mechanisms involved in the formation of SG cast iron are not simple, and there have been many attempts to explain this process.

The main difficulties to build a satisfactory model are associated to a lack of empirical evidence about what exactly occurs during solidification. The importance of simulation in this field of science and engineering can not be overstated. There are tremendous difficulties in the experimental work, which would be the subject of a paper in itself, mainly because one needs to investigate a process without full access to it, and also because any measuring device interferes with the very process that it is trying to investigate. There is another phase change that occurs in solid state during cooling; this is present in the experimental results but would be complex to include as part of the same solidification process modeled here.

Simulation by itself, on the other hand, is not sufficient because there is a strong need to have evidence regarding the evolution of the microstructure. Thus, it seems clear that further advances in this field require both experimental evidence and computational simulation of the process, in which the latter may help to understand the consequences of the assumptions made in the physical theories.

Early work performed to model solidification phenomena has been restricted to the macroscopical level [1], which is governed by the energy equation

$$\rho c\dot{T} + \rho L\dot{f}_{pc} = \nabla(k\,\nabla\,T) \tag{1}$$

where ρ is the density, c is the specific heat, k is conductivity, T is temperature, L is the specific latent heat associated to phase change, f_{pc} is the phase change function ($0 \leqslant f_{pc} \leqslant 1$), ∇ is the gradient operator, and the dot on top of a variable indicates time derivative. This is a nonlinear problem, on account of the changes that take place in the material parameters with the temperature evolution. The solution has been carried out using a space discretization with finite elements and a time discretization using finite differences (see, for example, Ref. [1]).

Microscopic models formulated in the past to deal with solidification in metals do not use an explicit phase change function but used its time variation as a function of the time variation of different independent state variables. For equiaxial solidification problems, it is possible to write

$$\dot{f}_s = A_N\dot{N} + A_R\dot{r} \tag{2}$$

where fs is the solid fraction, N is the density of nuclei, r is the average grain size, and A_N and A_R are nucleation and grain growth functions that depend on the specific kinetics model.

For the solidification process, the phase change function is the liquid fraction, i.e., $f_{pc}=1-fs$. In a macroscopic analysis, the phase change f_{pc} is an explicit function of T, so that temperature becomes the only independent variable in the problem. But such an analysis cannot predict microstructural properties for the different phases that develop with solidification, including grain size, eutectic or dendritic spacing, type of microstructure, and percentages of each component. All those aspects can only be taken into account by employing a microstructural model.

At present, most authors agree that graphite nucleates directly in the liquid with spherical shape. There are two main theories to

Contributed by the Applied Mechanics Division of ASME for publication in the JOURNAL OF APPLIED MECHANICS. Manuscript received June 14, 2005; final manuscript received January 26, 2006. Review conducted by C. Buscaglia. Discussion on the paper should be addressed to the Editor, Prof. Robert M. McMeeking, Journal of Applied Mechanics, Department of Mechanical and Environmental Engineering, University of California—Santa Barbara, Santa Barbara, CA 93106-5070, and will be accepted until four months after final publication of the paper itself in the ASME JOURNAL OF APPLIED MECHANICS.

explain other details of the solidification behavior of SG cast iron. In the uninodular theory [2–9], the growth of graphite nodules occurs by carbon depositing directly from the liquid or by diffusion through a layer of solid austenite that surrounds a nodule (both graphite and austenite having spherical shape) or by a combination of both mechanisms. In the multinodular theory [10–18], on the other hand, austenite nucleates independently and grows in dendritic form, while graphite grows with spherical shape [13]. Initially, graphite grows in contact with liquid, but as it gains contact with austenite then the spherical nodules are surrounded by austenite. Once graphite is wrapped by austenite, the graphite spheres grow by diffusion of carbon, from the liquid, through the austenite. Simulations employing the multinodular theory have not yet been developed, with some exceptions of extremely simplified models [13,21,22].

This paper presents a numerical model for the simulation of equiaxial solidification of eutectic SG cast iron according to multinodular assumptions. Details of the microstructural model are given in Sec. 2, and results are shown in Sec. 3.

2 Microstructural Model of Solidification

2.1 Main Assumption at Microstructural Level. This model assumes the independent nucleation of austenite as a function of the cooling rate but in an instantaneous way. Continuous nucleation of graphite is assumed as a function of the liquid treatment and of undercooling. Austenite has dendritic growth, whereas graphite grows with spherical shape, but a distinction is made in the latter between growth in the interdendritic liquid and growth in the intergranular liquid. Mass balance of carbon is satisfied at all times. Moreover, a sequential computation of austenite and graphite evolutions is assumed, i.e., both evolutions are coupled, but to simplify the computations they are evaluated separately in a staggered form.

2.2 Carbon Concentration at Equilibrium in the Interfaces. To evaluate carbon concentrations at the equilibrium state of each phase at each temperature, the influence of silicon is taken into account in the equilibrium diagram Fe–C–Si. Following Heine [23], a two-dimensional equilibrium diagram is used, in which the liquidus and solidus lines and eutectic temperature are defined by functions that depend on the silicon and carbon contents. The carbon concentrations at equilibrium are given by

$$C^{l/\gamma} = \frac{1}{97.3}(1569 - T - 24.32Si)$$

$$C^{\gamma/l} = \frac{1}{177.9}(1528.4 - T - 32Si)$$

$$C^{l/gr} = \frac{1}{389.1}(T - 129.7Si + 503.2) \tag{3}$$

where $C^{l/\gamma}$ is the concentration of the liquid in contact with austenite, $C^{\gamma/l}$ is the concentration of austenite in contact with liquid, and $C^{l/gr}$ is the concentration of liquid in contact with graphite, all at temperature T and at equilibrium, and Si is the silicon content. All the concentrations are expressed in weight percent (wt. %) while the temperature in degrees celsius).

Silicon concentration is computed using Scheil law, in which a uniform concentration of silicon is assumed in the liquid and zero diffusion of such element is taken for the solid. This law has also been applied in Refs. [13,22].

2.3 Dendritic Equiaxial Growth. Several researchers have studied dendritic growth at a microstructural level [24–26]. Following Rappaz and Thévoz [24,25], the equiaxial dendritic growth of individual grains can be substituted by a spherical grain with a given fraction of the solid volume. The main assumptions made by Rappaz are as follows:

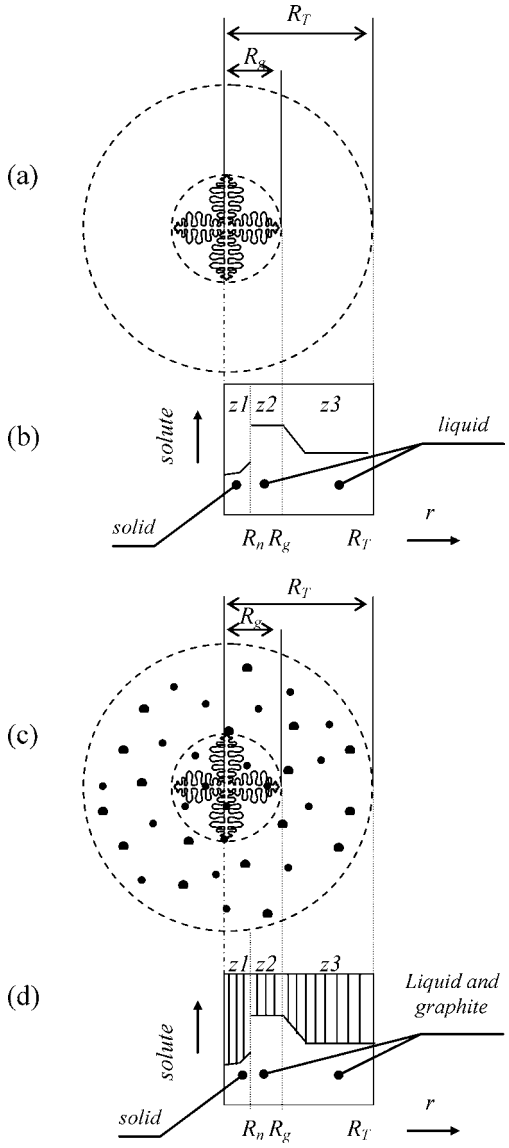

Fig. 1 (*a*) Schematic representation of equiaxial dendrite grain, (*b*) spherical solute concentration, (*c*) schematic representation of equiaxial dendrite grain and spherical graphite nodules, and (*d*) spherical solute concentration. Spherical symmetry is assumed in this work.

- The development of the microstructure is controlled by diffusion of solute.
- Temperature is uniform in a grain, so that the concentration of liquid in contact with the dendritic surface is also uniform and is equal to the concentration indicated by the line of liquidus in the corresponding equilibrium diagram at the considered temperature.
- Interdendritic liquid has a uniform composition.
- No diffusion of solute occurs in solid.
- Spherical diffusion of solute occurs in the intergranular liquid.
- The velocity of growth at the tips of the main dendrites is given by the kinetic equation governing the growth of isolated dendrites.

Figure 1(*a*) shows the equiaxial dendritic growth of an assumed spherical grain. The total grain radius R_T, is computed at the moment of instantaneous nucleation. The radius R_g corresponds to a spherical surface at the tip of the dendrites and grows during the

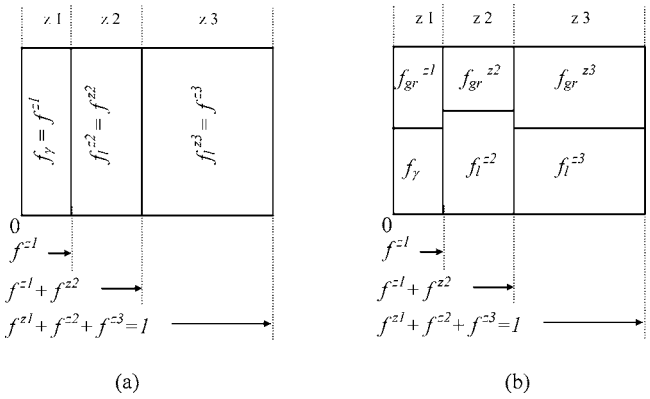

Fig. 2 (*a*) Component fractions of an equiaxial dendritic grain in the solidification of one phase and (*b*) Component fractions of an equiaxial dendritic grain in the solidification of an eutectic SG iron

solidification until it reaches the value R_T. Three spherical symmetric zones are identified in Fig. 1(*b*), in order to produce a simplified description of the solute concentration. Zone 1, defined as a sphere with radius R_n, shows the evolution of the solute contents in solid and covers the volumetric fraction corresponding to the total solid volume of the grain. Zone 2 covers a total volumetric fraction of $(4/3\pi(R_g^3 - R_n^3))$ and shows a uniform distribution of solute in the interdendritic liquid. Zone 3 covers $(4/3\pi(R_T^3 - R_g^3))$, with a variation of solute concentration in the intergranular zone. Changes are necessary in Figs. 1(*a*) and 1(*b*) if the solidification of an eutectic is analyzed, in which case a simultaneous dendritic solidification of austenite and the spherical solidification of the graphite nodules occurs, because changes occur in the solid fractions and solute concentrations in each zone; see Figs. 1(*c*) and 1(*d*).

2.4 Evaluation of Volumetric Fractions in the Eutectic Grain. The external rectangle in Fig. 2 represents the total grain volume, which is divided into three zones. Figure 2(*a*) shows the components of the whole volume of the grain for the case where only austenite solidification occurs. Figure 2(*b*) shows the components of the whole volume of the grain for the case where both dendritic austenite and graphite nodules distributed in the total grain volume solidify. In Fig. 2(*b*), zone 1 has austenite and graphite surrounded by austenite; zone 2 is formed by interdendritic liquid and graphite, and zone 3 has intergranular liquid and graphite. To compute those fractions, the following relations are used:

$$f^{z1} = \frac{R_n^3}{R_T^3} = f_\gamma + f_{gr}^{z1}$$

$$f^{z2} = \frac{(R_g^3 - R_n^3)}{R_T^3} = f_l^{z2} + f_{gr}^{z2}$$

$$f^{z3} = \frac{(R_T^3 - R_g^3)}{R_T^3} = f_l^{z3} + f_{gr}^{z3} \tag{4}$$

where f^{zn} is the volumetric fraction of zone n, and

$$f_\gamma = \frac{R_n^3}{R_T^3} - f_{gr}^{z1} = f^{z1} - f_{gr}^{z1} \tag{5}$$

where f_γ is the total volumetric fraction for the austenite. Furthermore,

$$f_{gr}^{z1} = \frac{\sum_{j=1}^{k} N_{grj}^{oz1} R_{grj}^{z13}}{R_T^3} = \frac{4}{3}\pi \sum_{j=1}^{k} N_{grj}^{z1} R_{grj}^{z13}$$

$$f_{gr}^{z2} = \frac{\sum_{j=1}^{k} N_{grj}^{oz2} R_{grj}^{3}}{R_T^3} = \frac{4}{3}\pi \sum_{j=1}^{k} N_{grj}^{z2} R_{grj}^{3}$$

$$f_{gr}^{z3} = \frac{\sum_{j=1}^{k} N_{grj}^{oz3} R_{grj}^{3}}{R_T^3} = \frac{4}{3}\pi \sum_{j=1}^{k} N_{grj}^{z3} R_{grj}^{3} \tag{6}$$

where f_{gr}^{z1}, f_{gr}^{z2}, and f_{gr}^{z3} are the total volumetric fraction of graphite in zone 1 (already surrounded by austenite), zone 2 (interdendritic), and zone 3 (integranular), $N_{gr}^{z1}, N_{gr}^{z2}, N_{gr}^{z3}$ are the number of graphite nodules in zones 1, 2, and 3, per unit volume of total grain, $N_{gr}^{oz1}, N_{gr}^{oz2}, N_{gr}^{oz3}$ are the number of graphite nodules in zones 1, 2, and 3, and R_{gr}^{z1}, R_{gr} are the radius of graphite nodules for zones 1, 2, and 3. The subscript j denotes the nodule group associated to a specific nucleation time and k stands for the total number of nodule groups.

Finally, the solid fraction may be written as

$$f_s = f_\gamma + f_{gr}^{z1} + f_{gr}^{z2} + f_{gr}^{z3} = f^{z1} + f_{gr}^{z2} + f_{gr}^{z3} \tag{7}$$

During the numerical analysis of solidification, a sequential computation of austenite and graphite evolutions is assumed and, therefore, some volumetric fractions need to be computed several times at each time step in order to properly take into account the coupling effects existing in the model. For example, the graphite fractions in each zone f_{gr}^{zn} have variations, in a given time step, with the nucleation and growth of nodules and with the increase in the radius R_n and R_g.

2.5 Nucleation and Grain Size in Eutectic Austenite. Nucleation of eutectic austenite is assumed to occur as soon as the eutectic temperature T_E is reached. There is experimental evidence [19,20] that a larger number of grains is obtained as a consequence of increasing cooling rate. The opposite occurs for lower cooling rates. This is due to the fact that, in most cases, an increase of the cooling rates leads to larger undercoolings. However, an instantaneous nucleation is assumed in the present model for austenite and, as an approximation, a linear function is proposed as

$$N_\gamma = A\frac{dT}{dt} \tag{8}$$

where N_γ is the density of austenite grains; A is a parameter that depends on the characteristics of liquid such as composition, superheating, and holding time. For simplicity, the final shape of the grains in equiaxial solidification is assumed to be spherical with radius R_T.

Based on the number of austenite grains that nucleate per unit volume, the total radius R_T is computed at each point of the spatial discretization, and it is kept constant during the whole analysis. At each representative volume, just one grain size is found, with a radius given by

$$R_T = \sqrt[3]{\frac{3}{4\pi N_\gamma}} \tag{9}$$

2.6 Nucleation of Graphite Nodules. Graphite nucleation is modeled as a continuous process, and occurs when:

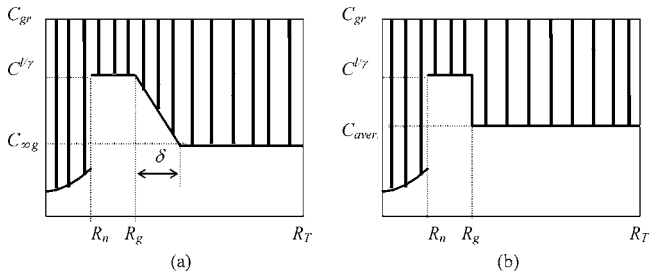

Fig. 3 (*a*) Carbon concentration considering the solute layer thickness and (*b*) carbon concentration without consideration of the solute layer

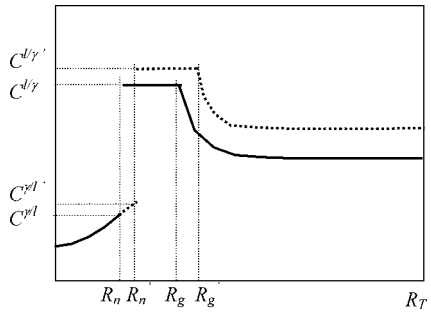

Fig. 4 Changes in the carbon concentration in a time step

- the temperature is below the eutectic temperature, and is lower than the lowest temperature reached since the beginning of the solidification process.
- the liquid fraction is not yet equal to zero.

A group of nodules nucleates with a given density, $N_{gr\,j}$, where index j identifies the nucleation group considered. Some of the nodules nucleate in the interdendritic liquid in zone 2 ($R_n < r < R_g$), and some in the intergranular liquid in zone 3 ($r > R_g$). Each time a group of nodules nucleates, its distribution is established between the two zones.

The nucleation of graphite is modeled in each zone by an exponential law, which takes the form [13]

$$N_{grj}^{z2} = \left[b\Delta T \exp\left(\frac{-c}{\Delta T}\right)(1 - f^{z1} - f_{gr}^{z2} - f^{z3})\Delta t \right]_j$$

$$N_{grj}^{z3} = \left[b\Delta T \exp\left(\frac{-c}{\Delta T}\right)(1 - f^{z1} - f^{z2} - f_{gr}^{z3})\Delta t \right]_j \qquad (10)$$

where N is the nodule density (nodules per unit volume) that nucleate during the time interval Δt, ΔT is the undercooling, and b and c are parameters that depend on the composition and liquid treatment. The nucleation remains very small until a "critical undercooling," which depends on the value of the interfacial energy between the nucleating phase and the substrate, is reached [13]. For larger undercoolings the nucleation rate markedly increases. The critical undercooling is directly proportional to the value of the parameter c. Equation (10) takes into account the decrease in the liquid fraction.

2.7 Austenite Growth. In a situation in which just austenite grows, the variation of concentration of carbon would be like in Fig. 1(*b*); however, for solidification of the eutectic, the graphite nodules are assumed distributed in the volume of the grain, then the variation of carbon would look like in Fig. 1(*c*) and Fig. 3(*a*). It is seen that there are discontinuities due to the presence of nodules with carbon contents of 100%. An even more simplified variation of concentration is shown in Fig. 3(*b*), for a uniform concentration of carbon C_{average} in all zone 3. In the present model, the concentration C_{average} is obtained through a mass balance carried out after the growth computation of R_n and the graphite nodules located in zone 3. Once the values of C_{average}, $C^{l/\gamma}$, δ, and R_g are known, the solute mass balance equation leads to the following expression of $C_{\infty g}$

$$C_{\infty g} = \frac{C^{l/\gamma}\delta(6R_g^2 + 4R_g\delta + \delta^2) + C_{\text{average}}(-R_T^3 + R_g^3)}{4R_g^3 + 6R_g^3\delta + 4R_g\delta^2 + \delta^3 - 4R_T^3} \qquad (11)$$

The growth of the tips of the main dendrites (R_g) is controlled by undercooling ($C^{l/\gamma} - C_{\infty g}$); furthermore, an increase of the total austenite fraction, which occurs through the growth produced on R_n, is obtained by a mass balance.

2.7.1 Kinetics of Growth at The Tip of a Dendrite. The growth of dendrite tips is assumed to be controlled by the diffusion of solute, and the influence of the thermal undercooling is neglected because the temperature is assumed constant for the whole grain. The velocity of growth of the tip of a dendrite is taken from Ref. [27], which was previously employed by several authors [24–26], in the form

$$\frac{dR_g}{dt} = \frac{DmC_0}{\pi^2\Gamma(k-1)}\left(\frac{C^{l/\gamma} - C_{\infty g}}{C_0}\right)^2 \qquad (12)$$

where D is the coefficient of diffusion of carbon in liquid, m is the slope of the austenite liquidus T_{AL}, Γ is the Gibbs-Thompson coefficient, C_0 is the initial concentration of carbon, and k is the coefficient that relates the concentrations of solid and liquid in equilibrium (distribution or partition coefficient). $C_{\infty g}$ is the concentration of carbon in intergranular liquid away from the limit zone δ (equivalent boundary layer).

2.7.2 Growth of R_n Due to Solidification of Austenite. Figure 4 shows the variation of carbon concentration at a time step, but to simplify the drawing, the concentrations of nodules are not represented. Concentrations and radius are given for time t, while those with a dash, R_n', R_g', $C^{\gamma/l\prime}$, and $C^{l/\gamma\prime}$, are associated to time $t+\Delta t$.

Assuming that there is no carbon diffusion through the spherical surface of radius R_T at the limit of a grain, the variation of solute distribution during solidification should be such that the contents of carbon in the grain is constant, so that the sum of the variation in the carbon content in the three zones becomes zero.

The variation of the mass carbon in zone 1 for time step Δt, assuming constant concentration in the solid in $[R_n, R_n']$ and equal to $kC^{l/\gamma}$, plus carbon variations in zones 2 and 3 at the same time step, is equal to zero. The mass balance equation is simplified by assuming a uniform (non-discrete) distribution of the volume of graphite nodules in the volume of zones 2 and 3. To achieve this, the model uses U_{gr}^{zn} (the carbon volume of the nodules per unit volume of the zone), which is computed as

$$U_{gr}^{zn} = \frac{4}{3}\pi\sum_{j=1}^{k} N_{grj}^{\circ zn}\frac{R_{grj}^3}{V_{zn}} = \frac{f_{gr}^{zn}}{f^{zn}} \quad \text{with} \quad n = 2,3 \qquad (13)$$

This U_{gr}^{zn} plays a role in the mass balance equation for each zone. The mass balance equation reads

$$\int_{R_n}^{R_g}(C^{l/\gamma'}-C^{l/\gamma})(1-U_{gr}^{z2})4\pi\rho_\gamma r^2dr + \int_{R_g}^{R_g'}C^{l/\gamma'}(1-U_{gr}^{z3})4\pi\rho_\gamma r^2dr - \int_{R_n}^{R_n'}C^{l/\gamma'}(1-U_{gr}^{z2})4\pi\rho_\gamma r^2dr + \int_{R_g}^{R_g'}C_{gr}U_{gr}^{z3}4\pi\rho_{gr}r^2dr - \int_{R_n}^{R_n'}C_{gr}U_{gr}^{z2}4\pi\rho_{gr}r^2dr + \int_{R_g}^{R_T}\frac{\partial C}{\partial t}\Delta t(1-U_{gr}^{z3})4\pi\rho_\gamma r^2dr - \int_{R_g}^{R_g'}C'_{(r)}(1-U_{gr}^{z3})4\pi\rho_\gamma r^2dr - \int_{R_g}^{R_g'}C_{gr}U_{gr}^{z3}4\pi\rho_{gr}r^2dr + \int_{R_g}^{R_T}\frac{\partial C}{\partial t}\Delta t(1-U_{gr}^{z3})4\pi\rho_\gamma r^2dr - \int_{R_g}^{R_g'}C'_{(r)}(1-U_{gr}^{z3})4\pi\rho_\gamma r^2dr\int_{R_g}^{R_g'}C_{gr}U_{gr}^{z3}4\pi\rho_{gr}r^2dr=0 \quad (14)$$

If the same nucleation law is used for zones 2 and 3, and the growth of the radius of nodules in those zones is computed as an average, then $U_{gr}^{z2}=U_{gr}^{z3}$. Therefore, it is possible to show that integration of the above equation leads to an expression for R_n' in the form

$$R_n'=\sqrt[3]{\frac{3DR_g^3\left.\frac{dC}{dr}\right|_{R_g}\Delta t+C^{l/\gamma}(1-k)R_n^3+(C^{l/\gamma'}-C^{l/\gamma})R_g^3}{C^{l/\gamma}(1-k)+(C^{l/\gamma'}-C^{l/\gamma})}} \quad (15)$$

The gradient in R_g, which is required to compute R_n' is here given by Zener's approximation [25–27]

$$\left.\frac{dC}{dr}\right|_{r=R_g}=\frac{C^{l/\gamma}-C_{\infty g}}{\frac{\delta}{2}} \quad \text{where} \quad \delta=\frac{2D}{\frac{dR_g}{dt}} \quad (16)$$

2.8 Distribution of Already Existing Nodules. The radius R_n and R_g change, so that some nodules that initially belonged to zone 2 may later belong to zone 1, while nodules in zone 3 will be later in zone 2. Note that the model assumes that the nodules do not move and the change in zones is only due to a modification of the boundaries given by radius R_n and R_g.

The variations in the densities of nodules in each zone for each group j in a given time step are

$$\Delta N_{grj}^{z1}=\frac{N_{grj}^{z2}}{f^{z2}}\frac{\frac{4}{3}\pi[(R_n+\Delta R_n)^3-R_n^3]}{V_T}$$

$$\Delta N_{grj}^{z2}=\left\{\frac{N_{grj}^{z3}}{f^{z3}}\frac{4}{3}\pi[(R_g+\Delta R_g)^3-R_g^3]-\frac{N_{grj}^{z2}}{f^{z2}}\frac{4}{3}\pi[(R_n+\Delta R_n)^3-R_n^3]\right\}/V_T$$

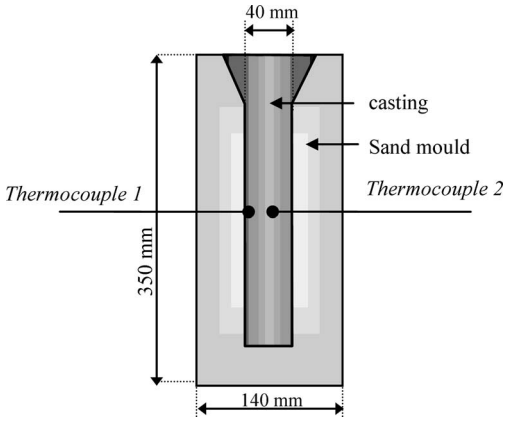

Fig. 5 Geometry of the coupon and the mold

$$\Delta N_{grj}^{z3}=-\frac{N_{grj}^{z3}}{f^{z3}}\frac{\frac{4}{3}\pi[(R_g+\Delta R_g)^3-R_g^3]}{V_T} \quad (17)$$

With a growth in radius R_n, some of the nodules that were before in zone 2 with radius $R_{gr\ j}^{z2}$, migrate to zone 1, in which the radius of the nodules of group j is $R_{gr\ j}^{z1}$. When this occurs, new radius $R_{gr\ j}^{z1}$ are computed, so that mass balance of carbon is satisfied

$${}^fR_{grj}^{z1}=\sqrt[3]{\frac{N_{grj}^{z1\ i}R_{grj}^{z1}+N_{grj}^{z2}\Delta f^{z1}R_{gr}}{N_{grj}^{z1}+N_{grj}^{z2}\Delta f^{z1}}} \quad (18)$$

2.9 Growth of Graphite Nodules in Liquid. The growth of austenite and graphite occurs at the same time; however, the computations in this step-by-step analysis are carried out by increasing austenite with a constant value in the number and size of graphite nodules, and vice versa. Graphite nodules grow in both the interdendritic and the intergranular liquids, but with different rates because zones 2 and 3 have different carbon concentrations, named $C^{l/\gamma}$ and $C_{\infty g}$ respectively. The growth of graphite nodules due to diffusion is modeled here using Zener's equation for a spherical isolated particle in a matrix with low saturation [2,13,28]. For nodules in zone 2, Zener's equation yields

$$\frac{dR_{gr}}{dt}=\frac{D\rho_l(C^{l/\gamma}-C^{l/gr})}{2R_{gr}\rho_{gr}(C_{gr}-C^{l/gr})} \quad (19)$$

For zone 3, it becomes

$$\frac{dR_{gr}}{dt}=\frac{D\rho_l(C_{\infty g}-C^{l/gr})}{2R_{gr}\rho_{gr}(C_{gr}-C^{l/gr})} \quad (20)$$

As soon as zone 3 vanishes, i.e., the main dendrite tips reach radius R_T, Eq. (19) is multiplied by $(1-f\gamma)$ to account for the event that some nodules are partially covered by austenite.

3 Numerical Results and Comparison to Other Techniques

Some examples are presented in this section to illustrate the behavior of the solidification of a SG cast iron. First, a cylindrical coupon cast in a sand mold is studied (see Fig. 5), for which experimental results were obtained in Ref. [13]. A refractory material is placed at the bottom of the coupon, and the top part is also isolated once casting is complete. The material properties, given in Table 1, correspond to ductile cast iron at the eutectic composition with Si=2.4 wt. %. The ambient temperature and the initial temperature of the mold is 25 °C. The initial temperature of the alloy is 1245 °C.

Table 1 Material properties, taken from [13]

Ductile Iron Properties	
Thermal conductivity [W/m°C]:	solid=30, mushy=25, liquid=30
Density (kg/m^3)	7000
Specific heat (kJ/kg°C)	$cp=0.61+1.214\times10^{-4}\times T$ for $777\,^\circ\mathrm{C}<T\leqslant1130\,^\circ\mathrm{C}$
	$cp=0.915$ for $T>1130\,^\circ\mathrm{C}$
Latent heat (kJ/kg)	185
Diffusion coefficient of C (m^2/s)	in liquid$=5.0\times10^{-10}$ in austenite$=9.0\times10^{-11}$
Nucleation parameters	$b=9.0\times10^{11}$ $c=250$ $A=1.0\times10^{08}$
Sand Properties	
Thermal conductivity (W/m°C)	1.1
Density (kg/m^3)	1500
Specific heat (kJ/kgK)	$cp=0.782+5.71\times10^{-4}\times T-1.88\times10^{-4}\times T^{-2}$ for $T\leqslant846$ K
	$cp=1.00+1.35\times10^{-4}\times T$ for $T>846$ K

Because of the isolation at both ends, together with the long axial dimension of the coupon, heat flow at the center occurs in radial direction and the problem is modeled considering a two-dimensional strip at the center. A finite element analysis was carried out using a special purpose program with 90 plane equiaxial elements with four nodes and Lagrangian interpolation.

Computational and experimental results of cooling curves are shown in Fig. 6, with good agreement not only at the center but also at the surface of the coupon. The evolution of liquid, austenite and graphite fractions at an intermediate location (half way between the central axis and the surface) has been plotted in Fig. 7. The velocity of growth of austenite increases as the nucleation of the graphite nodules becomes more intense due to the mass balance established in the model. The growth of the radius R_T, R_g, and R_n at an intermediate point is shown in Fig. 8. It can be seen that the tips of the main dendrites reach the edge of the grain; thus, that for most of the solidification time there are only two zones.

An important aspect of the solution is the distribution of graphite volume with identification of the radius of the nodules; this is shown in Fig. 9 for a point which is close to the surface of the coupon. Most of the total graphite volume is concentrated in nodules with a radius of ~15 μm. The density of nodules computed at a point located at half the radius from the central axis is 1.18×10^{13}, whereas the value recorded experimentally in Ref. [13] is 1.10×10^{13}.

4 Conclusions

This paper presented a new microstructural model to simulate the equiaxial solidification of an eutectic SG cast iron. This model can be coupled to the macro level, in which the heat flow problem is solved. The specific model is based on a plurinodular theory of solidification, in which there is independent nucleation of austenite and graphite. The problem includes both the spherical nodules of graphite and the dendritic growth of austenite, and the mass balance of solute (carbon) is satisfied at all steps of the process.

From the present model it is possible to obtain microstructural features arising from the solidification process, such as the density and distribution of the size of graphite nodules, and this has a direct consequence on the mechanical properties of the material. Furthermore, such predictions allow the identification of the grain size of austenite, which influences the mechanical properties

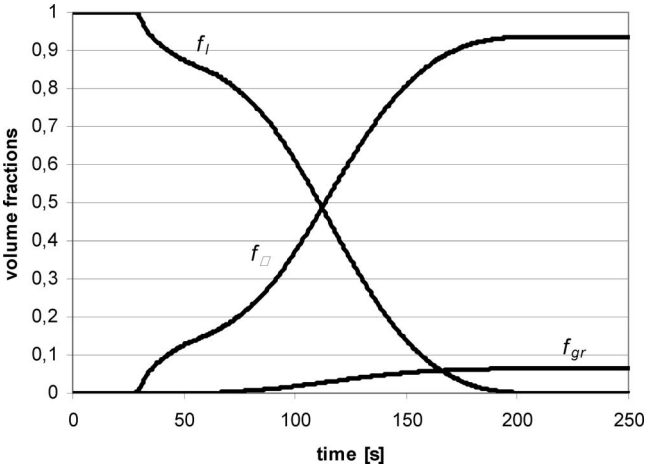

Fig. 7 Evolution of liquid (f_l), austenite ($f\gamma$), and graphite (f_{gr}) fractions at an intermediate location

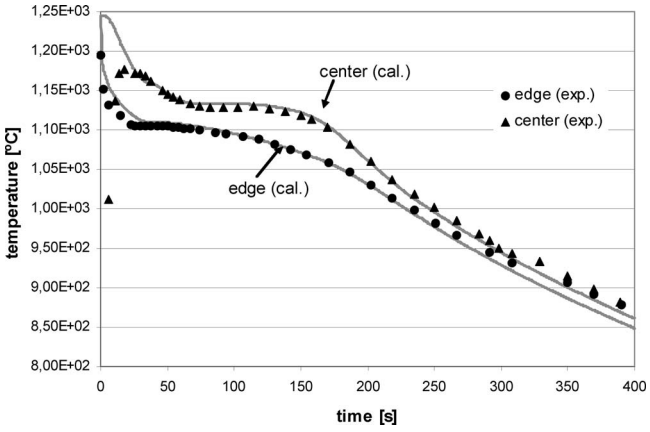

Fig. 6 Computational and experimental cooling curves at the casting edge and at the casting center

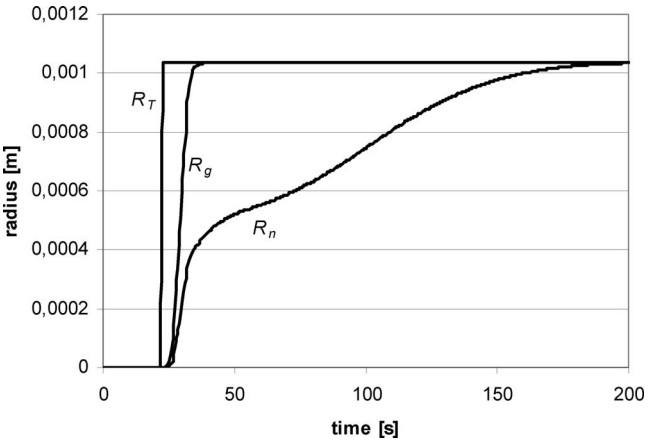

Fig. 8 Growth of the radii R_T, R_g, and R_n

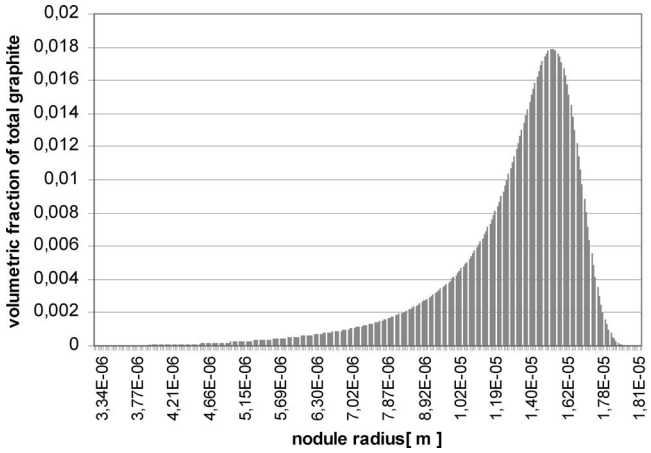

Fig. 9 Graphite volume distribution computed near the casting edge

through the distribution of microsegregation and its incidence on the phase changes that occur after solidification, leading to the final microstructure of the material. Those aspects serve to highlight the importance of an adequate modeling of solidification of austenite as the basis for simulations carried out during the eutectoid transformation.

The model implemented can serve to investigate changes in the laws of nucleation and growth, as well as the parameters of the microstructure; as such, this may help in the identification of adequate properties before testing is carried out to produce final technological decisions.

Acknowledgment

The support provided by the Science Research Council of Argentina (CONICET), the Chilean Council of Research and Technology CONICYT (FONDECYT Project 1060139) and the Department of Technological and Scientific Research at the University of Santiago Chile (DICYT-USACH) and gratefully acknowledged.

References

[1] Celentano, D., 1994, "Un Modelo Termomecánico para Problemas de Solidificación de Metales," Ph.D. thesis, Universidad Politécnica de Catalunya, Barcelona (in Spanish).

[2] Su, K., Ohnaka, I., Yamauchi, I., and Fukusako, T., 1984, "Computer Simulation of Solidification of Nodular Cast Iron," *Proceedings of the Third International Symposium on the Metallurgy of Cast Iron*, Stockholm, Elsevier, New York, pp. 181–189.

[3] Fras, E., 1984, "A Computer-aided Simulation of the Kinetics of Solidification of the Eutectic Ductile Cast Iron," *Proceedings of the Third International Symposium on the Metallurgy of Cast Iron*, Stockholm, Elsevier, New York, pp. 191–199.

[4] Fredriksson, H., and Svensson, I., 1984, "Computer Simulation of the Struture Formed During Solidification of Cast Iron," *Proceedings of the Third International Symposium on the Metallurgy of Cast Iron*, Stockholm, Elsevier, New York, pp. 273–284.

[5] Castro, M., Alexandre, P., Lacaze, J., and Lesoult, G., 1989, "Microstructures and Solidification Kinetics of Cast Irons: Experimental Study and Theoretical Modelling of Equiaxed Solidification of S. G. and Grey Cast Iron," *Proceedings of the Fourth International Symposium on the Metallurgy of Cast Iron*, Tokyo, Materials Research Society, Warrendale, PA, pp. 433–440.

[6] Onsoien, M. I., Grong, O., Gundersen, O., and Skaland, T., 1999, "A Process Model for the Microstructure Evolution in Ductile Cast Iron: Part I. The Model," Metall. Mater. Trans. A, **30**, pp. 1053–1068.

[7] Onsoien, M. I., Grong, O., Gundersen, O., and Skaland, T., 1999, "A process Model for the Microstructure Evolution in Ductile Cast Iron: Part II. Applications of the Model," Metall. Mater. Trans. A, **30**, pp. 1069–1079.

[8] Liu, B. C., Zhao, H. D., Liu, W. Y., and Wang, D. T., 1999, "Study of Microstructure Simulation of Spheroidal Graphite Cast Iron," Cast Met. Res. J., **11**(5), pp. 471–476.

[9] Zhao, H., and Liu, B., 2001, "Modeling of Stable and Metastable Eutectic Transformation of Spheroidal Graphite Iron Casting," ISIJ Int., **41**(9), pp. 986–991.

[10] Rickert, A., and Engler, S., 1984, "Solidification Morphology of Cast Irons," *Proceedings of the Third International Symposium on the Physical Metallurgy of Cast Iron*, Stockholm, Elsevier, New York, pp. 165–174.

[11] Hummer, R., 1984, "A Study of the Shrinkage and Dilatation During Solidification of Nodular Cast Iron—Its Relation to the Morphology of Crystallisation," *Proceedings of the Third International Symposium on the Metallurgy of Cast Iron*, Stockholm, Elsevier, New York, pp. 213–222.

[12] Stefanescu, D. M., and Bandyopadhyay, D. K., 1989, "On the Solidification Kinetics of Spheroidal Graphite Cast Iron," *Proceedings of the Fourth International Symposium on the Physical Metallurgy of Cast Iron*, Tokio, Materials Research Society, Warrendale, PA, pp. 15–26.

[13] Boeri, R., 1989, "The Solidification of Ductile Cast Iron," Ph.D. thesis, University of British Columbia, Canada.

[14] Sikora, J., Rivera, G., and Biloni, H., 1990, "Metallographic Study of the Eutectic Solidification of Gray, Vermicular and Nodular Cast Iron," *Proceedings of F. Weimberg International Symposium on Solidification Processing*, Pergamon Press, New York, pp. 280–288.

[15] Rivera, G., Boeri, R., and Sikora, J., 1995, "Revealing the Solidification Structure of Nodular Iron," Cast. Met., **8**(1), pp. 1–5.

[16] Rivera, G., Boeri, R., and Sikora, J., 1997, "Counting Eutectic Grains in SG Cast Iron," Adv. Mater. Res. (N.Y.), **4**, pp. 169–174.

[17] Rivera, G., Boeri, R., and Sikora, J., 1999, "Influence of the Solidification Microstructure on the Mechanical Properties of Ductile Iron," Cast Met. Res. J., **11**(5), pp. 267–272.

[18] Rivera, G., 2000, "Estructura de Solidificación de Fundiciones de Hierro con Grafito Esferoidal," Ph.D. thesis, Universidad Nacional de Mar del Plata, Mar del Plata (in Spanish).

[19] Sikora, A., Boeri, R., and Rivera, G., 2001, "Characteristics of Austenite in Ductile Iron: Its Influence on the Microstructure and Properties," *Proceedings of the International Conference on the Science of Casting and Solidification*, Editura Lux Libris, Brasov, Romania, pp. 321–329.

[20] Boeri, R., Sikora, A., 2001, "Solidification Macrostructure of Spheroidal Graphite Cast Iron," Cast Met. Res. J., **13**, pp. 307–313.

[21] Dardati, P. D., Celentano, D. J., Godoy, L. A., Boeri, R. E., 2002, "Simulación Numérica del Proceso de Solidificación de la Fundición Dúctil," Mecánica Computacional, XXI, pp. 2855–2874 (in Spanish).

[22] Dardati, P. D., Celentano, D. J., Godoy, L. A., and Boeri, R. E., 2006, "Numerical Simulation of Solidification Processes of Spheroidal-Graphite Cast Iron," J. Comput. Methods Sci. Eng. (accepted for publication).

[23] Heine, H., 1986, "The Fe–C–Si solidification diagram for cast irons," AFS Transactions, **71**, pp. 391–402.

[24] Rappaz, M., and Thévoz, P., 1987, "Solute Diffusion Model for Equiaxed Dendritic Growth," Acta Metall., **35**(7), pp. 1487–1497.

[25] Rappaz, M., and Thévoz, P., 1987, "Solute Diffusion Model for Equiaxed Dendritic Growth:Analitical Solution," Acta Metall., **35**(12), pp. 2929–2933.

[26] Nastac, L., and Stefanescu, D., 1996, "Simulation of Microstructure Evolution During Solidification of Inconel 718," AFS Trans., **104**, pp. 96–193.

[27] Kurz, W., and Fisher, D. J., 1986, *Fundamentals of Solidification*, Trans Tech Publications, Switzerland.

[28] Wetterfall, S. E., Fredriksson, H., and Hillert, M., 1972, "Solidification Process of Nodular Cast Iron," J. Iron Steel Inst., London, **210**, pp. 323–333.

Javier Quinteros
Laboratorio de Tectónica Andina,
Departamento de Geología,
Facultad de Cs. Exactas y Naturales – UBA,
Buenos Aires, Argentina
e-mail: jquinte@dc.uba.ar

Pablo M. Jacovkis
Departamento de Computación
and Instituto de Cálculo,
Facultad de Cs. Exactas y Naturales – UBA,
Buenos Aires, Argentina
e-mail: jacovkis@dc.uba.ar

Victor A. Ramos
Laboratorio de Tectónica Andina,
Departamento de Geología,
Facultad de Cs. Exactas y Naturales – UBA,
Buenos Aires, Argentina

Evolution of the Upper Crustal Deformation in Subduction Zones

The uplift and evolution of a noncollisional orogen developed along a subduction zone, such as the Andean system, is a direct consequence of the interrelation between plate tectonic stresses and erosion. Tectonic stresses are related to the convergence velocity and thermal state, among other causes. In this paper, a new model designed to investigate the evolution of the topography and the upper crustal deformation of noncollisional orogens in a subduction zone produced by the oceanic crust being subducted is presented. The mechanical behavior of the crust was modeled by means of finite elements methods to solve Stokes equations for a strain-rate-dependent viscoplastic rheology. The model takes into account erosion effects using interface-tracking methods to assign fictitious properties to nonmaterial elements. [DOI: 10.1115/1.2204962]

1 Objectives

The modeling of the processes related to crustal deformation, due to compression or extension, has been approached in a number of different ways in the last decade. On one side, models that analyze small scale crustal deformation have reached accurate and satisfactory results using mainly formal numerical methods [1]. On the other side, the development of numerical models to study the large-scale crustal deformation is continuously evolving because of the multiplicity of processes that take part in the whole evolution of the deformation. Some of these are models based in geometrical properties, considering isotropic rocks [2], whereas others try to represent more complicated mechanical and rheological properties [3–5]. In the last few years, many authors [6–8] have used the method proposed by Fullsack [9] for the study of orogens formed by the collision of two plates. In this work, a model for noncollisional formed mountain belts (orogens) and well suited for subduction zones is developed. (see Fig. 1)

2 Geological Concepts

In the last few years, several authors have discussed the importance of the different factors that control the uplift of an orogen like the Andes. Some of them suggest that the absolute motion and direction of the plate movement and its convergence velocity are the main causes for the development of an orogen [10], while others relate it to the amount of sediments in the trench [11] or the absolute velocity of the plates [12,13]. Anyway, there is actually some consensus on the idea that, in an orogen like the Andes, all these factors can contribute to the generation of stresses along the plate interface. This fact controls the development of the general tectonics of an Andean orogen [11]. The deformation will also be strongly conditioned by the position of the magmatic arc, which implies a higher thermal flux in the zone.

In some subduction systems, depending on the coupling between both plates and its features, friction may imply huge quantities of material removal from the overriding plate. This process is known as *crustal (or subduction) erosion* and has been proved to be one of the main causes of the magmatic arc shifting. The reason is that if the angle of subduction is kept unchanged, the magmatic arc should always be at the same distance from the trench. But, as the trench has moved into the overriding plate, because of the material eroded, the magmatic arc shall migrate in order to keep the distance [14].

At the same time that tectonic stresses deform the upper crust and the orogen develops, erosion can affect the surface, resulting in deeper rocks being exhumated. One of the main causes of erosion is precipitation. It is common that when the orogen reaches a certain yield altitude, precipitation concentrates on the side where the humid winds come from [15]. When the difference in precipitation is considerable, the phenomenon is known as *orographic rain shadow*.

3 Numeric Model

The model presented in this paper consists of three different parts. First, a tectonic model was developed to predict the upper (continental) crustal deformation as a result of the forces applied by the oceanic slab being subducted. In second place, a surface and subduction erosion model was implemented. Finally, an isostatic compensation model takes into account the flexural behavior of the lithosphere. All these models are coupled at each time step modifying the deformation produced by the compression.

3.1 Tectonic Model. Although the upper crust is made of rigid solid material, large-scale long-term deformation (tens of thousands of years) is usually modeled by means of fluid dynamics equations [9]. In this case, Stokes equations were employed because the process is considered quasi-static and inertial terms are negligible [16]. The dimensionless Reynolds number was considered to be zero in order to model the fluid as laminar and without turbulence. The problem was posed as two-dimensional (2D) and in a plane-strain state. The transect (vertical section) was designed with a 700 km long bidimensional mesh consisting of 1881 nodes (Fig. 2).

Finite elements used are Q_2-P_1 type [17], capable of biquadratic interpolation for velocities (nine nodes) and lineal interpolation for pressures (three nodes). It has been proved that this element satisfies the inf-sup condition [18,19], the basic mathematical criterion that determines whether a finite element discretization is stable and convergent, and avoids side-effects as the

Contributed by the Applied Mechanics Division of ASME for publication in the JOURNAL OF APPLIED MECHANICS. Manuscript received June 27, 2005; final manuscript received April 17, 2006. Review conducted by G. C. Buscaglia. Discussion on the paper should be addressed to the Editor, Prof. Robert M. McMeeking, Journal of Applied Mechanics, Department of Mechanical and Environmental Engineering, University of California – Santa Barbara, Santa Barbara, CA 93106-5070, and will be accepted until four months after final publication of the paper itself in the ASME JOURNAL OF APPLIED MECHANICS.

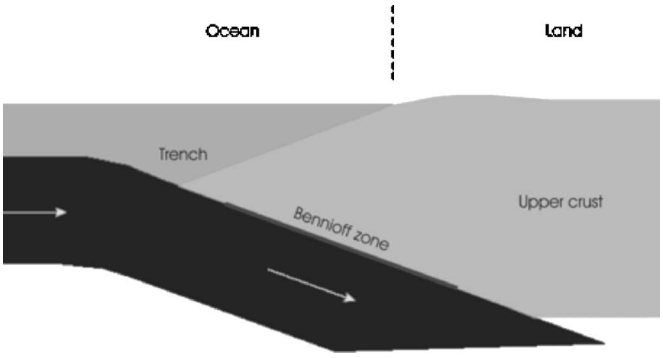

Fig. 1 Schematic graphic of a subduction zone

checkerboard distribution of pressure [19].

3.1.1 Finite Elements Resolution. The Cauchy stress tensor (σ) is defined as

$$\sigma_{ij} = S_{ij} + P \,.\, \delta_{ij} \tag{1}$$

where S is the deviatoric stress tensor, P is the trace of the stress tensor or hydrostatic component, and δ is the Kronecker δ function. The governing differential equations are the incompressibility equation (Eq. (2)) and the equilibrium equation (Eq. (3))

$$\nabla \underline{v} = 0 \tag{2}$$

$$\nabla \sigma + \rho \underline{g} = 0 \tag{3}$$

The constitutive relation is

$$S_{ij} = 2\mu \dot{\varepsilon}_{ij} \tag{4}$$

Here $\underline{v}$ is the velocity of the fluid, ρ is the density, $\underline{g}$ is the gravity acceleration, μ is viscosity, and $\dot{\varepsilon}$ is the strain rate. The latter is defined as

$$\dot{\varepsilon}_{ij} = \frac{1}{2}\left[\frac{\partial v_i}{\partial x_j} + \frac{\partial v_j}{\partial x_i}\right] \tag{5}$$

where v_i is the velocity of the fluid in the i direction.

Starting with the virtual work principle

$$\int_V \sigma_{ij} \delta \dot{\varepsilon}_{ij} \, \partial V = \int_V f_i^B \delta v_i \, \partial V + \int_\Pi f_i^S \delta v_i \, \partial \Pi \tag{6}$$

and splitting strain rate in a deviatoric and a volumetric part

$$\dot{\varepsilon}_{ij} = \dot{e}_{ij} + \frac{\dot{\varepsilon}_v}{3}\delta_{ij} \tag{7}$$

Equation (1) and (7) can be replaced into Eq. (6) namely,

$$\int_V (S_{ij} \delta \dot{e}_{ij} + P \delta \dot{\varepsilon}_v) \, \partial V = \int_V f_i^B \delta v_i \, \partial V + \int_\Pi f_i^S \delta v_i \, \partial \Pi \tag{8}$$

Including the constitutive relation (Eq. (4)), it can be rewritten it as

$$\int_V \delta\varepsilon^T \left(I - \frac{1}{3}mm^T\right)^T 2\mu \left(I - \frac{1}{3}mm^T\right) \delta\dot{\varepsilon} \, \partial V + \int_V \delta\varepsilon^T mP \, \partial V = \int_V f_i^B \delta v_i \, \partial V + \int_\Pi f_i^S \delta v_i \, \partial \Pi \tag{9}$$

where $m=[1,1,0,1]$.

After discretization and some algebraic simplification,

$$\left[\int_V B^T \left(I - \frac{1}{3}mm^T\right)^T 2\mu \left(I - \frac{1}{3}mm^T\right) B \, \partial V\right] U + \int_V B^T m H_P P \, \partial V = \left[\int_V Hb \, \partial V + \int_\Pi H^S t \, \partial \Pi\right]$$

is derived, where H is the velocity shape functions matrix, B is the velocity derivative functions matrix, and H_P is the pressure shape functions matrix.

Finally, the following system of equations:

$$K_{uu} U + K_{up} P = R \tag{10}$$

is obtained, where

$$K_{uu} = \int_V B^T \left(I - \frac{1}{3}mm^T\right)^T 2\mu \left(I - \frac{1}{3}mm^T\right) B \, \partial V \tag{11}$$

$$K_{up} = \int_V B^T m H_P \, \partial V \tag{12}$$

$$R = \int_V Hb \, \partial V + \int_\Pi H^S t \, \partial \Pi \tag{13}$$

Rewriting Eq. (2),

$$\int_V \delta P (\nabla v) \, \partial V = 0 \tag{14}$$

$$\int_V \delta P^T H_P^T \dot{\varepsilon}_V \, \partial V = 0 \tag{15}$$

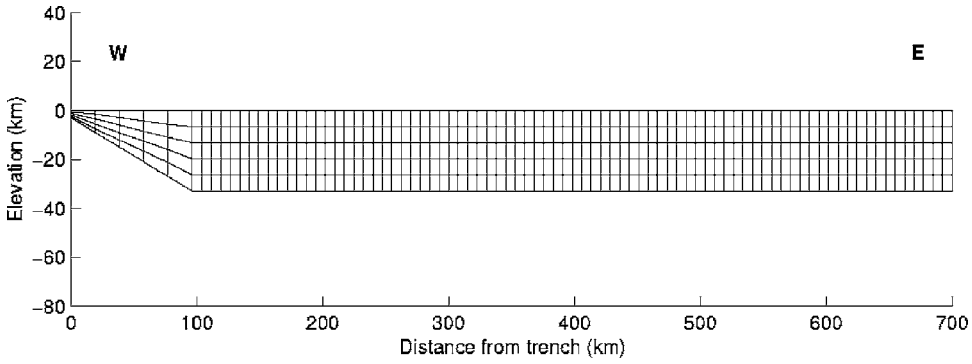

Fig. 2 Geometry of the vertical section and mesh used

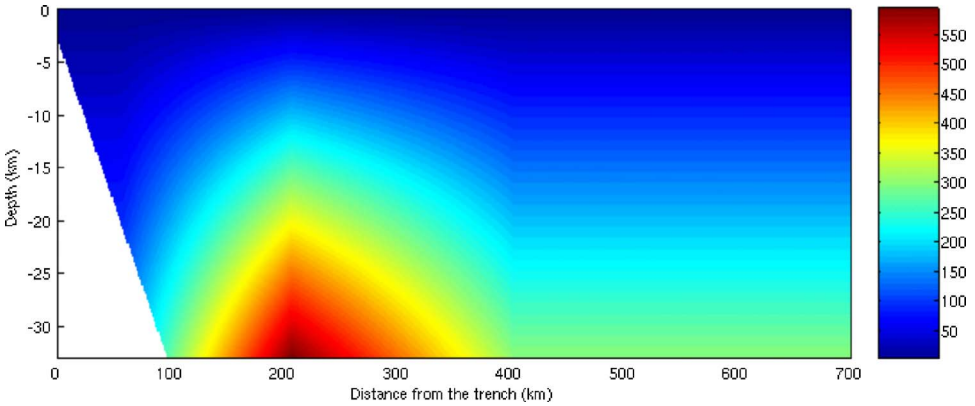

Fig. 3 Temperature distribution at the beginning of simulation

$$\delta P^T \left[\int_V H_P^T m^T B \, \partial V \right] U = 0 \tag{16}$$

where

$$\int_V H_P^T m^T B \, \partial V = K_{up}^T \tag{17}$$

Finally, the system given in Eqs. (10) and (16) can be expressed as

$$\begin{bmatrix} K_{uu} & K_{up} \\ K_{up}^T & 0 \end{bmatrix} \begin{bmatrix} U \\ P \end{bmatrix} = \begin{bmatrix} R \\ 0 \end{bmatrix} \tag{18}$$

3.1.2 Rheology: Dependence and Numerical Resolution. Temperature in a subduction zone is highly variable from the spatial point of view but quite stable through time, especially when considering large-scale modeling. As the viscosity of a rock (μ) is related to the temperature to which it is exposed, the variation in viscosity can be of several orders of magnitude between minimum and maximum values. Penalization techniques were avoided because of this, as it is probable that the precision needed turns the matrix to being ill-conditioned. Mixed elements are used instead in order to achieve the totally incompressible solution.

Temperature is considered to have a bidimensional distribution, as can be seen in Fig. 3, and is based on the classical study of Ernst [20]. The magmatic arc position (the warmest part) is consistent with the subduction angle, the supposed depth where the magmas were produced and the geological evidence.

In the uppermost part of the lithosphere, temperature, and pressure are relatively low, and fractures and frictional sliding define the mechanical behavior. That is known as *brittle regime*. When depth increases, and also temperature and pressure, plastic flow is the default mechanical behavior [21]. That process is called *ductile regime*.

Many authors have studied the behavior of the different rocks and the varying temperature and pressure conditions to which they are exposed [22,23]. Although sometimes, exclusively, temperature-dependent viscosity is used in modeling [7], it is usual to consider more than one variable for rheology that has to be used in large-scale modeling, particularly strain rate $\dot{\varepsilon}$, material rigidity A, temperature T, activation energy Q, and a power-law exponent n, among others (Eq. (19)). Many of these constants can be seen in Table 1. The viscosity is defined as

$$\mu = A^{(-1/n)} \cdot \dot{\varepsilon}_{II}^{(1-n)/n} \cdot e^{Q/nRT} \tag{19}$$

where $\dot{\varepsilon}_{II}$ is the second invariant of the strain-rate tensor and R is the universal gas constant [24].

In order to be consistent with the *brittle regime*, shear stress at any point cannot be greater than the maximum shear stress supported by rocks (σ_y) [25] that can be expressed as

$$\sigma_y = \sigma_0 + \frac{\Phi - 1}{\Phi} \rho g z \tag{20}$$

where σ_0 is the frictional cohesive strength, $(\Phi - 1)/\Phi$ is the coefficient of friction,

$$\Phi = [(1 + \eta^2)^{1/2} - \eta]^{-2} \tag{21}$$

and

$$\eta = \tan(\theta) \tag{22}$$

θ being the angle of internal friction considered.

Because of the nonlinearity produced due to the strain-rate dependence, an iterative algorithm (Table 2) is used until a desired level of convergence is achieved.

For the first iteration, the viscosity μ is calculated as a function of temperature T and a reference strain rate $\dot{\varepsilon}_0$. The viscosity distribution calculated is used to assemble the finite element matrix and to calculate the pressures and velocities. Later, the strain rate is recalculated using the velocity, and the viscosity is updated based on the resulting strain rate.

For elements in which the resulting shear stress (Eq. (4)) is greater than the frictional failure criterion (Eq. (20)), the effective viscosity μ is reset to

$$\mu = \frac{\sigma_y}{2\dot{\varepsilon}_{II}} \tag{23}$$

Once the viscosity difference between two iterations is considered to be small enough (lesser than a tolerance (TOL)), iteration ends.

Table 1 Model parameters

Parameter	Definition	Value	Units
A	Material strength constant	2.91×10^{-3}	$MPa^{-1}\ s^{-1}$
Q	Molar activation energy	151	$kJ\ mol^{-1}$
n	Power law exponent	1.8	
R	Universal gas constant	8.3144	$J\ mol^{-1}\ K^{-1}$
T	Temperature		K
$\dot{\varepsilon}_o$	Reference strain rate	10^{-14}	s^{-1}
σ_0	Frictional cohesive strength	50	MPa
Θ	Angle of internal friction	15	deg
S_w	Initial atmospheric water (vapor) flux	8×10^{11}	$mm^2\ yr^{-1}$
Δt	Time step	10^4	yr
hs	Altitude scale		
mpc	Minimum precipitation coefficient		
apc	Available precipitation coefficient		

Table 2 Algorithm to calculate deformation due to tectonic compression

1: **procedure** STOKES	
2: $\mu_0 \leftarrow f(T, \dot{\varepsilon}_0)$	▷ Start with a reference strain rate
3: **repeat**	
4: $K \leftarrow K(\mu_k)$	▷ Assemble stiffness matrix
5: $P=(K_{up}^T K_{uu}^{-1} K_{up})^{-1} K_{up}^T K_{uu}^{-1} R$	▷ Calculate pressure
6: $U=K_{uu}^{-1}[R-K_{up}P]$	▷ Calculate velocity
7: $\dot{\varepsilon}_{ij}=\frac{1}{2}\left[\frac{\partial v_i}{\partial x_j}+\frac{\partial v_j}{\partial x_i}\right]$	▷ Calculate strain rate
8: k++	▷ Go to the next step
9: $\mu_k \leftarrow f(T, \dot{\varepsilon}_{II})$	▷ Recalculate viscosity
10: **If** $S > \sigma_y$ **then**	▷ If stress > failure criterion
11: $\mu_k=\frac{\sigma_y}{2\dot{\varepsilon}_{II}}$	▷ Reset viscosity
12: **end if**	
13: **until** $\|\mu_k-\mu_{k-1}\| < \mathrm{TOL}$	
14: **end procedure**	

3.1.3 Interface Tracking and Numerical Treatment. In this model, two interfaces are defined (Fig. 4):

- a surface interface, that tracks the shape of the topography resulting from the tectonic deformation and the erosion produced by the precipitation. This divides the material that has been eroded from the one that is still part of the crust.
- a Benioff interface, that separates the crust removed by subduction erosion from the remaining one.

Both interfaces are defined by several particles (an arbitrary number) whose movement through time is interpolated from the velocities calculated in the procedure defined in Table 2.

The surface interface is defined at the beginning of the model in the same position as the upper limit of the domain. The Benioff interface is defined as the western limit of the domain (Fig. 1). The model keeps record of the element to which every point of the interfaces belongs. Once the velocity of each Eulerian node is calculated, we check whether the point still belongs to the same element by means of the inverse of the affine transformation used in the elemental matrix calculation step. Otherwise, we find to which element the point has moved.

Later, the velocity of the interface point v_p is calculated interpolating the velocities from the four corner nodes v_i of the element using the form functions h_i of a four-node quadrilateral element (Eq. (24)), namely,

$$v_p = \sum_{i=1}^{4} h_i v_i \tag{24}$$

After that, the amount of erosion is calculated for every point (see Sec. 3.2) in the interface and its position corrected.

Both interfaces will be fully inside the domain in a few time steps because of the acting erosion processes. That means that there will be material that has been eroded, but it is still part of the Eulerian mesh. Different numerical treatments need to be implemented for the material eroded by precipitation and subduction.

At every Gauss point that belongs to material removed by precipitation, two things have to be addressed when the stiffness matrix is assembled: it should have zero density

$$\rho_{\mathrm{rem}} = 0 \tag{25}$$

and a fictitious viscosity several orders of magnitude less than the minimum value found in natural conditions

$$\mu_{\mathrm{rem}} \ll \min(\mu) \tag{26}$$

In this way, the material can be numerically *removed*, ensuring that the results are accurate.

In the case of the Benioff interface, tracking is not done based on the velocities resulting from the FEM calculations, because the velocity of the interface is known a priori. It moves with a constant horizontal velocity that has been determined by previous studies based on geological evidence. This velocity is obviously greater than the boundary condition imposed by the subduction compression.

All the material eroded (located to the left of the interface) is considered to be *rigid* material. Rigidity is achieved by assigning viscosity values several orders of magnitude greater than the maximum found in natural conditions

$$\mu_{\mathrm{rem}} \gg \max(\mu) \tag{27}$$

so the boundary conditions can *bypass* the material and be virtually imposed at the Benioff interface.

The time tracking of the problem is treated through the deformation of the Eulerian mesh at each time step (Table 1), based on the velocities calculation. The mesh is checked before any calculation in case an element has been affected by a large deformation that turns it to being ill-suited for the numeric resolution, although that never happened in any experiment because of the small CFL (Courant-Friedrichs-Lewy) number related to the boundary conditions and mesh grid.

3.2 Erosion Model. Apart from the tectonic processes, the topography is modified by erosion in different ways. Wind erosion and landslides can be considered as short-range processes, [26] whereas precipitation and the establishment of a natural drainage are long-range processes. As the main objective is to develop a

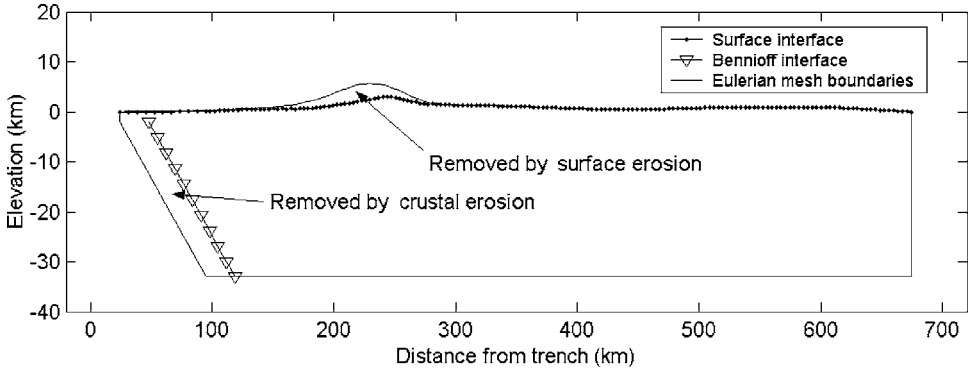

Fig. 4 Interfaces defined in the model to represent the surface and the Benioff zone

Table 3 Algorithm for erosion due to precipitation

```
1: procedure SURFACE EROSION (initwater)
2: S_w(1) ← initwater                                   ▷ Initialize available water
3: for x ← 2, interfacenodes do
4: R(x) ← (h(x)/hs + mpc)^2 S_w(x)/aps                  ▷ Calculate precipitation
5: If R(x) < 0 then
6: R(x) ← 0                                             ▷ Precipitation cannot be negative
7: end if
8: S_w(x) = S_w(x−1) − R(x)[pos(x) − pos(x−1)]          ▷ Discount water precipitated
9: end for
10: end procedure
```

coarse large-scale evolution of the topography, the erosion due to precipitation was considered a first-order approximation to the surface acting processes.

In order to estimate the erosion rate, the analysis is focused on three factors that favor erosion efficiency: millimeters of rain precipitated R, altitude h, and slope sl. Howard and Kerby [27] proposed a quantitative erosion law, based on empirical results, that includes all these factors. Recently, Willett expressed that the linear form of this law is able to capture the most important physical processes and provides the feedback mechanisms between orogen growth and erosion [28]. In this way, erosion rate (k) could be expressed as

$$k(x) = R(x)h(x)sl(x) \tag{28}$$

An initial atmospheric water (vapor) flux S_w is considered to be transported by the humid winds from the west [16]. Elevation determines how much of the available water is precipitated at every point, namely,

$$R(x) = \left(\frac{h(x)}{hs} + \text{mpc}\right)^2 \frac{S_w(x)}{\text{aps}} \tag{29}$$

Appropriate values for the different parameters (hs, mpc, aps) were calibrated taking into account present-day topography and precipitation distribution.

Surface slope ($sl(x)$) is included as a factor in Eq. (28) because it is supposed to determine the effectiveness of the erosion in a linear way [28].

After that, the water precipitated, taking into account the distance to the next node (c_L), is discounted from the total water flux (Eq. (30)), and the latter is moved to the east.

$$S_w(x+1) = S_w(x) - R(x)c_L(x) \tag{30}$$

The complete algorithm can be seen in Table 3.

3.3 Isostatic Compensation Model. The behavior of the lithosphere under conditions of tectonic uplift is similar to the behavior of a beam under load. Whenever a mountain rises, the deflection of the lithosphere occurs because of tectonic stacking of the crust, which produces relief and consequent extra weight [29]. It is known that lithosphere is in a state of equilibrium whenever it is at sea level height, which means that its thickness is about 33 km [30]. More (or less) than 33 km of thickness must be compensated, which means that it will bend until the system reaches equilibrium again.

The mechanical behavior of a beam can be expressed by means of Timoshenko's theory. Under this theory, a section of the beam that is initially normal to the neutral plane, remains as a plane and with the same length after deformation. Because of the shear deformations, this section does not remain normal to the neutral axis. Then, the total rotation of the plane β is given by the rotation of the tangent to the neutral axis ($\partial w/\partial x$) and the shear deformation γ (Eq. (31)),

$$\beta = \frac{\partial w}{\partial x} - \gamma \tag{31}$$

w being the vertical deflection.

The deformation of a cross section of the beam and the different angles of Eq. (31) can be seen in Fig. 5.

The equation that describes the deflection of a beam is

$$D\frac{\partial^4 w}{\partial x^4} + P\frac{\partial^2 w}{\partial x^2} = q(x) \tag{32}$$

where D is the flexural rigidity, P the horizontal forces exerted on the plate, and $q(x)$ the load applied. Anyway, for this type of geodynamical problems, horizontal forces are usually considered to be negligible ($P=0$) [30]; thus, the second term of the equation is discarded, namely,

$$D\frac{\partial^4 w}{\partial x^4} = q(x) \tag{33}$$

3.3.1 Finite Elements Resolution. By the way the problem is posed, and under the assumptions of Timoshenko's beam theory, the following variational formula can be derived from the virtual work principle (Eq. (6)):

$$EI\int_0^L \left(\frac{\partial \beta}{\partial x}\right)\delta\left(\frac{\partial \beta}{\partial x}\right)\partial x + \kappa GA\int_0^L \left(\frac{\partial w}{\partial x} - \beta\right)\delta\left(\frac{\partial w}{\partial x} - \beta\right)\partial V - \int_0^L p\,\delta w + m\,\delta\beta\,\partial x = 0 \tag{34}$$

where E is the Young's modulus, G is the shear modulus, A is the area of the yz cross section, p and m are the transverse and moment loading per unit length, respectively, and $\kappa = 5/6$ is a shear correction factor based on equating the shear strain energy yield by the constant shearing stress across the section and the actual shearing stress [31].

Displacements and rotations vector is defined as

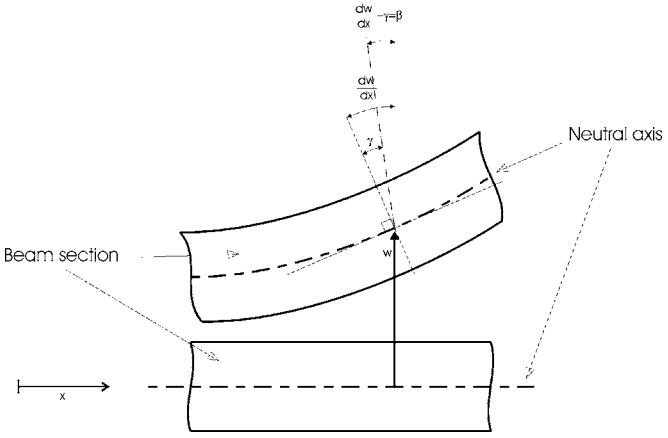

Fig. 5 Deformation of a beam cross section

$$U^T = [w_1, w_2, \ldots, w_N, \beta_1, \ldots, \beta_N] \tag{35}$$

where w_i is a displacement related with vertical deflection of node i, β_i is the rotation at the node, and N is the number of nodes.

Then, all the usual isoparametric formulations are employed in order to interpolate, namely,

$$w = H_w U \tag{36}$$

$$\frac{\partial w}{\partial x} = B_w U \tag{37}$$

$$\beta = H_\beta U \tag{38}$$

$$\frac{\partial \beta}{\partial x} = B_\beta U \tag{39}$$

Replacing into Eq. (34) and after some algebraic steps, we get

$$\left[EI \int_0^L B_\beta^T B_\beta \, \partial x + GA\kappa \int_0^L (B_w - H_\beta)^T (B_w - H_\beta) \, \partial x \right] U = \int_0^L H_w^T p \, \partial x + \int_0^L H_\beta^T m \, \partial x \tag{40}$$

The system of equations can be expressed as

$$KU = R \tag{41}$$

where

$$K = EI \int_0^L B_\beta^T B_\beta \, \partial x + GA\kappa \int_0^L (B_w - H_\beta)^T (B_w - H_\beta) \, \partial x \tag{42}$$

$$R = \int_0^L H_w^T p \, \partial x + \int_0^L H_\beta^T m \, \partial x \tag{43}$$

and where the terms of K are related to flexure and shear stress, respectively.

But in the context of an elastic plate overlying a fluidlike mantle, there is one process that has to be included in the equation: the isostatic restoring force (buoyancy) [29]. When the material added as tectonic load above the crust causes the lithosphere to bend, material from the mantle is displaced beneath the crust. The resistance of the underlying mantle related to the load can be addressed by including another term in the equation.

In this way, the governing equation can be expressed as

$$D \frac{\partial^4 w}{\partial x^4} + \Delta\rho g w = q(x) \tag{44}$$

where $\Delta\rho$ is the density contrast between the load and the upward restoring mantle and g is the acceleration of gravity.

Thus, K is modified in order to include this term in the system of equations, namely,

$$K = EI \int_0^L B_\beta^T B_\beta \, \partial x + GA\kappa \int_0^L (B_w - H_\beta)^T (B_w - H_\beta) \, \partial x + \int_0^L \Delta\rho g H_w \, \partial x \tag{45}$$

3.3.2 From the Beam to the Crust. The continental lithosphere is considered as a beam whose deflection under a certain load can be described by Eq. (44). As the lithosphere is in a state of equilibrium when its thickness is ~33 km, the tectonic load will be considered as the real thickness of the lithosphere minus the thickness of equilibrium state (33 km) [30].

Finding the correct flexural rigidity parameter D is not trivial and is a specific issue that must be addressed. In many cases, the lithosphere is not completely homogeneous and there can be zones of weakness due to temperature anomalies or to the history of the crust among other factors. In this case, the temperature is considered to be the most important factor. It is known that the higher the thermal flux, the weaker the zone is, which results in a locally compensated load [32].

These variations are treated through the correct setup of the effective elastic thickness T_e. Geodynamic researchers agree that this is not the real depth of the crust but a *mechanical* property related to its behavior when loaded [32]. Anyway, it is the depth that must be used in order to calculate the deflection because it reflects the strength of the crust.

In this direction, we follow the guidelines of previous works (see, for instance, Ref. [33]) that establish that the effective elastic thickness of the lithosphere is the depth at which the isotherm of 450°C is located. In this way, flexural rigidity D can be expressed as

$$D = \frac{EaT_e^3}{12} \tag{46}$$

where T_e is the effective elastic thickness and a is the width of the beam. Thus, in warmer zones, the isotherm is near the surface, T_e is smaller, and the beam is weaker.

At each time step, the deflection of the base of the upper crust is calculated by defining a one-dimensional (1D) beam with the same length as the lower boundary of the domain. The beam is considered to have no deflection or rotation at both boundaries. The load is calculated from the tectonic model topography. The density difference between the load applied and the material displaced by the deflection is calculated, taking into account how much of the deflection is filled. Namely, the density considered for the load is proportional to the infill of the deflection.

Once the deflection is calculated for the nodes of the beam, it is added to the vertical component of the tectonic velocity for each node in the domain. An example of the topography calculated by the tectonic model and the resulting topography after the compensation is shown in Fig. 6.

4 Geological Setting

The Southern Andes, as defined by Gansser [34], encompass the orogen developed along the Pacific margin of South America between 46°30′S (Gulf of Penas) and 56°S. The segment to the North of the Strait of Magallanes is known as the Patagonian Andes. Subduction has been continuous since early Cenozoic times (more than 65 My (millions of years)), although the main development of this segment took place after the late Oligocene (30–28 My) [35]. The sudden change in plate kinematics and the strong acceleration in the convergence rate [36] controlled the deformation until the late Miocene-Pliocene (10–3 My) [37], when an oceanic spreading ridge was subducted [38,39].

The Southern Patagonian Batholith is considered the backbone of the Patagonian Andes. It runs with a NNW trend continuously along all the segment and has an average width of 120 km [40]. The exhumation of the batholith indicates that it has suffered an extreme denudation, which was climaxed later by the establishment or enhancement of an orographic rain shadow by the middle Miocene (17–16 My). The rain shadow caused drastic climatic and ecologic changes as a result of more than 1 km uplift [41]. The total denudation estimated by fission track analysis ranges from 4 to 9 km west of the present-day water divide and decreases to <3 km to the east [42].

The facts that the batholith is located in the present forearc and that early Miocene magmatism activity evidence (Punta Daphne ca. 48°S) is found around 120 km from the present trench are considered to be proofs for subduction erosion occurring in this segment [42]. The apparent subduction angle at that moment [43] and the depth at which a typical magma should have been produced indicate that the original position of these could have been

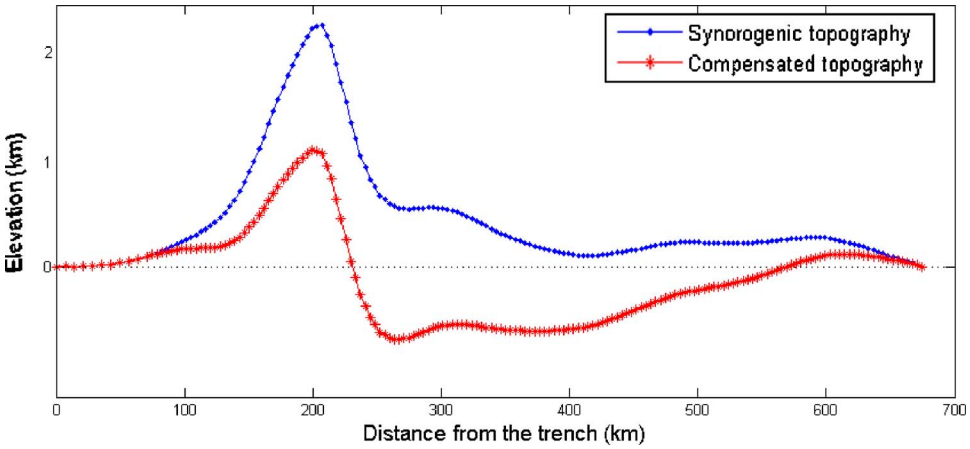

Fig. 6 Example of topography calculated by tectonic stresses before and after the isostatic compensation

more than 200 km away from the early Miocene trench. These facts indicate an approximate rate of more than 3 km/My of trench retreat.

4.1 Boundary Conditions for the Tectonic Model. As can be seen in Fig. 7, the upper (sea-level) side is defined as a free stress surface that represents the topography resulting from the tectonic process, not taking into account the acting erosion. The western side represents the contact between the eastward subducting Nazca plate and the South America continental plate. On that side, the subduction imposes a horizontal velocity of 3 mm/y to the east [36], and the vertical velocity is zero. The lower side represents the limit of the crust and was established at 33 km depth because of the rheological contrast with the deeper lithosphere. The vertical velocity was considered to be zero and the horizontal velocity was left free in the whole segment. On the eastern side all the nodes have a nonslip boundary condition; thus, the deformation is restricted.

5 Results

The model was applied to a transect (vertical section) at ~47°S. The results show that, at the beginning of the simulation, the deformation and uplift concentrate in the magmatic arc as a consequence of the thermal conditions. The high thermal flux in the magmatic arc causes the material to have low-viscosity values (Fig. 8), which results in a higher initial strain rate (Fig. 9) and in a weaker zone where material flows/deforms easily.

It can also be seen in Fig. 10 the change of orientation for the maximum strain rate, which moved from the "Retro-shear" to the

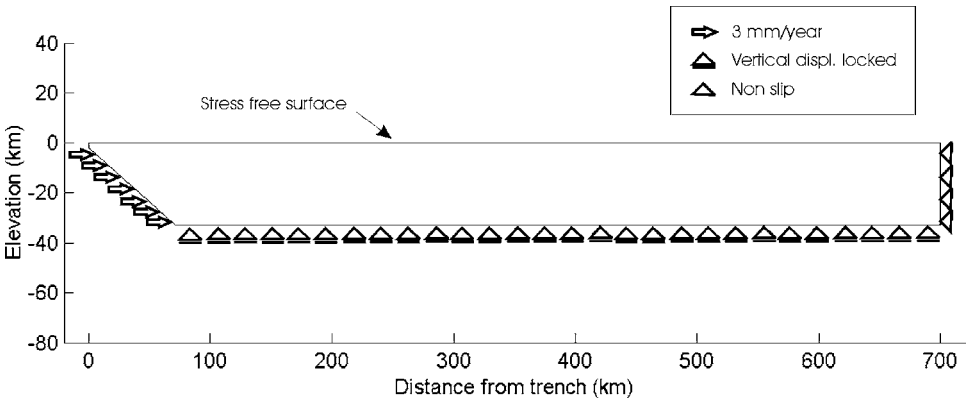

Fig. 7 Boundary conditions

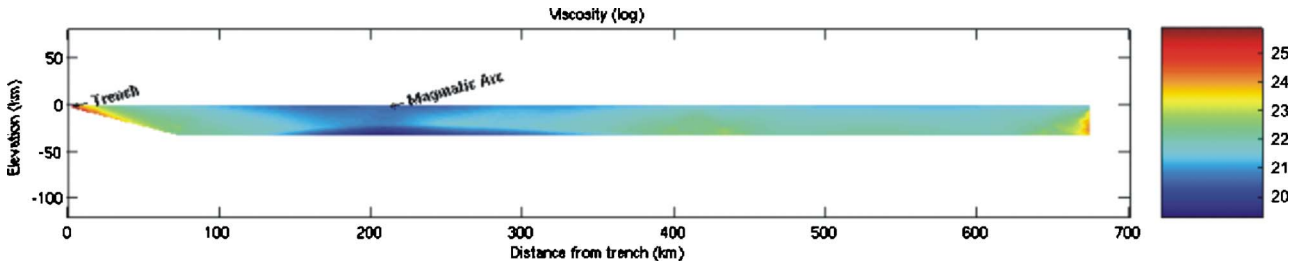

Fig. 8 Viscosity at the beginning of the simulation

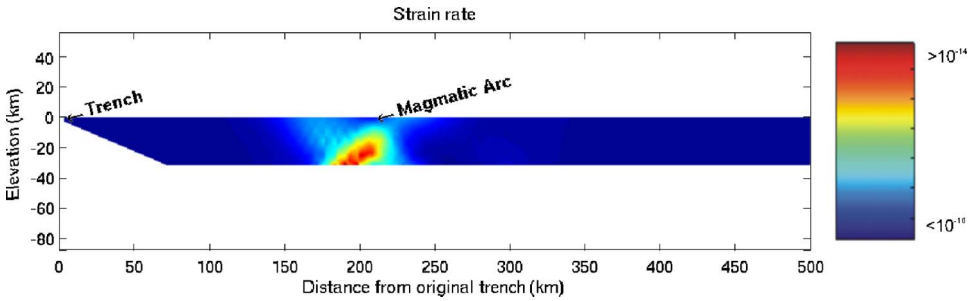

Fig. 9 Strain rate at the beginning of the simulation

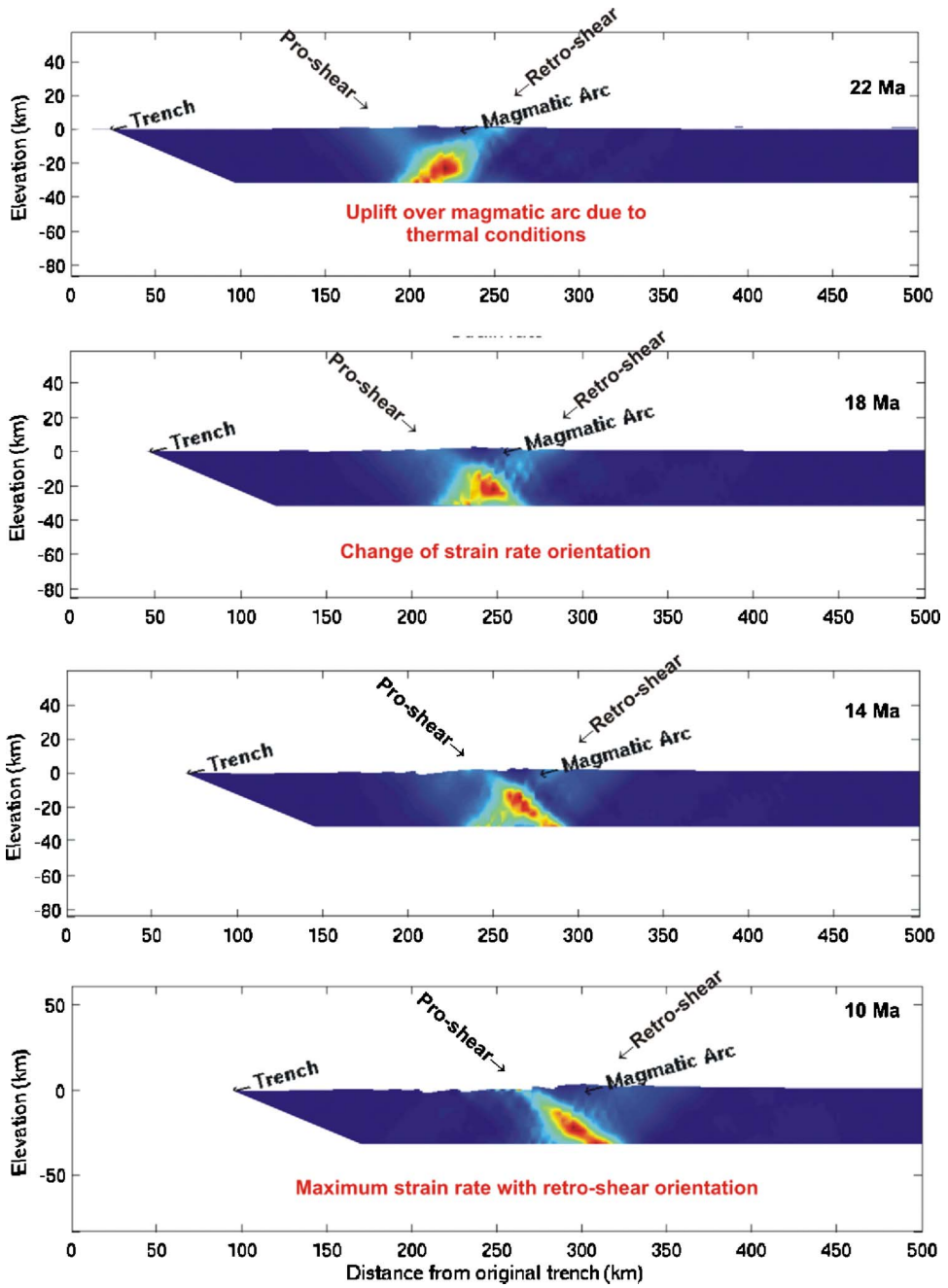

Fig. 10 Strain rate at 3, 7, 11, and 15 My from the beginning

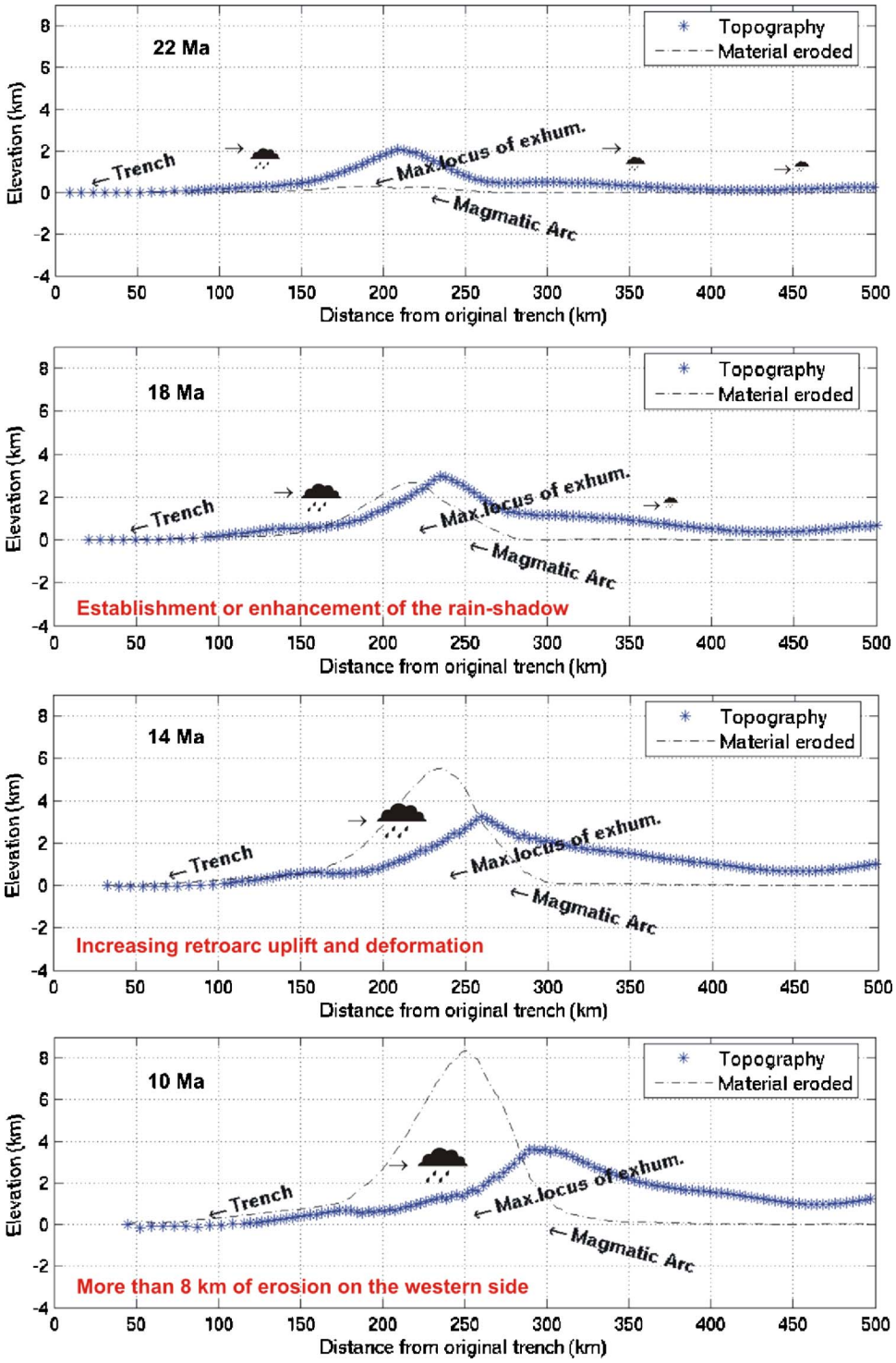

Fig. 11 Topography and surface erosion at 3, 7, 11, and 15 My from the beginning

"Pro-shear" zone. Among the factors that favor this, we can mention the strong erosion acting on the western side of the orogen. This is in complete coincidence with the results of Beaumont et al. [16] who found that when erosion removes mass from a plateau or its flanks, strain rates increase where erosion has occurred. Strong crustal erosion also favors this process because, due to the migration of the arc, the lowest viscosity values and maximum strain rates can be found to the east and near the bottom boundary of the domain.

The evolution of the topography during early and middle Miocene was predicted (Figs. 11 and 12(*a*)).

As the orogen grows, erosion turns more effective, resulting in a higher erosion rate. When it reaches a certain yield altitude, humid winds cannot bypass the water divide, causing an asymmetric precipitation pattern with the western side heavily eroded (Fig. 11). At the same time, as subduction erosion forces the shifting of the magmatic arc, eastern zones are heated and deformed (Fig. 10) resulting in a consequent surface uplift. The combination

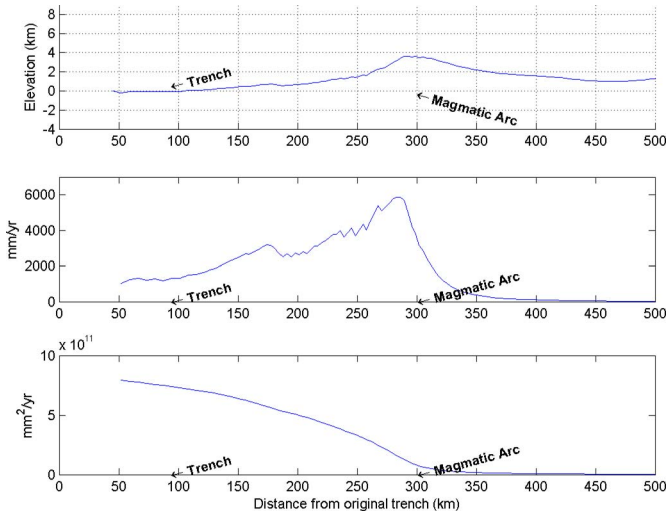

Fig. 12 Topography, precipitation, and available water flux calculated by the model at approximately middle Miocene (12 My)

of both processes results in a progressive migration of the maximum locus of exhumation toward the east, as can be seen in Fig. 11.

The amount of denudation along the transect in our simulation is in complete agreement with the studies of Thomson et al. [42], who were able to quantify approximately the eroded material in the zone. They demonstrated by means of fission track analysis that the surface erosion since ca. 30 Ma. in the western side of the water divide was between 4 and 9 km, while in the eastern side is, at most, 3 km. It can be seen in Fig. 11 that the calculated denudation is up to 8 km in some parts of the transect and only considering the period modeled, which would imply a good correspondence with Thomson's figures. Also, the volume (per unit width) of the material eroded from the surface in the section considered is about 700 km^2. This is coherent in orders of magnitude with the volume of material sedimented to the east of the orogen. The deposits are known as *Santa Cruz Formation* [44] and extend from almost the present water divide to the Atlantic coast. The period encompassed by this formation is almost the same as the one of the simulation.

It is important to remark that the exhumation pattern shown in Fig. 11 has exactly the same features as the one proposed by Willett for orogens with an asymmetric pattern of erosion (higher in prowedge), with a broad domal exhumation pattern across the prowedge interior [28]. The main difference between both experiments is that in Willett's work there was no crustal erosion; thus, the process reaches a steady state at some point of the evolution and there is no surface uplift in the retrowedge. In the case of our simulation, the migration of the magmatic arc toward the east favors some deformation and surface uplift on the retrowedge.

The total shortening obtained in the simulation during the considered period is ~45 km. This shortening is in complete agreement with the detailed field evidence published by Ramos where the absolute minimum shortening for this period ranges from 22 to 45 km [37].

Another important result is that the model predicts the establishment and posterior enhancement of the orographic rain shadow in similar circumstances as the ones described by Blisniuk et al. [41], who published data that support the drastic ecological and climate changes were caused by this process. The asymmetric pattern of precipitation predicted for middle Miocene can be seen in Fig. 12(*b*). Precipitation reaches its maximum value almost at the topographic divide in coincidence with present-day distribution.

6 Conclusions

The results obtained with this model, particularly developed to study subduction zones, are widely satisfactory. The capability of following the topographic evolution through millions of years, quantifying eroded volumes of rock and the time where it could have happened, knowing the tectonic stresses distribution inside the upper crust, understanding the way in which thermal conditions are related to mechanical properties of the crust, and achieving the flexibility to adapt to multiple geometries and configurations through a correct setting of parameters, among other features, turns this model into a powerful and flexible formal framework for a geologist researching large-scale evolution of noncollisional orogens formed parallel to subduction zones.

In this particular case, it is important to remark that the modeling of the acting processes in this region during such a long period of time is completely novel, contributing to support some geological hypotheses about the Miocene deformation of the Andes at these latitudes.

Acknowledgment

This research was funded by "Fundación Antorchas." Javier Quinteros wants to thank the financial support from CONICET (Consejo Nacional de Investigaciones Científicas y Técnicas de Argentina). The authors want to thank Dr. Gustavo Buscaglia and two anonymous reviewers for their positive and helpful suggestions, which contributed to the improvement of our paper.

References

[1] Cristallini, E. O., and Allmendinger, R. W., 2001, "Pseudo 3-D Modeling of Trishear Fault-Propagation Folding," J. Struct. Geol., **23**, pp. 1883–1899.
[2] Hindle, D., Besson, O., and Burkhard, M., 2000, "A Model of Displacement and Strain for Arc-Shaped Mountain Belts Applied to the Jura Arc, " J. Struct. Geol., **22**, pp. 1285–1296.
[3] Pysklywec, R. N., and Beaumont, C., 2004, "Intraplate Tectonics: Feedback Between Radioactive Thermal Weakening and Crustal Deformation Driven by Mantle Lithosphere Instabilities," Earth Planet. Sci. Lett., **221**, pp. 275–292.
[4] Babeyko, A. Y., Sobolev, S. V., Trumbull, R. B., Oncken, O., and Lavier, L. L., 2002, "Numerical Models of Crustal Scale Convection and Partial Melting Beneath the Altiplano-Puna Plateau," Earth Planet. Sci. Lett., **199**, pp. 373–388.
[5] Gemmer, L., Nielsen, S. ren B., and Bayer, U., 2003, "Late Cretaceous-Cenozoic evolution of the North German Basin: Results from 3D Geodynamic Modelling," Tectonophysics, **373**, pp. 39–54.
[6] Willett, S. D., 1999, "Rheological Dependence of Extension in Wedge Models of Convergent Orogens," Tectonophysics, **305**, pp. 419–435.
[7] Pysklywec, R. N., and Shahnas, M. H., 2003, "Time-Dependent Surface Topography in a Coupled Crust-Mantle Convection Model," Geophys. J. Int., **154**, pp. 268–278.
[8] Behn, M. D., Lin, J., and Zuber, M. T., 2002, "A Continuum Mechanics Model for Normal Faulting Using a Strain-Rate Softening Rheology: Implications for Thermal and Rheological Controls on Continental and Oceanic Rifting," Earth Planet. Sci. Lett., **202**, pp. 725–740.
[9] Fullsack, P., 1995, "An Arbitrary Lagrangian-Eulerian Formulation for Creeping Flows and its Application in Tectonic Models," Geophys. J. Int., **120**, pp. 1–23.
[10] Pardo-Casas, F., and Molnar, P., 1987, "Relative Motion of the Nazca (Farallon) and South American Plates Since Late Cretaceous Time," Tectonics, **6**, pp. 233–248.
[11] Lamb, S., and Davis, P., 2003, "Cenozoic Climate Change as a Possible Cause for the Rise of the Andes," Nature (London), **425**, pp. 792–797.
[12] Silver, P. G., Russo, R. M., and Lithgow-Bertelloni, C., 1998, "Coupling of South American and African Plate Motion and Plate Deformation," Science, **279**, pp. 60–63.
[13] Sobolev, S. V., and Babeyko, A. Y., 2005, "What Drives Orogeny in the Andes?," Geology, **33**, pp. 617–620.
[14] Kay, S. M., Godoy, E., and Kurtz, A., 2005, "Episodic Arc Migration, Crustal Thickening, Subduction Erosion, and Magmatism in the South-Central Andes," Bull. Geol. Soc. Am., **117**, pp. 67–88.
[15] Ruddiman, W. F., Raymo, M. E., Prell, W. L., and Kutzbach, J. E., 1997, "*The Uplift-Climate Connection: A Synthesis*", *Tectonic Uplift and Climate Change*, W. F. Ruddiman, ed., Plenum Press, New York, pp. 471–515.
[16] Beaumont, C., Fullsack, P., and Hamilton, J., 1992, "*Erosional Control of Active Compressional Orogens*", Thrust tectonics, K. R. McClay, ed., Chapman and Hall, New York, pp. 19–31.
[17] Girault, V., and Raviart, P.-A., 1986, *Finite Element Methods for Navier-Stokes Equations*, Springer-Verlag, Berlin.
[18] Brezzi, F., and Fortin, M., 1991, *Mixed and Hybrid Finite Elements Methods*, Springer-Verlag, Berlin.

[19] Bathe, K.-J., 1996, *Finite Element Procedures*, Prentice-Hall, Englewood Cliffs, NJ.
[20] Ernst, W. G., 1975, "Systematics of Large-Scale Tectonics and Age Progressions in Alpine and Circum-Pacific Blueschist Belts," Tectonophysics, **26**, pp. 229–246.
[21] Kohlstedt, D. L., Evans, B., and Mackwell, S. J., 1995, "Strength of the Lithosphere: Constraints Imposed by Laboratory Experiments," J. Geophys. Res., **100**, pp. 17587–17602.
[22] Jaoul, O., Tullis, J., and Kronenberg, A., 1984, "The Effect of Varying Water Contents on the Creep Behavior of Heavytree Quartzite," J. Geophys. Res., **89**, pp. 4298–4312.
[23] Mackwell, S. J., Zimmerman, M. E., and Kohlstedt, D. L., 1998, "High Temperature Deformation of Dry Diabase with Application to Tectonics on Venus," J. Geophys. Res., **103**, pp. 975–984.
[24] Tsenn, M. C., and Carter, N. L., 1987, "Upper Limits of Power Law Creep of Rocks," Tectonophysics, **136**, pp. 1–26.
[25] Byerlee, J., 1978, "Friction of Rocks," Pure Appl. Geophys., **116**, pp. 615–626.
[26] Flemings, P., and Jordan, T. E., 1989, "A Synthetic Stratigraphic Model of Foreland Basin Development," J. Geophys. Res., **94**, pp. 3851–3866.
[27] Howard, A. D., and Kerby, D., 1983, "Channel Changes in Badlands," Bull. Geol. Soc. Am., **94**, pp. 739–752.
[28] Willett, S. D., 1999, "Orogeny and Orography: The Effects of Erosion on the Structure of Mountain Belts," J. Geophys. Res., **104**, pp. 28957–28981.
[29] Turcotte, D. L., and Schubert, G., 1982, *Geodynamics: Applications of Continuum Mechanics to Geological Problems*, Wiley, New York.
[30] Allen, P. A., and Allen, J. R., 1990, *Basin Analysis, Principles & Applications*, Blackwell Scientific Publications, Oxford.
[31] Crandall, S. H., Dahl, N. C., and Lardner, T. J., 1978, *An Introduction to the Mechanics of Solids*, 2nd ed., McGraw-Hill, New York.
[32] Burov, E. B., and Diament, M., 1995, "The Effective Elastic Thickness (T_e) of Continental Lithosphere: What Does It Really Mean?," J. Geophys. Res., **100**, pp. 3905–3927.
[33] Karner, G. D., Steckler, M. S., and Thorne, J. A., 1983, "Long-Term Thermo-Mechanical Properties of the Lithosphere," Nature (London), **304**, pp. 250–252.
[34] Gansser, A., 1973, "Facts and Theories of the Andes," J. Geol. Soc. (London), **129**, pp. 93–131.
[35] Pankhurst, R. J., Weaver, S. D., Hervé, F., and Larrondo, P., 1999, "Mesozoic-Cenozoic Evolution of the North Patagonian Batholith in Aysén, Southern Chile," J. Geol. Soc. (London), **156**, pp. 673–694.
[36] Somoza, R., 1998, "Updated Nazca (Farallon) - South America Relative Motions During the Last 40 My: Implications for Mountain Building in the Central Andean Region," J. S. A. Earth Sci., **11**, pp. 211–215.
[37] Ramos, V. A., 1989, "Andean Foothills Structures in Northern Magallanes Basin, Argentina," Am. Assoc. Pet. Geol. Bull., **73**, pp. 887–903.
[38] Cande, S. C., and Leslie, R. B., 1986, "Late Cenozoic Tectonics of the Southern Chile Trench," J. Geophys. Res., **91**, pp. 471–496.
[39] Ramos, V. A., 2005, "Seismic Ridge Subduction and Topography: Foreland Deformation in the Patagonian Andes," Tectonophysics, **399**, pp. 73–86.
[40] Hervé, F., Demant, A., Ramos, V. A., Pankhurst, R. J., and Suárez, M., 2000, "*The Southern Andes*", Tectonic Evolution of South America, U. G. Cordani, E. J. Milani, A. T. Filho, and D. A. Campos, eds., International Geological Congress, Rio de Janeiro, pp. 605–634.
[41] Blisniuk, P. M., Stern, L. A., Chamberlain, C. P., Idleman, B., and Zeitler, P. K., 2005, "Climatic and Ecologic Changes During Miocene Surface Uplift in the Southern Patagonian Andes," Earth Planet. Sci. Lett., **230**, pp. 125–142.
[42] Thomson, S. N., Hervé, F., and Stöckhert, B., 2001, "Mesozoic-Cenozoic Denudation History of the Patagonian Andes (Southern Chile) and its Correlation to Different Subduction Processes," Tectonics, **20**, pp. 693–711.
[43] Bourgois, J., Martin, H., Moigne, J. L., and Frutos, J., 1996, "Subduction Erosion Related to Spreading-Ridge Subduction: Taitao Peninsula (Chile Margin Triple Junction Area)," Geology, **24**, pp. 723–726.
[44] Nullo, F. E., and Combina, A. M., 2002, "Sedimentitas Terciarias Continentales," *Geología y Recursos Naturales de Santa Cruz. Relatorio del XV Congreso Geológico Argentino. El Calafate*, M. J. Haller, ed., Asociación Geológica Argentina, Buenos Aires, Vol. I-16, pp. 245–258.

P. J. Sánchez
e-mail: psanchez@intec.unl.edu.ar

V. Sonzogni

Centro Internacional de Métodos Computacionales en Ingeniería, INTEC-UNL-CONICET, Güemes 3450, S3000 GLN Santa Fe, Argentina

A. E. Huespe

J. Oliver

Technical University of Catalonia, Campus Nord, Modul C1, c/Jordi Girona 1-3, 08034 Barcelona, Spain

Stabilized Mixed Finite Elements With Embedded Strong Discontinuities for Shear Band Modeling

A stabilized mixed finite element with elemental embedded strong discontinuities for shear band modeling is presented. The discrete constitutive model, representing the cohesive forces acting across the shear band, is derived from a rate-independent J_2 plastic continuum material model with strain softening, by using a projection-type procedure determined by the Continuum-Strong Discontinuity Approach. The numerical examples emphasize the increase of the numerical solution accuracy obtained with the present strategy as compared with alternative procedures using linear triangles.
[DOI: 10.1115/1.2190233]

1 Introduction

Shear bands in plastic solids arise as a typical deformation mode due to a strain localization phenomenon, during the inelastic deformation processes, when the material becomes unstable. Numerical modeling of shear bands using discontinuous velocity fields was previously proposed by several authors (see, for example, Armero et al. [1], Regueiro et al. [2], and Samaniego et al. [3]).

In a number of problems, a large stable process of irreversible isochoric plastic deformation precedes the inception of a strain localized mode. In these cases, and from a computational point of view, it should be considered the deficient response provided by standard finite elements when kinematics incompressibility constraints are present. This particular aspect of the numerical approach is a classical, and extensively studied, issue in computational mechanics (see Zienkiewicz et al. [4], Hughes [5]).

In this paper we present a stabilized mixed finite element formulation, which has been recently developed for J_2 plasticity [6,7]. The kinematics is enriched with the addition of an embedded strong discontinuity mode with elemental support, like that proposed in Oliver [8,9], for capturing the characteristic shear band type deformation mechanisms. The idea of using a well behaved finite element for plasticity in conjunction with an embedded strong discontinuity kinematics is not new in shear band modelling. Armero et al. [1] have used a triangular MINI element and Regueiro et al. [2] the classical quadrilateral BBAR element, both of them enriched with an embedded strong discontinuity. Nevertheless, the authors understand that the problem remains open since, in their opinion, the linear triangle has a number of advantages which make it particularly suitable to be enriched with embedded discontinuities. The stabilized element here presented is a linear triangle.

The Continuum-Strong Discontinuity Approach [10] adopted in this work, determines the shear strain rate-traction rate separation law of the shear band. A characteristic of this procedure is that the resulting discrete law governing the shear band evolution, i.e., the cohesive force acting across the shear band surface, is a projection onto the discontinuity surface of the bulk material constitutive model. In this work, the nonlocalized (bulk) material behavior follows a rate-independent J_2 elastoplastic law with strain softening response.

Alternative models for simulating shear bands have been numerous in the past. Recently, Cervera et al. [11] have presented a model that uses the same stabilized mixed finite element shown here, but without introducing the embedded strong discontinuity mode into the finite element. However, the authors think that the additional features provided by the CSDA deserve to be studied too.

The paper proceeds as follows: In Sec. 2, we present the enriched kinematics with the strong discontinuity mode and the discrete constitutive model governing the shear band evolution. Section 3 presents the finite element formulation with the stabilization procedure and Sec. 4 its numerical implementation. In the present work, we are interested in the analysis of the numerical stabilization effect, its influence on the shear-band capturing and the subsequent post-critical response, particularly when embedded strong discontinuities are used. This analysis is presented in Sec. 5 by means of two numerical applications. In the first case, a slope instability problem, we compare the numerical response obtained by different finite element implementations, including standard and stabilized mixed linear triangles with and without embedded strong discontinuities, quadrilaterals, etc. Also, we analyze the convergence rate of the solution with the finite element mesh size. In the second example, the near incompressibility constraint is imposed already at the beginning of elastic regime. In this context, again we study the ability of the model to capture the shear band and the obtained peak load is compared with an analytical solution taken from the literature. Finally, the conclusions are presented.

2 Problem Settings

2.1 Strong Discontinuity Kinematics. Let Ω be a body which experiences a shear band failure mode. The material surface $\mathcal{S}$, with normal $\boldsymbol{n}$ intersecting the body Ω, represents the zone with localized strain rate, as it is shown in Fig. 1. The appropriate kinematics describing this phenomenon should account for a discontinuous velocity field across $\mathcal{S}$, such as the following one:

$$\dot{\boldsymbol{u}}(\boldsymbol{x},t) = \dot{\bar{\boldsymbol{u}}}(\boldsymbol{x},t) + \mathcal{H}_{\mathcal{S}}(\boldsymbol{x})\dot{\boldsymbol{\beta}}(\boldsymbol{x},t) \tag{1}$$

where $\dot{\bar{\boldsymbol{u}}}(\boldsymbol{x},t)$ represents a continuum field, $\mathcal{H}_{\mathcal{S}}(\boldsymbol{x})$ is the Heaviside's step function shifted to $\mathcal{S}$ ($\mathcal{H}_{\mathcal{S}}(\boldsymbol{x})=1\ \forall \boldsymbol{x}\in\Omega^+$ and $\mathcal{H}_{\mathcal{S}}(\boldsymbol{x})$

Contributed by the Applied Mechanics Division of ASME for publication in the JOURNAL OF APPLIED MECHANICS. Manuscript received July 1, 2005; final manuscript received February 13, 2006. Review conducted by G. C. Buscagila. Discussion on the paper should be addressed to the Editor, Prof. Robert M. McMeeking, Journal of Applied Mechanics, Department of Mechanical and Environmental Engineering, University of California—Santa Barbara, Santa Barbara, CA 93106-5070, and will be accepted until four months after final publication of the paper itself in the ASME JOURNAL OF APPLIED MECHANICS.

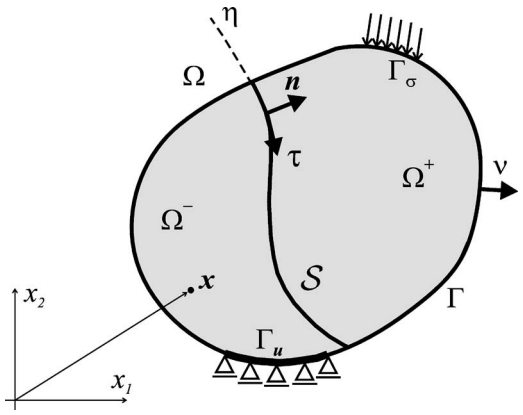

Fig. 1 Strong discontinuity problem

$=0\,\forall \boldsymbol{x}\in\Omega^-$), that, multiplied by the velocity jump vector $\dot{\boldsymbol{\beta}}$, introduces the discontinuity term into the velocity field.

The infinitesimal strain rate being compatible with this velocity field, is a generalized function in Ω:

$$\dot{\boldsymbol{\varepsilon}}(\boldsymbol{x},t)=(\nabla\dot{\boldsymbol{u}})^{\mathrm{sym}}=\dot{\bar{\boldsymbol{\varepsilon}}}+\delta_S(\dot{\boldsymbol{\beta}}\otimes\boldsymbol{n})^{\mathrm{sym}} \tag{2}$$

composed of a regular term $\dot{\bar{\boldsymbol{\varepsilon}}}=(\nabla\dot{\bar{\boldsymbol{u}}})^{\mathrm{sym}}+\mathcal{H}_S(\nabla\dot{\boldsymbol{\beta}})^{\mathrm{sym}}$ and a singular one, given by the Dirac's delta function (δ_S) shifted to $\mathcal{S}$.

The boundary value problem (BVP) of a quasi-static elastoplastic body showing a strong discontinuity kinematics, such as a shear band, is described (in rate form) by the following equations:

$$\nabla\cdot\dot{\boldsymbol{\sigma}}+\rho\dot{\boldsymbol{b}}=\boldsymbol{0}\quad\forall\,\boldsymbol{x}\in\Omega/\mathcal{S} \tag{3}$$

$$\dot{\boldsymbol{u}}=\dot{\boldsymbol{u}}^{*}\quad\forall\,\boldsymbol{x}\in\Gamma_{\boldsymbol{u}} \tag{4}$$

$$\dot{\boldsymbol{\sigma}}\cdot\boldsymbol{\nu}=\dot{\boldsymbol{t}}^{*}\quad\forall\,\boldsymbol{x}\in\Gamma_{\boldsymbol{\sigma}} \tag{5}$$

where the Cauchy's equation (3), relating the stress rate $\dot{\boldsymbol{\sigma}}$ with the rate of volumetric forces $\rho\dot{\boldsymbol{b}}$, and ignoring the inertial effects, is defined in the regular part of the body ($\Omega/\mathcal{S}$), i.e., the points in Ω excluding those in $\mathcal{S}$ and where no strain rate localization effects are observed. The boundary condition in velocities $\dot{\boldsymbol{u}}^{*}$ and rate of tractions $\dot{\boldsymbol{t}}^{*}$ are imposed on $\Gamma_{\boldsymbol{u}}$ and $\Gamma_{\boldsymbol{\sigma}}$ (Eqs. (4) and (5)), respectively. Furthermore, the equilibrium condition across the discontinuity surface $\mathcal{S}$ requires that:

$$\dot{\boldsymbol{t}}^{+}=\dot{\boldsymbol{\sigma}}^{+}\cdot\boldsymbol{n}=\dot{\boldsymbol{\sigma}}^{-}\cdot\boldsymbol{n}=\dot{\boldsymbol{t}}^{-}\quad\forall\,\boldsymbol{x}\in\mathcal{S} \tag{6}$$

where $\dot{\boldsymbol{t}}^{+}$ ($\dot{\boldsymbol{t}}^{-}$) is the traction vector applied to the body part Ω^{+} (or Ω^{-}) on the boundary $\mathcal{S}$. If cohesive tractions ($\boldsymbol{t}_{\mathcal{S}}$) are considered in the shear band interface, the equilibrium condition in rates also requires:

$$\dot{\boldsymbol{t}}_{\mathcal{S}}=\dot{\boldsymbol{\sigma}}_{\mathcal{S}}\cdot\boldsymbol{n}=\dot{\boldsymbol{\sigma}}^{+}\cdot\boldsymbol{n}=\dot{\boldsymbol{t}}^{+}\quad\forall\,\boldsymbol{x}\in\mathcal{S} \tag{7}$$

where, and consistently with the Continuum-Strong Discontinuity Approach, a fundamental hypothesis has been adopted: A stress state $\boldsymbol{\sigma}_{\mathcal{S}}$ exists into the discontinuity zone $\mathcal{S}$ (where singular strain rates are present), which is defined by a regularized version of the constitutive model that describes the regular part of the body $\Omega/\mathcal{S}$, see [8,12,13].

2.2 Continuum Constitutive Model and Discrete Cohesive Law. We assume for the $\Omega/\mathcal{S}$ domain a rate-independent J_2 elastoplastic material model with strain softening described by the equations:

$$\dot{\boldsymbol{\sigma}}=\boldsymbol{C}:(\dot{\boldsymbol{\varepsilon}}-\dot{\boldsymbol{\varepsilon}}^{p});\quad\boldsymbol{C}=\lambda(\mathbb{1}\otimes\mathbb{1})+2\mu\boldsymbol{I} \tag{8}$$

$$\dot{\boldsymbol{\varepsilon}}^{p}=\gamma\partial_{\boldsymbol{\sigma}}\phi=\gamma\boldsymbol{M} \tag{9}$$

$$\dot{\alpha}=\gamma\partial_q\phi=\gamma \tag{10}$$

$$\dot{q}=-H\dot{\alpha}=-H\gamma \tag{11}$$

$$\phi(\boldsymbol{\sigma},q)=J_2(\boldsymbol{\sigma})-(\sigma_y-q);\quad J_2(\boldsymbol{\sigma})=\sqrt{\frac{3}{2}(\boldsymbol{S}:\boldsymbol{S})} \tag{12}$$

$$\gamma\geqslant 0;\quad\phi\leqslant 0;\quad\gamma\phi=0 \tag{13}$$

where $\boldsymbol{C}$ is the fourth order elastic constitutive tensor depending on the Lamé's parameters (λ and μ), with $\mathbb{1}$ and $\boldsymbol{I}$ being the second and fourth order unit tensors, respectively, $\dot{\boldsymbol{\varepsilon}}^{p}$ is the plastic strain rate tensor, q and α are scalar internal variables and ϕ is the yield function describing the elastic domain depending on the deviatoric stress tensor $\boldsymbol{S}=\boldsymbol{\sigma}^{\mathrm{dev}}$ (through the second invariant J_2) and the yield strength σ_y. We denote $\boldsymbol{M}$ the plastic deviatoric strain rate direction (being $tr(\boldsymbol{M})=0$) and γ the plastic multiplier. From Eqs. (10)–(12), α is identified as the total equivalent plastic strain. Special attention should be paid, in the present setting, to the softening modulus $H(H<0)$, which plays a main role in the localization condition.

In the Continuum-Strong Discontinuity Approach, followed in the present work, it is assumed that the stress $\boldsymbol{\sigma}_{\mathcal{S}}$ is determined by a regularized version of the model given by Eqs. (8)–(13). This stress state, which due to equilibrium conditions must be a bounded tensor, defines the cohesive behavior of the interface $\mathcal{S}$.

Following Simo et al. [12] and Oliver [10], and considering the regularized sequence of functions $\delta_S=\lim_{h\to 0}(\mu_S/h)$ (where $\mu_S(\boldsymbol{x}\in\mathcal{S})=1$, $\mu_S(\boldsymbol{x}\notin\mathcal{S})=0$), it can be shown that (variables with subindex $(\cdot)_{\mathcal{S}}$ are referred to their evaluation at the domain $\mathcal{S}$):

$$\dot{\boldsymbol{\sigma}}_{\mathcal{S}}=\boldsymbol{C}:(\dot{\boldsymbol{\varepsilon}}_{\mathcal{S}}-\dot{\boldsymbol{\varepsilon}}^{p}_{\mathcal{S}})=\boldsymbol{C}:[\dot{\bar{\boldsymbol{\varepsilon}}}_{\mathcal{S}}+\delta_{\mathcal{S}}(\boldsymbol{n}\otimes\dot{\boldsymbol{\beta}})^{\mathrm{sym}}-\dot{\boldsymbol{\varepsilon}}^{p}_{\mathcal{S}}] \tag{14}$$

is a bounded term whenever:

$$\delta_{\mathcal{S}}(\boldsymbol{n}\otimes\dot{\boldsymbol{\beta}})^{\mathrm{sym}}-\dot{\boldsymbol{\varepsilon}}^{p}_{\mathcal{S}}=\boldsymbol{0} \tag{15}$$

Condition (15) can be verified by introducing a singular measures for the plastic multiplier γ and the inverse of the softening modulus H:

$$\gamma_{\mathcal{S}}=\delta_{\mathcal{S}}\bar{\gamma};\quad H^{-1}_{\mathcal{S}}=\delta_{\mathcal{S}}\bar{H}^{-1};\quad\bar{H}=\frac{\sigma_y^2}{2G_f} \tag{16}$$

where $\bar{H}$ is an intrinsic softening modulus, determined by the material fracture energy G_f. Therefore, from Eqs. (11) and (16), $\dot{q}$ becomes a regular term, even when $\dot{\boldsymbol{\varepsilon}}_{\mathcal{S}}$ is singular:

$$\dot{q}_{\mathcal{S}}=-\bar{\gamma}\bar{H} \tag{17}$$

and replacing Eq. (9) into Eq. (14), yields:

$$\bar{\gamma}\boldsymbol{M}_{\mathcal{S}}=(\boldsymbol{n}\otimes\dot{\boldsymbol{\beta}})^{\mathrm{sym}} \tag{18}$$

which has been termed the "strong discontinuity equation" [10]. Recalling that:

$$\boldsymbol{M}_{\mathcal{S}}=\sqrt{\frac{3}{2}}\frac{\boldsymbol{S}_{\mathcal{S}}}{\|\boldsymbol{S}_{\mathcal{S}}\|} \tag{19}$$

and given the particular structure of tensor $(\boldsymbol{n}\otimes\dot{\beta})^{\mathrm{sym}}$, Eq. (18) imposes the strong discontinuity condition on $\boldsymbol{\sigma}_{\mathcal{S}}$, which establishes that $\boldsymbol{\sigma}_{\mathcal{S}}$ is only characterized by the traction vector $\boldsymbol{t}_{\mathcal{S}}$, see Fig. 2. Additional details on this aspect can be found in [10].

This result allows us to rewrite the constitutive model only as a function of the traction vector and velocity jumps ($\boldsymbol{t}_{\mathcal{S}}$ versus $\dot{\boldsymbol{\beta}}$). Let the traction vectors $\boldsymbol{t}_{\mathcal{S}}$ and $\boldsymbol{t}^{\mathrm{dev}}_{\mathcal{S}}$ be identified by the components $\boldsymbol{t}_{\mathcal{S}}=\{(\sigma_{nn})_{\mathcal{S}},(S_{n\tau})_{\mathcal{S}},(S_{n\xi})_{\mathcal{S}}\}\in\mathbb{R}^3$, where the identity between the shear components of $\boldsymbol{\sigma}$ and $\boldsymbol{S}$ are used, $\boldsymbol{t}^{\mathrm{dev}}_{\mathcal{S}}=\{0,(t_\tau)_{\mathcal{S}},(t_\xi)_{\mathcal{S}}\}$, see Fig. 2, and let the vector of plastic strain rate direction $\boldsymbol{m}_{\mathcal{S}}$ be

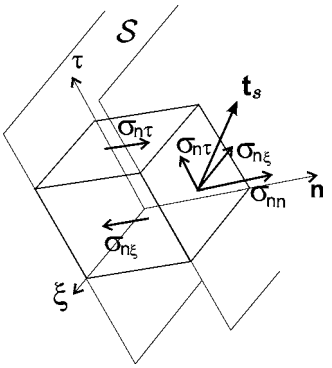

Fig. 2 Stress tensor structure in $\mathcal{S}$

given by $\boldsymbol{m}_{\mathcal{S}}=\sqrt{3}\boldsymbol{t}_{\mathcal{S}}^{\mathrm{dev}}/(\|\boldsymbol{t}_{\mathcal{S}}^{\mathrm{dev}}\|)\in\mathbb{R}^3$. Then, the yield function and the consistency equation, in a loading process, can be written as follows:

$$\phi_{\mathcal{S}}=\sqrt{3\boldsymbol{t}_{\mathcal{S}}^{\mathrm{dev}}\cdot\boldsymbol{t}_{\mathcal{S}}^{\mathrm{dev}}}-(\sigma_y-q_{\mathcal{S}});\quad \dot{\phi}_{\mathcal{S}}=\boldsymbol{m}_{\mathcal{S}}\cdot\dot{\boldsymbol{t}}_{\mathcal{S}}^{\mathrm{dev}}-\bar{\gamma}\bar{H}=0 \quad (20)$$

We remark that $\boldsymbol{t}_{\mathcal{S}}^{\mathrm{dev}}$ is normally termed the Schmidt resolved shear stresses for the slip plane $\mathcal{S}$, see [14].

In a loading state ($\bar{\gamma}>0$), Eqs. (18) and (20b) determine the velocity jump $\dot{\boldsymbol{\beta}}$:

$$\dot{\boldsymbol{\beta}}=\left(\frac{\boldsymbol{m}_{\mathcal{S}}\cdot\dot{\boldsymbol{t}}_{\mathcal{S}}^{\mathrm{dev}}}{\bar{H}}\right)\boldsymbol{Q}_e^{-1}\cdot(\boldsymbol{n}\cdot\boldsymbol{C}:\boldsymbol{M}_{\mathcal{S}});\quad \boldsymbol{Q}_e=\boldsymbol{n}\cdot\boldsymbol{C}\cdot\boldsymbol{n} \quad (21)$$

Equation (21) is consistent with a classical constitutive assumption on the slip phenomenon in single-crystal plasticity: The shear rate ($\dot{\zeta}=\|\dot{\boldsymbol{\beta}}\|$), in a slip system, depends on the stresses only through the Schimdt resolved shear stress ($\boldsymbol{t}_{\mathcal{S}}^{\mathrm{dev}}$). Implicit in Eq. (21) is the fact that the velocity jump $\dot{\boldsymbol{\beta}}$ is compatible with a slip line mode ($\dot{\boldsymbol{\beta}}\cdot\boldsymbol{n}=0$) and that:

$$\boldsymbol{Q}_{ep}|_{(H=0)}\cdot\dot{\boldsymbol{\beta}}=0;\quad \boldsymbol{Q}_{ep}|_{(H=0)}=\boldsymbol{n}\cdot\boldsymbol{C}_{ep}\cdot\boldsymbol{n} \quad (22)$$

where $\boldsymbol{C}_{ep}$ is the perfectly plastic constitutive tensor and $\boldsymbol{Q}_{ep}$ is the so-called "localization tensor."

The degenerated (projected) cohesive model, traction-separation law, derived from the continuum model and induced by a strong discontinuity kinematics, is displayed in Eqs. (23)–(26):

$$\dot{\beta}=\bar{\gamma}\boldsymbol{Q}_e^{-1}\cdot(\boldsymbol{n}\cdot\boldsymbol{C}:\boldsymbol{M}_{\mathcal{S}}) \quad (23)$$

$$\dot{q}_{\mathcal{S}}=-\bar{\gamma}\bar{H} \quad (24)$$

$$\phi_{\mathcal{S}}\leqslant 0;\quad \bar{\gamma}\geqslant 0;\quad \bar{\gamma}\phi_{\mathcal{S}}=0 \quad (25)$$

$$\phi_{\mathcal{S}}=\sqrt{3\boldsymbol{t}_{\mathcal{S}}^{\mathrm{dev}}\cdot\boldsymbol{t}_{\mathcal{S}}^{\mathrm{dev}}}-(\sigma_y-q_{\mathcal{S}}) \quad (26)$$

3 Stabilized Mixed Variational Formulation Using Embedded Strong Discontinuities

Decomposing the stress rate into its deviatoric $\dot{\boldsymbol{S}}$, and spherical $-\dot{p}\mathbb{1}$ $\left(\dot{p}=-\frac{1}{3}tr(\dot{\boldsymbol{\sigma}})\right)$, parts:

$$\dot{\boldsymbol{\sigma}}=-\dot{p}\mathbb{1}+\dot{\boldsymbol{S}}\quad \forall\,\boldsymbol{x}\in\Omega/\mathcal{S} \quad (27)$$

and considering from the constitutive model that $\dot{p}=-\kappa\nabla\cdot\dot{\boldsymbol{u}}$, where κ is the volumetric modulus, the BVP can be set within a classical variational mixed (velocity, pressure) format: find $\dot{\boldsymbol{u}}\in\mathcal{V}_{\boldsymbol{u}}$ and $p\in Q$ such that:

$$\mathcal{L}(\dot{\boldsymbol{u}},\dot{p};\boldsymbol{\eta},q)=\int_\Omega\left[(\nabla\boldsymbol{\eta})^{\mathrm{sym}}:\dot{\boldsymbol{\sigma}}+q\left(\nabla\cdot\dot{\boldsymbol{u}}+\frac{\dot{p}}{\kappa}\right)-\boldsymbol{\eta}\cdot\dot{\boldsymbol{f}}^{(\mathrm{ext})}\right]d\Omega$$
$$=0\quad\forall\,\boldsymbol{\eta}\in\mathcal{V}_\eta,\quad\forall\,q\in\mathcal{Q} \quad (28)$$

The admissible functional space for q is $\mathcal{Q}\equiv L^2_{(\Omega/\mathcal{S})}$. We define the space of admissible functions for velocities $\mathcal{V}_{\boldsymbol{u}}$ by assuming the existence of nonsmooth terms representing the velocity jumps developed in the shear band zone. These terms are included via the embedded strong discontinuity technique. Let the velocity space $\mathcal{V}_{\boldsymbol{u}}$ be defined by:

$$\mathcal{V}_{\boldsymbol{u}}=\{\dot{\boldsymbol{u}}(\boldsymbol{x})=\bar{\dot{\boldsymbol{u}}}(\boldsymbol{x})+\mathcal{M}_{\mathcal{S}}(\boldsymbol{x})\dot{\boldsymbol{\beta}};\bar{\dot{\boldsymbol{u}}}\in\bar{\mathcal{V}}_u\} \quad (29)$$

$$\mathcal{M}_{\mathcal{S}}(\boldsymbol{x})=\mathcal{H}_{\mathcal{S}}-\varphi(\boldsymbol{x}) \quad (30)$$

where $\mathcal{M}_{\mathcal{S}}$ is the so-called elemental unit jump function [9], whose support is a given domain Ω_h that includes $\mathcal{S}$. The $\varphi(\boldsymbol{x})$ term can be taken as an arbitrary smooth function such that: $\varphi(\boldsymbol{x}\in\Omega^+)=1$ and $\varphi(\boldsymbol{x}\in\Omega^-)=0$. Also $\dot{\boldsymbol{\beta}}\in\mathbb{R}^{\mathrm{dim}}$, with dim standing for the space dimension, is the velocity jump vector. The virtual (kinematically admissible) velocities lie on the space:

$$\mathcal{V}_{\boldsymbol{\eta}}=\{\boldsymbol{\eta}=\bar{\boldsymbol{\eta}}(\boldsymbol{x})+\mathcal{M}_{\mathcal{S}}(\boldsymbol{x})\delta\boldsymbol{\beta};\ \bar{\boldsymbol{\eta}}|_{\Gamma_u}\in\bar{\mathcal{V}}_{\boldsymbol{u}}^o(\bar{\boldsymbol{\eta}}|_{\Gamma_u}=0)\} \quad (31)$$

It should be mentioned that $\bar{\dot{\boldsymbol{u}}}$ and $\bar{\boldsymbol{\eta}}$ are smooth functions ($\bar{\mathcal{V}}_{\boldsymbol{u}}\subset H^1$).

Introducing the spaces (29) and (31) into Eq. (28), the governing equations can be alternatively written as follows:

$$\int_{\Omega/\mathcal{S}}(\dot{\boldsymbol{S}}-\dot{p}\mathbb{1}):(\nabla\bar{\boldsymbol{\eta}})^{\mathrm{sym}}d\Omega=P_{\boldsymbol{u}}^{(\mathrm{ext})}\quad\forall\,\bar{\boldsymbol{\eta}}\in\bar{\mathcal{V}}_{\boldsymbol{u}}^o \quad (32a)$$

$$\int_{\Omega/\mathcal{S}}q\left(\frac{\dot{p}}{\kappa}+(\nabla\cdot\dot{\boldsymbol{u}})\right)d\Omega=0\quad\forall\,q\in\mathcal{Q} \quad (32b)$$

$$\int_\Omega\dot{\boldsymbol{\sigma}}:(\nabla\mathcal{M}_{\mathcal{S}}\otimes\delta\boldsymbol{\beta})^{\mathrm{sym}}d\Omega=0\quad\forall\,\delta\boldsymbol{\beta}\in\mathbb{R}^{\mathrm{dim}} \quad (32c)$$

where $P_{\underline{\boldsymbol{u}}}^{(\mathrm{ext})}$ is the virtual power of the body forces and external loads.

Recalling that $\nabla\mathcal{M}_{\mathcal{S}}=(\delta_{\mathcal{S}}\boldsymbol{n}-\nabla\varphi)$, then Eq. (32*c*) imposes a weak traction continuity condition on the discontinuity surface and it can be rewritten as:

$$\int_{\mathcal{S}}\dot{\boldsymbol{\sigma}}_{\mathcal{S}}\cdot\boldsymbol{n}d\mathcal{S}-\int_{\Omega/\mathcal{S}}(\dot{\boldsymbol{S}}-\dot{p}\mathbb{1})\cdot\nabla\varphi d\Omega=\int_\Omega\tilde{\boldsymbol{G}}^S\dot{\boldsymbol{\sigma}}d\Omega=\boldsymbol{0} \quad (33)$$

where we have identified the matrix $\tilde{\boldsymbol{G}}^S$ with the operator $\nabla\mathcal{M}_{\mathcal{S}}$ applied to stresses. A widely used variational nonsymmetric (not-consistent) formulation, redefines the weak traction continuity Eq. (33) by exchanging $\nabla\varphi$ by $\boldsymbol{n}$, in the second left hand side term, and computing the mean values of the traction continuity [15]:

$$\frac{1}{l_{\mathcal{S}}}\int_{\mathcal{S}}\dot{\boldsymbol{\sigma}}_{\mathcal{S}}\cdot\boldsymbol{n}d\mathcal{S}-\frac{1}{\Omega}\int_{\Omega/\mathcal{S}}(\dot{\boldsymbol{S}}-\dot{p}\mathbb{1})\cdot\boldsymbol{n}d\Omega=\int_\Omega\tilde{\boldsymbol{G}}^N\dot{\boldsymbol{\sigma}}d\Omega=\boldsymbol{0} \quad (34)$$

where $l_{\mathcal{S}}$ is the length of discontinuity $\mathcal{S}$ intersecting the finite element, see Fig. 4. In the numerical examples, we present solutions considering both procedures. We use the term "symmetric formulation" when Eq. (33) is implemented and "nonsymmetric formulation" if condition Eq. (34) governs the traction continuity.

3.1 Stabilization. It is well known that mixed formulations like Eq. (28) suffer from numerical instability issues [4,5]. The instability problem becomes particularly serious when piecewise

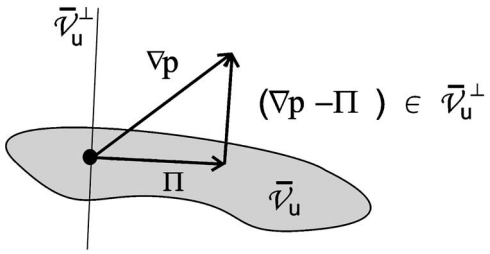

Fig. 3 Projection of the pressure gradient

linear polynomial functions of continuity C^0 are chosen for interpolation of both spaces $\bar{\mathcal{V}}_u$ and $\mathcal{Q}$, because in that case the so-called Ladyzhenskya-Babuska-Brezzi condition (or simply LBB) is not satisfied [16]. A remedy for this unwanted effect has been the introduction of stabilization terms $\mathcal{S}_{st}$ into the variational principle Eq. (28). Particularly, this term is added to the left hand side of Eq. (32*b*).

The stabilization term used in this work has been introduced by Codina [17] in the fluid mechanics context and extended by Cervera et al. [6] to J_2-plasticity problems. It has been termed the orthogonal sub-scale method, PGP, and is defined by:

$$\mathcal{S}_{st} = \int_{\Omega/\mathcal{S}} \nabla q \cdot (\tau(\nabla \dot{p} - \dot{\mathbf{\Pi}}))d\Omega \tag{35}$$

where $\dot{\mathbf{\Pi}}(\in \bar{\mathcal{V}}_u)$ is the projection-$L^2_{(\Omega/\mathcal{S})}$ of the discrete pressure rate gradient $(\nabla \dot{p})$ on the regular finite element approximation space $(\bar{\mathcal{V}}_u)$, see Fig. 3:

$$\int_{\Omega/\mathcal{S}} ((\nabla \dot{p} - \dot{\mathbf{\Pi}}) \cdot \boldsymbol{\chi})d\Omega = 0; \quad \forall\, \boldsymbol{\chi} \in \bar{\mathcal{V}}_u \tag{36}$$

This procedure considers the term $\mathcal{S}_{st}$ proportional to a stabilization factor τ, depending on the shear modulus μ and a characteristic finite element size h (we have adopted h to be the square root of the finite element area):

$$\tau = c\frac{h^2}{2\mu} \tag{37}$$

where the scalar coefficient c is a constant parameter ($c \approx \mathcal{O}(1)$).

Introducing the stabilization term (35) into the variational equation (28), and considering that Eq. (36) shall be included as an additional restriction, it is possible to rewrite the variational principle, in $(\dot{\bar{\boldsymbol{u}}}, \dot{\boldsymbol{\beta}}, \dot{p}, \dot{\mathbf{\Pi}})$, as follows:

$$\int_{\Omega/\mathcal{S}} (\dot{\boldsymbol{S}} - \dot{p}\mathbf{1}):(\nabla \bar{\boldsymbol{\eta}})^{\text{sym}} d\Omega = P^{(\text{ext})}_{\bar{\boldsymbol{u}}} \quad \forall\, \bar{\boldsymbol{\eta}} \in \bar{\mathcal{V}}^o_u \tag{38a}$$

$$\int_{\Omega/\mathcal{S}} q\left(\frac{\dot{p}}{\kappa} + \nabla \cdot \dot{\boldsymbol{u}}\right)d\Omega + \int_{\Omega/\mathcal{S}} \nabla q \cdot (\tau(\nabla \ddot{p} - \dot{\mathbf{\Pi}}))d\Omega = 0 \quad \forall\, q \in \mathcal{Q} \tag{38b}$$

$$\int_{\Omega/\mathcal{S}} (\nabla \dot{p} - \dot{\mathbf{\Pi}}) \cdot \boldsymbol{\chi} d\Omega = 0 \quad \forall\, \boldsymbol{\chi} \in \bar{\mathcal{V}}_u \tag{38c}$$

$$\int_{\mathcal{S}} \dot{\boldsymbol{\sigma}}_{\mathcal{S}}:(\boldsymbol{n} \otimes \delta\boldsymbol{\beta})^{\text{sym}} d\mathcal{S} - \int_{\Omega/\mathcal{S}} (\dot{\boldsymbol{S}} - \dot{p}\mathbf{1}):(\nabla\varphi \otimes \delta\boldsymbol{\beta})^{\text{sym}} d\Omega = 0 \quad \forall\, \delta\boldsymbol{\beta} \in \mathbb{R}^{\dim} \tag{38d}$$

Equations (38*a*)–(38*d*) at time t, can be alternatively written in terms of the total stresses and displacements.

4 Numerical Implementation

Considering $\Omega \in \mathbb{R}^2$, simplicial finite elements (linear triangles) with C^0 piecewise linear interpolation polynomials for pressure and regular displacement fields have been chosen for the present implementation.

4.1 Displacement Field Approximation. The continuous part of the displacement $\bar{\boldsymbol{u}} = \{\bar{u}_x, \bar{u}_y\}^T$ is interpolated in the standard way by using piecewise linear shape functions $\boldsymbol{N}^e_{\boldsymbol{u}}(\boldsymbol{x})$ (supra index $(\cdot)^e$ refers to element e). The elemental unit jump function $\mathcal{M}^e_{\mathcal{S}}(\boldsymbol{x}) = \mathcal{H}^e_{\mathcal{S}}(\boldsymbol{x}) - (N^e_u)^{\text{node+}}(\boldsymbol{x})$ is built by using the linear shape function $(N^e_u)^{\text{node+}}$ corresponding to that nodes belonging to the Ω^+ region, see Fig. 4. The support of $\mathcal{M}^e_{\mathcal{S}}$ is, therefore, one element:

$$\boldsymbol{u}^e(\boldsymbol{x},t) = \boldsymbol{N}^e_{\boldsymbol{u}}(\boldsymbol{x})\hat{\bar{\boldsymbol{u}}}^e(t) + \mathcal{M}^e_{\mathcal{S}}(\boldsymbol{x}) + \boldsymbol{\beta}^e(t); \quad \forall\, \boldsymbol{x} \in \Omega^e \tag{39}$$

where $(\hat{\cdot})$ refers to nodal values.

The strains, in a vectorial format $(\boldsymbol{\varepsilon}^e = \{\varepsilon^e_x, \varepsilon^e_y, \varepsilon^e_{xy}\}^T)$, can be written as follows:

$$\boldsymbol{\varepsilon}^e(\boldsymbol{x},t) = \boldsymbol{B}^e\hat{\bar{\boldsymbol{u}}}^e + \boldsymbol{G}^e\boldsymbol{\beta}^e; \quad \forall\, \boldsymbol{x} \in \Omega^e \tag{40}$$

where $\boldsymbol{B}^e = (\nabla \boldsymbol{N}^e_{\boldsymbol{u}})^{\text{sym}}$ is the strain-displacement matrix and $\boldsymbol{G}^e$ is the matrix given by:

$$\boldsymbol{G}^e = \delta_{\mathcal{S}}\begin{bmatrix} n_x & 0 \\ 0 & n_y \\ n_y & n_x \end{bmatrix} - \begin{bmatrix} \partial_x(N^e_u)^{\text{node+}} & 0 \\ 0 & \partial_y(N^e_u)^{\text{node+}} \\ \partial_y(N^e_u)^{\text{node+}} & \partial_x(N^e_u)^{\text{node+}} \end{bmatrix} \tag{41}$$

4.2 Interpolations of the Pressure and L^2-Projected Pressure Gradient Fields. The L^2-projected pressure gradient field $(\mathbf{\Pi}^e)$ is interpolated by using identical shape functions to those

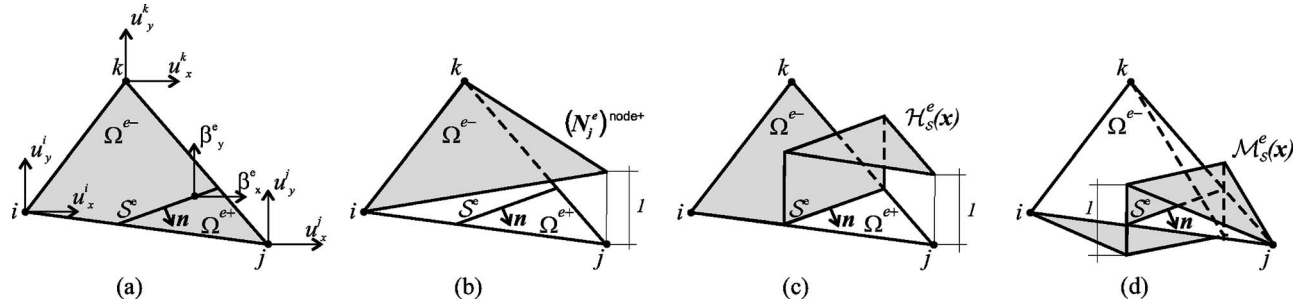

Fig. 4 Displacement field interpolation: (*a*) Element d.o.f.'s, (*b*) $\varphi^e(\boldsymbol{x})$ function, (*c*) Heaviside's step function $\mathcal{H}^e_{\mathcal{S}}(\boldsymbol{x})$, (*d*) Elemental unit jump function $\mathcal{M}^e_{\mathcal{S}}(\boldsymbol{x})$

chosen for the velocity approximation. In the same way, the pressure is also interpolated by means of C^0 piecewise linear functions:

$$\boldsymbol{\Pi}^e(\boldsymbol{x},t)=\boldsymbol{N}_{\boldsymbol{u}}^e(\boldsymbol{x})\hat{\boldsymbol{\Pi}}^e(t);\quad p^e(\boldsymbol{x},t)=\boldsymbol{N}_p^e(\boldsymbol{x})\hat{p}^e(t);\quad \forall\,\boldsymbol{x}\in\Omega/\mathcal{S}^e$$

$$\boldsymbol{\chi}^e(\boldsymbol{x})=\boldsymbol{N}_{\boldsymbol{u}}^e(\boldsymbol{x})\hat{\boldsymbol{\chi}}^e;\quad q^e(\boldsymbol{x})=\boldsymbol{N}_p^e(\boldsymbol{x})\hat{q}^e;\quad \forall\,\boldsymbol{x}\in\Omega/\mathcal{S}^e \tag{42}$$

where $\boldsymbol{N}_p^e$ are, again, the classical linear shape functions.

4.3 Discrete Equations. Internal Force Evaluation. The discrete version of the variational principle Eq. (38) can be formulated as follows: Find $\hat{\boldsymbol{u}}$, $\hat{p}$, $\hat{\boldsymbol{\Pi}}$, and $\boldsymbol{\beta}$ such that they verify the essential boundary condition Eq. (4) and the following system of equations:

$$\boldsymbol{F}^{(\mathrm{int})}-\boldsymbol{F}^{(\mathrm{ext})}=\boldsymbol{0} \tag{43}$$

where the internal $\boldsymbol{F}^{(\mathrm{int})}$ and external $\boldsymbol{F}^{(\mathrm{ext})}$ generalized forces are defined as:

$$\boldsymbol{F}^{(\mathrm{int})}=\begin{bmatrix}\boldsymbol{F}_{\bar{\boldsymbol{u}}}^{(\mathrm{int})}\\ \boldsymbol{F}_p^{(\mathrm{int})}\\ \boldsymbol{F}_\beta^{(\mathrm{int})}\end{bmatrix}=\begin{bmatrix}\mathop{\mathbf{A}}_{e=1}^{nel}\left[\int_{\Omega/\mathcal{S}^e}\boldsymbol{B}^{eT}\boldsymbol{S}^{e(n+1)}d\Omega\right]-\boldsymbol{G}_0\hat{\boldsymbol{p}}^{(n+1)}\\ -\boldsymbol{G}_0^T\hat{\bar{\boldsymbol{u}}}^{(n+1)}-\left[\frac{1}{\kappa}\boldsymbol{M}_p+\boldsymbol{L}\right]\hat{\boldsymbol{p}}^{(n+1)}-\boldsymbol{Q}\boldsymbol{\beta}^{(n+1)}\\ \mathop{\mathbf{A}}_{e=1}^{nel}\left[\int_{\Omega^e}\tilde{\boldsymbol{G}}^{eT}\Delta\boldsymbol{\sigma}^e d\Omega\right]\end{bmatrix} \tag{44}$$

$$\boldsymbol{F}^{(\mathrm{ext})}=\begin{bmatrix}\boldsymbol{F}_{\bar{\boldsymbol{u}}}^{(\mathrm{ext})}\\ \boldsymbol{F}_p^{(\mathrm{ext})}\\ \boldsymbol{F}_\beta^{(\mathrm{ext})}\end{bmatrix}=\begin{bmatrix}\boldsymbol{F}_{\bar{\boldsymbol{u}}}^{(\mathrm{ext})}\\ -\boldsymbol{H}^T\hat{\boldsymbol{\Pi}}^{(n)}\\ \boldsymbol{0}\end{bmatrix} \tag{45}$$

$\mathbf{A}$ being the finite element assembling operator, and matrices $\boldsymbol{G}_0$, $\boldsymbol{M}_p$, $\boldsymbol{M}_u$, $\boldsymbol{L}$, $\boldsymbol{H}$, and $\boldsymbol{Q}$ are computed as follows:

$$\boldsymbol{G}_0=\mathop{\mathbf{A}}_{e=1}^{nel}\left[\int_{\Omega/\mathcal{S}^e}\boldsymbol{B}^{eT}\mathbb{I}\boldsymbol{N}_p^e d\Omega\right];\quad \boldsymbol{M}_p=\mathop{\mathbf{A}}_{e=1}^{nel}\left[\int_{\Omega/\mathcal{S}^e}\boldsymbol{N}_p^{eT}\boldsymbol{N}_p^e d\Omega\right] \tag{46}$$

$$\boldsymbol{M}_{\boldsymbol{u}}=\mathop{\mathbf{A}}_{e=1}^{nel}\left[\int_{\Omega/\mathcal{S}^e}\boldsymbol{N}_{\boldsymbol{u}}^{eT}\tau\boldsymbol{N}_{\boldsymbol{u}}^e d\Omega\right];$$

$$\boldsymbol{L}=\mathop{\mathbf{A}}_{e=1}^{nel}\left[\int_{\Omega/\mathcal{S}^e}(\nabla\boldsymbol{N}_p^e)^T\tau(\nabla\boldsymbol{N}_p^e)d\Omega\right] \tag{47}$$

$$\boldsymbol{H}=\mathop{\mathbf{A}}_{e=1}^{nel}\left[\int_{\Omega/\mathcal{S}^e}\boldsymbol{N}_{\boldsymbol{u}}^{eT}\tau(\nabla\boldsymbol{N}_p^e)d\Omega\right];\quad \boldsymbol{Q}=\mathop{\mathbf{A}}_{e=1}^{nel}\left[\int_{\Omega/\mathcal{S}^e}\boldsymbol{N}_p^{eT}\mathbb{I}^T\boldsymbol{G}^e d\Omega\right] \tag{48}$$

Implicitly, Eqs. (43)–(45) introduce the strategy of assuming the uncoupling of the field $\hat{\boldsymbol{\Pi}}$. Its value at the end of step $n(\hat{\boldsymbol{\Pi}}^{(n)})$, that is determined by using Eq. (38*c*) with the previously known variable $\hat{\boldsymbol{p}}^{(n)}$:

$$\hat{\boldsymbol{\Pi}}^{(n)}=\boldsymbol{M}_{\boldsymbol{u}}^{-1}\boldsymbol{H}^{(n)}\hat{\boldsymbol{p}}^{(n)} \tag{49}$$

is used for solving the system Eqs. (43)–(45) at step $n+1$. This strategy has been previously utilized by Codina et al. and Chiumenti et al. [17–19], allowing for a more efficient computational treatment of the problem.

Following the same integration procedure presented in Oliver [9], one additional Gauss point is considered for evaluation of strains and stresses at $\mathcal{S}$. Thus, integrals on $\mathcal{S}$ in Eq. (44), are referred to terms evaluated in those additional Gauss point multiplied by an adequate weight.

4.4 Tangent Matrix. The use of the Newton-Raphson scheme for solving Eqs. (43)–(45) requires the evaluation of the system jacobian matrix $\boldsymbol{J}$. Considering that $\boldsymbol{X}=[\hat{\bar{\boldsymbol{u}}}\ \hat{\boldsymbol{p}}\ \boldsymbol{\beta}]^T$ is the independent variable vector, $\boldsymbol{J}$ can be evaluated as follows:

$$\underbrace{\begin{bmatrix}\delta\boldsymbol{F}_{\bar{\boldsymbol{u}}}^{(\mathrm{int})}\\ \delta\boldsymbol{F}_p^{(\mathrm{int})}\\ \cdots\cdots\\ \delta\boldsymbol{F}_\beta^{(\mathrm{int})}\end{bmatrix}}_{\delta\boldsymbol{F}^{(\mathrm{int})}}=\underbrace{\begin{bmatrix}\boldsymbol{K}_{\bar{u}\bar{u}} & \boldsymbol{K}_{\bar{u}p} & \vdots & \boldsymbol{K}_{\bar{u}\beta}\\ \boldsymbol{K}_{p\bar{u}} & \boldsymbol{K}_{pp} & \vdots & \boldsymbol{K}_{p\beta}\\ \cdots\cdots & \cdots\cdots & \cdot & \cdots\cdots\\ \boldsymbol{K}_{\beta\bar{u}} & \boldsymbol{K}_{\beta p} & \vdots & \boldsymbol{K}_{\beta\beta}\end{bmatrix}}_{\boldsymbol{J}=\frac{\partial\boldsymbol{F}^{(\mathrm{int})}}{\partial\boldsymbol{X}}}\underbrace{\begin{bmatrix}\delta\hat{\bar{\boldsymbol{u}}}\\ \delta\hat{\boldsymbol{p}}\\ \cdots\cdots\\ \delta\boldsymbol{\beta}\end{bmatrix}}_{\delta\boldsymbol{X}} \tag{50}$$

where submatrices $\boldsymbol{K}_{ij}$ result:

$$\boldsymbol{K}_{\bar{u}\bar{u}}=\mathop{\mathbf{A}}_{e=1}^{nel}\left[\int_{\Omega/\mathcal{S}^e}\boldsymbol{B}^{eT}\mathbb{C}^{\mathrm{dev}}\boldsymbol{B}^e d\Omega^e\right];\quad \boldsymbol{K}_{\bar{u}p}=\boldsymbol{K}_{p\bar{u}}^T=\underbrace{-\boldsymbol{G}_0}_{\Omega/\mathcal{S}^e} \tag{51}$$

$$\boldsymbol{K}_{\bar{u}\beta}=\mathop{\mathbf{A}}_{e=1}^{nel}\left[\int_{\Omega/\mathcal{S}^e}\boldsymbol{B}^{eT}\mathbb{C}^{\mathrm{dev}}\boldsymbol{G}^e d\Omega^e\right];\quad \boldsymbol{K}_{pp}=-\underbrace{\left[\frac{1}{\kappa}\boldsymbol{M}_p+\boldsymbol{L}\right]}_{\Omega/\mathcal{S}^e} \tag{52}$$

$$\boldsymbol{K}_{\beta p}=\mathop{\mathbf{A}}_{e=1}^{nel}\left[-\int_{\Omega/\mathcal{S}^e}\tilde{\boldsymbol{G}}^{eT}\mathbb{I}\boldsymbol{N}_p^e d\Omega^e\right];\quad \boldsymbol{K}_{p\beta}=\underbrace{-\boldsymbol{Q}}_{\Omega/\mathcal{S}^e} \tag{53}$$

$$\boldsymbol{K}_{\beta\bar{u}}=\mathop{\mathbf{A}}_{e=1}^{nel}\left[\int_{\Omega/\mathcal{S}^e}\tilde{\boldsymbol{G}}^{eT}\mathbb{C}^{\mathrm{dev}}\boldsymbol{B}^e d\Omega^e\right]+\mathop{\mathbf{A}}_{e=1}^{nel}\left[\int_{\mathcal{S}^e}\tilde{\boldsymbol{G}}^{eT}\mathbb{C}\boldsymbol{B}^e d\mathcal{S}^e\right] \tag{54}$$

$$\boldsymbol{K}_{\beta\beta}=\mathop{\mathbf{A}}_{e=1}^{nel}\left[\int_{\Omega/\mathcal{S}^e}\tilde{\boldsymbol{G}}^{eT}\mathbb{C}^{\mathrm{dev}}\boldsymbol{G}^e d\Omega^e\right]+\mathop{\mathbf{A}}_{e=1}^{nel}\left[\int_{\mathcal{S}^e}\tilde{\boldsymbol{G}}^{eT}\mathbb{C}\boldsymbol{G}^e d\mathcal{S}^e\right] \tag{55}$$

5 Numerical Simulations

The numerical response of the present model is analyzed by means of two bidimensional problems. Particularly, we are addressing our study to determine the ability of the numerical model for capturing the strain localization mode and the structural peak load. Also, we analyze other fundamental aspects in failure mechanics analysis under softening regime, such as the objectivity of the numerical results with independence of the finite element mesh size and orientation.

The mathematical verification and consistency of the model is studied by comparing alternative finite element formulations, which are denoted using the nomenclature in Table 1. As it can be seen there, the set of elements that we use for this comparison belongs either to the generalized displacement finite element formulation (the constant strain triangle STDSD in the Table and the BBAR quadrilateral element taken from Simo et al. [20]) or to the mixed (pressure-velocity) formulations including the PGP stabilization scheme. All of them, excepting the first one, are enriched with an embedded strong discontinuity kinematics with elemental support. The traction continuity condition is implemented using both procedures: The symmetric element type given by Eq. (33) and the nonsymmetric element type given by Eq. (34).

Table 1 Element formulations

Nomenclature	Element topology	Kinematics	Incompressibility treatment	Element type
PGP	Triangle	Smooth Velocity	PGP (mixed) Scheme	
STDSD-N	Triangle	Strong Disc.	None (displacement)	Nonsymmetric
STDSD-S	Triangle	Strong Disc.	None (displacement)	Symmetric
PGPSD-N	Triangle	Strong Disc.	PGP (mixed) Scheme	Nonsymmetric
PGPSD-S	Triangle	Strong Disc.	PGP (mixed) Scheme	Symmetric
BBARSD-N	Quadrilateral	Strong Disc.	BBAR Formulation	Nonsymmetric
BBARSD-S	Quadrilateral	Strong Disc.	BBAR Formulation	Symmetric

In the PGP formulation without embedded strong discontinuities (denoted "smooth velocity kinematics" in the Table 1), solutions have been obtained by regularization of the softening modulus H, redefining it in accordance with:

$$H^{\text{reg}} = h\bar{H} \tag{56}$$

where h is the characteristic size of the element and $\bar{H}$ the intrinsic softening modulus computed as in Eq. (16).

A comparison of the relative computational cost between PGPSD and BBARSD elements is also reported. For this purpose, it must be considered that the examples have been run in a PC equipped with a single Pentium 4 −3.0 GHz, 512 MB Ram—processor.

For all cases, a stability factor "c" near to unity (see Eq. (37)) was adopted to perform the numerical tests.

5.1 2D Slope Stability Problem. When undrained loading conditions are assumed, the constitutive behavior of saturated cohesive soils can be approximately modeled by an associative deviatoric plastic flow law. In this context, we use a J2 model to simulate a typical plane strain geotechnical slope stability problem and its corresponding shear band failure mode. A similar example was presented in Regueiro et al. [2] and in Oliver et al. [21] where a BBAR element with embedded strong discontinuities was used. Due to the lack, at least up to the author's knowledge, of an analytical or exact solution for this problem, the above mentioned strategies (denoted as BBARSD-N in Table 1), will be used as a reference solution to compare quantitative results.

The effects of including, or not, the strong discontinuity mode are particularly remarked in the present analysis. Also, the numerical stabilization influence on the solution, which is contrasted with similar formulations that do not use such strategy, is studied.

The dimensions and boundary conditions of the physical model are shown in Fig. 5. The test consists of the application of an incremental downward prescribed displacements "$\delta\mathbf{u}$" at the middle of a rigid foot (point **A** in the same figure). This situation leads to an instability problem and to the development of a shear band that propagates through the soil embankment. The material properties used in the simulation (a J2 plasticity model equipped with linear softening) are: $E=1.0e7$[Pa] (Young's modulus), $\nu=0.45$ (Poisson's ratio), $\sigma_y=1.0e5$[Pa] (yield strength), $H=-2.0e5$[Pa] (softening modulus), $G_f=8e3$[N/m] (fracture energy).

Three meshes of triangular elements have been considered for numerical purposes: M1, M2, and M3 (see Figs. 6(*a*)–6(*c*)), with characteristic element size $h\approx 1$[m], $h\approx 0.5$[m], and $h\approx 0.25$[m], respectively. Notice the particular mesh configuration that has been intentionally generated against to the expected strain localization path. This situation represents a challenge for the linear triangle kinematics. A fourth mesh, of quadrilaterals (M4 in Fig. 6(*d*)), with element size similar to M3, is used to obtain the BBARSD-N reference solution.

Figure 7 shows, in gray color, the evolution of those PGPSD-N elements that are subjected to plastic loading conditions in four different stages, as the process advances along the time. It is clear from this figure how the strain localization phenomenon is developed, inducing the shear band mode.

In Fig. 8 again we show, in gray color, those elements in the meshes M1, M2, and M3 and using the PGPSD-N approach, that are post bifurcation regime (were the strong discontinuity is active) at the end of the simulated process. We can observe that the three meshes display a qualitative agreement respect to the shear band trajectory, with a clear tendency to converge with the mesh refinement, toward a well defined curve which compares well with that reported by Regueiro et al. [2]).

Figures 9(*a*) and 9(*b*) compare the deformed mesh solutions obtained using the mixed stabilized formulations either without embedded strong discontinuity (PGP) or with it (PGPSD-N). In the first case, it is observed that the zone of strain localization has a pronounced trend to follow the mesh direction (mesh bias). Furthermore, the solution of the PGP procedure presents a more diffuse deformation pattern respect to that shown by the PGPSD-N. Both effects determine a noticeable difference in the structural response (see Fig. 9(*c*)), mainly in the limit load prediction.

Next, we report the structural response in terms of load versus the vertical displacement $\delta\boldsymbol{u}$ curves (point A). Figure 10(*a*) shows

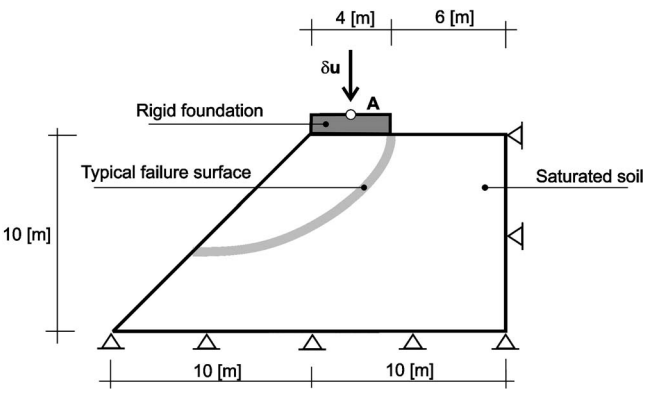

Fig. 5 Slope stability problem: Geometry and boundary condition

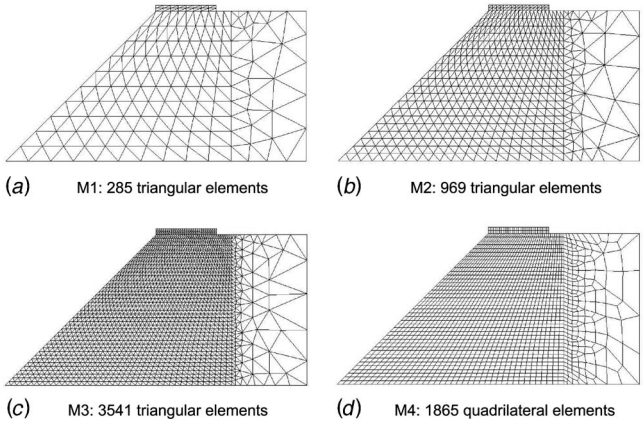

Fig. 6 Slope stability problem: Finite element discretizations

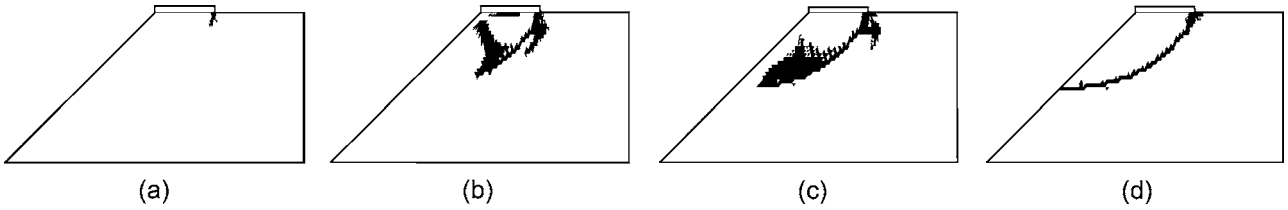

Fig. 7 Slope stability problem: Evolution of plastic loading states using the PGPSD-N element (M3)

these results, which correspond to the PGPSD-N element and different meshes. The M3 solution compares well with those obtained using the BBARSD-N strategy. In Fig. 10(*b*) we plot the same results corresponding to the M3 mesh, but using different finite element formulations. The two responses obtained with the STDSD procedure reveals a locking (spurious) effect produced by the isochoric deformation constraints, overestimating the dissipated energy and peak load.

It must be observed that the PGPSD-N scheme shows a good prediction of the limit load P_u, as compared with the reference solution, and also in terms of the dissipated energy during the localization process. To quantify both features, we plot in Fig. 11 the convergence analysis of the PGPSD-N and STDSD-N solutions. Figure 11(*a*) displays in a logarithmic plot the linear regression curve of the dissipated energy error ($\|e\|_{L^2}$) as a function of the mesh size h. The relative error ($\|e\|_{L^2}$) of every solution $S_{(Mi)}$,

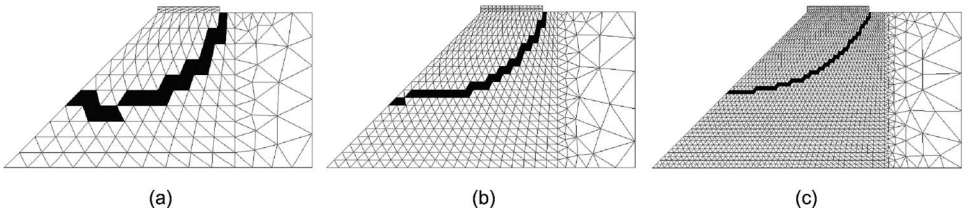

Fig. 8 Slope stability problem. PGPSD-N elements in post-bifurcation condition at the end of the analysis: (*a*) Mesh M1. (*b*) Mesh M2. (*c*) Mesh M3.

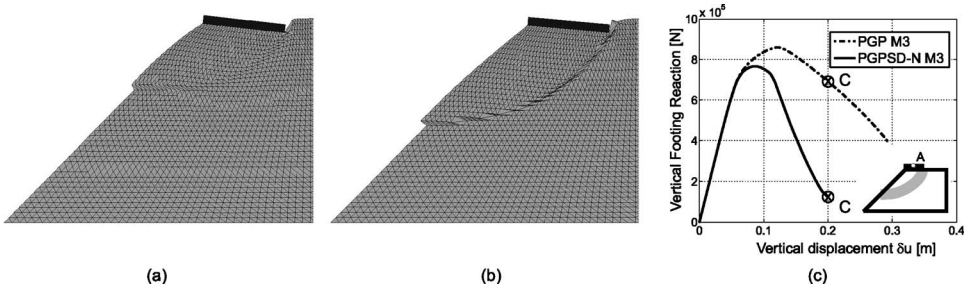

Fig. 9 Slope stability problem. Deformed configuration at point "C" in the equilibrium path: (*a*) PGP Formulation; (*b*) PGPSD-N Formulation; (*c*) Comparison of the Load-Displacement (δu) curves for both strategies.

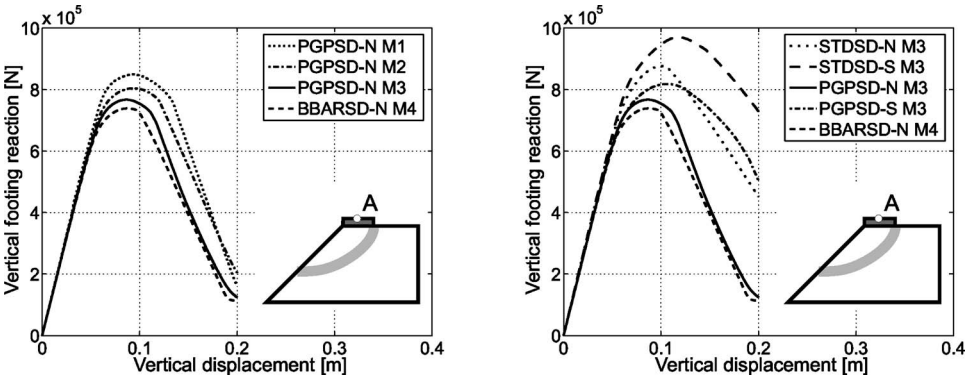

Fig. 10 Slope stability problem. Load-displacement (δu) curves: (*a*) PGPSD-N Convergence. (*b*) Comparison of elements.

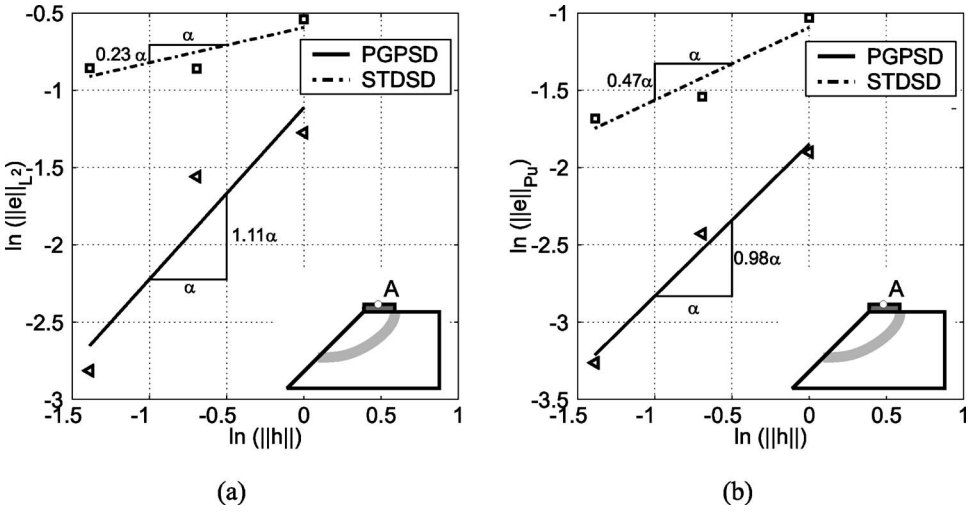

Fig. 11 Slope stability problem. Relative errors vs element size: (*a*) Load-displacement response (in terms of L^2-norm). (*b*) Ultimate load *Pu*.

where $S_{(Mi)}$ is the load vs. displacement ($\delta \boldsymbol{u}$) curve of the mesh M_i ($i=1,2,3$), is computed in terms of a L^2 norm as follow:

$$\|e\|_{L^2} = \frac{\|S_{(Mi)} - S_{(REF)}\|_{L^2}}{\|S_{(REF)}\|_{L^2}} = \frac{\sqrt{\int_0^{\tau_{\max}} (S_{(Mi)} - S_{(REF)})^2 d\tau}}{\sqrt{\int_0^{\tau_{\max}} (S_{(REF)})^2 d\tau}}; \quad i = 1,2,3 \tag{57}$$

where the integration parameter τ corresponds to the vertical displacement ($\delta \boldsymbol{u}$) and $\tau_{\max} = \max(\delta \boldsymbol{u})$ is the same for all cases, while $S_{(REF)} = S^{BBARSD\text{-}N}_{(M3)}$ is the reference solution.

Similarly, Fig. 11(*b*) displays the linear regression curve of the limit load prediction error as a function of the size mesh h. The relative error of the peak load solution is determined by means of:

$$\|e\|_{Pu} = \frac{\|Pu_{(Mi)} - Pu_{(REF)}\|}{\|Pu_{(REF)}\|}; \quad i = 1,2,3 \tag{58}$$

where $Pu_{(Mi)}$ is the maximum value of the vertical footing reaction displayed by mesh M_i and $Pu_{(REF)} = Pu^{BBARSD\text{-}N}_{(M3)}$.

From Fig. 11 it is clearly observed a higher accuracy and convergene rate, either in limit load prediction as also in the dissipated energy, of the PGPSD-N model if compared with athe STDSD-N element.

Finally, the comparative computational cost for PGPSD-N element, relative to BBARSD-N formulation, is outlined in Table 2. Every mesh M1, M2, and M3 of PGPSD-N elements is compared with an equivalent mesh of quadrilateral BBAR elements having identical number of nodes and element sizes.

Table 2 2D slope problem. Relative computational cost.

Mesh	Residual forces	Stiffness matrix	Solver	Total time
M1	1.44	1.16	2.10	1.37
M2	1.44	1.12	1.25	1.30
M3	1.48	1.06	1.33	1.31

5.2 Center Cracked Panel. A square (10×10[cm^2]) cracked panel subjected to uniaxial vertical displacement is analyzed.

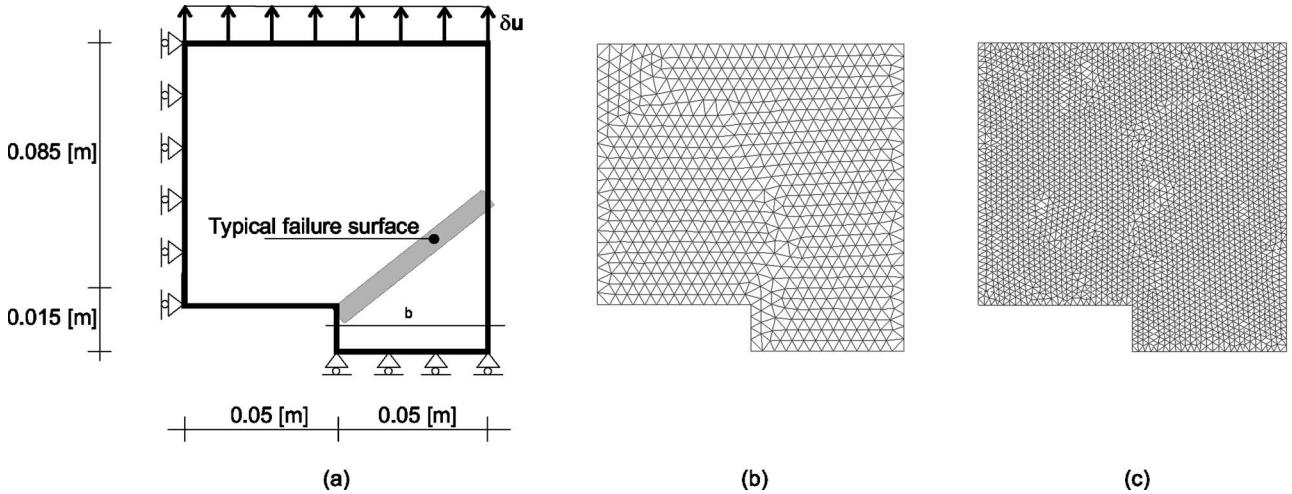

Fig. 12 2D cracked panel: (*a*) Geometry and boundary conditions. (*b*) Mesh M1: 1301 elements ($h \approx 4$[mm]). (*c*) Mesh M2: 5252 elements ($h \approx 2$[mm]).

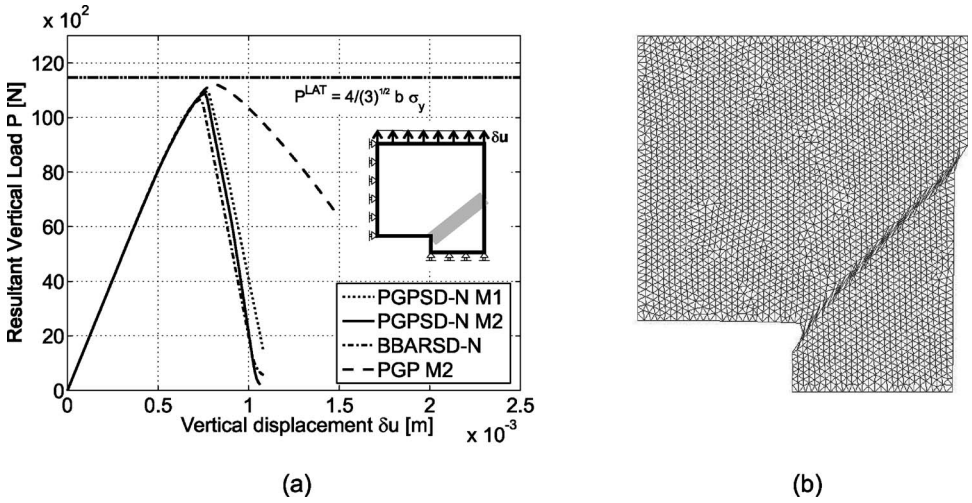

Fig. 13 2D cracked panel: (*a*) Load-displacement equilibrium paths. (*b*) Deformed configuration PGPSD-N (M2).

Plane strain conditions are assumed and, due to symmetry, only a quarter of the model is considered for the simulation (see Fig. 12(*a*)). A quasi-incompressible elastic J2 plastic constitutive model with linear softening is used, based on the following material parameters: $E=1.0e7$[Pa], $\nu=0.499$, $\sigma_y=1.0e5$[Pa], $H=-2.0e5$[Pa], $G_f=4e3$[N/m]. Unlike the previous example, an arbitrary distribution of elements is now adopted, see the meshes M1 and M2 in Figs. 12(*b*) and 12(*c*).

The analytical peak load solution for a problem with sharp crack type and considering perfect elastoplasticity, is available from Limit Analysis Theory (LAT) [22].

Figure 13(*a*) shows the equilibrium curves (vertical displacement versus resultant force P) obtained for both meshes, using the PGPSD-N formulation, and also the PGP without discontinuous enriching modes. Again, in the first case, an adequate convergence can be observed with mesh refinement toward the BBARSD-N solution, and a reasonable accuracy respect to the analytical peak load solution. It must be reported that the standard triangle (STDSD-N) fails, dramatically, in simulating this near incompressible test.

In addition, the deformed mesh configuration of the PGPSD-N model, see Fig. 13(*b*), displays the predicted collapse mechanism.

6 Conclusions

The main contribution of the present work is the presentation of a new simplicial finite element, called PGPSD, which appears as an improvement respect to previous models, leading to robust and accurate simulations for shear band problems induced by strain softening in plastic material models. It has been developed within the context of the Continuum-Strong Discontinuity Approach. The proposed formulation is based on a consistent coupling of two techniques:

(i) The pressure gradient projection stabilization scheme (PGP);
(ii) the elemental embedded strong discontinuity kinematics.

From the study reported in the above examples, we can extract the following conclusions in reference with the PGPSD model in general, and in particular with the PGPSD-N implementation:

- The PGPSD-N element has shown an adequate performance when the strain localization phenomenon happens in a dominant quasi incompressible regime;
- The numerical behavior of the PGPSD-N element has been proven quantitatively through a classical convergence study based on a structured mesh refinement from a reference solution taken from different sources ([2,23]);
- The PGPSD element shows an improvement in the convergence rates and diminution in the relative error magnitude in comparison with the standard (nonstabilized) enriched element (STDSD) and also with respect to the nonenriched PGP strategy. In addition, it compares very well with BBARSD formulation.
- The computational cost, for the two bidimensional cases presented in this work, seems to be reasonable (1.3 to 1.4 times greater than that obtained with the BBARSD procedure) considering that both set of d.o.f.'s, $\mathbf{\Pi}$ and β, can be decoupled and statically condensed in the numerical implementation respectively.

However, we have observed some troubles that must be remarked. The linear kinematics of the simplicial elements (triangle), before the activation of enriched modes, seems to be fairly stiff, which produces a noticeable effect on the bifurcation conditions, delaying the activation of the shear-band. This effect induces, in certain pathological mesh orientations, a serious kinematical locking. This unsolved limitation and the extension to 3D context, motivate future research works.

Acknowledgment

This work has received partial financial support from Consejo Nacional de Investigaciones Científicas y Técnicas (CONICET) through Grant No. PIP 2000/2552. The first author was supported by the "Programme Alβan, the European Union Programme of High Level Scholarships for Latin American, scholarship No.(E04D035536AR)." The third and fourth authors acknowledge the financial support from the Spanish Ministry of Science and Technology, through Grant No. BIA 2004-07289-C03-02.

References

[1] Armero, F., and Garikipati, K., 1996, "An Analysis of Strong Discontinuities in Multiplicative Finite Strain Plasticity and Their Relation With the Numerical Simulation of Strain Localization in Solids," Int. J. Solids Struct., **33**(20–22), pp. 2863–2885.
[2] Regueiro, R., and Borja, R., 1999, "A Finite Element Model of Localized Deformation in Frictional Materials Taking a Strong Discontinuity Approach," Finite Elem. Anal. Design, **33**, pp. 283–315.
[3] Samaniego, E., and Belytschko, T., 2005, "Continuum-Discontinuum Modeling of Shear Bands," Int. J. Numer. Methods Eng., **62**, pp. 1857–1872.
[4] Zienkiewicz, O. C., and Taylor, R. L., 2000, *The Finite Element Method*, Butterworth-Heinemann, Oxford, UK.

[5] Hughes, T. J. R., 1987, *The Finite Element Method. Linear Static and Dynamic Finite Element Analysis*, Prentice-Hall,Englewood Cliffs, NJ.
[6] Cervera, M., Chiumenti, M., Valverde, Q., and Agelet de Saracibar, C., 2003, "Mixed Linear/Linear Simplicial Elements for Incompressible Elasticity and Plasticity," Comput. Methods Appl. Mech. Eng., **192**, pp. 5249–5263.
[7] Sanchez, P., Sonzogni, V., and Huespe, A., 2004, "Evaluation of a Stabilized Mixed Finite Element for Solid Mechanics Problems and its Parallel Implementation," Comput. Struct. (to be published).
[8] Oliver, J., 1996a, "Modeling Strong Discontinuities in Solids Mechanics via Strain Softening Constitutive Equations. Part 1: Fundamentals," Int. J. Numer. Methods Eng., **39**(21), pp. 3575–3600.
[9] Oliver, J., 1996b, "Modeling Strong Discontinuities in Solids Mechanics via Strain Softening Constitutive Equations. Part Numerical Simulation," Int. J. Numer. Methods Eng., **39**(21), pp. 3601–3623.
[10] Oliver, J., 2000, "On the Discrete Constitutive Models Induced by Strong Discontinuity Kinematics and Continuum Constitutive Equations," Int. J. Solids Struct., **37**, pp. 7207–7229.
[11] Cervera, M., Chiumenti, M., and Agelet de Saracibar, C., 2004, "Shear Band Localization via Local j2 Continuum Damage Mechanics," Comput. Methods Appl. Mech. Eng., **193**, pp. 849–880.
[12] Simo, J., Oliver, J., and Armero, F., 1993, "An Analysis of Strong Discontinuities Induced by Strain-Softening in Rate-Independent Inelastic Solids," Comput. Mech., **12**, pp. 277–296.
[13] Oliver, J., Cervera, M., and Manzoli, O., 1999, "Strong Discontinuities and Continuum Plasticity Models: The Strong Discontinuity Approach," Int. J. Plast., **15**(3), pp. 319–351.
[14] Asaro, R. J., 1983, "Micromechanics of Crystals and Polycrystals," Adv. Appl. Mech., **23**, pp. 1–115.
[15] Oliver, J., Huespe, A., and Samaniego, E., 2003, "A Study On Finite Elements for Capturing Strong Discontinuities," Int. J. Numer. Methods Eng., **56**, pp. 2135–2161.
[16] Brezzi, F., and Fortin, M.1991, *Mixed and Hybrid Finite Element Methods*, Springer, Berlin.
[17] Codina, R., 2000, "Stabilization of Incompressibility and Convection Through Orthogonal Sub-Scales in Finite Element Method," Comput. Methods Appl. Mech. Eng., **190**, pp. 1579–1599.
[18] Codina, R., Blasco, J., Buscaglia, G. C., and Huerta, A., 2001, "Implementation of a Stabilized Finite Element Formulation for the Incompressible Navier-Stokes Equations Based on a Pressure Gradient Projection," Int. J. Numer. Methods Eng., **37**, pp. 419–444.
[19] Chiumenti, M., Valverde, Q., Agelet de Saracibar, C., and Cervera, M., 2002, "Una Formulación Estabilizada Para Plasticidad Incompresible Usando Triangulos y Tetraedros con Interpolaciones Lineales en Desplazamientos y Presiones," *Métodos Numéricos en Ingeniería V*.
[20] Simo, J. C., and Hughes, T. J. R., 1998, *Computational Inelasticity*, Springer, New York.
[21] Oliver, J., Huespe, A. E., Blanco, S., and Linero, D. L., 2005, "Stability and Robustness Issues in Numerical Modeling of Material Failure in the Strong Discontinuity Approach," Comput. Methods Appl. Mech. Eng. (in press).
[22] Kanninen, M. F., and Popelar, H., 1985, *Advanced Fracture Mechanics*, Oxford University Press, New York.
[23] Oliver, J., Huespe, A. E., Pulido, M. D. G., Blanco, S., and Linero, D. L., 2004, "Recent Advances in Computational Modeling Of Material Failure," in *Proc. European Congress on Comput. Methods in Appl. Sciences and Eng.*, P. Neittaanmäki, T. Rossi, K. Majava, and O. Pironneau, eds, ECOMAS 2004, Jyväskylä.

Approximation of the Vibration Modes of a Plate and Shells Coupled With a Fluid

E. Hernández
Departamento de Matemática,
Universidad Técnica Federico Santa María,
Casilla 110-V, Valparaiso, Chile
e-mail: Erwin.Hernandez@usm.cl

We consider a method to compute the vibration modes of an elastic thin structure (shell or plate) in contact with a compressible fluid. For the structure, the classical Naghdi equations, based on the Reissner–Mindlin hypothesis, are considered and its approximation using the mixed interpolation of tensorial component 4 finite element method. The fluid equations are discretized by using Raviart–Thomas elements, and a non-conforming coupling is used on the fluid-solid interface. Numerical experiments are reported, assessing the efficiency of this coupled scheme. [DOI: 10.1115/1.2173675]

1 Introduction

In this paper we are interested in the numerical computation of the vibration modes of a fluid-structure interaction problem in a three-dimensional (3D) domain. This is a very important engineering problem (e.g., for treatment of noise in cars or planes) and a large amount of work has been devoted to this subject (see for example [1]). One problem of this kind is to compute elastoacoustic vibrations when the structure is an elastic shell and the fluid is ideal and compressible, both subject to small displacements.

When a thin structure is considered, a big amount of work has been developed by different communities under different points of view. There exist two main ways of approximating shell problems: Finite element methods resulting from the discretization of classical shell models (see [2,3]) and methods based on "degenerating a 3D solid finite element into a shell element" using some kinematical assumption in the thickness direction (see [4]). We are interested in the first case: we consider classical two-dimensional (2D) shell models, namely, Naghdi equations, which are based on Reissner–Mindlin hypotheses. To discretize them we use the mixed interpolation of tensorial component (MITC) finite element methods, introduced by Bathe and Dvorkin in [5], which are very likely the most used in practice (see [4]).

For these MITC elements some mathematical analysis can be found applied to Reissner–Mindlin plate equations (see, for example, [6,7]). In particular, we use the low-order MITC4 method, which is the most common isoparametric quadrilateral element of this family. The performance of this approach has been recently tested for both plates and shells vibration problems [8].

To approximate the fluid we consider the displacement vector field as primary variable, which presents some important properties like, for example, the fact that compatibility and equilibrium through the fluid-structure interface satisfy automatically (see [9]). Though, it is well known that the displacement formulation suffers from the presence of zero-frequency spurious modes with no physical meaning. We consider lowest-order Raviart–Thomas finite elements whose degrees of freedom (DOF) are located at the element faces and represent the normal component of the field through them.

Finally, on the fluid-solid interface we use a non-conforming coupling: the kinematic constraint (i.e., equal normal displacement for fluid and shell), imposing it in a weak sense. Because of this, the fluid and shell meshes do not need to be compatible on the common interface.

In Sec. 2 we state the vibration coupled problem. In Sec. 3 we treat the particular case of a plate. Finally, in Sec. 4, we apply the method to calculate the vibrations of a thin cylinder full of fluid.

2 Statement of the Problem

Let Ω be the three-dimensional domain occupied by the fluid. We consider that $\partial\Omega$ is the union of the 2D surfaces $\Gamma_0, \Gamma_1, \ldots, \Gamma_J$ and we assume that Γ_0 is in contact with the shell, whereas the remaining surfaces are in contact with perfectly rigid walls.

To describe the free small amplitude motions of the fluid, we consider the displacement formulation; we denote by $W=(W_1, W_2, W_3)$ the displacement fluid field.

For the shell, we assume that there exists a single chart ϕ that is a one-to-one mapping, which applies a 2D domain Γ onto the midsurface of the shell. Then, we consider the Naghdi shell model, which is written in terms of the rotations $\Theta=(\Theta_1, \Theta_2)$ of the fibers initially normal to the shell midsurface and the three-dimensional vector field $U=(U_1, U_2, U_3)$ which corresponds to the displacement of the midsurface. Note that these vectors are function defined on the reference domain Γ. Moreover, for simplicity we suppose that the fluid is in contact with the midsurface Γ.

The space of kinematically admissible displacements is denoted by $\mathcal{U}$ and defined by

$$\mathcal{U} := \{(U,\Theta,W): U,\ \Theta,\ W \text{ sufficiently smooth},\ (U_3 \circ \phi^{-1}) = W \cdot n,\ \text{and } \mathcal{BC}\}$$

where $\mathcal{BC}$ symbolically denotes the prescribed essential boundary conditions (see [3,4] for notation and details). The expression $(U_3 \circ \phi^{-1}) = W \cdot \mathrm{n}$ denotes the equality of the normal displacements of both mediums.

Let $a(\cdot,\cdot)$ be the bilinear form defined by:

$$a[(U,\Theta,W),(V,\Upsilon,Z)] := A(W,Z) + t^3 D^b[(U,\Theta),(V,\Upsilon)] + tD^m(U,V) + tkD^s[(U,\Theta),(V,\Upsilon)]$$

Here A is the fluid stiffness and the shell stiffness is written as the sum of a bending term D^b, a membrane term D^m, and a shear term D^s as follows:

$$A(W,Z) := \int_\Omega \rho_F c^2 \operatorname{div} W \operatorname{div} Z dV$$

Contributed by the Applied Mechanics Division of ASME for publication in the JOURNAL OF APPLIED MECHANICS. Manuscript received July 7, 2005; final manuscript received January 5, 2006. Review conducted by G. C. Buscaglia. Discussion on the paper should be addressed to the Editor, Prof. Robert M. McMeeking, Journal of Applied Mechanics, Department of Mechanical and Environmental Engineering, University of California—Santa Barbara, Santa Barbara, CA 93106-5070, and will be accepted until four months after final publication of the paper itself in the ASME JOURNAL OF APPLIED MECHANICS.

$$D^b[(U,\Theta),(V,\Upsilon)] := \int_\Gamma \frac{E^{\alpha\beta\lambda\mu}}{12}\chi_{\alpha\beta}(U,\Theta)\chi_{\lambda\mu}(V,\Upsilon)\sqrt{\det(a)}dS$$

$$D^m(U,V) := \int_\Gamma E^{\alpha\beta\lambda\mu}\gamma_{\alpha\beta}(U)\gamma_{\lambda\mu}(V)\sqrt{\det(a)}dS$$

$$D^s[(U,\Theta),(V,\Upsilon)] := \int_\Gamma G^{\alpha\beta}\varphi_\alpha(U,\Theta)\varphi_\beta(V,\Upsilon)\sqrt{\det(a)}dS$$

Moreover, c is the sound speed in the fluid, the tensors χ, γ, and φ are the well-known bending, membrane, and shear strain operators, respectively (see [2,4]). The tensors present in the stiffness term $E^{\alpha\beta\lambda\mu}$ and $G^{\alpha\beta}$ correspond to the material properties and depend on Young's modulus and Poisson's ratio for the structure, E and ν, respectively. By k we denote a correction factor for the shear term.

Then the coupled system in the frequency domain is the following:

SP: *Find* $\omega>0$ *and* $0\neq(U,\Theta,W)\in\mathcal{U}$ *such that*

$$a[(U,\Theta,W),(V,\Upsilon,Z)] = \omega^2 b[(U,\Theta,W),(V,\Upsilon,Z)] \quad \forall\,(V,\Upsilon,Z)\in\mathcal{U}$$

The bilinear form $b(\cdot,\cdot)$ is given by

$$b[(U,\Theta,W),(V,\Upsilon,Z)] := \int_\Gamma \rho_S\left(ta^{\alpha\beta}U_\alpha V_\beta + tU_3V_3 + \frac{t^3}{12}a^{\alpha\beta}\Theta_\alpha\Upsilon_\beta\right)\sqrt{\det(a)}dS + \int_\Omega \rho_F W\cdot Z dV$$

where ρ_S and ρ_F are the density of the shell and the fluid, respectively. Here, the matrix $(a^{\alpha\beta})$ is the contravariant form of the first fundamental form of the midsurface of the shell (see [2–4] for further details); Greek indices range over 1 and 2. We use the convention of summation over indices repeated up and down.

According to [10], to avoid typical spurious modes in the fluid-solid coupled system (i.e., the eigenfunctions related to the frequency $\omega=0$, arise because no irrotational constraint is imposed to fluid displacements), the approximation of the fluid displacement vector field is made by using Raviart–Thomas element. This element discretizes the whole vector field instead of each of its components separately (see [11], for further details).

We use MITC4 elements for the shell structure. This method is based on discretizing the bending and membrane terms using the usual isoparametric quadratic finite elements and relaxing the shear term by using reduced integration.

Let us now specify this method in our context. Let $\{\mathcal{T}_h\}$ be a family of partitions in hexahedra of Ω and $\{\mathcal{T}_h^\Gamma\}$ be a family of decompositions of Γ into convex quadrilaterals. Here h stands for the maximum diameter of the elements in $K\in\mathcal{T}_h^\Gamma$ or $\mathbf{K}\in\mathcal{T}_h$, respectively. Let $\hat{K}$ be the unit square reference element. We denote by $Q_{i,j}(\hat{K})$ the space of polynomials of degree less than or equal to i in the first variable and to j in the second one. We set $Q_k(\hat{K}) := Q_{k,k}(\hat{K})$. We denote by F_K the bilinear mapping of $\hat{K}$ onto K, and we set $Q(K) := \{p : p\circ F_K\in Q_1(\hat{K})\}$.

For the definition of admissible discrete variables, we impose weakly the kinematic interface constraint because to do it strongly would be too stringent (see [10]). The integrals to do this are imposed on the fluid mesh faces in contact with the shell. More precisely, let $\mathcal{C}_h := \{\mathcal{F}: \mathcal{F}$ is a face of the fluid meshes lying on $\Gamma\}$, we consider

$$\mathcal{U}_h := \left\{(U_h,\Theta_h,W_h):\ U_h|_K\in Q_1(K)^3,\ \ \Theta_h|_K\in Q_1(K)^2\ \forall\,K \in\mathcal{T}_h^\Gamma,\ \ W_h|_{\mathbf{K}}\in RT(\mathbf{K})\ \forall\,\mathbf{K}\in\mathcal{T}_h,\ \int_{\mathcal{F}}(U_{3h}\circ\phi^{-1})dS = \int_{\mathcal{F}} W_h\cdot n dS\ \forall\,\mathcal{F}\in\mathcal{C}_h,\ \text{and } \mathcal{BC}\right\}$$

where $RT(\mathbf{K})$ denotes the lowest-order Raviart–Thomas hexahedron, whose degrees of freedom are the fluxes through each of the six faces of $\mathbf{K}$. Recall that $\mathcal{BC}$ denotes the prescribed essential boundary conditions.

Then, the discrete variational problem reads:

SP$_\mathbf{h}$: *Find* $\omega_h>0$ *and* $0\neq(U_h,\Theta_h,W_h)\in\mathcal{U}_h$ *such that*

$$a_h[(U_h,\Theta_h,W_h),(V_h,\Upsilon_h,Z_h)] = \omega_h^2 b[(U_h,\Theta_h,W_h),(V_h,\Upsilon_h,Z_h)]\ \forall\,(V_h,\Upsilon_h,Z_h)\in\mathcal{U}_h$$

The bilinear form $a_h(\cdot,\cdot)$ is a perturbed form of $a(\cdot,\cdot)$; more precisely, it comes from introducing in the shear term D^s an appropiated reduction operator $\varphi\mapsto\mathbf{R}\varphi$. In this particular case, the operator $\mathbf{R}$ is defined such that $\mathbf{R}\varphi|_K\in Q_{0,1}(K)\times Q_{1,0}(K)\,\forall K\in\mathcal{T}_h^\Gamma$ (For details in the case of plate see, for example, [7], and for cylindrical shell see [12]). Thus we obtain

$$D_h^s[(U_h,\Theta_h),(V_h,\Upsilon_h)] := \int_\Omega G^{\alpha\beta}[\mathbf{R}\varphi(U_h,\Theta_h)]_\alpha[\mathbf{R}\varphi(V_h,\Upsilon_h)]_\beta\sqrt{\det(a)}dV$$

Let us emphasize that, for the shell structure, this MITC4 finite element procedure is based on meshes that are constructed in a reference 2D domain, and the numerical computations require an extensive use of the chart ϕ (see [8] for details).

3 Plates

Now, we consider the case of a plate. The Reissner–Mindlin formulation for plates can be seen as a special case of the Naghdi shell model, where the plate transversal displacement terms appear separately from the in-plane terms. Thus the fluid-solid interaction can be expressed in terms only of the plate transversal displacement, the fiber rotations, and the fluid displacements. Then finite element space is

$$\mathcal{U}_h^P := \left\{(U_{3h},\Theta_h,W_h):\ U_{3h}|_K\in Q_1(K),\ \ \Theta_h|_K\in Q_1(K)^2\ \forall\,K \in\mathcal{T}_h^\Gamma,\ \ W_h|_{\mathbf{K}}\in RT(\mathbf{K})\ \forall\,\mathbf{K}\in\mathcal{T}_h,\ \int_{\mathcal{F}}U_{3h}dS = \int_{\mathcal{F}} W_h\cdot n dS,\ \text{and } \mathcal{BC}\right\}$$

Then to compute the free vibration modes we must solve the problem (see [6,13]):

PP$_\mathbf{h}$: *Find* $\omega_h>0$ *and* $0\neq(U_{3h},\Theta_h,W_h)\in\mathcal{U}_h^P$ *such that*:

$$t^3\tilde{a}(\Theta_h,\Upsilon_h) + \kappa t\int_\Gamma \mathbf{R}(\nabla U_{3h}-\Theta_h)\cdot\mathbf{R}(\nabla V_{3h}-\Upsilon_h)dS + \int_\Omega \rho_F c^2\,\mathrm{div}\,W_h\,\mathrm{div}\,Z_h dV = \omega_h^2\rho\left(t\int_\Gamma U_{3h}V_{3h}dS + \frac{t^3}{12}\int_\Gamma\Theta_h\cdot\Upsilon_h\right)dS + \int_\Omega\rho_F W_h\cdot Z_h dV\ \forall\,(V_{3h},\Upsilon_h,Z_h)\in\mathcal{U}_h^P$$

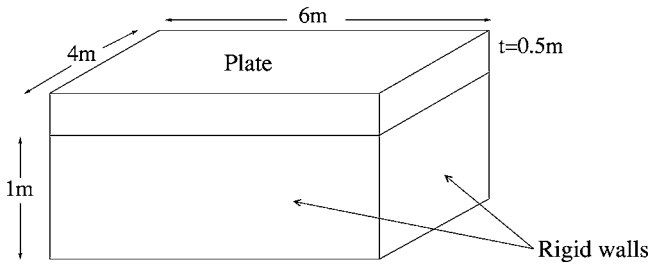

Fig. 1 A 3D cavity filled with fluid

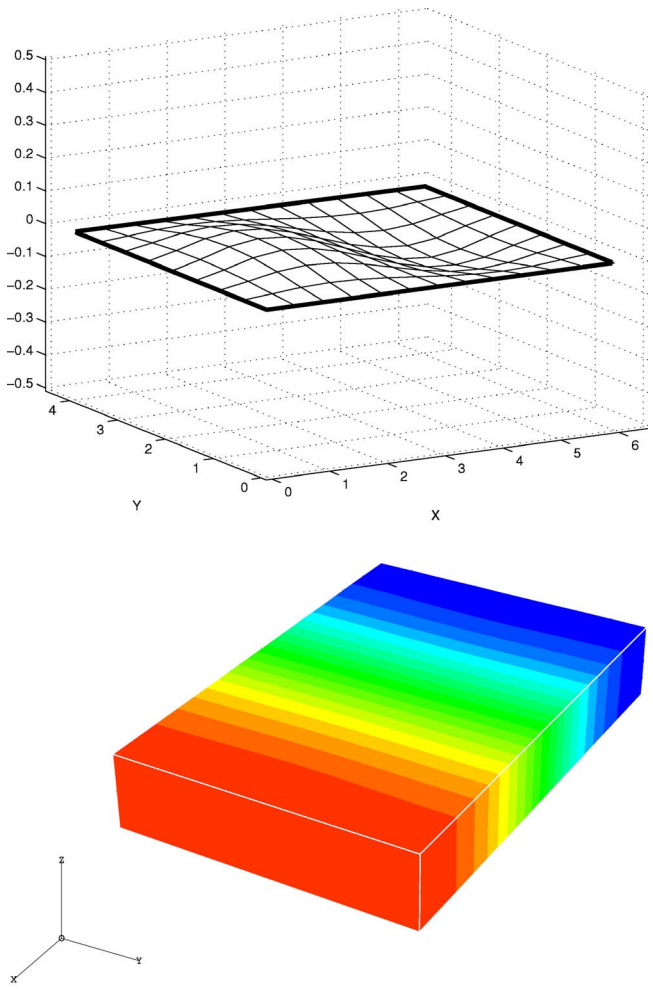

Fig. 2 Vibration mode of frequency ω_1. Deformed plate and fluid pressure.

Here $\kappa := Ek/2(1+\nu)$ is the shear modulus, meanwhile the bilinear form a is defined by

$$\tilde{a}(\Theta_h, \Upsilon_h) := \frac{E}{12(1-\nu^2)} \int_\Gamma \left[\sum_{i,j=1}^{2} (1-\nu)\varepsilon_{ij}(\Theta_h)\varepsilon_{ij}(\Upsilon_h) + \nu \operatorname{div} \Theta_h \operatorname{div} \Upsilon_h \right] dS$$

where ε_{ij} denotes the components of the linear strain tensor.

Recently, this coupled problem has been mathematically analyzed in [13], where hexahedra Raviart–Thomas elements for the fluid and MITC4 elements for the plate were used. Optimal order error estimates have been obtained for the solution of $\mathbf{PP_h}$, which are valid uniformly on the plate thickness t. These results have been, previously, proved for MITC3 and tetrahedral Raviart–Thomas elements in [6].

We have considered a steel 3D cavity completely filled with water with all of its walls being perfectly rigid, except for one of them which is a plate. The geometric parameters are given in Fig. 1. We consider the physical parameters of plate and fluid: $\rho_P = 7700\ \mathrm{kg/m^3}$, $E = 1.44 \times 10^{11}$ Pa, $\nu = 0.35$, $\rho_F = 1000\ \mathrm{kg/m^3}$, $c = 1430$ m/s, $k = 5/6$.

Table 1 shows the frequencies of the three lowest-frequency vibration modes computed on different meshes. Here, N stands for the number of layers of elements for the fluid domain in the vertical direction. The number of layers in the other two direction being $2N$ and $3N$, respectively. The plate meshes are induced by the fluid meshes. We also include more accurate values computed by extrapolating those obtained with the most refined meshes.

Table 2 shows the results obtained for the lowest-frequency vibration mode for plates of different thickness. To allow for comparison we scale the frequencies. Note that the convergence behavior does not depend on the plate thickness.

Figures 2 and 3 show the deformed plate and the fluid pressure field for the two first modes in Table 1.

4 Shells

In this section we present numerical results corresponding to the solution of problem $\mathbf{SP_h}$ in the case of circular cylindrical shells filled with fluid. First, to validate our code, we compare the results with those in [14]. As a second test, to show the clear advantage of using a 2D model for the structure, we apply our method to a problem considered in [15].

By using cylindrical coordinates, we are led to a reference domain $\Omega = [0, 2\pi] \times [0, H]$, with H being the height of the cylindrical shell. We have used uniform meshes of rectangles with 2^{N+2} and 2^{N+1} element edges on each side of Ω, respectively (see Fig.

Table 1 Lowest vibration frequencies of a steel plate in contact with water

Mode	$N=4$	$N=5$	$N=6$	$N=7$	Exact
ω_1	745.5411	744.6309	744.1355	743.8364	743.002848
ω_2	1126.6920	1123.8563	1122.3137	1121.3828	1118.786303
ω_3	1354.1576	1351.3917	1349.8881	1348.9811	1346.471972

Table 2 Scaled lowest frequency for plates of different thickness coupled with fluid

Thickness	$N=4$	$N=5$	$N=6$	$N=7$	Exact
0.5	745.54	744.63	744.13	743.83	743.0028
0.05	747.51	746.63	746.15	745.87	745.0697
0.005	747.53	746.65	746.18	745.89	745.0913
0.0005	747.53	746.65	746.18	745.89	745.0915

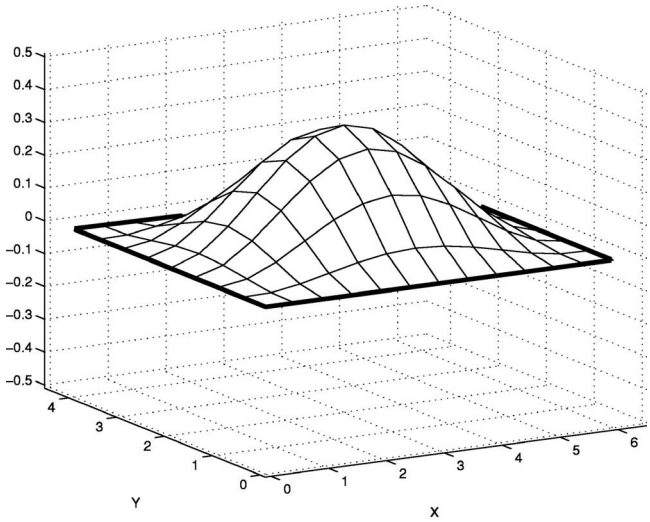

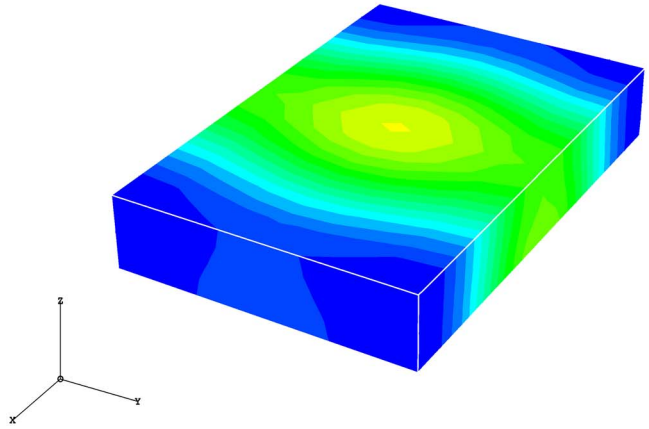

Fig. 3 Vibration mode of frequency ω_2. Deformed plate and fluid pressure.

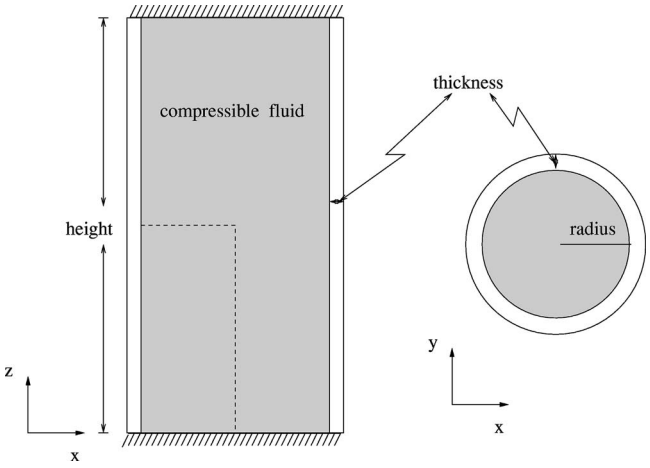

Fig. 5 Used meshes for $N=3$

4). For a given mesh (i.e., a fixed N), we denote by (DOF) its total number of degrees of freedom. We have used three meshes in both experiments, those corresponding to $N=3$ (4956 DOF), $N=4$ (11168 DOF), and $N=5$ (21100 DOF).

In the first case, we have considered a clamped circular cylindrical thin shell completely filled with a compressible fluid (see Fig. 5). The dimensions of the shell are radius 0.1 m, height 0.3 m, and thickness 0.002 m. The physical properties of the materials, which correspond to aluminum and water, are the following: $\rho_P=2700$ kg/m^3, $E=69\times10^9$ Pa, $\nu=0.3$, $\rho_F=1000$ kg/m^3, $c=1483$ m/s, $k=5/6$.

Table 3 shows the computed lowest vibration frequencies. They are ordered according to their circumferential and axial mode numbers n and m, respectively. This table also includes "exact" values of the vibration frequencies obtained by extrapolating the frequencies computed with these meshes. In the last column, we include the results reported in [14], which are obtained with an analytical method based on a finite Fourier series expansion. Note that in all cases the difference between the exact values and those in [14] are smaller than 3.0%.

It can be seen from Table 3 that the method appears locking free for the computation of vibration modes with low circumferential number ($n=0$ and $n=1$). Instead, for larger circumferential numbers ($n=2$, $n=3$, etc.), the computed values of the vibration frequencies are close to the exact ones only for highly refined meshes. This suggests that the method locks for circumferential numbers greater than 1 in this case. This observation agrees with the results reported in [8] for a cylindrical shell in vacuum.

For the second test, we have considered a moderately thick circular cylinder clamped by both ends and filled with fluid. We have used the same material properties as in the example of the plate from the previous section, i.e., a steel structure filled with water. The height of the cylinder is 3.5 m, its inner diameter length is 2.0 m, and its thickness 0.1 m.

Table 4 shows the lowest vibration frequencies computed with the method described in this paper. We have used the same meshes as in the previous example. We denote by ω_s^i and ω_f^i the shell and

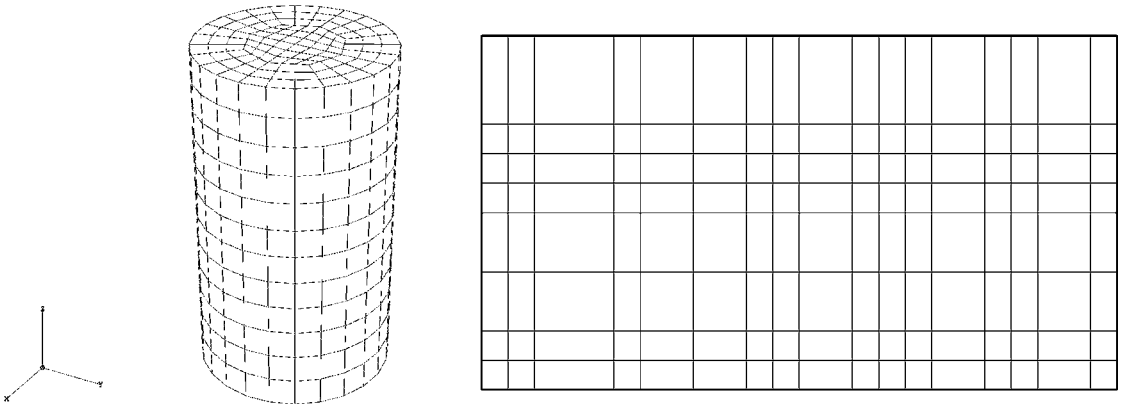

Fig. 4 Cylinder filled with fluid

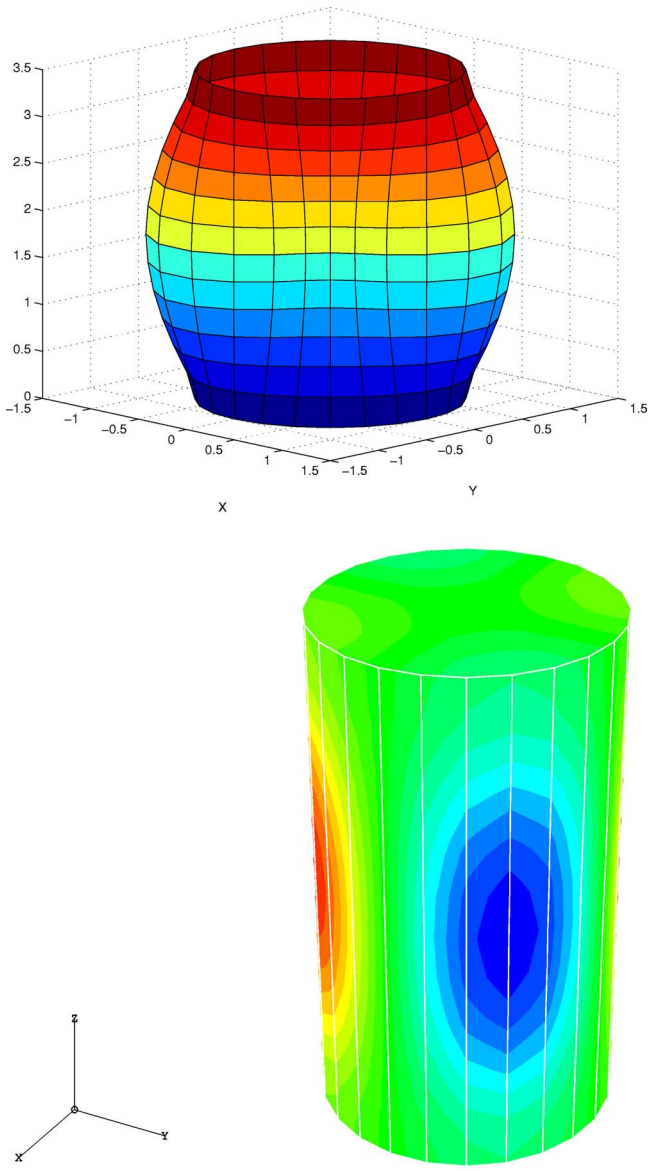

Fig. 6 Vibration mode of frequency ω_s^1. Deformed shell and fluid pressure.

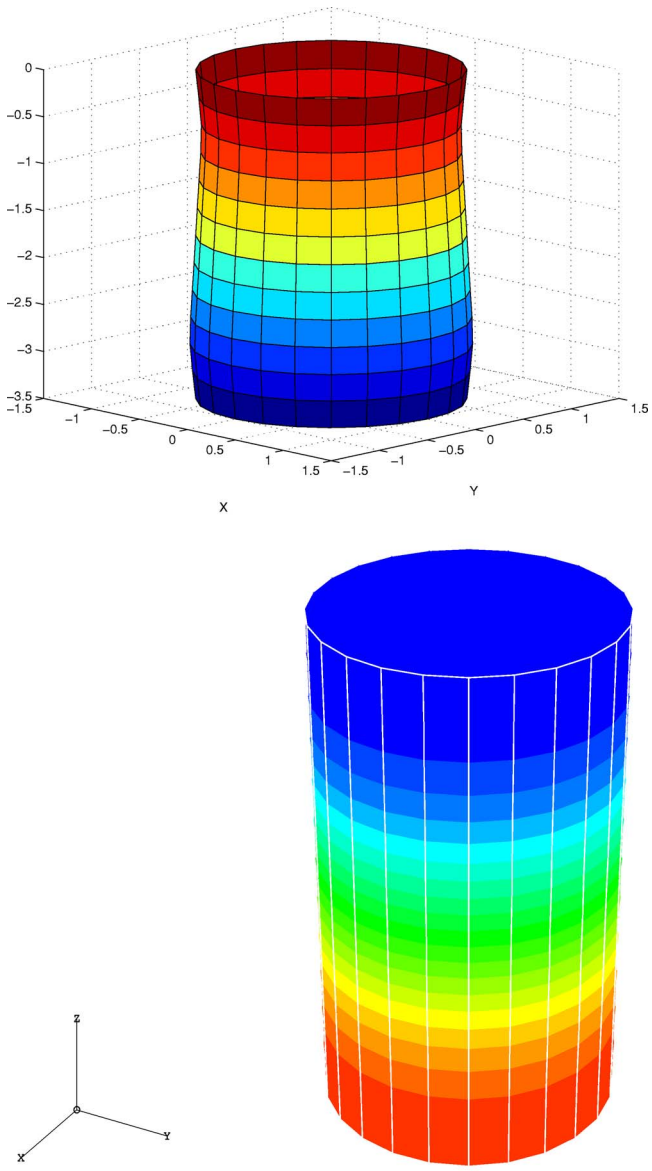

Fig. 7 Vibration mode of frequency ω_f^1. Deformed shell and fluid pressure.

fluid mode, respectively. We also include the exact values of the vibration frequencies obtained by extrapolating the computed frequencies. In the last column we include the discrepancy (in percent) between the values computed on the finest mesh and the exact values. Let us remark that ω_s^2 is a shell mode with circumferential number $n=2$; this is the reason why the discrepancy is larger for this mode.

To allow for comparison, we reproduce in Table 5 some results reported in [15]. In this reference, the same problem has been solved, but considering the structure as a three-dimensional elastic solid. The total numbers of DOF used in each mesh are also given in the table. Let us recall that the corresponding numbers of DOF

Table 3 Vibration frequencies for a thin cylindrical shell filled with fluid

Mode	$N=3$	$N=4$	$N=5$	Exact	[14]
$n=1$, $m=1$	1020.3491	1013.3759	1010.1519	1004.4146433	1007.5
$n=1$, $m=2$	1727.6673	1713.7354	1707.3111	1695.9488040	1699.5
$n=2$, $m=1$	841.9886	792.0624	768.7160	726.1533379	728.6
$n=2$, $m=2$	1539.8293	1499.4937	1481.1173	1449.6221483	1453.9
$n=3$, $m=1$	956.2804	793.6864	712.6670	539.6201194	553.0
$n=3$, $m=2$	1433.4752	1310.1966	1253.4812	1153.8148361	1156.2
$n=4$, $m=1$	1337.5487	1023.6297	863.8526	502.6526781	516.8
$n=4$, $m=2$	1631.5230	1355.9940	1226.7993	989.8001371	985.5

Table 4 Vibration frequencies for a moderately thick cylindrical shell filled with fluid

Mode	$N=3$	$N=4$	$N=5$	Exact	Discrepancy
ω_f^1	1162.5606	1160.2396	1159.1665	1157.2567655	0.165%
ω_f^2	2288.0000	2270.9296	2263.1405	2249.6966024	0.597%
ω_s^1	1213.3284	1204.3192	1200.1554	1192.8062219	0.616%
ω_s^2	1014.5626	948.2604	916.9248	858.3380240	6.825%

Table 5 Vibration frequencies reported in [15]

Mode	Mesh 1 (8544 d.o.f.)	Mesh 2 (57720 d.o.f.)	Mesh 3 (183840 d.o.f.)
ω_f^1	1188.4430	1166.6490	1158.6870
ω_f^2	2348.5520	2281.9990	2255.3540
ω_s^1	1311.8430	1237.6660	1219.2640
ω_s^2	1701.5000	1153.6710	1009.3770

of the meshes in Table 4 are 4956, 11,168, and 21,100, respectively. The impressive advantage of using the present 2D model can be clearly observed.

Finally, Figs. 6 and 7 show the deformed shell and the fluid pressure field for the two lowest-frequency vibration modes in Table 4.

Acknowledgment

This work was supported by USM 12.05.26 and FONDECYT (Chile) through grant no. 1040341.

References

[1] Morand, H. J.-P., and Ohayon, R., 1995, *Fluid-Structure Interactions*, Wiley, New York.
[2] Bernadou, M., 1996, *Finite Element Methods for Thin Shell Problems*, Wiley, New York.
[3] Chapelle, D., and Bathe, K. J., 1998, "Fundamental Considerations for the Finite Element Analysis of Shell Structures," Comput. Struct., **66**, pp. 19–36.
[4] Chapelle, D., and Bathe, K. J., 2003, *The Finite Element Analysis of Shells: Fundamentals*, Springer, Verlag.
[5] Bathe, K. J., and Dvorkin, E. N., 1985, "A Four-Node Plate Bending Element Based on Mindlin/Reissner Plate Theory and a Mixed Interpolation," Int. J. Numer. Methods Eng., **21**, pp. 367–383.
[6] Durán, R., Hervella-Nieto, L., Liberman, E., Rodríguez, R., and Solomin, J., 2000, "Finite Element Analysis of the Vibration Problem of a Plate Coupled With a Fluid," Numer. Math., **86**, pp. 591–616.
[7] Durán, R., Hernández, E., Hervella-Nieto, L., Liberman, E., and Rodríguez, R., 2004, "Error Estimates for Low-Order Isoparametric Quadrilateral Finite Element for Plates," SIAM (Soc. Ind. Appl. Math.) J. Numer. Anal., **41**, pp. 1751–1772.
[8] Hernández, E., Hervella-Nieto, L., and Rodríguez, R., 2003, "Computation of the Vibration Modes of Plates and Shells by Low Order MITC Quadrilateral Finite Elements," Comput. Struct., **81**, pp. 615–628.
[9] Gamallo, P., 2002, "Métodos Numéricos de Elementos Finitos en Problemas de Interacción Fluido-Estructura," Ph.D. thesis, U. de Santiago de Compostela, Spain.
[10] Bermúdez, A., and Rodríguez, R., 1994, "Finite Element Computation of the Vibration Modes of a Fluid-Solid System," Comput. Methods Appl. Mech. Eng., **119**, pp. 355–370.
[11] Bermúdez, A., Gamallo, P., and Rodríguez., R., 2001, "A Hexahedral Face Element Method for the Displacement Formulation of Structural Acoustics Problems," J. Comput. Acoust., **9**, pp. 911–918.
[12] Malinen, M., and Pitkäranta, J., 2000, "A Benchmark Study of Reduced-Strain Shell Finite Elements: Quadratic Shemes," Int. J. Numer. Methods Eng., **48**, pp. 1637–1671.
[13] Hernández, E., 2004, "Approximation of the Vibration Modes of a Plate Coupled With a Fluid by Low-Order Isoparametric Finite Elements," Math. Modell. Numer. Anal., **38**, pp. 1055–1070.
[14] Kyeong-Hoon, J., and Kwi-Ja, K., 1998, "Free Vibration of a Circular Cylindrical Shell Filled With Bounded Compressible Fluid," J. Sound Vib., **217**, pp. 197–221.
[15] Bermúdez, A., Hervella-Nieto, L., and Rodríguez, R., 1999, "Finite Element Computation of Three Dimensional Elastoacoustic Vibrations," J. Sound Vib., **219**, pp. 277–304.

New Mass-Conserving Algorithm for Level Set Redistancing on Unstructured Meshes

Fernando Mut[1]
e-mail: fmut@gmu.edu

Gustavo C. Buscaglia[2]
e-mail: gustavo@cab.cnea.gov.ar

Enzo A. Dari[2]
e-mail: darie@cab.cnea.gov.ar

Instituto Balseiro,
Universidad Nacional de Cuyo and CNEA,
8400 Bariloche,
Argentina

The level set method is becoming increasingly popular for the simulation of several problems that involve interfaces. The level set function is advected by some velocity field, with the zero-level set of the function defining the position of the interface. The advection distorts the initial shape of the level set function, which needs to be re-initialized to a smooth function preserving the position of the zero-level set. Many algorithms re-initialize the level set function to (some approximation of) the signed distance from the interface. Efficient algorithms for level set redistancing on Cartesian meshes have become available over the last years, but unstructured meshes have received little attention. This presentation concerns algorithms for construction of a distance function from the zero-level set, in such a way that mass is conserved on arbitrary unstructured meshes. The algorithm is consistent with the hyperbolic character of the distance equation ($\|\nabla d\|=1$) *and can be localized on a narrow band close to the interface, saving computing effort. The mass-correction step is weighted according to local mass differences, an improvement over usual global rebalancing techniques.*
[DOI: 10.1115/1.2198244]

1 Introduction

The level set method (LSM) has become a popular choice for numerically handling problems with interfaces. The basic idea is to represent the interface (which we will denote by $\mathcal{S}$) as the zero-level set of a level set (LS) function ϕ. The normal to the interface thus satisfies

$$\boldsymbol{n}(\boldsymbol{x}) = \frac{\nabla\phi}{\|\nabla\phi\|} \tag{1}$$

for all $\boldsymbol{x}$ such that $\phi(\boldsymbol{x})=0$. The curvature of $\mathcal{S}$ can also be obtained from ϕ, i.e.

$$\kappa(\boldsymbol{x}) = \operatorname{div}\boldsymbol{n} = \operatorname{div}\left(\frac{\nabla\phi}{\|\nabla\phi\|}\right) \tag{2}$$

It is evident that, if $\boldsymbol{\beta}$ is any vector field such that $c_n=\boldsymbol{\beta}\cdot\boldsymbol{n}$ is the interface speed, then ϕ must satisfy the LS equation

$$\frac{\partial\phi}{\partial t} + \boldsymbol{\beta}\cdot\nabla\phi = 0 \tag{3}$$

at least locally at $\mathcal{S}$.

In multiphase flows, $\mathcal{S}$ represents the boundary between two immiscible fluids. Let us assume that just two fluids (A and B) are present inside a domain Ω, so that the region occupied by fluid A is

$$\Omega_A = \{\boldsymbol{x} \in \Omega, \phi(\boldsymbol{x}) > 0\} \tag{4}$$

If $\boldsymbol{\beta}$ (assumed smooth enough) is solenoidal inside Ω_A, then the volume of fluid A (denoted by $|\Omega_A|$) will be conserved since

$$\frac{d|\Omega_A|}{dt} = \int_{\mathcal{S}} c_n d\Gamma = \int_{\mathcal{S}} \boldsymbol{\beta}\cdot\boldsymbol{n}\, d\Gamma = \int_{\Omega_A} div\,\boldsymbol{\beta}\, d\Omega = 0 \tag{5}$$

It is important to remark that though Eq. (3) is a transport equation, it does not arise from a conservation law. Usual methods to deal with Eq. (3) have been designed to conserve mass when ϕ is a density; i.e., they conserve $\int_\omega \phi d\omega$ for some family of subdomains ω. This conservation property is, in fact, useless in LS formulations, since it does not imply that the zero-level set of ϕ will propagate at the correct speed, and thus in general mass of each fluid will be created or destroyed at the interface due to numerical error. Please notice that, strictly speaking, it is the volume of each fluid that is created or destroyed. We, however, speak of mass conservation (implicitly assuming the fluids to be homogeneous and incompressible) to stress the physical significance of the matter we are addressing.

Much effort has lately been devoted to improving the LSM so as to minimize numerical inaccuracies in the zero-level set propagation [1–7]. The underlying idea is that if the initial data $\phi_0(\boldsymbol{x}) = \phi(\boldsymbol{x}, t=0)$ are smooth in a neighborhood of $\mathcal{S}$, then any high-order numerical method for Eq. (3) will propagate the interface without significant error from $t=0$ to some time $t=T$ provided that the mesh is fine enough. The time bound T arises because, in general, ϕ will not remain smooth indefinitely and will thus be more prone to numerical inaccuracies.

The most popular approach for initializing ϕ as a function that is smooth close to $\mathcal{S}$ is to choose ϕ as the signed distance d to the interface. Of course, after some simulation time (smaller than T) the function ϕ is re-initialized (or "redistanced"), so that LS distortion is kept under control. This re-initialization was originally introduced by Chopp [8] to avoid spurious phenomena at boundaries when computing minimal surfaces with the LS formulation.

In the present paper we describe a general method for computing d in unstructured meshes, which is related to fast-marching methods developed for Cartesian grids [9,10]. The method is developed for simplices (triangles in two dimensions (2D), tetrahedra in three dimensions (3D)), and is consistent with the hyperbolic character of the distance equation $\|\nabla d\|=1$.

However, no matter how accurately d is computed at the mesh nodes, the function ϕ which coincides with d at the nodes will not

[1]Presently at the School of Computational Sciences, George Mason University, 4400 University Drive, MSN 4C7, Fairfax, VA 22030-4444.
[2]Also at the Centro Atómico Bariloche, CNEA, and at CONICET, Argentina.

Contributed by the Applied Mechanics Division of ASME for publication in the JOURNAL OF APPLIED MECHANICS. Manuscript received April 12, 2005; final manuscript received February 1, 2006. Review conducted by N. Sri Namachchivaya. Discussion on the paper should be addressed to the Editor, Prof. Robert M. McMeeking, Journal of Applied Mechanics, Department of Mechanical and Environmental Engineering, University of California – Santa Barbara, Santa Barbara, CA 93106-5070, and will be accepted until four months after final publication of the paper itself in the ASME JOURNAL OF APPLIED MECHANICS.

preserve the exact location of the interface. This may result in an additional spurious local mass loss or gain, which is added to that coming from numerical errors in the solution of Eq. (3). Almost all re-distancing algorithms thus involve some sort of mass-correction step [5,11,12]. Our method includes one such step that is local and involves no adjustable parameter.

We are leaving aside many other sources of error that play a role in LS formulations of multi-fluid flows. Among others, the numerical difficulty of correctly computing the transport velocity $\boldsymbol{\beta}$ close to the interface, where density and viscosity are discontinuous. Very comprehensive accounts of the LSM for fluid interfaces are available [13,14].

2 Redistancing Algorithm

2.1 Preliminaries. In this section we recall some elementary properties of distance functions stated in the form that adapts best for distance-computing algorithms.

We consider an arbitrary triangulation $\mathcal{T}_h$ of the domain Ω, where h is a characteristic mesh size, and the associated space V_h of continuous functions that are linear inside each simplex. Let $\phi_h \in V_h$ be a function, and let $\mathcal{S}$ be its zero-level set. Our aim is to find a function $\tilde{\phi}_h \in V_h$ which approximates the signed distance function d to $\mathcal{S}$, defined for any closed set $\mathcal{S}$ as

$$d(\boldsymbol{x}) = \text{sign}[\phi_h(\mathbf{x})] \min_{\mathbf{y}\in\mathcal{S}} \|\boldsymbol{x}-\boldsymbol{y}\| \tag{6}$$

This function satisfies $\|\nabla d\| = 1$ almost everywhere in Ω, but does *not*, in general, belong to V_h. In what follows we will assume Ω to be bounded, and all curves (in 2D) or surfaces (in 3D) to be compact (adding the adherence points if the curve or surface intersects the boundary of Ω).

The algorithm we consider is based on the following basic property of the distance function to a compact set $\mathcal{S}$:

PROPOSITION 2.1. *Let $\mathcal{C}$ be a surface in $\mathbb{R}^n$ (of co-dimension 1) which divides $\mathbb{R}^n$ into two open sets, ω^+ and ω^-, such that $\mathcal{S} \subset \omega^-$. Then, for any $\boldsymbol{y} \in \omega^+$*

$$|d(\boldsymbol{y})| = \min_{\mathbf{x}\in\mathcal{C}} [|\boldsymbol{y}-\boldsymbol{x}| + |d(\boldsymbol{x})|] \tag{7}$$

Proof. Let $\boldsymbol{s} \in \mathcal{S}$ satisfy $|d(\boldsymbol{y})| = |\boldsymbol{y}-\boldsymbol{s}|$, and let $\boldsymbol{a}$ be the intersection of the segment $\overline{ys}$ with $\mathcal{C}$ (which exists because $\mathcal{C}$ divides $\mathbb{R}^n$). Notice first that $|d(\boldsymbol{a})| = |\boldsymbol{a}-\boldsymbol{s}|$ because, if there existed a point $\boldsymbol{w}$ such that $|\boldsymbol{a}-\boldsymbol{w}| < |\boldsymbol{a}-\boldsymbol{s}|$, then

$$|\boldsymbol{y}-\boldsymbol{w}| \leqslant |\boldsymbol{y}-\boldsymbol{a}| + |\boldsymbol{a}-\boldsymbol{w}| < |\boldsymbol{y}-\boldsymbol{a}| + |\boldsymbol{a}-\boldsymbol{s}| = |\boldsymbol{y}-\boldsymbol{s}| = |d(\boldsymbol{y})|$$

in contradiction with the definition of $|d(\boldsymbol{y})|$ as the minimal distance from $\boldsymbol{y}$ to any point in $\mathcal{S}$. Defining now

$$\xi(\boldsymbol{y}) = \min_{\mathbf{x}\in\mathcal{C}} [|\boldsymbol{y}-\boldsymbol{x}| + |d(\boldsymbol{x})|] \tag{8}$$

it is easy to show that $\xi(\boldsymbol{y}) \leqslant |d(\boldsymbol{y})|$. In fact

$$\begin{aligned} |d(\boldsymbol{y})| &= |\boldsymbol{y}-\boldsymbol{s}| = |\boldsymbol{y}-\boldsymbol{a}| + |\boldsymbol{a}-\boldsymbol{s}| = |\boldsymbol{y}-\boldsymbol{a}| + |d(\boldsymbol{a})| \\ &\geqslant \min_{\mathbf{x}\in\mathcal{C}} [|\boldsymbol{y}-\boldsymbol{x}| + |d(\boldsymbol{x})|] = \xi(\boldsymbol{y}) \end{aligned}$$

It remains to show that $\xi(\boldsymbol{y}) \geqslant |d(\boldsymbol{y})|$. To see this, let $\boldsymbol{z} \in \mathcal{C}$ satisfy $\xi(\boldsymbol{y}) = |\boldsymbol{y}-\boldsymbol{z}| + |d(\boldsymbol{z})|$ and let $\boldsymbol{w} \in \mathcal{S}$ satisfy $|d(\boldsymbol{z})| = |\boldsymbol{z}-\boldsymbol{w}|$. Then

$$\xi(\boldsymbol{y}) = |\boldsymbol{y}-\boldsymbol{z}| + |\boldsymbol{z}-\boldsymbol{w}| \geqslant |\boldsymbol{y}-\boldsymbol{w}| \geqslant |d(\boldsymbol{y})|$$

and the proof is complete. □

The previous proposition shows that the distance function can be computed "layer after layer," using the values computed on some surface $\mathcal{C}$ to compute the values of d at points that lie "outside" $\mathcal{C}$. With these new values, one can redefine $\mathcal{C}$ as the new boundary of the subdomain in which d is already known, and in this way march outwards from $\mathcal{S}$ until d is known everywhere. The idea of a *marching method* [9,10] has been made evident in the previous argument.

But what happens when one considers *perturbations* of the original problem? We have already recalled that the exact function d does not belong to V_h. Let $\mathcal{P}$ be the set of nodal points that are adjacent to the zero-level set of ϕ_h, in the sense that they are vertices of simplices inside which ϕ_h changes sign. If one makes the simple assignment $\tilde{\phi}_h(\boldsymbol{X}) = d(\boldsymbol{X})$ for all $\boldsymbol{X} \in \mathcal{P}$, there is a volume loss (or gain) which could render the algorithm useless for physical simulations. To be precise, assigning $\tilde{\phi}_h(\boldsymbol{X}) = d(\boldsymbol{X})$ results in $\int_{\phi_h(\boldsymbol{x})<0} d\boldsymbol{x} \neq \int_{\tilde{\phi}_h(\boldsymbol{x})<0} d\boldsymbol{x}$.

The values of $\tilde{\phi}_h$ at the nodes adjacent to the zero-level set must thus be "adjusted" so as to preserve volume, and the function $\tilde{\phi}$ must be calculated at the remaining nodes using the adjusted values at $\mathcal{P}$. In general, this adjusted distance $\tilde{\phi}_h$, linearly interpolated from the nodal values, is *not* the distance to some adjusted set $\mathcal{S}'$. This is a perturbation of the problem considered in Prop. 2.1, and it is appropriate to adapt the result to consider this case. Simultaneously, we will rephrase the result in a way that motivates the algorithm we are using (which is not a marching method).

PROPOSITION 2.2. *Let $\mathcal{S}$ be a closed set in $\mathbb{R}^n$ and let ψ be a continuous, positive function on $\mathcal{S}$. Let us define*

$$\eta(\boldsymbol{y}) = \min_{\mathbf{x}\in\mathcal{S}} [\psi(\boldsymbol{x}) + |\boldsymbol{y}-\boldsymbol{x}|] \tag{9}$$

(notice that $\eta(\boldsymbol{y}) = |d(\boldsymbol{y})|$ if $\psi = 0$), and let $\boldsymbol{y}$ be arbitrary in $\mathbb{R}^n \backslash \mathcal{S}$. Then, for any surface $\mathcal{C}$ (as in Prop. 2.1) such that $\mathcal{S} \subset \omega^-$ and $\boldsymbol{y} \in \omega^+$

$$\eta(\boldsymbol{y}) = \min_{\mathbf{x}\in\mathcal{C}} [\eta(\boldsymbol{x}) + |\boldsymbol{y}-\boldsymbol{x}|] \tag{10}$$

Proof. Let

$$\xi(\boldsymbol{y}) = \min_{\mathbf{x}\in\mathcal{C}} [\eta(\boldsymbol{x}) + |\boldsymbol{y}-\boldsymbol{x}|] \tag{11}$$

We must prove that $\eta(\boldsymbol{y}) = \xi(\boldsymbol{y})$. Let $\boldsymbol{s}$ verify $\eta(\boldsymbol{y}) = \psi(\boldsymbol{s}) + |\boldsymbol{y}-\boldsymbol{s}|$, and let $\boldsymbol{a}$ be the intersection of the segment $\overline{ys}$ with $\mathcal{C}$. From Eq. (9)

$$\eta(\boldsymbol{a}) \leqslant \psi(\boldsymbol{s}) + |\boldsymbol{a}-\boldsymbol{s}| = \psi(\boldsymbol{s}) + |\boldsymbol{y}-\boldsymbol{s}| - |\boldsymbol{y}-\boldsymbol{a}| = \eta(\boldsymbol{y}) - |\boldsymbol{y}-\boldsymbol{a}|$$

implying that

$$\eta(\boldsymbol{y}) \geqslant \eta(\boldsymbol{a}) + |\boldsymbol{y}-\boldsymbol{a}| \geqslant \xi(\boldsymbol{y})$$

It remains to prove that $\eta(\boldsymbol{y}) \leqslant \xi(\boldsymbol{y})$. Let $\boldsymbol{z} \in \mathcal{C}$ satisfy $\xi(\boldsymbol{y}) = \eta(\boldsymbol{z}) + |\boldsymbol{y}-\boldsymbol{z}|$ and let $\boldsymbol{w} \in \mathcal{S}$ satisfy $\eta(\boldsymbol{z}) = \psi(\boldsymbol{w}) + |\boldsymbol{z}-\boldsymbol{w}|$. Then

$$\xi(\boldsymbol{y}) = \psi(\boldsymbol{w}) + |\boldsymbol{z}-\boldsymbol{w}| + |\boldsymbol{y}-\boldsymbol{z}| \geqslant \psi(\boldsymbol{w}) + |\boldsymbol{y}-\boldsymbol{w}| \geqslant \eta(\boldsymbol{y})$$

which completes the proof. □

Remark 2.3. In the proof above it is not difficult to see that $\boldsymbol{y}$, $\boldsymbol{w}$, and $\boldsymbol{z}$ are aligned. Let $\boldsymbol{b}$ be the intersection of the segment $\overline{yw}$ with $\mathcal{C}$. If $\boldsymbol{b} \neq \boldsymbol{z}$, then

$$\begin{aligned} \xi(\boldsymbol{y}) &= \psi(\boldsymbol{w}) + |\boldsymbol{y}-\boldsymbol{z}| + |\boldsymbol{z}-\boldsymbol{w}| > \psi(\boldsymbol{w}) + |\boldsymbol{b}-\boldsymbol{w}| + |\boldsymbol{y}-\boldsymbol{b}| \\ &\geqslant \eta(\boldsymbol{b}) + |\boldsymbol{y}-\boldsymbol{b}| \end{aligned}$$

in contradiction with Eq. (10). The alignment implies that, if $\boldsymbol{s}$ is as before such that $\eta(\boldsymbol{y}) = \psi(\boldsymbol{s}) + |\boldsymbol{y}-\boldsymbol{s}|$, then for any $\boldsymbol{z}$ in the straight segment $\overline{ys}$, $\eta(\boldsymbol{z}) = \psi(\boldsymbol{s}) + |\boldsymbol{z}-\boldsymbol{s}|$. The curves that join each point of the domain with the minimizing argument of the right hand side of Eq. (9) are straight lines ("rays," by analogy with optics).

Remark 2.4. It is also possible to prove that, at points where η is differentiable, $|\nabla \eta| = 1$ in much the same way as $|\nabla d| = 1$, which is a particular case corresponding to $\psi = 0$. To see this, first notice that along the rays the directional derivative of η is equal to one. It remains to prove that along a direction perpendicular to the local ray direction the derivative vanishes, assuming that it exists. Let $\boldsymbol{y}$ and $\boldsymbol{s}$ be as before, and let $\boldsymbol{D}$ be a unit vector orthogonal to the segment $\overline{ys}$. Because of the orthogonality

$$|\boldsymbol{y}+\epsilon\boldsymbol{D}-\boldsymbol{s}| = |\boldsymbol{y}-\boldsymbol{s}| + \frac{1}{2}\frac{\epsilon^2}{|\boldsymbol{y}-\boldsymbol{s}|} + \mathcal{O}(\epsilon^4)$$

Now, using also Eq. (9)

$$\eta(\boldsymbol{y}+\epsilon\boldsymbol{D}) \leqslant \psi(\boldsymbol{s}) + |\boldsymbol{y}+\epsilon\boldsymbol{D}-\boldsymbol{s}| \leqslant \psi(\boldsymbol{s}) + |\boldsymbol{y}-\boldsymbol{s}| + \mathcal{O}(\epsilon^2)$$
$$= \eta(\boldsymbol{y}) + \mathcal{O}(\epsilon^2)$$

From this it is immediate that, if η is differentiable at $\boldsymbol{y}$, then its derivative along $\boldsymbol{D}$ must vanish.

2.2 Computing the Distance. It is clear that the sign of $\tilde{\phi}_h$ adds no difficulty, since it simply equals that of ϕ_h. We will thus describe the calculation of $\tilde{\phi}_h$ just on Ω_A, where ϕ_h is positive. Let $\mathcal{P}$ be the set of nodal points that are adjacent to the zero-level set of ϕ_h, in the sense that they are vertices of simplices inside which ϕ_h changes sign, and let $\mathcal{P}_A$ be the subset of $\mathcal{P}$ with positive values of ϕ_h (i.e., $\mathcal{P}_A = \mathcal{P} \cap \Omega_A$). We assume $\tilde{\phi}_h$ given on $\mathcal{P}_A$ (its calculation is described later). The rest of the nodes in Ω_A are denoted by $\mathcal{R}_A$.

Step 1 (*Initialization*). There exist several options for initializing $\tilde{\phi}_h$ over $\mathcal{R}_A$.

(**a**) Let I be a node in $\mathcal{R}_A$, and let C_I be the set of nodes connected to I, I not included (notice that $C_I \subset (\mathcal{P}_A \cup \mathcal{R}_A)$). The initial guess we use for $\tilde{\phi}_h$ is a distance-along-edges approximation, i.e., the unique function satisfying

$$\tilde{\phi}_h(\boldsymbol{X}_I) = \min_{J \in C_I}[\tilde{\phi}_h(\boldsymbol{X}_J) + |\boldsymbol{X}_I - \boldsymbol{X}_J|]$$

In the process of initializing $\tilde{\phi}_h$ with this option, the elements can be ordered so as to render the algorithm more effective.

(**b**) If one wants to calculate $\tilde{\phi}_h$ up to a distance δ from $\mathcal{S}$, one simply initializes $\tilde{\phi}_h$ as equal to δ over $\mathcal{R}_A$.

Step 2 (*Evaluation*). The simplices in the mesh are swept until $\tilde{\phi}_h$ no longer changes. For each simplex, and for each node I of the simplex (coordinates denoted by $\boldsymbol{X}_I$), $\tilde{\phi}_h$ is interpolated linearly on the opposite face F_I, using the current values at the nodes. Then, a tentative new value η_I of $\tilde{\phi}_h$ at node I is calculated as

$$\eta_I = \min_{\mathbf{x} \in F_I}[\tilde{\phi}_h(\boldsymbol{x}) + |\boldsymbol{X}_I - \boldsymbol{x}|] \tag{12}$$

Finally, $\tilde{\phi}_h(\boldsymbol{X}_I)$ is updated to the value η_I *if the current value is greater than* η_I.

Equation (12) is the key operation in the computation of the distance. It is computed *exactly*. This is not difficult since $\tilde{\phi}_h$ is a linear function and the minimum is calculated over F_I, which is a simplex (a segment in 2D, a triangle in 3D). The possibilities of the minimum being attained in the interior of F_I or at its boundary have of course to be considered (in 3D, this latter case decomposes in turn into attaining the minimum either inside an edge or at a vertex). It can be shown that the proposed algorithm, like others discussed, for example, by Osher and Fedkiw [14], correctly approximates more complex distance problems such as computing geodesics, optical paths with varying refraction index, and distances around obstacles.

Remark 2.5. Notice that the discretization error in the distance computation is a direct consequence of the linear interpolation of $\tilde{\phi}_h$ on F_I from the values computed at the nodes. Since the distance is a smooth function almost everywhere, this interpolation error is of order h^2 (with h the mesh size) on each segment (in 2D) or triangle (in 3D). The error propagates away from the interface, being thus of order h^2 at distances of the order of the mesh size from the interface, and of order h at distances comparable to L (with L the domain size).

2.3 Volume Preservation. The key in preserving volume in the algorithm is the correct computation of $\tilde{\phi}_h$ on the set of nodes adjacent to the interface (denoted by $\mathcal{P}$). Let us define $\mathcal{K}(\phi_h)$ as the set of simplices in which ϕ_h changes sign, so that $\mathcal{S} \subset \mathcal{K}(\phi_h)$. The objective is thus to calculate $\tilde{\phi}_h$ such that it approximates the signed distance d while at the same time preserving the volume

$$V(\phi_h) = \int_{\mathcal{K}(\phi_h)} H(\phi_h(\boldsymbol{x}))d\boldsymbol{x} \tag{13}$$

where H is the Heaviside function ($H(s)=1$ if $s>0$, $H(s)=0$ otherwise). The contribution to this volume of each simplex $K \in \mathcal{K}(\phi_h)$ is

$$V_K(\phi_h) = \int_K H(\phi_h(\boldsymbol{x}))d\boldsymbol{x} \tag{14}$$

The algorithm is again structured in a sequence of steps.

Step 1 (*Initialization*). The function $\tilde{\phi}_h$ is initialized, over the nodes in $\mathcal{P}$, to a first estimate $\tilde{\phi}_h^0$, calculated as the true signed distance to $\mathcal{S}$.

Step 2 (*Evaluation of a simplex-wise correction*). In general, the initialization ends up with a function $\tilde{\phi}_h^0$ for which $V_K(\tilde{\phi}_h^0) \neq V_K(\phi_h)$, though the difference is quite small. We then solve, on K, the nonlinear system

$$R_K(\Delta_K) = V_K(\tilde{\phi}_h^0 + \Delta_K) - V_K(\phi_h) = 0 \tag{15}$$

to determine which (constant over K) value should be added to $\tilde{\phi}_h^0$ to achieve local volume preservation. The values Δ_K are computed using a simple secant algorithm $\Delta_K^{(i+1)} = \Delta_K^{(i)} - R_K^{(i)}(\Delta_K^{(i)} - \Delta_K^{(i-1)})/(R_K^{(i)} - R_K^{(i-1)})$, which converges in very few steps, and stored.

Step 3 (*Node-wise correction*). From the previous step, simplex-wise values that should be added to $\tilde{\phi}_h^0$ to preserve volume for all $K \in \mathcal{K}(\phi_h)$ are available. We now compute a node-wise direction ψ_h by averaging over the simplices that share a node. Let I be a node in $\mathcal{P}$, and let N_I be the number of simplices in $\mathcal{K}(\phi_h)$ that contain I, then we define

$$\psi_h(\boldsymbol{X}_I) = \frac{1}{N_I}\sum_{\substack{K \in \mathcal{K}(\phi_h) \\ I \in K}} \Delta_K \tag{16}$$

The value of $\tilde{\phi}_h$ on $\mathcal{P}$ is finally calculated over $\mathcal{P}$ as

$$\tilde{\phi}_h = \tilde{\phi}_h^0 + C\psi_h \tag{17}$$

where C is the value of C such that

$$\int_{\mathcal{K}(\phi_h)} H[\tilde{\phi}_h^0(\boldsymbol{x}) + C\psi_h(\boldsymbol{x})]d\boldsymbol{x} = \int_{\mathcal{K}(\phi_h)} H[\phi_h(\boldsymbol{x})]d\boldsymbol{x} \tag{18}$$

The nonlinear system for C is again solved by a simple secant method and converges in very few iterations.

Remark 2.6. The mass correction Eq. (17) is of the same generic form as those proposed in other papers, the difference being in the choice of ψ_h. A common approach is simply to propose $\psi_h = 1$, so that a uniform value is added to $\tilde{\phi}_h^0$ to correct the mass [15]. This is, however, not optimal, since mass loss/gain is not uniform over the interface. In fact, the loss/gain in mass tends to concentrate in regions of higher curvature. In other approaches the function $\tilde{\phi}$ is obtained as the steady state of the heuristic equation

$$\frac{\partial\tilde{\phi}}{\partial t} + S(\phi)(|\nabla\tilde{\phi}| - 1) = 0, \quad \tilde{\phi}(\boldsymbol{x},0) = \phi(\boldsymbol{x})$$

in which S is a sign function or a suitably smeared approximation thereof. We refer to the book by Osher and Fedkiw ([14], p. 65),

for a thorough discussion on re-initialization procedures. Our approach is similar to that proposed by Sussman and Fatemi for structured grids [11], in that it proposes a function $\tilde{\phi}_h$ that has no free parameters and concentrates the correction locally where the loss/gain in mass is higher, thus automatically accounting for curvature, mesh distortion, etc.

3 Numerical Examples in Pure Transport

In this section we couple the redistancing algorithm with a numerical method for transport. The numerical method we use for Eq. (3) is a streamline upwind Petrov-Galerkin (SUPG) finite element method [16], with Implicit-Euler (θ=1 below) or Crank-Nicolson (θ=0.5) treatment of the time derivative.

Let V_h be the space of piecewise linear functions on the triangulation $\mathcal{T}_h$ of Ω. To make explicit the numerical method, let $\phi_h^n \in V_h$ denote the numerical solution at time $t=n\Delta t$, where Δt is the time step. Then, assuming ϕ_h^n given, ϕ_h^{n+1} is obtained as the unique solution in V_h of the discrete variational formulation

$$\int_\Omega \left\{ \left[\frac{\phi_h^{n+1} - \mathcal{G}(\phi_h^n)}{\Delta t} + \boldsymbol{\beta} \cdot \nabla(\theta \phi_h^{n+1} + (1-\theta)\mathcal{G}(\phi_h^n)) \right] (v_h + \tau \boldsymbol{\beta} \cdot \nabla v_h) \right\} d\boldsymbol{x} = 0 \tag{19}$$

for all v_h in V_h. In Eq. (19) we have introduced the mapping $\mathcal{G}: V_h \to V_h$, which allows us to incorporate the re-initialization step. We thus compare the plain algorithm ($\mathcal{G}(\phi_h)=\phi_h$) to the re-initialized one (with or without the mass-correction substep), $\mathcal{G}(\phi_h)=\tilde{\phi}_h$. Also in Eq. (19), τ is the SUPG characteristic time, which we calculate as $\tau=h_\beta/(2|\boldsymbol{\beta}|)$. The local streamwise element size h_β is defined as one half the length of the element in the direction of $\boldsymbol{\beta}$.

3.1 Zalezak's Disk. The problem we consider is the rigid body rotation of the so-called Zalezak's disk, a usual benchmark for level set formulations [5,11]. The domain is $\Omega=(0,1)\times(0,1)$. The initial data correspond to fluid A inside a slotted circle centered at (0.50, 0.75) with a radius of 0.15. The slot length is 0.25 and its width 0.05. The velocity field is given by

$$\boldsymbol{\beta} = \frac{\pi}{314}(0.5 - x_2, x_1 - 0.5)$$

so that the disk completes one revolution every 628 time units.

In addition, we calculate the accuracy of the interface location using the L_1 norm of the error between the corresponding characteristic functions [5]:

$$E_1 = \frac{1}{L}\int_\Omega |H(\phi_{\text{expected}}) - H(\phi_{\text{computed}})| d\boldsymbol{x} \tag{20}$$

where L is the length of the expected interface. This integral is calculated exactly. We used a uniform unstretched triangulation of 80,000 elements for all tests. The distance algorithm was set to compute $\tilde{\phi}_h$ up to a distance of 0.04 from the zero-level set (Zalesak's disk).

Figure 1 shows an example of the evolution of the disk as it turns around the center of the domain. Four different instants are plotted (t_1=0, t_2=157, t_3=314, and t_4=471), superposed to the exact solution to put into evidence the distortion of the iso surface due to transport alone.

We now turn to quantitative comparisons of the different algorithms. In Fig. 2 we show the evolution of the disk's volume and the L_1 distance in time for Δt=0.5 and θ=0.5. This figure also contains a comparison between initial and final states.

Algorithms "Plain," where no-re-initialization is present, and "Re-initialized+MC," where re-initialization is done with the mass-correction substep, show a similar behavior. This is mainly because the time step and mesh size are small enough for the transport of the level set to be done without significant error. However, the case Re-initialized, in which the mass-correction substep is omitted, shows that the errors introduced in the re-initialization substep accumulate, destroying the global mass conservation. From the figure we can see that these errors are located in zones with greater curvature. Some authors (e.g., [9], p. 140) recommend to restrict redistancing to a minimum because of this phenomenon. The example just described shows that our *local* mass-conservation procedure allows redistancing to be safely performed at every time step. We recall that, when the mass-correction substep is performed, the re-initialization procedure strictly preserves the volume. The changes that nevertheless arise occur at the transport substep, and our algorithm does not attempt at solving them.

The second example was done with a fully implicit scheme replacing the Crank-Nicolson one presented above. The idea is to

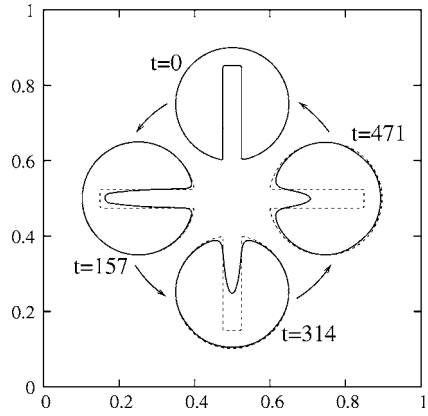

Fig. 1 Zalesak's disk at four different instants: t_1=0, t_2=157, t_3=314, and t_4=471. The first one corresponds to the initial state. A uniform unstructured unstretched grid of 80,000 elements was used. Δt=1 and θ=0.5 was set in the transport algorithm.

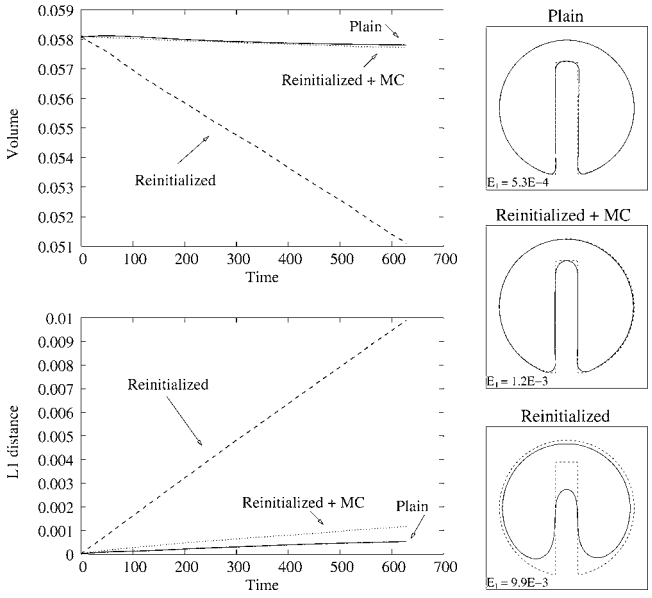

Fig. 2 Zalesak's disk: Volume and L_1-distance evolution for Δt=0.5 and θ=0.5. Comparison between initial and final states (after one revolution). Domain is a uniform unstructured unstretched grid of 80,000 elements.

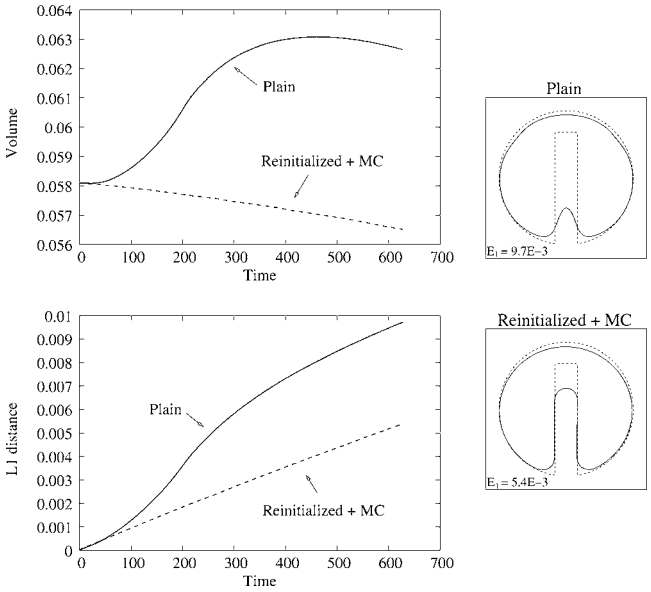

Fig. 3 Zalesak's disk: Volume and L_1-distance evolution for $\Delta t=0.5$ and fully implicit scheme ($\theta=1$). Comparison between initial and final states (after one revolution). Domain is a uniform unstructured unstretched grid of 80,000 elements.

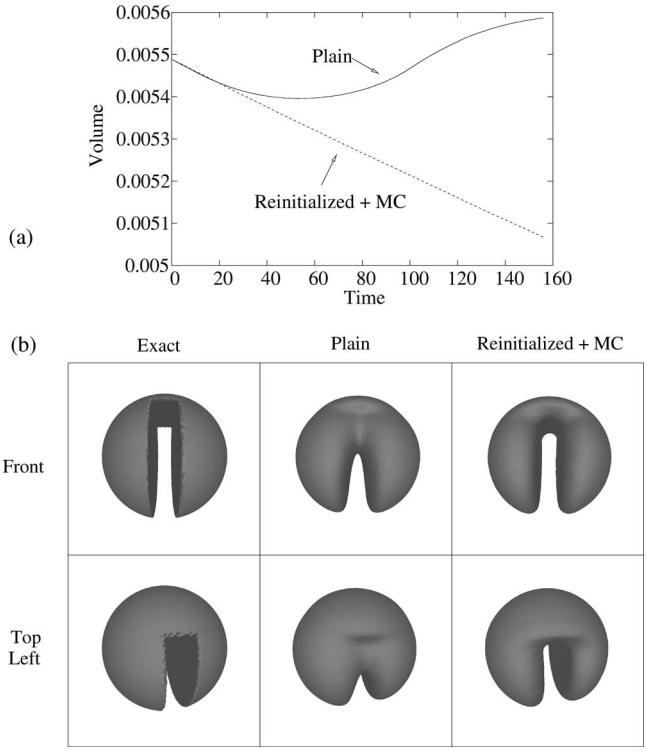

Fig. 5 Notched sphere: (*a*) Volume evolution for $\Delta t=1$ and fully implicit scheme. (*b*) Comparison between initial and final states ($t=157$) for the runs with and without reinitialization.

investigate the effects of more diffusive transport algorithms. Figure 3 shows the evolution of the volume and of the L_1 distance in time for $\Delta t=0.5$.

From the comparison between initial and final states, it is evident that the diffusive behavior is again concentrated in zones with greater curvature. This is consistent with the increase of the volume in the case Plain, since the slot quickly disappears. In case Re-initialized+MC the damage to the slot is greatly reduced, also reducing the global mass change. In addition, the geometry is preserved much more accurately.

Finally, the last test investigates the effect of re-initialization in simulations with large time steps. In Fig. 4 we show the evolution of the volume of fluid and the L_1 distance in time for $\Delta t=2$ (Crank-Nicolson scheme).

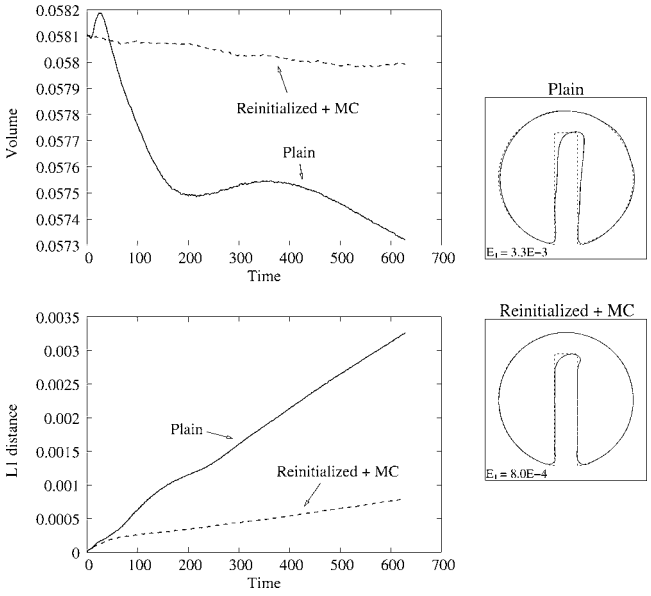

Fig. 4 Zalesak's disk: Volume and L_1-distance evolution for $\Delta t=2$ and Crank-Nicolson scheme. Comparison between initial and final states (after one revolution). Domain meshed with a uniform unstructured unstretched grid of 80,000 elements.

For algorithm Plain the total mass loss is 1.35%, while for Re-initialized+MC the amount of mass loss is 0.19%. From the comparison between initial and final states we see again that the re-initialization step helps preserve the original geometry.

3.2 Notched Sphere. This test is the three-dimensional analog of Zalezak's disk. The sphere's radius is 0.15, from which a sector of width 0.05 and depth 0.20 has been removed. The velocity field is the same rigid rotation as before. We use an unstructured uniform isotropic mesh of 2.76×10^6 tetrahedra, with the same mesh size as in the 2D case. The final time is $t=156$ (a quarter of a turn) with a time step $\Delta t=1$ and $\theta=1$.

We compare here two runs, Plain and Re-initialized+MC. The re-initialization, performed at each time step, includes the mass-correction step (otherwise the results are extremely bad). In Fig. 5(*a*) we compare the evolution of the volume along the two runs. Mass conservation is comparable for the two runs, but part 5(*b*) of the same figure shows that the shape is much better preserved in the re-initialized run.

4 Conclusions

In this work we developed an algorithm to compute the signed distance function on general unstructured meshes in two and three dimensions. A mass-correction step, which is weighted according to local mass differences, is proposed as part of the general algorithm in order to maintain the total mass during the re-initialization step.

We reported the well-known Zalezak's-disk and notched-sphere tests to assess the behavior of the algorithm in transport cases. We showed that a mass-correction step during the re-initialization is indeed necessary. Moreover, this step must be done in a local sense in order to preserve the original geometry. In addition, we observed that when numerical methods used to solve the transport

equation have significant errors (e.g., excessive diffusion) the re-initialization step helps to both preserve the geometry and to reduce global mass loss/gain.

Let us remark, however, that re-initialization techniques only work if the mesh is fine enough. For too-coarse meshes, in which the error is dominated by the spatial discretization of the transport step, re-distancing does not provide significant improvement.

Acknowledgment

This work was partially supported by ANPCyT through Grant No. 12-9848.

References

[1] Chang, Y. C., Hou, T. Y., Merriman, B., and Osher, S., 1996, "A Level Set Formulation of Eulerian Interface Capturing Methods for Incompressible Fluid Flows," J. Comput. Phys., **124**, pp. 449–464.

[2] Adalsteinsson, D., and Sethian, J. A., 1999, "The Fast Construction of Extension Velocities in Level Set Methods," J. Comput. Phys., **148**, pp. 2–22.

[3] Tezduyar, T., Aliabadi, S., and Behr, M., 1998, "Enhanced-Discretization Interface-Capturing Technique (EDICT) for Computation of Unsteady Flows With Interfaces," Comput. Methods Appl. Mech. Eng., **150**, pp. 235–248.

[4] Codina, R., and Soto, O., 2002, "A Numerical Model to Track Two-Fluid Interfaces Based on a Stabilized Finite Element Method and the Level Set Technique," Int. J. Numer. Methods Fluids, **40**, pp. 293–301.

[5] Enright, D., Fedkiw, R., Ferziger, J., and Mitchell, I, 2002, "A Hybrid Particle Level Set Method for Improved Interface Capturing," J. Comput. Phys., **183**, pp. 83–116.

[6] Lakehal, D., Meier, M., and Fulgosi, M., 2002, "Interface Tracking Towards the Direct Simulation of Heat and Mass Transfer in Multiphase Flows," Int. J. Heat Fluid Flow, **23**, pp. 242–257.

[7] Cruchaga, M., Celentano, D., and Tezduyar, T., 2005, "Moving-Interface Computations With the Edge-Tracked Interface Locator Technique (ETILT)," Int. J. Numer. Methods Fluids, **47**, pp. 451–469.

[8] Chopp, D., 1993, "Computing Minimal Surfaces via Level Set Curvature Flow," J. Comput. Phys., **106**, pp. 77–91.

[9] Sethian, J. A., 1998, "Fast Marching Methods and Level Set Methods for Propagating Interfaces," von Karman Institute Lecture Series, Computational Fluid Mechanics.

[10] Barth, T. J., and Sethian, J. A., 1998, "Numerical Schemes for the Hamilton-Jacobi and Level Set Equations on Triangulated Domains," J. Comput. Phys., **145**, pp. 1–40.

[11] Sussman, M., and Fatemi, E., 1999, "An Efficient, Interface-Preserving Level-Set Redistancing Algorithm and Its Application to Interfacial Incompressible Fluid Flow," SIAM J. Sci. Comput. (USA), **20**(4), pp. 1165–1191.

[12] Chopp, D. L., 2001, "Some Improvements of the Fast Marching Method," Clin. Anat., **23**(1), pp. 230–244.

[13] Sethian, J. A., and Smereka, P., 2003, "Level Set Methods for Fluid Interfaces," Annu. Rev. Fluid Mech., **35**, pp. 341–372.

[14] Osher, S., and Fedkiw, R., 2003, *Level Set Methods and Dynamic Implicit Surfaces*, **153**, Springer, New York.

[15] Aliabadi, S., and Tezduyar, T. E, 2000, "Stabilized-Finite-Element/Interface-Capturing Technique for Parallel Computation of Unsteady Flows With Interfaces," Comput. Methods Appl. Mech. Eng., **190**, pp. 243–261.

[16] Hughes, T., and Brooks, A., 1979, "A Multi-Dimensional Upwind Scheme With No Crosswind Diffusion," *Finite Element Methods for Convection Dominated Flows*, AMD-Vol. 34, ASME, New York pp. 19–35.

Numerical Simulation of Transient Free Surface Flows Using a Moving Mesh Technique

Laura Battaglia
e-mail: lbattaglia@ceride.gov.ar

Jorge D'Elía
e-mail: jdelia@intec.unl.edu.ar

Mario Storti
e-mail: mstorti@intec.unl.edu.ar

Norberto Nigro
e-mail: nnigro@intec.unl.edu.ar

Centro Internacional de Métodos Computacionales en Ingeniería,
Instituto de Desarrollo Tecnológico para Industria Química,
Universidad Nacional del Litoral - CONICET,
Güemes 3450, 3000-Santa Fe,
Argentina

*In this work, transient free surface flows of a viscous incompressible fluid are numerically solved through parallel computation. Transient free surface flows are boundary-value problems of the moving type that involve geometrical nonlinearities. In contrast to more conventional computational fluid dynamics problems, the computational flow domain is partially bounded by a free surface which is not known a priori, since its shape must be computed as part of the solution. In steady flow the free surface is obtained by an iterative process, but when the free surface evolves with time the problem is more difficult as it generates large distortions in the computational flow domain. The incompressible Navier-Stokes numerical solver is based on the finite element method with equal order elements for pressure and velocity (linear elements), and it uses a streamline upwind/Petrov-Galerkin (SUPG) scheme (Hughes, T. J. R., and Brooks, A. N., 1979, "A Multidimensional Upwind Scheme With no Crosswind Diffusion," in Finite Element Methods for Convection Dominated Flows, ASME ed., **34**. AMD, New York, pp. 19–35, and Brooks, A. N., and Hughes, T. J. R., 1982, "Streamline Upwind/Petrov-Galerkin Formulations for Convection Dominated Flows With Particular Emphasis on the Incompressible Navier-Stokes Equations," Comput. Methods Appl. Mech. Eng., **32**, pp. 199–259) combined with a Pressure-Stabilizing/Petrov-Galerkin (PSPG) one (Tezduyar, T. E., 1992, "Stablized Finite Element Formulations for Incompressible Flow Computations," Adv. Appl. Mech., **28**, pp. 1–44, and Tezduyar, T. E., Mittal, S., Ray, S. E., and Shih, R., 1992, "Incompressible Flow Computations With Stabilized Bilinear and Linear Equal Order Interpolation Velocity-Pressure Elements," Comput. Methods Appl. Mech. Eng., **95**, pp. 221–242). At each time step, the fluid equations are solved with constant pressure and null viscous traction conditions at the free surface and the velocities obtained in this way are used for updating the positions of the surface nodes. Then, a pseudo elastic problem is solved in the fluid domain in order to relocate the interior nodes so as to keep mesh distortion controlled. This has been implemented in the PETSc-FEM code (PETSc-FEM: a general purpose, parallel, multi-physics FEM program. GNU general public license (GPL), http://www.cimec.org.ar/petscfem) by running two parallel instances of the code and exchanging information between them. Some numerical examples are presented.*
[DOI: 10.1115/1.2198246]

1 Introduction

Free surface flows are very common in engineering problems. They include, for instance, the sloshing case which appears in vehicle, ship, or aerospace engineering, when the back-and-forth splashing of a liquid fuel in its tank can lead to problems of stability and control in ground or launch vehicles. Another case is the sloshing in a liquid storage tank subjected to seismic action when high impact loads on the tank roof and walls can damage the liquid storage tank. Early simulations of the liquid sloshing problem in a liquid carrier or storage tanks have mostly been performed with waves of small steepness assuming low sloshing so that the nonlinear boundary conditions can be neglected.

The most commonly applied classic idealization for estimating liquid response in excited rigid tanks is Housner's [5]. The hydrodynamic pressures are divided into two components: the impulsive pressure caused by the portion of liquid accelerating with the tank, and the convective pressure caused by the portion of liquid sloshing in the tank. These hydrodynamic pressures result in added masses which can duplicate forces and moments exerted by a liquid on a vibrating tank, as shown in the computations reported in Ref. [6]. Sloshing in a more general context is extensively reviewed by Biswal et al. [7].

From a numerical point of view, several techniques have been developed for the solution of free surface flows as initial value problems. These techniques are roughly classified by Shyy et al. [8] as Eulerian, Lagrangian, or mixed Eulerian-Lagrangian.

In Eulerian-like (volume-tracking) approaches (see Fig. 1), the mesh remains stationary or moves in a predetermined manner. Moreover, the free surface is not explicitly tracked but it is reconstructed from other field properties such as the fluid fractions. Then, the fluid moves in/out of the computational flow domain. Under this scope, Aliabadi and Tezduyar [9] perform a numerical simulation of sloshing in tanker trucks during turning with a stabilized finite element formulation which is implemented in parallel using the message-passing interface libraries. The level set method, the well-known marker-and-cell (MAC) method, and immersed boundary methods are schemes of this type (e.g., see Perot and Nallapati [10]). They can handle large displacements without loss of accuracy. However, it is rather difficult to impose the free boundary conditions, due to a lack of a sharp definition, see Nickell et al. [11], Silliman and Scriven [12], Ruschak [13], and Kawahara and Miwa [14]. In Lagrangian-like (surface-tracking) approaches, the mesh is configured to conform to the shape of the

Contributed by the Applied Mechanics Division of ASME for publication in the JOURNAL OF APPLIED MECHANICS. Manuscript received July 19, 2005; final manuscript received February 28, 2006. Review conducted by G. C. Buscaglia. Discussion on the paper should be addressed to the Editor, Prof. Robert M. McMeeking, Journal of Applied Mechanics, Department of Mechanical and Environmental Engineering, University of California – Santa Barbara, Santa Barbara, CA 93106-5070, and will be accepted until four months after final publication of the paper itself in the ASME JOURNAL OF APPLIED MECHANICS.

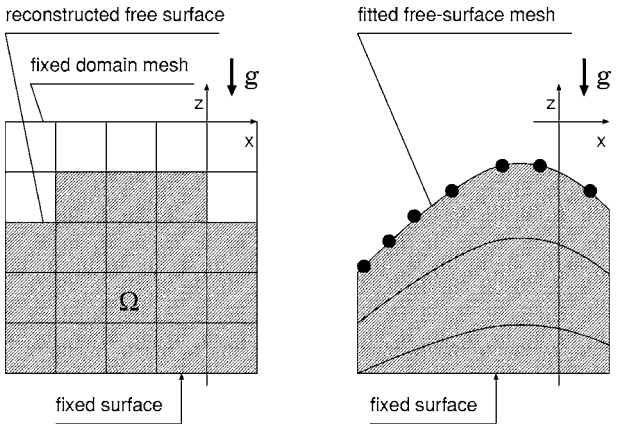

Fig. 1 A flow domain with a free surface discretized by domain-like schemes: Eulerian-type (left) and Lagrangian-type (right) methods

free surface, i.e., it continually adapts to it. The free surface is a discontinuity whose evolution is explicitly tracked as an $(n-1)$ dimensional entity in an n-dimensional space. No modeling is necessary to define the free surface or its effects on the flow field because the grid points move with the local fluid particles. However, mesh movement or remeshing is usually necessary for large deformations, see Bach and Hassager [15] and Ramaswamy and Kawahara [16]. In mixed Eulerian Lagrangian-like approaches, or arbitrary Lagrangian-Eulerian (ALE) formulations, the advantages of both methods are taken into account, see Hughes et al. [17], or more recently Sung et al. [18]. Other mixed approaches are also proposed. For example, the "emplicit" method uses an explicit-implicit time integration oriented to seakeeping ship motions, see Huang and Sclavounos [19], while the "material point" method, see York et al. [20], uses unconnected Lagrangian points and a background Eulerian mesh for solving fluid-membrane interaction.

While kinematic and dynamic laws govern the displacement of the computational flow domain at the moving boundaries, in Lagrangian-like (surface-tracking) approaches the motion of the internal nodes is largely arbitrary. A primary criterion is to achieve absorption of expected boundary displacements while keeping or controlling the distortion of the mesh elements, which are assumed to be well shaped at the start of the simulation. A number of possibilities have been proposed; they can be roughly classified in three main strategies (e.g., see Tezduyar et al. [21]):

1. *algebraic mesh update*: it applies an explicit algebraic expression for the displacement of each interior node as a function of the displacement of one or more boundary nodes;
2. *pseudo-elastic mesh update* [22,23]: it embeds the mesh in an elastic pseudo-solid governed by a fictitious constitutive relation and solves a boundary value problem with imposed boundary displacements. The mesh updates based on using different ratios of the Lamé constants were introduced by Johnson and Tezduyar [23], and results were reported as a function of that ratio;
3. *mesh update through regeneration*: it performs an entirely new mesh based on the updated boundary locations and projects the solution from the old mesh to the new one.

In a previous study [24], a Lagrangian-type panel method in the time domain was proposed for inviscid potential flows with a moving free surface where the instantaneous velocity-potential and normal displacement on the moving free surface were obtained by means of a time-marching scheme after a spatial semi-discretization with a low-order scheme. Later [25], a surface reallocation strategy for the instantaneous wet hull surface caused by changes in the position of the intersection curve between the free surface and hull surface was shown.

In this work, a mesh-movement technique for transient flow domains with a free surface of a viscous and incompressible fluid is addressed in the context of a finite element approach and solved by parallel computation.

2 Governing Equations

The flow of an incompressible and viscous fluid of the Newtonian type is considered. The governing flow equations are the Navier-Stokes (NS) ones

$$\rho(\partial_t \boldsymbol{v} + \boldsymbol{v}\cdot\nabla\boldsymbol{v} - \boldsymbol{f}) - \nabla\cdot\boldsymbol{\sigma} = 0$$
$$\nabla\cdot\boldsymbol{v} = 0 \tag{1}$$

on the flow domain $\Omega_t = \Omega(t)$ at time t, for all $t \in [0,T]$, where $\boldsymbol{v}$ is the fluid velocity, $\boldsymbol{f}$ is the body force, ρ is the fluid density, and T is a final time. The fluid stress tensor $\boldsymbol{\sigma}$ is decomposed into its isotropic $-p\boldsymbol{I}$ and deviatoric $\boldsymbol{T}$ parts

$$\boldsymbol{\sigma} = -p\boldsymbol{I} + \boldsymbol{T} \tag{2}$$

where p is the pressure and $\boldsymbol{I}$ is the identity tensor. As only Newtonian fluids with constant physical properties are considered, its deviatoric part $\boldsymbol{T}$ is related linearly to the strain rate tensor with

$$\boldsymbol{T} = 2\mu\boldsymbol{\epsilon}; \quad \boldsymbol{\epsilon} = \frac{1}{2}[\nabla\boldsymbol{v} + (\nabla\boldsymbol{v})^T] \tag{3}$$

where μ and $\nu = \mu/\rho$ are the dynamic and kinematic viscosity of the fluid and $(\ldots)^T$ denotes the transpose. The boundary conditions are

$$\boldsymbol{v} = 0 \quad \text{at } \Gamma_{\text{wall}}$$
$$p = P_{\text{atm}} \quad \text{at } \Gamma_{\text{FS}} \tag{4}$$
$$\boldsymbol{\tau}\cdot\boldsymbol{n} = 0 \quad \text{at } \Gamma_{\text{FS}}$$

where Γ_{wall} is the boundary on the solid walls while Γ_{FS} is the free surface. Note that as no restriction is imposed on velocity at the free surface, then the normal velocity there can be non-null. This normal velocity is responsible of the free surface movement. The boundary conditions at the free surface are similar to those normally imposed at an outlet boundary. ALE terms [17] are included in order to take into account the advection of momentum caused by the relocation of the nodes.

The discretization of this system of partial differential equations is carried out by a finite element method based on the streamline upwind/Petrov-Galerkin (SUPG) [1,2] and pressure-stabilizing/Petrov-Galerkin (PSPG) [3,4] formulations. This leads to a set of ordinary differential equations (ODE) in time, which is discretized by a finite difference method. A trapezoidal integration rule is employed for solving this ODE, which has been verified to be second order for $\alpha = 0.5$ in the numerical examples (it is often used $\alpha = 0.6$).

At each time step, a non-linear system of equations of the form

$$\boldsymbol{F}\left(\frac{\boldsymbol{v}^{n+1} - \boldsymbol{v}^n}{\Delta t}, \boldsymbol{p}^{n+1}\right) = \boldsymbol{0} \tag{5}$$

is obtained so that having setting the state of the fluid at time t^n and a mesh for the domain $\Omega(t^n)$, the velocity and pressure unknowns at time t^{n+1} can be solved. As the velocity may be non-null at the free surface in a Lagrangian approach, the nodes there should move with velocity

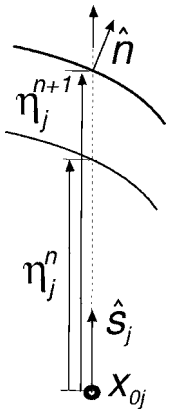

Fig. 2 Notation for the spines-like employed in the mesh movement

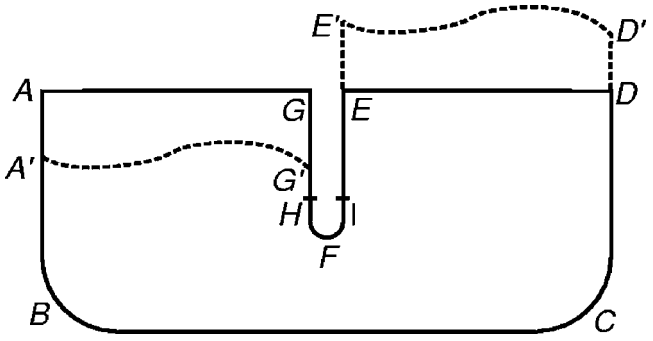

Fig. 3 Boundary conditions for the pseudo elastic problem for a mesh movement: nodes can move freely at the solid walls *ABCD*, *GH* and *IE* (slip boundary condition) and non-slip one in portion *HFI* to prevent large distortions of elements near the tip *F* of the separator

$$\boldsymbol{v}_j^{n+1} \approx \frac{\boldsymbol{x}_j^{n+1} - \boldsymbol{x}_j^n}{\Delta t} \tag{6}$$

However, displacements of the nodes tangential to the free surface are considered irrelevant so that it is necessary to verify only the normal component of this equation

$$\left(\frac{\boldsymbol{x}_j^{n+1} - \boldsymbol{x}_j^n}{\Delta t} - \boldsymbol{v}_j^{n+1} \right) \cdot \boldsymbol{n}_j^n = 0 \tag{7}$$

In addition, the movement of the free surface nodes are constrained along a fixed direction $\hat{\boldsymbol{s}}_j$, then

$$\boldsymbol{x}_j(t) = \boldsymbol{x}_{0,j} + \eta_j(t)\hat{\boldsymbol{s}}_j \tag{8}$$

where η_j is a scalar coordinate along some "*spine*" whose direction is $\hat{\boldsymbol{s}}_j$ and starting point $\boldsymbol{x}_{0,j}$, see Fig. 2. Then Eq. (5) gives an equation for the increment in η coordinate

$$\Delta \eta_j^{n+1} = \eta_j^{n+1} - \eta_j^n = \Delta t \frac{\boldsymbol{v}_j^{n+1} \cdot \hat{\boldsymbol{n}}_j^n}{\hat{\boldsymbol{s}}_j \cdot \hat{\boldsymbol{n}}_j^n} \tag{9}$$

Note that the spines $(\boldsymbol{x}_{0,j}, \hat{\boldsymbol{s}}_j)$ do not change with time. The only requirement is that the spine direction and the normal be nonorthogonal at each node at each time step, which means that the fixed direction can be defined almost arbitrary. However, it is convenient to choose them as parallel as possible to the expected surface normal. For example, the spines for a spillway are usually drawn perpendicular to the main profile of the structure. These spines are only used for the movement of the free surface nodes, that is, the interior ones are relocated by solving the pseudo elastic problem regardless of spines directions. On the other hand, the normal to the free surface at node $\boldsymbol{x}_j$ is computed at each time step using

$$\hat{\boldsymbol{n}} \propto \int_{FS} N_j(\boldsymbol{x}) \hat{\boldsymbol{n}}(\boldsymbol{x}) d\boldsymbol{\Sigma}_{FS}$$
$$\|\hat{\boldsymbol{n}}_j\| = 1 \tag{10}$$

where $N_j(\boldsymbol{x})$ is the finite element interpolation for the j node and $\hat{\boldsymbol{n}}(\boldsymbol{x})$ is the normal to the free surface at point $\boldsymbol{x}$. The integration is carried out over the whole free surface, but, due to the local support of the finite element interpolation function, it involves only those elements that are connected to the j-node. For linear tetrahedral elements in the fluid, this amounts to the weighted average of the normals of the triangular panels around the j-node.

Other limitations of the method of spines are inclined walls or high velocity normal to the spines, all situations that could also appear simultaneously. Considering that displacements are projected onto the direction of the spines, all these cases produce loss of information or instabilities over the free surface. An alternative to reduce negative aspects of spines direction is proposed by Behr and Abraham [26], who treated in the referenced paper an application for inclined walls problems. It must be emphasized that, unlike this method, which uses the projection over fixed spines only for the free surface, other proposals project the displacements of all the nodes over fixed directions. As a consequence of this, the mesh updated by the elastic solver is less distorted than in other proposals.

3 Moving Mesh Strategy

Once the displacements of the free surface nodes at time step $n+1$ are known, the positions of the internal nodes can be moved so as to reduce the distortion of the mesh elements. Here, an implementation of the *pseudo-elastic mesh update* strategy is employed. It is based on solving an artificial elastic problem with imposed displacements at the free surface, and slip or non-slip conditions at solid walls and other boundaries, see Tezduyar et al. [22] or Johnson [23]. Consider, for instance, a typical case of a truck container as in Fig. 10 with a separating wall. Under longitudinal accelerations of the truck, the fluid tends to go from one half to the other causing large displacements of the fluid surface with extreme positions as shown in Fig. 3. Under these circumstances, the best boundary conditions for the pseudo elastic problem may be to let the nodes move freely at the solid walls *ABCD*, *GH* and *IE* (slip boundary condition). However, these can cause large distortions of the elements near the tip *F* of the separator, so a non-slip one is imposed in a small region around the tip, such as the portion *HFI*.

The pseudo elastic problem may be posed as

$$\sigma_{ij,j} = 0$$
$$\sigma_{ij} = 2\tilde{\mu}\epsilon_{ij} + \tilde{\lambda}\delta_{ij}\epsilon_{kk} \tag{11}$$
$$\epsilon_{ij} = \frac{1}{2}(u_{i,j} + u_{j,i})$$

where $\boldsymbol{u}$ is the mesh node displacements

$$\boldsymbol{u}_j = \boldsymbol{x}_j^{n+1} - \boldsymbol{x}_j^0 \tag{12}$$

where $\tilde{\mu}$ and $\tilde{\lambda}$ are the Lamé elastic constants for the fictitious elastic material and δ_{ij} is the Kronecker tensor. Of course, the pseudo elastic problem is invariant under a multiplicative constant in the elastic coefficients since only Dirichlet conditions are used. The only relevant parameter is the ratio between them, or its equivalent, the Poisson ratio $\tilde{\nu}$. The Lamé constants $\tilde{\mu}$ and $\tilde{\lambda}$ can be expressed in terms of more familiar modulus of elasticity $\tilde{E}$ with

$$\tilde{\mu} = \frac{\tilde{E}}{2(1+\tilde{\nu})}; \quad \tilde{\lambda} = \frac{\tilde{\nu}\tilde{E}}{(1+\tilde{\nu})(1-2\tilde{\nu})} \tag{13}$$

It is not clear which values are more appropriate for $\tilde{\nu}$ but for $\tilde{\nu} \to 1/2$ the material is nearly incompressible and the pseudo elastic problem will become ill conditioned. The increment of the Poisson ratio towards the incompressible limit ($\tilde{\nu}=0.5$) tends to increase the ability to admit larger displacements of the free surface without collapse but for small deformations of the free surface, lower values of $\tilde{\nu}$ can be used. In Ref. [23], this moving mesh method was reported, including several examples and the study of the influence of the Lamé constants was considered. The interest in using lower values of $\tilde{\nu}$ is achieving a better conditioning of the pseudo-elastic problem, and then a lower computational cost. In the numerical examples, $\tilde{\nu}=0.3$ was used for moderate free surface deformations and $\tilde{\nu}=0.45$ for larger ones.

The boundary conditions are

$$\boldsymbol{u} = \Delta \boldsymbol{x}^{n+1} \quad \text{at free surface } AG + ED \tag{14}$$

$$\boldsymbol{u} = 0 \quad \text{at non-slip boundary } HFI \tag{15}$$

$$\boldsymbol{u} \cdot \hat{\boldsymbol{n}} = 0 \quad \text{at slip boundary } ABCD + GH + IE \tag{16}$$

where $\Delta \boldsymbol{x}^{n+1} = \boldsymbol{x}^{n+1} - \boldsymbol{x}^0$. The pseudo elastic problem is solved in the reference mesh Ω_0, where the choice between slip and non-slip boundary condition at solid walls is problem dependent and is specified by the user. Once this problem is solved, the updated position of the internal nodes $\boldsymbol{x}^{n+1}$ is obtained with Eq. (12).

Several alternatives for the mesh relocation problem could be devised. Non-linear elastic material behavior could be used in order to reduce distortion but in the linear version shown here the computing time per time step and memory requirements are lower than the ones needed for the fluid, and it was able to solve problems with relatively large distortions, as shown in the examples below.

4 Free Surface Elevation Smoothing

The whole algorithm as described so far is unstable for gravity waves of high frequency and must be stabilized, mainly due to the fully explicit character of the free surface update given by Eq. (9). This has been also reported by other authors [27]. In this study, a smoothing operator is applied to the free surface elevation so that Eq. (9) is replaced by

$$\Delta \tilde{\eta}_j^{n+1} = \frac{\boldsymbol{v}_j^{n+1} \cdot \hat{\boldsymbol{n}}_j^n}{\hat{\boldsymbol{s}}_j \cdot \hat{\boldsymbol{n}}_j^n}$$
$$\Delta \eta_j^{n+1} = \mathcal{S}(\Delta \tilde{\eta}_j^{n+1}) \tag{17}$$

where $\mathcal{S}$ is a smoothing operator based on solving the heat equation with a diffusivity α adjusted so as to have a characteristic spreading length γh, where h is a characteristic global mesh size, and γ is a user chosen parameter; usually, $\gamma=2$ is employed.

5 Moving Contact Line

As described so far, the nodes at the contact line (i.e., the intersection of the free surface with a wall boundary, also called waterline) have null velocity due to how boundary conditions are imposed, leading to large elevation gradients near the wall. The non-slip condition may be relaxed at the contact line and replaced by the Navier slip condition

$$(\boldsymbol{I} - \boldsymbol{nn}) \cdot (\boldsymbol{n} \cdot \boldsymbol{\sigma}) = -\frac{1}{\beta}(\boldsymbol{I} - \boldsymbol{nn}) \cdot (\boldsymbol{v} - \boldsymbol{v}_{\text{wall}}) \tag{18}$$

where $\boldsymbol{v}$ is the fluid velocity at the contact line, $\boldsymbol{v}_{\text{wall}}$ is the wall velocity, $\boldsymbol{I}-\boldsymbol{nn}$ is the projector onto the tangent plane and β is an empirical slip coefficient. For $\beta=0$ the non-slip condition is considered, whereas for $\beta \to \infty$ the perfect slip condition is recovered.

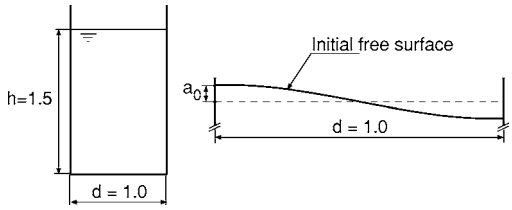

Fig. 4 Dimensions in m and initial free surface position for the sloshing problem with known solution

In the cases evaluated up to now, the contact line movement is implemented over a thin strip of nodes near the free surface or only those nodes which define the contact line, over the walls, whose nodal displacements are controlled by this condition.

6 Numerical Results

6.1 Some Comments on the Viscous Incompressible Navier-Stokes Solver. This section depicts the ability of the incompressible Navier-Stokes module implemented in the PETSc-FEM library [3] to capture the physics involved in the flow of a viscous incompressible fluid, i.e., vorticity, transport, and dissipation. Both the Navier-Stokes solver and the linear system solver, based on domain decomposition techniques, were applied to different benchmarks in order to prove its validity, accuracy, and efficiency [28–30].

In particular, the laminar flow past a circular cylinder at moderated Reynolds numbers is proposed. Much research work focused on the description of this problem, from the experimental and numerical point of view, covering a wide range of Reynolds numbers, see Refs. [31–39]. This fact had pushed the computational fluid dynamics (CFD) community to use this test as a benchmark to validate CFD code development. Results obtained from PETSc-FEM show good agreement with those published in the references above. A maximum error of 0.5% in the prediction of the Strouhal number is verified, while a maximum error of 2.5% in the predicted lift and drag forces is encountered.

6.2 Analytic Validation: 2D Viscous Sloshing. For validating the proposed method, a two-dimensional (2D) sloshing test with analytical solution is performed, following Rabier and Medale [40]. This test mainly shows how a numerical scheme predicts, besides the frequency, the damping rate governed by the fluid viscosity. It consists in solving the initial-value problem of the small-amplitude motion of the free surface of a viscous fluid in a rectangular tank (see Fig. 4), whose free surface is in an initial position given by

$$h(x) = 1.5 + a_0 \sin[\pi(1/2 - x)] \tag{19}$$

where a_0 is the amplitude of the initial sinusoidal perturbation of the movement. The fluid is submitted to gravity acceleration, and viscous forces are responsible for the damping of movement. The boundary conditions chosen are perfect slip on solid boundaries, as mentioned in Sec. 5, i.e., null normal velocity and tangential stresses, and over the free surface, $p=P_{\text{atm}}$ and $\boldsymbol{\tau} \cdot \boldsymbol{n} = 0$. The analytical solution of the linearized case is given by Prosperetti [41] as

$$a(t) = \frac{4\nu^2 k^4}{8\nu^2 k^4 + \omega_0^2} a_0 \operatorname{erfc}(\nu k^2 t)^{1/2} + \sum_{i=1}^{4} \frac{z_i}{Z_i} \left(\frac{\omega_0^2 a_0}{z_i^2 - \nu k^2} \right)$$
$$\times \exp[(z_i^2 - \nu k^2)t] \operatorname{erfc}(z_i t^{1/2}) \tag{20}$$

where ν is the kinematic viscosity of the fluid, k is the wave number, $\omega_0^2 = gk$ is the inviscid natural frequency, each z_i is the root of the following algebraic equation

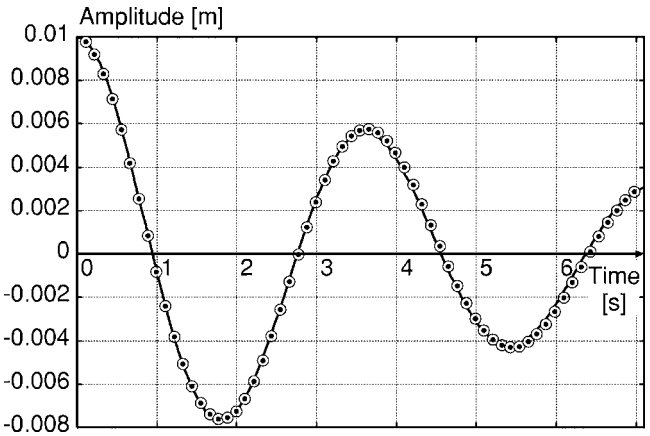

Fig. 5 Analytic solution curve and numerical results (dots) calculated for the sloshing problem

$$z^4 + k^2\nu z^2 + 4(k^2\nu)^{3/2}z + \nu^2 k^4 + \omega_0^2 = 0 \tag{21}$$

where $Z_1=(z_2-z_1)(z_3-z_1)(z_4-z_1)$ with Z_2, Z_3, Z_4 obtained by circular permutation of the indices and erfc(…) is the error function for complex variable. This expression is valid for small-amplitude flat waves in an infinite depth domain.

The example was solved for the chosen geometry, with initial maximum perturbation $a_0=0.01$ m, kinematic viscosity $\nu=0.01$ m^2/s, unit gravity acceleration $g=1.0$ m/s^2, and a mesh of 40×60 quadrangular elements for the container of $h=1.5$ m height and $d=1.0$ m wide, with a time-step $\Delta t=2.12\ 10^{-2}$ s.

In Fig. 5, the vertical position of the upper left node versus time is plotted over the curve calculated analytically.

The results obtained allow validation of the method, considering the capture of the frequency and the rate of viscous damping in the experiment.

6.3 Analytic Validation: 3D Quasi-Inviscid Sloshing. The proposed case corresponds to a right cylinder of annular base, as shown in Fig. 6. The nature of this problem is clearly three dimensional (3D) because of the initial condition imposed, which produces fluid circulation from one side to the other of the tank. This test mainly shows how the numerical scheme simulates the eigenvalues and eigenmodes of the free surface, e.g., see Papaspyrou et al. [42].

The internal radius of the cylinder is $R_i=1.0$ m, and the external one $R_e=2.0$ m. The initial condition proposed, represented also in Fig. 6, is the free surface perturbed by displacements given by the natural frequency $n=1$, with maximum amplitude $a_0=0.05$ m over fluid height, $h=1.0$ m. In this way, the movement is not influenced by natural modes other than the one used as initial condition.

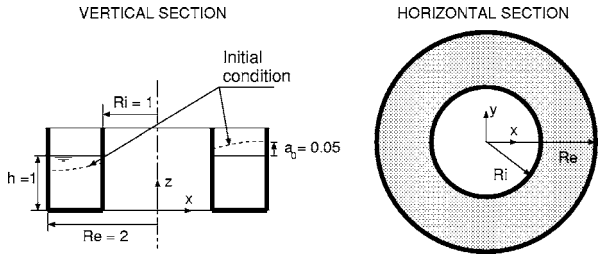

Fig. 6 Vertical and horizontal sections of a right vertical cylinder with annular base for a three-dimensional quasi-inviscid sloshing test. Initial free surface and reference axis. Dimensions in m.

As in the precedent case, boundary conditions are imposed as follows: $p=P_{\text{atm}}$ and $\boldsymbol{\tau}\cdot\boldsymbol{n}=0$ over the free surface, and perfect slip on solid walls.

The results obtained are contrasted with equations developed by Moiseev and Petrov [43], which calculate natural frequencies of sloshing for inviscid liquids in this kind of domain. As this analytical value is computed under the inviscid hypothesis, it is not expected that the numerical viscous values converge to it, even when $\nu\to0$ and the mesh is refined. However, it is expected to give a good approximation with a small percentage of relative error.

For the natural frequency ω, the wave number k and the dimensionless coefficient $c=R_e/R_i>1$, the equations considered are

$$k_m^{(n)} = \frac{(\omega_m^{(n)})^2}{g} \tag{22}$$

$$k_m^{(n)} = \kappa_m^{(n)}\tanh[\kappa_m^{(n)}h] \tag{23}$$

where $\kappa_m^{(n)}$ is the mth root of the equation

$$J_n'(\kappa)\cdot N_n'(c\kappa) - N_n'(\kappa)\cdot J_n'(c\kappa) = 0 \tag{24}$$

in which $J_n(\ldots)$ and $N_n(\ldots)$ are Bessel functions of first and second kind, respectively. Besides, $n=1$ was adopted corresponding to the lowest frequency mode. The higher periods calculated by applying this method are $T_1=9.94$ s, $T_2=3.47$ s, $T_3=2.49$ s, and $T_4=2.04$ s, considering that $T=2\pi/\omega$. As the first is the leading one, $T_a=9.94$ s is used as an analytical period for comparing to numerical results.

The finite element problem for this case was solved with a mesh of 32,000 hexahedral eight-node elements and 35,721 nodes, with gravity $g=1.0$ m/s^2, kinematic viscosity $\nu=10^{-3}$ m^2/s, and $\Delta t=0.1$ s.

Numerical results are plotted in Fig. 7, where vertical displacements of four representative nodes are plotted making it possible to distinguish the period T of the movement. A global way to show the sloshing is proposed, in this case the free surface nodal displacements weighted with a "first moment function" (see Fig. 8). This function calculates the sum of nodal vertical displacements multiplied by its distance to the axis of the cylinder, allowing the estimation of the experimental period for the whole tank, as the average of time differences between the zeros of the function. The period of movement calculated in this way is $T_e=10.33$ s. The relative error between the numerical viscous solution and the inviscid one is under 4%.

Several analyses were made for studying convergence of the method, taking the period of the movement as the main parameter. The variables considered were the mesh mean step h and the time step, keeping the quotient between them constant. Considering that the finite element approximation applied is $O(h^2)$, the results were used to make a Richardson's extrapolation which gave an asymptotic $T_0=10.315$ s for $h\to0$. In Fig. 9, the calculated points are plotted, as well as T_0.

6.4 Example: Tank With Internal Buffer. A truck-like container tank with an internal buffer subject to an impulsive deceleration is considered (see Fig. 10). The container is moving right at velocity 0.5 m/s and suddenly stops at $t=0$ s. The tank length and width are $L=1.20$ m and $L_y=L/2$ m, respectively, and the curvature radius of tank corners is $R_C=0.15$ m. The length of wall edge separation is $W=0.15$ m. The starting height of fluid in the tank is $H_f=0.36$ m. In this example, the perfect slip condition (see Sec. 5) is used on the contact line and the nodes on a thin strip near the contact line, whose width is $H_s=0.2\times H_f=0.072$ m. The number of elements in fluid movement direction is 80, the same as in the wall-to-wall directions and in the crossing one (see Fig. 11). The time step is $\Delta t=0.02$ s, the gravity acceleration g

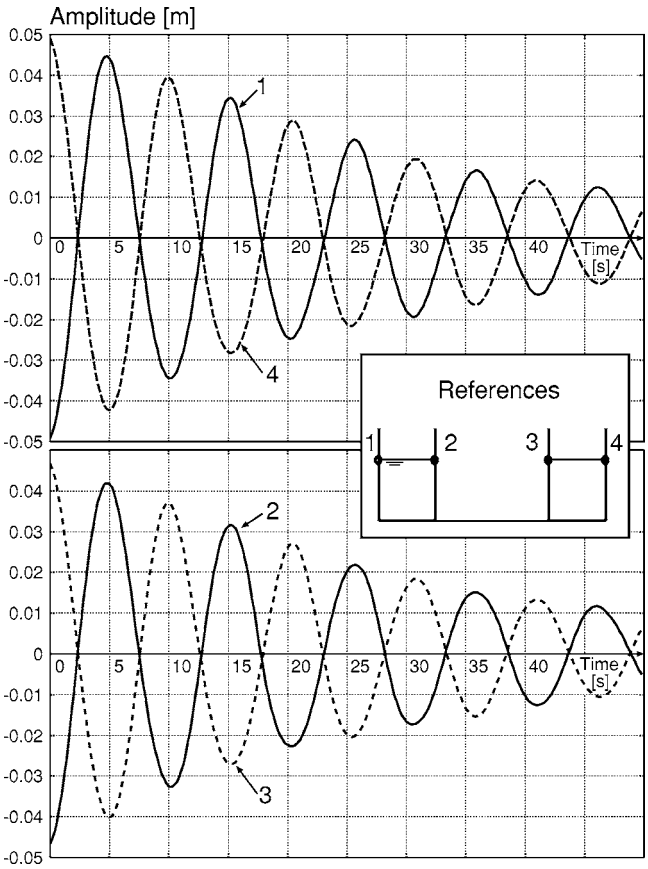

Fig. 7 Displacements time evolution for some representative mesh nodes in the tank of annular base

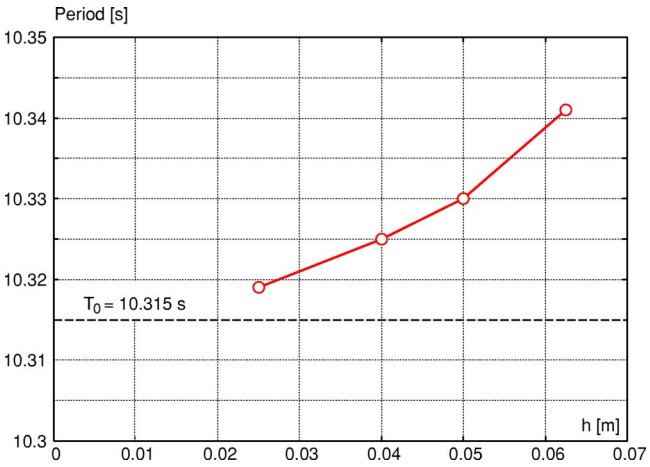

Fig. 9 Period of movement *T* versus mesh mean step *h* for the sloshing 3D test

$=9.81\ \mathrm{m/s^2}$, and the kinematic viscosity is $\nu=3\times10^{-5}\ \mathrm{m^2/s}$.

The internal buffer is a wall edge separation that is placed to break the fundamental longitudinal sloshing mode. Nevertheless, with this geometrical container configuration and under longitudinal accelerations or decelerations, there is a transient back-and-forth splashing of the liquid, as a hydraulic pendulum. The observed period of the main mode is $T_h \approx 1.7$ s. As the fluid passes from the right half to the left one there is a strong viscous friction near the tip of the separator. This causes emission of vortices, which are the main energy dissipation mechanism. Figures 12 and 13 correspond to time instants near the point of maximum height in the left half. A forming vortex is clearly seen in Fig. 12 on the left wall of the separator near the tip. In Fig. 13 it has already been separated from the wall. Once the vortices are shed, they are transported by the fluid and in Figs. 14 and 15 the vortex is passing to the right half and a new vortex is forming on the right half.

The Reynolds number (Re) observed in the region where the vortices are shed is low enough (Re $\approx$100) to make a turbulence model unnecessary, so the vorticity is a result of the averaged Navier-Stokes equations, which are accurately solved by the corresponding PETSc-FEM module, as mentioned in Sec. 6.1.

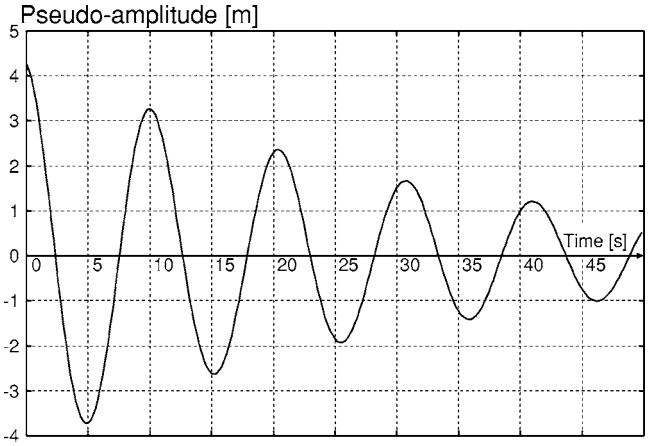

Fig. 8 Filtered nodes movement on the free surface for the 3D cylindrical tank

7 Conclusions

In this study a moving mesh technique for transient free surface flows of an incompressible and viscous fluid of Newtonian type, in the context of SUPG and PSPG formulations for finite elements is shown.

The combined fluid and moving mesh problem was formulated within the picture of the multi-physics programming paradigm, and was implemented reusing pre-existent fluid and elastic modules which are not specifically oriented to the free surface case.

Numerical tests show that the frequency and damping of sloshing modes are accurately predicted. Even if the surface elevation is updated with an explicit strategy, time steps as large as one twentieth of the main sloshing mode period can be used. The simple moving mesh strategy based on a linear pseudo-elastic operator proved to be robust enough, allowing large surface elevation amplitudes.

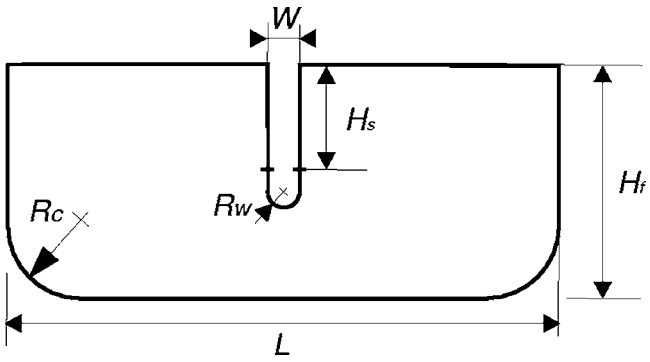

Fig. 10 Main geometrical dimensions of a truck-like container with a separating wall

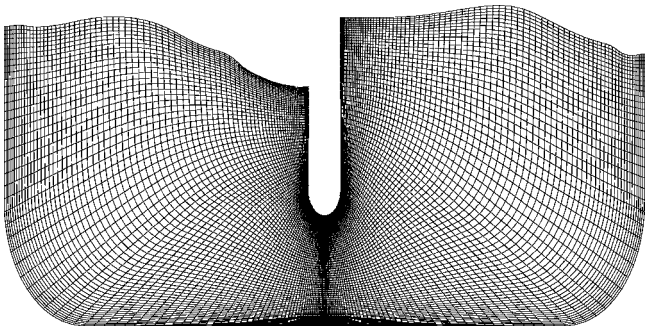

Fig. 11 Updated mesh with a pseudo elastic strategy

The right cylinder of annular base example shows that the method can be applied in 3D and more complex geometries with structured or unstructured meshes composed of any combination of tetrahedral, hexahedral, and wedge elements.

The advantages of this technique over those with remeshing are related to the computational cost of the pseudo elastic problem, which is smaller than a whole remeshing, and the possibility of parallelizing the pseudo-elastic problem.

Future work will involve the inclusion of more complex moving mesh strategies involving non-linear pseudo-elastic models. In sloshing applications, modeling will be focused on how to couple the dynamics of the fluid with the container dynamics, for instance, the simulation of sloshing in containers on tanker trucks with accelerations during turning.

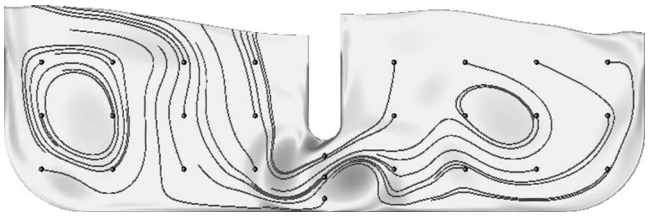

Fig. 12 Vorticity and streamlines at time step n_t=209. A forming vortex is clearly formed on the left wall of the separator near the tip.

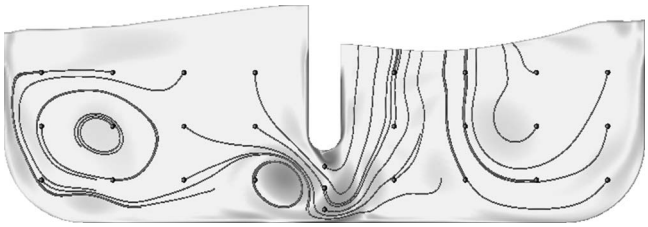

Fig. 13 Vorticity and streamlines at time step n_t=217. The previously formed vortex has been separated from the wall.

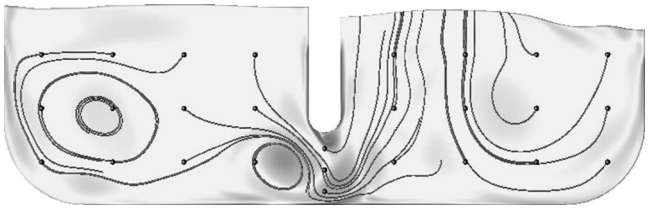

Fig. 14 Vorticity and streamlines at time step n_t=224. Once the vortices are shed they are transported by the fluid.

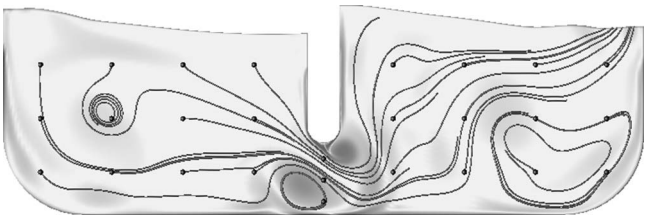

Fig. 15 Vorticity and streamlines at time step n_t=230. A new vortex forming on the right half.

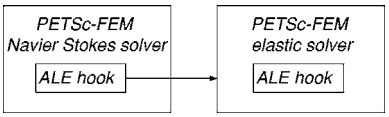

Fig. 16 PETSc-FEM hooks that exchange information and data for the synchronization of the global execution of the fluid and pseudo elastic solvers

Acknowledgment

This work was partially performed with the Free Software Foundation/GNU-Project resources as `GNU/Linux OS` and `GNU/Octave`, as well another Open Source resources as `PETSc`, `MPICH` and `OpenDX`, and supported through Grant Nos. CONICET-PIP-02552/2000, ANPCyT-FONCyT-PME-209 Cluster, ANPCyT-FONCyT-PID-99-74 Flags, ANPCyT-PICT-6973-BID-1201/OC-AR Proa and CAI+D-UNL-2000-43.

Appendix: Parallel and Multi-Physics Implementation Details

Besides being relevant from the physical and engineering point of view, this problem is interesting as a paradigm of multi-physics programming. Even if it is perfectly possible to implement it as a module, it is interesting to see how it is implemented reusing preexistent fluid and elastic modules which are not specifically oriented to the free surface case. The proposed algorithm is implemented in the PETSc-FEM [28,44] code, which is a parallel multi-physics finite element program based on the Message Passing Interface (MPI) [45] and the Portable Extensible Toolkit for Scientific Computations (PETSc) [46]. Among CFD applications, this flow solver includes, for instance, hydrology [29] and free surface flows [24,47].

The pseudo-elastic and fluid problems are run in independent PETSc-FEM instances, both in parallel. In general, there is a PETSc-FEM process for the flow problem and another for the pseudo-elastic one at each computing node. The key point in the implementation is the data exchange and synchronization between both parallel processes. This could be done by modifying the PETSc-FEM sources or by writing a small script or C++ external code that communicates with both PETSc-FEM processes. Instead

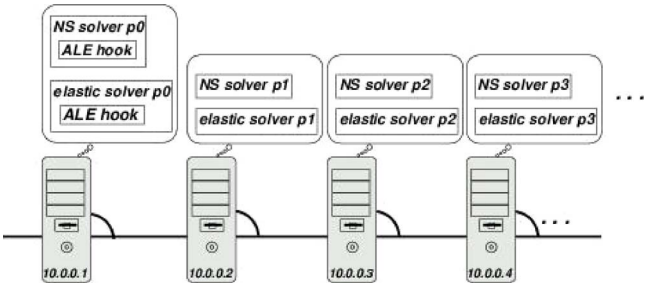

Fig. 17 The master processes of both PETSc-FEM (fluid and mesh-movement) are executed at the same computing node

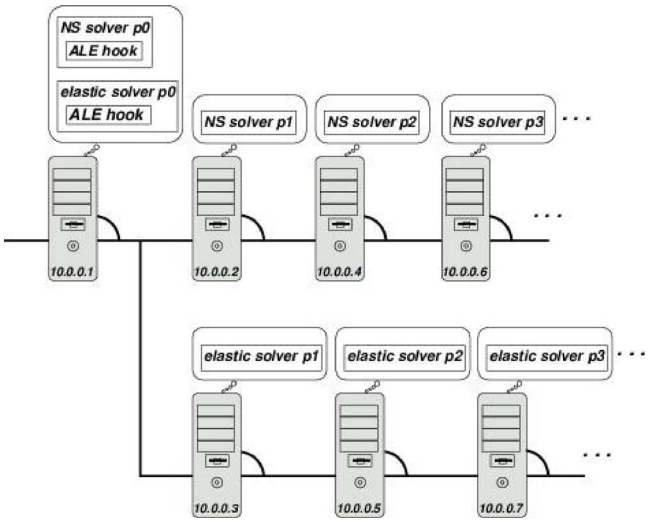

Fig. 18 The PETSc-FEM parallel runs (fluid and mesh movement) are running in different node sets but their master processes (MPI rank 0) must be the same

of these alternatives, PETSc-FEM has a feature called "*hooks*" that are C++ modules, or eventually shell scripts (bash, Perl, Python or other), that are run at certain specific points in the program. This concept was borrowed from the GNU Emacs editor and also from the Linux [48] kernel. The C++ hooks are compiled and dynamically loaded at runtime, so that it is not necessary to link them against PETSc-FEM or modify the sources. Currently, the Navier-Stokes PETSc-FEM module launches hooks at four points in the execution thread: before the beginning of the time step loop, at the beginning and end of each time step, and after the time step loop.

For the problem at hand two PETSc-FEM C++ hooks were written, one that is executed from the NS process and the other from the pseudo-elastic mesh-relocation process. Both hooks exchange information and data for the synchronization of the global execution through a first in first out (FIFO), also called a "*named pipe*," with an ad hoc protocol, see Fig. 16. This is an efficient and portable way of communication between processes and is part of the standard C library ("*libc*"). There is a restriction related to this implementation: inter-process communication via FIFO can only be done between processes in the same host, constraining the master processes of both PETSc-FEM modules to be executed at the same computing node. That is, the parallel runs (fluid and mesh movement) can be executed on the same set of nodes (see Fig. 17), or in different ones. However, their master processes (MPI rank 0) must be the same (see Fig. 18). This restriction could be removed by replacing the FIFO by a socket.

The sequence of the process is the following. First, the Navier-Stokes solver calculates the state in the fluid. Then, the velocities on the surface nodes are sent to the pseudo-elastic solver which computes the new free surface node positions and solves the pseudo-elastic problem. The new fluid nodes coordinates are sent back to the fluid solver, which computes the fluid node mesh velocities, needed for computing the ALE terms. Then the fluid solver computes the fluid state and the whole process is restarted. In summary, the communication between the modules at each time step amounts only to sending the free surface velocities to the pseudo-elastic solver, and the fluid nodes positions back. Note that, as the mesh partitioning for both modules is the same, much of this traffic is *inside* each processor, so that no communication overhead is caused.

Further developments and examples of free surface flows with mesh movement solved by parallel computation were published by Tezduyar et al. [21] and Johnson and Tezduyar [23].

References

[1] Hughes, T. J. R., and Brooks, A. N., 1979, "A Multidimensional Upwind Scheme With No Crosswind Diffusion," *Finite Element Methods for Convection Dominated Flows*, ASME, ed., **34**. AMD, New York, pp. 19–35.

[2] Brooks, A. N., and Hughes, T. J. R., 1982, "Streamline Upwind/Petrov-Galerkin Formulations for Convection Dominated Flows With Particular Emphasis on the Incompressible Navier-Stokes equations," Comput. Methods Appl. Mech. Eng., **32**, pp. 199–259.

[3] Tezduyar, T. E., 1992, "Stabilized Finite Element Formulations for Incompressible Flow Computations," Adv. Appl. Mech., **28**, pp. 1–44.

[4] Tezduyar, T. E., Mittal, S., Ray, S. E., and Shih, R., 1992, "Incompressible Flow Computations With Stabilized Bilinear and Linear Equal Order Interpolation Velocity-Pressure Elements," Comput. Methods Appl. Mech. Eng., **95**, pp. 221–242.

[5] Housner, G. W., 1957, "Dynamic Pressures on Accelerated Fluid Containers," Bull. Seismol. Soc. Am., **47**, pp. 15–35.

[6] Storti, M. A., and D'Elía, J., 2005, "Added Mass of an Oscillating Hemisphere at Very-Low and Very-High Frequencies," J. Fluids Eng., **126**(6), pp. 1048–1053.

[7] Biswal, K. C., Bhattacharyya, S. K., and Sinha, P. K., 2004, "Dynamic Response Analysis of Liquid-Filled Cylindrical Tank With Annular Baffle," J. Sound Vib., **274**(1), pp. 13–97.

[8] Shyy, W., Udaykumar, H. S., Rao, M. M., and Smith, R. W., 1996, *Computational Fluid Dynamics with Moving Boundaries*, Taylor and Francis, London.

[9] Aliabadi, S., and Tezduyar, T. E., 2000, "Stabilized-Finite-Element/Interface-Capturing Technique for Parallel Computation of Unsteady Flows with Interfaces," Comput. Methods Appl. Mech. Eng., **190**, pp. 243–261.

[10] Perot, B., and Nallapati, R., 2003, "A Moving Unstructured Staggered Mesh Method for the Simulation of Incompressible Free-Surface Flows," J. Comput. Phys., **184**(1), pp. 192–214.

[11] Nickell, R. E., Tanner, R. I., and Caswell, B., 1974, "The Solution of Viscous Incompressible Jet and Free-Surface Flows Using Finite Element Method," J. Fluid Mech., **65**, pp. 189–206.

[12] Silliman, W. J., and Scriven, L. E., 1980, "Separating Flow Near a Static Contact Line: Slip at the Wall and Shape of a Free Surface," J. Comput. Phys., **34**(3), pp. 287–313.

[13] Ruschak, K. J., 1980, "A Method for Incorporating Free Boundaries with Surface Tension in Finite Element Fluid Flow Simulation," Int. J. Numer. Methods Eng., **15**(5), pp. 639–648.

[14] Kawahara, M., and Miwa, T., 1984, "Finite Element Analysis of Wave Motion," Int. J. Numer. Methods Eng., **20**(7), pp. 1193–1210.

[15] Bach, P., and Hassager, O., 1985, "An Algorithm For the Use of the Lagrangian Specification in Newtonian Fluid Mechanics and Applications to Free Surface Flows," J. Fluid Mech., **152**, pp. 173–190.

[16] Ramaswamy, B., and Kawahara, M., 1987, "Lagrangian Finite Element Analysis Applied to Viscous Free Surface Fluid Flow," Int. J. Numer. Methods Fluids, **7**(9), pp. 953–984.

[17] Hughes, T. J. R., Liu, W. K., and Zimmermann, T. K., 1981, "Lagrangian-Eulerian Finite Element Formulation for Incompressible Viscous Flows," Comput. Methods Appl. Mech. Eng., **29**, pp. 329–349.

[18] Sung, J., Choi, H. G., and Yoo, J. Y., 2000, "Time-Accurate Computation of Unsteady Free Surface Flows Using an ALE-Segregated Equal-Order FEM," Comput. Methods Appl. Mech. Eng., **190**, pp. 1425–1440.

[19] Huang, Y., and Sclavounos, P. D., 1998, "Nonlinear Ship Motions," J. Ship Res., **42**(2), pp. 120–130.

[20] York, A. R., Sulsky, D., and Schreyer, H. L., 2000, "Fluid-Membrane Interaction Based on the Material Point Method," Int. J. Numer. Methods Eng., **48**(6), pp. 901–924.

[21] Tezduyar, T., Aliabadi, S., Behr, M., Johnson, A., and Mittal, S., 1993, "Parallel Finite-Element Computation of 3D Flows," Computer, **26**, pp. 27–36.

[22] Tezduyar, T. E., Behr, M., Mittal, S., and Johnson, A. A., 1992, "Computation of Unsteady Incompressible Flows With the Stabilized Finite Element Methods-Space-Time Formulations, Iterative Strategies and Massively Parallel Implementations," *New Methods in Transient Analysis*, PVP-VOL. 246/AMD-143, ASME, New York, pp. 7–24.

[23] Johnson, A. A., and Tezduyar, T. E., 1994, "Mesh Update Strategies in Parallel Finite Element Computations of Flow Problems With Moving Boundaries and Interfaces," Comput. Methods Appl. Mech. Eng., **119**, pp. 73–94.

[24] D'Elía, J., Storti, M. A., Oñate, E., and Idelsohn, S. R., 2002, "A Lagrangian Panel Method in the Time Domain for Moving Free-Surface Potential Flows," Int. J. Comput. Fluid Dyn., **16**(4), pp. 263–275.

[25] D'Elía, J., Storti, M. A., and Idelsohn, S. R., 2001, "A Surface Remeshing for Floating-Like Bodies With a Moving Free Surface," *Mecánica Computacional*, Vol. 20, XII Congress on Numerical Methods and Their Applications-ENIEF 2001, pp. 462–467.

[26] Behr, M., and Abraham, F., 2002, "Free-Surface Flow Simulations in the Presence of Inclined walls," Comput. Methods Appl. Mech. Eng., **191**, pp. 5467–5483.

[27] Güler, I., Behr, M., and Tezduyar, T., 1999, "Parallel Finite Element Computation of Free-Surface Flows," Comput. Mech., **23**(2), pp. 117–123.

[28] Sonzogni, V. E., Yommi, A. M., Nigro, N. M., and Storti, M. A., 2002, "A Parallel Finite Element Program on a Beowulf Cluster," Adv. Eng. Software, **33**, pp. 427–443.

[29] Paz, R. R., and Storti, M. A., 2005, "An Interface Strip Preconditioner for Domain Decomposition Methods. Application to Hidrology," Int. J. Numer. Methods Eng., **62**(13), pp. 1873–1894.

[30] Paz, R. R., Nigro, N. M., and Storti, M. A., 2006, "On the Efficiency and Quality of Numerical Solutions in CFD Problems Using the Interface Strip Preconditioner for Domain Decomposition Methods," Int. J. Numer. Methods Fluids (in press).
[31] Braza, M., Chassaing, P., and Minh, H., 1986, "Numerical Study and Physical Analysis of the Pressure and Velocity Fields in the Near Wake of a Circular Cylinder," J. Fluid Mech., **165**, pp. 79–130.
[32] Tezduyar, T. E., and Shih, R., 1991, "Numerical Experiments on Downstream Boundary of Flow Past Cylinder," J. Eng. Mech., **117**, pp. 854–871.
[33] Behr, M., Liou, J., Shih, R., and Tezduyar, T. E., 1991, "Vorticity-Stream Function Formulation of Unsteady Incompressible Flow Past a Cylinder: Sensitivity of the Computed Flow Field to the Location of the Outflow Boundary," Int. J. Numer. Methods Fluids, **12**, pp. 323–342.
[34] Cantwell, B. J., and Coles, D., 1983, "An Experimental Study of Entrainment and Transport in the Turbulent Near Wake of a Circular Cylinder," J. Fluid Mech., **136**, pp. 321–374.
[35] Roshko, A., 1961, "Experiments on the Flow Past a Circular Cylinder at Very High Reynolds Number," J. Fluid Mech., **10**, pp. 345–356.
[36] Williamson, C. H. K., 1996, "Vortex Dynamics in the Cylinder Wake," Annu. Rev. Fluid Mech., **28**, pp. 477–539.
[37] Gushchin, V., Kostomarov, A., Matyushin, P., and Pavlyukova, E., 2002, "Direct Numerical Simulation of the Transitional Separated Fluid Flows Around a Sphere and a Circular Cylinder," J. Wind. Eng. Ind. Aerodyn., **90**, pp. 341–358.
[38] Mittal, R., and Balachandar, S., 1995, "Effect of Three-Dimensionality on the Lift and Drag of Nominally Two-Dimensional Cylinders," Phys. Fluids, **7**(8), pp. 1841–1865.
[39] Norberg, C., 2001, "Flow Around a Circular Cylinder: Aspects of Fluctuating Lift," J. Fluids Struct., **15**, pp. 459–469.
[40] Rabier, S., and Medale, M., 2003, "Computation of Free Surface Flows with a Projection FEM in a Moving Mesh Framework," Comput. Methods Appl. Mech. Eng., **192**, pp. 4703–4721.
[41] Prosperetti, A., 1981, "Motion of Two Superposed Viscous Fluids," Phys. Fluids, **24**(7), pp. 1217–1223.
[42] Papaspyrou, S., Karamanos, S. A., and Valougeorgis, D., 2004, "Response of Half Full Horizontal Cylinders Under Transverse Excitation," J. Fluids Struct., **19**(7), pp. 985–1003.
[43] Moiseev, N. N., and Petrov, A. A., 1966, "The Calculation of Free Oscillations of a Liquid in Motionless Container," *Advances in Applied Mechanics*, **8**. Academic, New York, pp. 91–155.
[44] PETSc-FEM: A general purpose, parallel, multi-physics FEM program. GNU General Public License (GPL), http://www.cimec.org.ar/petscfem
[45] Message Passing Interface (MPI). http://www.mpi-forum.org/docs/docs.html
[46] Balay, S., Gropp, W., Mclnnes, L. C., and Smith, B., 1997, *Petsc 2.0 Users Manual.* Tech. Rep. No. UC-405, Argonne National Laboratory.
[47] D'Elía, J., Storti, M. A., and Idelsohn, S., 2000, "A Panel-Fourier Method for Free Surface Flows," J. Fluids Eng., **122**(2), pp. 309–317.
[48] Linux. The Linux Documentation Project, http://www.gnu.org

G. Etse
e-mail: getse@herrera.unt.edu.ar

S. M. Vrech

Centro de Métodos Numéricos y
Computacionales en Ingeniería,
University of Tucuman,
Muñecas 730,
10A, 4000 Tucumán,
Argentina

Geometry Method for Localization Analysis in Gradient-Dependent J_2 Plasticity

In this work the geometrical method for the assessment of discontinuous bifurcation conditions is extended to encompass gradient-dependent plasticity. To this end, the gradient-dependent localization condition is cast in the form of an elliptical envelope condition in the coordinates of Mohr. The results in this work demonstrate the capability of thermodynamically consistent gradient-dependent elastoplastic model formulations to suppress the localized failure modes of the classical plasticity that take place when the hardening/softening modulus $\bar{H}$ equals the critical value for localization $\bar{H}_c$, provided the characteristic length l remains positive. [DOI: 10.1115/1.2202348]

1 Introduction

Finite element solutions of boundary value problems involving strain-softening materials are strongly affected by mesh-dependency when the governing equations turn ill-posed. This is related to the formation of spatial discontinuities of kinematic fields and consequently, to a discontinuous bifurcation condition, see among others, Nadai [1], Thomas [2], Hill [3], and Rudnicki and Rice [4]. To reduce the loss of objectivity of the related computational results, two strategies are at hand: to improve the finite element technology or to regularize the description of the material behavior at the constitutive level.

To solve the mesh sensitivity of the computational predictions of strain softening material models, two possible strategies are at hand. On one hand, to improve the finite element technology by developing both standard finite element formulations, which are able to follow the post-bifurcation localization using realignment methods, and enhanced finite elements with discontinuous interpolation capabilities. On the other hand, to regularize the description of the material behavior at the constitutive level. However, a combination of both approaches seems to be the most effective one.

The regularization strategy leads to enriched material formulations that are mostly based on nonlocal approaches. Thereby, the gradients of the displacement function are evaluated in the vicinity of the material point, thus a spatial average is taken into account to evaluate the point value. This is accomplished by defining suitable weighted averages (nonlocal formulations) or gradients (gradient formulations) of a selection of thermodynamic variables.

In the literature, gradient-dependent material theories have been advocated within two different conceptual settings. On the one hand, within the classical hypoelastic framework which does not have a thermodynamic law, e.g., Zbib and Aifantis [5], Fleck and Hutchinson [6], Zbib [7]. Related to this type of material formulation Sluys et al. [8], de Borst et al. [9,10], and Pamin [11] have proposed numerical algorithms for the stress integrations at the local and finite element level.

On the other hand, gradient-dependent material formulations were analyzed and advocated within a thermodynamic framework, e.g., Valanis [12], Dillon and Kratochvil [13], and more recently Valanis [14] and Svedberg and Runesson [15]. In this last case the nonlocal character of the constitutive equations is restricted to the internal variables, leading to an additive expression of the free energy density.

A detailed discussion regarding the different gradient models of plasticity is given in Fleck and Hutchinson [16,17] and where the subtle differences in regularizing softening and in introducing size effects is highlighted.

In this work, the localization properties of the thermodynamically consistent gradient-dependent J_2 plasticity model with isotropic hardening/softening law are analyzed by means of the geometrical method.

To this end, the gradient-dependent elastoplastic localization properties are cast in the form of an elliptical envelope condition in the $\sigma_N - \tau_N$ coordinates of Mohr, see Pijaudier-Cabot and Benallal [18], Liebe and Willam [19]. Therefore, the tangency condition between the localization ellipse and the major principal circle defines the existence of localized failure mode and the corresponding critical directions. In the present analysis, the geometrical localization condition is defined in terms of the degree of nonlocality of the constitutive model that in case of gradient plasticity is represented by the characteristic length.

2 Gradient-Dependent Elastoplasticity

We follow the thermodynamically consistent gradient-dependent material theory by Svedberg and Runesson [15]. After reviewing the relevant thermodynamic and constitutive equations, the J_2 gradient elastoplastic model is presented, in which the nonlocal character is restricted to the internal plastic variables.

2.1 Thermodynamic Consistency. Under consideration of small strain kinematics, the free energy density of a strain gradient elastoplastic continuum can be expressed in an additive form as

$$\rho\Psi(\boldsymbol{\varepsilon}^e, \kappa, \nabla\kappa) = \rho\Psi^e(\boldsymbol{\varepsilon}^e) + \rho\Psi^{p,\mathrm{loc}}(\kappa) + \rho\Psi^{p,g}(\nabla\kappa) \qquad (1)$$

where ρ is the material density. The elastic free energy density is defined as $\rho\Psi^e(\boldsymbol{\varepsilon}^e) = (1/2)\boldsymbol{\varepsilon}^e : \mathbf{E}^e : \boldsymbol{\varepsilon}^e$, $\boldsymbol{\varepsilon}^e$ and $\mathbf{E}^e$ being the elastic strain tensor and the fourth-order elastic operator, respectively.

The local and gradient free energy density contributions due to inelastic strains $\Psi^{p,\mathrm{loc}}$ and $\Psi^{p,g}$ are expressed in terms of the scalar hardening/softening variable κ. We observe in Eq. (1) that the gradient effects are only restricted to hardening/softening behavior via the inclusion of $\nabla\kappa$.

From the Coleman's relations follow the constitutive equations

Contributed by the Applied Mechanics Division of ASME for publication in the JOURNAL OF APPLIED MECHANICS. Manuscript received September 21, 2005; final manuscript received April 6, 2006. Review conducted by G. C. Buscaglia. Discussion on the paper should be addressed to the Editor, Prof. Robert M. McMeeking, Journal of Applied Machanics, Department of Mechanical and Environmental Engineering, University of California–Santa Barbara, Santa Barbara, CA 93106-5070, and will be accepted until four months after final publication of the paper itself in the ASME JOURNAL OF APPLIED MECHANICS.

$$\boldsymbol{\sigma} = \rho \frac{\partial \Psi}{\partial \varepsilon} \quad \boldsymbol{\sigma} = \mathbf{E}^e : \boldsymbol{\varepsilon}^e \tag{2}$$

whereby $\boldsymbol{\sigma}$ is the stress tensor and $\boldsymbol{\varepsilon}$ the strain tensor. The dissipative stress within the continuum is defined as

$$K = K^{\mathrm{loc}} + K^g \tag{3}$$

being

$$K^{\mathrm{loc}} = -\rho \frac{\partial \Psi^{p,\mathrm{loc}}}{\partial \boldsymbol{\kappa}} \quad K^g = \boldsymbol{\nabla} \cdot \left(\rho \frac{\partial \Psi^{p,g}}{\partial (\boldsymbol{\nabla} \boldsymbol{\kappa})} \right) \tag{4}$$

while on the boundary $\partial\Omega$, the dissipative stress due to the gradient in the second equation in Eq. (4) turns

$$K^{(g,b)} = -\mathbf{m} \cdot \rho \frac{\partial \Psi^{p,g}}{\partial (\boldsymbol{\nabla} \boldsymbol{\kappa})} \tag{5}$$

with the (outward) normal $\mathbf{m}$ to $\partial\Omega$.

2.2 Constitutive Equations

2.2.1 General Case. Considering a convex set B of plastically admissible states defined as $B=\{(\boldsymbol{\sigma},K)\,|\,\Phi(\boldsymbol{\sigma},K)\leqslant 0\}$ with the convex yield function $\Phi=\Phi(\boldsymbol{\sigma},K)$, and a dissipative potential $\Phi^*=\Phi^*(\boldsymbol{\sigma},K)$, which turns Φ in case of associated plasticity. Then, the rate equations for the inelastic strains $\dot{\boldsymbol{\varepsilon}}^p$ and the scalar hardening/softening variable $\dot{\kappa}$, take the forms

$$\dot{\boldsymbol{\varepsilon}}^p = \dot{\lambda} \frac{\partial \Phi^*}{\partial \boldsymbol{\sigma}} \quad \text{and} \quad \dot{\kappa} = \dot{\lambda} \frac{\partial \Phi^*}{\partial K} \tag{6}$$

where $\dot{\lambda}$ is the rate of the plastic parameter.

From the Prandtl-Reuss additive decomposition of the total strain rate tensor into the elastic and plastic components that characterized the flow theory of plasticity and considering Eqs. (2), (4), and (6) follow the constitutive equations (in rate form)

$$\dot{\boldsymbol{\sigma}} = \dot{\boldsymbol{\sigma}}^e - \dot{\lambda} \mathbf{E}^e \frac{\partial \Phi^*}{\partial \boldsymbol{\sigma}} \quad \text{with} \quad \dot{\boldsymbol{\sigma}}^e = \mathbf{E}^e : \dot{\boldsymbol{\varepsilon}} \tag{7}$$

$$\dot{K}^{\mathrm{loc}} = -\dot{\lambda} \mathbf{H} \frac{\partial \Phi^*}{\partial K} \tag{8}$$

and

$$\dot{K}^g = l^2 \boldsymbol{\nabla} \cdot \mathbf{H}^g \cdot \left[\boldsymbol{\nabla} \dot{\lambda} \frac{\partial \Phi^*}{\partial K} + \dot{\lambda} \boldsymbol{\nabla} K \frac{\partial^2 \Phi^*}{\partial K^2} \right] \tag{9}$$

which on the boundary turns

$$\dot{K}^{(g,b)} = -l^2 \mathbf{m} \cdot \mathbf{H}^g \cdot \left[\boldsymbol{\nabla} \dot{\lambda} \frac{\partial \Phi^*}{\partial K} + \dot{\lambda} \boldsymbol{\nabla} K \frac{\partial^2 \Phi^*}{\partial K^2} \right] \tag{10}$$

In the above equations, two types of state parameters were considered. On the one hand, the *local* hardening/softening modulus H and, on the other hand, the second-order tensor of *nonlocal gradient* state parameters $\mathbf{H}^g$ defined as

$$\mathbf{H}^g = \rho \frac{1}{l^2} \frac{\partial^2 \Psi^{p,g}}{\partial (\boldsymbol{\nabla} \boldsymbol{\kappa}) \otimes \partial (\boldsymbol{\nabla} \boldsymbol{\kappa})} \tag{11}$$

with

$$\det(\mathbf{H}^g) \geqslant 0 \tag{12}$$

As pointed out by Svedberg and Runesson [15], there are three possible interpretations for the characteristic length l in Eq. (11): as a convenient dimensional parameter which allows that both H and $\mathbf{H}^g$ get the same dimension, as a physical entity that defines the characteristic measure of the microstructure, and as a parameter that brings numerical stabilization to the local constitutive theory.

The Kuhn-Tucker conditions complete the rate formulation of the gradient-dependent plasticity in terms of hardening variables which, similar to the local theory, are defined by

$$\dot{\lambda} \geqslant 0 \quad \Phi(\boldsymbol{\sigma},K) \leqslant 0 \quad \dot{\lambda}\Phi(\boldsymbol{\sigma},K) = 0 \tag{13}$$

2.2.2 J_2 Material Model. The expression of the von Mises yield criterium, corresponding to J_2 materials, yields

$$\Phi(\boldsymbol{\sigma},K) = \sigma_e - \sigma_y - K \quad \sigma_e = \sqrt{\frac{3}{2}}|\mathbf{s}| \tag{14}$$

with σ_y the yield stress, K the dissipative stress and $\mathbf{s}$ the deviatoric stress tensor

$$\mathbf{s} = \boldsymbol{\sigma} - \mathbf{I}\sigma_0 \quad \text{with} \quad \sigma_0 = \frac{\sigma_{ii}}{3} \quad \text{and} \quad i = 1,2,3 \tag{15}$$

$\mathbf{I}$ being the second-order identity tensor.

The flow and hardening rules are of the associative type, therefore the rate equations for the internal variables in Eq. (6) are

$$\dot{\boldsymbol{\varepsilon}}^p = \dot{\lambda} \frac{3\mathbf{s}}{2\sigma_e} \quad \text{and} \quad \dot{\kappa} = -\dot{\lambda} \tag{16}$$

The explicit expression of the dissipative stress K in Eq. (14) follows from Eqs. (3) and (4), where the local and gradient free energy densities take the forms

$$\rho \Psi^{p,\mathrm{loc}} = \tfrac{1}{2} H \kappa^2 \tag{17}$$

$$\rho \Psi^{p,g} = \frac{1}{2} l^2 \boldsymbol{\nabla} \kappa \cdot \mathbf{H}^g \cdot \boldsymbol{\nabla} \kappa \tag{18}$$

Therefore, the components K^{loc} and K^g of K result now

$$K^{\mathrm{loc}} = -H\kappa \tag{19}$$

$$K^g = l^2 \boldsymbol{\nabla} \cdot (\mathbf{H}^g \cdot \boldsymbol{\nabla} \kappa) \tag{20}$$

3 Condition for Localized Failure

From the continuum mechanic's viewpoint, localized failure modes are related to discontinuous bifurcations of the equilibrium path, and lead to the loss of ellipticity of the equations that govern the static equilibrium problem.

The inhomogeneous or localized deformation field exhibits a plane of discontinuity that can be identified by the singularity condition of the acoustic or localization second-order tensor, see Ottosen and Runesson [20] and Willam and Etse [21].

Local and gradient flow theories of plasticity both result in the tangential equation that reads

$$\dot{\boldsymbol{\sigma}} = \mathbf{E}^{ep} : \dot{\boldsymbol{\varepsilon}} \tag{21}$$

where $\mathbf{E}^{ep}$ denotes the elastoplastic material operator that can be expressed by means of the encompassing equation

$$\mathbf{E}^{ep} = \mathbf{E}^e - \frac{1}{(h + h_g)} \mathbf{E}^e : \frac{\partial \Phi^*}{\partial \boldsymbol{\sigma}} \otimes \frac{\partial \Phi}{\partial \boldsymbol{\sigma}} : \mathbf{E}^e \tag{22}$$

with the *local* and *nonlocal* generalized plastic moduli

$$h = \frac{\partial \Phi}{\partial \boldsymbol{\sigma}} : \mathbf{E}^e : \frac{\partial \Phi^*}{\partial \boldsymbol{\sigma}} + \bar{H} \tag{23}$$

and

$$h^g = \begin{cases} 0 & \text{for local plasticity} \\ \mathbf{n}_l \cdot \bar{\mathbf{H}}^g \cdot \mathbf{n}_l \left(\frac{2\pi l}{\delta}\right)^2 & \text{for gradient-dependent plasticity} \end{cases} \tag{24}$$

δ being the width of the localization zone, $\mathbf{n}_l$ the normal direction to the discontinuous surfaces, and

$$\bar{H} = H \frac{\partial \Phi}{\partial K} \frac{\partial \Phi^*}{\partial K} \tag{25}$$

$$\bar{\mathbf{H}}^g = \mathbf{H}^g \frac{\partial \Phi}{\partial K} \frac{\partial \Phi^*}{\partial K} \tag{26}$$

From Eq. (26) and for the particular case of gradient isotropy, we obtain

$$\bar{\mathbf{H}}^g = \bar{H}^g \mathbf{I} \tag{27}$$

with $\bar{H}^g$ a positive, nonzero scalar. As $\mathbf{n}_l$ is a unit vector, results

$$\mathbf{n}_l \cdot \bar{\mathbf{H}}^g \cdot \mathbf{n}_l = \bar{H}^g \tag{28}$$

and, from the second equation in Eq. (24)

$$h^g = \bar{H}^g \left(\frac{2\pi l}{\delta}\right)^2 \tag{29}$$

In case of localized failure forms associated with discontinuous bifurcation we resort to the gradient elastoplastic localization tensor defined as

$$\mathbf{Q}^{epg} = \mathbf{Q}^e - \frac{1}{h + h^g} \mathbf{a}^* \otimes \mathbf{a} \tag{30}$$

with the elastic-localization tensor

$$\mathbf{Q}^e = \mathbf{n}_l \cdot \mathbf{E}^e \cdot \mathbf{n}_l \tag{31}$$

and

$$\mathbf{a}^* = \frac{\partial \Phi^*}{\partial \boldsymbol{\sigma}} : \mathbf{E}^e \cdot \mathbf{n}_l \tag{32}$$

$$\mathbf{a} = \frac{\partial \Phi}{\partial \boldsymbol{\sigma}} : \mathbf{E}^e \cdot \mathbf{n}_l \tag{33}$$

The localized failure condition in case of gradient-dependent elastoplasticity

$$\det(\mathbf{Q}^{epg}) = 0 \tag{34}$$

leads to the analysis of the spectral properties of $\mathbf{Q}^{epg}$. Its smallest eigenvalue, with respect to the metric defined by $\mathbf{Q}^e$, has the expression

$$\lambda^{(1)} = 1 - \frac{\mathbf{a}(\mathbf{n}_l) \cdot [\mathbf{Q}^e(\mathbf{n}_l)]^{-1} \cdot \mathbf{a}^*(\mathbf{n}_l)}{h + h^g} = 0 \tag{35}$$

In case of gradient isotropy, the explicit form of Eq. (35) is

$$\mathcal{H} + \frac{\partial \Phi}{\partial \boldsymbol{\sigma}} : \mathbf{E}^e : \frac{\partial \Phi^*}{\partial \boldsymbol{\sigma}} - \mathbf{a} \cdot [\mathbf{Q}^e]^{-1} \cdot \mathbf{a}^* = 0 \tag{36}$$

with

$$\mathcal{H} = \bar{H}_c^g \left(\frac{2\pi l}{\delta}\right)^2 + \bar{H}_c \tag{37}$$

The localization condition in Eq. (36) serves as a basis for analytical and numerical evaluations of the localization directions $\mathbf{n}_l$ and of the corresponding graphical maximum hardening/softening parameters $\bar{H}_c(\mathbf{n}_l) = \max[\bar{H}(\mathbf{n}_l)]$ in case of local plasticity, and $\bar{H}_c^g(\mathbf{n}_l) = \max[\bar{H}^g(\mathbf{n}_l)]$ in gradient-dependent plasticity.

4 Geometrical Localization Analysis

In this section, the geometrical method for localization analysis is derived for the thermodynamically consistent gradient-dependent J_2 elastoplastic model formulation detailed in Sec. 2.2.2. The approach is based on the original proposal by Benallal [22], which was further developed by Pijaudier-Cabot and Benallal [18] and Liebe and Willam [19] for classical plasticity.

Equation (36) defines an ellipse in the $\sigma_N - \tau_N$ coordinates of Mohr

$$\sigma_N = \mathbf{n}_l \cdot \boldsymbol{\sigma} \cdot \mathbf{n}_l \quad s = \mathbf{n}_l \cdot \mathbf{s} \cdot \mathbf{n}_l \tag{38}$$

$$\tau_N^2 = (\mathbf{n}_l \cdot \mathbf{s}) \cdot (\mathbf{n}_l \cdot \mathbf{s}) - (\mathbf{n}_l \cdot \mathbf{s} \cdot \mathbf{n}_l)^2 \tag{39}$$

The critical direction $\mathbf{n}_l$, normal to the plane where the Mohr components are evaluated, and the maximum hardening/softening parameters $\bar{H}_c$ and $\bar{H}_c^g$ for localization are obtained when the Mohr circle of stresses

$$(\sigma_N - \sigma_c)^2 + \tau_N^2 = R^2 \tag{40}$$

contacts the elliptical localization envelope

$$\frac{(\sigma_N - \sigma_0)^2}{A^2} - \frac{\tau_N^2}{B^2} = 1 \tag{41}$$

where the center and radius of the Mohr circle, Eq. (40), are

$$\sigma_c = \frac{\sigma_1 + \sigma_3}{2} \tag{42}$$

and

$$R = \frac{\sigma_1 - \sigma_3}{2} \tag{43}$$

with σ_1 and σ_3, the major and minor principal stresses, respectively, and the center σ_0 and half axes A and B of the localization ellipse are defined in the following.

5 Localization Properties of J_2 Gradient-Dependent Elastoplasticity

Considering for the elastic tensor $\mathbf{E}^e$ the expression

$$\mathbf{E}^e = 2G\mathbf{I}_4 + \Lambda \mathbf{I} \otimes \mathbf{I} \tag{44}$$

with the shear module G and the Lamé's constant Λ, the traction vectors in Eqs. (32) and (33) can then be rewritten as

$$\mathbf{a}^* = \mathbf{a} = 2G\mathbf{n}_l \cdot \mathbf{s} \tag{45}$$

and from Eq. (31), the inverse of the localization tensor $\mathbf{Q}^e$ shields

$$[\mathbf{Q}^e]^{-1} = \frac{1}{G}\left[\mathbf{I} - \frac{1}{2(1-\nu)} \mathbf{n}_l \otimes \mathbf{n}_l\right] \tag{46}$$

with the Poisson's modulus ν. Replacing Eq. (46) in Eq. (36), and combining with Eqs. (38) and (39), the center σ_0 and the half axes A and B of the localization ellipse, Eq. (41), results

$$\sigma_0 = \tfrac{1}{3} I_1 \tag{47}$$

$$B^2 = J_2 \left(\frac{\mathcal{H}}{G} + 1\right) \tag{48}$$

$$A^2 = 2\frac{1-\nu}{1-2\nu} B^2 \tag{49}$$

In the particular case of classical elastoplasticity the inhomogeneous differential Eq. (36) turns

$$\bar{H}_c = -\frac{\partial \Phi}{\partial \boldsymbol{\sigma}} : \mathbf{E}^e : \frac{\partial \Phi^*}{\partial \boldsymbol{\sigma}} + \mathbf{a} \cdot [\mathbf{Q}^e]^{-1} \cdot \mathbf{a}^* \tag{50}$$

therefore, the parameter B^2 representing the vertical axis of the ellipse in Eq. (41) now takes now the form

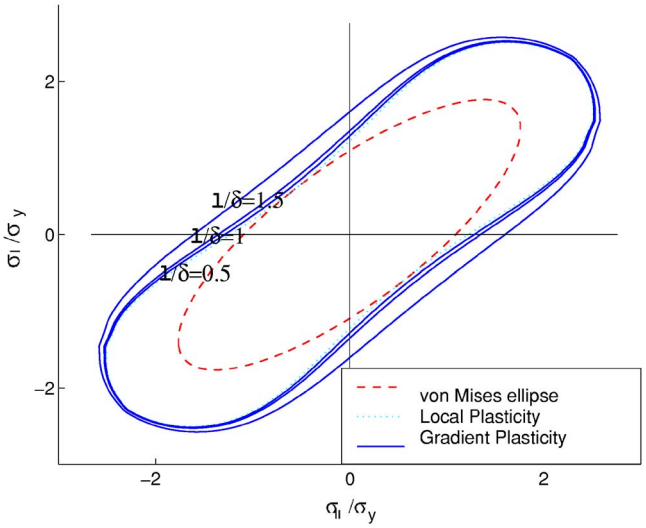

Fig. 1 Localization in local and gradient von Mises yield criterion in the principal stress space

$$B^2 = J_2\left(\frac{\bar{H}_c}{G} + 1\right) \tag{51}$$

So, the thermodynamically consistent gradient-dependent plasticity formulation allows a simple extension of the geometrical localization method as demonstrated in this section. Thereby, the nonlocal effects in terms of the characteristic length and of the gradient hardening/softening modulus only affect the expression of the localization ellipse half axes A and B.

5.1 Graphical Analysis. The localization properties of the thermodynamically consistent gradient-dependent J_2 elastoplastic model are analyzed for the plane strain condition when $\sigma_z = \nu(\sigma_x + \sigma_y)$ and $\bar{H} = \bar{H}_c$, $\bar{H}$ being the particular hardening/softening modulus of the gradient-dependent model and $\bar{H}_c$ the critical one for localization of the local elastoplastic model. As follows from Eqs. (41), (48), and (37), the localization properties of the gradient-dependent J_2 elastoplastic model depend on the ratio δ/l. As the purpose of this work is to evaluate the performance of the condition for localized failure of the model by means of the geometrical method and not the calibration of the model, the analysis in this section will mainly focus on the sensitivity of the localized failure indicator performance regarding the variation of the ratio δ/l but not on the evaluation of the most appropriate value of this ratio for different types of metals.

The results in terms of $\det(\mathbf{Q})$ are depicted in Fig. 1 in the principal stress space. The adopted internal material length equals the width of the localization zone $l = \delta$. As can be observed in Fig. 1, the gradient-regularized plasticity is able to suppress the fulfilment of the localization condition, i.e., discontinuous bifurcation, for the whole range of limit stress states of the von Mises material, in the plane strain regime.

The geometrical localization analysis of the nonlocal gradient J_2 material formulation is performed for the simple shear, uniaxial compression, and uniaxial tensile tests and the results are shown on the left side of Figs. 2–4, respectively. These results illustrate the influence of the characteristic length l in the mode of failure. When $l > 0$, no contact is observed between the localization ellipses of the gradient-dependent plasticity model and the Mohr circle corresponding to the analyzed limit stress state. Thus, diffuse failure mode takes place for all three limit stress states. However, as $l/\delta \to 0$ the gradient-based localization ellipses approaches that of the local model which contacts the Mohr circle, indicating that the localization condition is fulfilled and therefore, discontinuous bifurcation takes place.

To verify the previous geometrical results regarding the capacity of the J_2 gradient-dependent model to suppress discontinuous bifurcations of the related local model formulation, a numerical localization study is performed at the constitutive level. The diagrams in the right side of Figs. 2–4 show the variation of the normalized localization indicator $\det(\mathbf{Q}^{epg})/\det(\mathbf{Q}^{e})$ with the in-plane failure angles at peak of the pure shear, uniaxial compression, and tensile test, respectively. Both the local and the no-local gradient J_2 test are considered. These results demonstrate the capabilities of the J_2 gradient-dependent elastoplastic model formulation to eliminate discontinuous bifurcation in the form of localized failure.

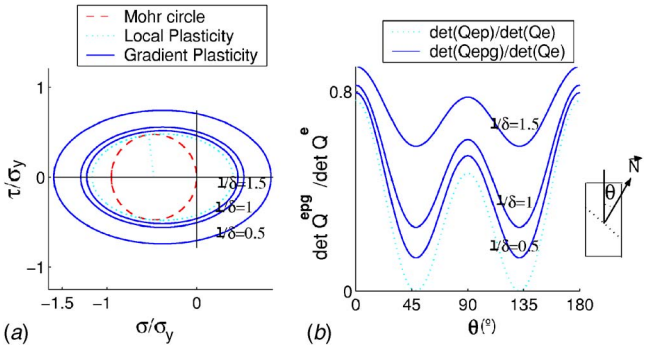

Fig. 3 Geometric localization analysis at peak of the uniaxial compression test. Local and gradient-dependent plasticity. J_2 material model.

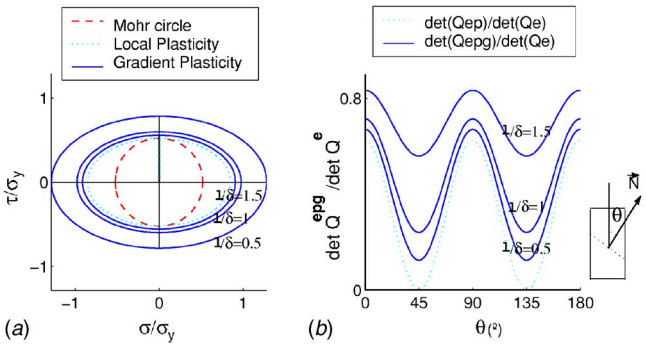

Fig. 2 Geometric and localization analysis at peak of the simple shear test. Local and gradient-dependent plasticity. J_2 material model.

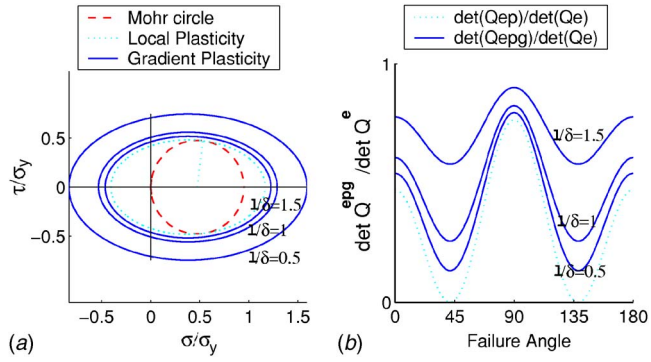

Fig. 4 Geometric localization analysis at peak of the uniaxial tensile test. Local and gradient-dependent plasticity. J_2 material model.

6 Conclusions

In this work the geometrical localization method was extended for the analysis of the discontinuous bifurcation properties of the J_2 gradient-dependent elastoplasticity. The localization condition was expressed in terms of the coordinates of Mohr to obtain an ellipse that represents the envelope of localization for each particular state of stress. Thereby, localized failure mode is geometrically signalized by the tangency condition between the localization ellipse and the major principle circle of Mohr, while the critical localization direction is defined by the inclination of the Mohr circle radius to the tangential point with the localization ellipse.

The results of the geometrical localization analysis indicate that the J_2 gradient-dependent elastoplastic formulation suppresses the discontinuous bifurcations of the classical elastoplasticity when the selected hardening/softening modulus $\bar{H}$ equals the critical one for localization of the local material formulation $\bar{H}_c$.

The regularization capability of the gradient formulation reduces as $l/\delta \to 0$. Therefore, the characteristic length l defines the level of diffusion of the failure mode. When l approaches zero, a continuous transition from non-local gradient to local elastoplasticity is obtained. In the extreme case, when $l=0$, see Eqs. (37), (48), and (51), the local formulation is fully recovered.

Acknowledgment

The authors acknowledge the financial support for this work by FONCYT (Argentina Agency for the promotion of research and technology) through Grant No. PICT 12/9870 and by FUDETEC (Foundation for Technology Advancement). S.M.V. acknowledge the partial financial support to this work by CONICET (National Council for Science and Technology) through Grant No. PIP 3006 and by the University of Tucuman, Argentina, through Grant No. 26/E217.

References

[1] Nadai, A., 1931, *Plasticity*, McGraw-Hill, New York.
[2] Thomas, T., 1961, *Plastic Flow and Fracture in Solids*, Academic, London.
[3] Hill, R., 1962, J. Mech. Phys. Solids, **10**, p. 1.
[4] Rudnicki, J., and Rice, J., 1975, J. Engrg. Mech. Div., **23**, p. 371.
[5] Zbib, H., and Aifantis, E., 2002, Acta Mech., **92**, p. 209.
[6] Fleck, N., and Hutchinson, J., 1993, J. Mech. Phys. Solids, **41**, p. 1825.
[7] Zbib, H., 1994, ASME Mater. Instabil., **92**, p. 19.
[8] Sluys, L., de Borst, R., and Muhlhaus, M., 1993, Int. J. Solids Struct., **30**, p. 1153.
[9] de Borst, R., Pamin, J., and Sluys, L., 1995, *Continuum Models for Materials With Micro-Structure*, H. B. Muhlhaus, ed., Wiley, New York, p. 159.
[10] de Borst, R., Pamin, J., and Sluys, L., 1995, *Computational Plasticity, Fundamentals and Applications*, D. R. J. Owen, E. Onate, and E. Hinton, eds., Pineridge, Swansea, p. 509.
[11] Pamin, J., 1994, Ph.D. thesis, TU-Delft, The Netherlands.
[12] Valanis, K. C., 1968, "Unified Theory of Thermomechanical Behavior of Viscoplastic Materials," *Mechanical Behavior of Materials Under Dynamic Loads Symposium*, Springer, New York, pp. 343–364.
[13] Dillon, O., and Kratochvil, J., 1970, Int. J. Solids Struct., **6**, p. 1513.
[14] Valanis, K., 1998, Acta Mech., **127**, p. 1.
[15] Svedberg, T., and Runesson, K., 1997, Int. J. Plast., **13**, p. 669.
[16] Fleck, N., and Hutchinson, J., 1998, *Material Instabilities in Solids*, R. de Borst and E. van der Giessen eds., Wiley, New York, p. 507.
[17] Fleck, N., and Hutchinson, J., 2001, J. Mech. Phys. Solids, **49**, p. 2245.
[18] Pijaudier-Cabot, G., and Benallal, A., 1993, Int. J. Solids Struct., **30**, p. 1761.
[19] Liebe, T., and Willam, K., 2001, ASCE JEM, **127**(6), p. 616.
[20] Ottosen, N., and Runesson, K., 1991, Int. J. Solids Struct., **27**, p. 401.
[21] Willam, K., and Etse, G., 1990, "Failure Assessment of the Extended Leon Model for Plain Concrete," *Proceedings of Sci-C*, Second International Conference held at Zell am See, Austria, N. Bicanic and H. Mang, eds., Pineridge Press, Swansea, pp. 851–870.
[22] Benallal, A., 1992, Arch. Mech., **44**, p. 15.

Kinematic Laplacian Equation Method: A Velocity-Vorticity Formulation for the Navier-Stokes Equations

Fernando L. Ponta[1]
College of Engineering,
University of Buenos Aires,
Paseo Colón 850,
Buenos Aires C1063ACV,
Argentina
e-mail: fponta@fi.uba.ar

In this work, a novel procedure to solve the Navier-Stokes equations in the vorticity-velocity formulation is presented. The vorticity transport equation is solved as an ordinary differential equation (ODE) problem on each node of the spatial discretization. Evaluation of the right-hand side of the ODE system is computed from the spatial solution for the velocity field provided by a new partial differential equation expression called the kinematic Laplacian equation (KLE). This complete decoupling of the two variables in a vorticity-in-time/velocity-in-space split algorithm reduces the number of unknowns to solve in the time-integration process and also favors the use of advanced ODE algorithms, enhancing the efficiency and robustness of time integration. The issue of the imposition of vorticity boundary conditions is addressed, and details of the implementation of the KLE by isoparametric finite element discretization are given. Validation results of the KLE method applied to the study of the classical case of a circular cylinder in impulsive-started pure-translational steady motion are presented. The problem is solved at several Reynolds numbers in the range $5 < \mathrm{Re} < 180$ *comparing numerical results with experimental measurements and flow visualization plates. Finally, a recent result from a study on periodic vortex-array structures produced in the wake of forced-oscillating cylinders is included.* [DOI: 10.1115/1.2198245]

1 Introduction

During the last three decades several studies appeared concerning the representation of the Navier-Stokes equations in terms of non-primitive variables (namely the vorticity and the velocity potentials) instead of the classical formulation in terms of the primitive variables velocity and pressure. This family of approaches is generally known as vorticity-stream function ($\boldsymbol{\omega},\boldsymbol{\psi}$) methods. More recently, together with those works on the vorticity-stream function formulation and as a natural extension of them, a comparatively smaller number of studies were presented using a hybrid formulation in terms of the primitive and non-primitive variables velocity and vorticity. As several authors pointed out [1–3], the vorticity-velocity ($\boldsymbol{\omega},\boldsymbol{v}$) methods (as they are generally known) present some advantages compared with the classical formulation on primitive variables or with the vorticity-stream function methods, namely: (a) The pair of variables involved is particularly suited for a dynamic description of incompressible viscous flows. The vorticity is governed by a well understood dynamical equation while the velocity, which embodies the kinematical aspect of the problem, can be related to the vorticity by a simple elliptic equation. In vortex-dominated flows the vorticity advection is a fundamental process determining the dynamics of the flow, hence the vorticity-velocity description is closer to physical reality. (b) The variety of boundary conditions that can be chosen for the velocity potentials due to the nonuniqueness of the velocity representation is avoided since the velocity is supplemented by unique boundary conditions. (c) In some specific situations like that of external flows, boundary conditions at infinity are easier to implement for the vorticity than for the pressure. (d) The noninertial effects only enter the solution procedure of the ($\boldsymbol{\omega},\boldsymbol{v}$) formulation via the proper implementation of the initial and boundary conditions. Hence, the general applicability of an algorithm based on the ($\boldsymbol{\omega},\boldsymbol{v}$) formulation is enhanced because it is independent of whether or not the frame of reference is inertial.

The first uses of the ($\boldsymbol{\omega},\boldsymbol{v}$) formulation of the incompressible Navier-Stokes equations were reported by Fasel [4] who analyzed the stability of boundary layers in two dimensions and by Dennis, Ingham, and Cook [5] who derived a numerical method for computing steady-state three-dimensional flows. Both approaches were based on finite difference techniques. Since then several investigations have been conducted on incompressible hybrid variable models using variations of the finite difference approach (e.g., see [6–8], among others). A vorticity-velocity finite element solution of the three-dimensional compressible Navier-Stokes equations have been presented by Guevremont et al. [9] who investigated the steady state flow in a cubic cavity for several Mach numbers. More recently Clercx [2], then Davies and Carpenter [10], introduced pseudospectral procedures for the ($\boldsymbol{\omega},\boldsymbol{v}$) formulation. Lo and Young [11] presented an arbitrary Lagrangian-Eulerian ($\boldsymbol{\omega},\boldsymbol{v}$) method for two-dimensional free surface flow, using finite difference discretization for the free surface and finite element discretization for the interior of the domain.

A disadvantage of the vorticity-velocity formulation, compared with the formulation in primitive variables, is that in the most general three-dimensional case the ($\boldsymbol{\omega},\boldsymbol{v}$) formulation requires a total of six equations to be solved instead of the usual four of the primitive-variable approach [2]. The objective of the present study is to introduce a new method based on the ($\boldsymbol{\omega},\boldsymbol{v}$) formulation which aims to tackle this six-unknown question and to improve some other aspects of the numerical implementation of the ($\boldsymbol{\omega},\boldsymbol{v}$)

[1]Also at the Department of Theoretical and Applied Mechanics, University of Illinois at Urbana-Champaign, 104 S. Wright Street, Urbana, IL 61801.

Contributed by the Applied Mechanics Division of ASME for publication in the JOURNAL OF APPLIED MECHANICS. Manuscript received September 24, 2005; final manuscript received February 4, 2006. Review conducted by G. C. Buscaglia. Discussion on the paper should be addressed to the Editor, Prof. Robert M. McMeeking, Journal of Applied Mechanics, Department of Mechanical and Environmental Engineering, University of California – Santa Barbara, Santa Barbara, CA 93106-5070, and will be accepted until four months after final publication of the paper itself in the ASME JOURNAL OF APPLIED MECHANICS.

approach. This alternative method is characterized by a complete decoupling of the two variables in a vorticity-in-time/velocity-in-space split algorithm, thus reducing to three the number of unknowns to solve in the time integration process. As we shall see later on, this time-space splitting also favors the use of adaptive variable-step size/variable-order ordinary differential equation (ODE) algorithms which enhances the efficiency and robustness of the time integration process.

A comprehensive study of the theoretical basis of the vorticity-velocity formulation in two and three dimensions can be found in Chapter 4 of Quartapelle [1], including a series of theorems proving the equivalence between the $(\boldsymbol{\omega},\boldsymbol{v})$ formulation of the incompressible Navier-Stokes equations and their classical formulation in primitive variables (velocity-pressure).

1.1 Vorticity Boundary Conditions. A common problem to all the methods based on nonprimitive or hybrid variables is the absence of boundary conditions for the vorticity in the presence of no-slip boundary conditions for the velocity. In the case of the $(\boldsymbol{\omega},\boldsymbol{\psi})$ formulation it also implies that the Poisson problem for the stream function with both Dirichlet and Neumann conditions is overdetermined. There are several different ways of overcoming this difficulty. Some earlier approaches like the *boundary vorticity formula* or the *vorticity creation* methods use different techniques to define the boundary values of vorticity in terms of the stream function (or the velocity) by means of some approximate formula applied locally at the no-slip boundary. They are roughly equivalent, however their implementation may differ remarkably depending on the type of discretization used (see [1,12–14]).

An alternative viewpoint has been introduced by Quartapelle and Valz-Gris [15,16]. They showed that in order to satisfy the no-slip boundary conditions for the velocity, the vorticity should be subject to an integral constraint. This integral condition enforces the orthogonality of the abstract projection of the vorticity field with respect to the linear space of the harmonic functions defined on the domain. This condition is a direct consequence of the boundary conditions on the velocity, and ensures satisfaction of essential conservation laws for the vorticity. An important aspect of the integral vorticity conditions is their nonlocal character: the vorticity distribution in the interior of the domain and on its boundary is affected each time by the instantaneous values of the tangential and normal components of the velocity along the entire boundary. In other words, the distribution of the vorticity in the whole domain is constrained by the velocity boundary values. A detailed description of the mathematical basis and the different numerical implementations of the orthogonal-projection operation of the vorticity field for the $(\boldsymbol{\omega},\boldsymbol{\psi})$ formulation can be found in [1].

In our method, the issue of the vorticity boundary conditions on the no-slip surface is dealt with by a sequence of two solutions of the kinematic Laplacian equation (KLE) under a different set of velocity boundary conditions. Thus, inside each time step, we perform two projectional operations of integral character applied on the velocity field which ensures that the vorticity evolves in time in a way compatible with the time-dependent velocity boundary values.

2 Laplacian Approach as a Vorticity-Velocity Method: KLE

Starting from the well-known vector identity

$$\nabla^2\boldsymbol{v} = \boldsymbol{\nabla}\cdot\boldsymbol{\nabla}\boldsymbol{v} = \boldsymbol{\nabla}(\boldsymbol{\nabla}\cdot\boldsymbol{v}) - \boldsymbol{\nabla}\times(\boldsymbol{\nabla}\times\boldsymbol{v}) \tag{1}$$

We found that a variational form of this "Laplacian" expression could be advantageously used as the spatial counterpart of the vorticity transport equation in a new type of vorticity-velocity method.

Let us consider the full three-dimensional incompressible Navier-Stokes equation in vorticity form for a flow domain Ω with solid boundary $\partial\Omega$ and *external* boundary of Ω in the far field, in a moving frame of reference fixed to the solid

$$\frac{\partial\boldsymbol{\omega}}{\partial t} = -\boldsymbol{v}\cdot\boldsymbol{\nabla}\boldsymbol{\omega} + \nu\nabla^2\boldsymbol{\omega} + \boldsymbol{\omega}\cdot\boldsymbol{\nabla}\boldsymbol{v} \tag{2}$$

If we have the velocity field $\boldsymbol{v}$ in Ω at a certain instant of time, we can rewrite Eq. (2) as

$$\frac{\partial\boldsymbol{\omega}}{\partial t} = -\boldsymbol{v}\cdot\boldsymbol{\nabla}(\boldsymbol{\nabla}\times\boldsymbol{v}) + \nu\nabla^2(\boldsymbol{\nabla}\times\boldsymbol{v}) + (\boldsymbol{\nabla}\times\boldsymbol{v})\cdot\boldsymbol{\nabla}\boldsymbol{v} \tag{3}$$

and solve for $\boldsymbol{\omega}$ at each point of the discretization of Ω by integration of Eq. (3) using an ODE solver.

Now, let us revisit Eq. (1) but this time impose a given distribution for the vorticity field and the rate of expansion

$$\nabla^2\boldsymbol{v} = \boldsymbol{\nabla}\mathcal{D} - \boldsymbol{\nabla}\times\boldsymbol{\omega} \tag{4}$$

$$\boldsymbol{\nabla}\cdot\boldsymbol{v} = \mathcal{D} \tag{5}$$

$$\boldsymbol{\nabla}\times\boldsymbol{v} = \boldsymbol{\omega} \tag{6}$$

Here $\boldsymbol{\omega}$ is the vorticity field in Ω given by Eq. (3) and $\mathcal{D}$ is the corresponding rate of expansion (i.e., the divergence field). The KLE is essentially defined as a solution of Eq. (4) in its weak form under the simultaneous constraints (5) and (6).

The imposition of the corresponding distributions for both the rate of expansion and the vorticity is needed in order to obtain a unique solution for the complete velocity field from Eq. (4). The first constraint defines the irrotational-not-solenoidal component of the velocity field, and the latter the solenoidal-not-irrotational component. If those two components are given, the remaining component (which is both solenoidal and irrotational) is uniquely determined for prescribed boundary conditions. A comprehensive treatment of this subject may be found in [17] Secs. 2.4–2.7. Usually, in other vorticity-velocity approaches the Poisson Eq. (4) is solved simultaneously with the vorticity transport equation together with an imposition of the incompressibility condition (i.e., a constant zero rate of expansion). With the KLE, instead, the objective is to uncouple the velocity and vorticity solutions. Hence, the imposition of the vorticity distribution is needed as a second constraint in order to obtain an independent solution of the velocity field. To clarify this point, let us consider the orthogonal decomposition of the velocity field in its irrotational not-solenoidal component $\boldsymbol{v}_{\mathcal{D}}$, its solenoidal not-irrotational component $\boldsymbol{v}_{\omega}$ and its irrotational and solenoidal (i.e., harmonic) component $\boldsymbol{v}_h$. Under prescribed boundary conditions for the normal component of the velocity and given distributions for the vorticity $\boldsymbol{\omega}$ and the rate of expansion $\mathcal{D}$, this decomposition $\boldsymbol{v}=\boldsymbol{v}_{\mathcal{D}}+\boldsymbol{v}_{\omega}+\boldsymbol{v}_h$ is uniquely determined [17]. Constraints (5) and (6) ensure that $\boldsymbol{v}_{\mathcal{D}}$ and $\boldsymbol{v}_{\omega}$ are properly solved.

$$\boldsymbol{\nabla}\cdot\boldsymbol{v} = \boldsymbol{\nabla}\cdot\boldsymbol{v}_{\mathcal{D}} = \mathcal{D} \tag{7}$$

$$\boldsymbol{\nabla}\times\boldsymbol{v} = \boldsymbol{\nabla}\times\boldsymbol{v}_{\omega} = \boldsymbol{\omega} \tag{8}$$

Now, applying the orthogonal decomposition to the total velocity field $\boldsymbol{v}$ in Eq. (4) we have

$$\nabla^2(\boldsymbol{v}_h + \boldsymbol{v}_{\mathcal{D}} + \boldsymbol{v}_{\omega}) = \nabla^2\boldsymbol{v}_h + \boldsymbol{\nabla}(\boldsymbol{\nabla}\cdot\boldsymbol{v}_{\mathcal{D}}) - \boldsymbol{\nabla}\times(\boldsymbol{\nabla}\times\boldsymbol{v}_{\omega})$$
$$= \boldsymbol{\nabla}\mathcal{D} - \boldsymbol{\nabla}\times\boldsymbol{\omega} \tag{9}$$

substituting Eqs. (7) and (8) in Eq. (9) yields

$$\nabla^2\boldsymbol{v}_h = 0 \tag{10}$$

which provides the solution of the harmonic component $\boldsymbol{v}_h$. Thus, the KLE construction ensures that all three components of the velocity field are properly solved.

For incompressible cases, such as discussed here, $\mathcal{D}$ is simply set to zero. For compressible cases, $\mathcal{D}$ can be a general distribution given by a solution analogous to Eq. (3) but for the divergence transport equation (i.e., the momentum equation in divergence form) together with a solution of the mass transport

equation and adding to Eqs. (2) and (3) the terms eliminated by the application of the incompressibility condition.

Now, provided that we can find a way of imposing on the velocity field the no-normal-flow condition

$$\boldsymbol{v}\cdot\boldsymbol{n}=0 \tag{11}$$

and the no-slip condition

$$\boldsymbol{v}\cdot\boldsymbol{\tau}=0 \tag{12}$$

on the solid boundary $\partial\Omega$ in a way compatible with the vorticity distribution at that time, we obtain a compatible solution for the velocity. Then, from this velocity field we produce the right-hand side of Eq. (3) required to advance the time-integration process to the next step. In order to impose the no-normal-flow and no-slip conditions on $\partial\Omega$ together with the correspondingly compatible boundary conditions on the vorticity, we designed a scheme based on two consecutive solutions of the KLE: the first under free-slip and the second under no-slip boundary conditions on the solid surface. The algorithmic sequence described below is repeatedly performed inside the time-iteration process commanded by an adaptive variable-step size ODE solver. The solution is checked by the adaptive step size control by monitoring of the local truncation error, which proved to be quite stable for this application. The algorithmic sequence goes as follows:

(i) Given a velocity field for the previous time-step $\boldsymbol{v}^{n-1}$ (which is compatible with the correspondent vorticity field $\boldsymbol{\omega}^{n-1}$), compute the next vorticity field $\tilde{\boldsymbol{\omega}}^n$ by time integration of Eq. (3) at each node of the spatial discretization. The vorticity field $\tilde{\boldsymbol{\omega}}^n$ is still incompatible with the velocity boundary conditions on the solid surface $\partial\Omega$.

(ii) Get $\tilde{\boldsymbol{\omega}}_0^n$ by setting homogeneous conditions on $\partial\Omega$ for $\tilde{\boldsymbol{\omega}}^n$. As the nodal values of $\tilde{\boldsymbol{\omega}}^n$ are given from step (i), this step is accomplished by simply setting to zero the nodal values of $\tilde{\boldsymbol{\omega}}^n$ on $\partial\Omega$.

(iii) Compute a *free-slip* velocity field, $\boldsymbol{v}^n$, by solving the KLE (i.e., solving Eq. (4) in its week form under the simultaneous constraints (5) and (6), with $\mathcal{D}=0$). This solution uses $\tilde{\boldsymbol{\omega}}_0^n$ as input, applying only the no-normal-flow ($\boldsymbol{v}\cdot\boldsymbol{n}=0$) condition on $\partial\Omega$ with the normal derivative of the tangential velocity set to zero.

(iv) From $\boldsymbol{v}^n$, compute the new vorticity field as $\boldsymbol{\omega}^n=\boldsymbol{\nabla}\times\tilde{\boldsymbol{v}}^n$ applying both the no-normal-flow ($\boldsymbol{v}\cdot\boldsymbol{n}=0$) and the no-slip condition ($\boldsymbol{v}\cdot\boldsymbol{\tau}=0$) on $\partial\Omega$. Thus, $\boldsymbol{\omega}^n$ is a modified vorticity field produced in response to the induced slip which is compatible with the velocity boundary conditions on $\partial\Omega$. This is the analog of the *vorticity creation* process of the early methods mentioned above, where vorticity is *created* in response to the induced slip [12–14].

(v) Compute the final velocity field $\boldsymbol{v}^n$, by solving again the KLE but this time using $\boldsymbol{\omega}^n$ as input and applying both the no-normal-flow and the no-slip condition on $\partial\Omega$. In this way, $\boldsymbol{v}^n$ gives the weak solution for the velocity field at time-step n, which satisfies the time-dependent boundary conditions for the velocity, and simultaneously, its correspondent vorticity field $\boldsymbol{\omega}^n$ is compatible with those velocity boundary conditions.

In steps (iii)–(v) we apply the corresponding time-dependent, Dirichlet conditions for the velocity on $\partial\Omega_\infty$, the *external* boundary of Ω in the far field.

It is interesting to note that all the physics of the problem is contained in step (i) and it is solved as an ODE problem on the vorticity. Steps (ii)–(v) are concerned with the computation of a spatial solution for the velocity field which is compatible with both: the time-evolved vorticity distribution obtained in (i) and the time-dependent boundary conditions for the velocity. Setting homogeneous conditions on $\partial\Omega$ in step (ii) makes the vorticity field consistent with the *free-slip* solution of the velocity field to be computed in step (iii). Then, enforcing of the no-slip condition on $\partial\Omega$ in step (iv) gives the vorticity values in the boundary in response to the induced slip. As was mentioned above, this is the analog of the *vorticity-creation* process typically found in early hybrid and nonprimitive methods. Thus, we obtain our compatible vorticity boundary conditions on the solid surface by sequence of two solutions of the KLE under a different set of velocity boundary conditions. These two projectional operations of integral character applied on the velocity field (and performed inside each time step) ensure that the vorticity evolves in time in a way compatible with the time-dependent velocity boundary values. As was mentioned above, the algorithmic sequence defined in (i)–(v) is repeatedly performed inside the time-iteration process commanded by an adaptive variable-step size ODE solver. We tested a predictor-corrector (ABM-PECE) solver and a fifth-order adaptive Runge-Kutta solver (see [18]), both with satisfactory results.

The algorithmic sequence defined in (i)–(v) has the advantage of producing a complete decoupling between the time integration of the vorticity transport equation and the space solution of the Poisson equation for the velocity field. The linear spatial solution defined in (4)–(6) (i.e., the KLE) can be implemented in just one variational formulation. This implementation leads to a global matrix which is independent both of time and of the particular constitutive relation of the continuum media. Then, this matrix can be factorized at the moment of assembling and its triangular factors used as many times as needed so long as we are using the same grid. As we said, this is so even for problems with different constitutive relations because all the physics of the problem is taken into account only in the time-integration process for the vorticity, i.e., the spatial solution is purely *kinematic*. Thus, the space solution performed at each time step reduces to a pair of back-substitution processes where we simply change the right-hand side vector of the linear system in order to impose the boundary conditions consecutively (11) and (12). This scheme simplifies the issue of obtaining the vorticity in order to satisfy the boundary conditions on the velocity. Note that it is not a purely local manipulation performed on the boundary; this double solution of the velocity field is calculated over the entire domain involving two projectional operations of nonlocal character.

3 Numerical Implementation of KLE Method

The KLE method is more a mathematical model than a numerical discretization scheme and is in itself independent of the particular interpolation adopted for the spatial discretization. Here, we adopted the tri-quadrilateral finite element method (FEM) technique for this first implementation of the method because it was well suited to the kind of problems we were interested in studying (i.e., the vortex structure of wakes for different body shapes). The generality of the KLE method allows further exploration of different techniques for discretization in space (like advanced triangular FEM, spectral elements, etc.) and time (implicit ODE methods), which is the author's intention. The actual discretization is based on the use of nine-node biquadratic isoparametric finite elements, which, though "expensive" in computational terms, possess a high convergence rate and, due their biquadratic interpolation of the geometric coordinates, provide the additional ability of reducing the so-called skin error on curvilinear boundaries when compared to linear elements. Figure 1 shows the biquadratic interpolation functions (h^k, $k=1,\ldots,9$) of the nine-node isoparametric element on its natural system of coordinates (r,s) (for a detailed description of the isoparametric-element technique and its corresponding interpolation functions see [19]).

In order to combine the advantages of the nine-node quadrilateral isoparametric element with the geometrical ability of a triangular grid to create suitable non-structured meshes with gradual and smooth changes of density, we implemented what we called

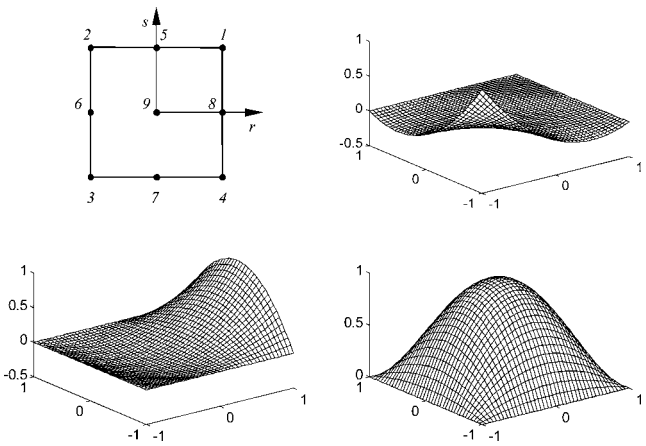

Fig. 1 Interpolation functions of the nine-node isoparametric element showing its natural system of coordinates, node numeration, and three examples of functions: for a corner node (node 3), for a central-lateral node (node 8), and for the central node (node 9)

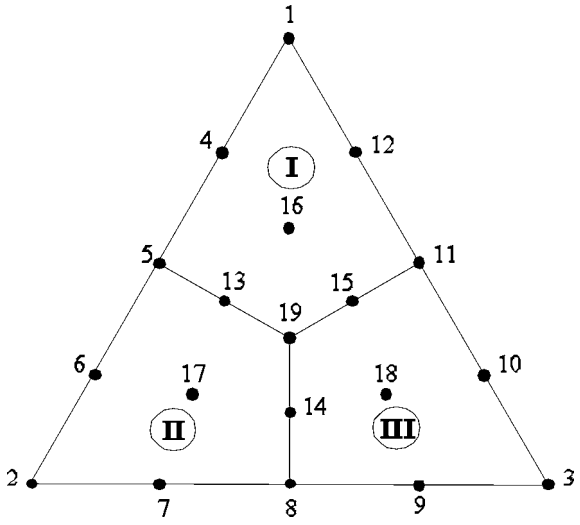

Fig. 3 Schematic view of the internal topology of the tri-quadrilateral element. Subelements (I)–(III) are modeled by standard nine-node isoparametric interpolation. Numbers 1–19 indicate the in-triangle nodal numeration.

tri-quadrilateral isoparametric elements [20,21]. The tri-quadrilateral elements consist of an assembling of three quadrilateral nine-node isoparametric elements in which each triangle of a standard unstructured mesh is divided into. Figure 2 shows a schematic example of a mesh of tri-quadrilateral finite elements obtained from the original triangular discretization.

By static condensation of the nodes that lie inside the triangle, we can significantly reduce the number of nodes to solve in the final system, subsequently recovering the values for the internal nodes from the solution on the non-condensable nodes. Figure 3 shows a schematic view of the internal topology of the tri-quadrilateral element including the in-triangle global numeration of the nodes and indicating the three nine-node subelements (I)–(III). The internal nodes 13–19 may be expressed in terms of nodes 1–12 which lay on the elemental boundary following the classical procedure for elemental condensation (see [19]). This process of condensation allows us to reduce the size of the new system to solve to approximately 40% of the original system. The use of the static condensation procedure is attractive not only because it reduces the size of the stiffness matrices arising in finite-element and spectral-element methods but also because it improves the condition number of the final condensed system. This is related to the properties of the Schur-complement technique. The condensed system is essentially the Schur complement of the interior-node submatrix in the non-condensed original system.

A further advantage of the tri-quadrilateral scheme is that it may be directly extended to the use of quadrilateral spectral elements, which may handle complicated geometries while preserving the fast convergence properties of spectral discretizations.

As was mentioned above, none of the matrices involved in the finite element solution depend on $\boldsymbol{\omega}$ nor t, so they can be computed once for a given mesh, stored and used as many times as needed to compute the solution for the discrete velocity field $\hat{\boldsymbol{V}}$. The global matrix of the system is symmetric and positive definite, so it lends to factorization by Cholesky decomposition and its triangular factor is repeatedly used to solve $\hat{\boldsymbol{V}}$ through back substitution.

For the implementation of the time-integration procedure we evaluate the right-hand side of Eq. (3) applying the corresponding differential operators onto the discrete velocity field $\hat{\boldsymbol{V}}$ calculated following steps (ii)–(v) in Sec. 2. The normal procedure to calculate derivatives on the nodes of a mesh of isoparametric elements

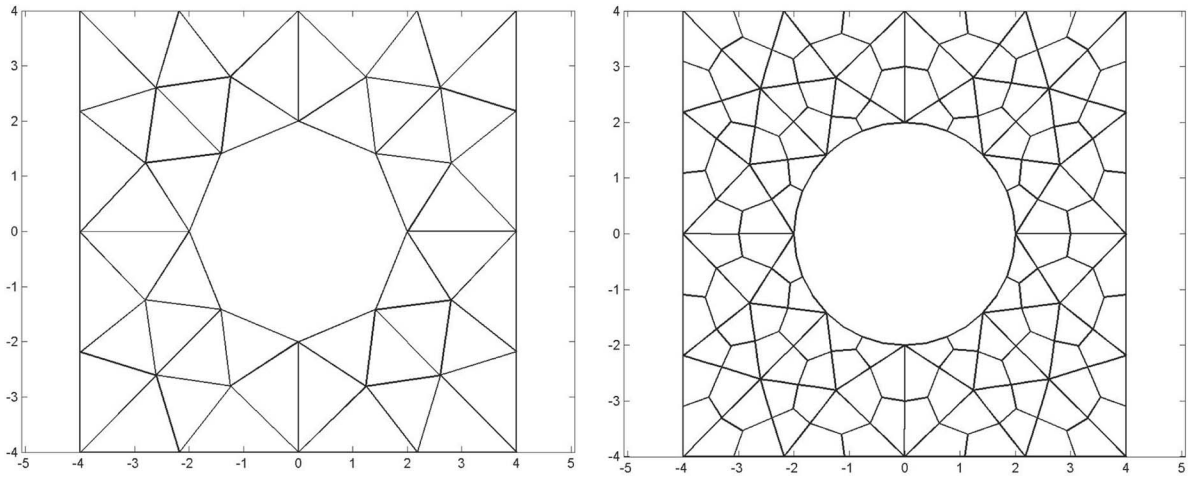

Fig. 2 An example of a mesh of tri-quadrilateral finite elements obtained from a standard triangular discretization

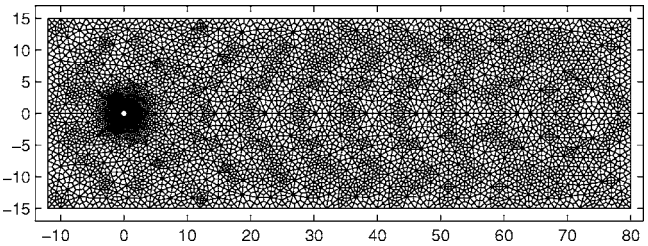

Fig. 4 An example of a mesh of 2828 tri-quadrilateral finite elements and 34,216 nodes used for the present analysis, which gives a total of 14,420 nodes after static condensation (geometrical coordinates are given in diameters)

consists in computing the derivatives in the Gaussian points adjacent to each node and interpolate their results following several alternatives techniques. A detailed description of this procedure can be found in [19]. In our case we used area-weighing interpolation which proved to be very effective. The contribution of each Gaussian point to its corresponding node depends on the constitution of the mesh and can be calculated at the moment of assembling. A set of arrays that perform the differential operations is assembled simultaneously with the finite-element matrices, so they can also be computed once for a given mesh, stored and used as many times as needed to provide evaluation of Eq. (3) right-hand side for an advanced package ODE solver. We choose a multivalue variable-order Adams-Bashforth-Moulton predictor-corrector (ABM-PECE) solver with adaptive step size control which proved to be quite efficient for this application. We also tried a fifth order adaptive-step size Runge-Kutta algorithm with good results. For the first DNS low-Reynolds-number applications of the KLE method, the function proves to be smooth enough for the adaptive ABM-PECE algorithm to work very efficiently, in these smooth cases the predictor corrector outperforms other alternatives like the Bulirsch-Stoer method [18].

4 Some Examples of Application of KLE Method

We first show some results produced by the KLE method for the well-studied case of a circular cylinder started impulsively and then subjected to steady translational motion through fluid otherwise at rest. Figure 4 shows an example of a mesh of 2828 tri-quadrilateral finite elements and 34,216 nodes used for the present analysis, which gives a total of 14,420 nodes after static condensation.

We shall see results at several values of Reynolds number, $\mathrm{Re}=Ud/\nu$, where U is the horizontal translational speed of the cylinder, d its diameter, and ν the kinematic viscosity of the fluid. We compare our two-dimensional flow simulations on the range $5<\mathrm{Re}<180$ to experimental measurements and flow visualizations. Figure 5 shows velocity arrow plots taken from our computations superimposed on two aluminum-dust flow-visualization plates due to S. Taneda (taken from [22]). The arrows are plotted out of scale in order to make the flow direction visible, especially in the vicinity of stagnation points. This scaling tends to exaggerate minor alterations in symmetry due to round-off error.

In the range $5<\mathrm{Re}<40$ we measured the length (s) of the stationary twin-vortex wake from the rear stagnation point on the solid surface to the confluence point at the tail of the wake, and we compared our results to the classical experiments of [23]. The results for the non-dimensional length s/d against Re are shown in Fig. 6. Overall the agreement between computations and experiments is very good.

As a second test case we considered the formation of the familiar Kármán vortex street behind a translating cylinder. Figure 7 shows a comparison between a smoke-in-air flow visualization due to M. M. Zdravkovich (taken from [22]) and the vorticity field produced by our numerical method at the same Reynolds number.

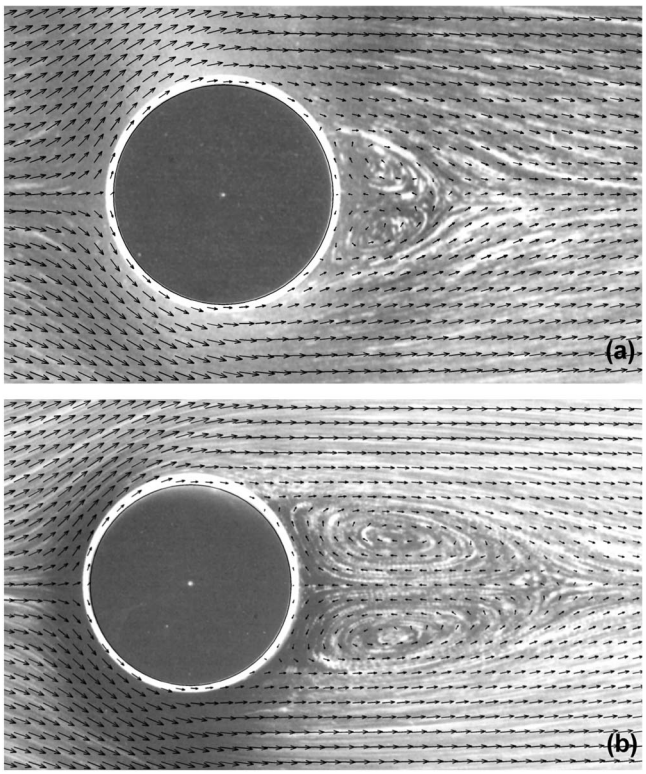

Fig. 5 Comparison of flow visualizations by Taneda and arrow plots from numerical results for the twin-vortex wake behind a cylinder at (*a*) Re=13.05 and (*b*) Re=26

We show a symmetric gray-scale map so areas of both positive and negative vorticity appear clear while zones of low vorticity appear dark. The smoke *signal* in the experimental photo, and the magnitude of vorticity displayed from the computation are, of course, not the same. Differences between the experimental image and the numerical plot are related to different diffusivity of smoke used as tracer in the experimental image and the diffusive properties of vorticity which is shown in the numerical plot. Nevertheless, due to the fact that in two-dimensional flow the vorticity transport equation coincides with the transport equation of a passive scalar, comparisons of vorticity plots with streakline flow-visualization images are very useful because they allow to check the structure of the wake. Those comparisons constitute a very strict test for any vorticity-velocity approach because they give an idea of the *history* of the wake. In unsteady flows streaklines represent the *integrated* development composed of all previous distortions incurred along the way from the point of introduction upstream of the point of observation. In a vorticity-velocity scheme, if the transport of vorticity is not accurate, the entire structure of the wake is affected. Here, the correspondence in the spacing, and even the shape of the vortices, lends considerable confidence to the fidelity of the numerical simulations. The typical CPU time to develop a Kármán-vortex-street wake 70-diam-long downstream of the cylinder for Re=140, using a mesh like the one shown in Fig. 4, is about 16 h in a standard Pentium-4 PC.

As our third test case, we measured the dominant frequency, f, of vorticity fluctuations at a set of points in the vortex street wake for the range of Reynolds numbers $50<\mathrm{Re}<180$, and we computed the corresponding value of the Strouhal number ($\mathrm{St}=fd/U$). The dominant frequency is the same for all the points probed, and it is clearly defined at an early stage of wake formation. The amplitude of the fluctuations, on the other hand, displays a transient state until it reaches its final, constant value somewhat

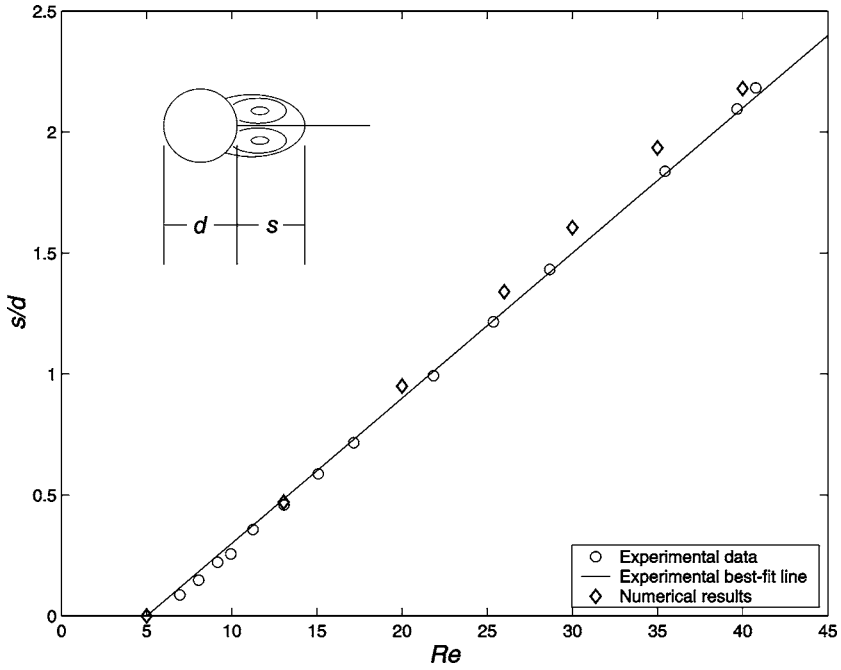

Fig. 6 Comparison of the wake length calculated by the kinematic Laplacian equation method and the experimental measurements by Taneda [23]

downstream. Plotting St versus Re, as shown in Fig. 8, compares very favorably with the experiments presented by Williamson [24].

Finally, we have recently started a study on the formation, shedding, and further evolution of periodic vortex-array structures produced in the wake of forced-oscillating cylinders. Several qualitatively distinct wake regimes were observed experimentally depending on the wavelength of the undulatory motion of the cylinder and the amplitude of the transverse undulations. For instance, for a certain range in the combination of the wavelength/amplitude parameters, a pattern in which one pair and a single vortex are shed in each cycle of the forced oscillation is produced. This pattern is commonly known as P+S (one pair plus one single vortex). Figure 9 shows a comparison of a gray scale plot of the vorticity field calculated by the KLE method with an experimental laser-fluorescene photograph for an oscillating cylinder at Re =140. This photo was kindly provided by Prof. C. H. K. Williamson. As in the previous case shown in Fig. 7, differences between the experimental image and the numerical plot are related to different diffusivity of fluorescene used as tracer in the experimental image and the diffusive properties of vorticity, which is shown in the numerical plot.

5 Conclusions and Outlook for Further Work

We have introduced a mathematical-computational approach to solve the time-dependent flow in a non-inertial frame of reference attached to a body in translational and/or roto-translational motion. The KLE method was validated for two-dimensional direct numerical simulation (DNS) applications against experimental results for incompressible flow around circular cylinders at low Reynolds number, finding very good agreement.

As we have seen above, the basic formulation of the KLE is three dimensional and has no special requirements on the rate-of-expansion distribution which is imposed. It implies that the

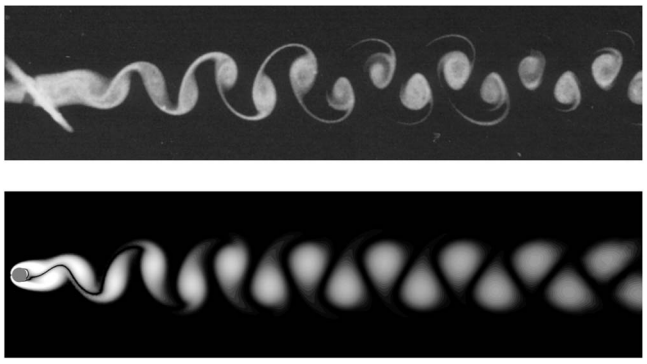

Fig. 7 Comparison of flow visualization of a Kármán vortex street behind a cylinder at Re=100 by M. M. Zdravkovich with a gray scale plot of the vorticity field produced by the kinematic Laplacian equation method at the same value of Reynolds number

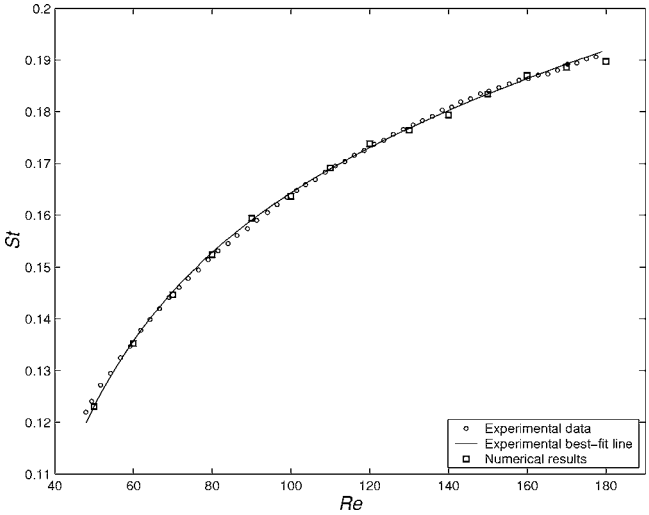

Fig. 8 Comparison of the Strouhal number calculated by the kinematic Laplacian equation method and the experimental measurements by Williamson [24] for Re<180

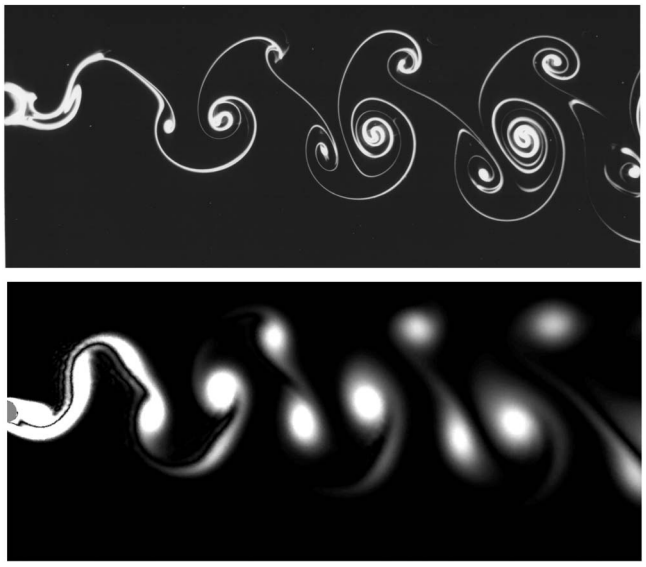

Fig. 9 Comparison of flow visualization of a P+S wake of an oscillating cylinder for Re=140 by C. H. K. Williamson (private communication to H. Aref) with a gray scale plot of the vorticity field produced by the KLE method at the same Reynolds number

method can be extended to the analysis of compressible flows, provided that we find a way of dealing with compatible boundary conditions for the rate of expansion in an analog way as we do with the vorticity.

Since it is a new approach, we are still exploring KLE method capabilities to manage higher Reynolds-number flows in DNS, and its potential to be extended to large eddy simulation (LES) applications. The fact that the linear spatial solution provided by the KLE is purely kinematic with all the nonlinearities and the material constitutive properties remitted to the high-order adaptive time integration, favors the solution of problems with more complex constitutive relations like non-Newtonian, plastic or viscoplastic flows. And the same argument may be applied to the adoption of turbulence models for a future LES implementation of the method.

The KLE is based on a universal vectorial relation, so it can be used to solve any vector field provided that we can solve a transport equation for its divergence and curl. This together with the fact that time is the only iteration variable present, makes it possible to extend its application to other physical problems like electromagnetic fields. It is also possible to couple the fluid analysis with other physical processes (e.g., heat transfer or chemical reaction) by adding more equations to the ODE system, using grids with different densities for problems with different scales.

Regarding the numerical implementation of the KLE method, the techniques mentioned above: Cholesky decomposition/back substitution for the spatial solution, and adaptive predictor-corrector solver for time integration, prove to be very efficient for a two-dimensional low Reynolds number implementation of the method in a sequential code. In view to solve problems in complex geometries in three-dimensional applications which will require a substantial number of nodes (leading to large sparse systems) for the spatial discretization, it will be necessary to turn to a parallel version of the KLE code. This can be done in a relatively easy way: there are several parallel-program packages including parallel versions of the top ODE solvers and evaluation of our right-hand-side term involves matrix products that can be easily parallelizable. Concerning the solution of our linear system, back substitution is essentially a sequential process, then it should be replaced by an iterative parallel linear solver. For a symmetric positive-definite matrix like ours, the preconditioned conjugate gradient method constitutes the first option, using the triangular factor from an incomplete Cholesky decomposition as preconditioner to accelerate convergence (like before, this incomplete Cholesky factor can be computed once an used repeatedly). Regarding the time integration process, the adaptive ABM-PECE solver works at its best for smooth functions. This situation could change when we try to extend the KLE method to problems with more complex constitutive relations or to the analysis of coupled physical processes where different time scales are likely to appear. If the function is no longer smooth, a recommendable alternative to the ABM-PECE solver is the adaptive Bulirsch-Stoer algorithm with modified midpoint integration and Richardson extrapolation [18]. If different time scales are present, the possibility of stiffness arises and then a Bulirsch-Stoer solver with semi-implicit midpoint integration is recommendable.

Finally, we may emphasize KLE flexibility to manage different trajectories with translational and rotational acceleration and its use of unstructured meshes. This method gives us a useful tool to study the vortex structure of wakes for different body shapes and motions. We are using this tool to explore complex vortex wake patterns in the wake of forced oscillating cylinders at low Reynolds number, focusing on the process of splitting which characterizes the formation of P+S and similar structures. We hope to use the numerical tool developed here to continue with such explorations in the future.

Acknowledgment

The author is indebted to Hassan Aref for his advice, support, and encouragement, and for many valuable discussions. He would like to acknowledge the financial support made available by the University of Buenos Aires through Grant No. UBACyT-Pr.2004/07(I-56) and by Fundación Antorchas. He also acknowledges the hospitality of the Department of Theoretical and Applied Mechanics at University of Illinois. This work was funded in part by research funds made available by the University of Illinois.

References

[1] Quartapelle, L., 1993, *Numerical Solution of the Incompressible Navier-Stokes Equations*, Birkäuser, Basel, Switzerland, Chap. 4.
[2] Clercx, H. J. H., 1997, "A Spectral Solver for the Navier-Stokes Equations in the Velocity-Vorticity Formulation for Flows With Two Nonperiodic Directions," J. Comput. Phys., **137**, pp. 186–211.
[3] Speziale, C. G., 1987, "On the Advantages of the Velocity-Vorticity Formulation of the Equations of Fluid Dynamics," J. Comput. Phys., **73**, pp. 476–480.
[4] Fasel, H., 1976, "Investigation of the Stability of Boundary Layers by a Finite Difference Model of the Navier-Stokes Equations," J. Fluid Mech., **78**, pp. 355–383.
[5] Dennis, S. C. R., Ingham, D. B., and Cook, R. N., 1979, "Finite Difference Methods for Calculating Steady Incompressible Flows in Three Dimensions," J. Comput. Phys., **33**, pp. 325–339.
[6] Gatski, T. B., Grosh, C. E., and Rose, M. E., 1989, "The Numerical Solution of the Navier-Stokes Equations for 3-Dimensional Unsteady Incompressible Flows by Compact Schemes," J. Comput. Phys., **82**, pp. 298–329.
[7] Napolitano, M., and Pascazio, G., 1991, "A Numerical Method for the Vorticity-Velocity Navier-Stokes Equations in Two and Three Dimensions," Comput. Fluids, **19**, pp. 489–495.
[8] Guj, G., and Stella, F., 1993, "A Vorticity-Velocity Method for the Numerical Solution of 3D Incompressible Flows," J. Comput. Phys., **106**, pp. 286–298.
[9] Guevremont, G., Habashi, W. G., Kotiuga, P. L., and Hafez, M. M., 1993, "Finite Element Solution of the 3D Compressible Navier-Stokes Equations by a Velocity-Vorticity Method," J. Comput. Phys., **107**, pp. 176–187.
[10] Davies, C., and Carpenter, P. W., 2001, "A Novel Velocity-Vorticity Formulation of the Navier-Stokes Equations With Applications to Boundary Layer Disturbance Evolution," J. Comput. Phys., **172**, pp. 119–165.
[11] Lo, D. C., and Young, D. L., 2004, "Arbitrary Lagrangian-Eulerian Finite Element Analysis of Free Surface Flow Using a Velocity-Vorticity Formulation," J. Comput. Phys., **195**, pp. 175–201.
[12] Anderson, C. R., 1988, "Observations on Vorticity Creation Boundary Conditions," *Mathematical Aspects of Vortex Dynamics*, R. E. Caflisch, ed., SIAM, Philadelphia, pp. 144–159.
[13] Chorin, A. J., 1973, "Numerical Study of Slightly Viscous Flow," J. Fluid Mech., **57**, pp. 785–796.
[14] Chorin, A. J., 1978, "Vortex Sheet Approximation of Boundary Layers," J. Comput. Phys., **27**, pp. 428–442.
[15] Quartapelle, L., and Valz-Gris, F., 1981, "Projection Conditions on the Vortic-

ity in Viscous Incompressible Flows," Int. J. Numer. Methods Fluids, **1**, pp. 129–144.
[16] Quartapelle, L., 1981, "Vorticity Conditioning in the Computation of Two-Dimensional Viscous Flows," J. Comput. Phys., **40**, pp. 453–477.
[17] Batchelor, G. K., 2000, *An Introduction to Fluid Dynamics*, Cambridge University Press, Cambridge, UK.
[18] Press, W. H., Teukolsky, S. A., Vetterling, W. T., and Flannery, B. P., 2002, *Numerical Recipes in C*, 2nd ed., Cambridge University Press, Cambridge, UK.
[19] Bathe, K. J., 1996, *Finite Element Procedures*, Prentice–Hall, Englewood Cliffs, NJ.
[20] Ponta, F. L., and Jacovkis, P. M., 2001, "A Vortex Model for Darrieus Turbine Using Finite Element Techniques," Renewable Energy, **24**, pp. 1–18.
[21] Ponta, F. L., and Jacovkis, P. M., 2003, "Constant-Curl Laplacian Equation: A New Approach for the Analysis of Flows Around Bodies," Comput. Fluids, **32**, pp. 975–994.
[22] Van Dyke, M., 1982, *An Album of Fluid Motion*, Parabolic Press, Stanford, CA.
[23] Taneda, S., 1956, "Experimental Investigation of the Wakes Behind Cylinders and Plates at Low Reynolds Numbers," J. Phys. Soc. Jpn., **11**, pp. 302–307.
[24] Williamson, C. H. K., 1989, "Oblique and Parallel Mode of Vortex Shedding in the Wake of a Circular Cylinder at Low Reynolds Numbers," J. Fluid Mech., **206**, pp. 579–627.

Constitutive Modeling and Discontinuous Bifurcation Assessment in Unsaturated Soils

Ricardo Schiava
Department of Civil Engineering,
Universidad Nacional de Santiago del Estero
(4200),
Santiago del Estero,
Argentina

Guillermo Etse
CONICET Department of Civil Engieering,
Universidad Nacional de Tucumán,
Munecas 730, 10A,
4000 Tucumán,
Argentina
e-mail: getse@herrera.unt.edu.ar

In this work an elastoplastic constitutive theory for unsaturated soils is presented. The proposed material model is formulated in the general framework of the theory of porous media and of the flow theory of plasticity. The model is based on an extension of the well-known MRS Lade model whereby the suction and the effective stress tensor are introduced as additional independent and dependent stress components, respectively. Consequently the cap and cone yield conditions of the MRS Lade model both in hardening and softening as well as the internal evolution laws in these regimes are redefined to include the dependency on the suction. The paper illustrates the predictive capability of the extended MRS Lade model for partially saturated soils. Finally, the condition for discontinuous bifurcation in elastoplastic partially saturated porous media as well as the localized failure predictions of the proposed material formulation for different suctions and stress states are also analyzed and discussed. [DOI: 10.1115/1.2202349]

1 Introduction

In the last years significant attention has been directed toward the development of constitutive theories for partially saturated soils. These materials are characterized by particular and complex response behaviors which strongly differ from those corresponding to both dry and saturated soils. Actually, the physics and engineering principles involved in dry soils are essentially the same as those involved in saturated soils. The main difference between a completely dry and a completely saturated soil is related to the compressibility of the pore fluid. The water in a saturated soil is basically incompressible. The water becomes compressible as air bubbles appear in the water.

From phenomenological observation we know that below the water table, the pore-water pressures are positive and the soils are, in general, saturated. However, above the water table, the pore-water pressures are, in general, negative. The negative pore-water pressures above the water table are mostly referenced to the pore-air pressure. The difference between the pore-air pressure and pore-water pressure is called the matric suction. Suction in an unsaturated soil is made up of two components, namely, matric suction and osmotic suction. The sum of the two components is called total suction. The osmotic suction is a function of the amount of dissolved salts acting in the pore fluid, and written in terms of a pressure. The matric suction is of primary interest because it is the stress variable which is strongly influenced by environmental changes.

Among the different experimental observation-based elastoplastic models for partially saturated soils in the literature, the model by Alonso et al. [1] is one of the most representative ones. They adopted two independent stress variables, i.e., the total stress in excess of pore air pressure and the suction. Similar to this model are the constitutive formulations proposed by Schrefler and Zhan [2], Cui et al. [3], Bolzon et al. [4], Wheeler and Sivakumar [5], and Kohgo et al. [6]. A comprehensive review of the different proposals is given by Gens [7]. Recently, Khalili [8] proposed a constitutive model based on the effective stress concept. However, in their detailed formulation of the model Loret and Khalili [9] included the suction as an independent variable in the yield function and plastic potential, in addition to the effective stress and the suction dependent hardening parameter.

Contrary to the formulation of constitutive equations for partially saturated soils, the analysis of the conditions for discontinuous bifurcation in the form of localized failure has not received considerable attention so far. Actually, the intrinsic hydromechanical coupling of partially saturated porous media and the presence of the suction in the constitutive equations strongly affects the localized failure indicators. As a consequence, both the solutions for discontinuous bifurcation as well as the critical directions for localization depend not only on the mechanical nonlinear properties of the material formulation, i.e., yield condition, nonassociativity, hardening/softening evolution law, etc., but also on the hydraulic features of the deformation history.

In this work an elastoplastic constitutive model for partially saturated soils is proposed. The model is an extension of the MRS-Lade model by Sture et al. [10], and is a further development of Lade's three-invariant model for cohesionless soils. The proposed elastoplatic material model, the extended MRS-Lade model, is described in the space of the three effective stress invariants and of the suction, which is introduced as a new independent variable.

The constitutive equations of the proposed model are also analyzed with regard to the solutions of discontinuous bifurcation. In this sense, the localized failure predictions and the critical directions for localization of the extended MRS Lade model are analyzed for different confinement pressures and suctions.

The results in this work demonstrate the proposed model's predictive capability of the response behavior of partially saturated soils. Also the strong influence of the suction on the failure mode and on the critical direction for localized failure is demonstrated.

Contributed by the Applied Mechanics Division of ASME for publication in the JOURNAL OF APPLIED MECHANICS. Manuscript received September 26, 2005; final manuscript received April 6, 2006. Review conducted by G. C. Buscaglia. Discussion on the paper should be addressed to the Editor, Prof. Robert M. McMeeking, Journal of Applied Mechanics, Department of Mechanical and Environmental Engineering, University of California—Santa Barbara, Santa Barbara, CA 93106-5070, and will be accepted until four months after final publication in the paper itself in the ASME JOURNAL OF APPLIED MECHANICS.

2 Constitutive Stress

Partially saturated soils are generally described in terms of the constitutive or effective stress tensor $\boldsymbol{\sigma}'$ and the suction s as a dependent and an independent stress variable, respectively, where

$$\boldsymbol{\sigma}' = \boldsymbol{\sigma} - \mathbf{I}p_w = \boldsymbol{\sigma}_n + \mathbf{I}s \tag{1}$$

$$s = (p_a - p_w) \tag{2}$$

thereby $\boldsymbol{\sigma}$ is the total stress tensor, $\boldsymbol{\sigma}_n$ the net stress tensor, p_a, p_w the pore air and pore water pressure, respectively, and $\mathbf{I}$ the second-order identity tensor. The term effective stress is due to Loret and Khalili [9], but as pointed out by Sheng et al. [11] who proposed the name *constitutive stress* instead, it is not an effective stress in Terzaghi's sense.

In many geotechnical applications the air pressure remains constant and, as a consequence, pore water pressure instead of the suction can be treated as a variable in the model formulation. Nevertheless, the constitutive formulation in this work is based on the suction allowing for the most general applications of the model.

3 Flow Rule-Based Elastoplastic Equations for Partially Saturated Soils

3.1 The General Formulation. Many plasticity models are characterized by yield surfaces, such as Tresca's, Mohr-Coulomb's, and a variety of cone-cap criteria. Each convex function $F_i(\boldsymbol{\sigma}', s, \boldsymbol{\kappa})$, that in case of partially saturated soils are defined in the space of the effective stress tensor and the suction, can be treated as an independent yield function, that depends on the set of hardening/softening variables represented by the array $\boldsymbol{\kappa}$. They are subsequently chosen as scalars κ_i that represent the plastic work or effective plastic strain measures in conjunction with the plasticity models presented in the following sections.

The intersection of all the sets of stresses defined by $F_i \leqslant 0$ defines the convex set $B\{\boldsymbol{\kappa}\}$ of plastically admissible constitutive stresses $\boldsymbol{\sigma}'$ and suction $\mathbf{s}$,

$$B\{\boldsymbol{\kappa}\} = \{\boldsymbol{\sigma}', s | F_i(\boldsymbol{\sigma}', s, \boldsymbol{\kappa}) \leqslant 0,\ i = 1,2,\ldots,U\} \tag{3}$$

Moreover, the space $B_{\lambda_i}\{\boldsymbol{\kappa}, \dot{\boldsymbol{\epsilon}}, \dot{s}\}$ can be introduced in the form

$$B_{\lambda_i}\{\boldsymbol{\kappa}, \dot{\boldsymbol{\epsilon}}, \dot{s}\} = \{\boldsymbol{\sigma}', s | F_i(\boldsymbol{\sigma}', \mathbf{s}, \boldsymbol{\kappa}) \leqslant 0, \quad \text{if } \dot{\lambda}_i(\dot{\boldsymbol{\epsilon}}, \dot{s}) > 0,\ i = 1,2,\ldots,U\} \tag{4}$$

to account for plastic loading and elastic unloading, where the parameters $\dot{\lambda}_i$, $i = 1,2,\ldots,U$, define the surfaces that are active. Plastic loading occurs when at least some $\dot{\lambda}_i > 0$.

Following Weihe [12], the flow rule can be formulated in terms of the space of sub-differentials ∂F_λ, representing a fan of admissible normals at each corner of the composite failure surface

$$\partial F_{\lambda_i}\{\boldsymbol{\sigma}', \dot{s}, \boldsymbol{\kappa}, \dot{\boldsymbol{\epsilon}}\} = \{\mathbf{a} | (\boldsymbol{\sigma}' - \boldsymbol{\sigma}'_o) : \mathbf{a} \geqslant 0,\ \forall\ \boldsymbol{\sigma}'_o,\ \in B_{\lambda_i}\{\boldsymbol{\kappa}, \dot{\boldsymbol{\epsilon}}, \dot{s}\}\} \tag{5}$$

The nonassociated flow rule-based general constitutive equations for partially saturated soils can, therefore, be expressed as

$$\dot{\boldsymbol{\sigma}}' = \mathbf{E} : (\dot{\boldsymbol{\epsilon}} - \dot{\boldsymbol{\epsilon}}_p) \tag{6}$$

$$(\boldsymbol{\sigma}' - \boldsymbol{\sigma}'_o) : \mathbf{A} : \dot{\boldsymbol{\epsilon}}_p \geqslant 0\ \forall\ \boldsymbol{\sigma}'_o \in B_{\lambda_i}\{\boldsymbol{\kappa}, \dot{\boldsymbol{\epsilon}}, \dot{s}\} \tag{7}$$

$$\dot{\boldsymbol{\kappa}} = h\{\dot{\boldsymbol{\epsilon}}_p\} \tag{8}$$

where $\dot{\boldsymbol{\epsilon}}_p$ is the plastic portion of total strain rate tensor $\dot{\boldsymbol{\epsilon}}$, the function h is a first degree homogeneous vector function, and Eq. (7) represents an associated flow rule for the transformed plastic strain rate $\mathbf{A} : \dot{\boldsymbol{\epsilon}}_p$ provided the fourth-order transformation operator $\mathbf{A}$ exists. An associated flow rule for the plastic strain rate $\dot{\boldsymbol{\epsilon}}_p$ is thus defined by $\mathbf{A} = \mathbf{I}$, $\mathbf{I}$ being the fourth-order identity tensor.

The *variational* form of the nonassociated flow rule in Eq. (7) can be reformulated using its *rate* form and the Kuhn-Tucker conditions

$$\dot{\boldsymbol{\epsilon}}_p = \sum_{i=1}^{U} \dot{\lambda}_i \mathbf{m}_i^\sigma \quad \dot{\lambda}_i \geqslant 0 \quad F_i \dot{\lambda}_i = 0 \tag{9}$$

where

$$\mathbf{m}_i^\sigma = \mathbf{A}^{-1} : \mathbf{n}_i^\sigma \quad \mathbf{n}_i^\sigma = \frac{\partial F_i}{\partial \boldsymbol{\sigma}'} \tag{10}$$

is the direction of the plastic flow associated with the yield function F_i. Thereby, and as indicated in Eq. (10), $\mathbf{m}_i^\sigma$ and $\mathbf{n}_i^\sigma$ represent the gradients to the plastic potential G_i and to the yield surface F_i, respectively, with respect to the constitutive stresses.

3.2 The Consistency Condition. In elastoplastic constitutive formulations, the consistency condition during plastic loading leads to the explicit form of the continuum material operator. In case of partially saturated soils the consistent condition takes the form

$$\dot{F}_i = \mathbf{n}_i^\sigma : \dot{\boldsymbol{\sigma}}' + n_i^s \dot{s} + r_i \dot{\kappa}_i = 0 \quad i = 1,2,\ldots,U \tag{11}$$

with

$$n_i^s = \frac{\partial F_i}{\partial s} \tag{12}$$

$$r_i = \frac{\partial F_i}{\partial \kappa_i} \tag{13}$$

$$\dot{\kappa}_i = \dot{\lambda}_i h_i(\mathbf{m}_i^\sigma) \tag{14}$$

As compared to the consistency condition of classical or conventional elastoplastic models, Eq. (11) has an additional term $n_i^s \dot{s}$ related with the evolution of the suction and the gradient of the yield surface with respect to the suction. As pointed out by Sheng et al. [11], many authors have simply neglected this additional term in their formulations of constitutive equations for partially saturated soils and, as a consequence, the resulting consistency conditions are mathematically not rigorous.

After replacing the stress-strain relation

$$\dot{\boldsymbol{\sigma}}' = \mathbf{E} : (\dot{\boldsymbol{\epsilon}} - \dot{\boldsymbol{\epsilon}}_p) \tag{15}$$

in Eq. (11), the explicit expression of the plastic multiplier $\dot{\lambda}$ can be obtained as

$$\dot{\lambda}_i = \frac{\mathbf{n}_i^\sigma : \mathbf{E} : \dot{\boldsymbol{\epsilon}} + \mathbf{n}_i^\sigma : \mathbf{I} \dot{s}}{\mathbf{n}_i^\sigma : \mathbf{E} : \mathbf{m}_i^\sigma - r_i h_i} \tag{16}$$

Substituting Eq. (16) into the *rate* form of the flow rule and then into Eq. (15) leads to the compact form of the constitutive equations

$$\dot{\boldsymbol{\sigma}}' = \mathbf{D}_{ep} : \dot{\boldsymbol{\epsilon}}' \tag{17}$$

whereby, and according to Sheng et al. [14], the extended strain rate field $\dot{\boldsymbol{\epsilon}}'$ was introduced. This extended field is composed by the classical strain rate tensor $\dot{\boldsymbol{\epsilon}}$ and the suction rate $\dot{\mathbf{s}}$ which is treated as an extra strain rate field

$$\dot{\boldsymbol{\epsilon}}' = \begin{pmatrix} \dot{\boldsymbol{\epsilon}} \\ \dot{s}\mathbf{I} \end{pmatrix} \tag{18}$$

The material operator $\mathbf{D}_{ep}$ in Eq. (17) is defined as

$$\mathbf{D}_{ep} = (\mathbf{E}_{ep}\ \mathbf{E}_s) \tag{19}$$

with

$$\mathbf{E}_{ep} = \mathbf{E} - \sum_{i=1}^{U} \left[\frac{\mathbf{E} : \mathbf{m}^\sigma \otimes \mathbf{n}^\sigma : \mathbf{E}}{\mathbf{n}^\sigma : \mathbf{E} : \mathbf{m}^\sigma + H} \right]_i \tag{20}$$

$$\mathbf{E}_s = -\sum_{i=1}^{U}\left[\frac{\mathbf{E}:\mathbf{m}^{\sigma}\otimes n^{s}\mathbf{I}}{\mathbf{n}^{\sigma}:\mathbf{E}:\mathbf{m}^{\sigma}+H}\right]_i \tag{21}$$

being $i=1,2,\ldots,U$. The hardening/softening modulus H_i is defined as

$$H_i = -r_i h_i(\mathbf{m}_i^{\sigma}) \tag{22}$$

Replacing Eq. (17) in Eq. (1) we obtain the evolution of the total stress tensor

$$\dot{\boldsymbol{\sigma}} = \dot{\boldsymbol{\sigma}}' + \dot{p}_w\mathbf{I} = \begin{cases} \text{General case} & :\mathbf{E}_{ep}:\dot{\boldsymbol{\epsilon}} + [-\mathbf{I}+\mathbf{E}_s]:\mathbf{I}\dot{s} \\ \dot{p}_a = 0 \text{ case:} & :\mathbf{E}_{ep}:\dot{\boldsymbol{\epsilon}} - [-\mathbf{I}+\mathbf{E}_s]:\mathbf{I}\dot{p}_w \\ \dot{p}_a = \dot{p}_w = 0 \text{ case:} & :\dot{\boldsymbol{\sigma}}' = \mathbf{E}_{ep}:\dot{\boldsymbol{\epsilon}} \end{cases} \tag{23}$$

4 Constitutive Model for Partially Saturated Soils

The elastoplastic model proposed in this work for partially saturated soils is an extension of the cap-cone MRS-Lade model [10] for cohesive-frictional drive soils. The main features of the MRS-Lade model for sands are:

- The yield condition is defined by means of two surfaces: a cone and a cap.
- The hardening and softening rules both in the cone and cap regimes are defined in terms of the plastic work rate.
- It includes a nonassociated flow rule which only affects the volumetric component of the plastic strain in the cone regime.

These are also the features of the extended MRS-Lade model for partially saturated soils in this work. In the following the governing equations of the proposed model for unsaturated soils-like porous media are presented.

4.1 Yield Condition. The yield condition, see Ref. [13], is defined in terms of the first invariant of the effective stress tensor p', of the second and third invariant of the deviatoric stress tensor q and θ, respectively, and of the hardening/softening variables in the cone region κ_{cone}. Defining the effective pressure in terms of the net mean stress p_n and the suction s the generic shape of the cone takes the form

$$F_{\text{cone}} = F(p_n,q,\theta,s,\kappa_{\text{cone}}) = f(q,\theta) - \eta_{\text{cone}}(\kappa_{\text{cone}})[p_n + s - p_c] = 0 \tag{24}$$

with

$$f(q,\theta) = q\left[1+\frac{q}{q_a}\right]^{m} g(\theta) \tag{25}$$

m being a material constant controlling the curvature of the cone in the meridian (p_n,q) planes, with $0\leqslant m\leqslant 1$, q_a a positive reference deviator stress, η_{cone} the angle of internal friction, and

$$p_n = \frac{I_{n1}}{3} \tag{26}$$

$$q = \sqrt{3J_2} \tag{27}$$

$$\cos\theta = \frac{3\sqrt{3}}{2}\frac{J_3}{\sqrt{J_2}} \tag{28}$$

Thereby I_{n1} is the first invariant of the net stress tensor and J_2 and J_3 the second and third invariants of the deviatoric stress tensor, respectively. Finally, $g(\theta)$ is the Willam and Warnke [14] factor which assures a continuous and smooth variation of the shear strength in the deviatoric plane as long as the so-called eccentricity parameter e fulfills the condition $1/2\leqslant e\leqslant 1$.

Figure 1 illustrates the projection of the extended MRS-Lade model's yield surface in the meridian plane $\pi/3$ and its variation with the suction. The intersection of the yield surface with the p_n-s plane defines a loading collapse (LC) yield curve which accounts for the increase of the elastic regime with the increment of s while reducing this regime to its minimum when $s=0$ (saturated soil).

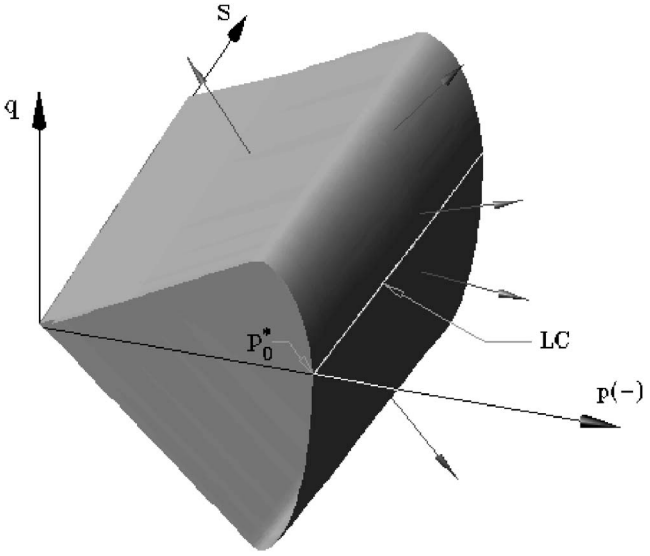

Fig. 1 Extended MRS-Lade model's failure envelope in compressive meridian

The formulation of the extended MRS-Lade model as the original one, implies that a plastic flow is associated for the capped yield surface. The cap surface is defined by

$$F_{\text{cap}}(p_n,q,\theta,s,\kappa_{\text{cap}}) = \left(\frac{p_n - p_{m2}}{p_r}\right) + \left(\frac{f}{f_r}\right)^2 - 1 \tag{29}$$

with

$$p_r = \frac{(1-\alpha)[\psi(1-\alpha)+\alpha]}{2\psi(1-\alpha)+\alpha}p_{\text{cap}}(\kappa_{\text{cap}}) \tag{30}$$

$$p_m = \frac{\alpha^2+\psi(1-\alpha^2)}{2\psi(1-\alpha)+\alpha}p_{\text{cap}}(\kappa_{\text{cap}}) \tag{31}$$

$$f_r = \eta_{\text{cone}}[\psi(1-\alpha)+\alpha]\left[\frac{\alpha}{2\psi(1-\alpha)+\alpha}\right]^{1/2} \tag{32}$$

$$\psi = \frac{\eta_{\text{cap}}}{\eta_{\text{cone}}} \text{ and } -\frac{\alpha}{2(1-\alpha)} < \psi \tag{33}$$

and

$$p_{\text{cap}}(\kappa_{\text{cap}}) = p_{\text{cap},0}(1+(\kappa_{\text{cap}})^{1/r}) \tag{34}$$

$$p_{\text{cap},0} = p_{0^*} + i\cdot s \tag{35}$$

whereby the dependency of the pressure $p_{\text{cap},0}$ on the suction in the last equation is due to Schrefler and Bolzon [15]. This function does fully define the dependency of the cap yield surface on the suction. The parameter p_{0^*} in Eq. (35) represents the preconsolidation pressure for saturated condition while αp_{cap} the pressure corresponding to the intersection between the cap and the cone yield surfaces, and i is a model parameter that takes into account the yield surface growth as increasing suction values.

4.2 Hardening/Softening Relations. The hardening and softening parameters κ_{cone} and κ_{cap} are defined in terms of the accumulated plastic work w^p that is dissipated during loading along the actual stress path

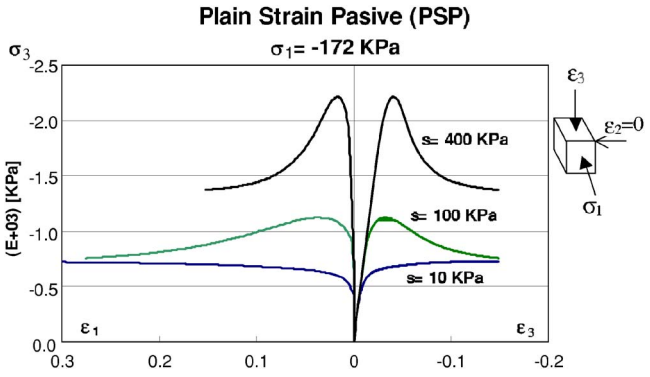

Fig. 2 Model predictions of plain strain passive (PSP) tests at $\sigma_1 = -172$ kPa for different suctions

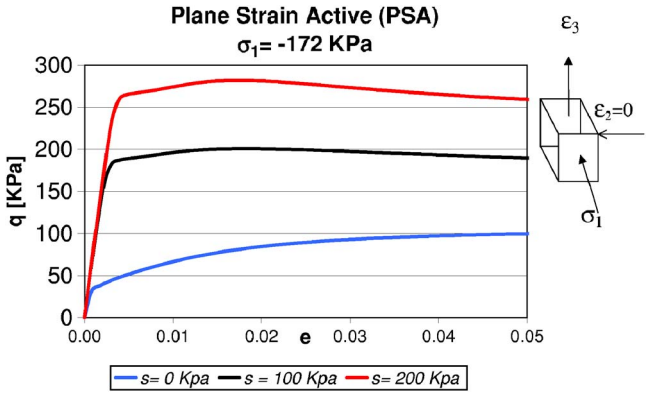

Fig. 3 Model predictions of plain strain active (PSA) tests at different suctions

$$\dot{w}^p = \int \boldsymbol{\sigma}_n : \dot{\boldsymbol{\epsilon}}_n^p dt \tag{36}$$

and are given in terms of the rate laws

$$\dot{\kappa}_{\text{cone}} = \frac{1}{c_{\text{cone}} p_a} \left(\frac{p + s - p_c}{p_a} \right)^{-l} \dot{w}^p \tag{37}$$

$$\dot{\kappa}_{\text{cap}} = \frac{1}{c_{\text{cap}} p_a \left(\frac{p_{\text{cap},0}}{p_a} \right)^{r}} \dot{w}^p \tag{38}$$

where c_{cone}, c_{cap}, p_a, l, and r are material constants. The hardening variables directly influence the yield surface, as described in Ref. [11]. Schematically, the relations are defined as $\eta_{\text{cone}} = \eta_{\text{cone}}(\kappa_{\text{cone}})$ and $p_{\text{cap}} = p_{\text{cap}}(\kappa_{\text{cap}})$, according to Eq. (34), such that the surface exhibits a smooth transition from the elastic to the plastic regime, that eventually leads to softening behavior.

4.3 Flow Rule. The flow rules devised for the extended MRS-Lade model assume, similarly to the original formulation by Sture et al. [10], nonassociated flow for the cone which only affects the volumetric flow. However, in the present formulation the level of volumetric nonassociativity in the cone regime is defined in terms of the suction in order to reproduce the tendency to associated flow of porous media, i.e., volumetric dilatancy reduction, with decreasing suction. In the present formulation the plastic potential function in the cone regime is defined in the form

$$G_{\text{cone}}(p,q,\theta,s) = f(q,\theta) - \left[n + (1-n) \left(\frac{s_{\max} - s}{s_{\max}} \right)^{t} \right] \eta_{\text{cone}}(\kappa_{\text{cone}})(p + s - p_c) \tag{39}$$

where $f(q,\theta)$ is defined in Eq. (25), n is a scalar parameter such that $0 \leqslant n \leqslant 1$, $s_{\max}$ is the maximum suction (water pressure) of the soil, and t is a parameter controlling the rate that the plastic flow approaches the normality condition when $s \to 0$, with $t \geqslant 1$. From the last equation it follows that the associated flow $G_{\text{cone}} = F_{\text{cone}}$ is obtained when $s = 0$ and that the maximum level of volumetric nonassociativity is reached when $s = s_{\max}$, i.e., for dry soils.

5 Discontinuous Bifurcation Condition

In this section the condition for localized failure modes in the form of discontinuous bifurcation is defined for unsaturated media. Discontinuous bifurcation or localized failure mode is detected by the formation of spatial discontinuities or jumps in the kinematic field across singularity surfaces that emerge in a stressed body. The analysis of localization leads to the same format and consequent relations as the propagation condition for plane acoustic waves in solid, see, e.g., Thomas [16] and Hill [17]. The formation of a *weak discontinuity* assumes that a second-order singularity appears in the strain rate field, while the displacement rates are still continuous

$$[[\dot{\mathbf{u}}]] = \dot{\mathbf{u}}^+ - \dot{\mathbf{u}}^- = 0 \tag{40}$$

$$[[\nabla_x \dot{\mathbf{u}}]] = \nabla_x \dot{\mathbf{u}}^+ - \nabla_x \dot{\mathbf{u}}^- \neq 0 \tag{41}$$

here the double brackets indicate the jump. Applying Maxwell's theorem [18], the jump condition of the velocity gradient must be a rank-one tensor

$$[[\nabla_x \dot{\mathbf{u}}]] = \dot{\gamma} \mathbf{M} \otimes \mathbf{N} \tag{42}$$

where $\mathbf{N}$ is the normal to the discontinuity surface, $\mathbf{M}$ defines the jump direction, and $\dot{\gamma}$ the jump magnitude. Using the strain definition of classical continua, the strain rate jump takes the form

$$[[\dot{\boldsymbol{\epsilon}}]] = \tfrac{1}{2} \dot{\gamma} (\mathbf{N} \otimes \mathbf{M} + \mathbf{M} \otimes \mathbf{N}) \tag{43}$$

Under the assumption of a continuous water pressure field, i.e. $[[\dot{s}]] = 0$ and assuming that at the onset of localization both sides of the singularity surface are in plastic loading state, the jump of the total stress state follows from the elastoplastic constitutive law (39) and the strain rate jump (43) as

$$[[\dot{\boldsymbol{\sigma}}]] = [[\dot{\boldsymbol{\sigma}}']] = \dot{\gamma} \mathbf{E}_{ep} : (\mathbf{N} \otimes \mathbf{M}) \tag{44}$$

According to Cauchy's lemma, the traction rate vector $\dot{\mathbf{t}}$ has to remain continuous across the singularity surface in the interior of a solid. Therefore, the localization condition takes the form

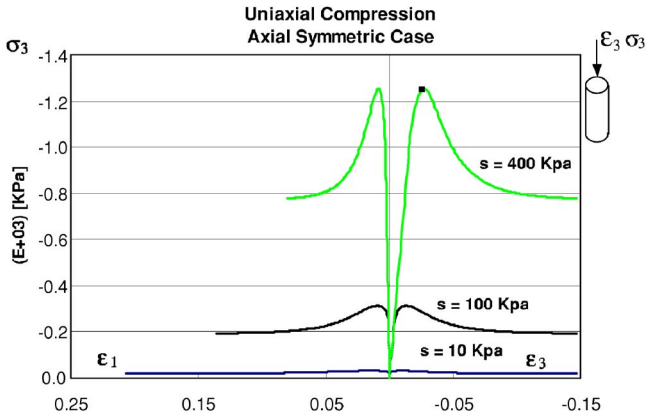

Fig. 4 Model predictions of uniaxial compression tests. Axial symmetric stress state (ASS).

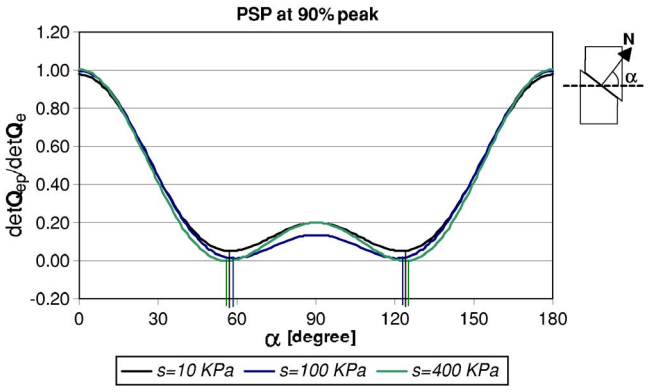

Fig. 5 Localization analysis at 90% of PSP test's peak stresses

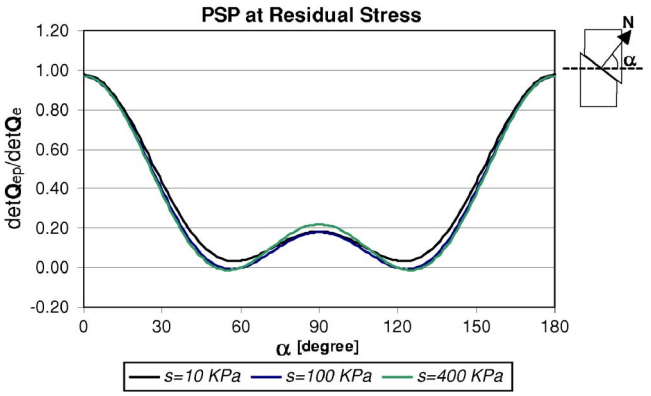

Fig. 7 Localization analysis at residual stress of PSP tests

$$\mathbf{0} = [[\dot{\mathbf{t}}]] = \mathbf{N} \cdot [[\dot{\boldsymbol{\sigma}}]] = (\mathbf{N} \cdot \mathbf{E}_{ep} \cdot \mathbf{N}) \cdot (\dot{\gamma}\mathbf{M}) = \mathbf{Q}_{ep} \cdot (\dot{\gamma}\mathbf{M}) \quad (45)$$

whereby

$$\mathbf{Q}_{ep} = \mathbf{N} \cdot \mathbf{E}_{ep} \cdot \mathbf{N} \quad (46)$$

is the localization tensor and $\mathbf{M}$ is the eigenvector that defines the direction of the strain rate jump. Thus, the discontinuity bifurcation begins when the localization tensor turns singular, i.e., when

$$\det(\mathbf{Q}_{ep}) = 0 \quad (47)$$

The last equality represents the localization condition in the present theory of partially saturated soils and, for the particular case of a continuous water pressure field considered here, coincides with that of classical continua. In the next section the localization condition will be analyzed during deformation histories of soils with different degrees of saturation.

6 Model Predictions

The model predictions of the failure response behavior of partially saturated soils are analyzed for different stress paths and deformation histories. Particularly, the influence of the suction in the response behavior is evaluated and discussed.

The numerical analyses in this section illustrate the predictive capability of the proposed model for the plane strain passive, plane strain active, and uniaxial compression tests.

Figure 2 shows the model predictions of the plane strain passive tests (PSP) for different suction levels in terms of the constitutive vertical stress versus the vertical and lateral strain component plots. This numerical analysis was performed in plain strain condition and under mixed control, i.e., the vertical strain increments, the constant lateral confinement stress, and the (null) out-of-plane strain are known while the vertical stress, the lateral strain, and the out-of-plain stress are unknown. The results in Fig. 2 clearly illustrate the strong influence of the suction in the response behavior of partially saturated soils in terms of the limit stress, the ductility, and the lateral strain. Particularly, we observe that with increasing suction a reduction of the ductility takes place together with an increment of the peak stress and of the lateral strain. This agrees very well with the features of the partially saturated soils response behavior.

Figure 3 illustrates the prediction of the model for the plane strain active tests (PSA) with a different level of the suction in terms of q and the second invariant of the deviatoric strain tensor e. These tests were also performed under mixed control. However, and contrary to the PSP case, the applied vertical strain in the PSA tests is in the tensile direction. The results in Fig. 3 as the previous ones in Fig. 2 demonstrate the significant influence of the suction in the response behavior of partially saturated soils under plane strain condition.

Finally, Fig. 4 depicts the proposed model predictions of the uniaxial compression tests in axial symmetric stress condition for different suction levels. Although a very ductile behavior is observed in the analysis with the lowest suction, $s=10$ kPa, the response behavior exhibits a peak load and a softening regime. This is a remarkable difference with the plane strain compression analysis in Fig. 2 whereby a continuous hardening regime without axial stress degradation can be observed when $s=10$ kPa. Actually, the more ductile behaviors in the PSP tests as compared to those of the uniaxial compression tests in axial symmetric stress state are mainly due to the presence of the confinement stress (σ_1) in the first ones. The comparative analysis between the results in Figs. 2 and 4 leads to the conclusion that the influence of the suction in the overall response behavior reduces with increasing confinement pressure, i.e., see the stronger dependency of the

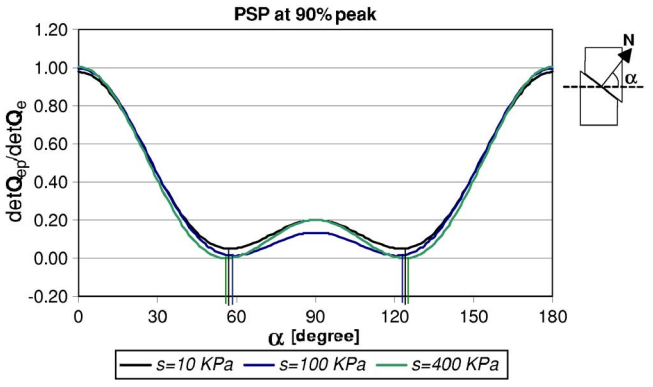

Fig. 6 Localization analysis at peak stress of PSP tests

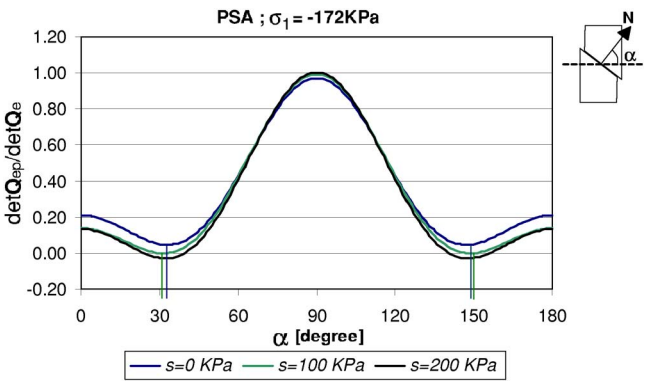

Fig. 8 Localization analysis at final stage of PSA tests

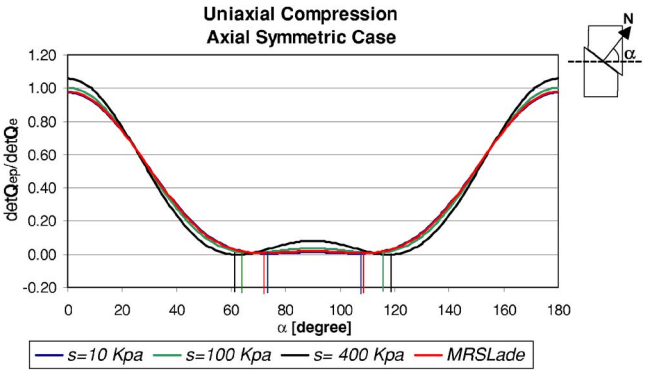

Fig. 9 Localization analysis at peak. Uniaxial compression test in axial symmetric state.

peak load on the suction in the tests without confinement pressure in Fig. 4 when compared to the results in Fig. 2.

7 Localized Failure Predictions

The localized failure condition was analyzed at different stress states along the PSP, the PSA, and the uniaxial compression tests of Figs. 2–4, respectively.

Figure 5 illustrates the localized failure analysis at 90% of the peak load performed in the PSP tests. At this level of the axial stress the conditions for localized failure are fulfilled for the first time in the PSP test with the largest suction $s=400$ kPa as can be observed in Fig. 6. The other two tests with $s=100$ kPa and $s=10$ kPa indicate diffuse failure as the localization tensor remains nonsingular. The results in Fig. 5 also indicate that the critical direction for localization varies with the suction. In other words, both the failure mode (diffuse or localized) as well as the orientation of the potential or critical shear band depend on the saturation degree of the soil.

The localization analysis in the PSP tests was also performed at peak and at the residual stress and the corresponding results are depicted in Figs. 6 and 7. We observe in these figures that the localization tensor remains positive defined up to the final stage in the test with the minimum suction $s=10$ kPa, while in the other two tests with larger suction the localization condition was fulfilled. Therefore, we conclude that the reduction of the suction suppresses localization or discontinuous bifurcation and lead to diffused or continuous failure modes. Moreover, the fact that already for $s=10$ kPa no localized failure is obtained in the PSP test also demonstrates that the stabilizing effect of the reducing suction takes place before full saturation of the soils.

The results of the localization analysis at residual stress of the PSA tests are shown in Fig. 8. As before, we observe that both the failure mode and the critical localization direction depends on the saturation degree of the soil. However, in the PSA tests the stabilizing effect of the reducing suction with regards to discontinuous bifurcation takes place for considerable lower values of the suction, corresponding almost to fully saturated soils. In other words, for the same level of confining pressure the dependency of the failure mode in the suction is more relevant in the PSP tests than in the PSA ones.

Finally, Fig. 9 describes the performance of the localized failure indicator at peak load of the uniaxial compression tests under axial symmetric stress state with $s=10$ kPa, $s=100$ kPa, and $s=400$ kPa. In this figure the performance of the localization indicator corresponding to the classical MRS-Lade model is also shown. These results agree with the observations by Peric [19] in the sense that the classical MRS-Lade model does not lead to localized failure in axial symmetric stress state. However, they show that even in this stress state the destabilizing effect associated with the increasing suction is important and leads in the extreme case, i.e., when $s=400$ kPa, to localized failure mode.

8 Conclusions

An elastoplastic constitutive theory for partially saturated soils is proposed on the basis of the well-known MRS-Lade model. The proposed model is defined in the space of the effective stresses and of the suction which strongly influence the shape of the maximum strength envelope and of the yield conditions. The flow rule of the so-called extended MRS-Lade model is based on a restricted nonassociate whereby only the volumetric plastic flow in the cone regime is nonassociate.

The predictive analysis of the proposed model demonstrates its capability to reproduce the most relevant features of partially saturated soil response behaviors. On the other hand, the localization analysis performed with the model demonstrates that the increment of the suction is related to a destabilizing effect as discontinuous bifurcations in the form of localized failure take place instead of diffuse or continuous failure modes. The results also illustrate the relevant influence of the suction in the critical directions for localization.

References

[1] Alonso, E., Gens, A., and Jose, A., 1990, "A Constitutive Model for Partially Saturated Soils," Geotechnique, **40**, pp. 405–430.
[2] Schrefler, B., and Zhan, X., 1993, "A Fully Coupled Model for Water Flow and Airflow in Deformable Porous Media," Water Resour. Res., **29**, pp. 155–167.
[3] Cui, Y., Delage, P., and Sultan, N., 1995, "An Elastoplastic Model for Compacted Soils," *Proceedings of the First International Conference on Unsaturated Soil*, E. Alonso and P. Delage, eds., Balkema, Rotterdam, Vol. 2, pp. 703–709.
[4] Bolzon, G., Schrefler, B., and Zienkiewicz, O., 1996, "Elastoplastic Soil Constitutive Laws Generalised to Partially Saturated States," Geotechnique, **46**, pp. 279–289.
[5] Wheeler, S., and Sivakumar, V., 1995, "An Elastoplastic Critical State Framework for Unsaturated Soil," Geotechnique, **45**, pp. 35–53.
[6] Kohgo, Y., Nakano, Y., and Miyazaki, T., 1993, "Theoretical Aspects of Constitutive Modelling for Unsaturated Soils," Soils Found., **33**, pp. 49–63.
[7] Gens, A., 1995, "Constitutive Modelling: Application to Compacted Soils," *Proceedings of the First International Conference on Unsaturated Soil*, E. Alonso and P. Delage, eds., Balkema, Rotterdam, Vol. 3, pp. 1179–1200.
[8] Khalili, N., 2000, "Application of the Effective Stress Principle to Volume Change in Unsaturated Soils," *Unsaturated Soils for Asia*, H. Rahardjo et al., eds., Balkema, Rotterdam, pp. 101–105.
[9] Loret, B., and Khalili, N., 2000, "A Three-Phase Model for Unsaturated Soils," Int. J. Numer. Analyt. Meth. Geomech., **24**, pp. 893–927.
[10] Sture, S., Runesson, K., and Macari-Pascualino, 1989, "Analysis and Calibration of a Three Invariant Plasticity Model for Granular Materials," Ing.-Arch., **59**, pp. 253–266.
[11] Sheng, D., Sloan, S. W., Gens, A., and Smith, D. W., 2003, "Finite Element Formulation and Algorithms for Unsaturated Soils. Theory," Int. J. Numer. Analyt. Meth. Geomech., **27**, pp. 745–765.
[12] Weihe, S., 1990, "Implicit Integration Schemes for Multi-Surface Yield Criteria Subjected to Hardening/Softening Behavior," M.Sc. thesis, University of Colorado at Boulder.
[13] Schiava, R., 2002, "Modelacion Elastoplastica de Suelos Cohesivo-Friccionales Parcialmente Saturados," M.Sc. thesis, Universidad Nacional de Santiago del Estero, Argentina.
[14] Willam, K., and Warnke, E., 1975, "Constitutive Models for the Triaxial Behaviour of Concrete," Int. Assoc. Bridge Struct. Engrg. Proc., **19**, pp. 1–30.
[15] Schrefler, B., and Bolzon, G., 1997, "Compaction in Gas Reservoirs Due to Capillary Effects," *Computational Plasticity*, CIMNE, Barcelona.
[16] Thomas, T., 1961, *Plastic Flow and Fracture in Solids*, Academic, New York.
[17] Hill, R., 1962, "Acceleration Waves in Solids," J. Mech. Phys. Solids, **10**, pp. 1–16.
[18] Maxwell, J. C., 1873, *A Treatise in Elasticity and Magnetism*, Oxford.
[19] Peric, D., 1990, "Localized Deformation and Failure Analysis of Pressure Sensitive Granular Materials," Ph.D. thesis, University of Colorado at Boulder.

José Risso

Alberto Cardona
e-mail: acardona@intec.unl.edu.ar

Andres Anca

CIMEC - INTEC (UNL/Conicet),
Güemes 3450,
(3000) Santa Fe,
Argentina

Violeta Colpachi
Research & Development,
Fundición San Cayetano,
L.M. Drago y Melián,
1852 Burzaco,
Argentina

Computation of Stress and Strain Evolution During Heat Treatment of Work Rolls

We present a numerical simulation of heat treatment of cast metallic alloys by the finite element method, to predict strains and stresses produced during the said process. From a computational point of view, this problem involves a coupled thermal-metallurgical-mechanical analysis modeled as a non-stationary and non-linear process. The calculation of metallurgical properties is coupled directly with thermal analysis. Material properties, which are dependent on temperature and microstructural composition, are rewritten for the purpose of the analysis as functions of temperature and time. Results of thermo-metallurgical analysis are taken as data for the subsequent mechanical analysis. The simulation was successful and proved the causes of failure during heat treatment of a centrifugally cast three-layered Hi-Chrome work roll. [DOI: 10.1115/1.2198247]

1 Introduction

Heat treatment of metallic alloys is a complex thermomechanical process involving solid state metallurgical transformations that change both the thermal and the mechanical properties of materials. This process is widely used in industrial applications to release internal stresses, reduce fragility, improve machinability, or modify properties like hardness or strength to satisfy the requirements of a definite application. However, a badly designed heat treatment can cause undesirable strains and stresses, and also cracking. This fact must be taken into account when designing the heating and cooling sequences in the process.

Numerical simulation of heat treatment has been the subject of much research work focusing either on thermal and mechanical analysis of the process [1–4] or on aspects of material modeling [5–8].

Material models capable of accounting for variations in thermal and mechanical properties due to temperature and metallurgical structure changes are a key point to simulate the thermomechanical evolution of parts subjected to heat treatment. A first type of models exists that describe the microstructure evolution as a function of alloy composition, temperature, and cooling time, reproducing either isothermal (TTT) or continuous cooling (CCT) diagrams for different alloys and chemical compositions [9–14]. Once the microstructure is known, a second type of model describes material properties as functions of microstructure, alloy composition, and temperature [7,8]. Using models of both types, we can predict the material properties needed for thermomechanical computations.

The latter procedure is useful to develop material models for a broad range of well-known alloys (carbon and low-alloy steels, austenitic stainless steels, etc.). However, as Taleb points out [15], its effectiveness is very limited for special alloys (e.g., for high-alloy white iron) since the model obtained is not able to represent with accuracy the material properties observed experimentally. Taleb proposed several corrections to the standard models to reproduce material properties in the alloys he modeled.

In this work, we follow an alternative way to represent material properties for heat treatment simulation. We redefined material properties as functions of time and temperature, by merging TTT/CCT diagrams with curves of dependency of thermo-mechanical properties in terms of temperature and metallurgical composition a priori. In this way, material properties were represented by piecewise linear interpolation of the final properties observed in experiments in terms of time and temperature. The simulations were done using a commercial finite element software which takes into account the dependence of material properties on time and temperature [16].

Section 2.1 describes the numerical model used to simulate thermo-mechanical processes in heat treatment of ferrous metals. In Sec. 2.2, a description of the proposed material model is given. Section 3 presents an application of this model to the simulation of the heat treatment of centrifugally cast three-layered Hi-Chrome work rolls, commonly used in steel mills. The simulation accounted for and reproduced the kind of actual failures observed during heat treatment of these types of work rolls.

2 Numerical Model

2.1 Thermomechanical Model. The numerical analysis of heat treatment processes can be made by modeling the time evolution of two coupled problems:

- A thermal problem which involves heating and cooling of parts and must take into account the variations of material properties (thermal conductivity and enthalpy) caused by temperature and microstructural transformations as well as heat releasing/absorption phenomena (related to latent heat), during metallurgical transformations.
- A mechanical problem which arises when it comes to predicting stresses and strains generated by thermal expansion/contraction produced by temperature changes and also by metallurgical phase transformations.

The thermal problem is nonlinear because material parameters depend on temperature. The mechanical problem is also nonlinear because thermal and transformation-induced strains often generate plastic deformations.

Provided there are no strong mechanical perturbations that could induce metallurgical transformations (e.g., transformation of retained austenite to martensite, induced by stresses generated by

Contributed by the Applied Mechanics Division of ASME for publication in the JOURNAL OF APPLIED MECHANICS. Manuscript received September 27, 2005; final manuscript received January 3, 2006. Review conducted by G. C. Buscaglia. Discussion on the paper should be addressed to the Editor, Prof. Robert M. McMeeking, Journal of Applied Mechanics, Department of Mechanical and Environmental Engineering, University of California – Santa Barbara, Santa Barbara, CA 93106-5070, and will be accepted until four months after final publication of the paper itself in the ASME JOURNAL OF APPLIED MECHANICS.

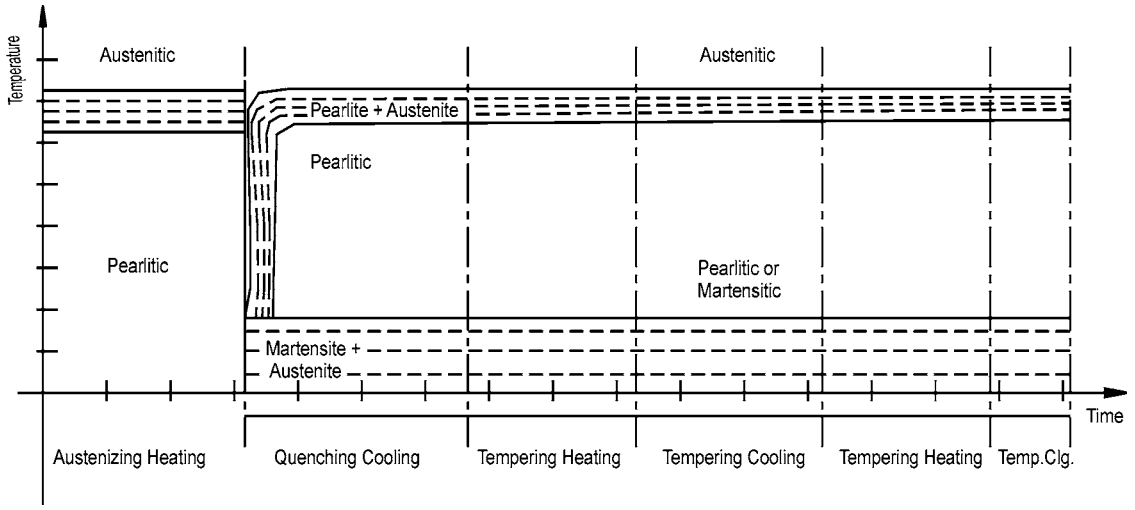

Fig. 1 Approximation of temperature-time transformation

external loads), mechanical phenomena do not affect thermal properties. Under this assumption we can ignore the dependency of the thermal model on the mechanical variables, which enables us to perform an uncoupled thermal analysis followed by a mechanical analysis that takes the thermal results as input.

The differential equation describing the thermal problem is

$$\rho(T)\frac{\partial H(T,m)}{\partial t} - \nabla(k(T,m)\,\nabla\, T) = 0 \tag{1}$$

where ρ is the density, H the enthalpy, t is the time, k the conductivity, T the temperature, and m accounts for the dependency of material parameters on microstructure.

By assuming both phases have the same density, the relationship between capacity and enthalpy in the presence of phase change is given by the following expression

$$\begin{aligned}\rho(T)H(T,m) &= \int_A^B \rho(T)c_{\text{eff}}(T,m)dT \\ &= \int_A^{\text{epc}} \varphi_1(T)\rho(T)c_1(T)dT + \rho(T)L_{pc} \\ &\quad + \int_{\text{spc}}^B \varphi_2(T)\rho(T)c_2(T)dT \end{aligned} \tag{2}$$

where c_{eff} is the effective (apparent) heat capacity, c_1 and c_2 are the specific heats for different microstructures, φ_1 and φ_2 are the fractions of initial and final microstructural components, L_{pc} is the latent heat necessary for a phase change, spc is the initial temperature of phase change, and epc the temperature at the end of phase change.

The dependence of the thermal problem on metallurgical transformations is simulated with an enthalpy model that takes into account heat capacity of metal, and latent heat exchange occurring during phase changes.

The dependence of the mechanical properties on material microstructure is simulated using material models that account for variations in metallurgical constituents with time. The thermal dependence of the mechanical problem is modeled using a temperature field calculated in the thermal simulation and given as input to evaluate the mechanical properties for the mechanical analysis and to compute the strains.

In the mechanical simulation, we use a classic elastoplastic model with isotropic hardening, in which the stresses are calculated as

$$\boldsymbol{\sigma} = \mathbf{C}(T,\varepsilon_p,m)\boldsymbol{\varepsilon}_e = \mathbf{C}(T,\varepsilon_p,m)(\boldsymbol{\varepsilon} - \boldsymbol{\varepsilon}_p - \boldsymbol{\varepsilon}_t), \tag{3}$$

where $\boldsymbol{\sigma}$ and $\boldsymbol{\varepsilon}$ are stress and strain vectors, $\mathbf{C}$ is the constitutive tensor, $\boldsymbol{\varepsilon}_\mathbf{e}$ is the elastic strain, $\boldsymbol{\varepsilon}_\mathbf{p}$ is the plastic strain, and $\boldsymbol{\varepsilon}_\mathbf{t}$ is the thermal-microstructural strain, which integrates the effect of thermal expansion and volume variations during metallurgical phase

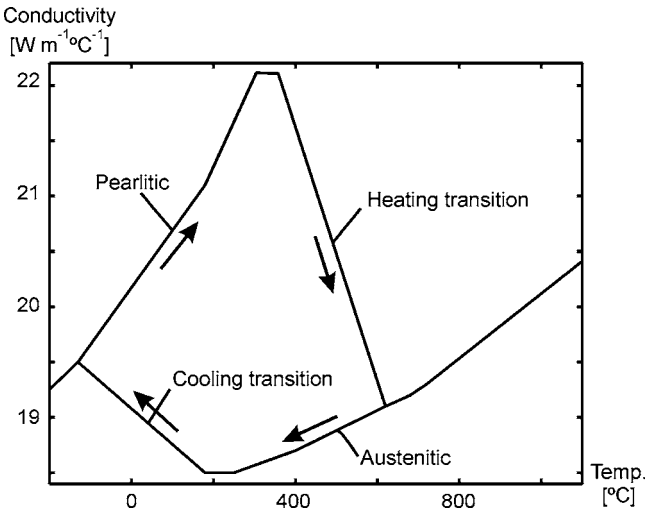

Fig. 2 Conductivity versus temperature approximation

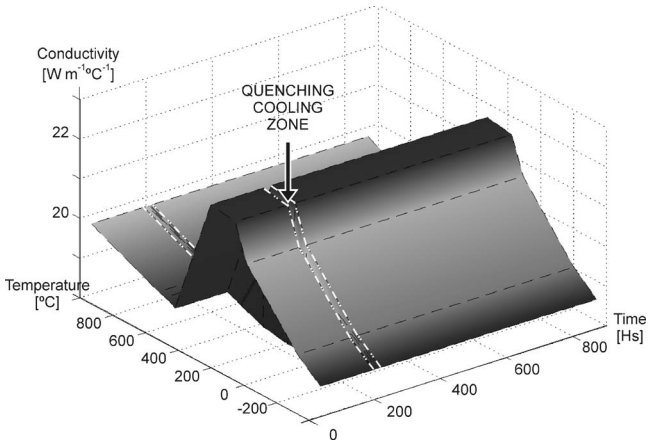

Fig. 3 Conductivity versus time/temperature diagram

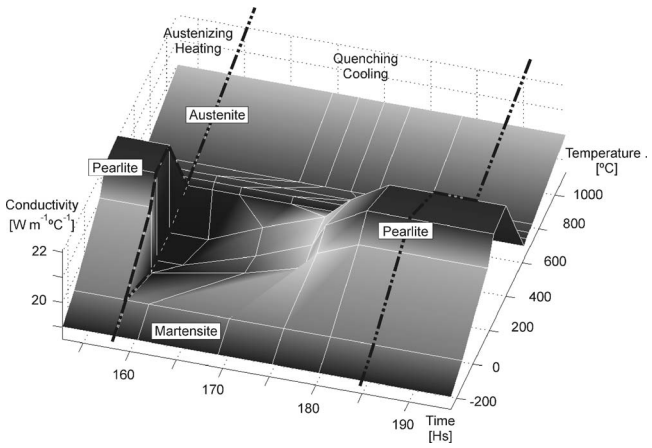

Fig. 4 Conductivity versus time/temperature diagram—detail in the quenching cooling zone

changes.

The stress field must satisfy a yield criterion (in this case, the isotropic Von Mises criterion)

$$\sigma_{eq} = \sqrt{\frac{1}{2}[(\sigma_x - \sigma_y)^2 + (\sigma_y - \sigma_z)^2 + (\sigma_z - \sigma_y)^2 + 6(\tau_{xy}^2 + \tau_{yz}^2 + \tau_{zx}^2)]} \leqslant Y(T, \varepsilon_{eq}, m) \quad (4)$$

Since the limit stress Y is a function of the temperature, of the equivalent plastic strain ε_{eq} and of the microstructure, the model can take into account the variation of material hardening behavior with temperature.

2.2 Material Model. Most material properties are functions of temperature and microstructure, and therefore have indirect dependency on variables such as time and maximum heating/cooling temperature which define material microstructure.

In austenizing processes (heating), the microstructure is modeled as a function of temperature only. In quenching processes (cooling), the microstructure is a function of temperature and time. In tempering processes (heating and cooling) the microstructure is considered as a function of temperature only (the dependency upon temperature and time could be modeled if data about transformations of retained austenite were available).

Then, for the whole process, we can formulate any general property μ as a function of temperature and time, as follows

$$\mu = \mu[T, m(T,t)] = \mu(T,t) \quad (5)$$

In order to define the material parameters, we first construct a map of microstructure as a function of temperature and time using data about heating and cooling periods, and isothermal (TTT) or continuous cooling (CCT) diagrams for the quenching cooling interval, as shown in Fig. 1. Then, for every definite material microstructure (i.e., austenitic, pearlitic, martensitic), we define the value of every property as a function of temperature. Figure 2 is an example for the case of conductivity. Finally, by combining the map of microstructure as a function of temperature and time with the curves of temperature dependence of the considered

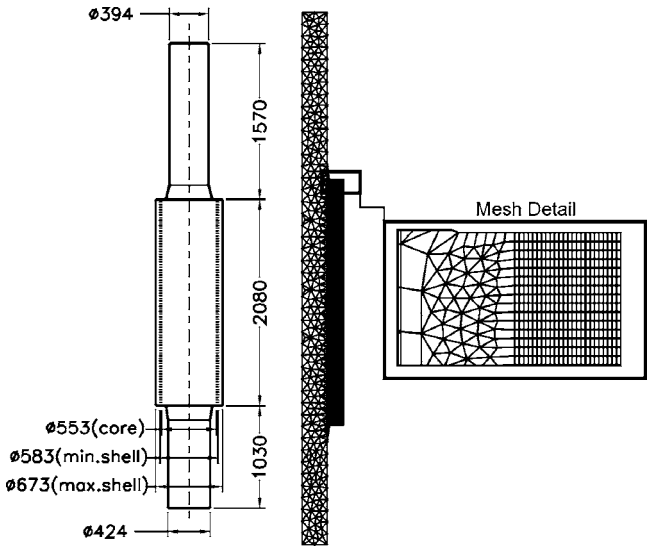

Fig. 5 (Left) Work roll main dimensions, (right) FEM mesh

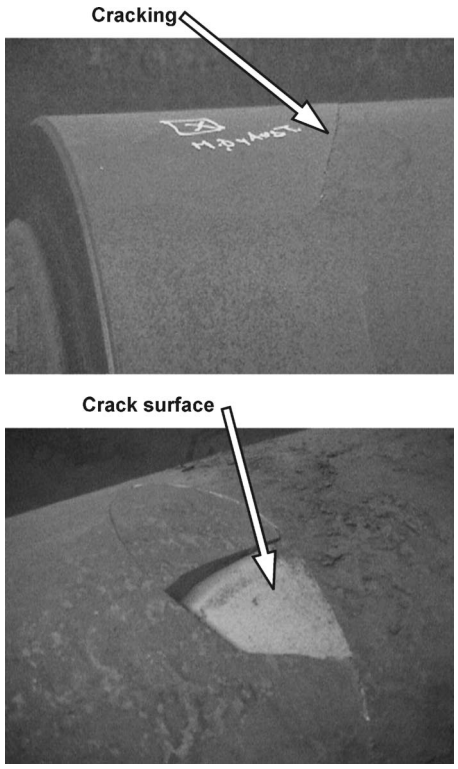

Fig. 6 Observed cracks in the barrel of work rolls

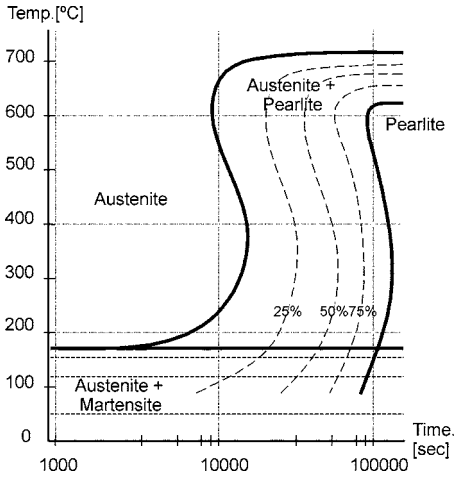

Fig. 7 Temperature-time-transformation diagram for Hi-Cr iron (shell)

Table 1 Convective boundary condition. Time variation of air temperature and heat transfer coefficients (intermediate values calculated by linear interpolation).

Time [s]	Temp. [°C]	Time [s]	Temp. [°C]	Time [s]	Heat transfer coefficient [W m^{-2} °C^{-1}]
0	25	1,590,000	520	0	40
160,000	170	1,620,000	490	<570,000	40
175,000	180	1,675,500	480	570,000	30
290,000	430	1,676,000	80	577,000	50
320,000	420	1,713,300	30	585,000	40
380,000	780	2,200,000	55	585,100	60
381,000	730	2,225,000	65	588,000	65
419,000	680	2,247,000	80	589,000	36
428,000	880	2,265,000	85	595,000	10
430,000	1080	2,311,600	160	599,000	15
440,000	1060	2,330,000	165	600,000	8
481,000	1090	2,380,000	310	613,000	12
500,000	1040	2,410,000	310	615,000	4
<570,000	1020	2,450,000	410	900,000	3
570,000	80	2,473,600	410	1,200,000	3
577,000	30	2,500,000	530	1,275,600	40
600,000	30	2,530,000	510	1,675,500	40
600,100	520	2,550,000	555	1,676,000	10
665,000	520	2,610,000	530	1,705,000	10
665,100	30	2,630,000	570	1,706,000	3
1,200,000	25	2,675,200	540	2,200,000	3
1,275,600	100	2,675,300	30	2,225,000	40
1,297,200	95	2,815,600	30	2,675,200	40
1,394,400	205	2,819,200	60	2,675,300	10
1,416,000	205	2,862,400	60	2,804,800	10
1,545,600	465	2,873,200	30	2,815,500	3
1,556,400	430			2,873,200	3

property, and by using the rule of mixtures for regions with mixed structure (e.g., austenite+pearlite), a map of the property as a function of temperature and time (continuous piecewise linear approximation) can be built, as shown in Fig. 3.

We used a commercial finite element code in which material properties can be defined as functions of temperature and time [16]. When using such a standard material model, special care must be taken to adapt the map of microstructure as a function of temperature and time to the real quenching cooling process (see Fig. 4) to avoid reversions in austenite-pearlite and austenite-martensite transformations. An improvement currently in progress is the development of a model with the ability to track microstructural evolution and avoid numerical reversion of physically irreversible phase changes.

In the thermal analysis, the material parameters are the enthalpy and the thermal conductivity. In the mechanical analysis, the material parameters are the Young (elastic) modulus, the Poisson coefficient, the thermal expansion coefficient, and the yield stress. All of them are modeled following the above-mentioned procedure to account for variations during the heat treatment process.

3 Application Case

3.1 Problem Description. The Hi-Chrome work rolls used in the initial stages of steel lamination have an exterior layer (shell) of Hi-Chrome white iron, an intermediate layer of low-alloy iron, and a core of spheroidal graphite iron. The first two layers are cast centrifugally in horizontal position, and afterwards the core is poured statically in vertical position. Typical as-cast dimensions are shown in Fig. 5.

After casting, rolls are heated from room temperature to 1020°C (with complete austenitization). Then, they are quenched by cooling in air at room temperature. Finally, they are subjected to two tempering processes at 480 and 540°C, each one followed by a slow cooling in air to room temperature.

After heat treatment, some rolls showed cracks near the corners of the barrel. In all cases the cracks had conic shape, starting at the end of the barrel in the vicinity of the interface between Hi-Chrome and interface layers, and ending at the external diameter of the barrel, approximately 250 mm away from the barrel's edge, as shown in Fig. 6.

Even though circumferential cracks in the external diameter of the roll were observed several hours after the end of the second tempering, when rolls were already at room temperature, the presence of black ferrous oxides in the initial zone of the cracks indicated that the cracking started in an intermediate stage of the heat treatment (at least previously to the last tempering heating). The aim of this analysis was to determine the stage where cracking starts, and to confirm the presence of residual stresses which may explain the advancement of the cracking front up to the external

Table 2 Properties for Hi-Cr iron (shell) in austenitic state

Temperature [°C]	Enthalpy [J kg^{-1}]	Conductivity [W m^{-1} °C^{-1}]	Young's modulus [Pa]	Secant thermal expansion coefficient [°C^{-1}]
180	0.62E5	18.50	2.07E11	−2.60E-5
250	1.06E5	18.50	2.04E11	−1.00E-5
400	2.11E5	18.60	1.95E11	0.23E-5
620	3.87E5	19.00	1.74E11	0.95E-5
650	4.11E5	19.07	1.69E11	1.01E-5
680	4.40E5	19.12	1.65E11	1.07E-5
720	5.25E5	19.20	1.62E11	1.13E-5
1030	7.91E5	20.00	0.75E11	1.90E-5

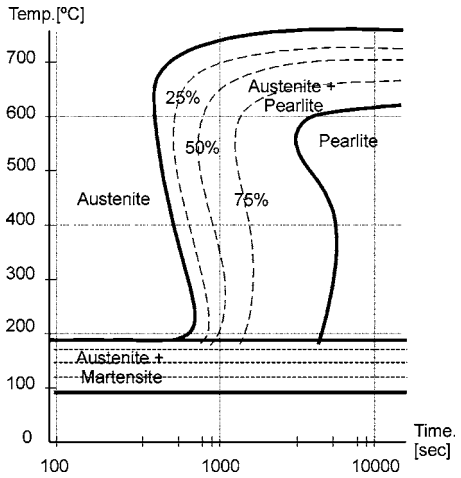

Fig. 8 Temperature-time-transformation diagram for SG iron (core)

diameter of the barrel.

Ignoring small circumferential temperature differences and small bending stresses generated by the horizontal mounting of cylinders in the heater, the problem can be modeled as an axisymmetrical one. The finite element mesh, built by using axisymmetric triangular elements, is shown in Fig. 5(*b*). The same mesh is used for the thermal and the mechanical analyses. A quadratic interpolation of unknowns (i.e., temperatures and displacements, respectively) is used in both cases.

Convective boundary conditions were set on the external surface of the roll for the thermal analysis. Convection coefficients ranging from 5 to 40 W m^{-2} C^{-1} were used in the different stages of heating and cooling, depending on the agitation of surrounding air, as seen in Table 1. The temperature evolution of air is also displayed in this table.

3.2 Shell Material Data (Hi-Chrome White Cast Iron). The TTT diagram of a similar alloy was used to determine the position of the pearlitic nose [17]. The cooling behavior of the shell material was determined using data of Hi-Cr white iron without Ni [18], with a correction of the transformation time to take into account the influence of Ni and Mo as suggested by Laird et al. [19]. The diagram is shown in Fig. 7.

The thermal conductivity as a function of temperature and microstructure was taken from data for high-alloy white iron [17,20]. Enthalpy values were calculated integrating the effective thermal capacity data [17,20] along the temperature range covered in the process. In order to calculate thermal-metallurgical strains, a secant expansion coefficient averaged from values found in bibliography [18,20] and based on a reference state of pearlitic structure at 20°C was used.

The elastic modulus as a function of temperature and chemical composition was obtained from data published by Belyakova et al. [19,21]. The Poisson coefficient was assumed constant and equal

Table 3 Properties for Hi-Cr iron (shell) in pearlitic-bainitic state

Temperature [°C]	Enthalpy [J kg^{-1}]	Conductivity [W m^{-1} °C^{-1}]	Young's modulus [Pa]	Secant thermal expansion coefficient [$°C^{-1}$]
−130	0.0	19.00	2.18E11	0.80E-5
180	1.07E6	19.50	2.12E11	0.88E-5
250	1.51E6	21.10	2.09E11	0.98E-5
400	2.56E5	22.00	2.00E11	1.18E-5
620	4.32E5	22.10	1.79E11	1.30E-5

Table 4 Yield stress for Hi-Cr iron (shell)

Temperature [°C]	Yield stress (austenitic) [Pa]		Yield stress (pearl./bain.) [Pa]	
	ϵ_{eq}=0.0	ϵ_{eq}=0.1	ϵ_{eq}=0.0	ϵ_{eq}=0.1
0	…	…	8.0E+8	10.0E+8
100	…	…	7.0E+8	8.9E+8
300	4.3E+8	5.3E+8	5.0E+8	6.4E+8
620	2.4E+8	3.0E+8	2.6E+8	3.2E+8
650	2.2E+8	2.6E+8	…	…
680	1.9E+8	2.3E+8	…	…
720	1.6E+8	1.9E+8	…	…
1030	0.4E+8	0.5E+8	…	…

Table 5 Properties for gray iron (layer) in austenitic state

Temperature [°C]	Enthalpy [J kg^{-1}]	Conductivity [W m^{-1} °C^{-1}]	Young's modulus [Pa]	Secant thermal expansion coefficient [$°C^{-1}$]
190	0.28E5	29.80	1.12E+11	−2.10E-5
400	1.40E5	31.00	1.06E+11	0.26E-5
600	2.85E5	31.80	0.97E+11	0.94E-5
650	3.31E5	32.00	0.95E+11	1.01E-5
675	3.59E5	32.10	0.94E+11	1.07E-5
700	4.30E5	32.20	0.92E+11	1.10E-5
750	5.52E5	32.50	0.89E+11	1.17E-5
1030	8.01E5	37.00	0.44E+11	1.95E-5

Table 6 Properties for gray iron (layer) in pearlitic-bainitic state

Temperature [°C]	Enthalpy [J kg^{-1}]	Conductivity [W m^{-1} °C^{-1}]	Young's modulus [Pa]	Secant thermal expansion coefficient [$°C^{-1}$]
0	0.0	42.50	1.22E+11	1.22E-5
190	0.91E5	42.90	1.18E+11	1.28E-5
400	2.08E5	39.90	1.12E+11	1.35E-5
600	3.48E5	37.10	1.04E+11	1.39E-5
650	3.89E5	36.25	1.01E+11	1.42E-5

Table 7 Properties for SG iron (core) in austenitic state

Temperature [°C]	Enthalpy [J kg^{-1}]	Conductivity [W m^{-1} °C^{-1}]	Young's modulus [Pa]	Secant thermal expansion coefficient [$°C^{-1}$]
190	0.28E5	18.00	1.51E11	−1.90E-5
400	1.43E5	18.20	1.43E11	0.23E-5
600	2.91E5	18.60	1.32E11	0.91E-5
650	3.36E5	18.70	1.29E11	1.01E-5
675	3.65E5	18.75	1.27E11	1.06E-5
700	4.36E5	18.80	1.25E11	1.10E-5
750	5.57E5	18.95	1.20E11	1.17E-5
1030	8.05E5	20.00	0.60E11	1.95E-5

Table 8 Properties for SG Iron (core) in pearlitic-bainitic state

Temperature [°C]	Enthalpy [J kg^{-1}]	Conductivity [W m^{-1} °C^{-1}]	Young's modulus [Pa]	Secant thermal expansion coefficient [$°C^{-1}$]
0	0.0	39.00	1.65E11	1.06E-5
190	0.93E5	36.65	1.59E11	1.15E-5
400	2.12E5	29.85	1.51E11	1.30E-5
600	3.60E5	25.49	1.40E11	1.36E-5
650	4.04E5	25.00	1.36E11	1.38E-5

Table 9 Yield stress for gray iron and SG iron (layer and core)

Temp. [°C]	Layer (austenitic) yield stress [Pa]		Layer (pearl./bain.) yield stress [Pa]		Core (austenitic) yield stress [Pa]		Core (pearl./bain.) yield stress [Pa]	
	ϵ_{eq}=0.0	ϵ_{eq}=0.1	ϵ_{eq}=0.0	ϵ_{eq}=0.1	ϵ_{eq}=0.0	ϵ_{eq}=0.1	ϵ_{eq}=0.0	ϵ_{eq}=0.1
0	…	…	6.60E+8	7.90E+8	…	…	7.00E+8	8.50E+8
100	…	…	6.20E+8	7.40E+8	…	…	6.50E+8	7.80E+8
300	4.30E+8	4.30E+8	4.50E+8	5.50E+8	4.50E+8	5.40E+8	4.80E+8	5.80E+8
620	1.60E+8	1.95E+8	1.70E+8	2.00E+8	1.80E+8	2.20E+8	1.90E+8	2.30E+8
650	1.50E+8	1.80E+8	…	…	1.70E+8	2.00E+8	…	…
680	1.30E+8	1.55E+8	…	…	1.45E+8	1.75E+8	…	…
720	0.97E+8	1.15E+8	…	…	1.10E+8	1.30E+8	…	…
1030	0.18E+8	0.22E+8	…	…	0.20E+8	0.25E+8	…	…

to 0.28. We assumed the yield stress dependence on temperature to be equal to that of the ultimate tensile stress for Hi-Cr white iron [19], scaled according to the room temperature yield stress of Hi-Cr. An isotropic hardening law was used.

Tables 2–4 show the values of these parameters in terms of temperature for austenitic and pearlitic/bainitic state. Data for material in martensitic state are not included because the evolution of temperatures during heat treatment of these rolls prevents the formation of martensitic structures.

3.3 Intermediate and Core Material Data (Gray and Spheroidal Graphite Cast Iron). Since the transformation curves of gray and spheroidal graphite cast iron are similar, the strategy used to determine their material parameters was the same for both. After determining the microstructure as a function of time and temperature, appropriate parameter values were selected. A TTT diagram for Ni-Mo ductile iron [22] was used to define the microstructure of the core material as a function of time and temperature in quenching. This diagram is shown in Fig. 8.

The thermal conductivity and the enthalpy as a function of heating and cooling temperature (obtained by integrating the apparent thermal capacity) were taken from data published by Auburn University researchers [23].

In order to compute thermal-metallurgical strains, a secant expansion coefficient based on a reference state of pearlitic structure at 20°C was calculated from tables of dilatometry in heating and cooling published by the Auburn Solidification Design Center [23]. The elastic modulus as a function of temperature was extrapolated from values at room temperature [17] and thermal de-

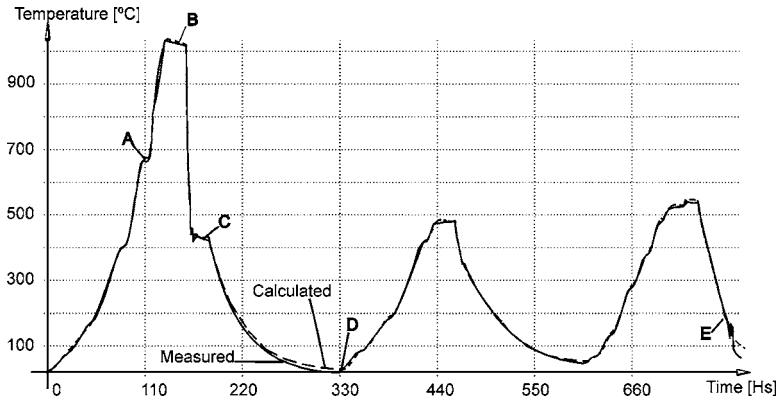

Fig. 9 Comparison between calculated and measured temperatures in barrel midpoint

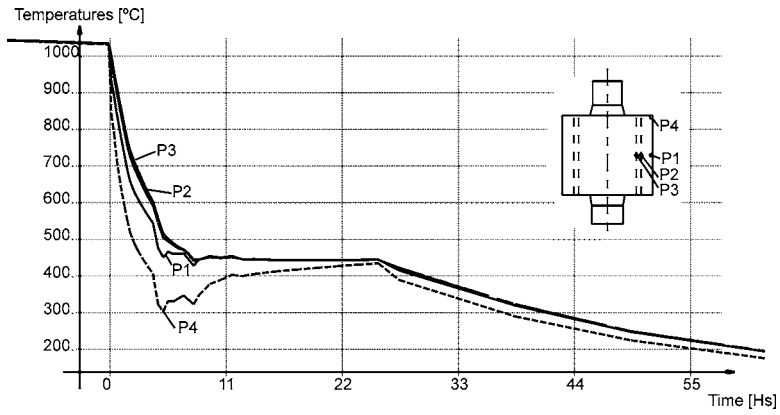

Fig. 10 Temperature evolution during quenching cooling

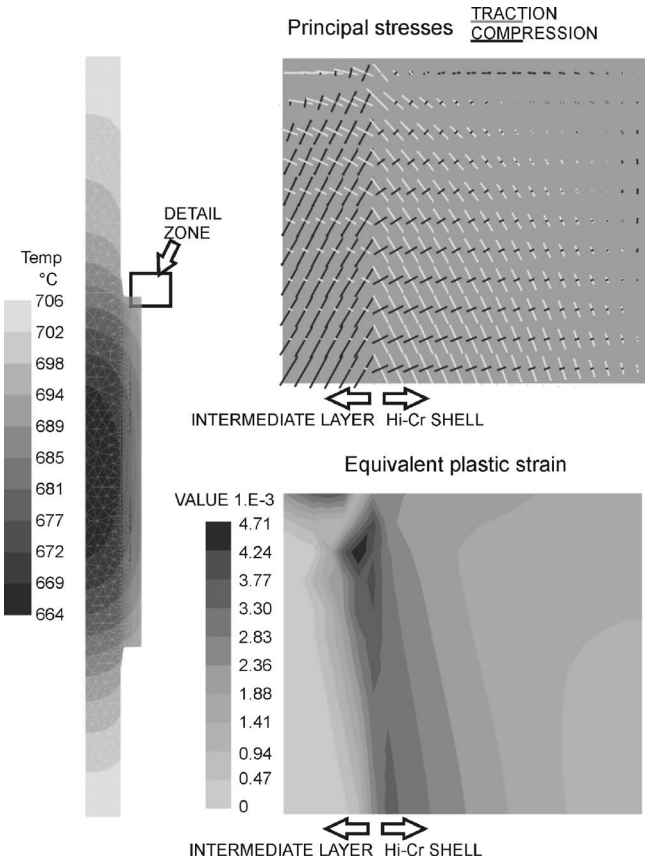

Fig. 11 Intermediate state during austenizing heating (point A, 110 h)

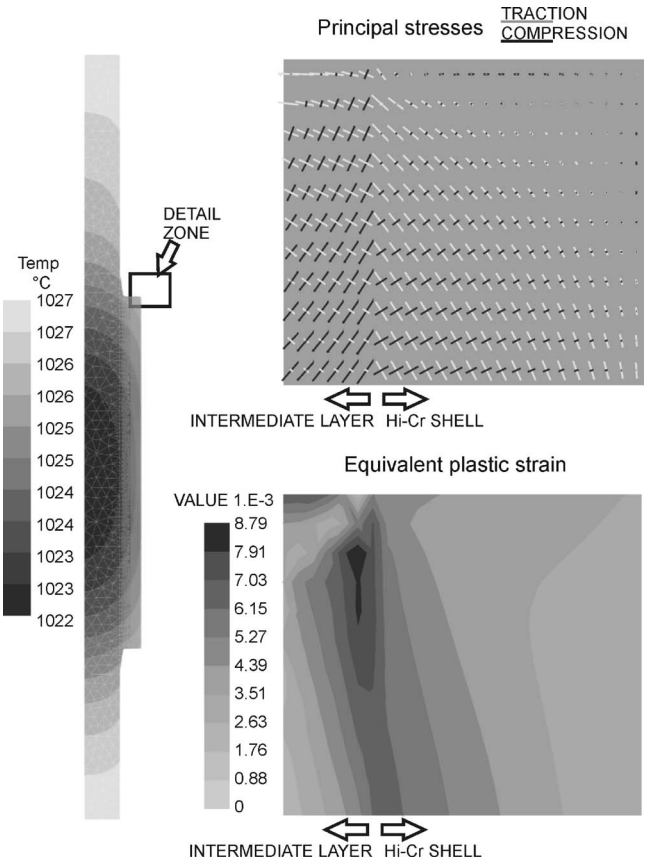

Fig. 12 End of austenizing heating (point B, 156 h)

pendency of this parameter for pearlitic steels. The Poisson coefficient was assumed constant and equal to 0.26. The yield stress dependence on temperature was taken from tables for gray and spheroidal graphite iron of similar composition [24].

Tables 5–9 show the values of these parameters as functions of temperature, for austenitic and pearlitic/bainitic state.

3.4 Results. A comparison between calculated (continuous line) and measured (dashed line) temperatures at the midpoint of the barrel surface is shown in Fig. 9. The agreement between curves is acceptable for the purposes of the analysis.

The largest differences between temperatures in different points of the roll, which define the maximum temperature gradients in the whole process, are found at the initial stage of quenching. Figure 10 shows a detail of the differences between points located in the surface of the barrel (P1, P4) and other points situated in the zones of transition between layers of different materials (P2, P3). The largest temperature difference predicted by computations between the surface and the core of the roll was lower than 300 °C, and occurred during quenching.

The evolution of temperatures, principal stresses, and equivalent plastic deformations near the barrel corner, at the zone of failure, are shown in Figs. 11–15. These plots correspond to different time instants along the complete heat treatment, which were referred to by letters A–E in Fig. 9.

During the austenizing heating, tensile axial stresses develop in the external shell. However, as plastic deformations occur during heating, in the quenching and in the tempering processes the axial stresses in the shell become compressive. Moreover, large residual stresses develop and remain at the end of the process because of the differential deformation of core and layers.

Figure 16 shows the evolution of equivalent plastic strains in different points near the barrel corner. Most inelastic deformations

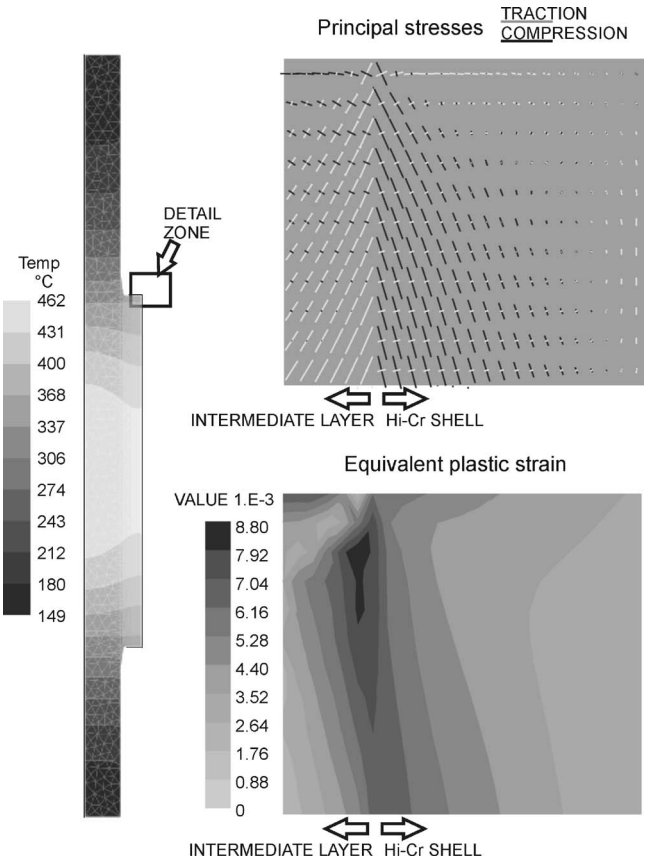

Fig. 13 Intermediate state during quenching cooling (point C, 166 h)

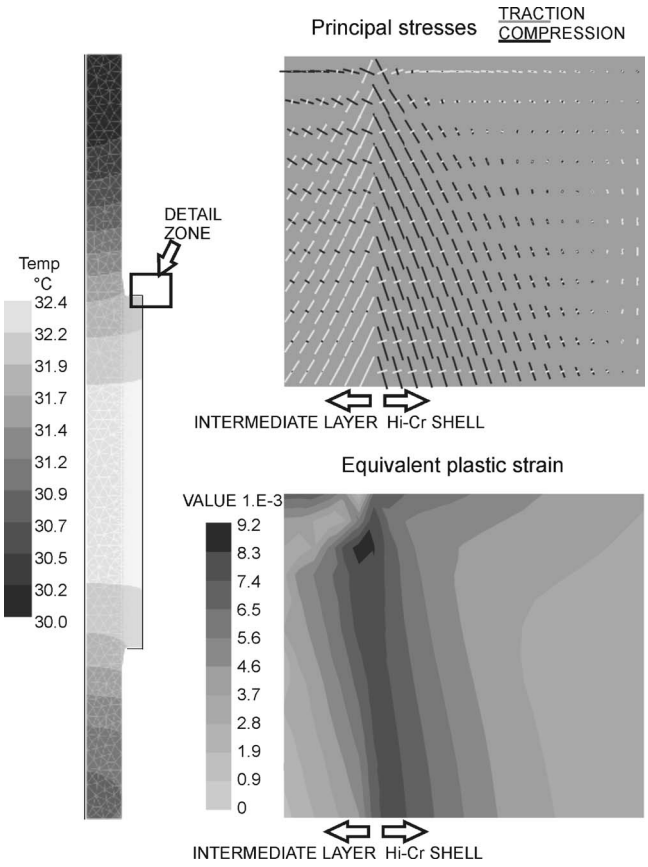

Fig. 14 End of quenching cooling (point D, 332 h)

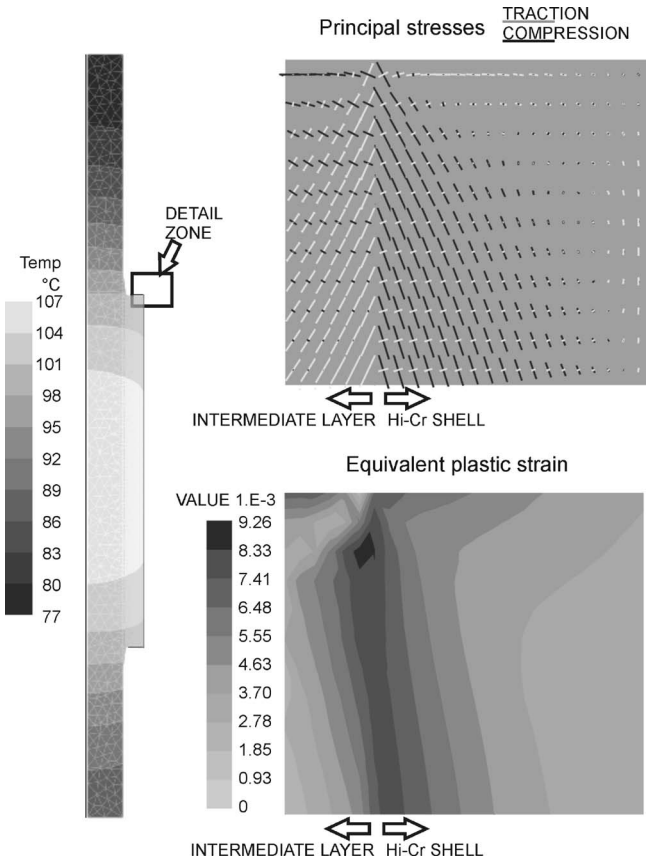

Fig. 15 End of second tempering cooling (point E, 792 h)

occur during the second half of the austenizing heating process and during the quenching process, as shown in the plots of evolution of equivalent plastic strain. Only a small increment in plastic strains is found during tempering processes. However, this result could be influenced by the lack of information about percentages of retained austenite after quenching and by transformations of retained austenite during tempering. The magnitude of inelastic strains found near the interface between shell and intermediate layers (close to 1%) is significant, specially if we take into account the brittle nature of Hi-Chrome white iron.

These two latter facts suggest that cracks started in the zone near the interface between shell and intermediate layers during the last stage of austenizing heating. The residual stresses observed at the end of the process (Fig. 15) are large enough to propagate these cracks in the plane perpendicular to the maximum tensile principal stresses up to the external surface of the barrel, in total coincidence with the observations (Fig. 6).

4 Conclusions

A model developed to simulate heat treatment of metals was presented. The approximation used to describe the behavior of thermo-mechanical variables, which was able to reproduce with accuracy the material properties observed experimentally, was found to be useful for special metal alloys. This type of parametrization allowed us to make an initial analysis with the small amount of data available in the literature for this special alloy. The analysis was very easily refined in regions of interest later on, when additional experimental data were obtained.

The main drawback of this approach is the need of knowing the approximate evolution of temperature in time a priori, in order to compute the resulting microstructure transformation at each point.

With regard to the analysis and design of work rolls, the results were of great aid in determining the causes of cracking failures and proposing preventive measures.

Finally, we should say that these results can be improved by using an initial stress field computed by an analysis of solidification in the casting process, and also by using data about the evolution of retained austenite in the shell material.

Acknowledgment

Financial support from Agencia Nacional de Promoción Científica y Tecnológica, Argentina, through Grant No. PID 99-76 and from Universidad Nacional del Litoral, through Grant No. CAI+D PE 214, is gratefully acknowledged.

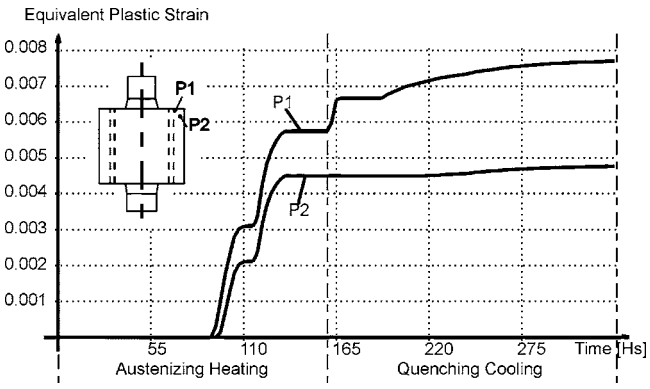

Fig. 16 Evolution of equivalent plastic strain

References

[1] Bergheau, J. M., Mangialenti, G., and Boitout, F., 1998, "Contribution of Numerical Simulation to the Analysis of Heat Treatment and Surface Hardening Processes," *Proc. of 18th ASM Heat Treating Conference and Exposition*, Wallis and Walton, eds., Rosemont, IL, pp. 681–690.

[2] Aliaga, C., and Massoni, E., 1998, "3D Numerical Simulation of Thermo-Elasto-Visco-Plastic Behavior Using a Stabilized Mixed F.E. Formulation: Application to Heat Treatment," *Simulation of Materials Processing: Theory, Methods and Applications, Proc. Numiform '98*, J. Huétink and F. Baaijens, eds., Balkema, Rotterdam, The Netherlands, p. 263–269.

[3] Sanchez Sarmiento, G., Gastón, A., and Vega, J., 1998, "Inverse Heat Conduction Coupled With Phase Transformations Problems in Heat Treating Processes," *Computational Mechanics—New Trends and Applications*, E. Oñate and S. Idelsohn, eds., CIMNE, Barcelona, Spain, CD-Book Part VI, Sec. 1, paper 16.

[4] Berglund, D., 2001, "Simulation of Welding and Stress Relief Heat Treatment in Development of Aerospace Components," Licentiate thesis, Lulea University of Technology, Sweden.

[5] Kirkaldy, J., Thomson, B., and Baganis, E., 1978, "Prediction of Multicomponent Equilibrium and Transformation Diagrams for Low Alloy Steels," *Hardenability Concepts With Applications to Steel*, J. Kirkaldy and D. Doane, eds., TMS-AIME, Warrendale, PA, pp. 82–125.

[6] Hömberg, D., 1996, "A Numerical Simulation of the Jominy End-Quench Test," Acta Mater., **44**(11), pp. 4375–4385.

[7] Alberg, H., 2003, "Material Modeling for Simulation of Heat Treatment," Licentiate thesis, Lulea University of Technology, Sweden.

[8] Saunders, N., Guo, Z., Li, X., Miodownik, A. P., and Schillé, J. P., 2003, "Using *JMatPro* to Model Materials Properties and Behavior," JOM, **55**(12), pp. 60–65.

[9] Johnson, W., and Mehl, R., 1939, "Reaction Kinetics in Processes of Nucleation and Growth," Trans. Am. Inst. Min., Metall. Pet. Eng., **135**, pp. 416–458.

[10] Lement, B. S., 1959, *Distortion in Tool Steels*, American Society for Metals, Metals Park, OH.

[11] Koistinen, D. P., and Marburger, R. E., 1959, "A General Equation Prescribing the Extent of the Austenite-Martensite Transformation in Pure Iron-Carbon Alloys and Plain Carbon Steels," Acta Metall., **7**, pp. 59–60.

[12] Leblond, J. B., Devaux, J., and Devaux, J. C., 1989, "Mathematical Modelling of Transformation Plasticity in Steels. I: Case of Ideal-Plastic Phases," Int. J. Plast., **5**, pp. 551–572.

[13] Leblond, J. B., 1989, "Mathematical Modelling of Transformation Plasticity in Steels. II: Coupling With Strain Hardening Phenomena," Int. J. Plast., **5**, pp. 573–591.

[14] Lusk, M., and Jou, H. H., 1997, "On the Rule of Additivity in Phase Transformation Kinetics," Metall. Mater. Trans. A, **28A**, pp. 287–291.

[15] Taleb, L., 2002, "Thermal, Metallurgical and Mechanical Interactions in the 16MND5 Steel," *Proc. of 1er Colloque interdisciplinaire sur les materiaux—Materiaux 2002*, October 21–25, Tours, France, pp. 1–5.

[16] Samtech, S. A., 2004, *Samcef/Mecano v10.1 User Manual*, Liege, Belgium.

[17] Betts, W., 2004, personal communication.

[18] Gundlach, R., and Doane, D., 2003, "Alloy Cast Irons," *ASM Metals Handbook*, ASM International, Materials Park, OH, Vol. 1, pp. 85–104.

[19] Laird, G., Gundlach, R., and Rörig, K., 2000, "Heat Treatment of High-Alloy AR Cast Irons," *Abrasion-Resistant Cast Iron Handbook*, American Foundry Society, Schaumburg, IL, Chap. 3.

[20] Stefanescu, D., 1995, "Physical Properties of Cast Iron," *Iron Castings Engineering Handbook*, G. Goodrich and W. Shaw, eds., American Foundry Society, Schaumberg, IL, pp. 223–244, Chap. 8.

[21] Belyakova, P. E., 1975, "Thermophysical Properties of Wear-Resisting Cast Irons," Metallovedenie I Termicheskaya Obrabotka Metallov., **12**, pp. 45–48.

[22] Boyer, H., 1977, *Atlas of Isothermal Transformations and Cooling Transformations Diagrams*, ASM International, Materials Park, OH, pp. II–68.

[23] Wang, D., 2001, "Thermophysical Property Data," Auburn Solidification Design Center, http://metalcasting.auburn.edu/data/data.html

[24] Lynch, C. T., 1975, *CRC Handbook of Materials Science—Vol. 2: Metals, Composites and Refractory Materials*, CRC, Boca Raton, FL.